

IntechOpen

Doppler Radar Observations
Weather Radar, Wind Profiler, Ionospheric
Radar, and Other Advanced Applications

Edited by Joan Bech and Jorge Luis Chau



**DOPPLER RADAR
OBSERVATIONS –
WEATHER RADAR, WIND
PROFILER, IONOSPHERIC
RADAR, AND OTHER
ADVANCED APPLICATIONS**

Edited by **Joan Bech** and **Jorge Luis Chau**

Doppler Radar Observations - Weather Radar, Wind Profiler, Ionospheric Radar, and Other Advanced Applications

<http://dx.doi.org/10.5772/2036>

Edited by Joan Bech and Jorge Luis Chau

Contributors

Franck Donnadieu, Shingo Shimizu, Ernesto Dos Santos Caetano, Baldemar Mendez, Masayuki Yamamoto, Mohammad Hossein Gholizadeh, Hamidreza Amindavar, Joan Bech, Bernat Codina, Jeroni Lorente, Adolfo Magaldi, Pak Wai Chan, Pengfei Zhang, Dusan Zrnic, Olivier Bousquet, Elena Saltikoff, Marco Gabella, Giovanni Perona, Riccardo Notarpietro, Marco Allegretti, Claudio Lucianaz, Oscar Rorato, Silvano Bertoldo, Andrea Prato, Jan Szturc, Katarzyna Ośródk, Anna Jurczyk, Chris G Collier, Erhan Kudeki, Marco Milla, David Hysell, Jorge Luis Chau, Günther Haase, Lars Norin, Clive Pierce, Alan Seed, Sue Ballard, Zhihong Li, David Simonin, Paul Joe

© The Editor(s) and the Author(s) 2012

The moral rights of the and the author(s) have been asserted.

All rights to the book as a whole are reserved by INTECH. The book as a whole (compilation) cannot be reproduced, distributed or used for commercial or non-commercial purposes without INTECH's written permission.

Enquiries concerning the use of the book should be directed to INTECH rights and permissions department (permissions@intechopen.com).

Violations are liable to prosecution under the governing Copyright Law.



Individual chapters of this publication are distributed under the terms of the Creative Commons Attribution 3.0 Unported License which permits commercial use, distribution and reproduction of the individual chapters, provided the original author(s) and source publication are appropriately acknowledged. If so indicated, certain images may not be included under the Creative Commons license. In such cases users will need to obtain permission from the license holder to reproduce the material. More details and guidelines concerning content reuse and adaptation can be found at <http://www.intechopen.com/copyright-policy.html>.

Notice

Statements and opinions expressed in the chapters are those of the individual contributors and not necessarily those of the editors or publisher. No responsibility is accepted for the accuracy of information contained in the published chapters. The publisher assumes no responsibility for any damage or injury to persons or property arising out of the use of any materials, instructions, methods or ideas contained in the book.

First published in Croatia, 2012 by INTECH d.o.o.

eBook (PDF) Published by IN TECH d.o.o.

Place and year of publication of eBook (PDF): Rijeka, 2019.

IntechOpen is the global imprint of IN TECH d.o.o.

Printed in Croatia

Legal deposit, Croatia: National and University Library in Zagreb

Additional hard and PDF copies can be obtained from orders@intechopen.com

Doppler Radar Observations - Weather Radar, Wind Profiler, Ionospheric Radar, and Other Advanced Applications

Edited by Joan Bech and Jorge Luis Chau

p. cm.

ISBN 978-953-51-0496-4

eBook (PDF) ISBN 978-953-51-4995-8

We are IntechOpen, the world's leading publisher of Open Access books Built by scientists, for scientists

3,800+

Open access books available

116,000+

International authors and editors

120M+

Downloads

151

Countries delivered to

Our authors are among the
Top 1%

most cited scientists

12.2%

Contributors from top 500 universities



WEB OF SCIENCE™

Selection of our books indexed in the Book Citation Index
in Web of Science™ Core Collection (BKCI)

Interested in publishing with us?
Contact book.department@intechopen.com

Numbers displayed above are based on latest data collected.
For more information visit www.intechopen.com



Meet the editors



Joan Bech is Associate Professor at the Department of Astronomy and Meteorology, University of Barcelona, Spain where he obtained his Physics degree and PhD. He participated in different research projects dealing with atmospheric physics, environmental quality, and meteorological remote sensing before joining the Meteorological Service of Catalonia where he worked 14 years in charge of remote sensing systems and applications, including a network of 4 C-band Doppler radars and a total lightning detection system. He was national delegate in several EU COST Projects related to weather radar applications and has participated in a number of projects related to anomalous propagation assessment, and in severe weather case studies including hailfalls, microbursts and tornadoes, as well as heavy rainfall events.



Jorge Chau is a Senior Researcher at the Radio Observatorio de Jicamarca, Peru where he has served as Director since 2001. His research has focused on radar studies of the equatorial neutral atmosphere and ionosphere. He is interested in the development of radar techniques to improve the atmospheric/ionospheric measurements as well as to improve the understanding of the atmospheric/ionospheric physics at low latitudes and/or tropospheric/stratospheric altitudes. Topics of ongoing research include the development of radio imaging techniques for 2D and 3D applications, incoherent scatter radar measurements at D and E region altitudes under the equatorial electrojet region, and meteor-head echo studies to determine the sources of the sporadic meteor population as well as other parameters of aeronautical and astronomical importance.

Contents

Preface XIII

**Part 1 Doppler Radar and
Weather Surveillance 1**

Chapter 1 **Doppler Radar for
USA Weather Surveillance 3**
Dusan S. Zrníc

Chapter 2 **Automated Processing of Doppler
Radar Data for Severe Weather Warnings 33**
Paul Joe, Sandy Dance,
Valliappa Lakshmanan, Dirk Heizenreder,
Paul James, Peter Lang,
Thomas Hengstebeck, Yerong Feng,
P.W. Li, Hon-Yin Yeung,
Osamu Suzuki, Keiji Doi and Jianhua Dai

Chapter 3 **Aviation Applications of Doppler
Radars in the Alerting of Windshear and Turbulence 75**
P.W. Chan and Pengfei Zhang

Part 2 Precipitation Estimation and Nowcasting 95

Chapter 4 **Nowcasting 97**
Clive Pierce, Alan Seed,
Sue Ballard, David Simonin and Zhihong Li

Chapter 5 **Use of Radar Precipitation Estimates
in Urban Areas: A Case Study of Mexico City 143**
Ernesto Caetano,
Baldemar Méndez-Antonio and Víctor Magaña

Chapter 6 **Measuring Snow with
Weather Radar 159**
Elena Saltikoff

- Chapter 7 **A Network of Portable, Low-Cost, X-Band Radars** 175
Marco Gabella, Riccardo Notarpietro, Silvano Bertoldo,
Andrea Prato, Claudio Lucianaz, Oscar Rorato,
Marco Allegretti and Giovanni Perona
- Part 3 Tropospheric Wind and Turbulence Observations** 203
- Chapter 8 **Retrieving High Resolution 3-D Wind Vector Fields from Operational Radar Networks** 205
Olivier Bousquet
- Chapter 9 **Multiple Doppler Radar Analysis for Retrieving the Three-Dimensional Wind Field Within Thunderstorms** 231
Shingo Shimizu
- Chapter 10 **New Observations by Wind Profiling Radars** 247
Masayuki K. Yamamoto
- Chapter 11 **Synergy Between Doppler Radar and Lidar for Atmospheric Boundary Layer Research** 271
Chris G. Collier
- Part 4 Weather Radar Quality Control and Related Applications** 287
- Chapter 12 **Quality Control Algorithms Applied on Weather Radar Reflectivity Data** 289
Jan Szturc, Katarzyna Ośródką and Anna Jurczyk
- Chapter 13 **Effects of Anomalous Propagation Conditions on Weather Radar Observations** 307
Joan Bech, Adolfo Magaldi, Bernat Codina and Jeroni Lorente
- Chapter 14 **Doppler Weather Radars and Wind Turbines** 333
Lars Norin and Günther Haase
- Part 5 Advanced Techniques for Probing the Ionosphere** 355
- Chapter 15 **Aperture Synthesis Radar Imaging for Upper Atmospheric Research** 357
D.L. Hysell and J.L. Chau
- Chapter 16 **Incoherent Scatter Radar – Spectral Signal Model and Ionospheric Applications** 377
Erhan Kudeki and Marco Milla

Part 6 Other Advanced Doppler Radar Applications 407

Chapter 17 **Volcanological Applications of
Doppler Radars: A Review and Examples
from a Transportable Pulse Radar in L-Band 409**
Franck Donnadieu

Chapter 18 **Doppler Radar Tracking Using Moments 447**
Mohammad Hossein Gholizadeh and Hamidreza Amindavar

Preface

Over the last decades Doppler radar systems have been instrumental to improve our understanding and monitoring capabilities of phenomena and processes taking place in the low, middle, and upper atmosphere. Weather radars, wind profilers, and incoherent and coherent scatter radars implementing Doppler techniques are now used routinely both in research and operational applications by scientists and practitioners. This book brings together a collection of essays by international leading authors devoted to different applications of ground based Doppler radars. The target audiences are graduate students looking for an introduction to the field or professionals intending to refresh or update their knowledge. The book is organized in eighteen chapters grouped into six different sections.

The first section deals with the use of Doppler radar in weather surveillance and is made up by three chapters. The first one gives a brief introduction to Doppler radar fundamentals and an overview of weather radar surveillance in the USA. The second one offers an updated description of operational processing systems used in severe weather monitoring, and the third chapter is focused on aviation applications of Doppler radars.

The second section, devoted to precipitation estimation and very short range forecasting, or *nowcasting*, has four different chapters. In the first one a description of historical and current development of *nowcasting* techniques is given in detail, while the second chapter describes a specific implementation of rainfall estimates in Mexico. The third chapter includes a description of snowfall estimates and related applications in cold climates, and a fourth chapter details an innovative network of portable radars designed to improve precipitation estimates.

Tropospheric wind and turbulence observations are the topic of the third section. In the first three chapters of this section readers will find several new methodologies developed in Japan and France to retrieve low level wind fields, along with an innovative approach to retrieve wind estimates with wind profilers. The section contains as well a chapter devoted to the complementary use of weather radar and lidar data to probe the atmospheric boundary layer.

The fourth section covers three chapters related to quality control of weather radar data and related topics. The first chapter offers a comprehensive methodology applied

in Poland to control radar data used for quantitative applications, and the second one describes the effects of anomalous propagation conditions on radar observations. Finally a study developed in Sweden examines the effects of wind turbines on weather radars.

The study of the ionosphere by Doppler radars with different techniques is covered in the fifth section, made up of two chapters. The first one covers the incoherent scatter technique, including recent improvements needed when the technique is applied to beams pointing perpendicular to the magnetic field. The second chapter presents advances in imaging aperture synthesis techniques applied to coherent echoes from ionospheric irregularities. Such techniques have been borrowed, improved, and adapted from the radio astronomy community.

The sixth section includes two chapters presenting other advanced techniques of Doppler radars. The first one depicts the use of Doppler radar for volcanological applications, and the second one describes a tracking technique based on the use of moments.

We finally would like to show our gratitude to all the contributing authors of this book for their eagerness and enthusiastic cooperation during the preparation and review of the chapters. We are particularly indebted to Dr Dusan Zrnic (National Severe Storms Laboratory, USA) and Professor David Hysell (Cornell University, USA) for their valuable suggestions and help with some chapter reviews. Last but not least we wish to thank our Intech editorial manager, Ms Marina Jozipovic, for her permanent assistance and professionalism. They all made this book possible and we sincerely hope that the readers will benefit from it.

Joan Bech

Department of Astronomy and Meteorology, University of Barcelona,
Spain

Jorge Chau

The Jicamarca Radio Observatory, Institute of Geophysics of Peru,
Peru

Part 1

Doppler Radar and Weather Surveillance

Doppler Radar for USA Weather Surveillance

Dusan S. Zrnica

*NOAA, National Severe Storms Laboratory
USA*

1. Introduction

Weather radar had its beginnings at the end of World War II when it was noticed that storms clutter radar displays meant to reveal enemy aircraft. Thus radar meteorology was born. Until the sixties only the return power from weather tracers was measured which offered the first glimpses into precipitation structure hidden inside clouds. Possibilities opened up to recognize hail storms, regions of tornadoes (i.e., hook echoes), the melting zone in stratiform precipitation, and even determine precipitation rates at the ground, albeit with considerable uncertainty.

Technology innovations and discoveries made in government laboratories and universities were quickly adopted by the National Weather Service (NWS). Thus in 1957 the Miami Hurricane Forecast Center commissioned the first modern weather radar (WSR-57) the type subsequently installed across the continental United States. The radar operated in the 10 cm band of wavelengths and had beamwidth of about 2°. In 1974 more radars were added: the WSR-74S operating in the band of 10 cm wavelengths and WSR-74C in the 5 cm band.

Development of Doppler radars followed, providing impressive experience to remotely observe internal motions in convective storms and infer precipitation amounts. Thus scientists quickly discovered tell tale signatures of kinematic phenomena (rotation, storm outflows, divergence) in the fields of radial velocities.

After demonstrable successes with this technology the NWS commissioned a network of Doppler radars (WSR-88D=Weather Surveillance Radars, year 1988, Doppler), the last of which was installed in 1997. Much had happened since that time and the current status pertinent to Doppler measurements and future trends are discussed herein.

The nineties saw an accelerated development of information technology so much so that, upon installation of the last radar, computing and signal processing capabilities available to the public were about an order of magnitude superior to the ones on the radar. And scientific advancements were still coming in strong implying great improvements for operations if an upgrade in processing power were to be made. This is precisely what the NWS did by continuing infusion of the new technology into the system. Two significant upgrades have been made. The first involved replacement of the computer with distributed workstations (on the Ethernet in about 2002) for executing algorithms for precipitation estimation, tornado detection, storm tracking, and other. The second upgrade (in 2005)

brought in fully programmable signal processor and replaced the analogue receiver with the digital receiver. In 2009 the NWS started the process of converting the radars to dual polarization which should be accomplished by mid 2013.

The number of radars used continuously for operations is 159 and there are two additional radars for other use. One is for supporting changes in the network brought by infusion of new science or caused by deficiencies in existing components (designated KCRI in Norman, OK). The evolution involves both hardware and software and the update in the former are typically made annually. The other (designated KOUN in Norman, OK, USA) is for research and development. Therefore its configuration is more flexible allowing experimental changes in both hardware and software.

Conference articles and presentation about the WSR-88D and its data abound and there are few descriptions of its basic hardware. Very recent improvements are summarized by Saxion & Ice (2011) and a look into the future is presented in Ice & Saxion (2011). Yet only few journal articles describing the system have been published. The one by Heiss et al. (1990) presents hardware details from the manufacturer's point of view. The paper by Crum et al. (1993) describes data and archiving and the one by Crum & Alberty (1993) contain valuable information about algorithms. The whole No. 2 issue of *Weather and Forecasting* (1998), Vol. 13 is devoted to applications of the WSR-88D with a good part discussing products that use Doppler information. A look at the network with the view into the future is summarized by Serafin & Wilson (2000).

As twenty years since deployment of the last WSR-88D is approaching there are concerns about future upgrades and replacements. High on the list is the Multifunction Phased Array Radar (MPAR). At its core is a phased array antenna wherein beam position and shape are electronically controlled allowing rapid and adaptable scans. Thus, observations of weather (Zrnich et al., 2007) and tracking/detecting aircraft for traffic management and security purposes is proposed (Weber et al., 2007). Another futuristic concept is exemplified in proposed networks for Cooperative Adaptive Sensing of the Atmosphere (CASA) consisting of low power 3 cm wavelength phased array radars (McLaughlin et al., 2009).

Very few books on weather radar have been written and most include Doppler measurements. Here I list some published within the last 20 years. The one by Doviak & Zrnich (2006) primarily concentrates on Doppler aspects and contains information about the WSR-88D. The book by Bringi & Chandrasekar (2001) emphasizes polarization diversity and has sections relevant to Doppler. Role of Doppler radar in aviation weather surveillance is emphasized in the book by Mahapatra (1999). The compendium of chapters written by specialists and edited by Meishner (2004) concentrates on precipitation measurements but has chapters on Doppler principles as well as application to severe weather detection. Radar for meteorologists (Rinehart, 2010) is equally suited for engineers, technicians, and students who will enjoy its easy writing style and informative content.

2. Basic radar

The surveillance range, time, and volumetric coverage are routed in practical considerations of basic radar capabilities and the size and lifetimes of meteorological phenomena the radar is supposed to observe. This is considered next.

2.1 Considerations and requirements for storm surveillance

Table 1 lists the radar parameters with which the surveillance mission is supported. Discussions of the reasons behind choices in volume coverage and other radar attributes of the WSR-88D network, with principal emphasis on Doppler measurements, follows.

Requirement	Values
Surveillance:	
Range	460 km
Time	< 5 min
Volumetric coverage	hemispherical
SNR	> 0 dB, for $Z = -8$ dBZ at $r = 50$ km (exceeded by ~ 5 dB)
Angular resolution	$\leq 1^\circ$
Range sampling interval:	
For reflectivity	$\Delta r \leq 1$ km; $0 < r \leq 230$ km; $\Delta r \leq 2$ km; $r \leq 460$ km
For velocity	$\Delta r = 250$ m
Estimate accuracy:	
Reflectivity	≤ 1 dB; SNR > 10 dB; $\sigma_v = 4$ m s ⁻¹
Velocity	≤ 1 m s ⁻¹ ; SNR > 8 dB; $\sigma_v = 4$ m s ⁻¹
Spectrum width	≤ 1 m s ⁻¹ ; SNR > 10 dB; $\sigma_v = 4$ m s ⁻¹

Table 1. Requirements for weather radar observations.

2.1.1 Range

Surveillance range is limited to about 460 km because storms beyond this range are usually below the horizon. Without beam blockage, the horizon's altitude at 460 km is 12.5 km; thus only the tops of strong convective storms are intercepted. Quantitative measurements of precipitation are required for storms at ranges less than 230 km. Nevertheless, in the region beyond 230 km, storm cells can be identified and their tracks established. Even at the range of about 230 km, the lowest altitude that the radar can observe under normal propagation conditions is about 3 km. Extrapolation of rainfall measurements from this height to the ground is subject to large errors, especially if the beam is above the melting layer and is detecting scatter from snow or melting ice particles.

2.1.2 Time

Surveillance time is determined by the time of growth of hazardous phenomena as well as the need for timely warnings. Five minutes for a repeat time is sufficient for detecting and confirming features with lifetime of about 15 min or more. Typical mesocyclone life time is 90 minutes (Burgess et al., 1982). Ordinary storms last tens of minutes but microbursts from these storms can produce dangerous shear in but a few minutes. Similarly tornadoes can rapidly develop from mesocyclones. For such fast evolving hazards a revisit time of less than a minute is desirable but not achievable if the whole three dimensional volume has to be covered. The principal driver to decrease the surveillance time is prompt detection of the tornadoes so that timely warning of their presence can be issued. Presently, the lead time for tornado warnings (i.e., the time that a warning is issued to the time the tornado does damage) is about 12 minutes (see Section 5).

2.1.3 Volumetric coverage

The volume scan patterns currently available on the WSR-88D have maximum elevations up to 20° and many are accomplished in about 5 minutes. Meteorologists have expressed a desire to extend the coverage to higher elevations to reduce the cone of silence. It is fair to state that the 30° elevation might be a practical upper limit for the WSR-88D. Top elevations higher than 20° have not been justified by strong meteorological reasons.

2.1.4 Signal to noise ratio

The SNR listed in Table 1 provides the specified accuracy of velocity and spectrum width measurements to the range of 230 km for both rain and snowfall rates of about 0.3 mm of liquid water depth per hour. That is, at a range of 230 km the SNR is larger than 10 dB thus the accuracy of Doppler measurements to shorter ranges is independent of noise and solely a function of number of samples and Doppler spectrum width.

2.1.5 Spatial resolution

The angular resolution is principally determined by the need to resolve meteorological phenomena such as tornados and mesocyclones to ranges of about 230 km, and the practical limitations imposed by antenna size at wavelength of 0.1 m. Even though beamwidth of 1° provides relatively high resolution, the spatial resolution at 230 km is 4 km. Because the beam of the WSR-88D is scanning azimuthally, the effective angular resolution in the azimuthal direction is somewhat larger (Doviak & Zrnic, 2006, Section 7.8); typically, about 40% at the 3 RPM scan rates of the WSR-88D. This exceeds many mesocyclone diameters, and thus these important weather phenomena, precursors of many tornadoes, can be missed. Tornadoes have even smaller diameters and therefore can not be resolved at the 230 km range.

The range resolution is indirectly influenced by the angular resolution; there is marginal gain in having range resolution finer than the angular one. For example better range resolution can provide additional shear segments and therefore improve detection of vortices at larger distance. The range resolution for reflectivity is coarser for two reasons: (1) reflectivity is principally used to measure rainfall rates over watersheds which are much larger than mesocyclones and (2) reflectivity samples at a resolution of 250 m are averaged in range (Doviak & Zrnic, 2006, Section 6.3.2) to achieve the required accuracy of 1 dB.

2.1.6 Precision of measurements

The specified 1 dB precision of reflectivity measurements (Table 1) provides about a 15% relative error of stratiform rain rate (Doviak & Zrnic, 2006, eq 8.22a). This has been accepted by the meteorological community. The specified precisions of velocity and spectrum width estimates are those derived from observations of mesocyclones with research radars. The 8 dB SNR is roughly that level beyond which the precision of velocity and spectrum width estimates do not improve significantly (Doviak & Zrnic, 2006, Sections 6.4, 6.5). But, it is possible that lower precisions can be tolerated and benefits can be derived therefrom. For example, it has been proposed (Wood et al., 2001) that velocity estimates be made with less samples (e.g., by a factor of two) in order to improve the azimuthal resolution. Although

this increases the error of the Doppler velocity estimates by the square root of two, the improved angular resolution can increase the range, by about 50% (Brown et al., 2002 and 2005), to which mesocyclones and violent tornadoes can be detected. Therefore in the recently introduced scanning patterns, the data (i.e., spectral moments) are provided at 0.5° increments in azimuth (Section 3.5).

2.2 Radar operation

The essence of the hardware (Fig. 1) is what radar operators see on the console. To the left of the data link (R,V,W,D) is the radar data acquisition (RDA) part consisting of the transmitter, antenna, microwave circuits, receiver, and signal processor. These components are located at radar site and data is transmitted to the local forecast office (LFO) where Radar Product Generation (RPG, Fig. 1) takes place. Operators at the LFO control (the block Control in Fig. 1) the radar and observe/analyze displays of data fields. At a glance of a console they can see the operating status of the radar and data flow. In the RPG the data is transformed into meteorologically meaningful information (Products in Fig. 1) by algorithms executed on Ethernet cluster of workstation.

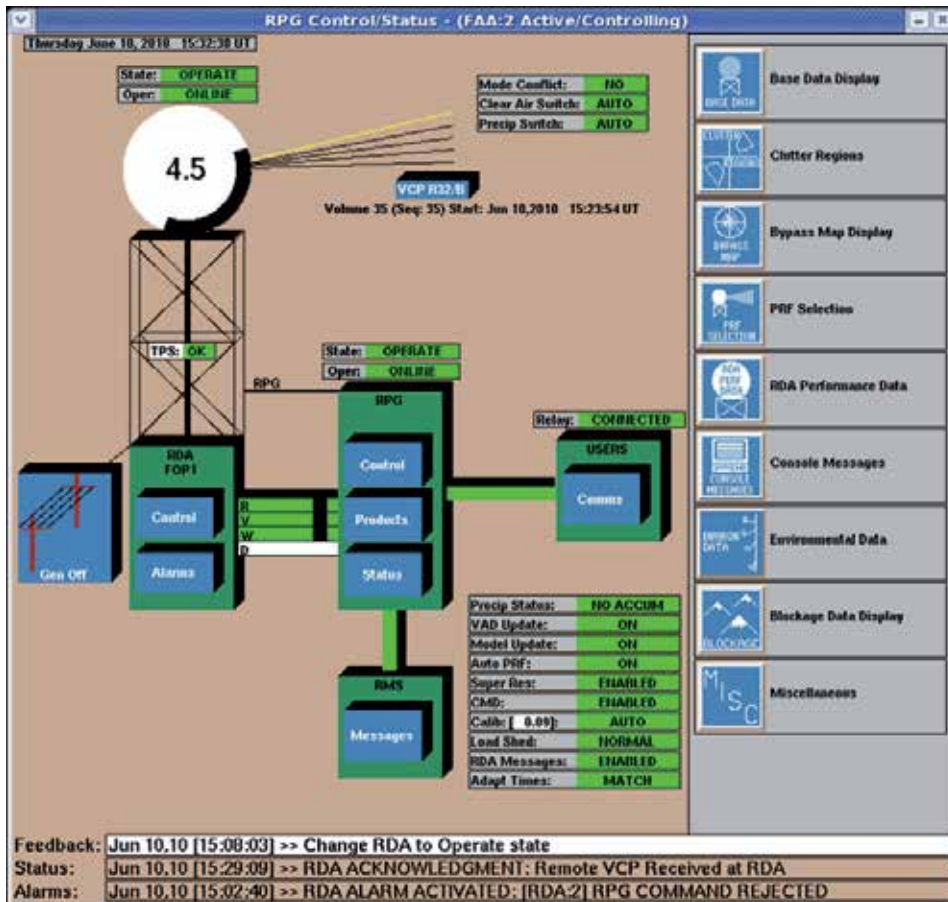


Fig. 1. Block diagram of the WSR-88D seen on the console of operators.

The radar is fully coherent pulsed Doppler and pertinent parameters are listed in Table 2 (see also Doviak & Zrnica, 2006 page 47). Each radar is assigned a fixed frequency in the band (Table 2), hence some values like the beamwidth and unambiguous velocities (not listed) depend on the exact frequency.

Frequency	2.7 to 3 GHz
Beamwidth	1°
Antenna gain	44.5 to 45.5 dB
Transmitter:	
Pulse power	750 kW
Pulse width	1.57 μs and 4.57 μs
Rf duty cycle	0.002
PRFs (Hz, 5 sets of 8, variation ~3%)	322, 446, 644, 857, 1014, 1095, 1181, 1282
Unambiguous range (km)	466, 336, 233, 175, 148, 137, 127, 117
Receiver linear:	
Dynamic range	94 dB at 1.57 μs pulse and 99 dB at 4.57 μs
Intermediate frequency (IF)	57.6 MHz
A/D converter at IF	14 bits
Sampling rate	71.9 MHz
Noise figure	-113 dBm at 1.57 μs and -118 dBm at 4.57 μs
Filter bandwidth or type:	
Front end analogue	6 MHz (3 dB bandwidth)
IF Digital matched, short/long pulse	Output samples spaced at 250 m/500m
Radial spacing in azimuth	1° or 0.5°

Table 2. Radar characteristics.

The data coming out of the RDA consist of housekeeping (time, pointing direction of the antenna, status, operating mode, and fields of reflectivity factor, mean radial velocity, and spread of velocities (designated as R, V, W in the console, Fig. 1), collectively called spectral moments. A wideband communication link is used to exchange base data and radar status/control between RDA and RPG. Depending on distance this link is by direct wire (up to 120 m), microwave line-of-site (to 38 km), or telephone company T1 line (unlimited).

Pulse of high peak power and narrow width (Table 2) generated at the output of the power amplifier is guided to the antenna. It is radiated in form of electromagnetic (EM) field confined within the narrow (1°) antenna beam. The propagating EM field interacts with intervening scatterers (precipitation, biological, and other). Part of the field is reflected forming a continuous stream at the antenna where it is intercepted and transformed for further processing by the receiver. Concise mathematical expression for the magnitude of the electric field at a distance r from the radar is

$$E = \left[\frac{P_a \eta}{\pi} \right]^{1/2} \frac{f(\theta, \phi)}{2r} \cos \left[2\pi f \left(t - \frac{r}{c} \right) + \psi_t \right] U(t - r/c), \quad (1)$$

where P_a is the power radiated by the antenna, r is the distance, $f(\theta, \phi)$ is the antenna pattern function (one way voltage), η is the free space impedance ($120\pi \Omega$), c speed of light, f radar frequency, and ψ_t arbitrary phase at the antenna. $U(t-r/c)$ designates the pulse function such that it is 1 if its argument is between 0 and τ (the pulse width).

2.2.1 Radar signal and Doppler shift

The effective beam cross section and pulse width define the intrinsic radar resolution volume but processing by the receiver increases it in range. Scatterers (hydrometeors such as rain, hail, snow and also insects, birds etc.,) within the resolution volume contribute to the backscattered electric field which upon reception by the antenna is transformed into a microwave signal. The signal is converted to an intermediate frequency f_{if} then passed through anti-alias filter (nominal passband ~ 14 MHz), digitized (as per Table 2), and down converted to audio frequencies (base band) for further processing.

At intermediate frequency the signal coming from a continuum of scatterers can be represented as $A(t)\cos(\omega_{if}t + \omega_d t)$ where the amplitude $A(t)$ fluctuates due to contribution by scatterers and ω_d is the instantaneous Doppler shift caused by their motions toward (positive shift) and/or away (negative shift) from the radar. To determine the mean sense of motion (sign of Doppler shift) the intermediate frequency is removed and the signal is decomposed into its sinusoidal and cosinusoidal components, the inphase I and quadrature phase Q parts. These carry information about the number and sizes of scatterers as well as their motion. Samples of I and Q components are taken at consecutive delays with respect to the transmitted pulse. The delays are proportional to the range within the cloud from which the transmitted pulse is reflected. Samples from the same range locations (delays) are combined to obtain estimates of the spectral moments: reflectivity factor Z , mean Doppler velocity v , and spectrum width σ_v (Doviak & Zrnic, 2006). The Doppler velocity v is related to the frequency shift f_d and wavelength λ via the Doppler equation

$$f_d = 2v/\lambda, \quad (2)$$

and so is the spectrum width.

Radars display (and store) equivalent reflectivity factor (often denoted with Z_e) which is computed from the power and other parameters in the radar equation (Doviak & Zrnic 2006) assuming the scatterers have refractive index of liquid water. For small (compared to wavelength) spherical scatterers, Z_e expressed as function of the distribution of sizes $N(D)$, equals

$$Z_e = \int_0^{D_{\max}} N(D)D^6 dD. \quad (3)$$

2.2.2 Processing path from signals to algorithms

Top left part in Fig 2 illustrates the continuum of returns (either I or Q), after each transmitted pulse from 1,...to M . Thus M samples at a fixed range delay (double vertical line) are operated on in various ways to produce estimates. There are as many estimates

along range time as there are samples. That is, sample spacing is typically equal to pulse duration and therefore consecutive samples are almost independent. Closer sampling (i.e., oversampling) has some advantages (Section 4.2).

Radials of spectral moments are transmitted to the RPG (a radial of velocities is in the top right part of Fig. 2). Spectral moments are displayed at Weather Forecast Offices, are recorded, and are also processed by algorithms to automatically identify hazardous weather features, estimate amounts of precipitation, and to be used in numerical models among other applications. Example displayed in Fig. 2 (right bottom) is the field of Doppler velocities obtained by the WSR-88D in Dove, North Carolina during the Hurricane Irene on Aug 28th, 2011 at 2:29 UTC. The end range on the display is 230 km which is also the range up to which quantitative measurements are currently being made. Extension to 300 km is planned.

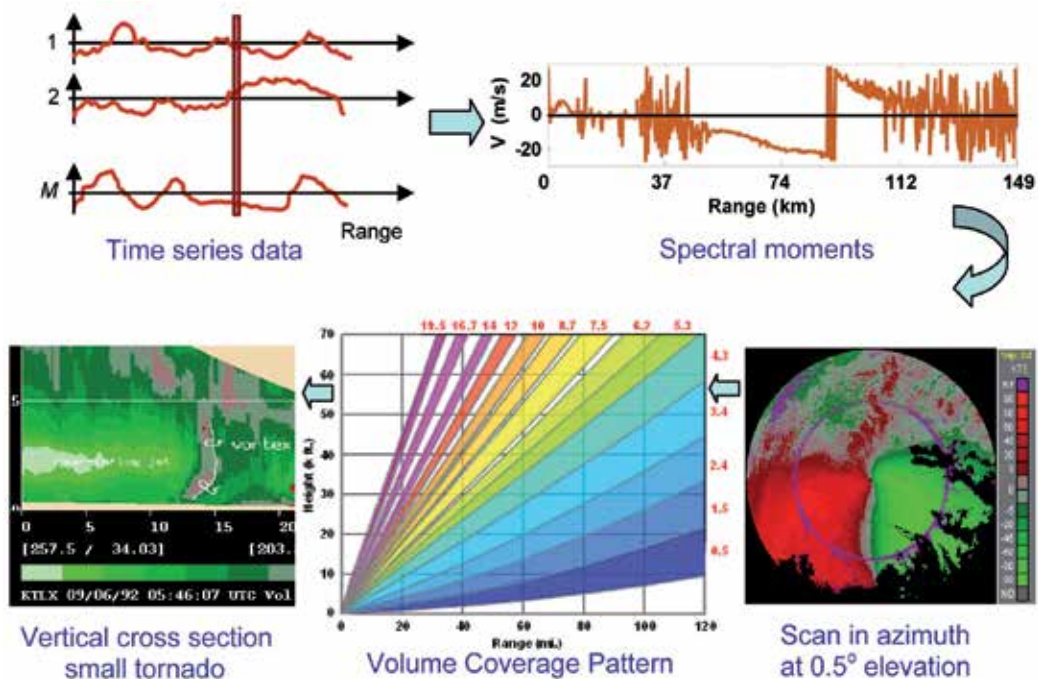


Fig. 2. Information path from time series to output of algorithms.

The radar is sufficiently sensitive to detect precipitation at much larger ranges where the beamwidth and observations high above ground make quantitative interpretation of impending weather on the ground. At the elevation of 0.5°, the radar makes two scans: one with the longest PRT (3.1 ms) for estimating reflectivities unambiguously up to 465 km in range, the other with one of the short PRTs to estimate unambiguously velocity over a sufficiently large span. The ambiguities in range and velocity are inherent to pulsed Doppler radars. Reflections from scatterers spaced by the unambiguous range ($r_a = cT_s/2$ where T_s is pulse repetition time) appear at the same delay with respect to the reference time (determined by the last of two transmitted pulses). Obvious increase in range can be made by increasing T_s . And this is fine for measurements of reflectivity but would harm measurements of velocity. At the 10 cm wavelength Doppler velocities are

estimated from the change in phase of the returned signal (Doviak & Zrnic 2006). Thus the WSR-88D is a phase sampling and measuring instrument. The change in phase of the return from one pulse to the next $2\pi f_d T_s$ is proportional to the Doppler velocity v as indicated in (2).

If the phase change caused by precipitation is outside the $-\pi$ to π interval it cannot be easily distinguished from the change within this interval. These limits define the unambiguous frequency $f_a = \pm 1/(2T_s)$ and through the Doppler relation (2) the unambiguous velocity as

$$v_a = \lambda / (4T_s). \quad (4)$$

Scatterers do cause a Doppler shift within the pulse as it is propagating and reflecting, but this shift is very small and can not be measured reliably as the following argument demonstrates. Consider the $\tau = 1.57 \mu\text{s}$ pulse width (WSR-88D) and scatterers moving at 10 m s^{-1} (36 km h^{-1}). The corresponding Doppler frequency shift is 200 Hz (at 10 cm wavelength) and it produces a phase difference of 0.11° ($2\pi f_d \tau$) between the beginning and end of the pulse return. This tiny difference can not be measured with sufficient accuracy to yield useful estimate.

To mitigate the ambiguity problem the WSR-88D has some options one of which is special phase coding and processing. The result is seen in Fig. 2 where the pink ring at 137 km indicates the unambiguous range for velocity measurements (see discussion in section 3.2.3); it represents censored data because the ground clutter from nearby range and weather signals from the second trip range are comparable in power and can not be reliably separated.

Operators of the WSR-88D have at their disposal preprogrammed volume coverage patterns (VCP – see example in Fig. 2). These are consecutive scans starting from elevation of 0.5° and incrementing until a top elevation is reached. Most algorithms require a full volume scan to generate a product. The one in Fig. 2 (bottom left) reconstructs a vertical profile of Doppler velocities along a radial; the radar is located to the right and green colors indicate velocities toward the radar in 5 m s^{-1} increments starting with 0 (gray color). Cylindrical protrusion below 5 km in the middle with some velocities toward the radar (red color) is indicative of a tornado.

3. Signal processing and display

The block diagram (Fig. 3) of the WSR-88D radar is typical for pulsed Doppler radars. Essential components are the Frequency and Timing generator, the transmitter and the receiver. Radar and antenna controls are omitted from the figure. Intermediate frequency (if) on the radars is 57.6 MHz , and the local oscillator (lo) frequency is adjustable to cover the range between 2.7 and 3 GHz (the operating band, see Table 2). The power amplifier is a klystron. The transmit/receive switch is comprised of a circulator and additional devices to protect the receiver from the transmitted high power pulse. The low noise amplifier (LNA) has a noise figure $\sim 0.8 \text{ dB}$ and the receiver bandwidth is 6 MHz up to the input of the digital receiver. The digital receiver is a proprietary product of SIGMET Co (now Vaisala) and its essence is described next.

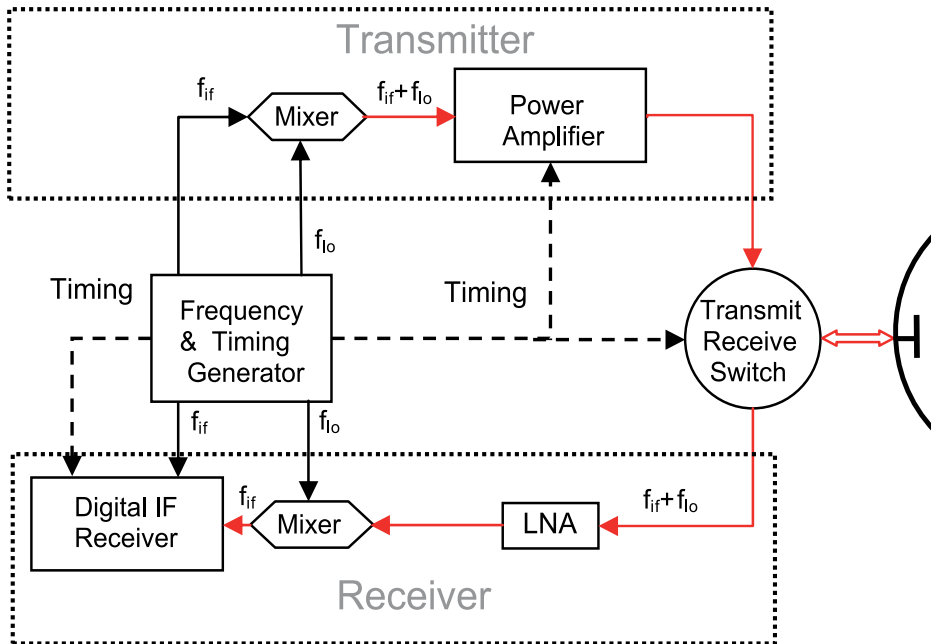


Fig. 3. Block diagram of the receiver (without signal processing part) and the transmitter.

3.1 Digital receiver

The analogue signal $A(t)\cos(\omega_{if}t + \omega_a t)$ is sampled at a rate of 71.9 MHz producing a stream (time t_i) of 14 bit numbers. These are multiplied (Fig. 4) with $\sin(\omega_{if}t_i)$ and $\cos(\omega_{if}t_i)$ and digitally filtered to obtain the base band I and Q components (at times t_k). Although the nominal short pulse duration is $1.57 \mu\text{s}$ same as sample spacing in range, 155 samples spaced at $\sim 13.8 \text{ ns}$ over $2.15 \mu\text{s}$ interval are used for multiplication and filtering (in the long pulse mode the number of samples is 470 over a $6.53 \mu\text{s}$ interval). The digital low pass filter is adjusted to match the shape of the transmitted long or short pulse. Matching is achieved by passing the attenuated transmitted pulse ("burst") through the receiver and taking the discrete Fourier transform of the output. The inverse of this transform gives the coefficients of the matched impulse response filter. Amplitude and phase of the "burst" is sampled upon each transmission to monitor power, compensate for phase instabilities, and use in phase codes for mitigating range ambiguities. The timing diagram (Fig. 5) illustrates the relations between transmitted sequence, digital oscillator samples, the sampled sequence from a point scatterer and its I and Q values (after the matched filter).

3.2 Transmitted sequences and volume scans

Several volume coverage patterns are available. With the exception of one all utilize the short pulse. The exception has a uniform sequence of long pulses at the longest PRT for observations in clear air or snow where weak reflections are from insects, birds, ice and/or refractive index fluctuations. For storm observations the volume coverage patterns have three distinct modes depending on the elevation.

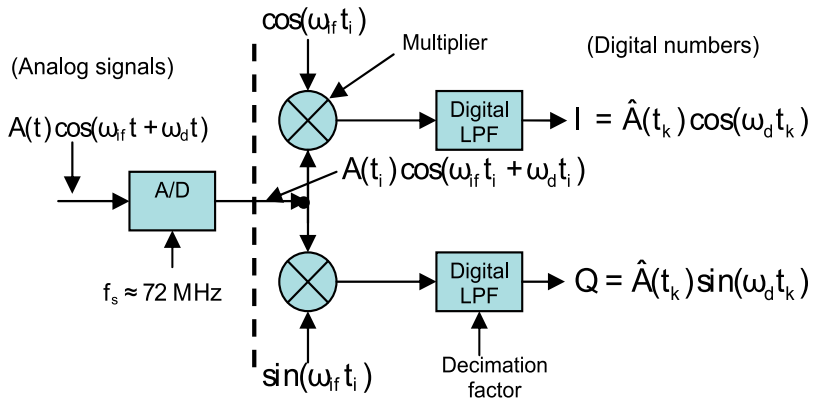


Fig. 4. Conceptual diagram of the digital receiver and down converter indicating the essential operations. The dashed vertical line shows where digital processing begins.

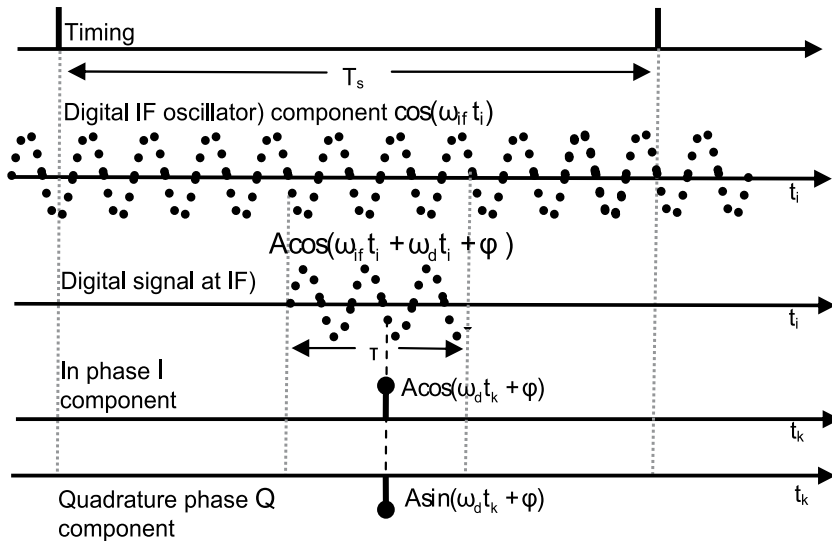


Fig. 5. Conceptual timing diagram of processes in the digital receiver. The return signal is assumed to be sinusoidal pulse such as would be produced by a single point scatterer.

3.2.1 Lowest elevation scans

At the lowest two (sometimes three) elevations ($< 1.6^\circ$) two consecutive scans at each elevation are made. For surveillance and reflectivity measurement the longest PRT is used so that the unambiguous range is $\sim 460 \text{ km}$. It is followed by one or more of the higher PRTs for measurement of Doppler velocity and spectrum width whereby the unambiguous velocity interval is larger than $\sim 20 \text{ m s}^{-1}$. Thus Doppler estimates can be ambiguous and overlaid in range. To determine the location of the Doppler estimates, powers along the radial at the same azimuth but in the surveillance scans are examined. The echoes from ranges spaced by $nPRTc/2$ of the Doppler scan, where n is 1, 2, 3, 4, can be overlaid in the Doppler scan; the echo for $n=1$ is said to come from the first trip because it corresponds to the round trip shorter than the separation between consecutive pulses. Powers from

locations spaced by $nPRTc/2$ are compared to determine the correct range of the Doppler estimates and presence of overlaid echoes. If one of the overlaid powers is larger than user specified threshold (typically 5 dB) the corresponding Doppler spectral moment is assigned to the correct range whereas the values at location of the other overlaid echoes are censored. If the powers are within 5 dB, the variables at all locations where the overlay is possible are censored. Because the Doppler spectral moments are computed and recorded only to the distance of at most twice the unambiguous range the censoring is also done to that distance.

There is a special VCP (Zittel et al., 2008) with three scans at same elevation on five consecutive lowest elevations whereby velocities from three PRFs (No. 4, 6, and 8 in table 2) are combined to increase the v_a and display it up to the distance of 175 km.

3.2.2 Scans at mid and high elevations

At elevations between 1.6° and 7° a “batch” sequence is transmitted. It is a dual PRF in which the first few (3 to 12) pulses are at the lowest PRF and the rest (between about 25 and 90) are transmitted at one of the four highest PRFs (shortest PRTs, Table 2). The lowest PRF pulses are for surveillance, reflectivity measurements, and censoring and assignment of range to Doppler spectral moments; just the same as in the lowest scans. To improve accuracy of the reflectivity estimates powers from the Doppler sequence (high PRF) are included in the averaging provided there is no contamination by overlaid echoes. Beyond 7° elevation uniform PRTs are transmitted because the tops of storms at locations where overlay can occur are below the radar beam.

3.2.3 Phase coding

To mitigate range overlay some volume scanning patterns at the lowest elevations ($<2^\circ$) have transmitted sequences encoded with the SZ(8/64) phase code (Sachidananda & Zrnic, 1999). The concept is depicted in Fig. 6 and explained in the caption. The prescribed phases Ψ_k (i.e., switching phases) are applied to the transmitted pulses. Formally this is represented by multiplication of the sequence with the switching code $a_k = \exp(j\Psi_k)$. The first trip return signal is made coherent by multiplying it with the conjugate $a_k^* = \exp(-j\Psi_k)$. With this multiplication the 2nd trip signal is phase modulated by the code $c_k = a_{k-1}a_k^*$. The 2nd trip can be made coherent by multiplying the incoming sequence with a_{k-1}^* , in which case the 1st trip signal is modulated by the code c_k^* . The code, a_k is designed such that the modulation code c_k has a phase shift given by $\varphi_k = \Psi_{k-1} - \Psi_k = 8\pi k^2 / 64$. The special property of this code is that its autocorrelation is unity for lags in multiples of 8 (lags $8n$; $n=0,1,2,\dots$), and is zero for all other lags. Therefore the power spectrum has only 8 non-zero coefficients separated by $M/8$ coefficients. The SZ(8/64) switching code is given by

$$a_k = \exp[-j \sum_{m=0}^k (\pi m^2 / 8)]; \quad k=0,1,2,\dots,63. \quad (5)$$

It has periodicity of 32 hence the number of samples M must be an integer multiple of 32. From (5) it is obvious that the phase sequence consists of a binary sub multiple of 360° hence it is generated without round-off errors using standard binary phase shifters. Because the

desired phase and actual phase might not be exactly equal, the transmitted phase is sampled and used in processing to precisely cohere the signal from the desired trip.

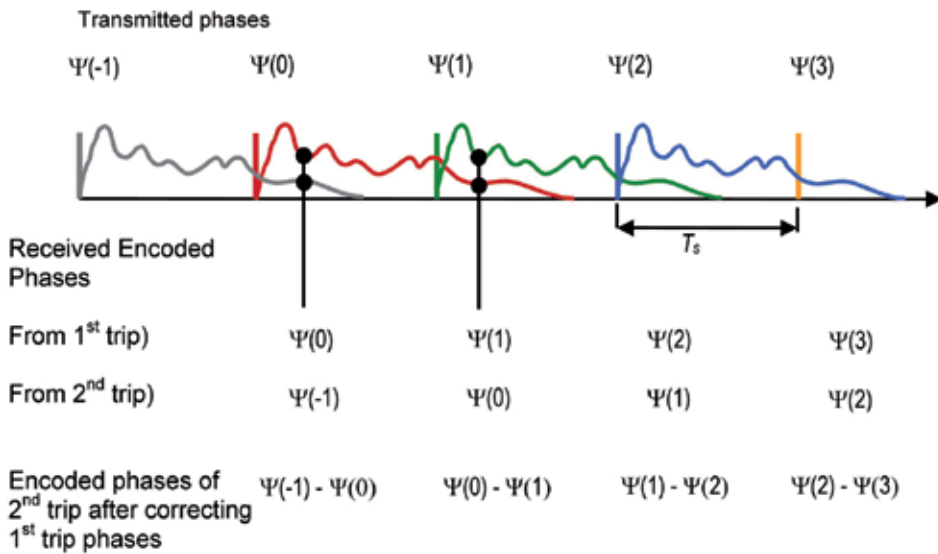


Fig. 6. Transmitted pulse sequence (vertical color lines) and the corresponding received powers (wiggly curves). The phases of the transmitted pulses are indicated and indexed from -1 to 3. The location of overlay at one fixed range is indicated by two black vertical lines. The phases of the received signals from the first and second trip are indicated as well as the phase of the second trip signal after subtracting (correcting) the phase of the first trip.

In case of overlaid echoes the phase coding allows separation of the contributions by the first and second trip signals. This is accomplished by first cohering (correcting) the phases of the stronger echo, then filtering it out. For example if first trip is cohered the second trip signal spectrum (complex with magnitudes and phases) is split into eight replicas over the unambiguous interval. Then frequency domain filtering of the first (strong) trip signal with a notch centered on its spectrum and having a width of $\frac{3}{4}$ unambiguous interval leaves two spectral replicas of the second trip signal spectrum. From these replicas it is possible to reconstruct the second trip spectrum and compute spectral moments. It turns out that cohering for the first trip signal induces 4 spectral replicas in the third trip signal and again eight replicas into the fourth trip signal; the fifth trip signal has two replicas and can not be recovered.

Determination of the ranges where overlaid echoes might be is made using powers from the surveillance scan (long PRT) which precedes the Doppler scan (phase coded short PRT). The overlay trip number and powers are needed to make proper cohering-recohering order and notch filter application. In case ground clutter is present Blackman window is applied to time series data and clutter is taken out with a special frequency domain filter (Sec 3.3). If there is no clutter contamination but overlaid echoes are present the von Hann window is chosen. An example of Doppler velocity fields obtained with the SZ(8/64) phase code is in Fig. 7 (left side). The same field obtained by processing and censoring with no phase coding is also plotted (right side); note the large pink area in the second trip region indicative of non recoverable velocities. Small pink areas in the first trip region (SE of radar) signify that

overlaid powers of first and second trip signals are within 10 dB and hence velocities can not be confidently recovered. There is a narrow pink ring of censored data in the image where phase code is applied. The beginning range of the ring is at the start of the second trip (175 km) and is caused by automatic receiver shut down during transmission followed by the strong first trip ground clutter overwhelming the weaker second trip signal.

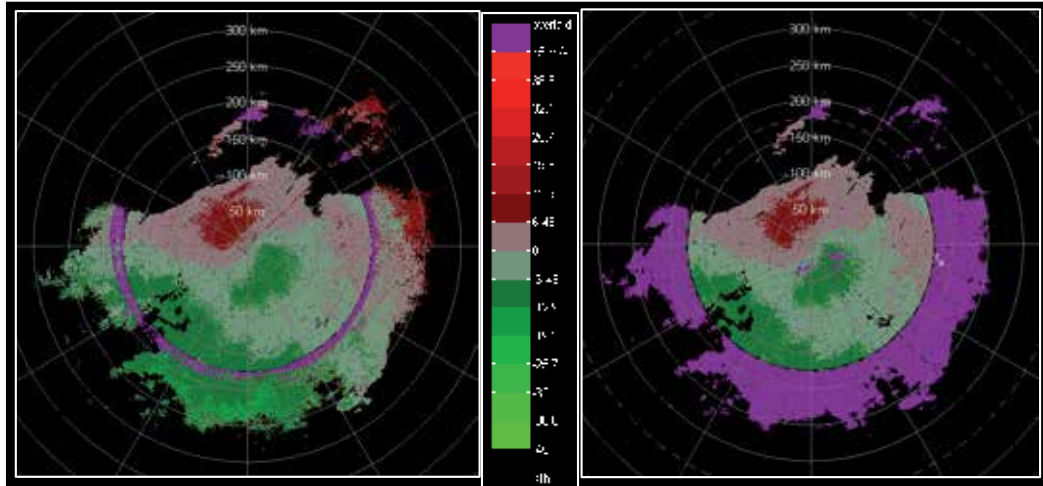


Fig. 7. Fields of Doppler velocities. Left: obtained from phased coded sequence. Right: obtained from non coded sequences. Elevation is 0.5° , the unambiguous velocity $v_a = 23.7 \text{ m s}^{-1}$ and range $r_a = 175 \text{ km}$. Data were collected on 10/08/2002 with the research WSR-88D (KOUN). The color bar indicates velocities in m s^{-1} . (Figure from Torres et al., 2004c).

3.3 Ground clutter filter

The ground clutter filter implemented on the network is a frequency domain filter with interpolation over the removed clutter spectral coefficients. The filter called Gaussian Model Adaptive Processing (GMAP) has been developed by Siggia and Passarelli (2004). Its first premise is: clutter has a Gaussian shape power spectrum with width linearly related to the antenna rotation rate; hence the width can be computed. The second is the signal spectrum has also Gaussian shape and has width larger than clutter's. The Blackman window is applied followed by Fourier transform. Receiver noise is externally provided to the filter and used to establish the spectral noise level which helps determine how many spectral coefficients either side of zero to remove (Fig. 8, blue peak is from ground clutter). The removed coefficients are replaced (iteratively) with a Gaussian curve obtained from Doppler moments and the spectrum of the weather signal (dotted curve) is restored. Then the inverse discrete Fourier transform is performed to obtain the autocorrelation at lag 1. The argument of the autocorrelation is linearly related to the mean Doppler velocity (see section 3.4).

Several options exist to decide where to filter clutter. One relies on the clutter map to locate azimuths and ranges. It is also possible but undesirable to apply clutter filter everywhere. The operators can select regions between azimuths and ranges where to turn the filter on. Recently an adaptive algorithm called Clutter Mitigation Decision has been implemented (Hubbert et al., 2009). It uses coherency of the clutter signal exemplified in what the authors

call Clutter Phase Alignment (CPA) defined as $CPA = |\sum V_k| / \sum |V_k|$, where V_k is the complex voltage ($I + jQ$) from a fixed clutter location at consecutive times (spaced by the PRT) indicated by time index k and the sum is over the total number of pulses in the dwell time. Local standard deviation (termed texture) of reflectivity factor Z_i in range (i index indicates adjacent values in range) and changes in sign of the differences $Z_{i+1} - Z_i$ are also used; the frequency of change in reflectivity gradient along range is obtained from this difference and it defines the spin variable. The CPA, texture, and spin are combined in a fuzzy classification scheme to identify locations where clutter filter should be applied.

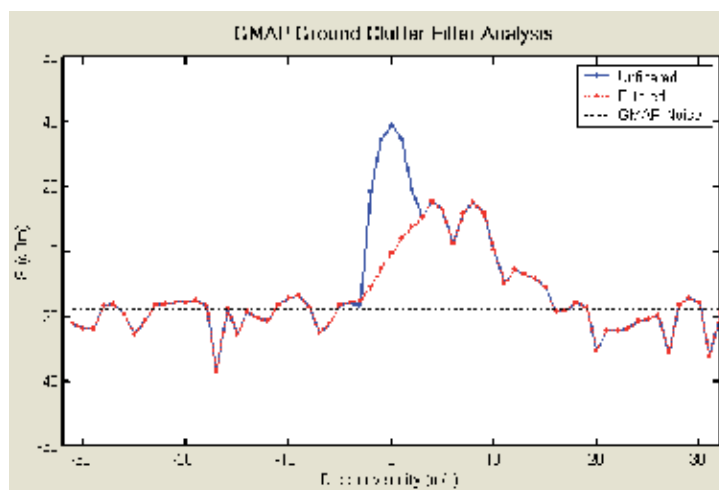


Fig. 8. Doppler spectrum of simulated weather signal (red) and clutter (blue). Interpolated (filtered) Gaussian part and estimated noise level are shown. The $v_a=32 \text{ m s}^{-1}$. (Figure as in Torres et al., 2004c).

The GMAP filter and censoring (Free & Patel, 2007) is applied to surveillance and Doppler scans. In the “batch” mode the number of samples is insufficient for spectral processing hence the average voltage (i.e., DC) from the samples spaced by the long PRT is removed.

The system also employs strong point clutter (typically caused by aircraft) removal along radials. It is done on each spectral moment independently by comparing the sample power with two adjacent values either side of it. If the value is outside prescribed criteria it is replaced by interpolation of neighboring values.

3.4 Computation of spectral moments

In computations of Z and σ_v receiver noise powers are subtracted from the returned powers. Thus, the receiver noise power is estimated at the end of each volume scan at high elevation angle. The noise depends on the elevation angle because contributions from ground radiation and air constituents are larger if the beam is closer to the ground. To account for the increase the noise is extrapolated to lower elevations using empirical relations.

The reflectivity factor is obtained by summing the pulse powers, subtracting the noise power, and using the radar equation (Doviak & Zrnic, 2006). At the lowest few elevations Z is computed from the long PRT (surveillance scan). At mid elevations (“batch mode”) the

reflectivity is computed from both the long and short PRTs if no overlay is indicated; otherwise only samples from the surveillance scan (long PRT) are used.

Computation of Doppler variables starts with the discrete Fourier transform. In absence of clutter, time series data is equally weighted (uniform window) and the power spectrum estimate (at some range location) is

$$\hat{S}(k) = \left| \frac{1}{M} \sum_{m=0}^{M-1} V(m) e^{-j \frac{2\pi mk}{M}} \right|^2, \quad k = 0, 1, \dots, M-1 \quad (6)$$

The discrete inverse Fourier transform applied to (6) produces the value of circular autocorrelation function at lag 1 (i.e., T_s) which contains one erroneous term, namely the product of first and last member of the time series (Torres et al., 2007). This term is subtracted so that the autocorrelation at lag one (i.e., T_s) becomes

$$\hat{R}(1) = \sum_{m=0}^{M-1} \hat{S}(k) e^{j \frac{2\pi k}{M}} - \frac{1}{M} V^*(M-1)V(0), \quad (7)$$

and the mean velocity estimate comes out to be (Doviak & Zrnic, 2006, eq 6.19)

$$\hat{v} = -\left(\frac{\lambda}{4\pi T_s}\right) \arg[\hat{R}(1)]. \quad (8)$$

The spectrum width for most VCPs is estimated by combining the lag one autocorrelation

and the signal power $\hat{P}_s = \sum_{m=0}^{M-1} |V(m)|^2 - P_n$, from which the noise power P_n is subtracted, as follows (Doviak & Zrnic 2006, eq 6.27)

$$\hat{\sigma}_v = \frac{\lambda}{2\sqrt{2}\pi T_s} \left| \ln \left(\frac{\hat{P}_s}{|\hat{R}(1)|} \right) \right|^{1/2}. \quad (9)$$

But, if the logarithm term is negative $\hat{\sigma}_v$ is set to zero. In case of phase coding and presence of overlaid echoes equation (9) is used for the weaker signal in the surveillance scan (long PRT). The spectrum width of the strong signal is computed for the Doppler scan using the ratio $\hat{R}(1)/\hat{R}(2)$ as in Doviak & Zrnic (2006, eq. 6.32), because it is not biased by presence of the weak signal.

3.5 Oversampling in azimuth (overlapping radials)

Until recent upgrades all VCPs had spacing of radials at 1° azimuth and reflectivities were averaged and recorded at 1 km range intervals but velocities retained inherent spacing of 250 m (Table 1). Newly added VCPs employ a strategy whereby at the lowest two elevations time series data from overlapping (in azimuth) beams are processed to produce spectral moments. Thus data obtained over one degree azimuth are weighted with the von Hann

window and so are data from the adjacent azimuth centered 0.5° off from the previous. This produces more radials of data (spaced by 0.5° as opposed to 1°) increasing resolution to facilitate recognition of small phenomena such as tornado vortices (Brown et al., 2002, and 2005). The contrast between the routine and enhanced resolution of a tornado vortex signature is evident in the example in Fig. 9. The reflectivity field (top figures in dBZ as indicated by the color bars) displays a “hook echo” associated with low level circulation. The crisp pattern (top right) is the result of the enhanced resolution.

The velocity field (bottom in Fig. 9) displays three circular features (“balls”) in its center: the lighter green and red adjacent to it in azimuth indicate cyclonic circulation (mesocyclone). Its diameter is about four km and it is estimated from the distance between maximum inbound (green) and outbound (red) velocities. The sharp discontinuity in the center (light green $\sim -30 \text{ m s}^{-1}$ to $> 30 \text{ m s}^{-1}$) is the tornado vortex signature (TVS). The transition between the red “ball” and the green one farther in range marks the zero radial velocity suggesting converging flow (i.e., red and green velocities pushing air toward each other) near ground. Bottom right: same as in the left but the resolution in azimuth is enhanced to 0.5° . The TVS is better defined and so are other small scale features.

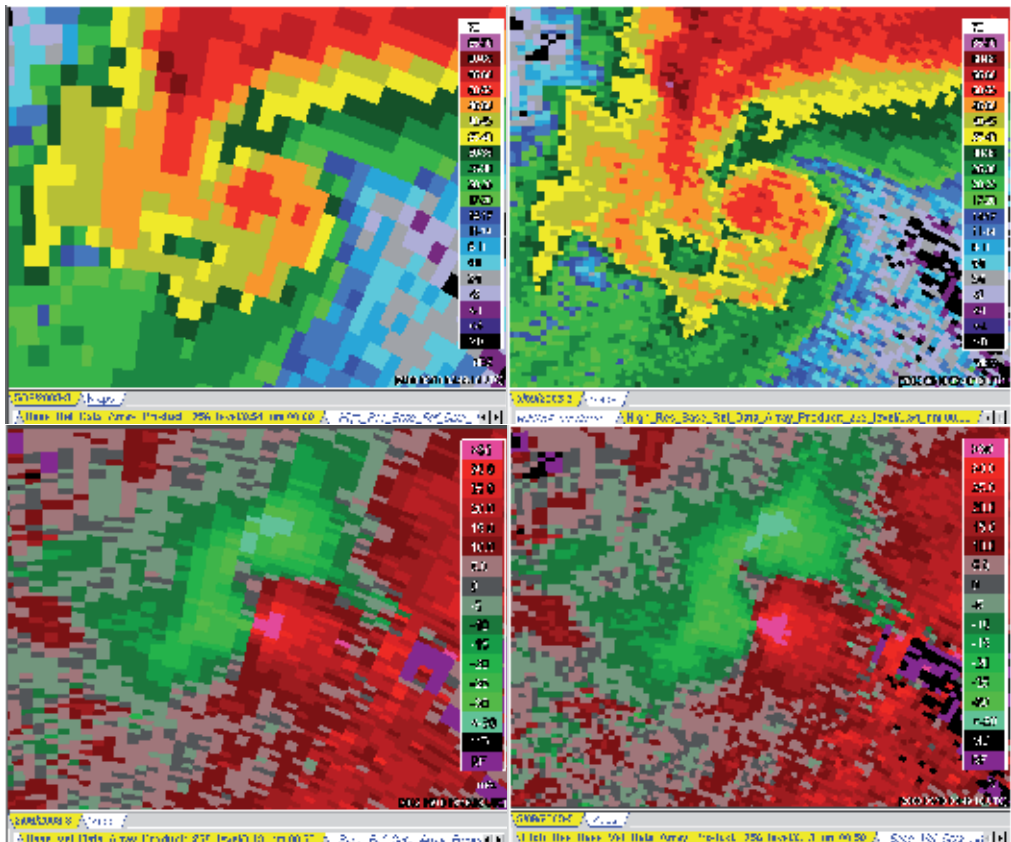


Fig. 9. Top Left: Z, resolution 1 km x 1° . Right: resolution 250 m x 0.5° . Bottom Left: V field, resolution 250 m x 1° . Right: resolution 250 m x 0.5° . X, Y sizes are 25 by 20 km; radar is at x= 4 km and y = -25 km with respect to each image left corner. (Courtesy, S. Torres).

4. Near term enhancements

Currently a significant transformation of the radars is ongoing; it is addition of dual polarization (Zrníc et al., 2008). By mid 2013 all radars on the network should have this capability. Although Doppler capability is not a prerequisite for dual polarization, the coherency of transmit-receive signals within one PRT is for differential phase measurement. Dual polarization offers ample possibilities for application of spectral analysis to polarimetric signals and these are being explored (e.g., to discriminate between insects and birds, Bachman & Zrníc, 2007; to suppress ground clutter, Unal, 2009; or to achieve adaptive clutter and noise suppression, Moisseev & Chandrasekar, 2009).

Three improvements approved for soon inclusion on the network are pending. These are staggered PRT, processing of range oversampled signals, and adaptive recognition and filtering of ground clutter. Brief description follows.

4.1 Staggered PRT

It is planned for mitigating range velocity ambiguities at mid elevation angles with possible use at the lower elevations. The scheme consists of alternating interval between transmitted pulses (Fig. 10) and estimating arguments of two autocorrelations at the two lags, $\arg[R(T_1)]$ and $\arg[R(T_2)]$. The velocities estimated from these arguments have a different unambiguous interval (each inversely proportional to the corresponding separation T_i , $i=1$ or 2) as can be deduced from eq. (8). Therefore the difference of the velocities uniquely tags the proper unambiguous interval for either PRT so that correct dealiasing can be achieved (Torres et al., 2004a) up to larger v_a than possible with only one of these PRTs. For the example in Fig. 10, $v_a = 3v_{a2} = 2v_{a1}$. Consider $T_1=1$ ms $T_2=1.5$ ms which produces $v_a = 50$ m s⁻¹ (unambiguous interval is -50 to 50 m s⁻¹) and unambiguous range of at least 150 km.

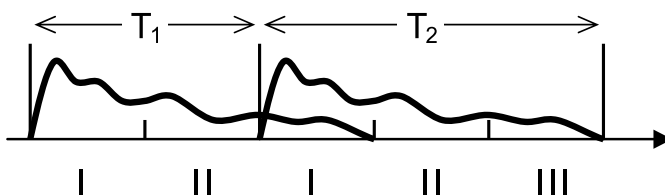


Fig. 10. Staggered PRT. The stagger ratio $T_1/T_2 = 2/3$. The continuous curve depicts the return from precipitation extending up to $cT_2/2$ but not further (from Torres et al., 2009 and adapted from Sachidananda & Zrníc, 2003).

Power estimates in range sections I, II, and III (Fig.10) are computed separately for the short PRT and the long PRT to check if data censoring is needed. Comparison of powers in the two PRT intervals indicates if there is overlay and how severe it is so that appropriate censoring can be applied. In Fig. 11 contrasted are two fields of velocities obtained with two radars (spaced about 20 km apart). The left field comes from the operational WSR-88D in Oklahoma City and was obtained with the “batch mode” and parameters as indicated. On the right is the same storm complex but obtained with staggered PRT on the research WSR-88D radar in Norman OK some 20 km SSW from Oklahoma City. Highlighted in yellow circles are regions where significant aliasing occurs on the operational radar (exemplified by abrupt discontinuities in the field, change from red to green) but are absent in the field from

the research radar. Also, the large pink area of overlaid echoes has almost disappeared in the measurement made utilizing the staggered PRT. The small circle closest to the radar origin indicates overlaid echo contaminating the first trip velocities of the operational radar.

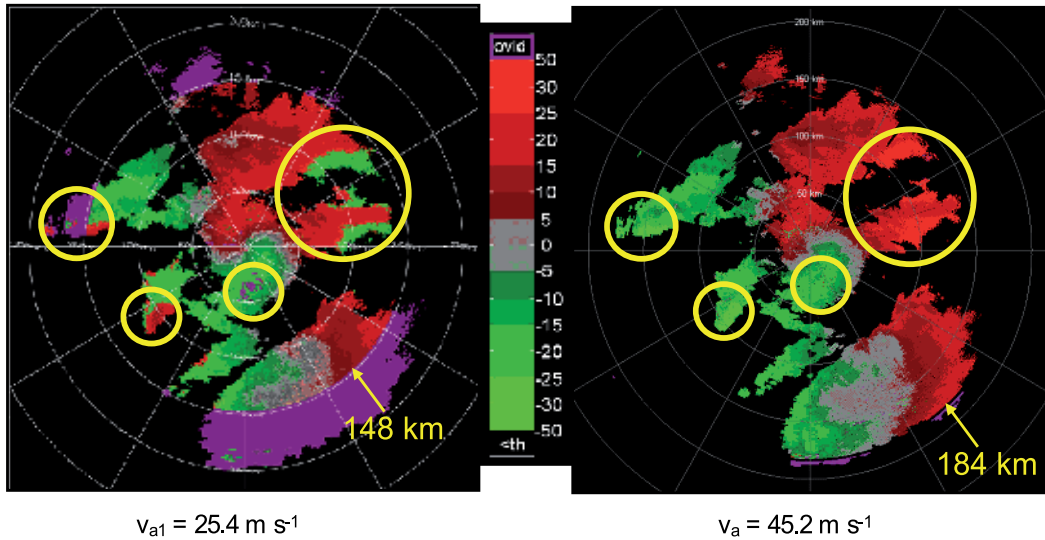


Fig. 11. Velocity fields of a storm system. Left: field obtained with the operational WSR-88D radar in Oklahoma City on April 06, 2003, elevation 2.5 deg, batch mode with unambiguous range of 148 km and velocity of 25.4 m s⁻¹. Pink regions locate censored velocities which can not be reliably recovered due to overlaid first and second trip echoes. Right: same as on the left but obtained with the research WSR-88D (KOUN) utilizing staggered PRT. This radar is about 20 km south from the operational radar. The color bar indicates velocities (m s⁻¹), red away from and green toward the radar. (Figure adapted from Torres et al., 2003).

4.2 Oversampling techniques

Oversampling here indicates spacing of I, Q samples smaller than the pulse duration. Operations on few of these range consecutive "oversamples" can reduce error in estimates and/or data acquisition time (Torres & Zrnica, 2003). Simplest of operations is averaging in range of oversampled spectral moments. Somewhat more involved is the whitening transformation in which the signal vector $\mathbf{v} = [V(m,0), V(m,1), \dots, V(m,l), \dots, V(m,L)]$ consisting of L oversampled correlated complex voltages is transformed into a set of L orthogonal voltages (Torres & Zrnica, 2003). The time index m refers to the usual sample time and l to the oversampled range time. The transformation takes the form $\mathbf{x} = \mathbf{H}^{-1} \mathbf{v}$ with \mathbf{H} related to the normalized correlation matrix \mathbf{C} of \mathbf{v} via $\mathbf{C} = \mathbf{H}^* \mathbf{H}^T$. The correlation matrix can be pre-computed (or measured e.g., Ivic et al., 2003) because it depends solely on the envelope of the transmitted pulse and the baseband equivalent receiver filter shape for a uniform Z . The L transformed samples are independent and averaging of spectral moments obtained from each (in absence of noise) yields smaller error of estimates. Whitening is effective at large SNRs but fails otherwise. To achieve L independent samples the receiver filter bandwidth needs to be increased L times over the matched filter bandwidth and this enhances the noise by the same factor. In addition the whitening transformation also increases the noise hence

the net SNR reduction is proportional to L^2 . Practical L is about 3 to 6, so the decrease is not catastrophic considering that weather SNRs are mostly larger than 20 dB. Another issue concerning whitening is the shape of the range weighting function compared to the matched filter. The two weighting functions have the same range extent but the one from whitening has rectangular shape smearing slightly its range resolution.

Increasing the number of independent samples when it is advantageous and gradually reverting to the matched filter has also been proposed (Torres et al. 2004b) and implemented (Curtis & Torres, 2011) on the National Weather Radar Testbed (NWRT), a phased array radar antenna powered by a WSR-88D transmitter (Zrnic et al., 2007). The processing is called adaptive pseudowhitening. It requires initial estimates of SNR and spectrum width.

Vivid example contrasting adaptive pseudowhitening to standard processing illustrates the much smoother fields obtained with the former (see Fig.12, and caption). The gradient of Doppler velocities (indicated with an arrow) is at the interface of the storms outflow and the environmental flow. This type of discontinuity is the key feature detected by algorithms for locating gust fronts and quantifying wind shear across the boundary; such information is extremely useful for air traffic management and safety at airports.

In contrast to whitening techniques pulse compression does not degrade the SNR (Doviak and Zrnic, 2006) but is not considered due to excessive bandwidth and current hardware constraints. A very simple alternative to speed volume coverage at lowest elevations (where tornadoes are observed) is a VCP with adaptive top elevation angle based on radar measurements (Chrisman et al., 2009). It will soon be added to the VCPs on the network.

4.3 Clutter detection and filtering

A novel way to recognize and filter ground clutter is planned. Its acronym CLEAN-AP stands for clutter environment analysis using adaptive processing (Warde & Torres, 2009). The essence of the technique is spectral analysis (decomposition) of the autocorrelation at lag 1 and use of its phase at and near zero Doppler shift. The conventional estimate

$$\hat{R}_b(1) = \frac{1}{M^2} \sum_0^{M-1} |Z(k)|^2 e^{j2\pi k/M}, \quad (10)$$

where $Z(k)$ is the discrete Fourier transform of the returned signal, is biased (indicated by subscript b) and can be unbiased as in (7). Another way to avoid the bias is by computing two Fourier transform as proposed by (Warde & Torres 2009). One, $Z_0(k)$ is the complex spectrum of $d(m)V(m)$, $d(m)$ =window function, and the other $Z_1(k)$ is the spectrum of $d(m)V(m+1)$ from the sequence shifted in time by one unit (T_s). Then the unbiased estimate is

$$\hat{R}(1) = \sum_{k=0}^{M-1} Z_0^*(k)Z_1(k) / M^2. \quad (11)$$

Individual terms $S_1(k) = Z_0^*(k)Z_1(k)$ constitute the spectral density (over Doppler index k) of the lag 1 autocorrelation function. Thus the autocorrelation spectral density is estimated in CLEAN-AP from the cross spectrum.

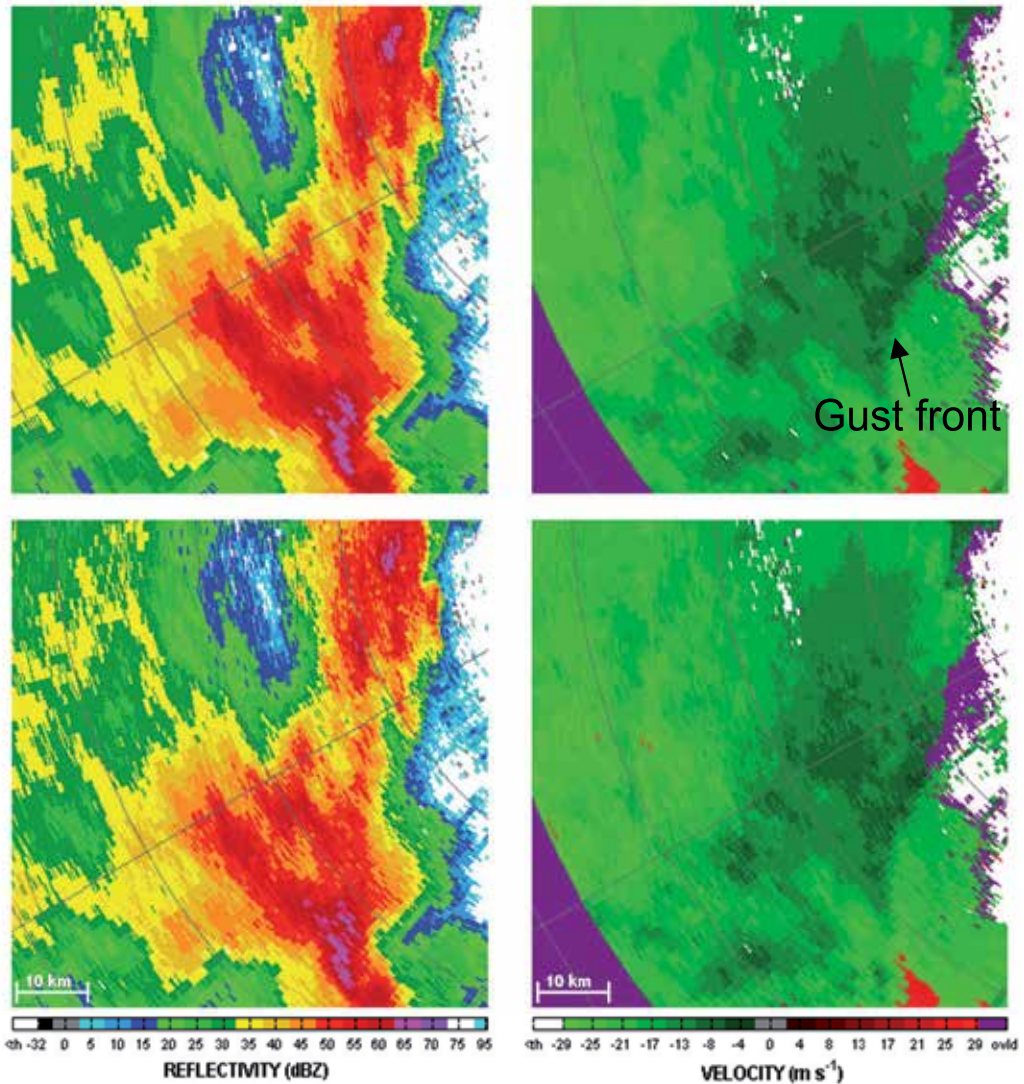


Fig. 12. Fields of reflectivity and velocity from a severe storm obtained on 2 Apr 2010 10:54 UTC, with the phased array radar (NWRT) in Norman, OK. Top two panels resulted for pseudowhitening applied to $L = 4$ samples of time series data; the number of samples M per radial was 12 for Z and 26 for v . Data in the lower panels have been obtained by processing as on the WSR-88D (16 for Z and 64 for v). The curved discontinuity in the velocity field delineates outflow boundary (gust front) generated by this storm. The peak reflectivity values of ~ 65 dBZ are likely caused by hail. (Adapted from Curtis & Torres, 2011).

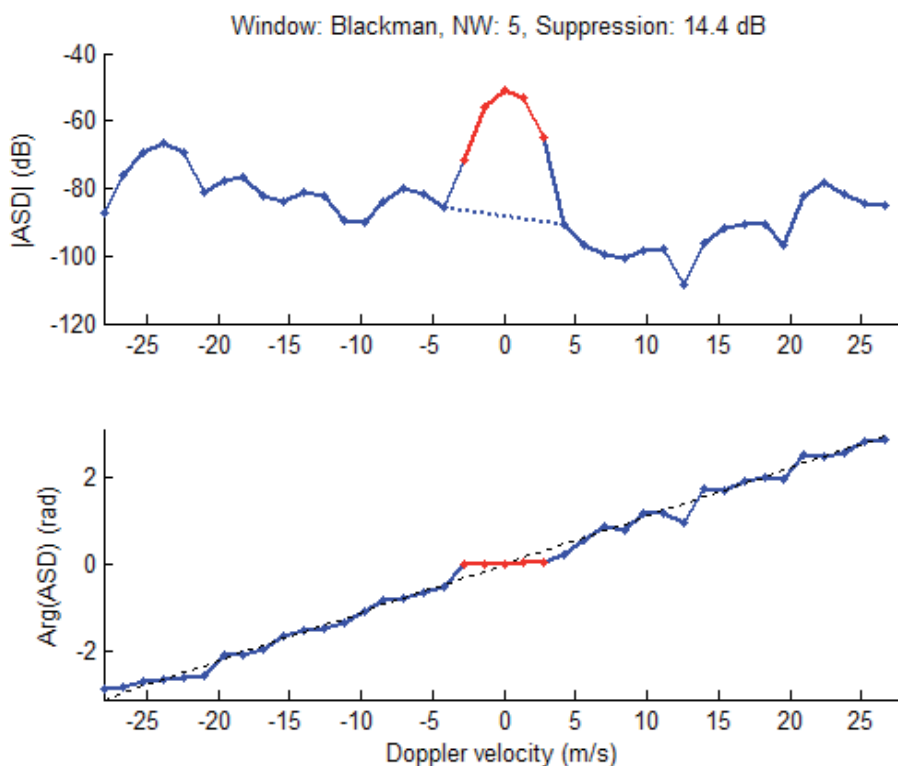


Fig. 13. Autocorrelation spectral density (ASD) of a radar return, top: magnitude and bottom: phase. Clutter is well defined with its peak at zero and flat phase (red). Based on this phase five coefficients are replaced with interpolated values resulting in 14.4 dB of suppression (defined as the ratio of total S+C power to remaining power). Interpolated powers are indicated by the dotted line; dash line represents linear phase; $v_a = 27 \text{ m s}^{-1}$. Data obtained with the phased array radar (NWRT). (Figure courtesy of Sebastian Torres).

The choice of window function $d(m)$ is very important because its sidelobes limit the amount of power that can be filtered. The clutter power is computed from the sum of $V(m)$ to obtain the clutter to noise ratio (CNR). Then the CNR is compared with the peak to first sidelobe level (PS_w) ratio of four windows (w =rectangular, von Hann, Blackman, and Blackman-Nuttall) and the window whose PS_w exceeds the CNR by the smallest amount is chosen. That way the leakage of the clutter signal away from zero will be below the noise level, while the notch width will be smaller than the one for the other windows satisfying the condition $PS_w > \text{CNR}$.

Data windows spread the phase of clutter's $S_1(k)$ either side of zero ($k=0$) Doppler (Fig. 13). Recognition of the flat phase identifies clutter's presence. Doppler index at which the phase begins to depart from zero (according to a set of criteria) defines the clutter filter width. In the mean the autocorrelation spectral density of noise has linear phase as seen in Fig.13 but semi coherent signals have flattened phases in the vicinity of their mean Doppler shifts. Panels in Fig. 14 demonstrate qualitatively performance of this clutter mitigation technique and the caption highlights results.

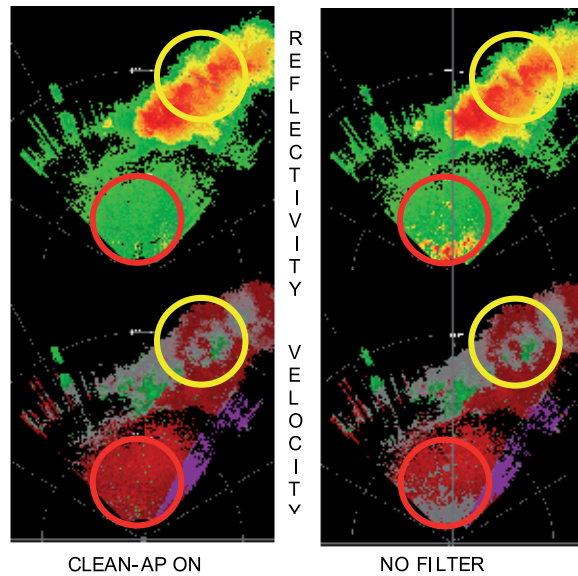


Fig. 14. Fields of reflectivities (top) and velocities (bottom) with no filter (right) and after application of the CLEAN-AP. Close to the radar the strong reflectivities in the top right panel encircled in red (red indicates > 50 dBZ) are caused by ground clutter which also biases the velocities toward zero (lower right panel). CLEAN-AP eliminates most of the clutter in both fields (left panels). To the NE within the yellow circle there are areas of near zero velocities (lower panels gray areas are velocities within ± 5 m s $^{-1}$). These appear unaffected by the filter. The data were collected with the agile beam phased array radar (NWRT) in Norman, OK. (Figure adapted from Warde & Torres, 2009).

4.4 Hybrid spectrum width estimator

The spectrum width estimator (9) is deficient at narrow widths where significant bias occurs. This shortcoming will be overcome with the Hybrid estimator which chooses an appropriate equation depending on a rough initial estimate of σ_v (Meymaris et al., 2009). Initial estimate of the spectrum width is made using the estimators (9), $\hat{R}(1) / \hat{R}(2)$ as in (Doviak & Zrnic, 2006 eq. 6.32) and an estimator based on $\hat{R}(1)$, $\hat{R}(2)$, and $\hat{R}(3)$. Criteria applied to the results produce three categories of widths, large, medium, and small. Then (9) is used as estimate for the large category, $\hat{R}(1) / \hat{R}(2)$ for the medium and $\hat{R}(1) / \hat{R}(3)$ for the small.

5. Observations of phenomena

Mesocyclone refers to a rotational part of storm with the diameter of maximum wind typically between 3 and 10 km. It is depicted with a couplet of Doppler velocity features (see Fig. 9). Storms having mesocyclones can produce devastating tornadoes (Fig. 9 exhibits a tornado vortex signature associated with the mesocyclone), strong winds, and hail. Thus, much effort has been devoted to detecting and quantifying these phenomena (No. 2 issue of *Weather and Forecasting*, 1998). One of the motivating reasons for installing Doppler radars

in the USA was the potential to detect mesocyclones and tornadoes. The investment in this technology paid off as demonstrated by the graph in Fig. 15. Trend of improvement is seen on all three performance indicators with the steepest rise in the years the Doppler radar network (NEXRAD) was being installed. This is logical: as the new tool was spreading across the country more forecasters were beginning to use it. Improvement continues few years past the completion of the network likely because it took time to train all forecasters and gain experience with the Doppler radar. The data indicates a plateau from about 2002 until present suggesting maturity of the technology with little room left for significant advancements. Further progress might come from combining radar data with short term numerical weather prediction models and/or introduction of rapidly scanning agile beam phase array radars (Zrnice et al., 2007 and Weber et al., 2007).

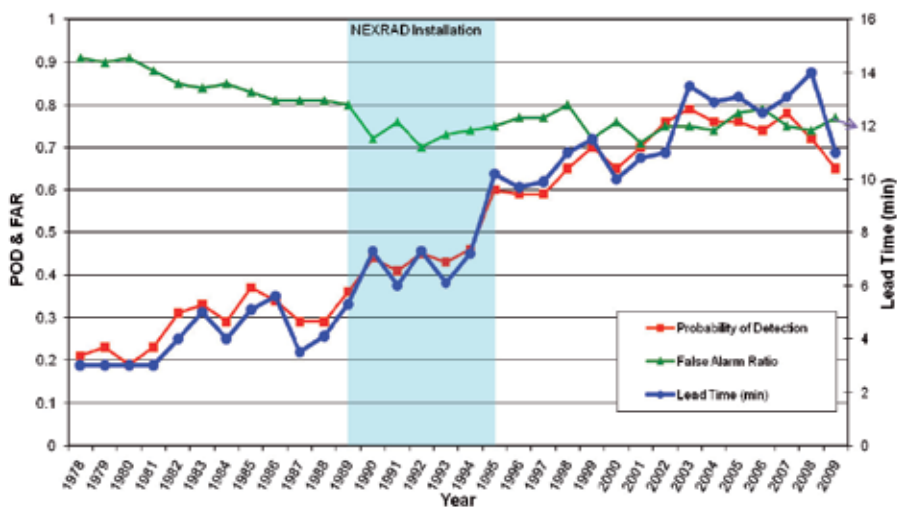


Fig. 15. Probability of detection, false alarms and lead time in tornado warnings issued by the National Weather Service as function of year. (Figure courtesy Don Burgess).

Doppler velocities are potent indicators of diverging (converging) flows such as observed in strong outflows from collapsing storms. These “microbursts” have been implicated in several aircraft accidents motivating deployment of terminal Doppler weather radars (TDWR) at forty seven airports in the USA (Mahapatra, 1999, sec 7.4). Vertical profiles of reflectivity and Doppler velocity in Fig. 16 indicate a pulsing microburst; the intense reflectivity core (red below 5 kft) near ground is the first precipitation shaft and the elongated portion above is the following shaft. On the velocity display the yellow arrows indicate direction of motion. Clear divergence near ground and at the top of the storm (in the anvil) is visible and so is the convergence over the deep mid storm layer (5 to 14 kft). The horizontal change in wind speed near ground of ~ 20 kts at this stage is not strong to pose treat to aviation (35 kts is considered significant for light aircraft).

An atmospheric undular bore (Fig. 17) was observed with the WSR-88D near Oklahoma City. This phenomena is a propagating step disturbance in air properties (temperature, pressure, velocity) followed by oscillation. Spaced by about 10 km the waves propagate in a surface-based stable layer. The layer came from storm outflow and the bore might have been

generated by subsequent storm. From the vertical cross section of the velocities it is evident that the positive velocity perturbation (toward the radar) ends at about 4000 ft, above which the ambient flow (green color) resumes. The velocities measured by the radar can quantify the structure of the perturbation, tell the thickness and wavelength. Propagation speed can be estimated by tracking the wave position in space and time.

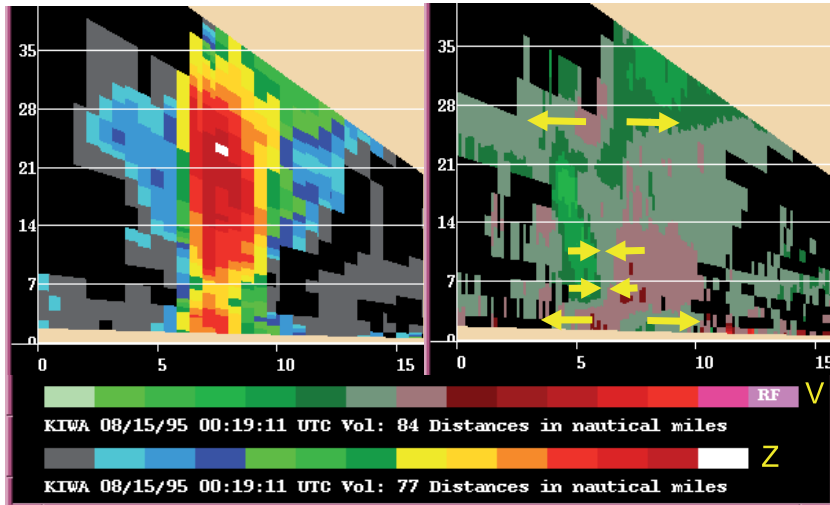


Fig. 16. Vertical cross sections of reflectivity field (left) and Doppler velocity field through a microburst reconstructed from conical scans (up to 19.5° elevation) of the WSR-88D radar in Phoenix Az on Aug 15, 1995. Height is in kft and distances are in nautical miles. The radar is located to the right of each cross section (at about 26 nautical miles). The top color bar depicts velocity categories in non linear increments with red away from the radar: light red = 0-5 kts, dark red 5 to 10, next 10-20; green indicates toward the radar in categories symmetric to red. The bottom bar refers to reflectivities starting at 0 dBZ in steps of 5 dBZ (white category indicates values larger than 65 dBZ).

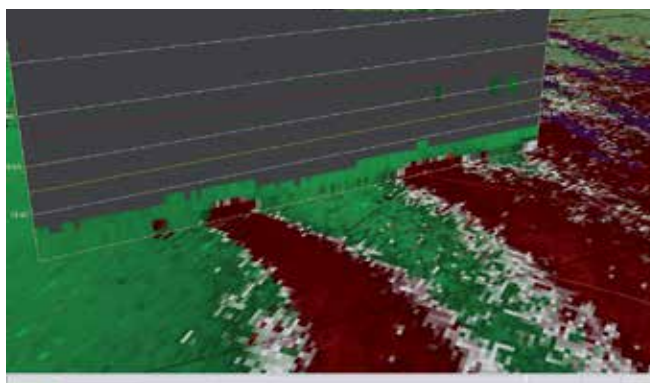


Fig. 17. Doppler velocities at 0.5° elevation and superposed vertical cross sections of the velocities obtained with Oklahoma City radar on Aug 10, 2011. Red color indicates motion away and green toward the radar located ESE of the bottom right corner. Height lines are in kft above ground level.

Doppler radar is valued for measuring winds in hurricanes and detecting tornadoes that can be imbedded in the bands. Combined with polarimetric capability, its utility greatly increases because of improved quantitative measurement of rainfall. Observation of hurricane Irene which swept the US East coast at the end of August 2011 is the case in point. Rotation speed of over 110 km h^{-1} is apparent in Fig. 18 where the color categories are too coarse to estimate the maximum values. The cyan color captures well Irene's rotational winds because they are aligned with radials. Color categories are coarse precluding precise estimation of velocities but recorded values are quantized to 0.5 m s^{-1} . Although the unambiguous velocity is $\sim 28 \text{ m s}^{-1}$ values more negative than -30 m s^{-1} are displayed. These and other outside the unambiguous interval have been correctly dealiased by imposing spatial continuity to the field.

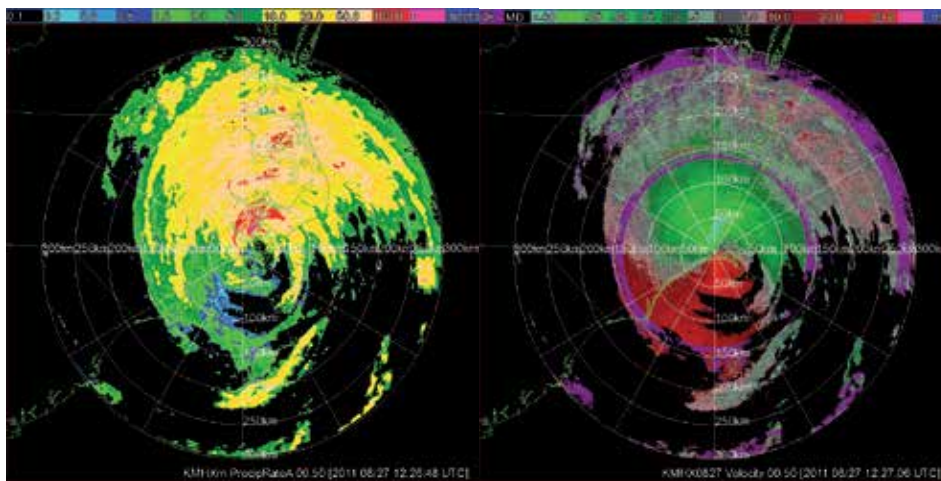


Fig. 18. Left: Rain rate in Hurricane Irene, obtained with a polarimetric algorithm using differential phase and reflectivity factor (surveillance scan with unambiguous range of $\sim 465 \text{ km}$). Right: Velocity field obtained with the SZ(2) phase code (Doppler scan with unambiguous range of $\sim 135 \text{ km}$ and velocity $\sim 28 \text{ m s}^{-1}$). Elevation is 0.5° , time 12:26 UTC, on Aug 27, 2011. The range circles are spaced 50 km apart. Color categories for rain rate are in mm h^{-1} and for velocity in m s^{-1} . (Figure courtesy of Pengfei Zhang).

The rain rate field depicts Irene's bands some containing values larger than 100 mm h^{-1} . These are instantaneous measurements and over time accumulations caused significant flooding which brought 43 deaths and ~ 20 billion \$ damage to the NE coast of the USA. The obviously large spatial extent of Irene amply justifies use of surveillance scan for maximum storm coverage and Doppler scan for wind hazard detection.

Atmospheric biota is routinely observed with the WSR-88D network (Rinehart, 2010). Examples are insects, birds, and bats. Many insects are passive wind tracers providing a way to estimate winds in the planetary boundary layer (extending up to 2 km above ground).

Biota can be tracked for ecological or other purposes. The radar can also provide location of bird migrating paths, roosts, and other congregating places; this could be important for aircraft safety. The three donut shaped features in Fig. 19 represent Doppler speeds of birds

leaving roost early in the morning. The critters are diverging away from the roost in search of food. Close to the radar the continuous field of velocities is principally from reflections off insects filling a good part of the boundary layer (this is deduced from polarimetric signatures, but not shown here).

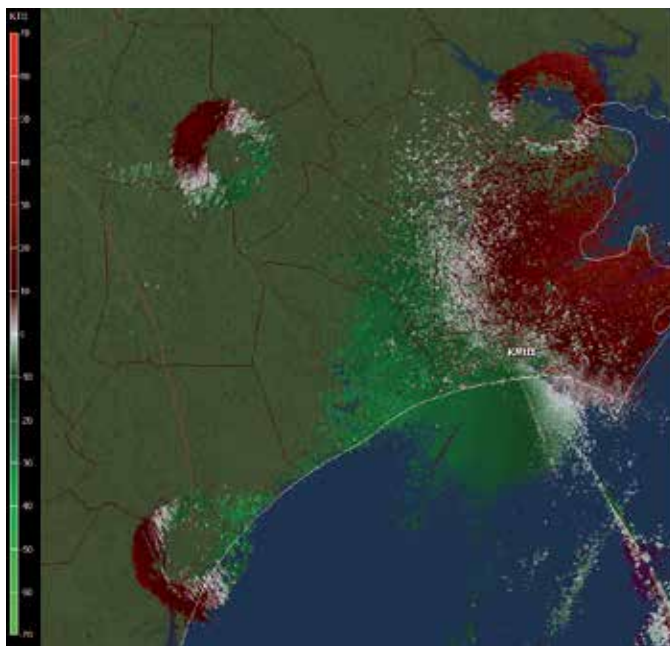


Fig. 19. Field of velocities obtained from the radar at Moorhead City, NC, on July 27, 2011 at 5:08 in the morning. The color bar indicates categories in kts; red away from the radar and green is toward. Elevation is 0.5°.

6. Epilogue

The WSR-88D network has been indispensable for issuing warnings of precipitation and wind related hazards in the USA. And its real time display of storm locations has become one of most popular and common applications on cellular phones. Its role in quantitative precipitation estimation is matching that of rain gages. So, what is beyond these achievements for the WSR-88D? Dual polarization upgrade combined with Doppler capability is the panacea a radar with the dish antenna on a rotating pedestal can achieve. Promising possibilities are: polarimetric confirmation of tornado touchdown at places where Doppler velocities indicate rotation; improvement of ground clutter filtering; polarimetric spectral analysis for extracting/separating features within radar resolution volume; significant improvement in data interpretation; inclusion of wind and precipitation type/amount in numerical prediction models; and other. Clearly the evolutionary trend continues and will do so at a decelerating pace until a plateau is reached. Complementary shorter wavelength (3 cm and 5 cm) surveillance radars are being considered for closing gaps or providing extra coverage at opportune places. (The TDWRs 5 cm wavelength radar data has been supplied to the NWS for several years). Explored are networks of tightly coordinated 3 cm wavelength radars for surveillance close to the ground.

One emerging technology is rapid scan agile beam phased array radar. This might be the ultimate radar providing it exceeds all the capabilities on the current network at faster scan rates. If in addition it proves to fulfill security and aviation needs (tracking of airplanes, missiles) it could revolutionize the current radar paradigm.

7. Acknowledgment

The author is grateful to Rich Ice, Darcy Saxion, Alan Free, and Dave Zittel for advice and valuable information about the WSR-88D. Sebastian Torres provided several figures and comments concerning technical aspects and designed signal processing for the MPAR. Dave Warde contributed figures and details about ground clutter and some VCPs. Collaboration with Dick Doviak is reflected in the requirements section. Allen Zahrai was in charge of engineering developments on MPAR and KOUN; Doug Forsyth lead the MPAR team in outstanding support and development of that platform.

8. References

- Bachmann, S., & D. Zrníc (2007). Spectral Density of Polarimetric Variables Separating Biological Scatterers in the VAD Display. *J. Atmos. Oceanic Technol.*, Vol. 24, pp.1186–1198.
- Bringi, V. N., & V. Chandrasekar (2001). *Polarimetric Doppler Weather Radar*. Cambridge University Press, Cambridge, UK.
- Brown, R. A., V. T. Wood, & D. Sirmans (2002). Improved tornado detection using simulated and actual WSR-88D data with enhanced resolution. *J. Atmos. Oceanic Technol.*, Vol. 19, pp. 1759-1771.
- Brown, R. A., B. A. Flickinger, E. Forren, D. M. Schultz, D. Sirmans, P. L. Spencer, V. T. Wood, & C. L. Ziegler (2005). Improved detection of severe storms using experimental fine-resolution WSR-88D measurements. *Weather and Forecasting*, Vol. 20, 3-14.
- Burgess, D. W., V. T. Wood, & R. A. Brown (1982). Mesocyclone evolution statistics, *Severe Storm Conf. Proc.*, pp. 422-424, AMS, Boston, MA, USA.
- Chrisman, J.N. (2009). Automated volume scan evaluation and termination (AVSET). *34th Conference on Radar Meteorology*, AMS, Williamsburg, VA, USA.
- Crum, T.D., & R.L. Alberty (1993). The WSR-88D & the WSR-88D operational support facility." *B. American Meteorological Society*, Vol. 74, pp. 1669-1687.
- Crum, T.D., R.L. Alberty, & D.W. Burgess (1993). Recording, archiving, and using WSR-88D data." *B. American Meteorological Society*, Vol. 74, pp. 645-653.
- Curtis, D.C., & S. M. Torres (2011). Adaptive range oversampling to achieve faster scanning and the national weather radar testbed phased array radar. *J. Atmos. Oceanic Technol.*, in press.
- Doviak, R.J., & D. S. Zrníc (2006). *Doppler radar and weather observations*. Second edition, reprinted by Dover, Mineola, NY, USA.
- Free, A.D., & N.K. Patel (2007). Clutter censoring theory and application for the WSR-88D. *32nd Conference on Radar Meteorology*, AMS, Albuquerque, NM, USA.
- Heiss, W.H, D.L McGrew, & D. Sirmans (1990). Next generation weather radar (WSR- 88D). *Microwave J.*, Vol. 33, pp. 79-98.

- Hubbert, J.C., M. Dixon, & S.M. Ellis (2009). Weather radar ground clutter. Part II) Real-time identification and filtering. *Jour. Atmosph. Oceanic. Tech.* Vol. 26, pp. 1181-1197.
- Ice, L.R., & D.S. Saxion (2011). Enhancing the foundational data from the WSR-88D) Part II, the future, *35th Conference on Radar Meteorology*, AMS, Pittsburgh, PA, USA.
- Ivic, R.I., D.S. Zrnica, & S. M. Torres (2003). Whitening in range to improve weather radar spectral moment estimates. Part II) Experimental evaluation. *J. Atmos. Oceanic Technol.*, Vol. 20, pp. 1449-1459.
- Mahapatra, P. (1999). *Aviation weather surveillance systems*. Published by IEE and AIAA, printed by Short Run Press, Ltd, Exeter, UK.
- Meischner, P. (2004). *Weather radar, principles and advanced applications*. Springer-Verlag, Berlin, Germany.
- Meymaris, G., J.K. Williams, & J.C. Hubbert (2009). Performance of a proposed hybrid spectrum width estimator for the NEXRAD ORDA. *25th Int. Conf. on IIPS*. AMS, Phoenix, AZ, USA.
- McLaughlin, D., & Coauthors (2009). Short-wavelength technology and the potential for distributed networks of small radar systems. *Bull. Amer. Meteor. Soc.*, Vol. 90, pp. 1797-1817.
- Moisseev, D.N., & V. Chandrasekar (2009). Polarimetric spectral filter for adaptive clutter and noise suppression. *J. Atmos. Oceanic Technol.*, Vol. 26, 215-228.
- Rinehart, R.E. (2010). *Radar for meteorologists*. Fifth edition. Rinehart Publications, Nevada, MO, USA.
- Sachidananda, M., & D.S. Zrnica (2003). Unambiguous Range Extension by Overlay Resolution in Staggered PRT Technique. *J. Atmos. Oceanic Technol.*, Vol. 20, pp. 673-684.
- Sachidananda, M., & D.S. Zrnica (1999). Systematic phase codes for resolving range overlaid signals in a Doppler weather radar. *J. Atmos. Oceanic Technol.*, Vol. 16, pp. 1351-1363.
- Saxion, D. S., & R. L. Ice (2011). Enhancing the foundational data from the WSR- 88D) Part I, a history of success. *35th Conference on Radar Meteorology*, AMS, Pittsburgh, PA.
- Serafin, R.J. & J.W. Wilson (2000). Operational weather radar in the United States Progress and opportunity. *Bull. Amer. Meteor. Soc.*, Vol. 81, pp. 501-518.
- Siggia, A.D., & R. E. Passarelli, Jr. (2004). Gaussian model adaptive processing (GMAP) for improved ground clutter cancellation and moment calculation. *Proceedings of ERAD (2004)*, pp. 67-73. Visby, Island of Gotland, Sweden.
- Torres, M.S., C.D. Curtis, D.S. Zrnica, & M. Jain (2007). Analysis of new Nexrad spectrum width estimator. *33rd Inter. Conf. on Radar Meteorology*, AMS, Cairns, Australia.
- Torres, M.S., Y.F. Dubel, & D.S. Zrnica (2004a). Design, implementation, and demonstration of a staggered PRT algorithm for the WSR-88D. *J. Atmos. Oceanic Technol.*, 21, 1389-1399.
- Torres, M.S., C.D. Curtis, & J.R. Cruz (2004b). Pseudowhitening of weather radar signals to improve spectral moment and polarimetric variable estimates at low signal-to-noise ratios. *IEEE Trans. Geosc. Remote Sens.* Vol. 42, pp. 941-949.
- Torres S., Sachidananda, M, & D. Zrnica (2004c). Signal Design and Processing Techniques for WSR-88D Ambiguity Resolution) Phase coding and staggered PRT, implementation, data collection, and processing. NOAA/NSSL Report, Part 8, available from http://publications.nssl.noaa.gov/wsr88d_reports/.

- Torres S., D. Zrnica, & Y. Dubel (2003). Signal Design and Processing Techniques for WSR-88D Ambiguity Resolution) Phase coding and staggered PRT, implementation, data collection, and processing. NOAA/NSSL Report, Part 7, available from http://publications.nssl.noaa.gov/wsr88d_reports/.
- Torres, S.M., & D.S. Zrnica (2003). Whitening in range to improve weather radar spectral moment estimates. Part I) Formulation and simulation. *J. Atmos. Oceanic Technol.*, Vol. 20, pp. 1443-1448.
- Unal, C. (2009). Spectral polarimetric radar clutter suppression to enhance atmospheric echoes. *J. Atmos. Oceanic Technol.*, Vol. 26, pp. 1781-1797.
- Warde, A. D., & S. M. Torres (2009). Automatic detection and removal of ground clutter contamination on weather radars. *34th Conference on Radar Meteorology*, AMS, Williamsburg, VA, USA.
- Weber, M., J.Y.N. Cho, J.S. Flavin, J. M. Herd, W. Benner, & G. Torok (2007). The next generation multi-mission U.S. surveillance radar network. *Bull. Amer. Meteorol. Soc.*, Vol. 88, pp. 1739-1751.
- Wood, V.T, R. A. Brown, & D. Sirmans (2001). Technique for improving detection of WSR-88D mesocyclone signatures by increasing angular sampling. *Weather and Forecasting*. Vol. 16, pp. 177-184.
- Zittel, W.D. , D. Saxion, R. Rhoton, & D.C. Crauder (2008). Combined WSR-88D technique to reduce range aliasing using phase coding and multiple Doppler scans. *24th IIPS Conference*, AMS. New Orleans.
- Zrnica, D. S., J. F. Kimpel, D. F. Forsyth, A. Shapiro, G. Crain, R. Ferek, J. Heimmer, W. Benner, T. J. McNellis, & R. J. Vogt (2007). Agile beam phased array radar for weather observations. *Bull. Amer. Meteorol. Soc.*, Vol. 88, pp. 1753-1766.
- Zrnica, D., S. V. M. Melnikov, & I. Ivic, 2008: Processing to obtain polarimetric variables on the ORDA (final version) NOAA/NSSL Report available from http://publications.nssl.noaa.gov/wsr88d_reports/.

Automated Processing of Doppler Radar Data for Severe Weather Warnings

Paul Joe¹, Sandy Dance², Valliappa Lakshmanan³, Dirk Heizenreder⁴, Paul James⁴, Peter Lang⁴, Thomas Hengstebeck⁴, Yerong Feng⁵, P.W. Li⁶, Hon-Yin Yeung⁶, Osamu Suzuki⁷, Keiji Doi⁷ and Jianhua Dai⁸

¹*Environment Canada*

²*Bureau of Meteorology,*

³*CIMMS/OU/National Severe Storms Laboratory,*

⁴*Deutcher Wetterdienst,*

⁵*Guandong Meteorological Bureau, China Meteorological Agency,*

⁶*Hong Kong Observatory,*

⁷*Japan Meteorological Agency,*

⁸*Shanghai Meteorological Bureau, China Meteorological Agency,*

¹*Canada*

²*Australia*

³*USA*

⁴*Germany*

⁷*Japan*

^{5,6,8}*China*

1. Introduction

Radar is the only operational tool that provides observations of severe weather producing thunderstorms on a fine enough temporal or spatial resolution (minutes and kilometers) that enables warnings of severe weather. It can provide a three-dimensional view about every five to ten minutes at a spatial resolution of the order of 1 km or less. The development and evolution of intense convective precipitation is closely linked to thunderstorms and so understanding of the microphysics and dynamics of precipitation is needed to understand the evolution of thunderstorms as diabatic and precipitation processes modify and create hazardous rain, hail, wind and lightning.

The characteristics and proportion of severe weather is climatologically or geographically dependent. For example, the highest incidence of tornadoes is in the central U.S. whereas the tallest thunderstorms are found in Argentina (Zipser et al, 2006). Warning services developed at National Hydrological and Meteorological Services (NHMS) often originate because of a particular damaging severe weather event and ensuing expectations of the public. Office organization, resources and expertise are critical considerations in the use of radar for the preparation of severe weather warnings. Warnings also imply a level of legal liability requiring the authority of an operational National Hydrological Meteorological

Service. All available data and timely access is critical and requires substantial infrastructure, ongoing support and maintenance. Besides meteorological data, eye witness observations and reports are also essential element in the issuance of tornado warnings (Doswell et al, 1999; Moller, 1978).

This contribution will discuss operational or operational prototypical radar processing, visualization systems for the production of convective severe weather warnings. The focus will be on the severe weather identification algorithms, the underlying philosophy for its usage, the level of expertise required, decision-making and the preparation of the warning. Radar is also used for the precipitation estimation and its application for flash flood warnings. This is discussed elsewhere (Wilson and Brandes, 1979). Only a few countries have convective thunderstorm warning services and the target audience for this contribution are those countries or NHMS' considering developing such a service. The intent is to provide a broad overview and global survey of radar processing systems for the provision of severe weather warning services. There is a considerable literature in convective weather forecasting and warning, this contribution can only explore a few aspects of this topic (Doswell, 1982; Doswell, 1985; Johns and Doswell, 1992; Wilson et al, 1998).

The forecasting and the warning of severe weather are very briefly described. Then, the underlying technique for the identification of severe thunderstorms using radar is presented. This forms the basis for the radar algorithms that identify the severe storm features. The basic components of the system are then described. Some details and unique innovations are incorporated in the global survey of operational or near operational use. This is concluded by a summary.

2. Forecasting/Nowcasting/Severe weather warnings

Severe weather predictions are divided into severe weather watches and severe weather warnings. In the preceding days, thunderstorm outlooks may be issued. Watches are predictions of the potential of severe weather. They are strategic in nature and fairly coarse in spatial and temporal resolution. They are often issued on a schedule or in conjunction with the public forecast. The expected behaviour is that the public would be aware of the possibility of severe weather and to listen for future updates. Warnings are predictions of the occurrence or imminent occurrence (with high certainty) of severe weather. They are tactical and more specific in location and time. They are also specific in weather element. They are a call to action and to protect one's property and one's self. They are issued and updated as necessary. Fig. 1 shows an overview of the process from the Japanese Meteorological Agency.

Weather advisories are issued if the weather is a concern but not hazardous. Specific types of warning, such as tornado or hail warnings may then be issued and generally after the more generic severe thunderstorm warning is issued.

The key difference is that the watch is a forecast or very short range forecast service as strategic in nature whereas the warning is a nowcast (based on existing data, precise in time, location and weather element) and tactical in nature.

2.1 Severe weather definition

Severe weather is defined here as heavy rains, hail, strong winds including tornadoes and lightning. In the production of warnings, thresholds need to be defined. The thresholds are necessarily locally defined by climatology, local infrastructure and familiarity will dictate what is extreme. Table 1-4 show the warning criteria for Canada circa 1995. Canada is a very big country covering many different weather climatologies and therefore is illustrative of the variation of the severe weather thresholds (see also Galway, 1989). For example, Newfoundland on the east coast of Canada is a very windy location and hence strong winds are a common occurrence and the people have adapted to their environment and therefore it has the highest wind threshold in Canada. Each service needs to define these for them selves.

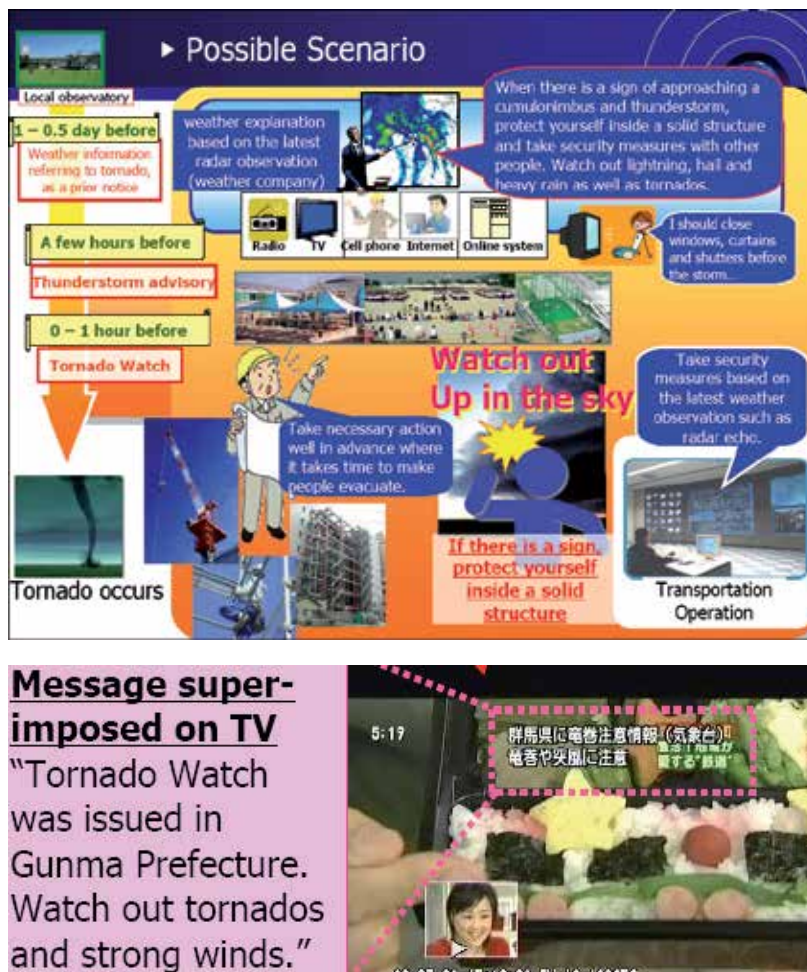


Fig. 1. The envisioned warning process from outlook to tornado watch. This is typical of the process that is used in most countries providing severe weather warning services. Getting the message out to and understood by the public is very important aspect of the utility of the warning service. Superimposing the warning on television, internet, mobile devices and directed messaging are critical to have the message heard.

Type	Description
Wind	Strong winds that cause mobility problems and possible damage to vegetation and structures.
Heavy Rainfall	Heavy or prolonged rainfall accumulating on a scale sufficient to cause local/widespread flooding.
Thunderstorm	One or more of the following: strong winds causing mobility difficulty, damage to structures due to wind and hail, heavy rain that may cause local flooding and lightning
Severe Weather	Presence of tornado(es), damaging hail, heavy rain, strong winds, life and property exposed to real threat, lightning
Tornado	Public has real potential to be exposed to tornado(es).

Table 1. Severe Weather Criteria in Canada: Warning Elements

Weather Centre	Wind	Rain	Hail	Remarks
Newfound-land	gusts of 90 km/h	25 mm/h	20 mm	No tornado criteria; no tornado warning; may mention hurricanes in marine warning.
Maritimes	gusts of 90 km/h	25 mm in 1 hr or 50 mm in 3 hrs	15 mm	Tornado or tornadic waterspout; no tornado warning; will issue hurricane prognostic message and information statements.
Quebec	gusts of 90 km/h	25 mm in 1 hr or 50 mm in 12 hrs	20 mm	Tornado, water spout, funnel cloud, windfall; no tornado warning
Ontario	gusts of 90 km/h	50 mm/hr for 1 hr; 75 mm for 3 hrs	20 mm	No tornado criteria in severe thunderstorm warning; tornado watch issued when confirmed tornadoes threaten to move into region or issued up to 6 hours in advance based on analysis or immediately for severe thunderstorms that indicate potential for becoming tornadic; tornado warning on forecast or observation.
Prairie	90 km/h	50 mm in 1 hr; 75 mm in 3 hr	20 mm	Tornado or waterspout probable; tornado warning issued when expected or observed.
Alberta	gust of 90 km/h	30 mm/h	20 mm	Tornado, waterspout or tornado warning exists; cold air funnel cloud warning when cold air funnels expected but not tornadoes.
Arctic	90 km/h	25 mm/hr	12 mm	Tornado, water spout, funnel cloud; tornado occurrence warning on a confirmed report.
Yukon	gust to 90 km/h	25 mm in 2 hr	significant hail	Potential of tornado; warning is for thunderstorms; no tornado warning.
Pacific	gusts of 90 km/h	25 mm in 1 hr	15 mm	Lightning intensity of 500 strikes in 1 hr over an area of 1 degree x 1 degree latitude/longitude; no watches for severe thunderstorms or tornadoes; no tornado warnings; thunderstorm warning issued on a less than severe thunderstorm; will issue hurricane prognostic messages and information statements.

Table 2. Severe Weather Criteria in Canada: Severe Thunderstorm Criteria

Weather Centre	Warning Criteria
Newfoundland	50 mm in 24 hrs
Maritimes	50 mm in 24 hrs
Quebec	50 mm in 24 hrs or 30 mm in 12 hrs during a spring thaw
Ontario	50 mm in 12 hrs; sodden ground/bare frozen ground: 25 mm in 24 hrs; spring: 25 mm in 24 hrs; slow moving thunderstorms: 50 mm/3 hrs or 25 mm/3 hrs if ground is sodden.
Prairie	80 mm in 24 hrs or 50 mm in 12 hrs
Alberta	50 mm in 24 hrs
Arctic	50 mm in 24 hr
Yukon	40 mm in 24 hr
Pacific	50 mm in 24 hr except in west Vancouver Island and northern coastal regions 100 mm in 24 hr and interior of B.C. 25 mm in 24 hr

Table 3. Severe Weather Criteria in Canada: Heavy Rainfall Warning

Weather Centre	Warning Criteria
Newfoundland	75 km/h and/or gusts of 100 km/h
Maritimes	65 km/h and/or gusts to 90 km/h
Quebec	50 km/h with gusts to 90 km/h or with only gust to 90 km/h
Ontario	60 km/h for 3 hours, or gusts of 90 km/h for 3 hrs
Prairie	60 km/h and/or gusts to 90 km/h for 1 hr
Alberta	60 km/h or gusts to 100 km/h except in Lethbridge Region: 70 km/h or gusts to 120 km/h.
Arctic	60 km/h or gusts of 90 km/h
Yukon	60 km/h for 3 hr or gusts to 90 km/h
Pacific	Mandatory 90 km/h expected over adjacent marine areas; discretionary if gale force winds (63 to 89 km/h) expected over marine areas; discretionary for interior B.C. 65 km/h or gusts of 90 km/h

Table 4. Severe Weather Criteria in Canada: Strong Wind Warning

Warnings for summer severe weather are for extreme or rare events - events that are at the high end of the spectrum of weather. In terms of statistics, rare events do not occur very often (by definition) and so statistical analyses are always suspect due to low numbers. It is difficult to easily demonstrate (using statistics) the efficacy of a warning program (Doswell et al, 1990; Ebert et al 2004). Qualitative analyses or case studies are required to understand the relationship between the provision of warnings and the saving of lives (Sills et al, 2004; Fox et al, 2004). The same applies to determining the efficacy of radar algorithms to the provision of weather warnings (Joe et al, 2004).

This has a significant impact on statistics but also on the "cry wolf" syndrome (AMS, 2001; Barnes et al, 2007; Schumacher et al, 2010; Westefeld et al, 2006). An accurate but useless tornado forecast could be by stating that "next year there will be a tornado in the U.S." This statement is a climatological or statistical forecast. It has a very high probability of being true. However, the phenomenon is very small, perhaps 10-20 km in length and 500 m in width and so this particular prediction is not very useful. The information is highly accurate

but not very precise in terms of location or time. Most, if not all, people would ignore the warning and take the risk. Another form of the "cry wolf" syndrome is where warnings are issued indiscriminately for a very precise time and location and with considerable lead time. However, particularly for rare events (those at the extreme end of a distribution), this is accompanied by a high false alarm rate. If too many false alarms are issued, then these will also be ignored. So, for rare extreme hazardous events, high probability of detection is needed but the false alarms need to be mitigated (Bieringer and Ray, 1996; Black and Ashley, 2011; Glahn 2005; Hoekstra et al, 2011; Polger et al, 1994).

So the issuance of warnings requires a very fine balance of decision-making that takes into account lead time, climatology, societal risk behaviour, social-economic infrastructure, warning service capacity and many other regional, political and societal factors (Baumgart et al, 2008; Dunn, 1990; Hammer and Schmidlin, 2002; Mercer et al, 2009; Schmeits et al, 2008; Westefeld et al, 2006; Wilson et al, 2004). Nowcasts in general are user dependent (Baumgart et al, 2008). Warnings are an extreme kind of nowcasts in which the thresholds apply to a very broad range of users (the public). However, in the future, one can envision very specific warnings or nowcasts issued at lower thresholds that may affect specific users requiring tailored communication techniques and technologies (Keenan et al, 2004; Schumacher et al, 2010).

The wind hazard deserves an extended discussion (Doswell, 2001). There are various kinds of wind hazards that have distinctive life times and spatial features. Straight line winds can originate in synoptic systems or typhoons and are ubiquitous, broad in spatial scale (~100+ km) and extended in duration (~hours/days). Derechos¹ are also straight line winds that originate out of mesoscale convective complexes (MCC; Davis et al, 2004; Evans and Doswell, 2001; Przybylinski, 1995; Weisman, 2001). The damaging portion exists at specific locations. They are smaller in size and temporal scale than the previous kind of winds. Gust fronts originate with the downdrafts of MCC's and depending on the nature of the MCC (isolated thunderstorm, multi-cellular, line echo wave pattern, bow echo, pulse storm); the gust front can take on many forms but generally emanate outwards from the MCC (Klingbe et al, 1987). They can extend for a long time and there may be extreme winds in portions of the gust front.

The downdrafts can also generate quasi-circular outward flowing winds called downbursts (generic term). If the downbursts are over airports, small in diameter (<4km) and intense (>10 m/s velocity differential) then they are given a very specific term called the microburst (McCarthy et al, 1982; Wilson et al, 1988; Wilson and Wakimoto 2001). It is arbitrarily defined this way in order to be very clear to aviators that they are hazardous and should not be transected. They originate with a descending intense precipitation core and the wind intensity is enhanced by evaporative cooling (Byko et al, 2009). If evaporation is strong, by the time the downburst reaches the surface, there may not be any precipitation associated with it. In this case, the feature is called a dry downburst. If there is precipitation then it is called a wet downburst or microburst as the case may be.

There are algorithmic radar techniques for the identification of all of these severe weather features (Dance and Potts, 2002; Donaldson and Desrochers, 1990; Johnson et al, 1998; Joe et

¹It is beyond the scope of this contribution to illustrate the various severe hazards in detail – see references for further information.

al, 2004; Kessler and Wilson, 1971; Lakshmanan et al, 2003; Lakshmanan and Smith, 2009; Lakshmanan et al, 2009; Lenning et al, 1998; Mitchell et al, 1998; Stumpf et al, 1998; Winston, 1998; Witt et al, 1998a, Witt et al, 1998b). The efficacy of the detection depends on the radar scan strategy and quality of the radar (range, azimuth resolution, cycle time, sensitivity, elevation angles, number of elevation tilts, etc (Brown et al, 2000; Heinselman et al, 2008; Lakshmanan et al, 2006; Marshall and Ballantyne, 1975; McLaughlin et al, 2009; Vasiloff, 2001).

2.2 Watches

Watches are based on the concept that the juxtaposition of dynamics, thermodynamics and a mechanism to create upward motion and/or a mechanism to remove inhibition factors exists. This is often called the ingredients approach as one looks to see where the various ingredients come together and that is where severe weather will occur. Historically, this is based on the original Fawbush and Miller Technique (1953) but it has gone through significant evolution (Doswell, 1980, 1982, 1985, 2001; Johns and Doswell, 1992; Moller, 2001; Moninger et al, 1991; Monteverdi et al, 2003; Rasmussen, 2003; Weiss et al 1980).

Fig. 2 shows the morphology of thunderstorms that theoretically develop under different wind shear and convective available potential energy (CAPE) situations (Brooks et al, 1993; Brooks et al, 1994; Markowski et al, 1998b; Weisman and Klemp, 1984; Weisman and Rotunno, 2000). Dynamics is represented by the 0-3 km magnitude of the wind shear. Other height limits may be used depending on the region and local operational usage. The atmospheric structure (low level moisture, mid level dry air, strength of inversions, etc) is important and the thermodynamics is represented by CAPE in this figure. While shear and CAPE are two basic indices that are often used, many other indices are investigated and used.

length of 0-6 km shear vector (kt)

		<20	20-45	>40
CAPE (J/kg)	<1000	ORDINARY	ORDINARY OR MULTICELL	ORDINARY OR SUPERCELL
	1000-2500	ORDINARY WITH SOME PULSE SEVERE	MULTICELL	SUPERCELL
	>2500	ORDINARY WITH SOME PULSE SEVERE	MULTICELL	SUPERCELL

Fig. 2. Thunderstorm type as a function of CAPE and Shear.

Watches are generally very broad in spatial nature due to the spatial density of the observations (soundings and surface observation), and models which are based on the observations, which is very sparse. The resulting analysis of severe weather potential is therefore necessarily broad. The situation is also very fluid and there can be many local factors such as topography or land-water boundaries or rural-urban differences, to name just a few (King et al, 2003; Wasula et al, 2002; Wilson et al, 2010). What are very difficult to identify are potential mechanisms to create upward motion (the trigger) or to overcome the convective inhibition (break the cap). On a synoptic scale, this could be lift generated by cold or warm fronts but on a smaller scale, they can be created by dry lines, thunderstorm outflows, lake-land breezes, urban hot spots, etc. Often they are very low level and therefore hard to observe. So forecasts of severe weather are indications that the potential ingredients exist. They are therefore very broad and strategic in nature.

2.3 Warnings

Weather warnings are issued when there is very high likelihood of severe weather. A broadly worded severe weather thunderstorm warning is most often first issued. If appropriate, it is followed by a more specific warning on a particular thunderstorm and specific severe weather element. This approach is not universal but is dependent on the climatology of severe weather and the level of the warning service that can or has been decided to provide. An important aspect of the detail of the warning is the ability to use the information by the end-user, which is often the public. The public may not know how to react. Given the "cry wolf" syndrome, there needs to be an education process (see Fig. 1). Often, a disaster is needed to get the attention of the public but the significance of the event can be lost in a few short years. Civil emergency services and hydro utilities can plan their post-event remediation actions/locations based on the warning areas and products. So, there can be many variations and underlying philosophies for the provision of warning services. This partially drives the design of the radar processing, visualization and warning preparations systems. It is one thing if severe weather is prevalent and there is a dedicated forecaster for a small area and the public is well attuned to the severity of the weather and have tornado shelters (Andra et al, 2002). It is another thing if the forecaster has to cover several radars and dealing with ill informed users (Leduc et al, 2002; Schumacher et al, 2010).

3. Identifying severe thunderstorms

3.1 Lemon technique

The specificity of the severe thunderstorm warning is primarily based on a radar feature identification technique attributed to Lemon (1977, 1980) and is based on a morphological approach (Moller et al, 1994). It is beyond the scope of this contribution to present or describe the various types of thunderstorms (Fig. 3 shows a small sample). As mentioned earlier, precipitation and precipitation cores form aloft and then descend.

The following features need to be identified:

- tilted updraft, and/or weak or bound weak echo region
- displaced echo top relative to the low-mid level core
- strong reflectivity gradients

- high low level reflectivity core displace towards the updraft
- concavity (hook echo)
- deviant motion (right or left mover, depending on hemisphere)
- rotation

This is a highly condensed version of the technique and there are many subtleties and morphological pathways as storms evolve. Severe storms begin as non-severe storms and algorithm developers and forecasters try very hard to extend lead times by trying to identify the severity of the future storm as early as possible. Note also that it is often in the collapsing stages of the storm (indicated by collapsing echo top or a descending core) when the severe weather reaches the surface (see Fig. 4).

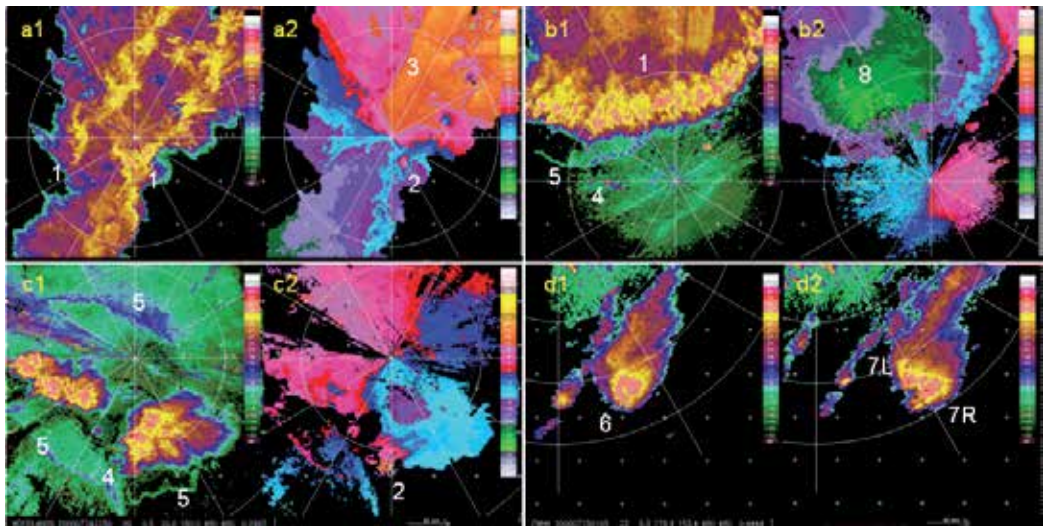


Fig. 3. It is obligatory to show radar images of severe convective storms. Linear convective storms are shown in (a) and (b) whereas isolated thunderstorms are shown in (c) and (d). Except for (d), reflectivity and radial velocity images are shown together. Fig. 3a shows double squall lines (1) with embedded cells and mesocyclones (2). (3) shows a shear line associated with a cold frontal passage, so the mesocyclones are pre-frontal and likely to have formed on a previously formed outflow boundary. Fig. 3b shows embedded thunderstorms on a bow echo. Note the boundaries (5) ahead of the bow echo. (8) shows a meso-scale intense straight line wind (nearing 48 m/s). Fig. 3c shows an isolated thunderstorm with a mesocyclone (4). Boundaries (5) can be seen and to be associated with the entire mesoscale convective complex and not just one individual cell. Fig. 3d shows the splitting of an isolated tornado producing storm. The yellow shading is the 40 dBZ contour. Often, cell identification thresholds are set lower (30 or 35 dBZ) in an attempt to get earlier cell detections but this demonstrates that this results in detecting different storm structures.

Not discussed here is the identification of the initiation phase of convective weather (Wilson et al, 1998). Significant progress has been made in the warning of air mass thunderstorms. In the past, these were considered random and unforecastable. Wilson et al (1998) demonstrate that they are not random but form on boundaries (see the fine lines on Fig. 3c). Roberts et al

(2006) discuss the tools to help bridge the convective initiation phase to the severe phase of thunderstorm nowcasting. The science or theory of thunderstorm is still evolving (Brooks et al, 1994; Brunner et al, 2007; Markowski, 2002; Rasmussen et al, 1994; Weisman and Rotunno, 2004).

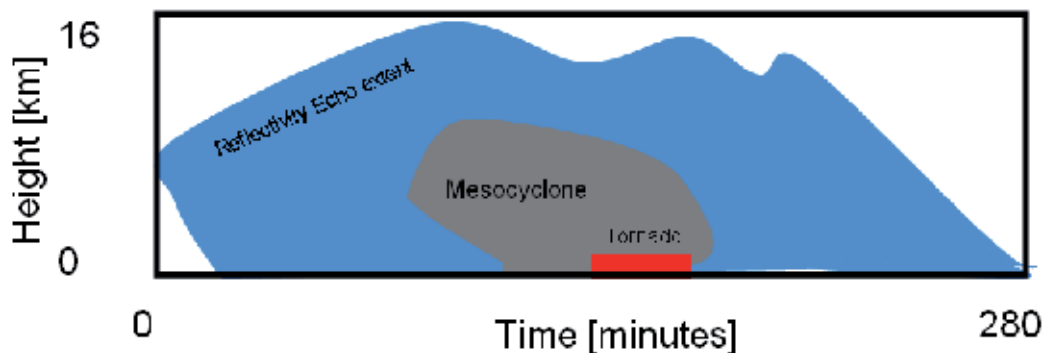


Fig. 4. A time-height diagram through the core of a long lived thunderstorm with a mesocyclone. The “nose” on the left side of the shading indicates the precipitation and the mesocyclone originate at mid-levels of the atmosphere and develop vertically up and down. In the collapse phase of the storm or mesocyclone top, the severe weather reaches the ground (adapted from Burgess et al, 1993; Lemon and Doswell, 1979).

3.2 Other data sets

This contribution focuses on radar and its use in the preparation of warnings. In fact, all sources of observations and information are used to validate and enforce the conceptual models used to produce the warnings. Satellite imagery, such as provided by MSG and the future GOES-R, will be able to provide 5 minute updates over limited areas. Lightning networks are now prevalent and often used as surrogates for radar data where none is available. They also directly observe the lightning hazard (Branick et al, 1992; Gatlin et al, 2010; Goodman et al, 1988; Knupp et al, 2003; Lang et al, 2004; Schultz et al, 2011). Even though a single lightning flash can cause serious harm or death, table 2 indicates that, in Canada, a propensity of lightning strikes is needed before a lightning warning will be issued. Surface wind reports can be also used. However, a tornado or a microburst is relatively small and most operational networks are too sparse to effectively sample the atmosphere for such a small feature. At some airports, a dense network of anemometers is established for this specific problem (Wilson et al, 1998). An important data set are eye witness reports (Doswell et al, 1999; Moller 1978; Smith, 1999). In the past, eye witness reports were required before a tornado warning would be issued. This made all tornado warnings “late” with negative lead times. This was done in order not to “cry wolf” and “alarm the public”. An emerging source of information is the use of high resolution NWP (Hoekstra et al 2011; Li, 2010; Stensrud et al 2009). While phase errors exist (time and location of the thunderstorm), the models appear to be able to capture the morphology of the storm (see Fig. 2). While radar is the core observation system for severe weather warnings at the convective scale, these are not available everywhere. A warning service that does not include radar has yet to be effectively demonstrated.

3.3 Radar dependencies

The Lemon technique implies that volume scanning radars are needed since many of the critical features originate aloft (see Fig. 4). Both, high data quality (Joe, 2009; Lakshmanan et al, 2007; Lakshmanan et al 2010; Lakshmanan et al, 2011) and rapid update cycles for the fast evolving thunderstorms (Crum and Alberty, 1993; Marshall and Ballantyne, 1975). In order to detect low level "clear air" boundaries important for the identification of convective initiation, high sensitivity is critical. Research literature often shows many examples of extensive clear air radar echoes that are not operationally observed. The operational question is whether it is a radar sensitivity issue or the lack of insect targets (the clear air targets have been identified as insects through dual-polarization signatures). Extensive clear air echoes are commonly reported observed on the WSR-88D and primarily in certain parts of the United States (Wilson et al, 1998). Table 5 shows the sensitivity of a small sample of radars including the WSR-88D, WSR-98D (S Band radars) and three C Band radars, one of which is a low powered (8 kW), travelling wave tube (TWT) solid state pulse compression radar (Joe, 2009; Bech et al, 2004; O'Hora and Bech, 2007). In units of dBZ, the sensitivity is a function of range. Fifty kilometer range is arbitrarily chosen to compare the radar sensitivities. The table shows that all these state of the art radars can have comparable sensitivity. Therefore, the apparent lack of clear air echoes is due to the lack of local clear air radar targets and not due to radar sensitivity or wavelength (for example, see May et al, 2004). In addition, due to the dependence of the backscatter on the inverse frequency squared, C Band radars should observe insects better than S Band radars.

Radar	MDS at 50 km
WSR-98D (TJ)	-6.0dBZ
WSR-98D (BJ)	-5.5 dBZ
WSR-88D (KTLX)	-7.5 dBZ
WSR-88D (KLCH)	-8.5 dBZ
WKR Conventional C Band (2 μ s pulse)	-11.0 dBZ
WKR Conventional C Band (0.5 μ s pulse)	-5.0 dBZ
CDV TWT (8kW) C Band (1 μ s pulse)	6.0 dBZ
CDV TWT (8kW) C Band (5 μ s pulse)	-7.0 dBZ
CDV TWT (8kW) C Band (NLFM 30 μ s pulse)	-6.0 dBZ
CDV TWT (8kW) C Band (NLFM 40 μ s pulse)	-9.0 dBZ
INM Conventional C Band (2 μ s pulse)	-9.0 dBZ

Table 5. Minimum Detectable Signal of Various Radars

4. Forecast process and system design

Perhaps the most important consideration in the design of the operational radar processing, visualization and decision-making is the underlying philosophy of the weather service, existing systems and, of course, the capabilities and resources available (Joe et al 2002). In many cases, the warning service requirements are driven not only by the scientific capabilities or the needs but also by the political, societal and economic norms. Often a warning service is an ethical and moral reaction by NHMS's to a damaging event or events and hence it is also a political reaction by governments. This varies considerably from place to place. These requirements are tempered by existing observational infrastructure. Are

there functioning radars or other data sources? Is there the capacity to design or even adopt a radar processing system? Is there the knowledge and capacity to interpret the data products to make effective warning decisions and issue warnings? And is there a way to reach the end-user in a timely fashion? It should not be forgotten that the end-user must be educated on the meaning of the warning and on how to react appropriately. Is there sufficient budget to develop a warning system? What is risk is acceptable? What level is the moral outrage?

An often overlooked design issue is the organization of the weather service. Warnings are provided for small areas (scale of the weather feature) in order to mitigate the "cry wolf" syndrome to be effective (Barnes et al, 2007; Hammer and Schmidlin, 2002). The critical issue is the capacity to provide the attention to the detail given the totality of the forecast responsibilities. The system design will be quite different if there are many forecast offices and few radars (one to one) compared to few offices and many radars (one office to ten radars as in Canada).

Of course, an overarching issue is the climatology of severe weather which ultimately is the core issue. For many countries, convective weather may occur year round and some only for the summer season. In the latter case, a design question is to determine the use case for the shoulder season where severe weather may occur unexpectedly and the warning service is seasonal.

Severe weather forecasting requires a unique forecasting skill set. In synoptic forecasting (for 12 hours and beyond), the forecaster compares current observations to numerical weather prediction models to evaluate the appropriateness of the model or to develop a conceptual model of the weather for the creation of the public forecast product (Doswell 2004). The product is usually produced on a fixed schedule. In severe weather forecasting, the observations need to be timely; there is urgency in the interpretation and the generation of the warning product. It is a "short fused" situation. These require different personality types and this also drives the design considerations. In order to mitigate the "cry wolf" situation while maintaining high probability of detection, a dedicated and separate warning forecaster function is required to be able to address the immediacy issues of the warning service. These are just some of the design considerations for a radar processing and visualization system and the forecast process for the provision of severe weather warnings. Forecast process refers to all components of the transformation of the data or observations into information used for decision- making and warning service production. It includes both the human and their tools and is often referred to as the man-machine mix. Given all the degrees of freedom in the chain, there are different models of the forecast process.

In the next section, a global survey (necessarily incomplete) is presented that will briefly examine the operational or near-operational systems that have been developed. Many have commonalities and only the underlying unique aspects will be highlighted.

5. Components of a basic system

In this section, the basic components or issues of severe weather radar processing/visualization are briefly discussed and a block diagram is provide in Fig. 5. The benefits of different radar types are discussed elsewhere (WMO, 2008).

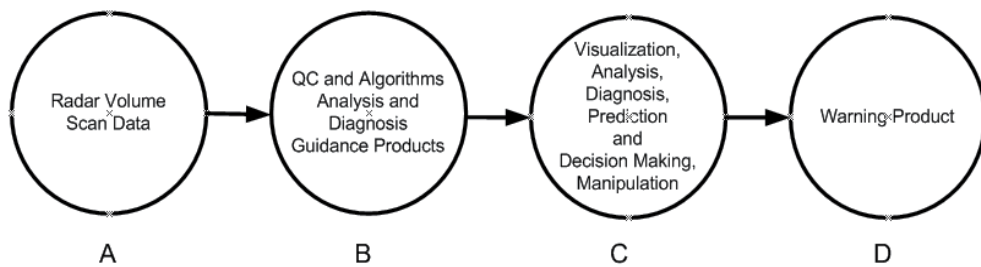


Fig. 5. The flow of the radar data to warning product is much the same in all systems. But the contents of each stage can be different. Except for one system described in this contribution, all the others require human decision-making at stage C before the warning product is issued to the public. In the case of KONRAD (see section 6.10), the product goes mainly to “sophisticated” users.

5.1 Data quality

Radar processing systems need quality controlled data. This can occur in a separate and independent process. In some cases, it is part of the adjustments and corrections that need to be made. Before the severe weather processing occurs (stage B in Fig. 5), it is assumed that the data is free of anomalous propagation, ground clutter and biases in power are adjusted. Second trip echoes and range folded may still be in the Doppler data (Joe 2009; Lakshmanan et al, 2010; Lakshmanan et al, 2011).

In high shear environments the assumption that the radial velocities within a range volume are uniform may not be satisfied (Holleman and Beekhuis 2003; Joe and May 2003). Fig 6ab shows a simulated Doppler velocity spectrum (based on an example in Doviak and Zrnic, 1984) of a tornado contained within a single range volume. The spectrum is bi-modal and the peaks are located at the speed of the radial components of the tornado. Normally it is unimodal and Gaussian in shape. Fig. 6cd show the measured spectrum given two different Nyquist limits. The spectrum is aliased and overlaps with itself. The smaller the Nyquist limit, the greater the overlap. In highly sheared regions, the velocity data is noisy and can be non-sensical. The chapter on quantitative precipitation estimation addresses many of the quality control issues.

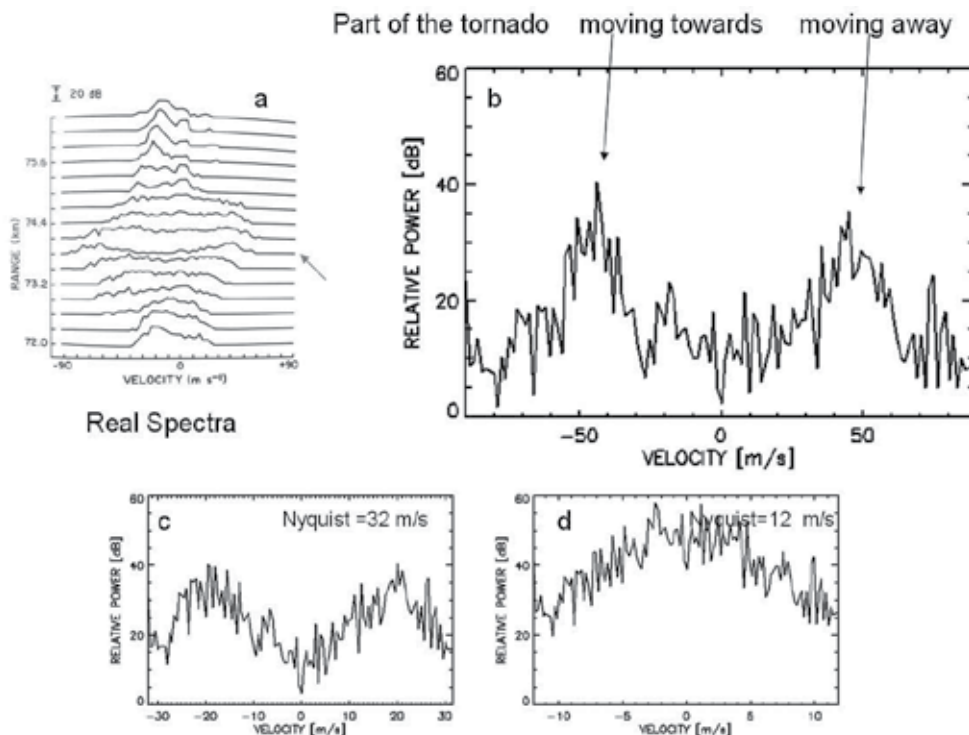


Fig. 6. (a) Doppler velocity spectra at different ranges made with a radar with a very large Nyquist interval. The arrow points to the tornado. The spectrum is bi-modal. (b) a simulation of the spectra. (c) and (d) are simulated measured spectra made with different Nyquist intervals. The spectrum overlaps and is aliased. In (c) the spectra is bi-modal still, would produce a radial velocity estimate near zero with a very broad variance. In (d), the mean is still zero, the spectra is uni-modal with a smaller variance.

6. Global survey

This section provides a necessarily brief global survey of various convective weather radar processing systems. In fact, there are only a few NHMS' that actually provide a severe weather warning service. The systems are presented in a sequence that approximately matches when they were developed and the reader can follow the progression of the system and philosophical developments.

6.1 RADAP – II, U.S.A.

The first radar processing system for severe weather was RADAP-II and it was built in the 1970's (Winston and Ruthi, 1986) and it followed from D/RADEX (Breidenbach et al, 1995; Saffle, 1976) within the National Weather Service. They used VIL (vertically integrated liquid water) and a significant innovation was the introduction of a SWP (Severe Weather Probability) product. They were using probabilistic and uncertainty concepts then! There were many innovations with RADAP-II but its deployment was curtailed due to the development of the Doppler upgrade called the WSR-88D (Crum and Alberty, 1993; Lemon et al, 1977; Wilson

et al, 1980). Crane (1979) developed the cell identification techniques based on peak detection. These systems left a legacy for the development of the WSR88D algorithms. McGill developed SHARP (Bellon and Austin, 1978) for precipitation nowcasting and developed the cross-correlation method for echo tracking which is still used today. It did not specifically address severe weather algorithms, which is the focus of this contribution.

6.2 WSR-88D, U.S.A., WSR-98D, China

Many of the innovations for the reflectivity-only algorithms of RADAP-II were adopted and significantly enhanced for the WSR88D (Crum and Alberty, 1993; Kitzmiller et al, 1995). Doppler algorithms were developed for mesocyclone and gust front detection (Hermes et al 1993; Uyeda and Zrnica, 1986; Zrnica et al, 1985). Considerable effort has been expended to improve upon these initial efforts. A search of the American Meteorological Society journal publications will illustrate that. Initially, the output from the WSR88D Radar Product Generator was displayed on a dedicated radar-only visualization system called the Principal User Product (PUP) display for the forecaster and later the forecaster workstation called AWIPS was used. This integrated all the data and products that the forecaster needed. WSR-88D algorithms were later deployed on the WSR-98D radars made by MetStar and used in China, Romania, India, Korea and other places.

A fundamental question arose as to the role of automated guidance products versus manual interpretation (Andra et al, 2002). It is clear that automated generated products are for guidance and it should not be mistakenly interpreted that warnings were automatically generated and issued without an intervening well trained decision-maker. Initially, there was an extensive radar training program for forecasters, up to 6 weeks for specialists. Clearly, the expectation was that an expert level of training was needed to interpret Doppler radar data for severe weather warnings. This was re-enforced by the work of Pliske et al (1997) who analyzed how to achieve the expected benefits of a modernization program. This resulted in the development of an on-going training program for decision-making at the appropriately named, Warning Decision Training Branch of the National Severe Storms Laboratory. Professionally trained instructors on cognitive principles interactively have the skills to tailor the material to the appropriate knowledge level, abilities and learning styles of the student. It is a model for professional training.

6.3 TITAN – NCAR

TITAN (Thunderstorm identification, tracking and nowcasting) was first developed in South Africa and then later at NCAR for support of weather modification programs. Dixon and Weiner (1993) described a simple but brilliant threshold technique for the identification of thunderstorm cell cores. This simplified the peak detection techniques of the Crane (1979) technique as the latter identified many weak cells and challenged the computing power of the day. It also described a methodology for tracking. It could be argued that this is the most widely used system in the world. It is freely available and requires some expertise to implement. It is used extensively in research environments (Lei et al, 2009). It is a stand alone system and integrating it into an operational environment has been done but there are capacity and support issues to consider. For example, it is used at the South African Weather Service.

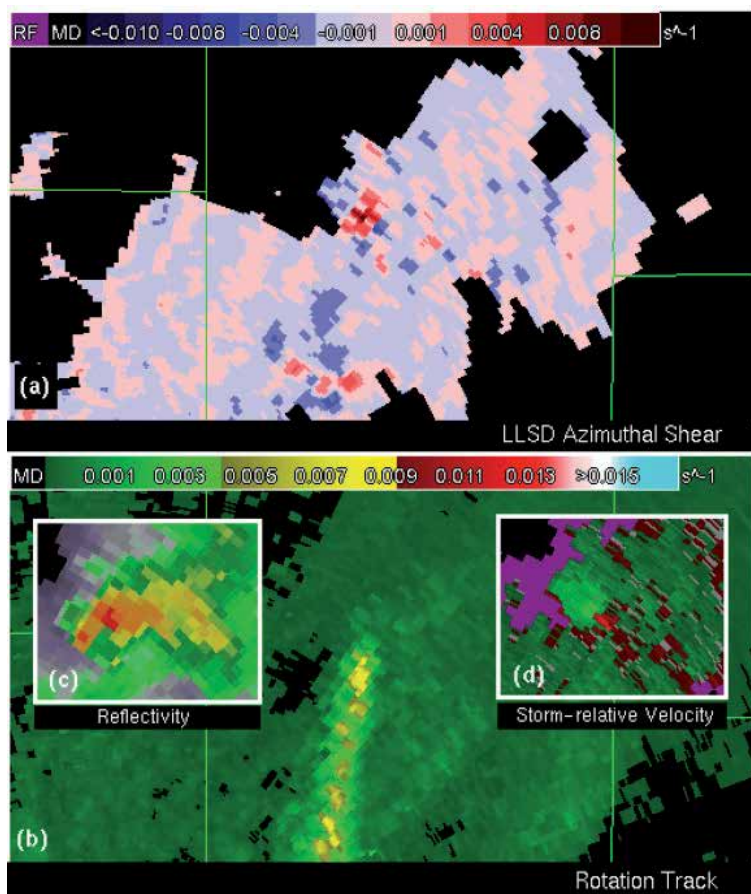


Fig. 8. In this system, there is a trend to go back to basic imagery products such as shear and aggregated shear to aid in the interpretation and utility of the data.

6.5 CARDS – Canada

The CARDS (Canadian Radar Decision Support) system was developed as part of the radar upgrade (Joe et al, 2002; Lapczak et al, 1999) and built on the previous concepts. In Canada, a single severe weather forecaster is responsible for the provision of warnings for the area coverage of about ten radars. This is in contrast to other countries, where it is approximately one radar for one forecaster. While this may seem like a work overload situation, there are some interesting side benefits. It has been estimated that in a one radar for one forecaster situation, a forecaster will likely face only one significant event in his career. In the Canadian scenario, a severe weather forecaster will therefore experience ten big events. It can be argued that these experienced forecasters will be better at decision making and will therefore make better warnings (Doswell, 2004). Forecasting is a complex process and it remains to be seen whether this is a true. Given these constraints, the weather service of Canada is arguably the most reliant on automated guidance products. They are critical in aiding the forecaster to diagnose those cells which need detailed interrogation to upgrade from a severe weather warning to a more specific warning.

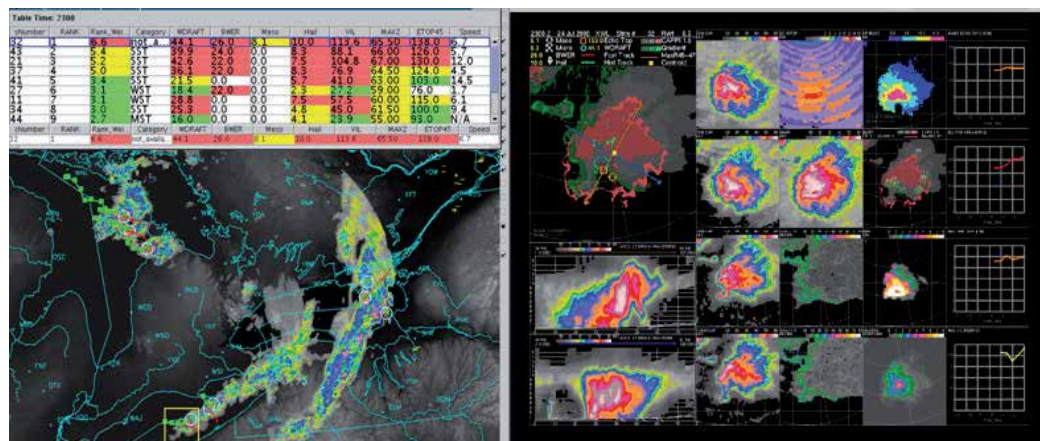


Fig. 9. An example of a CARDS composite, SCIT and cell view. The size of the forecast domain is about $\sim 2000 \text{ km} \times 1600 \text{ km}$. The image shows a zoomed image of the cells, tracks and lightning strikes. Eight Canadian radars and 12 US radars contribute to the image. The composite and the SCIT table products are invoked and displayed at the same time. The forecaster can either drill down to a CELL VIEW via the composite or via the SCIT table. They can also rapidly survey the cells from the SCIT table without invoking the CELL VIEW products. The colour coding indicates the categorical ranking. On the right is an example of a cell view. This shows a variety of images that allows the forecaster to quickly make a decision as to the severity of the storm. The product shows an ensemble product of the algorithms (upper left hand corner, not described), automatically determined cross-sections, four CAPPIs (1.5, 3.0, 7.0, 9.0 km), reflectivity gradient, MAXR, echo top, VIL density, Hail, BWER and 45 dBZ echo top and time graphs.

In an envisioned future exercise for the design of CARDS, it was identified that there was actually no hard requirement for single radar products. One of the main reasons for missed warnings was that the forecaster was so intent on one thunderstorm that they forgot about the others. There was a loss of situational awareness. This happens even with experienced forecasters or analysts and is common in many fields where critical decisions are made. A regional composite that could display and overlay the most popular products (CAPPI, EchoTop, etc) is the main product to maintain situational awareness. Thunderstorms cell locations are identified, ranked, color coded and displayed on the composite and in a table similar to the SCIT table. Selecting the cell of interest in the composite or in the table, the user is able to quickly and rapidly drill down to reveal a cell view product (Fig. 9) that contain all the products that the user would use to interrogate a cell and make decisions. The cell view has a legacy from Chisholm and Renick (1972). The design exercise also identified the critical reliance on automated guidance products.

Another important innovation is that the visualization tool for the image and data products is based on hypertext transfer protocol (http) which means that any computer regardless of operating system can access the full functionality of the radar data. Analyzing breakthroughs in the use of radar, access to the data and the products has been “the” key innovation. Recall the days of radar operators who hand drew radar maps or the facsimile

machine or the mono or color graphics terminal. Each innovation increased the capacity to deliver better products. In today's technology, every button press or mouse click that is eliminated delivers "a big bang for the buck". This key innovation allowed the data to be effectively used in the Sydney Olympic Command Centre (Joe et al, 2004; Keenan et al, 2004).

Similar to the SCIT of WDSS-I, CARDS implemented a fuzzy logic technique to rank storms. The technique is configurable (see Table 6). It shows the parameters that the users decided to use and the thresholds that they considered as weak, moderate, strong and severe (see also Doswell et al, 2006).

In the overlap region, cells are selected from one radar or the other, unlike WDSS-II. Due to attenuation concerns, lack of experience with the fuzzy logic storm severity technique and that reflectivity (and reflectivity based products) was still the prime parameter for determining storm severity; users selected the cell detection with the maximum reflectivity as the cell for visualization. However, this would likely not be the case anymore as nearest radar or maximum information or maximum severity ranking would be chosen today.

Thresholds	Rank (0-8)	BWER count	Meso m/s/km	Hail cm	Wdraft m/s	Vil density kg m ² / km	Max Z dBZ	45 dBZ ETop km
	0	0		0	0	0	0	0
Minimum	1 0-2	5-11		4	0.5	10	2.2	30
Weak	2 3-4	12-17		6	1.3	15	3	45
Moderate	3 5-6	18-21		8	2.3	20	3.5	50
Severe	4 7+	22-26		10	5	25	4	60

Notes:

Rank:	5-6 means a value of 5 or more but less than 7.
WER:	The number of directions where reflectivity increases determines a BWER (with low reflectivity below)
Meso:	Average Pattern Vector Shear (see Zrnice et al, 1985)
Hail:	Average Hail Size
WDRAFT:	Gust potential in m/s
Vil Density:	Similar to WDRAFT in pattern
VIL	if VIL for classification then 10 20 30 40 are the thresholds
Max Z:	Max reflectivity in the cell
45 dBZ Echotop Ht:	Reliable echo top parameter

Table 6. Fuzzy Logic Membership Functions for Parameters Used to Rank Storms.

6.6 SWIRLS and its variants – Hong Kong, China

In Hong Kong, lightning strikes and damaging squalls are major threats accompanying thunderstorms. In support of the Thunderstorm Warning operations, SWIRLS (Short-range Warning of Intense Rainstorms in Localized Systems) was developed to track and predict severe weather including rainstorms, cloud-to-ground (CG) lightning, damaging thunderstorm squalls and hail for the general public. The warning decision and message preparation are made by the Observatory's duty forecaster. Once issued, the warning message are disseminated automatically through various channels including radio and television broadcast automatic telephone enquiry system, Internet web page, as well as mobile apps for smart phones and social networking platforms such as Twitter.

An innovation is the DELITE (Detection of cloud Electrification and Lightning based on Isothermal Thunderstorm Echoes) algorithm for lightning warning. It selects radar and other parameters most relevant to the microphysical processes leading up to the electrification of a cumulus cloud (Fig. 10). This includes radar reflectivity at constant temperature levels (0°C, -10°C, and -20°C), the thermal profile of the troposphere (from either numerical weather model analysis or the latest available radiosonde data), the echo top height and the vertically integrated liquid (VIL). CG lightning initiation is expected if prescribed thresholds are exceeded.

The above severe weather analyses are performed on a cell basis and the threat areas are identified as elliptical cells in the corresponding interest fields with values greater than or equal to prescribed thresholds. For example, the detailed cell identification technique follows the GTrack algorithm of SWIRLS. For lightning and downburst, the interest fields are 3-km CAPPI and 0-5 km VIL respectively. The thresholds are 25 dBZ and 5 mm respectively.

MOVA (Multi-scale Optical flow by Variational Analysis) is a gridded echo-motion field that is derived from consecutive radar reflectivity fields by solving an optical-flow equation with a smoothness constraint. To capture multi-scale echo motions, the optical-flow equation is solved iteratively for a cascade of grids from coarse to fine resolutions (about 512 to 3 km).

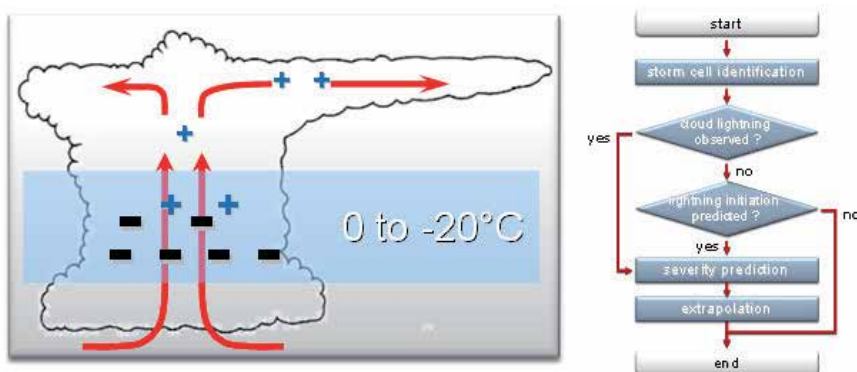


Fig. 10. (a) Conceptual model of CG lightning. The main source of electric charges is assumed to be located in the mixed-phase layer between 0 and -20°C. Prior to electrification, the updraft is expected to separate the charge carriers vertically. Negative charge carriers (i.e. graupel) are expected to reside mainly in the mixed-phase layer. The updraft pumps super-cooled rain water into this layer and wet the carriers. (b) Flow chart of the logic of the algorithm.

SWIRLS updates and outputs nowcast products at 6-minute intervals. For severe thunderstorms, the major results are visualized as an image product called the Severe Weather Map on its client workstation in the forecasting office, as well as a web page named SPIDASS (SWIRLS Panel for Integrated Display of Alerts on Severe Storms) dedicated for severe weather alerts (Fig. 11).

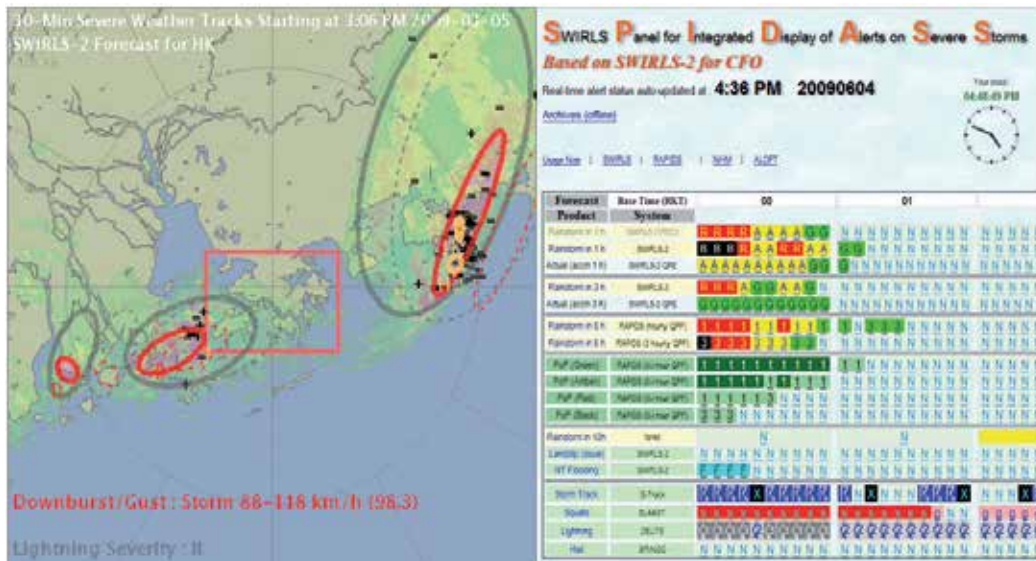


Fig. 11. (a) shows an example of the Severe Weather Map. Textual alerts with quantitative details were printed at the bottom. (b), the main panel of SPIDASS web page provides a compact view of all alerts arranged in rows and colour-coded for different severity levels.

The Hong Kong Observatory has also developed separate multi-sensor thunderstorm nowcasting systems for the aviation community and the public utilities services (Li, 2009). A lightning nowcasting system, named the Airport Thunderstorm and Lightning Alerting System (ATLAS), covers the Hong Kong International Airport (HKIA). It combines rapidly updated CG lightning strike information, radar reflectivity and TREC wind information to nowcast lightning strikes using a modified Semi-Lagrangian advection scheme. Depending on the predicted distance from HKIA, ATLAS will automatically generate RED (1km) or AMBER (5 km) alerts.

ATLAS is equipped with two ensemble algorithms, to take into account the possible rapid development nature of lightning (transient and sporadic). The Weighted Ensemble (WE) algorithm sums all available 12-minute CG forecasts with decreasing weight with time. If the sum exceeds an optimized threshold, alerts are created. WE has proved to be effective for alerting persistent and wide-spread thunderstorms. The Time Lagged Ensemble (TLE) algorithm sums the 1-minute forecasts valid at the same time from the twelve 1-minute forecasts provided in the past 12 minutes with decreasing weight over time. TLE is proved to be more skilful in predicting rapidly developing, small or wide-spread thunderstorms than WE. Figure 12 shows a snapshot of the ATLAS product.

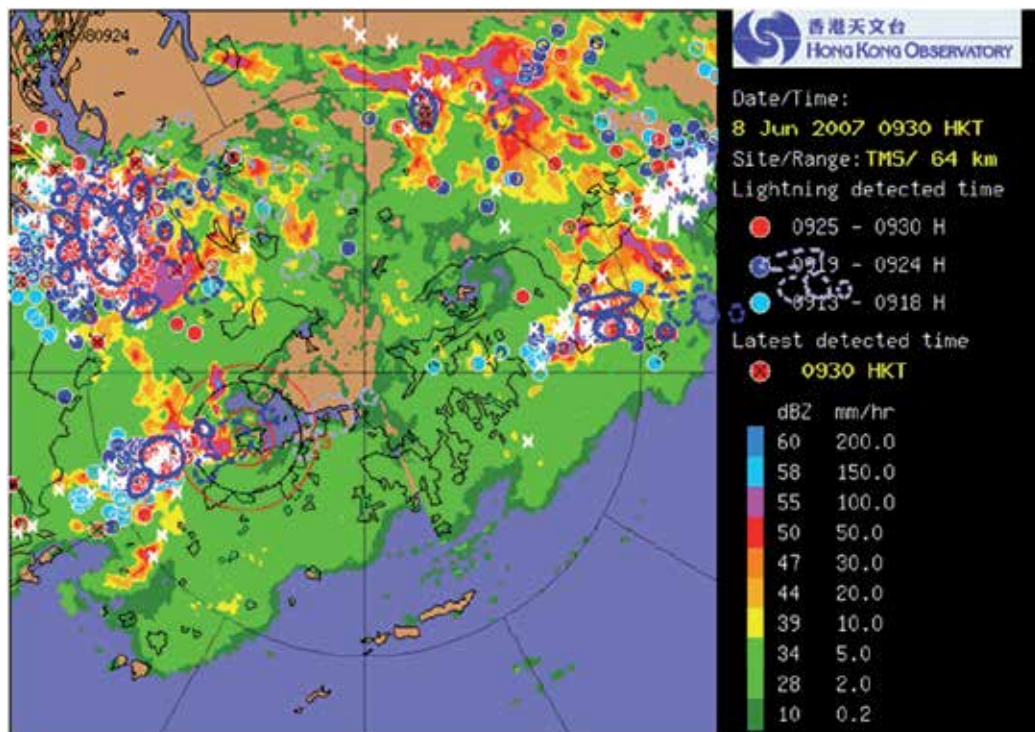


Fig. 12. A snapshot of ATLAS webpage. The image shows the actual position of the CGs (ellipses with solid line), the predicted CGs (ellipses with dashed line), the 12-minute forecast in blue and the 30-minute forecast in grey.

The Aviation Thunderstorm Nowcasting System (ATNS) has been developed to predict the movement of thunderstorms to help local Air Traffic Management to better manage the flight traffic over the Hong Kong Flight Information Region for the next few hours (Li and Wong, 2010). A blending approach is adopted to extend the forecast range and to capture the development and dissipation of thunderstorms. The NWP model used is a high resolution non-hydrostatic model with horizontal resolution of 5 km (Li et al. 2005; Wong et al. 2009). Volume radar reflectivity data are ingested into the model via the LAPS data assimilation system (Albers et al. 1996) and radar Doppler radial wind and 3D radar winds are assimilated via the JNoVA-3DVAR data assimilation system (Honda et al. 2005) to improve the initial moisture field and wind fields, respectively.

The blending algorithm is as follows: (i) SWIRLS radar forecast reflectivity is converted into surface precipitation using a dynamic reflectivity-rainfall (Z-R) relation; (ii) precipitation forecasts are extracted from the NHM; and (iii) then they are blended. The latter blending process involves: (i) Phase correction where a variational technique minimizes the root mean square error of the forecast rainfall field from a previous model run (usually initialized at 1-2 hours before) and the actual radar-raingauge derived precipitation distribution (Wong et al. 2009). (ii) Calibration of the QPF rainfall intensities is based on the observed radar-based quantitative precipitation estimate (QPE), and (iii) blending of calibrated model QPF with the radar nowcast out to 6 hours where the weighting is biased

to the nowcasts in the early stages and towards the model at the longer lead times. Figure 13 shows the comparison between the effects of ATNS using SWIRLS simple extrapolation (1-6 hours forecasts) and ATNS using SWIRLS-NHM blended forecasts for the case of 4 Jun 2009 (1-6 hour forecasts). The simple TREC extrapolation (left column) overpredicts the rainfall intensities in this case at long lead times (6 hours).

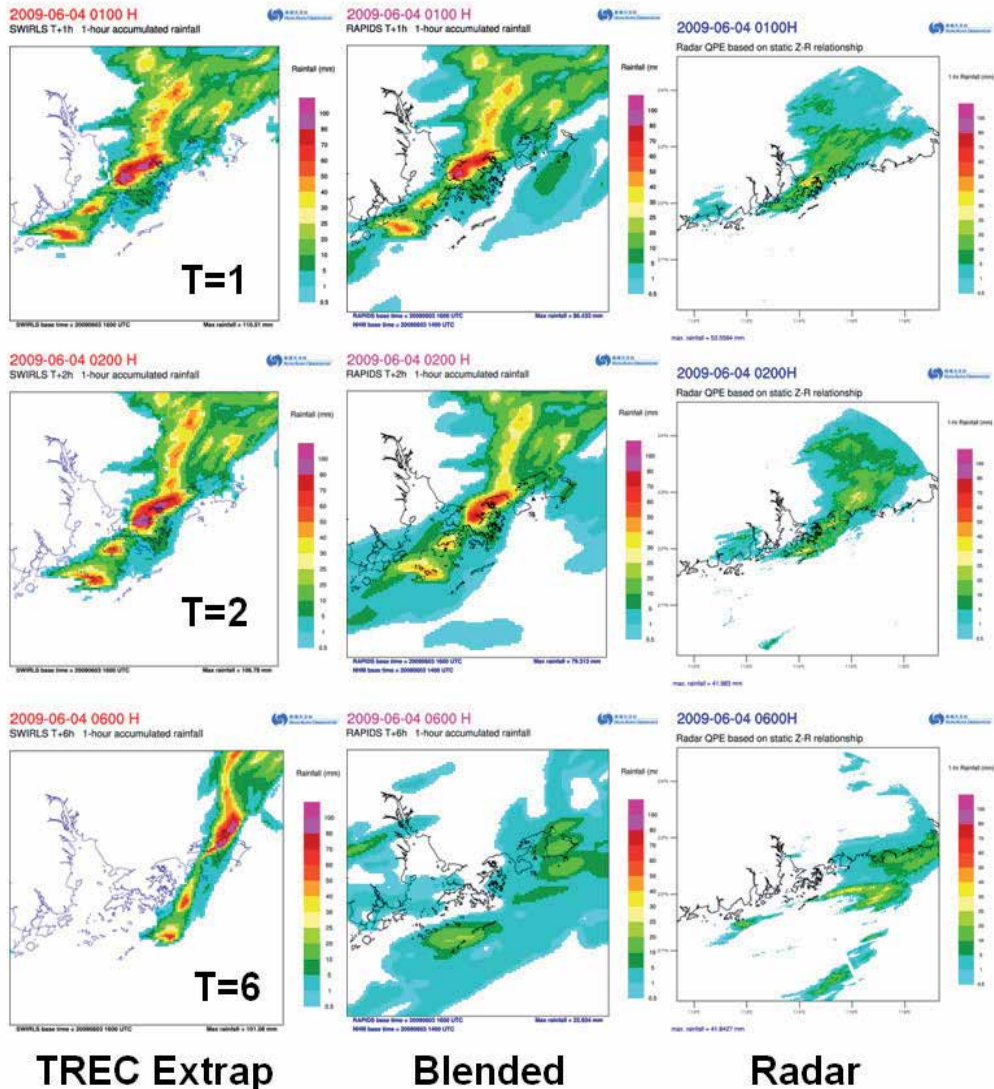


Fig. 13. An example showing the comparison between the effects of SWIRLS simple extrapolation and blending of SWIRLS and NHM rainfall. Figures from top to bottom are 1-hr, 2-hr and 6hr simple extrapolation (left column), AANS blended precipitation (middle column) forecasts and the radar-based QPE (different scale).

6.7 SIGOONS – France

Significant Weather Object Oriented Nowcast System (SIGOONS) is a component of the Synergie workstation (Brovelli et al, 2005). Thunderstorm cells are identified using the RDT (Rapidly Developing Thunderstorms) technique by Hering et al (2005) and are represented as objects. This database is updated every five minutes and is automatically quality controlled against other observational data. The objects may have deterministic and probabilistic attributes and have a time dimension – they can grow and decay. Products are automatically generated and tailored according to pre-defined customer requirements. Discrepancies are brought to the attention of the forecaster who can select persistence over linear extrapolation nowcasts. The forecaster can take additional initiative. The attributes of the weather objects can be manipulated and altered by forecasters.

6.8 THESPA and TIFS, Australia

Within the Bureau of Meteorology, forecasters use RAPIC to interactively interrogate the data. The innovation is the radar data is loaded on the graphics memory of the client computer and extremely rapid response of the display is achieved. To avoid dual-PRF dealiasing errors, only single PRF data is used resulting in a Nyquist interval of 16 m/s. This implies considerable forecaster training is required to interpret highly aliased Doppler data.

Thunderstorm Strike Probability (THESPA, Dance et al, 2010) generates probabilistic nowcasts. Using the historical statistics of the nowcast position errors as a function of lead time and detected storm properties, storm motion is modeled as a bivariate Gaussian distribution on storm speed and direction. For a given geographical point, the strike probability from all possible thunderstorms is computed for the forecast period (Fig. 14).

The algorithm is embedded in the Thunderstorm Interactive Forecast System (TIFS, Bally 2004). The Beijing Olympics provided an opportunity to explore and prototype new nowcasting techniques (Wang et al, 2010). TIFS was modified to ingest the storm locations and tracks from the CARDS, SWIRLS, WDSS and TITAN to create a poor man's ensemble. From each of the storms and tracks, THESPA was used to compute a consensus or ensemble strike probability (Fig. 14b). A warning product would be automatically generated. The analyst (B08 Forecast Demonstration Project team member) would evaluate the product and determine if intervention was needed. The analyst could then use the graphical interface and add, delete or modify cells or tracks. The analyst could view and modify any of the ensemble members and the strike probability display would update. Accepting the change would regenerate the automated warning product, be disseminated and overwriting the fully automated product.

6.9 NoCAWS – SMB

The Shanghai Meteorological Bureau's NoCAWS system was one of the nowcast systems used for the World Expo on Nowcasting Services (WENS) component of the Multi-hazard Early Warning Service project (MHEWS). It integrates observations, mesoscale models and nowcasts to host data displays; analysis tools, severe weather alerting tools to generate automatic forecasts and warning for forecasters. It covers the scales from outlooks to warnings. An innovative feature is lightning forecasts. COTREC winds are used to nowcast cell motions. Advection and statistical relationships between lightning and reflectivity are used to nowcast lightning (Fig. 15)

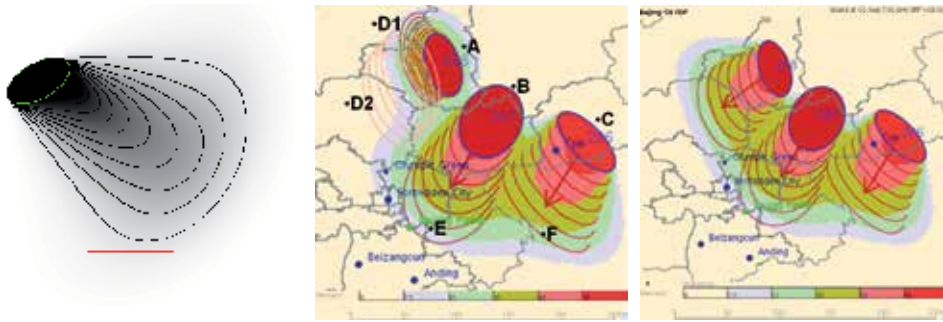


Fig. 14. (a) The detected thunderstorm is the ellipse oriented south-west to north-east. A motion to the south east is shown. The contours and shading show the probability that the thunderstorm will advect or propagate into those locations. The probabilities were verified for a season of storms around Sydney and Beijing, with excellent reliability, with a Brier skill score of between 0.36 and 0.44 with respect to an advected threat area forecast. (b) An example of a prototype TIFS strike probability product. Three cells are identified as A, B and C and represented as ellipses. The tracks of B and C are indicated by the partial ellipses and the colours indicate the strike probability, marked as E and F and appear consistent. The track for cell A is marked as D1 and appears anomalous. D2 is the track that the analyst has modified to produce the final strike probability map (c).

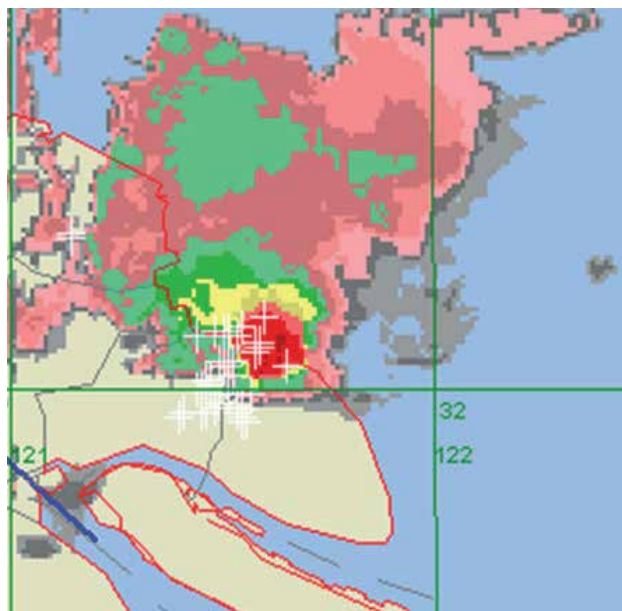


Fig. 15. This figure shows a nowcast of the reflectivity and lightning from NoCAWS. The plus signs are nowcasts of lightning strikes.

6.10 KONRAD/NinJo/NowCastMIX – DWD

There are several tools in the German Weather Service and include KONRAD (Lang et al, 2001), Mesocyclone detection (Hengstebeck et al, 2011), AutoWARN, EPM (editing, prediction, monitoring), Cellviews (Joe et al, 2003). All of these are integrated into the Ninjo system (Koppert et al, 2004). KONRAD was developed as a research prototype and uses a variable elevation angle PPI reflectivity product for the identification and warning potential of cells. The 10 minute volume scan product is used for further classification. The cells are displayed as abstractions and only a >28dBZ contour is displayed in the end user product (Fig. 16). Of all the systems discussed, it is the only truly automated system where the products go directly out to the end-user without human oversight. However, it targets sophisticated end-users such as emergency authorities, county administrators, fire departments and the military and not the public. One could argue that these are guidance products for external versus internal decision-makers for planning but not warning service. So the “cry wolf” syndrome is not a significant issue. This does demonstrate the potential use of fully automated products.

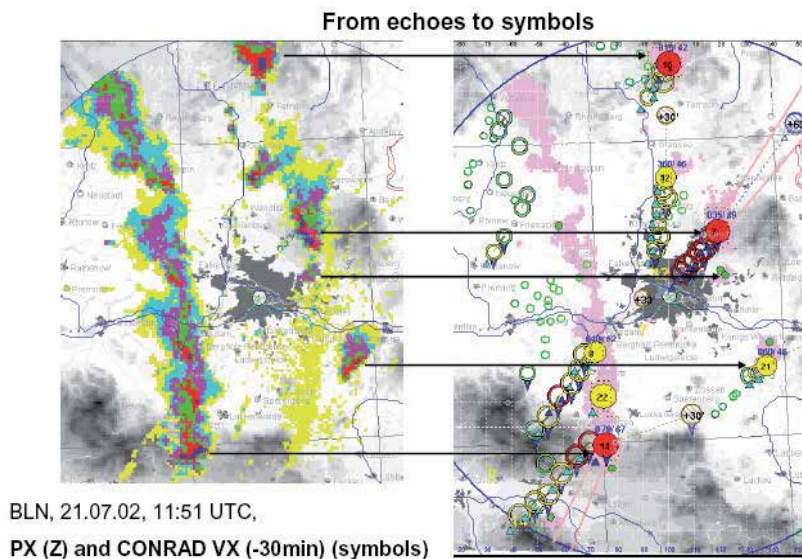


Fig. 16. An example of the abstraction from reflectivity to symbolic representation of thunderstorms from the KONRAD system. It is the only system described in the contribution that is totally automated. It is directed to “sophisticated users” for planning purposes.

The AutoWARN system in NinJo integrates various meteorological data and products in a warning decision support process, generating real-time warning proposals for assessment and possible modification by the duty forecasters. These warnings finally issued by the forecaster are then exported to a system generating textual and graphical warning products for dissemination to customers. On very short, nowcasting timescales, several systems are continuously monitored. These include the radar-based storm-cell identification and tracking methods, KONRAD and CellMOS; 3D radar volume scans yielding vertically integrated liquid water (VIL) composites; precise lightning strike locations; the precipitation prediction system, RadVOR-OP as well as synoptic reports and the latest high resolution numerical analysis and forecast data.

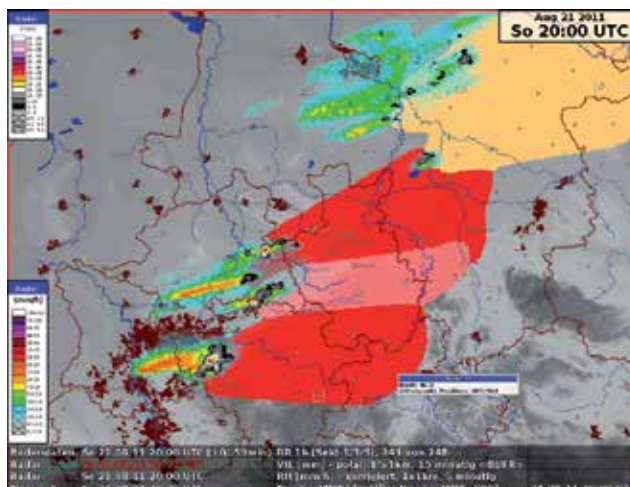


Fig. 17. An example of NowcastMix. It combines and merges the output from several nowcasting systems into a hazard map.

Since there are several nowcasting systems available, NowCastMIX processes these available nowcast products together in an integrated grid-based analysis, providing a generic, optimal warning solution with a 5-minute update cycle. The products are combined using a fuzzy logic approach (James et al 2011). The method includes estimates for the storm cell motion by combining raw cell tracking inputs from the KONRAD and CellMOS systems with vector fields derived from comparing consecutive radar images. Finally, the resulting gridded warning fields are spatially filtered to provide regionally-optimized warning levels for differing thunderstorm severities for forecasters. NowCastMIX delivers a synthesis of the various nowcasting and forecast model system inputs to provide consolidated sets of most-probable short-term forecasts (Fig. 17).

6.11 Japan – JMA

Japan Meteorological Agency initiated their hazardous wind warning program in 2007. A hazardous-wind-possibility-index is calculated based on the NWP prediction of wind and radar reflectivity exceeding a threshold. An innovation is the use of a template matching technique for the detection of mesocyclones. Rankine vortex and divergence flow field templates of different intensity and spatial scale are generated and matched to the radial velocity field. This is done every five minutes. Detections on two consecutive time steps are required as a quality controlled metric. Then the two estimates are combined every ten minutes to estimate a hazardous wind potential. Nowcasting is based on a motion analysis. Different thresholds are statistically established and the success ratio (1-FAR) and the probability of detection (POD) are used to categorize the hazard level (Table 7). If level 2 is exceeded (see Fig. 18), then it alerts a forecaster to issue Hazardous Wind Watch. A forecaster may ignore the level 2 information, when: (i) the storm is near the boundary of a warning area and it will be out before the time of warning or (ii) the quality of radar data seems poor (e.g. AP or sea clutter). A forecaster can issue a warning at level 1 when (i) reliable report of a tornado/tornadoes and/or and (ii) strong gust (say, greater than 30 m/s) caused by a convective cloud.

Warning Level	Criteria
2	Success Ratio = 1- FAR = 5- 10% with POD=20-30%
1	1-FAR= 1-5% and POD=60-70%

Table 7. Hazardous Criteria Level

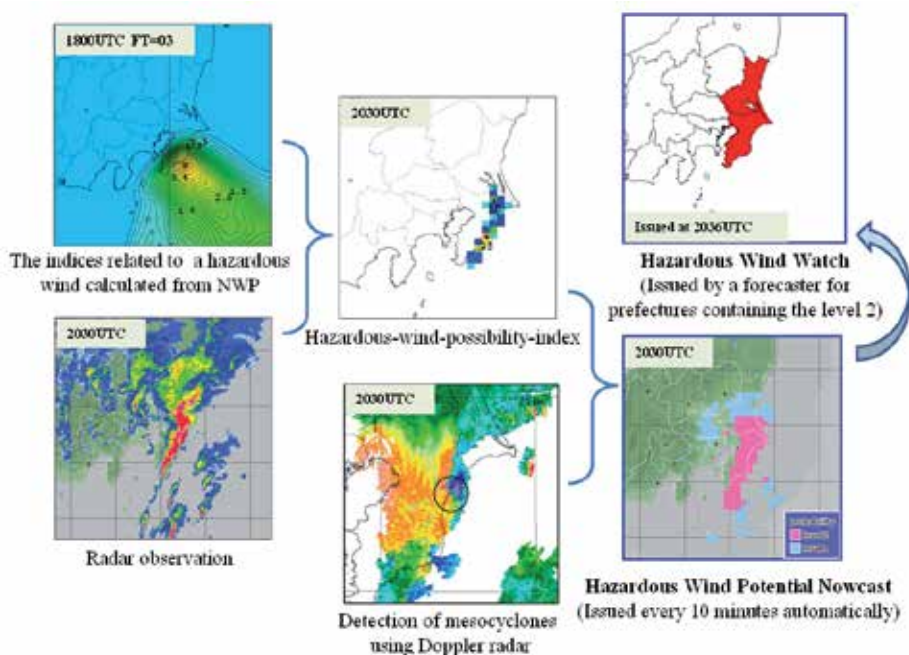


Fig. 18. The processing steps for hazardous wind potential at JMA. It is typical of current systems where mesoscale NWP predictions are assumed to be good enough to match with the observations.

6.12 SWAN – CHINA/CMA

In 2008, the China Meteorological Administration (CMA) launched a campaign on the development of its first version of integrated nowcasting system SWAN (Severe Weather Analysis and Nowcast system). This system aims at providing an integrated, state-of-the-art and timely severe weather nowcast platform for operational forecasters at all levels over China. SWAN ingests data from China's new generation Doppler radars (both S-band and C-band), automatic weather station, satellite, and mesoscale numerical weather prediction model. It offers a tool for severe weather monitoring, analysis, nowcasting and warnings such as flashing a real-time alert, driving next algorithm processes and sending a warning via SMS, etc.

The server application includes several modules, such as providing log files for monitoring system behavior, configuring network environment, setting data acquisition parameters, performing quality control for radar data and AWS data, generating 3D radar reflectivity mosaic, running algorithm for nowcast products, analyzing observation data and providing message for alerting the forecasters.

The client refreshes real-time observations cycled in 5 min from radars and AWS (automatic weather stations) and provides real-time alerts (sounding, flashing) for indication of severe weather events (meeting certain thresholds such as wind speeds or rainfall amounts). It also provides an interactive tool for preparing, editing and issuing Nowcast and warning for severe weathers

Based on quality control, a regional 3D reflectivity mosaic is produced by trying to fill the gaps that are generated by terrain blockage or AP. Products such as vertically integrated liquid (VIL), echo top (ET) and COTREC winds are then derived. QPE algorithm involves extraction of convective echoes from stratiform echoes by texture and horizontal gradient properties. Different Z-R relations are used for convective rain and stratiform rain. COTREC (continuous tracking radar echo by correlation) vectors are echo motion vectors that are derived from moving radar reflectivity patterns through grid-to-grid cross-correlation and then adjusted by a horizontal non-divergence constraint for hourly nowcasts of rainfall (Li et al, 1995). This is blended with mesoscale numerical prediction model output for 2-3 hour nowcasts.

SWAN provides real time verifications for storm tracking and reflectivity nowcasts. Storm track errors are shown as distance differences between observed storm tracks and predicted storm tracks (1h). Observed radar reflectivity are also verified against extrapolated forecasted reflectivity.

Severe weather warnings can be prepared and issued through SWAN by graphical interface by circling an area on the screen, clicking an icon and doing some minor wording (Fig. 19). A web-based version of SWAN has been developed and deployed in Guangdong Meteorological Bureau.

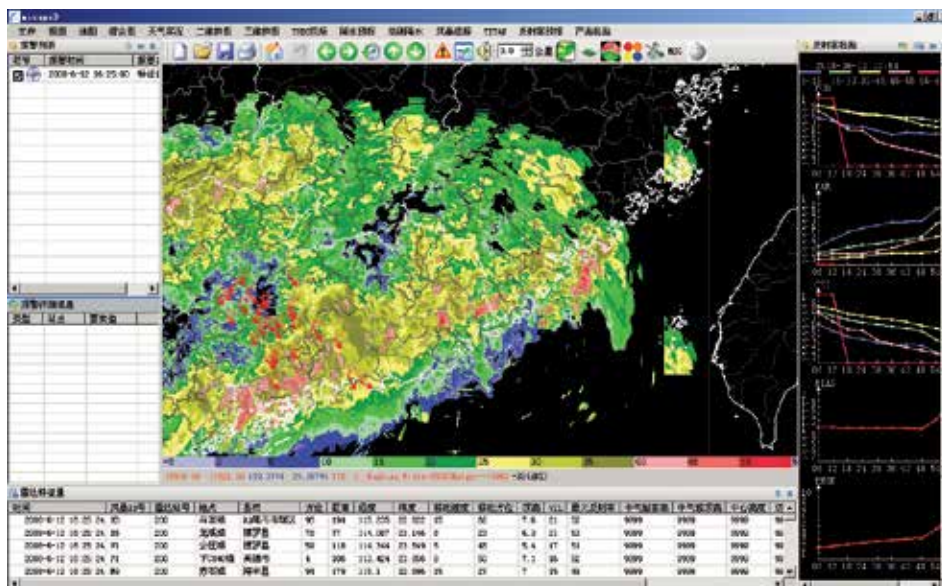


Fig. 19. A SWAN display showing cells/tracks (main screen), SCIT (bottom) and time histories of critical parameters (right). There are similarities with WDSS, NinJo and CARDS displays.

7. Conclusion

The objective of this contribution was to provide a broad overview of the use of radar and radar networks for the provision of severe weather warnings and to very briefly describe historical legacies and current practice. The target audience are those NHMS' who might be contemplating developing or enhancing such a service. Weather radar clearly plays a central role in this application. Not discussed are important applications such as nowcasting precipitation, quantitative precipitation estimation, wind retrieval, data assimilation for numerical weather prediction, etc. It also does not address the convective initiation aspects (Roberts et al, 2006; Sun et al, 1991; Sun and Crook, 1994). For a reliable warning service, design, infrastructure (reliable power and telecommunications), support and maintenance are critical and were not discussed in this contribution. These are major considerations but out of scope for this contribution.

The level and nature of the service will be determined by both meteorological and non-meteorological factors. The prevalence of severe weather, climatology and a defining event determine the impact, the exposure and the opportunity to develop a warning service. Socio-economic factors, risk persona, as well as the organizational structure, are particularly important in the design and expectations for the radar processing, visualization and dissemination systems. This contribution provided a short global survey of radar based systems to illustrate the commonality but also the differences in implementation. One solution does not fit all. Underlying these systems is the forecast process and it is emphasized that they all rely on human expertise in the decision-making process and so the human-machine mix is a critical item. This will drive the expertise and therefore the training requirements for the severe weather analyst.

This contribution highlighted the use of automation in the production of guidance products. Some systems rely on very little automation and totally rely on manual interpretation. All systems, except one, default to this mode. One of most highly automated systems is CARDS (Canada). Automation is necessary because of the need for look at details for warning preparation purposes while maintaining situational awareness in the situation where one forecaster is responsible for about ten radars. It processes radar data for identifying and ranking thunderstorm cells and features. It also creates highly processed image products to streamline and to guide the decision-making process. It still relies on human decision-making for the final preparation of the warning. KONRAD is the only system that produces totally automated products. However, it could be argued that these products are directed to "sophisticated users" for their specific planning and decision-making purposes and not warning purposes.

Given the limited space and time, all radar processing systems were inadequately described. There is room for improvement in describing all aspects of the processing chain from better algorithms (e.g. hail, hook echoes; Lemon, 1998; Wang et al, 2011) to advanced concepts where thermodynamic diagnostic fields, useful for understanding, are retrieved (Sun et al, 1991; Sun and Crook, 1994). Through the description of specific innovative aspects of individual systems, and since there are commonalities amongst them, the intent was to provide the reader with an overview of the capabilities of all the systems. There is fine work being done elsewhere that is not represented; to name a few, Italy, Switzerland and Finland. Another glaring oversight is the lack of description of systems by manufacturers. Some even

offer the possibility for the NHMS to add their own specialized products into their systems. Many of the countries mentioned above in fact use a combination of products from their own systems and those of the manufacturers. Information is readily available in trade shows or on their web sites. The ideal requirement is a seamless, user-friendly integrated visualization, decision-making and production system to cover all scales (the seamless prediction concept) and this is the trend in many NHMS' for all data, products and so radar only processing or visualization systems are an interim step towards this and requires investment, resources, time and effort to achieve. NinJo and AWIPS (not described here) provides an example of how radar is expected to be integrated into a comprehensive forecast analysis, diagnosis, prognosis and production tool.

The purpose of this contribution was to illustrate the issues faced by NHMS's. There is a push to use meteorological technology as much as possible and to automate as much as possible. Computing technology is still a limiting factor – computers, telecommunications and data/product storage are all continuing issues that can always be faster and bigger. If there is the time, the resources and the expertise, manual interpretation of basic radar products is still the best way to provide severe weather warning services and to optimally utilize the considerable capabilities of the forecasters. However, tools are needed to streamline and accelerate the process but this is highly dependent on organizational factors. Automated products introduce another level of complexity and knowledge requirement. They can be black boxes that bewilder the user. However, creating black boxes without diagnostic capabilities, providing poor tools and denying access to basic products and information, is self-defeating. It is a sure way of making smart people (appear) “dumb”. The algorithms aren't perfect given the need for high POD. They never will be and they can be better and substantial work on data quality, feature detection and prediction are needed. The systems described exhibit the great efforts and resources are expended to do this. Saving a single button click or a mouse movement can make the difference between a bad and a good system. This is difficult to describe as a requirement and prototyping and demonstration projects are the only way to appreciate this.

While reliable weather radars and expertise play a central role in the warning process, this is still a challenge for many countries. Satellite and lightning systems are now available that have minimal support requirements. Stand alone applications for severe weather can and are being developed for these system. In the absence of radars, there is no question that they will provide benefits but their efficacy, the forecast process and the service level for severe weather warnings need to be demonstrated. No doubt that they should also enhance existing systems that rely on weather radar networks. This is occurring but beyond the scope of this contribution. No convective scale warning service has been solely developed without radar and so this is a new area to investigate. Understanding the technology, interpretation of the data and the products will require more development, enhanced expertise, demonstration and decision-making skills.

For the convective weather problem, dual-polarization radar will have benefits in data quality, hail detection and rainfall estimation but this is again beyond the scope of this contribution (Frame et al, 2009). Earth curvature and beam propagation preclude low level detection and so many of the hazardous phenomena are not actually measured beyond a few tens of kilometer from the radar site and must therefore be inferred from measurements aloft. The CASA (Cooperative Adapting and Sensing of the Atmosphere) is a network of X

Band radars that address this issue but it is in early-transitional development (McLaughlin et al, 2009; Ruzanski et al, 2011). It also addresses the issue of rapid or adapting scan strategies (Heinselman et al, 2008) which is being investigated now but beyond the scope of this contribution. In any case, with increasing computing power, telecommunications, additional observations and new technology, these are exciting times.

8. References

- AMS, 2001: Expectations Concerning Media Performance during Severe Weather Emergencies (Adopted by the AMS Council 14 January 2001), Bulletin of the American Meteorological Society, 2001: Volume 82, Issue 4 705-70.
- Albers S., J. McGinley, D. Birkenheuer, and J. Smart 1996: The Local Analysis and Prediction System (LAPS): Analyses of clouds, precipitation, and temperature, *Wea. Forecasting*, 11, 273-287.
- Andra Jr., D. L., E. M. Quetone, W. F. Bunting, 2002: Warning Decision Making: The Relative Roles of Conceptual Models, Technology, Strategy, and Forecaster Expertise on 3 May 1999, *Weather and Forecasting*, Volume 17, Issue 3 (June 2002) 559-566.
- Bally, J., 2004: The Thunderstorm Interactive Forecast System: Turning Automated Thunderstorm Tracks into Severe Weather Warnings, *Weather and Forecasting*, Volume 19, Issue 1 (February 2004) 64-7.
- Barnes, L. R., E. C. Grunfest, M. H. Hayden, D. M. Schultz, C. Benight, 2007: False Alarms and Close Calls: A Conceptual Model of Warning Accuracy, *Weather and Forecasting*, Volume 22, Issue 5 (October 2007) 1140-114.
- Baumgart, L. A., E. J. Bass, B. Philips, K. Kloesel, 2008: Emergency Management Decision Making during Severe Weather, *Weather and Forecasting*, Volume 23, Issue 6 (December 2008) 1268-127.
- Bech, J., Vilaclara E., Pineda, N., Rigo, T., Lopez, J., O'Hora, F., Lorente, J., Sempere, D., Fabregas F.X., 2004: The weather radar network of the Catalan meteorological service: description and applications, ERAD, Visby, Sweden, 416-420.
- Bellon, A. and G. L. Austin, 1978: The Evaluation of Two Years of Real-Time Operation of a Short-Term Precipitation Forecasting Procedure (SHARP), *Journal of Applied Meteorology*, Volume 17, Issue 12, 1778-1787.
- Bieringer, P., P. S. Ray, 1996: Comparison of Tornado Warning Lead Times with and without NEXRAD Doppler Radar, *Weather and Forecasting*, Volume 11, Issue 1 (March 1996) 47-5.
- Black, A. W., W. S. Ashley, 2011: The Relationship between Tornadic and Nontornadic Convective Wind Fatalities and Warnings, *Weather, Climate, and Society*, Volume 3, Issue 1 (January 2011) 31-4.
- Branick, M. L., C. A. Doswell III, 1992: Polarity, An Observation of the Relationship between Supercell Structure and Lightning Ground-Strike, *Weather and Forecasting*, Volume 7, Issue 1) 143-14.
- Breidenbach, J. P., D. H. Kitzmiller, W. E. McGovern, R. E. Saffle, 1995: The Use of Volumetric Radar Reflectivity Predictors in the Development of a Second-Generation Severe Weather Potential Algorithm, *Weather and Forecasting*, Volume 10, Issue 2 (June 1995) 369-37.

- Brooks, H. E., C. A. Doswell III, J. Cooper, 1994: On the Environments of Tornadoic and Nontornadoic Mesocyclones, *Weather and Forecasting*, Volume 9, Issue 4 (December 1994) 606-61.
- Brooks, H. E., C. A. Doswell III, L. J. Wicker, 1993: STORMTIPE: A Forecasting Experiment Using a Three-Dimensional Cloud Model, *Weather and Forecasting*, Volume 8, Issue 3 (September 1993) 352-36.
- Brooks, H. E., C. A. Doswell III, R. B. Wilhelmson, 1994: The Role of Midtropospheric Winds in the Evolution and Maintenance of Low-Level Mesocyclones, *Monthly Weather Review*, Volume 122, Issue 1 (January 1994) 126-13.
- Brovelli, P., S. S en esi, E. Arbogast, P. Cau, S. Cazabat, M. Bouzom, J. Reynaud, 2005: Nowcasting thunderstorms with SIGOONS. A significant weather object oriented nowcasting system, M et eo-France, Toulouse, France, WSN05
- Brown, R. A., J. M. Janish, V. T. Wood, 2000: Impact of WSR-88D Scanning Strategies on Severe Storm Algorithms, *Weather and Forecasting*, Volume 15, Issue 1 (February 2000) 90-10.
- Brunner, J. C., S. A. Ackerman, A. S. Bachmeier, R. M. Rabin, 2007: A Quantitative Analysis of the Enhanced-V Feature in Relation to Severe Weather, *Weather and Forecasting*, Volume 22, Issue 4 (August 2007) 853-87.
- Burgess, D. W., R. J. Donaldson JR., and P. R. Desrochers, 1993: Tornado detection and warning by radar. *The Tornado: Its Structure, Dynamics, Prediction, and Hazards*, Geophys. Monogr., No. 79, Amer. Geophys. Union, 203-221.
- Byko, Z., P. Markowski, Y. Richardson, J. Wurman, E. Adelman, 2009: Descending Reflectivity Cores in Supercell Thunderstorms Observed by Mobile Radars and in a High-Resolution Numerical Simulation, *Weather and Forecasting*, Volume 24, Issue 1 (February 2009) 155-18.
- Chisholm, A. J. and J. Renick, 1972: The kinematics of multicell and supercell Alberta hailstorms, *Alberta Hail Studies*, 1972, Research Council of Alberta Hail Studies Rep. No. 72-2, 24-31.
- Crane, R. K., 1979: Automatic cell detection and tracking. *IEEE, Trans. Geosci. Electron.*, GE-17, 250-262.
- Crum, T. D. and R. L. Alberty, 1993: The WSR-88D and the WSR-88D Operational Support Facility, *Bulletin of the American Meteorological Society*, Volume 74, Issue 9, 1669-1687.
- Dance, S., E. Ebert, D. Scurrah, 2010: Thunderstorm Strike Probability Nowcasting, *Journal of Atmospheric and Oceanic Technology*, Volume 27, Issue 1) 79-9.
- Dance, S., R. Potts, 2002: Microburst Detection Using Agent Networks, *Journal of Atmospheric and Oceanic Technology*, Volume 19, Issue 5) 646-65.
- Davis, C., N. Atkins, D. Bartels, L. Bosart, M. Coniglio, G. Bryan, W. Cotton, D. Dowell, B. Jewett, R. Johns, D. Jorgensen, J. Knievel, K. Knupp, W. C. Lee, G. Mcfarquhar, J. Moore, R. Przybylinski, R. Rauber, B. Smull, R. Trapp, S. Trier, R. Wakimoto, M. Weisman, C. Ziegler, 2004: The Bow Echo and MCV Experiment: Observations and Opportunities, *Bulletin of the American Meteorological Society*, Volume 85, Issue 8 (August 2004) 1075-1093
- Dixon, M. and G. Weiner, 1993: TITAN, Thunderstorm Identification, Tracking, Analysis and Nowcasting - A Radar-based Methodology, *JAOT*, 10, 785-797.

- Donaldson, Jr., Ralph J., P. R. Desrochers, 1990: Improvement of Tornado Warnings by Doppler Radar Measurement of Mesocyclone Rotational Kinetic Energy, *Weather and Forecasting*, Volume 5, Issue 2 (June 1990) 247-25.
- Doswell III, C. A., 1980: Synoptic-Scale Environments Associated with High Plains Severe Thunderstorms, *Bulletin of the American Meteorological Society*, Volume 61, Issue 11 (November 1980) 1388-1400.
- Doswell, C. A. III, 1982: The operational meteorology of convective weather, Volume I: Operational Mesoanalysis, NOAA Tech Memo ERL NSSFC-5, 168p.
- Doswell, C. A. III, 1985: The operational meteorology of convective weather, Volume II: Storm Scale Analysis, NOAA Tech Memo ERL ESG-15, 240p.
- Doswell III, C. A., 2001: Severe Convective Storms, *Meteorological Monographs*, Volume 28, 561pp.
- Doswell III, C. A. 2004: Weather Forecasting by Humans – Heuristics and Decision Making. *Weather and Forecasting* 19:6, 1115-112.
- Doswell III, C. A., R. Davies-Jones, D. L. Keller, 1990: On Summary Measures of Skill in Rare Event Forecasting Based on Contingency Tables, *Weather and Forecasting*, Volume 5, Issue 4 (December 1990) 576-58.
- Doswell III, C. A., R. Edwards, R. L. Thompson, J. A. Hart, K. C. Crosbie, 2006: A Simple and Flexible Method for Ranking Severe Weather Events, *Weather and Forecasting*, Volume 21, Issue 6 (December 2006) 939-95.
- Doswell III, C. A., A. R. Moller, H. E. Brooks, 1999: Storm Spotting and Public Awareness since the First Tornado Forecasts of 1948, *Weather and Forecasting*, Volume 14, Issue 4 (August 1999) 544-557.
- Doviak, R. J., and D. S. Zrnica, 1984: *Doppler Radar and weather observations*, Academic Press, 458p.
- Dunn, L. B., 1990: Two Examples of Operational Tornado Warnings Using Doppler Radar Data, *Bulletin of the American Meteorological Society*, Volume 71, Issue 2 (February 1990) 145-15.
- Ebert, E. E., L. J. Wilson, B. G. Brown, P. Nurmi, H. E. Brooks, J. Bally, M. Jaeneke, 2004: Verification of Nowcasts from the WWRP Sydney 2000 Forecast Demonstration Project, *Weather and Forecasting*, Volume 19, Issue 1 (February 2004) 73-96
- Eilts, M. D., and Coauthors, 1996: Severe weather warning decision support system. Preprints, 18th Conf. on Severe Local Storms, San Francisco, CA, Amer. Meteor. Soc., 536-540.
- Evans, J. S., C. A. Doswell III, 2001: Examination of Derecho Environments Using Proximity Soundings, *Weather and Forecasting*, Volume 16, Issue 3 (June 2001) 329-34.
- Fawbush, E. J. and R. C. Miller, 1953: Forecasting Tornadoes, *USAF Air University Quarterly Review*, 1, 108-11.
- Fox, Neil I., R. Webb, J. Bally, M. W. Sleigh, C. E. Pierce, D. M. L. Sills, P. I. Joe, J. Wilson, C. G. Collier, 2004: The Impact of Advanced Nowcasting Systems on Severe Weather Warning during the Sydney 2000 Forecast Demonstration Project: 3 November 2000, *Weather and Forecasting*, Volume 19, Issue 1 (February 2004) 97-114
- Frame, J., P. Markowski, Y. Richardson, J. Straka, J. Wurman, 2009: Polarimetric and Dual-Doppler Radar Observations of the Lipscomb County, Texas, Supercell Thunderstorm on 23 May 2002, *Monthly Weather Review*, Volume 137, Issue 2 (February 2009) 544-56.

- Galway, J. G., 1989: The Evolution of Severe Thunderstorm Criteria within the Weather Service, *Weather and Forecasting*, Volume 4, Issue 4 (December 1989) 585-59.
- Gatlin, P. N., S. J. Goodman, 2010: A Total Lightning Trending Algorithm to Identify Severe Thunderstorms, *Journal of Atmospheric and Oceanic Technology*, Volume 27, Issue 1 (January 2010) 3-22.
- Glahn, B., 2005: Tornado-Warning Performance in the Past and Future—Another Perspective, *Bulletin of the American Meteorological Society*, Volume 86, Issue 8 (August 2005) 1135-114.
- Goodman, S. J., D. E. Buechler, P. J. Meyer, 1988: Convective Tendency Images Derived from a Combination of Lightning and Satellite Data, *Weather and Forecasting*, Volume 3, Issue 3 (September 1988) 173-188.
- Hammer, B., T. W. Schmidlin, 2002: Response to Warnings during the 3 May 1999 Oklahoma City Tornado: Reasons and Relative Injury Rates, *Weather and Forecasting*, Volume 17, Issue 3 (June 2002) 577-58.
- Heinselman, P. L., D. L. Prieognitz, K. L. Manross, T. M. Smith, R. W. Adams, 2008: Rapid Sampling of Severe Storms by the National Weather Radar Testbed Phased Array Radar, *Weather and Forecasting*, Volume 23, Issue 5 (October 2008) 808-824.
- Hengstebeck, T., D. Heizenreder, P. Joe, P. Lang, 2011: The Mesocyclone Detection Algorithm of DWD, 6th European Conference on Severe Storms, ECSS, 3-7 October 2011, Palma de Mallorca
- Hermes, L. G., A. Witt, S. D. Smith, D. Klinge-Wilson, D. Morris, G. J. Stumpf, M. D. Eilts, 1993: The Gust-Front Detection and Wind-Shift Algorithms for the Terminal Doppler Weather Radar System, *Journal of Atmospheric and Oceanic Technology*, Volume 10, Issue 5 (October 1993) 693-70.
- Hering, A. M., S. Senesi, P. Ambrosetti and I. Bernard-Bouissieres, 2005: Nowcasting thunderstorms in complex cases using radar data, WMO Symposium on Nowcasting and Very Short Range Forecasting, Toulouse France, paper 2. 14.
- Hoekstra, S., K. Klockow, R. Riley, J. Brotzge, H. Brooks, S. Erickson, 2011: A Preliminary Look at the Social Perspective of Warn-on-Forecast: Preferred Tornado Warning Lead Time and the General Public's Perceptions of Weather Risks, *Weather, Climate, and Society*, Volume 3, Issue 2 (April 2011) 128-14.
- Holleman, I. and H. Beekhuis, 2003: Analysis and correction of dual PRF velocity data, *JAOT*, 20(4), 443-453.
- Honda, Y., M. Nishijima, K. Koizumi, Y. Ohta, K. Tamiya, T. Kawabata and T. Tsuyuki, 2005: A pre-operational variational data assimilation system for a non-hydrostatic model at the Japan Meteorological Agency: Formulation and preliminary results. *Quart. J. Roy. Meteor. Soc.*, 131, 3465-3475.
- James, P. M., S. Treple, D. Heizenreder and B. K. Reichert, 2011: NowCastMIX – A fuzzy logic based tool for providing automatic integrated nowcasting systems, 11th EMS Annual Meeting, 10th European Conference on Applications of Meteorology, 12-16 Sept 2011., EMS2011-234,
- Joe, P., 2009: A First Look at Radar Data Quality for the Beijing 2008 Forecast Demonstration Project, in *Collection of Papers on the New Generation of China Radars*, (Xin Yi Dai, Tian Qi Leida Yewu Yingyoung Lunwenji, ISBN 978-7-5029-4468-1), edited by Xiaoding Yu (invited lead paper).

- Joe, P., D. Burgess, R. Potts, T. Keenan, G. Stumpf, A. Treloar, 2004: The S2K Severe Weather Detection Algorithms and Their Performance, *Weather and Forecasting*, Volume 19, Issue 1, 43-63.
- Joe, P., M. Falla, P. Van Rijn, L. Stamadianos, T. Falla, D. Magosse, L. Ing and J. Dobson, 2002: Radar Data Processing for Severe Weather in the National Radar Project of Canada, SELS, San Antonio, 12-16 August 2002, 221-224.
- Joe, P., P. T. May, 2003: Correction of Dual PRF Velocity Errors for Operational Doppler Weather Radars, *Journal of Atmospheric and Oceanic Technology*, Volume 20, Issue 4 (April 2003) 429-44.
- Johns, R. H., C. A. Doswell III, 1992: Severe Local Storms Forecasting, *Weather and Forecasting*, Volume 7, Issue 4 (December 1992) 588-61.
- Johnson, J. T., P. L. MacKeen, A. Witt, E. De W. Mitchell, G. J. Stumpf, M. D. Eilts, K. W. Thomas., 1998: The Storm Cell Identification and Tracking Algorithm: An Enhanced WSR-88D Algorithm, *Weather and Forecasting*, Volume 13, Issue 2, 263-27.
- Keenan, T., P. Joe, J. Wilson, C. Collier, B. Golding, D. Burgess, P. May, C. Pierce, J. Bally, A. Crook, A. Seed, D. Sills, L. Berry, R. Potts, I. Bell, N. Fox, E. Ebert, M. Eilts, K. O'Loughlin, R. Webb, R. Carbone, K. Browning, R. Roberts, C. Mueller, 2004: The Sydney 2000 World Weather Research Programme Forecast Demonstration Project: Overview and Current Status, *Bulletin of the American Meteorological Society*, Volume 84, Issue 8, 1041-1054.
- Kessler, E., J. W. Wilson, 1971: Radar in an Automated National Weather System, *Bulletin of the American Meteorological Society*, Volume 52, Issue 11, 1062-106.
- King, P. W. S., M. J. Leduc, D. M. L. Sills, N. R. Donaldson, D. R. Hudak, P. Joe, B. P. Murphy, 2003: Lake Breezes in Southern Ontario and Their Relation to Tornado Climatology, *Weather and Forecasting*, Volume 18, Issue 5 (October 2003) 795-807.
- Kitzmilller, D. H., W. E. McGovern, R. F. Saffle, 1995: The WSR-88D Severe Weather Potential Algorithm, *Weather and Forecasting*, Volume 10, Issue 1 (March 1995) 141-15.
- Klinge, D. L., D. R. Smith, M. M. Wolfson, 1987: Gust Front Characteristics as Detected by Doppler Radar, *Monthly Weather Review*, Volume 115, Issue 5 (May 1987) 905-91.
- Knupp, K. R., S. Paech, S. Goodman, 2003: Variations in Cloud-to-Ground Lightning Characteristics among Three Adjacent Tornadic Supercell Storms over the Tennessee Valley Region, *Monthly Weather Review*, Volume 131, Issue 1 (January 2003) 172-188
- Koppert, H. -J., Pedersen, T. S., Zuercher, B., Joe, P., 2004: How to make an international Meteorological Workstation project successful, *BAMS*, 1087-109.
- Lakshmanan, J. T. ., A. Fritz, T. Smith, K. Hondl, and G. J. Stumpf, 2007: An automated technique to quality control radar reflectivity data, *J. Applied Meteorology*, vol. 46, 288-305.
- Lakshmanan, V., K. Hondl, and R. Rabin, 2009: An efficient, general-purpose technique for identifying storm cells in geospatial images, *J. Ocean. Atmos. Tech.*, vol. 26, no. 3, 523-37.
- Lakshmanan, V., R. Rabin, and V. DeBrunner, 2003: Multiscale storm identification and forecast, *J. Atm. Res.*, vol. 67, 367-380.
- Lakshmanan, V. and T. Smith, 2009: Data mining storm attributes from spatial grids, *J. Ocea. and Atmos. Tech.*, vol. 26, no. 11, 2353-2365.

- Lakshmanan, V. and T. Smith, 2010: An Objective Method of Evaluating and Devising Storm-Tracking Algorithms, *Weather and Forecasting*, Volume 25, 701-709.
- Lakshmanan, V., T. Smith, K. Hondl, G. J. Stumpf, A. Witt, 2006: A Real-Time, Three-Dimensional, Rapidly Updating, Heterogeneous Radar Merger Technique for Reflectivity, Velocity, and Derived Products, *Weather and Forecasting*, Volume 21, Issue 5, 802-82.
- Lakshmanan, V., T. Smith, G. Stumpf, K. Hondl, 2007: The Warning Decision Support System-Integrated Information, *Weather and Forecasting*, Volume 22, Issue 3, 596-61.
- Lakshmanan, V., J. Zhang, K. Hondl, and C. Langston, 2011: A statistical approach to mitigating persistent clutter in radar reflectivity data, *IEEE J. Selected Topics in Applied Earth Observations and Remote Sensing*, vol. s, p. accepted.
- Lakshmanan, V., J. Zhang, and K. Howard, 2010, A technique to censor biological echoes in radar reflectivity data, *J. Applied Meteorology*, vol. 49, 435-462.
- Lang, P., 2001: Cell tracking and warning indicators derived from operational radar products, 30th International Radar Conference, AMS, Munich, Germany, 245-247.
- Lang, T. J., L. J. Miller, M. Weisman, S. A. Rutledge, L. J. Barker III, V. N. Bringi, V. Chandrasekar, A. Detwiler, N. Doesken, J. Helsdon, C. Knight, P. Krehbiel, Walter A. Lyons, D. Macgorman, E. Rasmussen, W. Rison, W. D. Rust, Ronald J. T., 2004: The Severe Thunderstorm Electrification and Precipitation Study, *Bulletin of the American Meteorological Society*, Volume 85, Issue 8 (August 2004) 1107-1125
- Lapczak, S., E. Aldcroft, M. Stanley-Jones, J. Scott, P. Joe, P. Van Rijn, M. Falla, A. Gagne, P. Ford, K. Reynolds and D. Hudak, 1999: The Canadian National Radar Project, 29th Conf. Radar Met., Montreal, AMS, 327-330.
- Leduc, M., P. Joe, M. Falla, P. Van Rijn, S. Lapczak, I. Ruddick, A. Ashton and R. Alsen, 2002: The July 4 2001 Severe Weather Outbreak in Southern Ontario as Diagnosed by the New Radar Data Processing System of the National Radar Project of Canada, SELS, San Antonio, 12-16 August 2002, 170-173.
- Lei H., S. Fu, L. Zhao, Y. Zheng, H. Wang and Y. Lin, 2009: 3D Convective Storm Identification, Tracking, and Forecasting – An Enhanced TITAN Algorithm, *Journal of Atmospheric and Oceanic Technology*, 2009: Volume 26, Issue 4) 719-73.
- Lemon, L. R., 1977: new severe thunderstorm radar identification techniques are warning criteria: a preliminary report, NWS NSSFC-1, PB 273049 60p.
- Lemon, L. R., 1980: new severe thunderstorm radar identification techniques are warning criteria, NWS NSSFC-1, PB 231409 60p.
- Lemon, L. R., 1998: The Radar “Three-Body Scatter Spike”: An Operational Large-Hail Signature, *Weather and Forecasting*, Volume 13, Issue 2 (June 1998) 327-34.
- Lemon, L. R., Ralph J. Donaldson, Jr., D. W. Burgess, R. A. Brown, 1977: Doppler Radar Application to Severe Thunderstorm Study and Potential Real-Time Warning, *Bulletin of the American Meteorological Society*, Volume 58, Issue 11, 1187-119.
- Lemon, L. R., C. A. Doswell III, 1979: Severe Thunderstorm Evolution and Mesocyclone Structure as Related to Tornadogenesis, *Monthly Weather Review*, Volume 107, Issue 9 (September 1979) 1184-119.
- Lenning, E., H. E. Fuelberg, A. I. Watson, 1998: An Evaluation of WSR-88D Severe Hail Algorithms along the Northeastern Gulf Coast, *Weather and Forecasting*, Volume 13, Issue 4 (December 1998) 1029-104.

- Li, P.W. 2009: Development of a thunderstorm nowcasting system for Hong Kong International Airport, AMS Aviation, Range, Aerospace Meteorology Special Symposium on Weather-Air Traffic Management Integration, Phoenix, Arizona, 11-15 Jan 2009.
- Li, P. W. and W.K. Wong, 2010: Development of an Advanced Aviation Nowcasting System by Including Rapidly Updated NWP Model in Support of Air Traffic Management, Proceedings 14th Conference on Aviation, Range and Aerospace Meteorology, Atlanta, Georgia, USA, 17-21 January 2010.
- Li, L., W. Schmid and J. Joss, 1995: Nowcasting of motion and growth of precipitation with radar over a complex orography, *JAM*, 34(6), 1286-1300
- Li, P. W. and S. T. Lai, 2004: Applications of radar-based nowcasting techniques for mesoscale weather forecasting in Hong Kong, *Meteorological Applications*, 11, 253-264.
- Li, P. W. and S. T. Lai, 2004a: Short-range quantitative precipitation forecasting in Hong Kong, *Journal of Hydrology*, 288, 189-209.
- Li, P.W., W.K. Wong and E.S.T. Lai, 2005: A New Thunderstorm Nowcasting System in Hong Kong, WMO/WWRP International Symposium on Nowcasting and Very-short-range Forecasting, Toulouse, France, 5-9 Sep. 2005.
- Markowski, P. M., 2002: Hook Echoes and Rear-Flank Downdrafts: A Review, *Monthly Weather Review*, Volume 130, Issue 4 (April 2002) 852-87.
- Markowski, P. M., E. N. Rasmussen, J. M. Straka, 1998a: The Occurrence of Tornadoes in Supercells Interacting with Boundaries during VORTEX-95, *Weather and Forecasting*, Volume 13, Issue 3 (September 1998) 852-85.
- Markowski, P. M., J. M. Straka, E. N. Rasmussen, D. O. Blanchard, 1998b: Variability of Storm-Relative Helicity during VORTEX, *Monthly Weather Review*, Volume 126, Issue 11 (November 1998) 2959-297.
- Marshall, J. S. and E. H. Ballantyne, 1975: Weather Surveillance Radar, *J. A. M.*, 14, 1317-1338.
- May, P. T., T. D. Keenan, R. Potts, J. W. Wilson, R. Webb, A. Treloar, E. Spark, S. Lawrence, E. Ebert, J. Bally, P. Joe, 2004: The Sydney 2000 Olympic Games Forecast Demonstration Project: Forecasting, Observing Network Infrastructure, and Data Processing Issues, *Weather and Forecasting*, Volume 19, Issue 1, 115-130.
- McCarthy, J., J. W. Wilson, T. T. Fujita, 1982: The Joint Airport Weather Studies Project, *Bulletin of the American Meteorological Society*, Volume 63, Issue 1) 15-1.
- McLaughlin, D., D. Pepyne, B. Philips, J. Kurose, M. Zink, D. Westbrook, E. Lyons, E. Knapp, A. Hopf, A. Defonzo, R. Contreras, T. Djaferis, E. Insanic, S. Frasier, V. Chandrasekar, F. Junyent, N. Bharadwaj, Y. Wang, Y. Liu, B. Dolan, K. Droegemeier, J. Brotzge, M. Xue, K. Kloesel, K. Brewster, F. Carr, S. Cruz-Pol, K. Hondl, P. Kollias, 2009: Short-Wavelength Technology and the Potential For Distributed Networks of Small Radar Systems, *Bulletin of the American Meteorological Society*, Volume 90, Issue 12, 1797-1817.
- Melnikov, V. M., D. W. Burgess, D. L. Andra JR., M. P. Foster, J. M. Krause, 2005: K. A. Scharfenberg, D. J. Miller, Terry J. Schuur, P. T. Schlatter, Scott E. Giangrande, 2005: The Joint Polarization Experiment: Polarimetric Radar in Forecasting and Warning Decision Making, *Weather and Forecasting*, Volume 20, 775-78.

- Mercer, A. E., Chad M. Shafer, C. A. Doswell III, Lance M. L., M. B. Richman, 2009: Objective Classification of Tornadoic and Nontornadoic Severe Weather Outbreaks, *Monthly Weather Review*, Volume 137, Issue 12 (December 2009) 4355-436.
- Mitchell, E. De W., S. V. Vasiloff, G. J. Stumpf, A. Witt, M. D. Eilts, J. T. Johnson, K. W. T., 1998: The National Severe Storms Laboratory Tornado Detection Algorithm, *Weather and Forecasting*, Volume 13, Issue 2, 352-36.
- Moller, A. R., 1978: The Improved NWS Storm Spotters' Training Program at Ft. Worth, Tex., *Bulletin of the American Meteorological Society*, Volume 59, Issue 12 (December 1978) 1574-1582
- Moller, A. R., 2001: Severe Local Storms Forecasting, *Meteorological Monographs*, Volume 28, Issue 50 (November 2001) 433-480
- Moller, A. R., C. A. Doswell III, M. P. Foster, G. R. Woodall, 1994: The Operational Recognition of Supercell Thunderstorm Environments and Storm Structures, *Weather and Forecasting*, Volume 9, Issue 3, 327-347
- Moninger, W. R., C. Lusk, W. F. R. s, J. Bullas, B. de Lorenzis, J. C. McLeod, E. Ellison, J. Flueck, P. D. Lampru, K. C. Young, J. Weaver, R. S. Philips, R. Shaw, T. R. Stewart, S. M. Zubrick, 1991: Shootout-89, A Comparative Evaluation of Knowledge-based Systems That Forecast Severe Weather, *Bulletin of the American Meteorological Society*, Volume 72, Issue 9 (September 1991) 1339-1354.
- Monteverdi, J. P., C. A. Doswell III, G. S. Lipari, 2003: Shear Parameter Thresholds for Forecasting Tornadoic Thunderstorms in Northern and Central California, *Weather and Forecasting*, Volume 18, Issue 2 (April 2003) 357-37.
- O'Hara, Fritz and Joan Bech, 2007: Improving weather radar observations using pulse-compression techniques, *Meteorological Applications*, 14, 389-401.
- Pliske, R., D. Klinger, R. Hutton, B. Crandall, B. Knight, and G. Klein, 1997: Understanding skilled weather forecasting: Implications for training and the design of forecasting tools. Contractor Rep. AL/HR-CR-1997-003, Material Command, Armstrong Laboratory, U. S. Air Force, 122
- Polger, P. D., B. S. Goldsmith, R. C. Przywarty, J. R. Bocchieri, 1994: National Weather Service Warning Performance Based on the WSR-88D, *Bulletin of the American Meteorological Society*, Volume 75, Issue 2 (February 1994) 203-21.
- Przybylinski, R. W., 1995: The Bow Echo: Observations, Numerical Simulations, and Severe Weather Detection Methods, *Weather and Forecasting*, Volume 10 (2) 203-21.
- Rasmussen. E. N., 2003: Refined Supercell and Tornado Forecast Parameters. *Weather and Forecasting* 18:3, 530-53.
- Rasmussen, E. N., J. M. Straka, R. Davies-Jones, C. A. Doswell III, F. H. Carr, M. D. Eilts, D. R. MacGorman, 1994: Verification of the Origins of Rotation in Tornadoes Experiment: VORTEX, *Bulletin of the American Meteorological Society*, Volume 75, Issue 6 (June 1994) 995-100.
- Ruzanski, E., V. Chandrasekar, Y. Wang, 2011: The CASA Nowcasting System. *Journal of Atmospheric and Oceanic Technology*, 28, 640-65.
- Roberts, Rita D., D. Burgess, M. Meister, 2006: Developing Tools for Nowcasting Storm Severity, *Weather and Forecasting*, Volume 21, 540-55.
- Saffle, R. E., 1976: D/RADEX products and field operation. 17th Conf. on Radar Meteorology, Seattle, AMS, Boston, MA., 555-559.

- Schaefer, J. T., 1990: The Critical Success Index as an Indicator of Warning Skill, *Weather and Forecasting*, Volume 5, 570-57.
- Schmeits, M. J., Kees J. Kok, D. H. P. Voegelezang, R. M. van Westrheden, 2008: Probabilistic Forecasts of (Severe) Thunderstorms for the Purpose of Issuing a Weather Alarm in the Netherlands, *Weather and Forecasting*, Volume 23, Issue 6 (December 2008) 1253-126.
- Schultz, C. J., W. A. Petersen, L. D. Carey, 2011: Lightning and Severe Weather: A Comparison between Total and Cloud-to-Ground Lightning Trends, *Weather and Forecasting*, Volume 26, Issue 5 (October 2011) 744-75.
- Schumacher, R. S., D. T. Lindsey, A. B. Schumacher, J. Braun, S. D. Miller, J. L. Demuth, 2010: Multidisciplinary Analysis of an Unusual Tornado: Meteorology, Climatology, and the Communication and Interpretation of Warnings, *Weather and Forecasting*, Volume 25, 1412-142.
- Serafin, R. J., J. W. Wilson, 2000: Operational Weather Radar in the United States: Progress and Opportunity, *Bulletin of the American Meteorological Society*.
- Sills, D. M. L., J. W. Wilson, P. I. Joe, D. W. Burgess, R. M. Webb, N. I. Fox, 2004: The 3 November Tornadic Event during Sydney 2000: Storm Evolution and the Role of Low-Level Boundaries, *Weather and Forecasting*, Volume 19, Issue 1, February 2004) 22-42
- Smith, P. L., 1999: Effects of Imperfect Storm Reporting on the Verification of Weather Warnings, *Bulletin of the American Meteorological Society*, Volume 80, 1099-110.
- Stensrud, D. J., L. J. Wicker, K. E. Kelleher, M. Xue, M. P. Foster, J. T. Schaefer, R. S. Schneider, S. G. Benjamin, S. Weygandt, J. T. Ferree, J. P. Tuell, 2009: Convective-Scale Warn-on-Forecast System, *Bulletin of the American Meteorological Society*, Volume 90, 1487-149.
- Stumpf, G. J., A. Witt, E. DeW. Mitchell, P. Spencer, J. T. Johnson, M. D. Eilts, K. W. Thomas, D. W. Burgess, 1998: The National Severe Storms Laboratory Mesocyclone Detection Algorithm for the WSR-88D, *Weather and Forecasting*, Volume 13, 304-32.
- Sun, J., and N. A. Crook, 1994: Wind and thermodynamic retrieval from single-Doppler measurements of a gust front observed during Phoenix-II. *Mon. Wea. Rev.*, 122, 1075-1091.
- Sun, J., D. Flicker, and D. K. Lilly, 1991: Recovery of three-dimensional wind and temperature from simulated single-Doppler radar data. *J. Atmos. Sci.*, 48, 876-890.
- Uyeda, H. and D. S. Zrnic, 1986: Automatic Detection of Gust Fronts, *Journal of Atmospheric and Oceanic Technology*, Volume 3, 36-5.
- Vasiloff, S. V., 2001: Improving Tornado Warnings with the Federal Aviation Administration's Terminal Doppler Weather Radar, *Bulletin of the American Meteorological Society*, Volume 82, 861-87.
- Wang, H. K., R. Mercer, J. Baron and P. Joe, 2011: Skeleton-based hook echo detection in radar reflectivity data, *J. Tech*, submitted.
- Wang, J. J., T. Keenan, P. Joe, J. Wilson, E. S. T. Lai, F. Liang, Y. Wang, B. Ebert, Q. Ye, J. Bally, A. Seed, M. X. Chen, J. Xue, B. Conway, 2010: Overview of the Beijing 2008 Olympics Forecast Demonstration Project, *China Meteorological Press*, 145pp.

- Wasula, A. C., L. F. Bosart, K. D. LaPenta, 2002: The Influence of Terrain on the Severe Weather Distribution across Interior Eastern New York and Western New England, *Weather and Forecasting*, Volume 17, Issue 6 (December 2002) 1277-1289.
- Weiss, S. J., C. A. Doswell III, F. P. Ostby, 1980: Comments on Automated 12-36 Hour Probability Forecasts of Thunderstorms and Severe Local Storms, *Journal of Applied Meteorology* Volume 19, Issue 11, 1328-1333.
- Weisman, M. L., 2001: Bow Echoes: A Tribute to T. T. Fujita, *Bulletin of the American Meteorological Society*, Volume 82, 97-116
- Weisman, M. L., J. B. Klemp, 1984: The Structure and Classification of Numerically Simulated Convective Storms in Directionally Varying Wind Shears, *Monthly Weather Review*, Volume 112, Issue 12 (December 1984) 2479-2498
- Weisman, M. L., R. Rotunno, 2000: The Use of Vertical Wind Shear versus Helicity in Interpreting Supercell Dynamics, *Journal of the Atmospheric Sciences*, Volume 57, Issue 9 (May 2000) 1452-1472
- Weisman, M. L., R. Rotunno, 2004: "A Theory for Strong Long-Lived Squall Lines" Revisited, *Journal of the Atmospheric Sciences*, Volume 61, Issue 4 (February 2004) 361-382
- Westefeld, J. S., A. R. Less, T. Ansley, H.S. Yi, 2006: Severe-Weather Phobia, *Bulletin of the American Meteorological Society*, 2006: Volume 87, 747-74.
- Wilson, J. W., E. A. Brandes, 1979: Radar Measurement of Rainfall – A Summary, *Bulletin of the American Meteorological Society*, Volume 60, 1048-105.
- Wilson, J., R. Carbone, H. Baynton, R. Serafin, 1980: Operational Application of Meteorological Doppler Radar, *Bulletin of the American Meteorological Society*, Volume 61, 1154-116.
- Wilson, J. W., N. A. Crook, C. K. Mueller, J. Sun, M. Dixon, 1998: Nowcasting Thunderstorms: A Status Report, *Bulletin of the American Meteorological Society*, Volume 79, 2079-209.
- Wilson, J. W., E. E. Ebert, T. R. Saxon, R. D. Roberts, C. K. Mueller, M. Sleigh, C. E. Pierce, A. Seed, 2004: Sydney 2000 Forecast Demonstration Project: Convective Storm Nowcasting, *Weather and Forecasting*, Volume 19, 131-15.
- Wilson, J. W., Y. Feng, Min Chen, Rita D. R. s, 2010: Nowcasting Challenges during the Beijing Olympics: Successes, Failures, and Implications for Future Nowcasting Systems, *Weather and Forecasting*, Volume 25, 1691-171.
- Wilson, J. W., J. A. Moore, G. B. Foote, B. Martner, T. Uttal, J. M. Wilczak, A. R. Rodi, 1988: Convection Initiation and Downburst Experiment (CINDE), *Bulletin of the American Meteorological Society*, Volume 69, 1328-134.
- Wilson, J. W., R. M. Wakimoto, 2001: The Discovery of the Downburst: T. T. Fujita's Contribution, *Bulletin of the American Meteorological Society*, Volume 82, 49-6.
- Winston, H. A., 1998: A Comparison of Three Radar-Based Severe-Storm-Detection Algorithms on Colorado High Plains Thunderstorms, *Weather and Forecasting*, Volume 3, 131-140.
- Winston, H. A., L. J. Ruthi, 1986: Evaluation of RADAP II Severe-Storm-Detection Algorithms, *Bulletin of the American Meteorological Society*, Volume 67, 145-15.
- Witt, A., M. D. Eilts, G. J. Stumpf, J. T. Johnson, E. De W. Mitchell, K. W. T., 1998a: An Enhanced Hail Detection Algorithm for the WSR-88D, *Weather and Forecasting*, Volume 13, 286-30.

- Witt, A., M. D. Eilts, G. J. Stumpf, E. De W. Mitchell, J. T. Johnson, K. W. T., 1998b: Evaluating the Performance of WSR-88D Severe Storm Detection Algorithms, *Weather and Forecasting*, Volume 13, 513-51.
- WMO, 2008: Commission on Instruments, Methods and Observations Guide, Chapter 9, 7th edition, available at <http://www.wmo.int/pages/prog/www/IMOP/publications/CIMO-Guide/CIMO%20Guide%207th%20Edition,%202008/Part%20II/Chapter%209.pdf>
- Wong, W. K., L. H. Y. Yeung, Y. C. Wang & M. Chen, 2009: Towards the Blending of NWP with Nowcast – Operation Experience in B08FDP, WMO Symposium on Nowcasting, 30 Aug-4 Sep 2009, Whistler, B. C., Canada.
- Wong K. Y., C. L. Yip and P. W. Li, 2007: A Novel Algorithm for Automatic Tropical Cyclone Eye Fix Using Doppler Weather Radar, *Meteorological Applications*, 14, 49-5.
- Yeung, L. H. Y., E. S. T. Lai & P. K. Y. Chan, 2008: Thunderstorm Downburst and Radar-based Nowcasting of Squalls, the Fifth European Conference on Radar in Meteorology and Hydrology, Helsinki, Finland 30 June - 4 July 200.
- Yeung, L. H. Y., W. K. Wong, P. K. Y. Chan & E. S. T. Lai, 2009: Applications of the Hong Kong Observatory nowcasting system SWIRLS-2 in support of the 2008 Beijing Olympic Games. WMO Symposium on Nowcasting, 30 Aug-4 Sep 2009, Whistler, B. C., Canada.
- Yeung, L. H. Y., E. S. T. Lai & S. K. S. Chiu, 2007: Lightning Initiation and Intensity Nowcasting Based on Isothermal Radar Reflectivity – A Conceptual Model, the 33rd International Conference on Radar Meteorology, Cairns, Australia, 6-10 August 2007.
- Zipser, E. J., C. Liu, D. J. Cecil, S. W. Nesbitt, D. P. Yorty, 2006: Where are the most intense thunderstorms on Earth?, *BAMS*, 87 (8), 1057-1071.
- Zrnic, D. S., D. W. Burgess, L. D. Hennington, 1985: Automatic Detection of Mesocyclonic Shear with Doppler Radar, *Journal of Atmospheric and Oceanic Technology*, Volume 2, 425-438.

Aviation Applications of Doppler Radars in the Alerting of Windshear and Turbulence

P.W. Chan¹ and Pengfei Zhang²

¹*Hong Kong Observatory, Hong Kong,*

²*University of Oklahoma, Norman, OK,*

¹*China*

²*USA*

1. Introduction

Doppler radars are indispensable nowadays in the assurance of aviation safety. In particular, many airports in the world are equipped with Terminal Doppler Weather Radar (TDWR) in the alerting of low-level windshear and turbulence. The microburst alerts from certain TDWR are taken as “sky truth” and the aircraft may not fly when microburst alerts are in force.

This chapter summarizes some recent developments on the aviation applications of TDWR in Hong Kong (Figure 1). It first starts with a case study of a typical event of microburst alert associated with severe thunderstorms. The applications of TDWR in the alerting of windshear and turbulence are then described, namely, in the calculation of windshear hazard factor using the radial velocity data from the radar, and the calculation of eddy dissipation rate based on the spectrum width data of the radar. It is hoped that this chapter could serve as an introduction to the aviation applications of TDWR, for the reference of the weather services of other airports.

2. A typical microburst event leading to missed approaches of aircraft

The missed approaches at the Hong Kong International Airport (HKIA) took place during the overnight period of 8 to 9 September 2010 when intense thunderstorm activity brought heavy rain and frequent lightning to the whole Hong Kong. During the period, an intense rain band with north-south orientation swept from east to west across Hong Kong. More than 50 millimeters of rainfall in an hour were generally recorded over the territory and a record-breaking number of 13,102 cloud-to-ground lightning strokes were registered during the hour just after midnight. When the thunderstorms edged close to the HKIA which is situated at the western part of the territory, gusty strong easterlies from the downdraft of the thunderstorm first affected the flight paths east of the airport resulting in an abrupt change in the prevailing winds from southwesterlies to easterlies.

Two flights, which tried to land as the thunderstorms approached HKIA, aborted landing and diverted to Macao eventually. Both flights approached the HKIA from the east under the prevailing southwesterly winds (Figure 2). The first aircraft went around twice. The first



Fig. 1. The locations of the Hong Kong TDWR (red dot) radar and Hong Kong International Airport (HKIA). The blue beams illustrate the radar beams over the runways corridor 07LA of the airport with 1° azimuth interval. Three yellow lines indicate the approach paths and their names are marked.



Fig. 2. Flight paths of the two aircraft which had to conduct missed approach. Red line indicated the flight path for the first aircraft and yellow for the second aircraft. Orange wind barbs showed the locations of aircraft when tailwind was encountered. The 1st and 2nd aircraft recorded tailwind of 37 and 22 knots respectively.

aborted landing was due to technical consideration. In the second approach at around 00:08 HKT (=UTC + 8 hours), it encountered strong tailwind. Landing was subsequently aborted and the aircraft diverted to Macao thereafter. Four minutes later, the second aircraft followed the same glide path of the first aircraft but also failed to land at the HKIA because of the same reason, i.e. the strong tailwind. The aircraft was also diverted to Macao at 00:12 HKT.

Flight data retrieved from the flight data recorders of the two aircraft was analyzed to reveal the meteorological conditions encountered by aircrafts. It appeared that the missed approach was attributable to the strong tailwind which exceeded the airline pre-defined threshold, namely 15 knots for tailwind landing.

According to the flight data, the first aircraft experienced more than 15 knots tailwind after it descended to below 1600 feet (Figure 3(a)) in its second approach. The tailwind increased from 25 knots when the aircraft descended to 780 feet (labeled 'A' in Figure 3(a)) and strengthened to 37 knots at 708 feet at 00:08 HKT (labeled 'B' in Figure 3(a)), which far exceed the limit for tailwind landing. As a result, diversion to other airport was conducted.

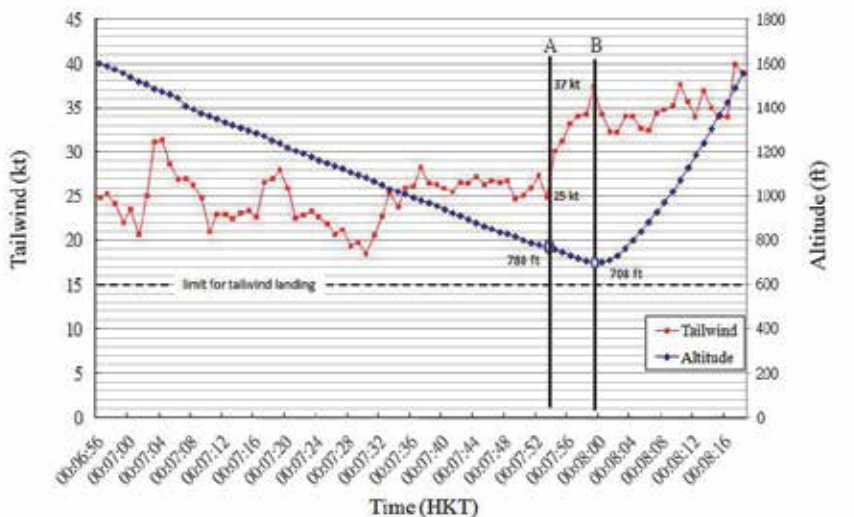
The second aircraft also experienced the tailwind of around 15 knots when it descended to around 1600 feet. The tailwind increased and reached 19 knots when the aircraft descended to 1423 feet (labeled 'C' in Figure 3(b)) but then decreased and fluctuated between 7 to 12 knots when the aircraft further descended to 1028 feet (labeled 'D' in Figure 3(b)). At around 00:12 HKT, the tailwind started to strengthen again and exceeded 15 knots. The maximum tailwind experienced by the aircraft was 22 knots, which also exceeded the limit for tailwind landing, at 859 feet above the runway (labeled 'E' in Figure 3(b)). Similar to the first aircraft, the second aircraft executed a missed approach due to the strong tailwind and was diverted to Macao.

The TDWR also captured the wind conditions when the two aircraft conducted missed approaches. Figures 4(a) and 4(b) showed the radial velocity measured by TDWR at 0008 HKT and 0012 HKT 9 September respectively. Gusts reaching 27 m/s (i.e. around 50 knots) were captured by the TDWR over the eastern part of the HKIA. The zero isotach, which marked the leading edge of the shear line, agreed well with that identified based on anemometer data.

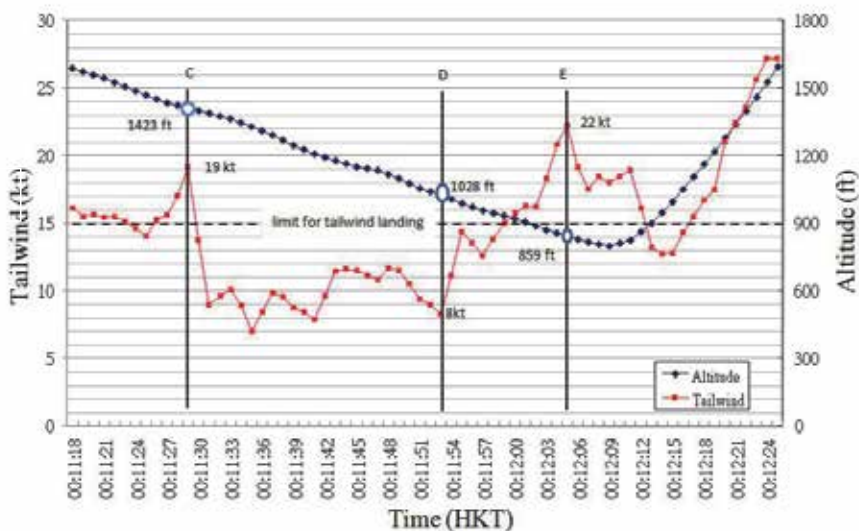
The HKO Windshear and Turbulence Alerting System (WTWS) integrates windshear and turbulence alerts generated by different algorithms such as Anemometer-based Windshear Alerting Rules-Enhanced (AWARE) (Lee, 2004), LIDAR Windshear Alerting System (LIWAS) (Shun and Chan, 2008), TDWR alerts and other algorithms. Alerts are then generated for 8 runway corridors (north runway and south runway have two arrival and two departure corridors each) and shown on a graphical display, the WTWS display.

At 0008 HKT, the zero isotach over the HKIA detected by the TDWR was analyzed as a gust front and was shown on the WTWS display (Figure 5(a)). In addition, microburst alerts, which represent windshear loss of 30 knots or more with precipitation, were provided by TDWR to the east of the HKIA; windshear alerts were generated from AWARE over the runways; turbulence alerts were in force due to the thunderstorm to the north of the HKIA. Over the 8 corridors of the HKIA, all had windshear alerts with magnitude ranging from +25 to +30 knots. At 0012 HKT, although the gust front was not detected by the TDWR

(Figure 5(b)) any more, using the surface anemometers and TDWR base data, windshear alerts with magnitude ranging from +15 to +25 knots were issued for the four western corridors. Meanwhile, areas with the microburst alerts shifted westwards and affected the eastern corridors. WTWS issued microburst alerts of -35 knots to the four eastern corridors. During the event, the WTWS functioned properly and was able to provide adequate warning to the aircraft of the windshear to be expected due to the thundery weather.

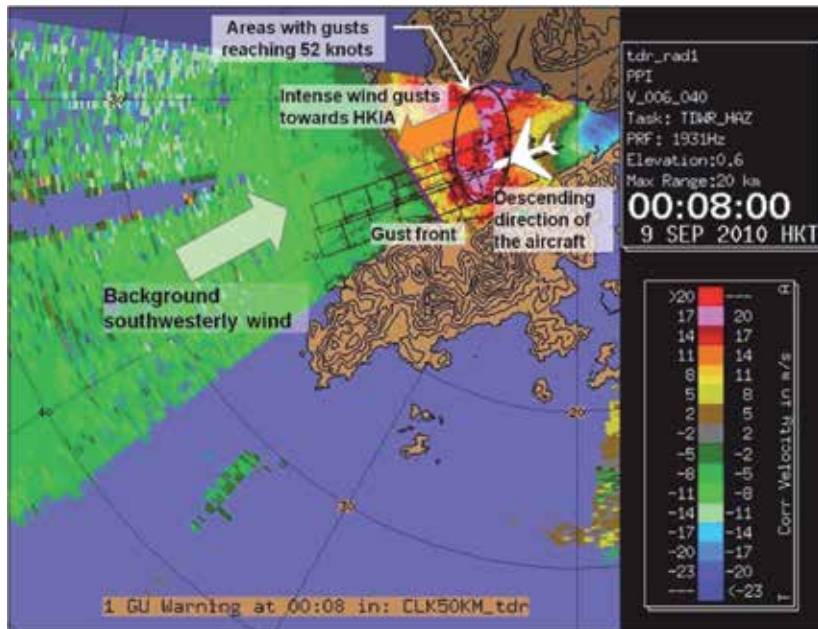


(a)

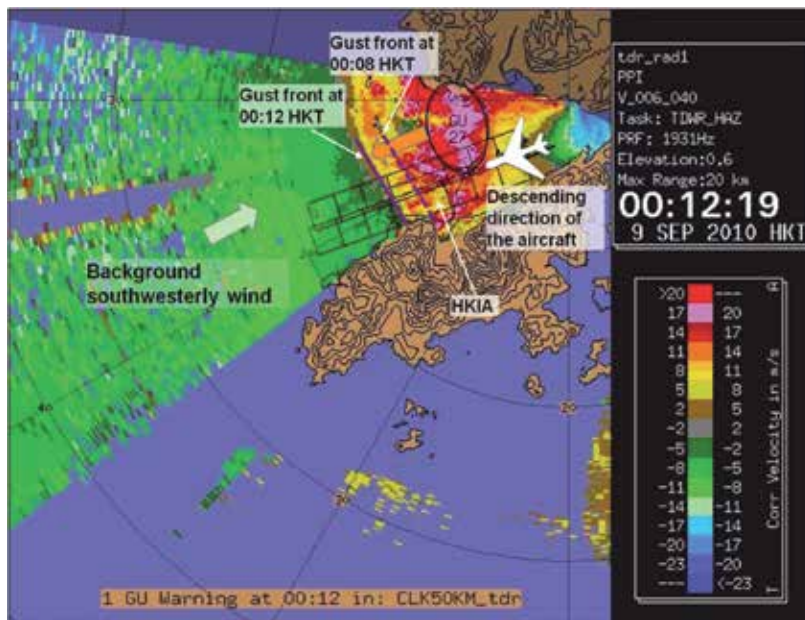


(b)

Fig. 3. Time series in HKT of tailwind in knots (red square) and aircraft altitude in feet (blue diamond) retrieved from the flight data recorders. (a) Flight data for the first aircraft. Tailwind reached 37 knots at 00:08 HKT. (b) Flight data for the second aircraft.

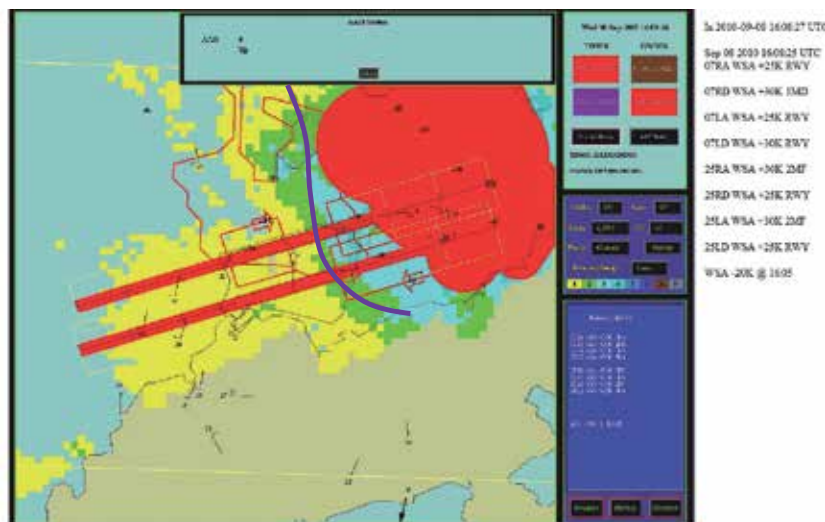


(a)

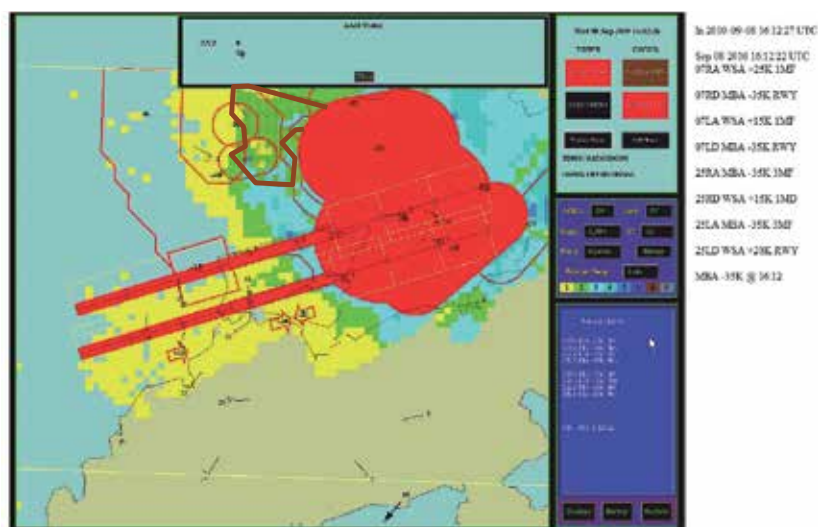


(b)

Fig. 4. Velocity measured by TDWR on 9 September 2010. The cool/warm colors represent winds towards/away from the TDWR. Area with gusts reaching 27 m/s was circled in black. The zero isotach (gust front) was in purple. (a) TDWR image at 0008 HKT; (b) TDWR images at 0012 HKT. The zero isotach (gust front) moved westwards to the western end of HKIA.



(a)



(b)

Fig. 5. WTWS display on 9 September 2010. Gust front analyzed by TDWR (purple line) over the HKIA; microburst alerts generated by TDWR (red solid band-aids); windshear alerts generated by AWARE (red hollow rectangles), by TDWR (red hollow irregular polygons); by LIDAR (red arrows, over the runways only); turbulence alert generated by TDWR (brown polygon with dots). Black numbers were the windshear magnitude in knots. (a) 0008 HKT on 9 September 2010. A gust front was over the HKIA. Windshear alerts were issued by the WTWS for all runway corridors. LIDAR data was highly attenuated by precipitation and could only detect windshear over the runway. (b) 0012 HKT on 9 September 2010. Microburst alerts of -35 knots were issued to the four eastern corridors. Windshear alerts with magnitude ranging from +15 to +25 knots were issued for the four western corridors.

3. Windshear hazard factor based on TDWR

In aviation meteorology, windshear refers to a sustained change of wind speed and/or wind direction that causes the aircraft to deviate from the intended flight path. Low-level windshear (below 1600 feet) could be hazardous to the arriving/departing aircraft. Hong Kong is situated in a subtropical coastal area and it is common to have intense convective weather in the spring and summer. To alert low-level windshear associated with microburst and gust front, a TDWR is operated by the Hong Kong Observatory (HKO) in the vicinity of HKIA (Figure 1). It is a C-band radar with 0.5-degree half-power beam width scanning over the airport and determines convergence/divergence features along the runway orientation from the Doppler velocities. Windshear alerts are generated when the velocity change is 15 knots or more.

Another index that quantifies the windshear threat is the F-factor (Proctor et al., 2000). It is based on the fundamentals of flight mechanics and the understanding of windshear phenomena. The F-factor could also be calculated from the Quick Access Recorder (QAR) data recorded on the commercial jets (Haverdings, 2000). In this study, an attempt is made to calculate F-factor for some typical microburst events at HKIA based on the TDWR measurements and the results are compared with the F-factor determined from the QAR data.

F-factor is calculated from TDWR's radial velocity data in two steps. First of all, convergence/divergence features are identified from the TDWR data. Then F-factor is determined from each convergence/divergence feature by assuming a wind field model of microburst. The two steps are briefly described below.

To compute convergence/divergence features, the method described in Merritt (1987) is adopted. The TDWR microburst detection algorithm identifies microburst by searching for significant velocity difference along a radial in a search window of 4 range gates (4 x 150 metres per gate = 600 metres in length, and one degree in azimuth). If the windshear along a search window is divergent (i.e. radial wind generally increases with increasing distance from the radar), the search window is taken to be a divergence shear segment. Likewise, convergence shear segment is also identified.

Two divergence/convergence segments are associated as a divergence/convergence shear features if their minimum overlap in range is 0.5 km or if their maximum angular spacing is 2 degrees azimuth. A divergence/convergence region contains at least 4 shear segments with a minimum length of 0.95 km and a minimum area of 1 km². Moreover, the maximum velocity difference among the shear segments inside a divergence region should be at least 5 m/s. As such, the shear within a divergence region is at least 5 m/s per 600 m, i.e. 0.008 m/s/m.

F-factor is related to the total aircraft energy and its rate of change, and is defined to be:

$$F = \frac{\dot{W}_x}{g} - \frac{w}{V_a} \quad (1)$$

where W_x is the component of atmospheric wind directed horizontally along the flight path (direction x) and \dot{W}_x its rate of change, g the acceleration due to gravity, w the updraft of

the atmosphere, and V_a the airspeed of the aircraft. By estimating the updraft from mass continuity constraint, it is shown to be equivalent to:

$$F = \frac{\partial W_x}{\partial x} \left[\frac{V_g}{g} + \frac{2h}{V_a} \right] \quad (2)$$

where V_g is the ground speed of the aircraft, and h the altitude above ground.

For each convergence/divergence feature captured by the TDWR, the velocity change ΔU and the distance over which this change occurs ΔR are calculated. It is shown in Hinton (1993) with reference to a microburst model that F-factor could be calculated from:

$$F = K \frac{\Delta U}{\Delta R} \left[\left(\frac{\Delta R}{L} \right)^2 - \left(\frac{\Delta R}{L} \right)^3 \frac{\sqrt{\pi}}{2\alpha} \operatorname{erf} \left(\frac{\alpha L}{\Delta R} \right) \right] \cdot \left[\frac{V_g}{g} + \frac{2h_r}{V_a} \right] \quad (3)$$

where $K = 4.1925$, $a = 1.1212$, h_r the above-ground-level (AGL) altitude of the TDWR radar beam, L the characteristic shear length of 1000 m, and $\operatorname{erf}(y)$ the error function.

The microburst model in Hinton (1993) includes a shaping function which describes the change in microburst outflow with altitude. This function is given by:

$$p(h) = \frac{e^{-0.22h/H} - e^{-2.75h/H}}{0.7386} \quad (4)$$

where h is the altitude above ground and H the altitude of maximum outflow speed (assumed to be 90 m). The F-factor F_1 from the TDWR at the radar beam altitude h_1 is then related to the F-factor F_2 of the aircraft at the altitude h_2 by the following equation:

$$F_2 = F_1 \frac{p(h_2) \left(\frac{V_g}{g} + \frac{2h_2}{V_a} \right)}{p(h_1) \left(\frac{V_g}{g} + \frac{2h_1}{V_a} \right)} \quad (5)$$

Combining (3) – (5) and with ΔU and ΔR determined, the F-factor associated with a divergence/convergence feature at the altitude of the aircraft along the glide path could be calculated.

For the formulation in (1), F-factor is positive if the windshear is performance decreasing (headwind decreasing or downdraft) and negative if the windshear is performance increasing (headwind increasing or updraft). As discussed in Proctor et al. (2000), for onboard windshear systems, the windshear is considered to be hazardous if F is greater than 0.1, and a *must alert* threshold is set to be 0.13. The *must alert* threshold means a wind shear alert must be issued when that threshold is reached/exceeded.

A microburst event that affected HKIA on 18 May 2007 is considered here as an illustration of the method. In the evening of that day, a surface trough of low pressure lingered around the south China coast, bringing unsettled weather to the region. Between 09 and 10 UTC (5 and 6 p.m. of 18 May 2007), a band of strong radar echoes with east-northeast to west-

southwest orientation moved southeastwards from inland areas across the coast. At HKIA, the TDWR issued microburst alerts of 30 knots headwind loss for the aircraft between 09:20 and 09:27 UTC.

Figure 6(a) shows the moment when a microburst associated with the thunderstorms affected the runway corridors to the east of HKIA. Divergent flow feature was found at 0.6-degree conical scan of TDWR. For an aircraft arriving at the north runway of HKIA (location in Figure 1) from the east, the windshear associated with the microburst is performance decreasing (due to decreasing headwind). Using the formulae above, the F-factor for the microburst is determined to be about 0.14, which exceeds the must alert threshold and the windshear associated with the microburst is considered to be hazardous to the aircraft. Flight data are obtained for an aircraft arriving at the north runway from the east at that time. They are processed by the algorithm in Haverdings (2000) and the variation of F-factor along the glide path is shown in Figure 6(b). At about the location of the microburst (near the eastern threshold of the north runway), the F-factor is found to be about 0.13, which is generally consistent with the value determined from TDWR data. Thus for microburst associated with the thunderstorm, the F-factor determined from TDWR measurements and that from QAR data of the aircraft are comparable with each other. The other peaks/troughs of F-factor from the QAR data (Figure 6(b)) are not revealed in the TDWR measurements. They may not be properly handled by the microburst model for F-factor calculation.

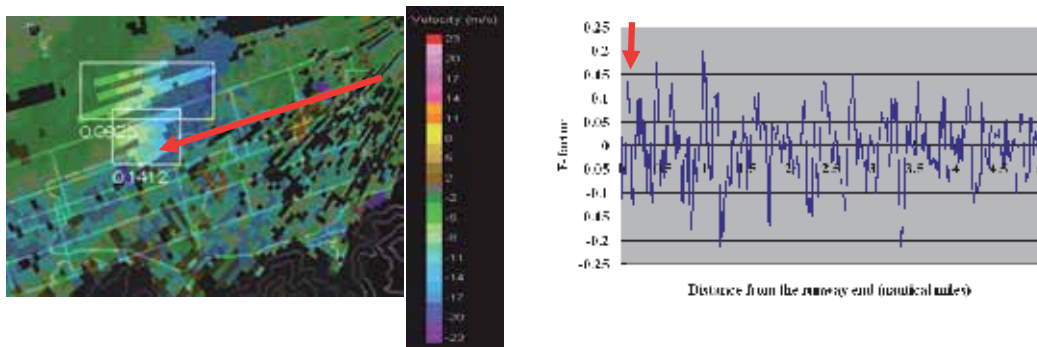


Fig. 6. (a) Divergence features (highlighted in lighter colours) associated with microburst on 18 May 2007, overlaid on the radial velocity from the TDWR (colour scale on the right). F-factor of each feature is given as a number next to the box indicating the location of the feature. (b) F-factor as recorded on an aircraft flying at about the same time as in (a) along the glide path shown as a red arrow in (a). The red arrow in (b) is the approximate location of the windshear feature encountered by the aircraft.

To study the change in the F-factor following the evolution of the microburst, the intense convective event on 8 June 2007 is considered. Severe gusts associated with thunderstorms and microburst with a recorded maximum of 35.9 m/s affected HKIA in the morning of that day. A helicopter parked on the apron toppled in strong winds during the passage of the intense storm cells. We just focus on the windshear hazard associated with the microburst. The divergence features determined from the radial velocity of the TDWR at 0.6-degree conical scans are shown in Figure 7. Stronger winds associated with the microburst got

closer to the ground level (about 260 m above mean sea level at the location of the microburst) in a short time interval within 3 minutes, with the maximum value of towards-the-radar velocity increasing from 18 m/s (dark blue in Figure 7) to 23 m/s (magenta in Figure 7). As a result, the F-factor increases in magnitude from 0.14 to 0.23, which exceeds the must alert threshold. The TDWR-based F-factor provides a good indication about the level of hazard associated with an evolving microburst.

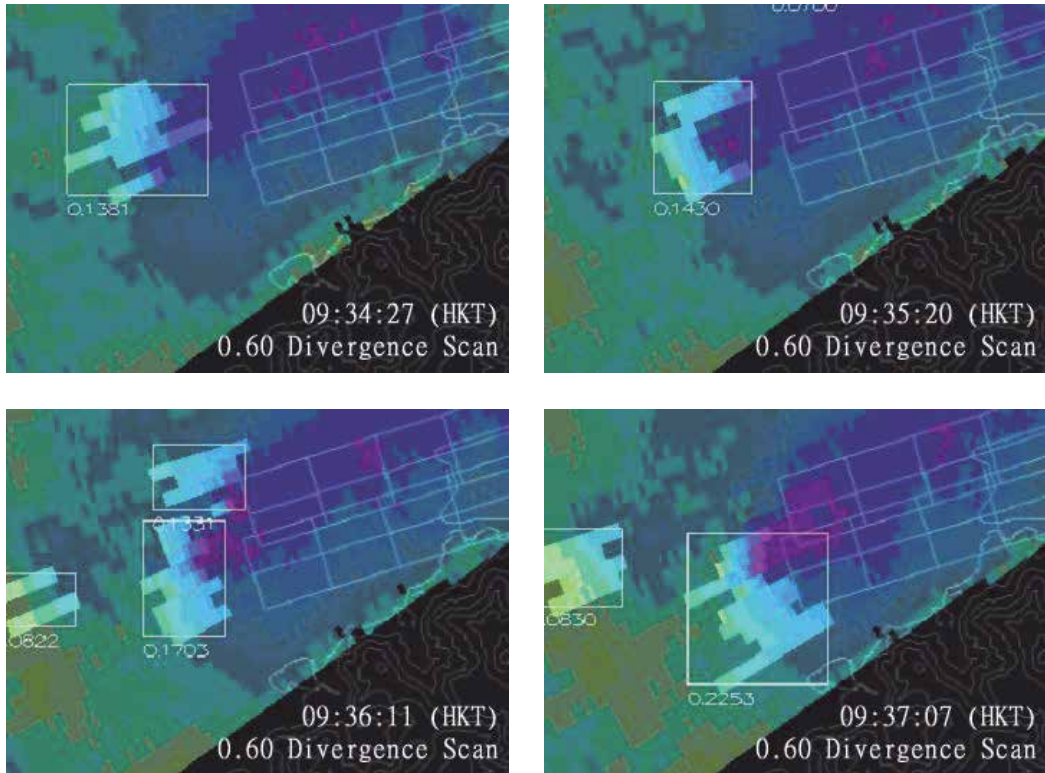


Fig. 7. Time series of the divergence feature associated with a microburst on 8 June 2007. The feature is highlighted in lighter colour and enclosed in a box. The number next to the box is the F-factor calculated for the feature. The background is the radial velocity from the TDWR, with the colour scale given in Figure 6.

Besides intense convective weather, the windshear hazard in terrain-disrupted airflow is also studied. The Typhoon Prapiroon case on 3 August 2006 is considered. On that day, Prapiroon was located at about 200 km to the southwest of Hong Kong over the South China Sea and tracked northwest towards the western coast of southern China. This typhoon brought about gale-force east to southeasterly airflow to Hong Kong. Due to complex terrain to the south of the airport, airflow disturbances occurred inside and around HKIA. Divergent flow features were observed near the airport from time to time. Figure 8(a) shows such a feature at 0.6-degree conical scan of the TDWR at about 4:47 a.m., 3 August. The F-factor associated with this feature is about 0.22, which exceeds the must alert threshold for windshear. An aircraft landed at the north runway of HKIA from the west at about that time (within one minute). The variation of the F-factor determined from QAR

data along the glide path is given in Figure 8(b). At the location of the microburst, the F-factor from the aircraft is comparable with that calculated from the TDWR data, even for this case of terrain-disrupted airflow. As discussed in the first case study, the other peaks/troughs of F-factor from the QAR data (Figure 8(b)) are not revealed in the TDWR measurements. They may not be properly handled by the microburst model for F-factor calculation.

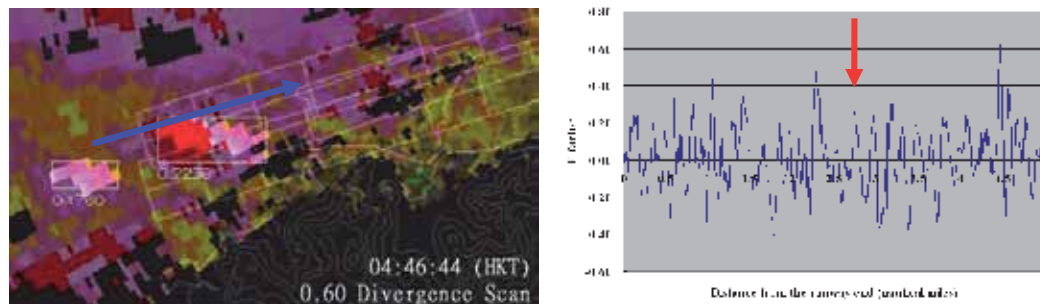


Fig. 8. (a) Divergence features (highlighted in lighter colours) associated with windshear in terrain-disrupted airflow on 3 August 2006, overlaid on the radial velocity from the TDWR (colour scale given in Figure 6). F-factor of each feature is given as a number next to the box indicating the location of the feature. (b) F-factor as recorded on an aircraft flying at about the same time as in (a) along the glide path shown as a blue arrow in (a). The red arrow in (b) is the approximate location of the windshear feature encountered by the aircraft.

4. Calculation of turbulence intensity

The measurement of spectrum width is determined not only by the Doppler velocity distribution and density distribution of the scatterers within the resolution volume, but also radar observation parameters like beamwidth, pulse width, antenna rotation rate, etc. According to Doviak and Zrnic (2006), there are five major spectral broadening mechanisms that contribute to the spectrum width measurements, which can be written as follow

$$\sigma_v^2 = \sigma_s^2 + \sigma_t^2 + \sigma_\alpha^2 + \sigma_d^2 + \sigma_o^2 \quad (6)$$

where σ_s represents mean wind shear contribution, σ_t represents turbulence, σ_α represents antenna motion, σ_d represents different terminal velocities of hydrometeors of different sizes, and σ_o represents variations of orientations and vibrations of hydrometeors. Except σ_s and σ_t , the rest of the terms on the right hand side of the Eq.(6) are considered to be negligible for the measurements of σ_v in this paper (Brewster and Zrnic, 1986). Thus the turbulence term σ_s can be obtained,

$$\sigma_t^2 = \sigma_v^2 - \sigma_s^2. \quad (7)$$

In the Eq.(7), mean wind shear width term σ_s can be decomposed into three terms due to mean radial velocity shear at three orthogonal directions in radar coordinate(Doviak and Zrnic, 2006):

$$\sigma_s^2 = \sigma_{s\theta}^2 + \sigma_{s\phi}^2 + \sigma_{sr}^2 = (r_0\sigma_\theta k_\theta)^2 + (r_0\sigma_\phi k_\phi)^2 + (\sigma_r k_r)^2, \quad (8)$$

where $\sigma_r^2 = (0.35c\tau/2)^2$, $\sigma_\theta^2 = \theta_1^2/16\ln 2$, and $\sigma_\phi^2 = \theta_1^2/16\ln 2$. Here $c\tau/2$ is range resolution, and θ_1 is the one-way angular resolution (i.e., beamwidth). k_θ , k_ϕ , and k_r are the components of shear along the three orthogonal directions.

In order to use σ_t to estimate eddy dissipation rate (EDR) ε , it must be assumed that within radar resolution volume turbulence is isotropic and its outer scale is larger than the maximum dimension of the radar's resolution volume (which is indicated as V_6). Under these assumptions, in the case of $\sigma_r \leq r\sigma_\theta$ the relation between turbulence spectrum width σ_t and EDR ε can be approximately written as (Labitt, 1981)

$$\varepsilon \approx \frac{0.72\sigma_t^3}{r\sigma_\theta A^{3/2}}, \quad (9)$$

where A is constant (i.e., about 1.6). When $\sigma_r \geq r\sigma_\theta$, the relation can be approximated by

$$\varepsilon \approx \left[\frac{\langle \sigma_t^2 \rangle^{3/2}}{\sigma_r (1.35A)^{3/2}} \right] \left(\frac{11}{15} + \frac{4}{15} \frac{r^2 \sigma_\theta^2}{\sigma_r^2} \right)^{-3/2} \quad (10)$$

Eqs. (9) and (10) are used to estimate EDR using Hong Kong TDWR observed spectrum width.

In hazardous weather mode, the Hong Kong TDWR conducts sector scans from azimuth 182° to 282° (i.e., confined to the approach and departure paths). Each sector scan takes about 4 minutes. Thus, the low altitude wind shear can be detected within a minute. The range and angular resolutions of the radar are 150 m and 0.5° respectively. The maximum range reaches 90 km. The radar data includes reflectivity, Doppler velocity, spectrum width, and signal-to-noise ratio (SNR) recorded with the azimuth interval of 1° .

Based on the Eqs. (9) and (10), EDR can be estimated when spectrum width observation is available. In this feasibility study, EDR estimation is only performed at the lowest elevation angle of 0.6° . The vertical wind shear contribution to the EDR is calculated by using spatially averaged mean Doppler velocity at two lowest elevation angles. Because the closest two elevation angles at lowest level are 0.6° and 1.0° at scans 11 and 12, vertical wind shear is calculated by using the Doppler velocity fields at these two scans. For simplicity, EDR is estimated at scan 17 with elevation angle of 0.6° . Azimuthal and radial wind shear is also calculated at this scan. So in the current algorithm, one EDR field at elevation angle of 0.6° will be generated for each volume scan.

The control of the TDWR spectrum width data quality is very important for EDR estimation. It has been found that there is a variety of sources of errors in spectrum width measurements in previous studies (Fang et al. 2004). Especially if signal to noise ratio (SNR) is low, spectrum width measurements have large variance. In this study, $\text{SNR} > 20$ dB is assigned as a simple and straightforward threshold for the EDR estimates. In other words, EDR at the gate with $\text{SNR} < 20$ dB is marked as missing data (MD) in our algorithm. In the future, more comprehensive quality control processor will be designed and implemented in our algorithm to deal with other error sources.

Following international practice, EDR values are classified into four categories in terms of the intensity of turbulence. For convenience and in line with alerting purpose of low-level turbulence, EDRs in the following figures and context will be labeled or indicated as insignificant (LL), light (L), moderate (M), and severe (S) instead of its value. It is also worth mentioning that EDR values presented in this paper are derived from the spectrum width data after smoothing by using a 9 point median filter along the radar beams in order to suppress the fluctuations in the determination of spectrum width values. This kind of fluctuation is expected, for instance, to arise from the limited and finite number of data points in the digitization of the spectrum of the return signal.

The spectrum width errors are large in region of low SNR. Here we selected a case to demonstrate the importance of the SNR threshold in the quality control of EDR data. Around 21 UTC on 6 June 2008, the TDWR radar observed thunderstorms over HKIA. Without SNR threshold, estimated EDR suggested severe turbulence region (red color; Figure 9(a)) in the region about azimuth of 270° and centered at about 25 km. High spectrum widths (~ 4.5 m/s) are indeed measured in this region (see Figure 9(c)). But reflectivity (Figure 9(e)) and SNR (Figure 9(d)) are around -8 dBZ and 10 dB respectively. The relatively large spectrum widths in this region can be caused by incorrect noise power estimates (Fang et al., 2004). To avoid such biases, we use a SNR threshold of 20 dB as recommended by Fang et al., (2004).

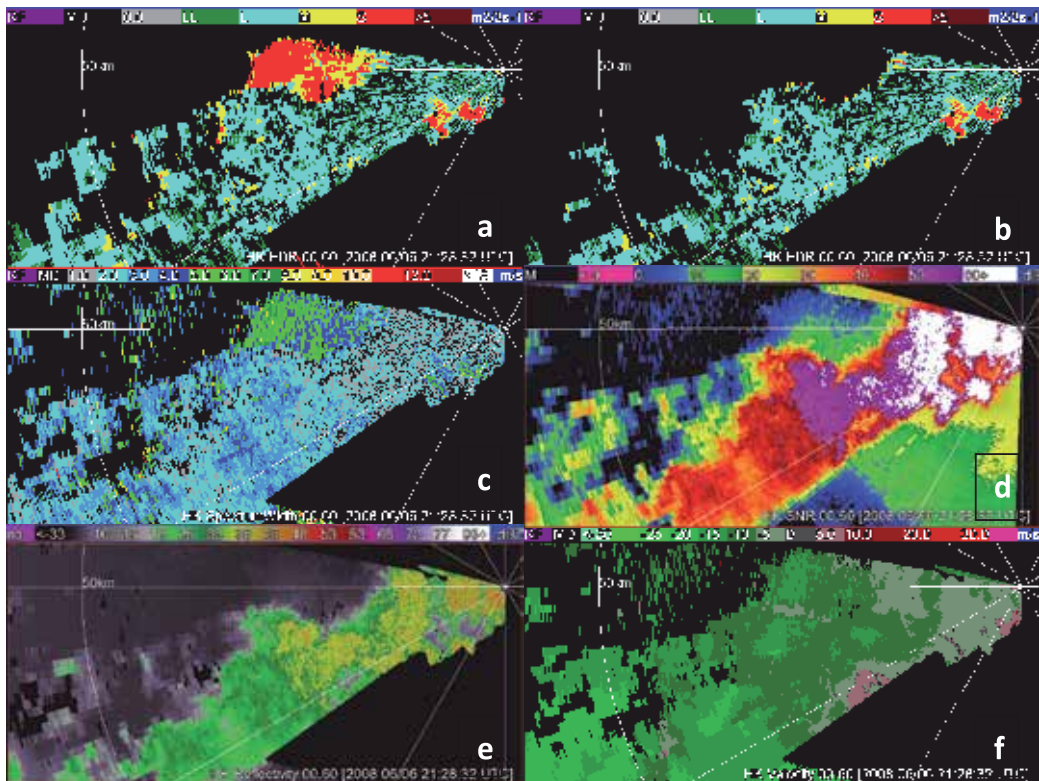


Fig. 9. (a) EDR, (b) EDR with SNR > 20 dB, (c) spectrum width, (d) SNR, (e) reflectivity, and (f) Doppler velocity at elevation angle of 0.6° at 21:28 UTC on 6 June 2008. Range ring is 50 km and azimuths are every 30° .

On the other hand, there are two small regions near the radar at the range of 6 km where EDR is also high. But in this region there is relatively strong horizontal shear of the radial wind component (Figure 9(f); green color identifies the wind has a component toward the radar and red color indicates wind is away from the radar). Furthermore, the reflectivity is about 10 dBZ and SNR is around 35 dB. Because this region is on the downwind side of Lantau Island, the ambient flow (green in Figure 9(f)) is blocked by the Island and back flow (red in Figure 9(f)) is induced. The wind shear contributions, computed using Eq. (8), have been removed from the calculation EDR presented in Figure 9(a). Thus the EDR should not be biased by strong shear of mean radial wind. Thunderstorm outflow may be another reason for the severe turbulence in this region. Because there is no strong horizontal shear of the Doppler velocity field in the region 270° and 25 km, we conclude that the large EDRs presented in that region of Figure 9(a) are unrealistic. After a threshold $SNR > 20$ dB is applied, it can be seen that these large EDR values are removed (Figure 9(b)).

Using the Hong Kong TDWR observations in 2006 and 2008, many EDR maps were produced and examined. Here wind shear contribution has been removed from spectrum width measurements. Here the mean wind shears in horizontal and vertical directions are calculated by using mean radial velocity field smoothed by a 9 points median filter along the radar beam in the Eq.(8). Figure 10 shows two typical EDR maps during light rain at 21:32 UTC on 27 April 2006 (Figure 10(a)) and during a thunderstorm at 13:17 UTC on 13 June 2008 (Figure 10(b)). For most of the scanned area, EDR is low and turbulence is classified as insignificant or light (green and light blue). Small pockets of moderate and severe turbulence (yellow and red) are scattered in the scanned area. Near the Lantau Island, moderate and severe levels of turbulence are frequently observed in the cases we studied. The blockage of the Island on the ambient flow may be a reason for the occurrence of the turbulent airflow. Based on the numerical simulations, Clark et al. (1997) and Chan (2009) found that mechanical effect of a mountainous island is a source of the generation of the turbulence.

Clear air cases have been investigated as well, but we found that SNR of the Hong Kong TDWR is too low to provide reliable and meaningful EDR maps.

After the EDR maps were generated, EDR profiles along the flight paths can be compared with aircraft measured EDR. A total of 14 cases are selected to make the comparison. The aircraft EDRs are estimated based on the vertical wind measured by aircraft (Cornman et al., 2004).

Radar derived EDR profile is constructed by selecting the EDR in a resolution volume V_6 closest to the flight path and at an elevation angle of 0.6°. There are still differences in the measurement heights between the aircraft and the radar beam for these two EDR datasets. Only a part of the flight path is covered by the radar beam. For example, aircraft approaching runway 25RA is in the radar beam only at the distance between 0.5 and 1.5 nm from the end of runway. From this point of view, EDRs estimated by aircraft and the radar would be compared within this distance interval. It should also be mentioned that radar estimated EDR is based on the spectrum width of the Doppler velocity, i.e. velocity in the radial direction along a radar beam. On the other hand, the aircraft estimated EDR is based on the vertical wind. As such, the two EDR datasets are derived from different components of the wind. Put aside errors in measurement, in order to have agreement turbulence must be isotropic.

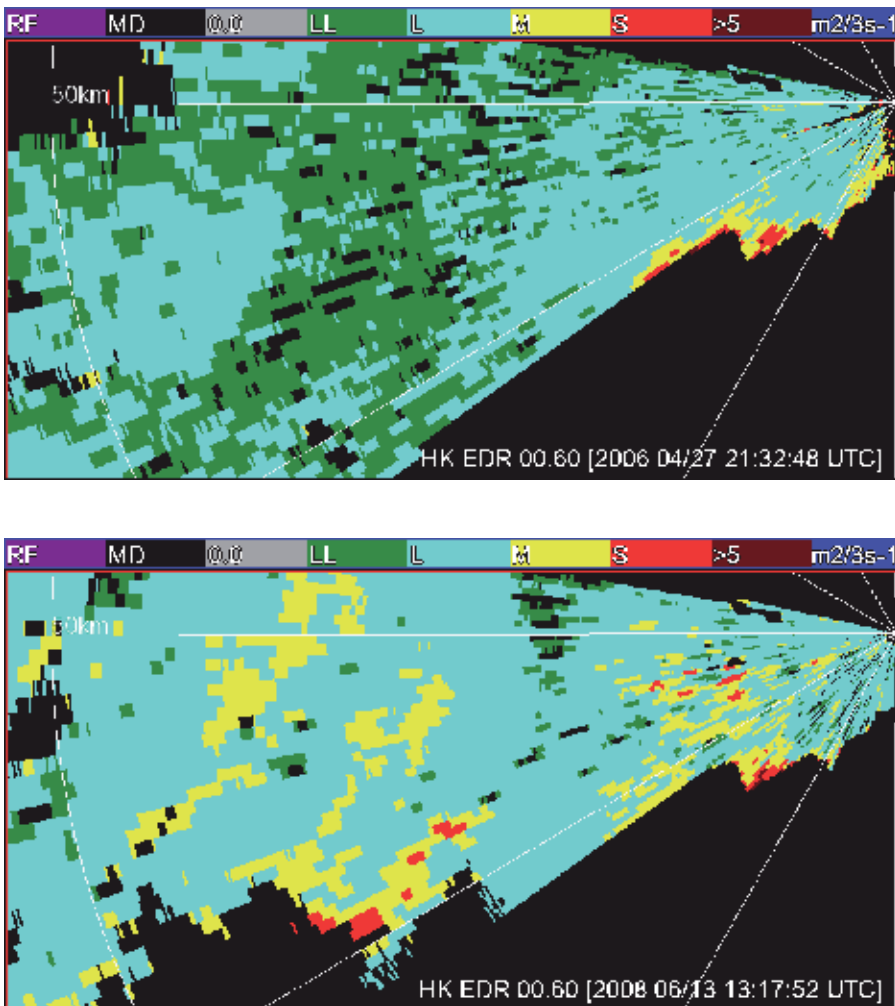


Fig. 10. EDR maps (a) at 21:32 UTC on 27 April 2006 and (b) 13:17 UTC on 13 June 2008. The mountainous Lantau Island is located to the south of the radar scans.

Another issue of the comparison is the contribution of mean wind shear to the measured spectrum width. For the estimation of EDR, the contribution of wind shear has to be extracted from the radar measured spectrum width. But for the comparison with aircraft measured EDR or even turbulence alert for aviation safety, wind shear might not need to be removed. For example if the aircraft experiences a sharp change in altitude, this may not be caused by isotropic turbulence but it is a measure of aircraft response to vertical shear of mean wind. As such, the aircraft estimated EDR based on vertical velocity may be slightly higher. Pilots and passengers in aircraft may also experience severe “turbulence”, which is a combination of the effects of both turbulence and wind shear.

Scatterplots of median and maximum EDR along the 5 nm of flight paths estimated by aircraft and radar are shown in Figure 11. Two plots for each are shown; one in which mean wind shear contributions to the observed spectrum widths are removed and a second plot in

which mean wind shear contribution has been retained. All median EDRs are smaller than $0.4 m^{2/3} / s$ (i.e., moderate or light turbulence). 13 of 14 median EDRs indicate turbulences are light. Based on maximum EDRs, two severe turbulent patches ($EDR > 0.5 m^{2/3} / s$) are detected by both aircraft and radar with wind shear, but they are not on the same flight paths. With wind shear contribution, median and maximum radar EDRs evidently increase.

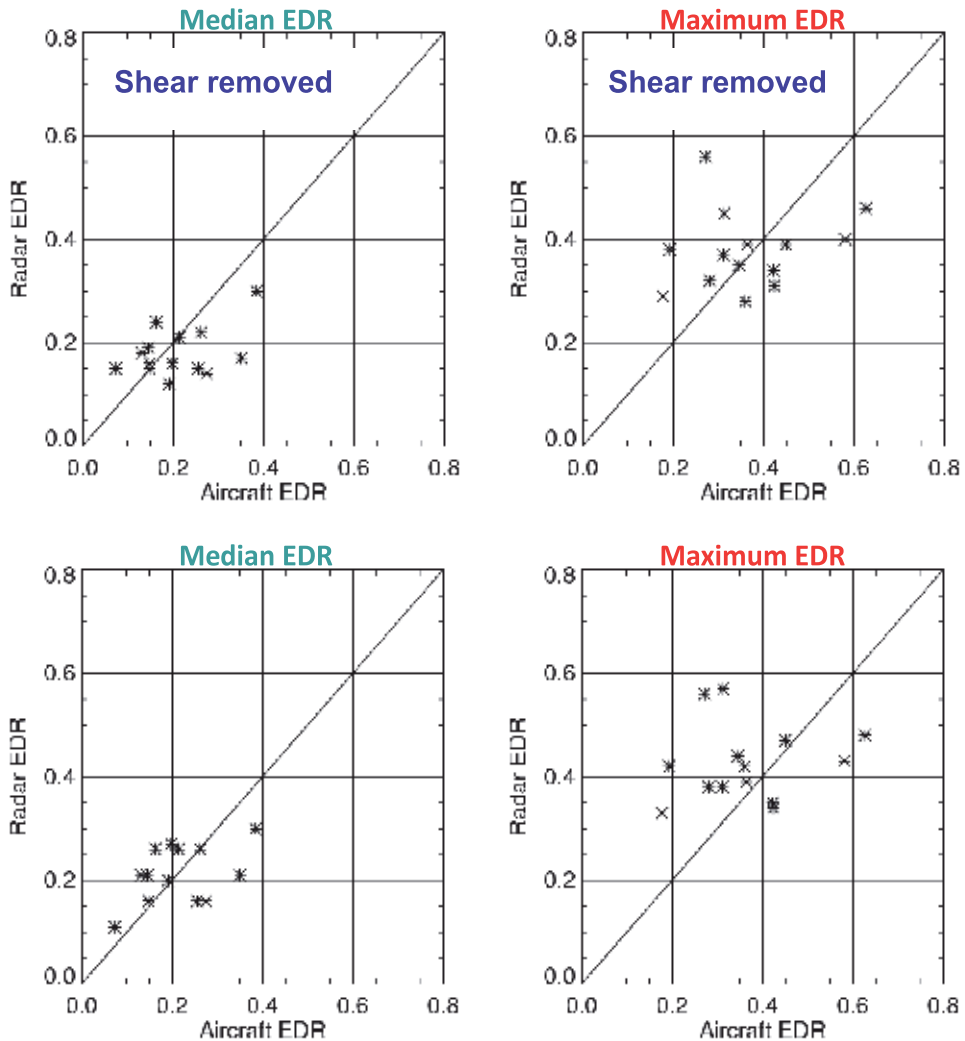


Fig. 11. Scatterplots of median and maximum EDR estimated by aircraft and radar along the 5 nm of flight paths for the selected 14 cases.

Comparing maximum intensity between aircraft and radar without wind shear, 8 of the 14 cases are in the same category. Seven of them are moderate turbulence. For 4 aircraft estimated light turbulence cases, the radar tends to overestimate them as moderate (3 cases) and severe (1 case) with wind shear contribution. After closer examination of the overestimation case at 07:17 UTC on 25 June 2008, it is found that the maximum severe

turbulence only occurs at one radar gate at the distance of 0 nm, closest to the end of the runway. It is noted that at this location, the radar beam is higher than the flight path by about 160m.

We have also compared aircraft and radar estimated EDR profiles including wind shear contribution along the aircraft flight path. For this case, aircraft B777 flew through a storm with maximum reflectivity of 42 dBZ and landed in clouds and light rain at HKIA.

Figure 12 shows the EDR estimated by aircraft and the radar along the flight path 25RA around 13:05 UTC on 19 April 2008. It is one of the two cases in which severe turbulence was encountered by the aircraft. Blue dots in Figure 13 represent the EDR estimated by the aircraft as it was landing at HKIA. Three peaks over $0.5 \text{ m}^{2/3} / \text{s}$, classified as severe turbulence, are recorded at distance of 0.77, 3.65, and 4.90 nm away from the runway end. EDR profiles estimated by using radar data at an elevation angle of 0.6° with the wind shear contribution included in the volume scans around 13:05 UTC are overlaid onto the aircraft estimated EDR in Figure 13. The radar estimated EDR profiles at 13:01, 13:05, and 13:09 UTC (brown dots, red squares, and green dots in Figure 13) matches well with aircraft EDR between distance of 0.5 and 1.5 nm, shaded in green color in Figure 13, where the aircraft was in a region common to the 0.6° radar beam. It means that radar and aircraft were measuring turbulence in approximately the same region at nearly the same time.

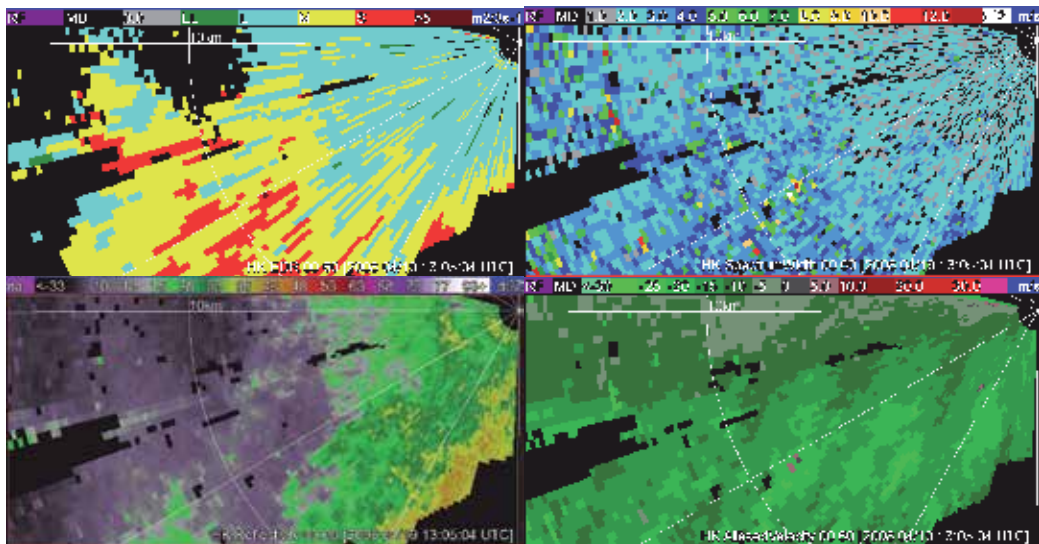


Fig. 12. (a) EDR, (b) spectrum width, (c) reflectivity factor, and (d) Doppler velocity at elevation angle of 0.6° at 13:05 UTC on 19 April 2008. Range ring is at 10 km.

The peaks of these 3 EDR profiles at 13:01, 13:05, and 13:09 UTC are in the green shaded interval and the maximum value is $0.48 \text{ m}^{2/3} / \text{s}$, just slightly smaller than $0.5 \text{ m}^{2/3} / \text{s}$. In order to find if there are higher EDR near the flight time (13:05 UTC), we examined the EDR for the two scans one minute before and after the passage of the aircraft at 13:05 UTC in the same volume scan at 13:05 UTC. The profiles are shown with light and dark purple dots in Figure 13. High EDRs with values of 0.69 and $0.76 \text{ m}^{2/3} / \text{s}$ are found within the shaded

interval. This convinces us that the EDR peak is not caused by random error of radar measurements.

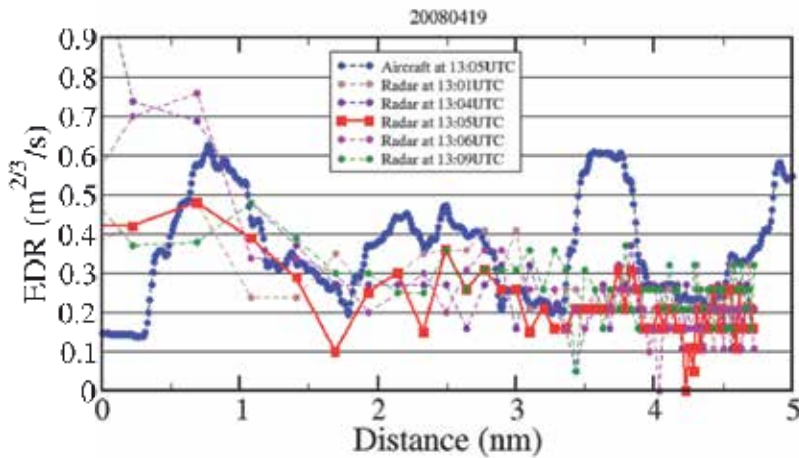


Fig. 13. EDR along the flight path estimated by the aircraft B777 (blue dots) at 13:05 UTC and by the TDWR radar at the time indicated in the legend on 19 April 2008. X axis is the distance between aircraft and the end of runway. The distance interval shaded by the green color indicates where the aircraft passes through the altitude interval observed with the 0.6° elevated beam.

It raises another question: the aircraft may contaminate the radar measurements of the atmospheric status, since the aircraft disturbs the atmosphere and changes the original atmospheric condition in the measurement region as it flies by. In addition, aircraft itself as a target embedded in other scatterers, such as raindrops, may contaminate the spectrum width measurements as well. Both of the two factors could affect spectrum width and EDR value.

It could also be seen that the radar EDR profiles do not match the two aircraft estimated EDR peaks at the distance of 3.65 and 4.90 nm. It might be caused by the spatial difference between the aircraft and the radar beams. The flight heights at the distance of 3.65 and 4.90 nm are higher than the radar beams by about 260 m and 400 m respectively.

Wind shear contribution to spectrum width measurement for this case has been examined. After removing wind shear contribution, the EDR peak at the distance of 0.69 nm is reduced from 0.48 to 0.46 $m^{2/3}/s$ (not shown) at 13:05 UTC. It means that wind shear contribution is small in this region. Because wind shear of the large scale mean wind should be persistent over the 4 minute for entire volume scan, the EDR peaks without wind shear contribution at 13:04 and 13:06 UTC at the distance of 0.69 nm are reduced to 0.67 and 0.74 $m^{2/3}/s$ respectively. It indicates severe turbulence that is matched with aircraft estimate at 13:05 UTC.

Note that the aircraft estimated EDR is considered as ground truth in the above analysis, but it also contains errors and requires significant QC effort, especially as airplane is climbing or descending (Gilbert et al., 2004).

5. Conclusion

This chapter discusses the aviation applications of TDWR. This radar issues microburst alerts which are crucial in the assurance of aviation safety. A typical case of microburst detection by TDWR in association with intense thunderstorms is described first in this chapter. Then the applications of TDWR in the alerting of windshear and turbulence are described. Windshear is alerted through the calculation of windshear hazard factor, which is a rather well established technology. On the other hand, the use of spectrum width data from the radar in the alerting of turbulence has a relatively shorter development history, and the technology is under exploration in Hong Kong.

Study is underway in Hong Kong to use X-band radar in the alerting of windshear and turbulence on experimental basis at the Hong Kong International Airport. The use of long-range S band radar in the alerting of turbulence for enroute aircraft is also under study. Such progress of these studies would be reported in the future.

6. References

- Brewster, K.A. and D.S. Zrnice, 1986: Comparison of eddy dissipation rate from spatial spectra of Doppler velocities and Doppler spectrum widths. *J. Atmos. Oceanic Technol.*, 3, 440-452.
- Chan, P.W., 2009: Atmospheric turbulence in complex terrain: verifying numerical model results with observations by remote-sensing instruments. *Meteorology and Atmospheric Physics*, 103, 145-157.
- Clark, T.L., T. Keller, J. Coen, P. Neille, H. Hsu, and W.D. Hall, 1997: Terrain-induced turbulence over Lantau Island: 7 June 1994 Tropical Storm Russ case study. *J. Atmos. Sci.*, 54, 1795-1814.
- Cornman, L. B., G. Meymaris, and M. Limber, 2004: An update on the FAA Aviation Weather Research Program's in situ turbulence measurement and reporting system. Preprints, Eleventh Conf. on Aviation, Range, and Aerospace Meteorology, Hyannis, MA, Amer. Meteor. Soc., P4.3.
- Doviak, R. J., and D. S. Zrnice, 2006: Doppler radar and weather observations. Dover Publications Inc., Mineola, New York, 562 pp. (except for the preface with links to online errata and supplements, this is an exact copy of the 1st and 2nd printing of the 1993 Academic Press edition).
- Fang, M., R.J. Doviak, and Melnikov, 2004: Spectrum width measured by the WSR-88D radar: Error sources and statistics of various weather phenomena. *J. Atmos. Oceanic Technol.*, 21, 888-904.
- Gilbert, D., L.B. Cornman, A.R. Rodi, R.G. Frechlich, and R.K. Goodrich, 2004: Calculating EDR from aircraft wind data during flight in and out of Juneau AK: Techniques and challenges associated with non-straight and level flight patterns. Preprints, 11th Conf. on Aviation, Range and Aerospace Meteorology. Hyannis, MA, Amer. Meteor. Soc., CD-ROM, 4.4.
- Haverdings, H., 2000: Updated specification of the WINDGRAD algorithm, NLR TR-2000-63, National Aerospace Laboratory, 2000.

- Hinton, D.A., 1993: Airborne derivation of microburst alerts from ground-based Terminal Doppler Weather Radar information - a flight evaluation, NASA Technical Memorandum 108990, NASA.
- Labitt, M., 1981: Coordinated radar and aircraft observations of turbulence. Project Rep. ATC 108, MIT, Lincoln Lab, 39 pp.
- Lee O.S.M. 2004. 'Enhancement of the Anemometer-based System for Windshear Detection at the Hong Kong International Airport.' Eighth Meeting of the Communications/Navigation/Surveillance and Meteorology Sub-Group (CNS/MET/SG/8) of APANPIRG, Bangkok, Thailand, 12 - 16 July 2004. International Civil Aviation Organization.
- Merritt, M.W., 1987: Automated detection of microburst windshear for Terminal Doppler Weather Radar, presented at SPIE Conference on Digital Image Processing and Visual Communications Technologies in Meteorology, 27-28 October 1987, Cambridge, MA, USA.
- Proctor, F.H., D.A. Hinton and R.L. Bowles, 2000: A windshear hazard index, presented at 9th Conference on Aviation, Range, and Aerospace Meteorology, 11-15 September 2000, Orlando, FL., USA.
- Shun C.M. and Chan P.W. 2008. Applications of an infrared Doppler Lidar in detection of wind shear. *Journal of Atmospheric and Oceanic Technology* 25: 637-655.

Part 2

Precipitation Estimation and Nowcasting

Nowcasting

Clive Pierce¹, Alan Seed², Sue Ballard³, David Simonin³ and Zhihong Li³

¹*Hydro-Meteorological Research, Met Office, FitzRoy Road, Exeter,*

²*Centre for Australian Weather and Climate Research, Bureau of Meteorology, Melbourne,*

³*Joint Centre for Mesoscale Meteorology, Met Office, Meteorology Building,
University of Reading, Earley Gate, Reading,*

^{1,3}UK

²Australia

1. Introduction

The somewhat inelegant term, *nowcasting*, was devised in the mid-1970s (Browning, 1980). It encapsulates a broad spectrum of observation intensive techniques developed for predicting the weather up to a few hours ahead. These techniques are reliant on the rapid processing of high resolution data sets collected by weather radars and satellites. As such, the evolution of nowcasting as a branch of operational meteorology has been closely bound up with post-second world war advances in remote sensing, telecommunications and digital computing. A comprehensive treatment of the subject matter is beyond the scope of this Chapter. In a book about Doppler radar the authors make no apology for focusing on radar based nowcasts of precipitation.

We begin with a brief justification for the use of nowcasts in operational meteorology. This is followed by an overview of nowcasting techniques. A description of some of the key, historical developments in nowcasting is followed by sections on deterministic extrapolation-based nowcasting techniques, errors in precipitation nowcasts and their treatment within nowcasting system frameworks. The remaining sections consider advances in high resolution Numerical Weather Prediction (NWP) model-based nowcasting and review some of the issues and developments surrounding the application of quantitative precipitation nowcasts (QPN) to hydrological forecasting and warning. The Chapter closes with a brief consideration of future prospects for nowcasting.

2. An overview of nowcasting techniques

Operational weather forecasts are produced by primitive equation models known collectively, as Numerical Weather Prediction models. The predictive skill of these models is limited by a number of factors including the accuracy and coverage of routinely available weather observations, the extent to which their model formulations and grid lengths allow the relevant physical and dynamical processes to be modelled accurately, and the non-linear response of the atmospheric system to small perturbations in its state.

Whilst current, operational NWP models are now beginning to resolve important processes such as convection (Lean et al., 2008), their predictive skill generally remains very limited at the convective scales. Furthermore, current computational constraints restrict their operational forecast update cycles to hours, whereas convective phenomena typically exhibit life times of tens of minutes. Thus, NWP-based forecasts of local weather (Browning, 1980) have tended to be rather poor and their use for local forecasting has, until very recently, often been limited to general guidance at the regional scale.

From the 1960s onwards, the availability in near real time of increasingly sophisticated, spatially contiguous, radar and satellite observations, particularly of precipitation or proxies for it, offered the prospect of very short range, local forecasting by extrapolation – the concept of exploiting persistence, either in an Eulerian or Lagrangian reference frame (Germann & Zawadzki, 2002), to make weather predictions with sufficient rapidity to circumvent the perishability of the data. Browning (1980) clarified the relative merits of extrapolation nowcasts and NWP forecasts (see Figure 1), suggesting that the former were of superior accuracy up to 6 hours ahead.

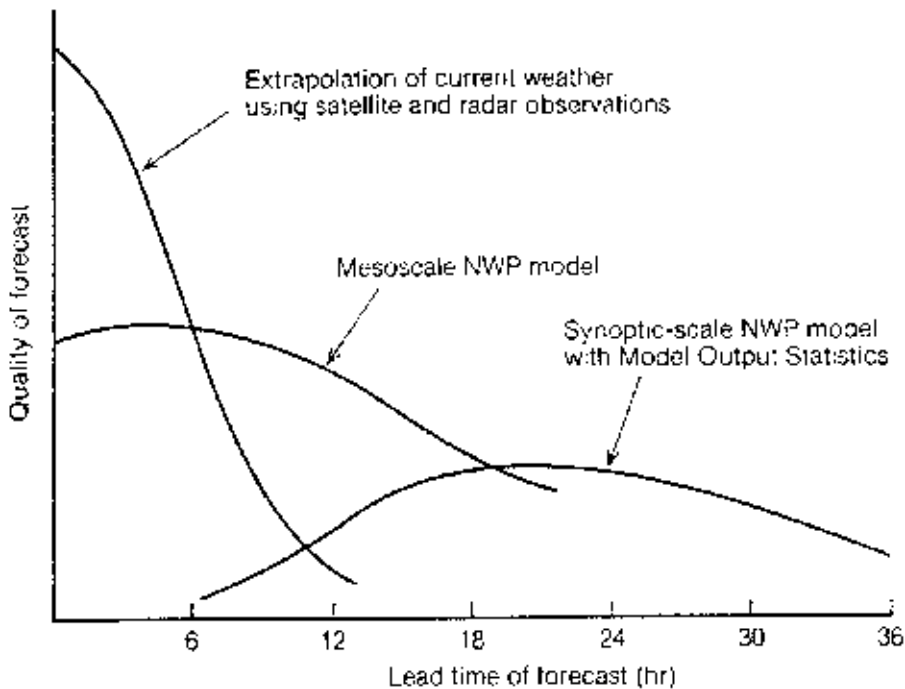


Fig. 1. A schematic diagram after Browning (1980) conceptualizing the relationship between forecasting methodology, skill and forecast range.

The predictability of extrapolation-based precipitation nowcasts and the forecast range at which these nowcasts must hand over to NWP to achieve optimal predictive skill have been explored by a number of authors (e.g. Browning, 1980; Zawadzki et al., 1994; Germann & Zawadzki, 2002; German et al., 2006; Bowler et al., 2006). Recent implementations of convective scale NWP model forecasts are now reducing the useful range of extrapolation-based nowcasts to a few hours ahead, as discussed later in this Chapter.

In the following section, we describe some of the key milestones in radar-based precipitation nowcasting and review these in the context of parallel advances in relevant areas of science and technology.

3. Radar-based nowcasting – A brief history

3.1 Origins of weather radar, and early research

Operational weather radar has its origins in the development of military radar during World War Two. The invention of the resonant cavity magnetron by John Randall and Harry Boot at the University of Birmingham in England in 1940 allowed the construction of high powered, centimeter-band radars, suitable for detecting precipitation. The sharing of this technology with American scientists early in the 1940s facilitated its subsequent development for meteorological applications.

Important early papers include those on rain drop size distributions (Marshall & Palmer, 1948) and shapes (Browne & Robinson, 1952; Hunter, 1954; Newell et al., 1955), the measurement of precipitation (Ryde, 1946; Byers, 1948; Bowen, 1951; Twomey, 1953; Battan, 1953; Stout & Neill, 1953), its vertical structure (Langille & Gunn, 1948) and associated estimation errors (Hitschfeld & Bordan, 1954), and those on thunderstorm identification, behaviour and dynamics (Wexler & Swingle, 1947; Byers & Braham, 1949; Wexler, 1951; Ligda, 1951; Battan, 1953).

3.2 Extrapolation techniques

The concept of extrapolating radar echoes for the short term prediction of precipitation was first proposed by Ligda (1953). The earliest demonstration of the application of objective extrapolation to radar echoes is described by Hilst and Russo (1960), whilst Noel and Fleischer (1960) were amongst the first radar meteorologists to explore the predictability of precipitation echoes using this approach. Further noteworthy papers are those published by Russo and Bowne (1962) and Kessler and Russo (1963). Kessler (1966) and Wilson (1966) explored the use of cross correlation statistics to diagnose a best estimate of echo pattern average motion. Wilson (1966) used the maximum value of the cross correlation coefficient as an indicator of pattern development.

Two important conclusions were drawn from these early studies. The first of these was the positive correlation between the predictability of precipitation features and their size: large features tend to be longer lived than small ones. The second conclusion is an adjunct to the first, namely that small scale features are generally short lived – typically a few tens of minutes. These findings are consistent with early investigations into the multi-scaling properties of the atmosphere and associated limits on atmospheric predictability (Lorenz, 1963; 1973).

The 1970s saw the further development of cross correlation-based nowcasting algorithms and their automation. Zawadzki (1973) developed an optical device for measuring the space-time statistical properties of radar inferred precipitation fields. Austin and Bellon (1974) evaluated an automated, computerized pattern matching programme for nowcasting precipitation up to 3 hours ahead. They concluded that the useful range of these nowcasts varied with the nature and extent of the precipitation. Nonetheless, this approach was shown to be consistently skilful up to one hour ahead over a wide range of events.

This latter work led to the operational implementation of an algorithm based upon global cross correlation at McGill University in the mid-1970s. Bellon and Austin (1978) reviewed the operational performance of this scheme, known as SHARP (Short-Term Automated Radar Prediction), on two years' worth of data. The experience gained allowed subsequent enhancement of their cross correlation method to enable independent tracking of different echoes (Austin & Bellon, 1982) using a nine vector motion field. Rinehart (1981) describes a similar, multi-vector, cross correlation approach to determine and extrapolate the motion of individual storms within a multi-storm system.

3.3 Cell tracking

Algorithms founded on the tracking of radar echo centroids evolved in parallel with field-based pattern matching techniques. These were developed specifically for nowcasting thunderstorms, initially in North America. Amongst the earliest of these echo centroid trackers were those described by Wilk and Gray (1970) and Zittel (1976). The extrapolation vectors were diagnosed using a linear least squares fit through successive positions of the echo centroids. Duda and Blackmer (1972) and Blackmer et al. (1973) formulated clustering techniques to resolve difficulties in cases involving the merging and splitting of echoes.

Refinements to these early techniques were subsequently developed and implemented within operational tools during the following decades. Several good examples are the Storm Cell Identification and Tracking (SCIT) algorithm (Witt & Johnson, 1993) and the Thunderstorm Identification, Tracking, Analysis and Nowcasting (TITAN) system (Dixon & Wiener, 1993).

3.4 Steady state versus growth and decay

The proto-type, operational nowcasting algorithms developed during the 1970s were generally reliant on the steady state assumption. Tsonis and Austin (1981) explored echo size and intensity trending with a view to improving the prediction of long lived convective cells. They found negligible improvement in skill, even using sophisticated non-linear time trending schemes. Wilson et al. (1998) drew similar conclusions in a study involving the use of the TITAN system (Dixon and Wiener, 1993). These results are consistent with the findings of theoretical and NWP modelling experiments showing that the evolution of convective scale features in the atmosphere is non-linear and, to a degree, chaotic (Tsonis, 1989).

3.5 Fractal properties of precipitation

During the 1980s and 1990s, an improved understanding of the chaotic influence of atmospheric processes such as turbulence on the predictability of precipitation was reflected in a growing number of publications exploring the so called *scaling* or *multi-fractal* attributes of meteorological fields, including those of radar derived precipitation fields. Scaling behaviour or self-similarity implies that similar features can be observed in the atmosphere over a wide range of space and time scales, and that the relationship between certain statistical attributes of a precipitation field measured at different scales can be described by equations which incorporate a scaling factor. The formative papers in this area include those by Lovejoy and Schertzer (1985, 1986).

3.6 Exploration of statistical and statistical-dynamical models of precipitation

This same period saw the development of a number of statistical (Krajewski & Georgakakos, 1985; Cox & Isham, 1988) and statistical-dynamical predictive models of precipitation (Georgakakos & Bras, 1984a, b; Lee & Georgakakos, 1990; French & Krajewski, 1994; Bell & Moore, 2000a). The latter were formulated to assimilate radar estimates and surface observations of precipitation and make forecasts using a simplified treatment of the governing atmospheric equations, focusing on the conservation of water mass. These studies were motivated by the operational forecasting requirements of the hydrological community and the limitations of “steady-state” nowcasting techniques and the first generation of operational, mesoscale NWP models.

3.7 Impact of forecast uncertainties

A growing recognition of the need to account for and communicate meteorological forecast uncertainty (Murphy & Carter, 1980; Krzysztofowicz, 1983), particularly in relation to precipitation, led to the development of a range techniques for probabilistic precipitation nowcasting. Andersson and Ivarsson (1991) evaluated an advection-based nowcasting scheme in which the probability of precipitation at a given location is estimated from the areal distribution of precipitation in a neighbourhood surrounding it (see also Schmid et al., 2000). This approach accounts for the impact of extrapolation errors on the location of advected precipitation. Other authors have adopted similar approaches. For example, Germann and Zawadzki (2004) used a local Lagrangian method to produce probabilistic extrapolation nowcasts.

The previously mentioned theoretical work on multi-fractals, and empirical studies supporting a scaling model representation of precipitation fields, laid the foundations for the development of a number of stochastic precipitation nowcasting schemes exploiting scale decomposition frameworks. Seed (2003) adopted a multi-scale decomposition framework in his S-PROG (Spectral-Prognosis) scheme to nowcast the space-time evolution of high resolution radar derived precipitation fields (see Figure 2); he highlighted the potential application of S-PROG to conditional simulation and design storm modelling.

In a similar vein, the McGill Algorithm for Precipitation Nowcasting by Lagrangian Extrapolation (MAPLE; Turner et al., 2004) exploits a wavelet transform to model the predictability of precipitation as a function of scale. The aim of the scale decomposition is to filter out the unpredictable scales in an extrapolation nowcast, and in so doing, minimize the Root Mean Square nowcast error (typically measured using rain gauge observations and/or radar inferred estimates of surface precipitation rate or accumulation).

Pegram and Clothier (2001) used a power law model to filter Gaussian distributed random numbers to generate stochastic realizations of radar precipitation fields in their String of Beads Model (SBM). Noise generation techniques similar to these were combined with a stochastic model of extrapolation velocity errors in the Short Term Ensemble Prediction System (STEPS, Bowler et al., 2006) to produce operational precipitation nowcasts quantifying uncertainties in phase as well as amplitude. In STEPS, the noise serves several purposes: it enables ensembles of equally likely nowcast solutions to be generated by perturbing predicted features as they lose skill; it also downscales an NWP forecast, injecting variance at scales lacking power (variance) relative to the radar.

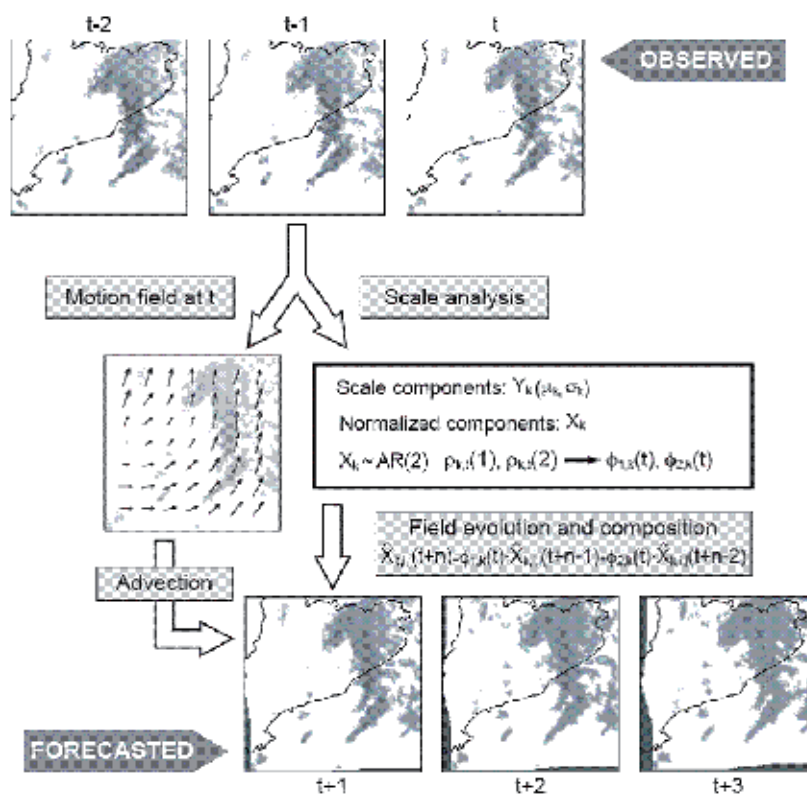


Fig. 2. The generation of an extrapolation nowcast using the Spectral-Prognosis (Seed, 2003) multi-scale decomposition (cascade) framework (after Berenguer et al., 2005). The motion of the precipitation field is derived from radar inferred analyses of precipitation rate valid at t and $t-1$ (typically a 10 or 15 minute time step). The temporal evolution of the extrapolated field is modelled on the hierarchy of scales produced by the cascade decomposition, using a hierarchy of second order auto-regressive (AR-2) models – one for each scale – and the analyses of precipitation rate valid at t , $t-1$ and $t-2$.

3.8 Improvements in extrapolation techniques

The past two decades have also seen further refinements to the extrapolation schemes exploited by precipitation nowcasting algorithms, notably in the form of COTREC (Li et al., 1995; Mecklenburg et al., 2000), Variational Echo Tracking (VET; Germann & Zawadzki, 2002) and optical flow (Bowler et al., 2004, Peura & Hohti, 2004). COTREC constrains the cross correlation diagnosed displacement vectors using the two dimensional continuity equation. This is equivalent to minimizing the divergence of velocities derived for adjacent blocks. The benefits over TREC (Rinehart and Garvey, 1978) were shown to be due to the elimination of spurious motion vectors caused by clutter, beam blockages and rapid changes in the precipitation pattern. In common with optical flow, the VET scheme diagnoses a field of motion by direct application of the optical flow constraint equation. Bowler et al. (2004) solve this equation before applying a smoothness constraint whereas Germann and Zawadzki (2002) uses a conjugate gradient method to minimize residuals from two constraints simultaneously.

3.9 NWP-based nowcasting

The 1990s saw the first attempts to run convection resolving NWP model forecasts assimilating radar data (Lin et al., 1993). These early experiments were focused on predicting convective storms.

Some success was demonstrated in cases involving convection strongly forced by the large scale environment. However, other studies showed that convective initiation in a weakly forced environment is difficult to predict because the location and timing of initiation are very sensitive to variations in low level temperature and moisture. It seems likely that the ability of convection resolving NWP models to predict convection is a function of the predominant scale of the associated forcing. In the UK, much of the convection is forced by small-scale orography, as demonstrated by the Convective Storms Initiation Project (Morcrette et al., 2007; Lean et al., 2008).

Despite these challenges, Lean et al. (2008) found that convection resolving models performed better in terms of convective initiation than a 12 km grid length model with parameterized convection, and a number of national weather services are now running operational, convection resolving NWP models. Indeed, some are trialling configurations with hourly or sub-hourly assimilation of radar data. NWP nowcast experiments in the UK show some improvements in NWP forecast skill in the nowcast time frame. Prospects for NWP nowcasting will be discussed in more detail later in this Chapter.

4. Conventional nowcasting techniques

4.1 Deterministic techniques

4.1.1 Cell tracking

Cell trackers or object-based nowcasting schemes are typically developed in areas where severe convective storms are a significant hazard, and are best suited to the generation of qualitative warnings of severe convective weather. In general, object-based algorithms are used to predict the location of a (convective) object in the future and thereby assign the properties of the object to that location. For example, a storm might be deemed to contain large hail, and therefore a warning of large hail will be issued for the locations on the forecast storm track.

The basic elements of cell tracking are:

1. devise a set of rules that will be used to identify the bounds of an object in either two or three dimensions;
2. analyse current data to identify objects and assign attributes to them (heavy rain, damaging wind, large hail etc);
3. link the objects to existing tracks and estimate the advection velocity;
4. predict the location of objects in the future.

Most cell tracking algorithms define an object, either as a set of contiguous points that exceed some threshold in radar reflectivity, typically 35, 40 or 45 dBz (e.g. Dixon & Weiner, 1993; Han et al., 2009), or as a small region of increased reflectivity (Crane, 1979), or both (e.g. Handwerker, 2002). Defining the object in three dimensions allows one to compute the volume and height of the cell. This adds value when assigning the elements of severe

weather or some sort of severity index, but does not necessarily add value to the identification and tracking of the cells. Rigo et al. (2010) used both 2D and 3D radar products and total lightning data to identify and track convective storms. A storm track is defined as a time series of cell positions. Assigning cells to tracks is the most complex aspect of these algorithms.

All cell tracking algorithms have to deal with cell initiation, mergers, splits, and terminations – the hatches, matches, and dispatches as it were – and this is often the point of differentiation between the various approaches. Errors in assigning the correct cell to a track are a major cause of error when estimating the cell velocity. The size of the object depends on the threshold that has been selected. Therefore, the predictability of the object decreases as the threshold is increased since the lifetime of a cell is related to its size. Using a high threshold to define the cell will make it more difficult to assign a cell to a track. This will increase the errors when estimating the track velocity. Using a low threshold will increase the longevity of the tracks, but will tend to limit the ability to forecast the location of the most severe cells within the storm. The concept of an “object” becomes less useful as the precipitation becomes more widespread. At some point (depending on the skill of the tracking algorithm), cell tracking algorithms fail to provide useful forecasts.

TITAN (Dixon & Weiner, 1993) and SCIT (Johnson et al., 1998) are good examples of what can be achieved in the object-tracking paradigm. Both TITAN and SCIT use the three-dimensional radar reflectivity data to identify a convective object that is defined by a reflectivity threshold. In TITAN, the current objects are linked to past objects through combinatorial optimization. This minimizes the total advection and change in cell volume between the previous and current time steps. Many other cell tracking algorithms, SCIT for example, assign the cell that is closest to the forecast location of an active track. Han et al. (2009) evaluated several extensions to TITAN including improvements in assigning cells to tracks and using TREC motion vectors to advect the cells. In assigning a cell to a track, they found that the most significant improvements were due to adding a requirement that the forecast cell from the track at the previous time step must overlap with the current cell.

4.1.2 Field-based advection

Field tracking algorithms generally divide a Cartesian grid of radar reflectivity or rain rate into a number of tiles and then find the advection of the tile that maximizes the cross correlation (or some other measure of similarity) between successive time steps in the data. The mean advection vector for each tile containing rain is then calculated by applying some form of constraint to minimize the divergence of the resulting vectors.

A number of the current field tracking-based nowcasting algorithms use COTREC (Li et al., 1995) as the basis for deriving the advection vectors. Examples include the system that has been developed at the Czech Hydrometeorological Institute (Novak, 2007), the Hong Kong Observatory system, SWIRLS (Li et al., 2000), and the system implemented at the Guangdong Meteorological Observatory system (Liang et al., 2010). Liang et al. (2010) determined that the optimum size of the tile was 30 km. Li et al. (2000) evaluated the performance of an advection scheme on a 93 x 93 grid using a 19 pixel tile: this equates to 20 km on their 256 km x 256 km domain.

Bowler et al. (2004) used the optical flow constraint (Horn & Schunck, 1981) approach that is used for computer vision applications to derive the mean advection vector for tiles with rain. Optical flow uses least squares to find the (u,v) that minimizes the two-dimensional conservation equation

$$\frac{dR}{dt} = u \frac{\partial R}{\partial x} + v \frac{\partial R}{\partial y} + \frac{\partial R}{\partial t} = 0 \quad (1)$$

over a local neighbourhood.

Bowler et al. (2004) smoothed the field using a moving average over a (15×15) pixel mask before calculating the partial derivatives using a finite difference scheme. The smoothed image was then partitioned into 48×48 km² tiles and least squares used to estimate the mean advection vector within the tile. The resulting vectors were then smoothed so as to minimize $\nabla^2 V$. Grecu and Krajewski (2000) used a similar approach over 40×40 km² tiles. Foresti and Pozdnoukhov (2011) used optical flow to track areas with rain rates that exceeded 10 mm/h. Essentially, this represents the application of optical flow to cell tracking.

Germann and Zawadzki (2002) used the Variational Echo Tracking (VET) method of Laroche and Zawadzki (1995) to derive the advection velocities. This technique partitions the field into small tiles and then uses the conjugate gradient method to minimize a cost function in one global minimization. The cost function includes a smoothness term. The difference between this approach and optical flow is that optical flow applies the smoothness constraint after the velocity field has been calculated for each tile, thereby avoiding an expensive global minimization (Bowler et al. 2004). Ruzanski et al. (2011) describe another approach using a linear least squares technique in the frequency domain.

Cell tracking algorithms assign a velocity to each object and this is advected with a constant velocity during the forecast period. Such an approach is not optimal for field tracking algorithms because it does not allow for changes in direction and speed of motion during the forecast period. Germann and Zawadzki (2002) undertook a detailed analysis of several advection algorithms and found that a modified semi-Lagrangian backward interpolation scheme was optimal. Bowler et al. (2004, 2006) used the simpler semi-Lagrangian scheme that is applied for each time step in the forecast time series. Semi-Lagrangian advection requires a velocity at each pixel in the field and the optical flow technique does not provide advection vectors for tiles that have no rainfall. Therefore the velocity at each pixel must either be interpolated from the tiles with rain, or provided by a hierarchical approach that progressively reduces the size of the tiles that are used in the analysis (e.g. Germann and Zawadzki, 2002).

Kernel-based methods have been employed for advection by Ruzanski et al. (2011) and Fox and Wikle (2005) using

$$\mathbf{y}_{t+1} = \mathbf{H}\mathbf{y}_t \quad (2)$$

where

$$\mathbf{y}_t = [y(s_1, t), y(s_2, t), \dots, y(s_n, t)]^T \quad (3)$$

is the vector of the n pixels in the image and $\mathbf{H} = \{h_{ij}\}$ is the $n \times n$ matrix of the advection operator.

Ruzanski et al. (2011) report that their approach is computationally efficient, although the time taken to derive the motion vectors was comparable to that required for optical flow. Furthermore, the advection algorithm was an order of magnitude slower than a simple implementation of a semi-Lagrangian backward interpolation scheme. Both Ruzanski et al. (2011) and Fox and Wikle (2005) demonstrated their methods using small images. The size of the advection operator is likely to become a constraint when using this technique to advect a large (say 10^6 pixels) image.

4.1.3 Analogues

Panziera et al. (2011) provide a good introduction on the assumptions and use of analogues in nowcasting. Advection-based tracking techniques rely on the assumption that precipitation fields evolve relatively slowly in Lagrangian coordinates and, therefore, their future state can be predicted largely by extrapolation. The assumption of Lagrangian persistence becomes a major limitation on the accuracy of nowcasts in situations where a field evolves rapidly, for example in situations where new storms are initiated or existing storms grow or decay. Data mining and analogue techniques seek to predict initiation, growth and decay by matching the current weather pattern with similar, past events and then use these past events as the basis for generating a forecast.

The first step in the use of analogues is to, either identify a set of regimes in the historical data, or identify a set of predictors that can be used as measures of similarity. Thereafter, the analogue that is closest to the current situation is selected and used as a basis for the forecast. This implies that the technique must be trained for each location, and that a significant historical record is available. Panziera et al. (2011) used predictors of mesoscale airflow and air-mass stability to select 120 analogues, and then employed two measures from the radar derived rainfall fields to select a set of 12 analogues to use as a forecast ensemble. Foresti and Pozdnoukhov (2011) derived maps of where orographic enhancement was likely to occur for a set of weather types. These could then be used to correct biases in advection forecasts.

4.2 Errors in precipitation nowcasts

4.2.1 Error sources and attribution

Sources of forecast errors include errors in the initial quantitative precipitation estimates (QPE), those arising from incorrect diagnosis of the field of motion, and changes in the motion and evolution of precipitation fields during the forecast period.

Approximately half of the total forecast error in the first hour of a forecast is due to errors in the radar derived rainfall analyses (Bellon & Austin, 1984; Fabry & Seed, 2009). This is because radar rainfall estimation errors, arising from variations in the relationship employed to convert the observed radar reflectivity to rainfall, have significant correlations over about an hour in time (Lee et al., 2007) and tens of kilometres in space (Velasco-Forero et al., 2009; Yeung et al., 2011).

Dance et al. (2010) used a year of TITAN tracks to investigate how cell tracking errors varied as a function of lead time, storm intensity, speed and duration. They found that the RMS errors in track speed and direction over the year were about 10 km/h and 30° respectively. Dance et al. (2010) found that tracking errors (both speed and direction) were large when the track speeds were less than 15 km/h; also, errors in track direction decreased with increasing speed.

Mecklenburg et al. (2000) investigated the tracking errors for TREC and COTREC and found that the mean absolute displacement and direction error for a 30-min forecast of convection was about 10 km and 20° respectively. Ebert et al. (2004) showed that TITAN cell tracking algorithms had a median error of about 10 km/h for intense cells. The median tracking error for the baseline field tracking algorithm – a correlation technique finding a single advection vector for the entire field of convective storms – was found to be 20 km/h using the same data.

Hourly accumulations of rainfall typically have correlation lengths of the order of 10 km (e.g. Anagnostou et al., 1999; Gebremichael & Krajewski, 2004). The tracking error after an hour is at least the same order of magnitude as the correlation length of the accumulations. Therefore, one would expect that enhancements to the current tracking algorithms should lead to improvements in the skill of nowcasts at lead times when tracking errors become a significant fraction of the correlation length of the rainfall field: this is likely to be around $T + 30$ minutes.

Berenguer et al. (2005) found that the temporal evolution of the advection field was not a significant source of error for nowcasts with lead times less than 60 minutes. Bowler et al. (2006) discovered that forecast errors due to the temporal evolution of the advection field were negligible in the first three hours of a nowcast and accounted for 10% of the total error after six hours.

It is interesting to note that the probability distribution of cell tracking errors is highly skewed (see, for example, Figure 20 of Ebert et al., 2004) and that the maximum 60 minute location error can be as high as 70 km. The fat tail in the distribution of tracking errors is a significant issue for operational nowcasting systems. Manual editing of the tracks (e.g. Bally, 2004) adds value to the automatic forecasts by eliminating the tracks that are regarded by the forecasters as being, either unimportant from a severe weather perspective, or incorrect.

Errors due to the initiation and decay of storms during the forecast period become increasingly dominant as the lead time extends beyond 60 minutes (Wilson et al., 2010). Zawadzki et al. (1994) evaluated the limits of predictability of rainfall fields as a function of space and time and found that the time for a Lagrangian persistence forecast to reach a correlation of 0.5 ranged from 40 to 112 minutes. They also found that these predictability times depended on the scales present in the rainfall field.

4.2.2 Space-time structure of errors and their treatment

Roca-Sancho et al. (2009) examined the spatial and temporal structure of forecast errors for MAPLE. They demonstrated that the temporal correlation of forecasts errors was very low after 60 minutes and that the spatial structure of the forecast errors progressively resembled that of rainfall with increasing lead time. The latter effect was due to increasing

errors in the location of rainfall. Fabry and Seed (2009) showed that forecasts of high rain rates were generally over-predictions and that the performance of advection forecasts in the recent past is not a good predictor of future performance. The best predictors were found to be raining fraction and the rate of change in mean areal precipitation over the forecast domain.

Germann and Zawadzki (2002) demonstrated that filtering the rainfall analysis field with a 64 km, low-pass filter increased Lagrangian life times by between 40 and 60 minutes, depending on the extent to which small scale features are embedded in larger-scale rain areas. Germann et al. (2006) state that the upper bound for an advection-based nowcasting system that does not include growth and dissipation of rainfall is about six hours. The typical lifetime of a storm is closely related to the scale of the storm, and is often represented as a power law of the scale (e.g. Marsan et al., 1996; Schertzer et al., 1997; Seed et al., 1999). Therefore, some nowcasting systems improve the accuracy (in the RMS error sense) of their predictions by progressively smoothing out the small scale features present in the analysis field (e.g. Seed, 2003; Turner et al., 2004). This removes features from the nowcast that are essentially unpredictable.

An alternative way of handling the perishability of the fine scale components in advected precipitation fields is to model them stochastically. This approach will be discussed in section 4.3.

4.2.3 Performance of nowcasting algorithms

The Critical Success Index is often used to report the accuracy of nowcasting algorithms presented in the literature. Ruzanski et al. (2011) found a CSI of approximately 0.5 after 10 minutes at a spatial resolution of 0.5 km. Liang et al. (2010) calculated a CSI of approximately 0.35 after 60 minutes for echoes in the 15-45 dBZ range at 2 km resolution. Berenguer et al. (2011) report a CSI for 60 minute forecasts of reflectivity (dBZ) at 1 km resolution of approximately 0.5 for widespread rainfall, and in the range of 0.1 to 0.3 for isolated convection. Poli et al. (2008) discovered that the CSI was generally low at the start and end of a storm, reaching a peak of around 0.4 for 1 km resolution T+60 minute forecasts of reflectivity greater than 30 dBZ.

Nine nowcasting systems were implemented for the Sydney 2000 Forecast Demonstration Project (Ebert et al., 2004) and eight nowcasting systems participated in the Beijing 2008 Olympics' Forecast Demonstration Project (Wang et al., 2009; Wilson et al., 2010). Wang et al. (2009) demonstrated that the overall performance of the nowcasting systems had improved during the years from 2000 to 2008. They showed that the maximum CSI for forecasts of hourly precipitation accumulation greater than 1 mm/h increased from 0.2 in 2000 to 0.45 in 2008, although the maximum CSI for rain greater than 10 mm/h was still only 0.15.

Lee et al. (2009) found that the CSI decreased with increasing rain rate and forecast lead time: the CSI for 60 minute rainfall forecasts decreased from 0.60 for 0.1 mm/h to 0.2 for 10 mm/h rain rates. Ebert et al. (2004) reported that the CSI for rain greater than 20 mm/h is essentially zero. This implies that the use of nowcasting techniques to predict the precise location of extreme rain for flash flood warning may not be viable.

In summary then, the accuracy of a nowcast depends on the accuracy of the initial radar derived rainfall field, the degree of spatial organization of the rain, the rain rate, and forecast lead time. Also, it is likely to be higher in the middle of the storm (in both space and time) than at the edges.

4.3 Probabilistic techniques

4.3.1 Justification

Given the magnitude of the errors in a 30 minute precipitation nowcast, it is reasonable to adopt a probabilistic approach to nowcasting and attempt to convey to the users the uncertainty that is associated with a particular weather situation. As explained earlier, within the extrapolation nowcast framework, errors can be categorized into those attributable to the radar observations and processing, inaccuracies in the field of motion used to advect the observations, and errors arising from assumptions made about the Lagrangian evolution of the advected precipitation field.

4.3.2 Methods of handling uncertainties

A number of techniques have been developed for modelling nowcast errors with a view to producing probabilistic precipitation nowcast products. One of the simplest entails time-lagging a consecutive series of deterministic nowcasts using techniques similar to those demonstrated in a NWP post-processing context (Mittermaier, 2007). Each member of the time-lagged ensemble is assigned a weight which is a function of lead time. SWIRLS generates probabilistic nowcasts using this approach (Wang et al., 2009).

Another approach relies on the assumption that errors in the diagnosed advection velocity field predominate. Consequently, the probability of exceeding a chosen precipitation threshold at a given location can be derived from the distribution of precipitation in a neighbourhood surrounding the forecast location. The neighbourhood size increases with lead time to reflect to the growth in advection errors (Andersson & Ivarsson, 1991; Schmid et al., 2000).

Germann and Zawadzki (2004) compared four methods of generating probabilistic precipitation nowcasts based upon radar extrapolation. They concluded that the most skilful method was one based upon the local Lagrangian technique. Essentially, this produces an advection forecast using a semi-Lagrangian backward advection scheme and then uses the probability distribution of forecast rain rates in some search area centred on a pixel to calculate the probability of exceeding a threshold at that location. The size of the search area increases with lead time to reflect the increasing forecast uncertainty. This approach has since been exploited by others, for example Megenhardt et al. (2004), and more recently, Kober et al. (2011).

Other authors have focused their attentions on modelling errors using stochastic space-time models. Pegram and Clothier (2001) used a power law model to filter Gaussian distributed random numbers to generate stochastic realizations of radar precipitation fields in their String of Beads model (SBM). Noise generation techniques similar to these were combined with a stochastic model of extrapolation velocity errors in the Short Term Ensemble Prediction System (STEPS; Bowler et al., 2006) to produce operational precipitation nowcasts

quantifying uncertainties in phase as well as amplitude. In STEPS, the noise serves several purposes: it enables ensembles of equally likely nowcast solutions to be generated by perturbing predicted features as they lose skill; it also downscales an NWP forecast, injecting variance at scales lacking power (variance) relative to the radar.

4.3.3 Treatment of observation errors

Uncertainties in nowcasts of precipitation also derive from errors in the radar observations and processing. Austin (1987) categorized radar errors into physical biases, measurement biases and random sampling errors. Historically, much effort has been invested in improving deterministic estimates of precipitation accumulation at the surface by correcting physical (e.g. ground clutter and beam blockage) and measurement (e.g. Z-R conversion) biases. However, more recently, a growing number of researchers have focused their attentions on the treatment of random sampling errors and how these can be utilized within stochastic, integrated system frameworks to improve hydro-meteorological nowcasting.

Two main approaches to the modelling of random sampling errors in QPE have been described in the literature: one entails a statistical description of the difference between the radar estimates and a reference (e.g. Ciach et al., 2007; Lloret et al., 2008; Germann et al., 2009); a second involves modelling the characteristics of individual sources of error (e.g. Jordan et al., 2003; Lee & Zawadzki, 2005a, 2005b, 2006; Lee, 2006; Lee et al., 2007). The challenge with the first approach is the need for a reference field: this is usually derived from a dense network of rain gauges. The difficulty with the second approach is that the true error structure of QPEs can vary significantly depending on the meteorological conditions and is therefore largely unknowable.

Germann et al. (2009) describe a radar ensemble generator using LU decomposition (factorization) of the radar-gauge error covariance matrix to derive an ensemble of precipitation fields. Each ensemble member is the sum of the bias corrected, deterministically derived radar precipitation field and a stochastic perturbation representing the random error. The stochastic term is generated such that it preserves the correct space-time error covariances. The authors present the results of the coupling of a real-time implementation of the radar ensemble generator with a semi-distributed hydrological model.

Norman et al. (2010) implemented several radar ensemble generators and compared their performance on a selection of case study events using rain gauges. An implementation of the Germann et al. (2009) scheme was found to be marginally superior to one comprising separate models of Z-R (Lee et al., 2007) and VPR (Jordan et al., 2003) errors. Pierce et al. (2011) integrated these two ensemble generators to produce ensembles of radar-based analyses of surface precipitation rate for input to STEPS. They evaluated the impact of these ensembles on the performance of STEPS ensemble precipitation nowcasts. Verification results demonstrated that accounting for QPE errors improved the ensemble spread-skill relationship in the first hour of the nowcasts.

One alternative to the stochastic QPE and QPN schemes described above is the use of historical analogues. Panziera et al. (2011) describe an analogue-based heuristic tool for nowcasting orographically forced precipitation. The system known as Nowcasting of Orographic Rainfall by means of Analogues, exploits the strong correlation between

orographic rainfall and predictors describing mesoscale flow and air mass stability, to identify past events with predictors similar to those derived from real time observations. The authors present verification results showing that NORA performs better than Eulerian persistence for nowcasts with lead times of more than an hour.

5. NWP-based nowcasting

5.1 Introduction

In the past few years, increasing availability of high powered computers and the implementation of non-hydrostatic models have made NWP at the convective scales (1 km–4 km horizontal grid length) a reality for national weather services. Many centres are already running these models operationally with update cycles of between 3 and 6 hours to generate short-range forecasts up to about T+36 hours. Traditionally, these forecasts have been deployed in combination with nowcasting techniques to deliver optimal guidance. However, recently, centres have begun to explore the use of NWP-based systems for nowcasting.

5.2 The challenges

For nowcasting purposes, the key component of NWP is the data assimilation of high resolution observations in space and time, especially radar and geostationary satellite data. Traditional nowcasting techniques use these observations to produce forecasts of rain, cloud and associated weather with observation derived advection velocities, or NWP forecast wind fields, or a combination of both. Nowcasts are also produced from analyses of other weather elements including screen temperature, visibility, 10 m wind and wind gusts. However, these systems do not use the observations in an optimal manner and may not use all available observation types.

Data assimilation into NWP models potentially offers the ability to use all observations in a consistent and synergistic manner to provide the best estimate of the state of the atmosphere from which to produce a nowcast. At this time, nudging, variational data assimilation (3D-Var and 4D-Var) and ensemble Kalman filters (EnKF; Sun, 2005b) for high resolution data assimilation are being used in weather services or are under development in research centres around the world. Indeed, some national weather services are already running operational NWP models with data assimilation at grid lengths in the range 1 km-10 km. Most of this work relies heavily on the exploitation of Doppler radar measured radial winds and reflectivity data or derived surface rain rates.

One challenge for NWP-based nowcasting is to match the skill of traditional methods in the first two hours. Traditional nowcasts closely fit the observations because they employ extrapolation techniques and so use the observations themselves (i.e. radar derived surface rain rate) at analysis time. This is challenging for NWP because unresolved scales are excluded from the model state, data assimilation systems are designed, not to match observations, but to achieve a good and balanced forecast over a longer period of time, and the T+0 fields from the NWP system are essentially a weighted fit to both the NWP forecast and the observations.

Also, traditional nowcasts can produce forecasts within a few minutes of data time, but complex data assimilation methods and numerical integration of the governing atmospheric equations are more costly and therefore take longer. However, if these techniques produce improved forecasts at longer lead times, the benefits outweigh the timeliness issue and reduced accuracy in the first 2 hours.

Another performance issue with NWP-based nowcasts relates to the latency of the boundary conditions. This arises because domain sizes are usually small and are nested in coarser resolution forecasts or larger domain forecasts with less frequent analysis cycling and later data cut-off times. The consequences are that the boundary conditions and synoptic scale forcing cannot be refreshed as frequently or as recently on the larger domain(s) as they are on the nowcast inner domain. This limits the skill at longer forecast ranges and possibly close to the boundaries.

Nonetheless, the advantage of NWP-based nowcasting lies in the fact that model formulation, dynamical equations and physical parameterizations can predict the non-linear evolution of weather elements and, in particular, the generation and decay of precipitating weather systems.

5.3 A status report

To investigate the direct use of NWP for nowcasting, the Met Office in the UK is developing an hourly cycling 4D-Var high resolution (1.5 km) NWP system to run on a domain covering southern England (see section 5.4). This is nested within the most recent forecasts for the whole of the UK (1.5 km resolution forecasts produced every 6 hours from 3 hourly 3D-Var data assimilation cycles at 3 km resolution) to obtain boundary conditions. The latter may be up to 6 hours old. Although 4D-Var is more expensive than 3D-Var, the aim is to evaluate the benefit of assimilating high time-frequency sub-hourly data (Ballard et al., 2011): see section 5.4 for more details.

Over the past 20 years, NCAR has undertaken many studies to explore the assimilation of radar data into high resolution cloud and NWP forecast models. These have included using the Variational Doppler Radar Assimilation System (VDRAS – Sun, 2005a, 2005b; Sun & Crook, 1994, 1997, 1998, 2001; Sun & Zhang, 2008) with 4D-VAR (Sun et al., 1991, 2012). These tend to use very short time-windows and have exploited the mesoscale model, MM5 3D-Var (Xiao et al., 2005) and the Weather Research & Forecasting Model (WRF) 3D-Var and 4D-VAR, or ensemble Kalman filter (Caya et al., 2005). These were run using VDRAS as part of the forecast demonstration project during the Beijing Olympics (Sun et al., 2010).

Meteo-France has a 2.5 km, 3-hourly cycling 3D-Var scheme covering France (the Application of Research to Operations at Mesoscale – AROME-France). This has been operational since December 2008 (Seity et al., 2011; Brousseau et al., 2011). Radial Doppler winds (Montmerle & Faccani, 2009) and humidity profiles derived from radar reflectivity (Caumont et al., 2010) are assimilated. Meteo-France is also undertaking a project entitled, “AROME-Nowcasting”, to adapt their 2.5 km grid length model, AROME, to meet the requirements of nowcasting. The main difference to AROME-France is the production of an analysis every hour, but without cycling. The potential benefits of a system called AROME-airport, based at Charles de Gaulle airport near Paris, are also being explored. This model will provide an input to a Wake-Vortex forecast model. The main goal is to add new,

dedicated observations, and to run a 500 m grid length model in a configuration comparable with conventional nowcasts (Ludovic Auger, MeteoFrance, personal communication WMO/WWRP Workshop on Use of NWP for Nowcasting, Boulder 2011).

DWD has a 2.8 km forecast model with a nudging assimilation scheme (Consortium for Small-scale Modeling, COSMO) covering Germany (COSMO-DE, Stephan et al., 2008) and is developing PP KENDA (Priority Project "KENDA" - Km-scale Ensemble-based Data Assimilation) for a 1 km-3 km scale Ensemble Prediction System known as LETKF (Local Ensemble Transform Kalman Filter; Ott et al., 2004). MeteoSwiss is running a 2 km version of COSMO. Various collaborating meteorological services are running, or are planning to run versions of these systems.

The HIRLAM (High Resolution Limited Area Model) European community run their 3D-Var system (Gustafsson et al., 2001) with the HIRLAM model at grid lengths down to about 3.3 km and are developing a new HARMONIE system to run at about 2.5 km. They have also run experiments comparing three hourly and hourly cycling at 11 km and are exploring the impact of GPS and Doppler radar radial wind data (Magnus Lindskog, HIRLAM personal communication WMO/WWRP Workshop on Use of NWP for Nowcasting, Boulder 2011 and HIRLAM Newsletter No. 58, November 2011).

In the USA, NCEP (National Center for Environmental Prediction) has an operational RUC (Rapid Update Cycle) system with hourly data assimilation (Benjamin et al., 2004). As of September 2011, this was due to be replaced by the Rapid Refresh. The RR uses a version of the WRF model (currently v3.2+) and the Grid-point Statistical Interpolation (GSI) analysis largely developed at NCEP/EMC (Environmental Modelling Center, NOAA), using hourly cycling and a 13 km grid length. NCEP also run a 3 km model nested in the RR, but this has no separate data assimilation (Steve Weygandt et al., Earth System Research Lab, Boulder, personal communication WMO/WWRP Workshop on Use of NWP for Nowcasting, Boulder 2011, Stensrud et al., 2009; Smith et al., 2008; Weygandt et al., 2008).

In Japan, JMA (Japan Meteorological Agency) runs a Mesoscale Model (MSM) for Japan and its surrounding areas using a 5 km grid length and 4D-VAR with forecasts every 3 hours to 15 or 33 hours (Honda et al., 2005; Saito et al., 2006). This is a non-hydrostatic model (JMA-NHM). Development of NWP at a higher resolution (Local Forecast Model, LFM) is also in progress to help produce sophisticated disaster-prevention and aviation information services.

A trial operation of a 9-hour LFM forecast run on a 2 km grid length was performed in 2010 and 2011, and operational implementation is scheduled to start in 2012. LFM also uses JMA-NHM as a forecast model, and its initial condition is generated from a 3D-Var rapid update cycle. The cycle uses the MSM forecast as the first guess, and runs a JMA non-hydrostatic model-based variational data assimilation system (JNoVA) – a 3DVar (a degenerate version of JNoVA-4DVar) analysis and 1-hour JMA-NHM forecast in turn – over 3 hours using a 5 km grid length.

The Korean Meteorological Agency (KMA) is currently running the WRF 3D-Var (Barker et al., 2004, Xiao et al., 2008) at 10 km but is planning to use the 1.5 km, variable resolution Met Office Unified Model (UM) system with 3D-Var in the near future. In the past they have tested a 3.3 km version of WRF 4D-Var (Huang et al., 2009).

Over recent years, CAPS (Center for Analysis and Prediction of Storms, Oklahoma, USA) has been carrying out experimental, real time forecasting including the generation of 1 km grid length forecasts on a continental U.S. domain once a day, and the production of rapidly updated NWP-model-based nowcasts producing two hour, 1 km forecasts every 10 minutes (Xue et al., 2011; Kong et al., 2011; Clark et al., 2011; Brewster et al., 2010). These forecasts assimilate US operational WSR-88D radar data and/or high-resolution experimental X-band radar data, with and without assimilation cycles.

Comparison forecasts show systematically positive impacts of assimilating radar data on short-range precipitation forecasting, lasting up to 12 hours on average. To address forecast uncertainty and to provide probabilistic forecast information, storm-scale ensemble predictions have also been carried out and the products have been evaluated at an experimental forecasting facility. Extensive research has also been undertaken using ensemble-based data assimilation methods for initializing storm-scale NWP models, with very promising results.

CAPS has investigated a Mesoscale Convective System/vortex case study exploiting nested 400m / 2 km grids and assimilating radar data at 5 min intervals using their Advanced Regional Prediction System (ARPS) 3DVAR+cloud analysis (Schenkman et al., 2011a) as well as EnKF (Snook et al., 2011). These show data impact on Collaborative Adaptive Sensing of the Atmosphere (CASA; Schenkman et al., 2011b) and probabilistic forecast skill with EnKF analyses (Snook et al., 2011; 2012).

Environment Canada has begun developing a convective-scale EnKF in order to examine the assimilation of radar data (e.g. over the Montreal region; Luc Fillion, personal communication WMO/WWRP Workshop on Use of NWP for Nowcasting, Boulder 2011). This is based on adaptation of the Global EnKF code available at Environment Canada (Houtekamer & Mitchell scheme) to a limited-area domain. The analysis step and the forecast model configuration (1 km horizontal grid length) are being validated.

5.4 Development of an NWP-based nowcasting system in the UK

5.4.1 Progress to date

The Met Office has run an operational, 4 km grid length NWP model for the UK (UK4) since December 2005. It has also run a 1.5 km UK configuration (UKV) routinely since summer 2010. Both models use three-hourly cycling 3D-Var and produce forecasts to 36 hours ahead with 70 levels. These are based on the Met Office's Unified Model (Davies et al., 2005) and variational data assimilation system (Lorenc et al., 2000; Rawlins et al., 2007), plus latent heat nudging (Macpherson et al., 1996; Jones & Macpherson, 1997; Dixon et al., 2009). They also include direct variational assimilation of analysed 3D cloud cover via associated relative humidity. The UKV has a 1.5 km grid length over the UK and a 4km stretched boundary nested in the 12 km NAE (North Atlantic and European) model. The UKV uses 3 km 3D-VAR over the whole domain. Collaborations with KMA and CAWCR (Centre for Australian Weather and Climate Research, Australian Government Bureau of Meteorology) are aiming to implement 1.5 km versions of the UM with 3D-Var or 4D-Var.

The Met Office's UK Post-Processing system (UKPP) incorporates a STEPS precipitation nowcast (Bowler et al., 2006). This combines a stochastic, radar-based extrapolation nowcast

with UK4 or UKV precipitation forecasts. An 8 member ensemble and control member (unperturbed) nowcast to T+7 h are produced every 15 minutes. Recent Root Mean Squared Factor error statistics for STEPS control member advection nowcasts and UK4 and UKV forecasts of precipitation have shown that STEPS nowcasts are superior in the first 2.5 hours (see Figure 3).

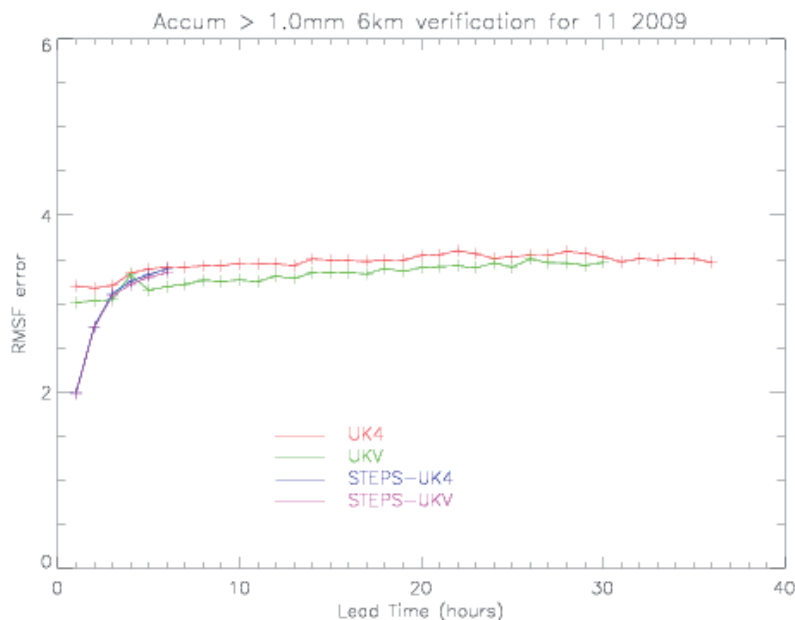


Fig. 3. Root Mean Squared Factor errors for November 2009 based on hourly accumulations greater than 1mm, smoothed to a scale of 6km, and measured using radar derived accumulations as the reference observation. The performance of 1.5 km (green) and 4 km (red) grid length, UK configurations of the Met Office's Unified Model are compared with control member STEPS nowcasts blending radar extrapolation with UM: 1.5 km (purple) and UM: 4km (blue) model forecasts. The performance of the STEPS nowcast blending extrapolation with the UM: 1.5 km forecast does not asymptote to that of UM: 1.5 km model because this was an experimental configuration run without prior calibration.

The implementation of an NWP-based nowcast system in the Met Office is focused on improving the prediction of convective storms for flood forecasting. The ultimate aim is to replace the existing extrapolation-based precipitation nowcasts and site specific forecasting techniques. Boundary conditions will be provided by the 6 hourly 1.5 km UKV system.

An hourly analysis and forecast system for southern England has been run experimentally for a limited number of cases of summer rain and convection, using conventional data and 3D-Var or 4D-Var, plus latent heat nudging of radar derived rain rates and humidity nudging based on analysed 3D cloud cover nudging (Macpherson et al., 1996; Jones & Macpherson, 1997; Dixon et al., 2009). The direct variational assimilation of cloud cover has not yet been tested in the hourly cycling system. This has used a fixed 1.5 km resolution configuration of the Unified Model and a 3 km resolution 4D-Var grid or 1.5 km and 3 km resolution 3D-Var grid.

The ultimate aim is to use 4D-VAR, if affordable and beneficial, in a real-time, routinely running NWP-based nowcast system. This will exploit high resolution (in time and space) Doppler radar measured radial winds and reflectivity or derived surface rain rates directly within the variational analysis scheme. Direct use in 4D-VAR should allow optimum extraction of information through interaction with other data sources, and the potential to modify the dynamical and physical forcing of precipitation and convective storms.

Research is also proceeding to investigate the background errors, balances and control variables required for use in convective scale data assimilation. The aim is to have a real-time system running continuously from summer 2012 for southern England.

5.4.2 A case study comparison of conventional and NWP-based nowcasts

Figure 4 compares T+1 hour, T+2 hour and T+3 hour STEPS control member nowcasts of surface precipitation rate, all valid at 2100 UTC on 3 June 2007 with a radar-based analysis of surface precipitation rate for the same time. At T+3 h, the STEPS nowcast is a combination of an extrapolation nowcast and UK4 forecast precipitation. The UK4 forecast tends to produce individual convective precipitation elements that are too large. It also fails to predict the full extent of the bands of convective precipitation to the east of the precipitation area lying through south-west England and west Wales. At T+2 hours, the STEPS scheme has re-produced the line of convection in the east but this is too narrow, possibly due to convergence in the diagnosed advection velocity field. By T+1 h, a reasonable nowcast has been produced.

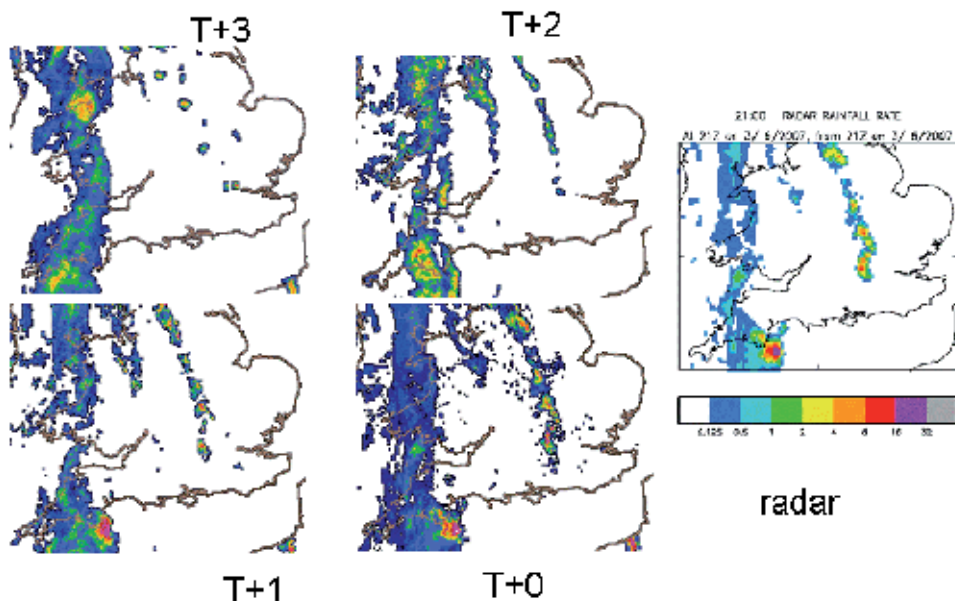


Fig. 4. STEPS T+0 h, T+1 h, T+2 h and T+3 h nowcasts of surface rain rate all valid at 2100 UTC on 3 June 2007. The key shown on the right-hand side represents precipitation rate in units of mm/h. Dry areas are shown in white. Note that dark blue areas in the STEPS nowcasts are not included in the colour key. These represent light drizzle.

Figure 5 shows the evolution of radar derived surface rain rate between 1200 UTC and 2100 UTC on 3 June 2007. It is apparent that a rain band in the west over Ireland at 1200 UTC reduces in intensity and moves only slightly eastward during the following 9 hours. However, bands to the east develop from about 1700 UTC onwards and intensify. The STEPS nowcast from 1800 UTC has not been able to reproduce the development of the eastern-most rain band seen in Figure 5. Nowcasts starting from later analysis times contain more precipitation but tend, incorrectly, to maintain the shape of individual features.

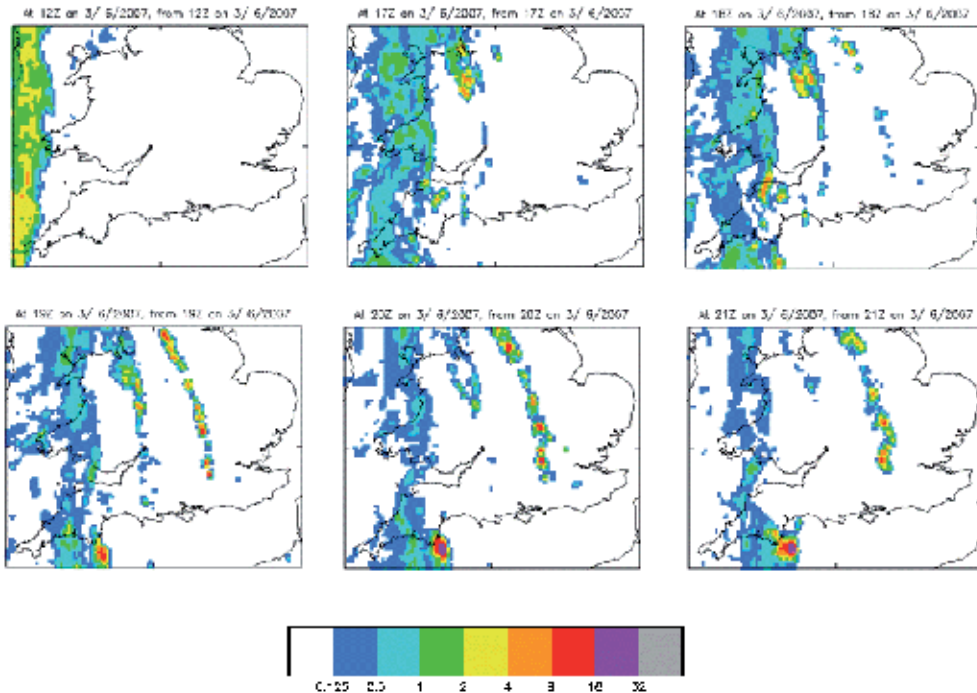


Fig. 5. Radar derived surface rain rates valid between 1200 UTC and 2100 UTC on 3 June 2007. The data for 1800 UTC, 1900 UTC, 2000 UTC and 2100 UTC were used to derive the T+3 h, T+2 h, T+1 h and T+0 h STEPS nowcasts shown in Fig. 4. The key shown below represents precipitation rate in units of mm/h. Note that dry areas are represented by the colour white.

Figure 6 compares T+1 hour, T+2 hour and T+3 hour 1.5 km NWP-based nowcasts of surface precipitation all valid at 2100 UTC on 3 June 2007 with radar derived precipitation rates for the same time. This model has used latent heat nudging of radar derived rain rates available every 15 minutes, and nudging of hourly humidity derived from 3-D cloud cover analyses in conjunction with hourly cycles of 4D-Var assimilation of conventional observations over 1 hour time windows. The NWP nowcasts improve at shorter lead times due to the benefit of data assimilation. In particular, they benefit from the latent heat nudging of surface precipitation rates derived from the sub-hourly radar data. In comparison with the STEPS nowcasts, the 1.5 km NWP nowcast has a better representation of the rain band in the east at both T+3 hours and T+2 hours. However, the representation of the rain in the south-west of England is inferior.

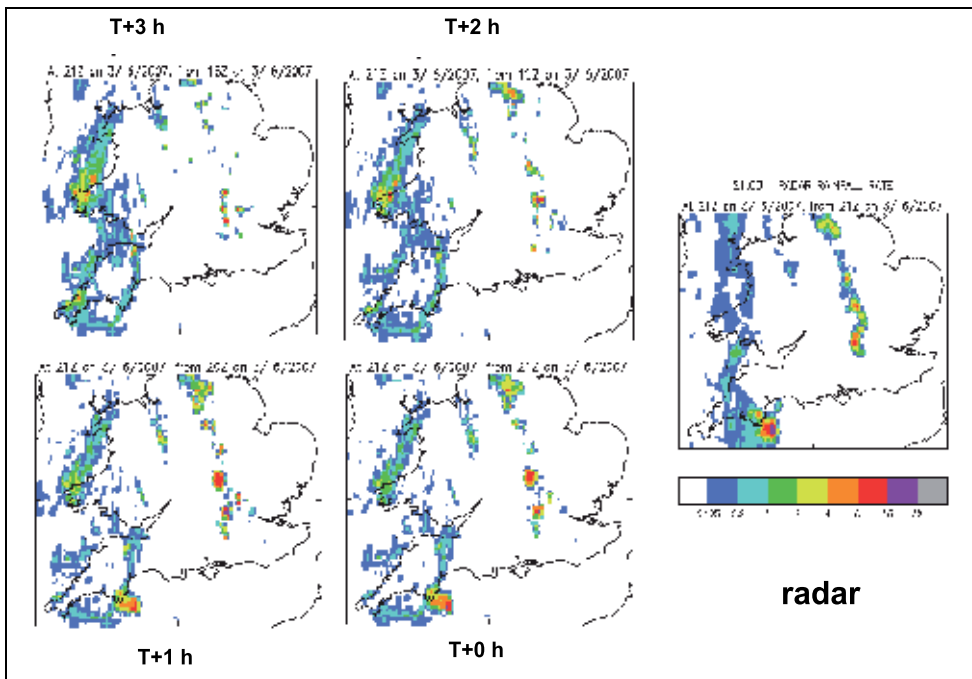


Fig. 6. A prototype Met Office NWP-based analysis (T+0 h) and T+1h, T+2h and T+3h nowcasts of surface rain rate generated using 4D-Var assimilation with latent heat nudging of the radar derived surface rain rates. All fields are valid at 2100 UTC on 3 June 2007. The area of coverage is the full domain of the prototype NWP-based nowcasting system. Note that dry areas are represented by the colour white.

Nonetheless, since this comparison is a first attempt without optimization of the data assimilation scheme and without the exploitation of more frequent conventional and Doppler radar measured radial wind observations, this is a very promising result. The forecast in the south-west can be improved by assimilation of 15 minute time frequency GPS water vapour data. At present, these are only available 90 minutes after data time so cannot be used in a nowcast system. Work is underway to make the UK GPS data available closer to data time.

Another potential source of water vapour information comes from radar refractivity by exploiting the interaction of the radar beam with ground clutter. Work is underway with Reading University to investigate the potential for obtaining this information from the UK weather radar network.

Direct assimilations of radar derived surface precipitation rates within 4D-Var is being investigated as well as direct or indirect assimilation of radar reflectivity, the latter through derived temperature and humidity increments from external 1D-Var assimilation of multiple beam elevations in vertical columns.

5.4.3 Use of Doppler radar derived winds

Potentially, weather radar provides a high resolution source of wind observations via the Doppler returns from hydro-meteors and insects. Currently, four weather radars in the south of England produce Doppler radial winds operationally every 5 minutes when there is precipitation (see Figure 7). The radars each perform scans at 5 elevations. The majority are at 1, 2, 4, 6 and 9 degrees, although one radar near London scans at 1, 2, 4, 5 and 5.5 degree elevations. Doppler winds are available to a range of about 100 km. This provides a small amount of dual or triple Doppler overlap in southern England as can be seen in Figure 7.

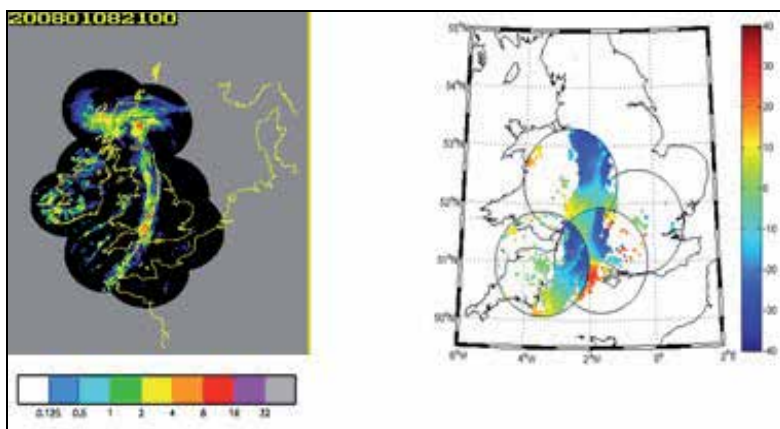


Fig. 7. A comparison of UK weather radar network coverage (left) and Doppler radar radial wind coverage (right) as of 8 January 2008. The key shown bottom-left represents precipitation rate in units of mm/hour. Note that dry areas in the left-hand graphic are represented by the colour black. The grey shading indicates areas without UK weather radar coverage.

Code has been developed to allow their processing, quality control, monitoring, super-obbing and data assimilation. Super-obbing is the process of combining observations that are of higher resolution than the forecast or analysis grid to reduce the data volume (Lorenç, 1981) and representativeness errors. Trials have been run to investigate the impact of Doppler radar radial winds on UK4 model forecasts using 3D-Var. The use of Doppler radar radial wind scans valid at analysis time was made operational in the UK configurations of the Unified Model in 2011. Three-hourly radial winds now replace hourly VAD winds from the same radars in the three-hourly 3D-Var cycles.

Much work has been done on specification of observation errors and investigating the impact of super-ob variances, errors derived from observation-background variances and errors derived from the Hollingsworth and Lonnerberg technique (Hollingsworth & Lonnerberg, 1986).

The impact of Doppler radar radial wind data has been assessed over southern England using a prototype nowcasting system with a 1.5 km grid length model and hourly cycling 1.5 km 3D-VAR. For the initial tests, only the radar scans closest to the analysis hour were selected from each radar for assimilation. Initial subjective and objective verification looks

promising. The location and coverage of precipitation is affected and improved in some situations. Figure 8 shows the increase in Fractional Skill Score (Roberts & Lean, 2008) of forecast hourly precipitation accumulations due to assimilation of radial winds from the four Doppler radars over southern England. These results are based on four case studies of about 10-19 cycles each, using hourly cycling 3D-Var and 11 hour forecasts. The results imply an hour's gain in skill in the earliest hours of the forecasts and a positive impact out to T+6 hours. The extent of the impact is limited by the small size of the domain and the spread of information from the boundary conditions into the domain.

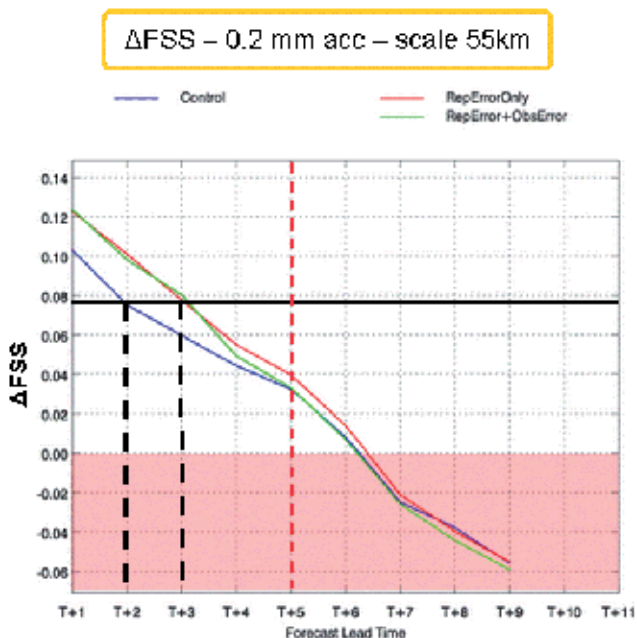


Fig. 8. Δ FSS for a 0.2 mm hourly precipitation accumulation threshold at a scale of 55km. Positive values of Δ FSS are indicative of forecast skill. The performance of the control forecast (blue) is compared with that of a forecast incorporating Doppler radial winds with a specified observation error derived from O-B statistics and referred to as representativeness error (red), and a similar forecast including Doppler radial winds with the representativeness error plus the super-observation standard deviation as the observation error (green).

Work continues on the specification of observation error and to test the impact of hourly and higher time frequency data in the 4D-Var prototyping nowcasting system. The impact and areal influence of observations in a NWP analysis depends on the background error correlation and covariances (i.e. the short range forecast error) at the analysis time, in addition to the observation error itself. The background errors can have a significant impact on forecast quality and the benefit afforded by the observations. Thus, work is underway to define improved errors for the 1.5 km grid length forecasts, both in terms of correlations between variables, length scales and error variances. These need to extract longer time and synoptic scale information as well as information at shorter time and spatial scales from radar data with high spatial and time resolutions. This is very challenging work.

Work with Reading University has been undertaken to look at the potential for use of winds derived from insect returns in fine weather (Rennie et al., 2010). This will continue in collaboration with CAWCR in Australia. Radar returns only give radial winds (i.e. in the direction of the radar beam) rather than 3-D wind components, so the additional information in areas of overlapping radars (dual-Doppler) may increase the impact of wind retrievals in those locations.

5.4.4 Conclusions and further work

1.5 km grid length NWP in the Met Office is showing promise in the very short range prediction of convection over the UK. Previous sections have highlighted the potential benefits of using radar derived precipitation rates through latent heat nudging on top of 4D-Var and of using Doppler radar derived radial winds in 3D-Var.

4D-Var has the potential to exploit higher time frequency observations and to extract more information from them than 3D-Var. Therefore, research is continuing on the use of high time frequency Doppler radial winds, direct application of radar derived surface precipitation rate, and direct and indirect use of multi-elevation volume scan reflectivity in 4D-Var. Although latent heat nudging is still showing benefit in forecasts, it cannot correctly represent resolved convection where latent heat release occurs in different locations to surface precipitation, so it is hoped to obtain benefits from direct 4D-Var or indirect 1D-Var assimilation of the reflectivity data.

Unfortunately, 4D-Var is computationally expensive on the super-computer currently available to the Met Office. Therefore, research and development is being undertaken with both 3D-Var and 4D-Var systems. With a super-computer upgrade due in 2012, the aim is to start running a prototype real-time NWP-based nowcast system in 2012, hopefully with 4D-Var if the upgrade provides sufficient computer resources.

Due to the tight time constraints imposed by operational schedules, it may be necessary to move away from use of a time window centred on the analysis time to one finishing at the analysis time. High quality data sources such as GPS, which provide information on low level humidity, are currently only available 90 minutes after data time, although less accurate but more timely data may become available. There are many sources of information on different variables (e.g. GPS, radar refractivity, satellite imagery and surface observations for low level humidity). The usefulness of the different data sources will be investigated to provide an optimum system. The initial experiments reported here were undertaken nested within the UK 4 km NWP forecast system. Now, the nowcasting system is being tested embedded in the UK 1.5 km NWP forecast system.

The skill of the convective scale nowcasts is very dependent on the accuracy of the synoptic forcing conditions both within the nowcast domain itself and the boundary conditions. Both the UK models and the embedded nowcast system use the same model and essentially the same data assimilation system. Errors in convective initiation can come from errors in the synoptic flow either as a result of lack of observations to correct model errors, or incorrect or sub-optimal use of observations. Finding the best way to extract synoptic scale and convective scale information from observations in both the nowcast system itself and in the forcing at the boundaries will be key to improvements in the skill of the nowcast.

Data sources such as GPS can be problematical because they are vertically integrated measurements depending on the accuracy of the specification of the forecast background errors, and interaction with other data sources to allocate changes to humidity in the vertical can have dramatic impacts on forecast precipitation. The use of high vertical and horizontal spatial and temporal resolution Doppler radar winds and reflectivity or rain rate data, and improvements in specification of forecast background errors, can lead to changes and improvements in the impact of different data sources and the accuracy of the precipitation in the early hours of the forecast.

NWP systems can suffer from imbalances in the initial conditions leading to spin-up or spin-down of precipitation in the initial stages of the forecast. Work to improve this will help to improve skill in the early hours of the nowcasts. Improvements in the skill of the forecast model itself in terms of precipitation biases are likely to help both the forecast and the ability to assimilate observations. We tend to use radar derived rain rates to verify the NWP forecasts, for assimilate into the models and to improve the formulation of the model. However, the radar data can have quality issues, for example relating to attenuation, and improvements in quality control and data processing are needed to ensure that the radar data are of high quality.

The entire UK network of weather radars will gradually be updated to produce Doppler radial winds and also dual-polarization data and radar refractivity measurements. The use of radar data in NWP high resolution variational data assimilation has the potential to improve on current extrapolation-based nowcasts. To achieve this we need high quality radar data, fast processing (techniques and computer power), careful specification of observation and forecast background error covariances and correlations through the scientific design of the data assimilation system, and a good representation of the dynamical and microphysical processes in the NWP forecast model.

In future it is hoped to exploit ensemble techniques in both the data assimilation and production of forecasts. If there is sufficient computer power available for hourly NWP forecasts to 12 hours, this will provide the potential for 6 hours of 1 hourly lagged ensemble forecasts and a measure of the predictability of the nowcasts.

6. Application of radar-based precipitation nowcasts to hydrological forecasting and warning

6.1 Overview

Documented uses of radar data in hydro-meteorology are many and varied. They include numerous studies of the space-time structure of radar inferred precipitation fields (e.g. Harris et al., 2001), the compilation of precipitation climatologies (Panziera et al., 2011), the estimation of Probable Maximum Precipitation (Cluckie, Pessoa & Yu, 1991; Collier & Hardaker, 1996), reservoir design and safety (Cluckie & Pessoa, 1988), design storm modelling (Seed, 2003), urban drainage and waste water management (Cluckie & Tyson, 1989; Schellart et al., 2009), river flow management (Lewin, 1986) and hydroelectric power generation (Baker, 1986).

In addition to the above, operational radar-based precipitation nowcasts can be of great value in fluvial (river) flood prediction because they extend the lead time of flood warnings

by reducing reliance on crude assumptions regarding future precipitation. For pluvial (surface water) flood forecasting, predictions of future precipitation are essential because the time between the precipitation reaching the ground and any consequent flooding is very short (Golding, 2009). In this section we review some of the key developments in the use of radar for fluvial (river) flood prediction and warning.

6.2 Hydrological requirements for precipitation observations

It was the prospect of accurate, contiguous observations of precipitation over large areas that first stimulated hydrologists to explore the use of radar data for the prediction of run-off and river flow. Early assessments of the value of radar data were mixed (Anderl et al., 1976; Barge et al., 1979). This is not surprising given the reliance of these early experiments on deterministic precipitation estimates of variable accuracy, and the many factors known to impact on hydrological forecast performance.

Hydrological requirements for precipitation observations and forecasts are a function of catchment size, morphology and land use, and the hydrological model used (Hudlow et al., 1981). Many operational, hydrological forecasting models are lumped conceptual models in which the catchment response is modelled as a whole and the precipitation input is an areal average estimate. A number of authors have emphasized that the benefits of radar derived, spatially contiguous precipitation estimates can only be fully realized if used as input to distributed, conceptual or physically-based hydrological models (e.g. Moore, 1987).

6.3 Impact of the spatial and temporal distribution of precipitation

Wilson et al. (1979) found that a failure to properly represent the spatial distribution of rainfall, due to reliance on point observations from rain gauges, could produce significant errors in the total volume, peak and time to peak of an estimated hydrograph, even when the rainfall depth and its temporal evolution were accurately recorded at rain gauge sites. Errors were largest in cases of localized convective storms. Bedient and Springer (1979) demonstrated that the peak flows in a catchment could be enhanced when the precipitation moved in the direction of the stream.

More recently, Bell and Moore (2000b) explored the sensitivity of lumped and distributed catchment rainfall-run-off models to time series of rainfall observations from radar and rain gauge, gridded to a range of spatial resolutions. For a small rural catchment, they confirmed the sensitivity of distributed model run-off to the spatial variability of rainfall. A comparison of the performances of lumped and distributed models showed similar levels of predictive skill in stratiform rain, but superior distributed model predictions during convective rainfall events.

Ball (1994) examined the impact of the temporal evolution of the precipitation pattern on the time of concentration and peak discharge in a catchment. The time of concentration was shown to be sensitive to the temporal evolution of excess rainfall over the catchment, where as catchment peak discharge was not. Thus, timing errors in predicted flows can result if the time interval between precipitation observations is too long. Collier (1996) suggests that a radar scan cycle of no more than 5 minutes is required to capture the time evolution of most convective precipitation fields.

6.4 Relationship between radar data resolution, catchment characteristics and hydrological model performance

Various studies have examined the impact of the spatial and temporal resolution of remotely sensed precipitation observations on hydrological model performance (Krajewski et al., 1991; Pessoa et al., 1993; Obled et al., 1994; Ogden & Julien, 1994; Ball, 1994; Faurès et al., 1995; Shah et al., 1996; Winchell et al., 1998; Bell & Moore, 2000b; Carpenter et al., 2001).

Ogden and Julian (1994) explored the relationship between catchment size, and the correlation length and horizontal resolution of the radar derived precipitation fields input to a two-dimensional, physically-based hydrological model. They defined two, dimensionless length parameters and considered their impacts on the accuracy of predicted run-off. *Storm smearing* describes a reduction in the horizontal gradient of precipitation rate as the horizontal resolution of the radar data approaches its correlation length. *Watershed smearing* occurs when the horizontal resolution of the radar data approaches the characteristic length scale of the catchment (square root of the catchment area). Watershed smearing was shown to be the main source of error in predicting river flow over small catchments. Berenguer et al. (2005) point out that the sensitivity of hydrological models to biases in mean areal rainfall are due to the fact that river catchments act as integrators of the precipitation falling on them.

Bell and Moore (2000b) emphasized the need to calibrate hydrological models with rainfall data for a given resolution. They found that the most skilful distributed rainfall-run-off model predictions were made with lower resolution rainfall data. This finding was interpreted as evidence for the need to improve distributed hydrological model formulation.

6.5 Impact of radar intensity resolution

The impact of the intensity resolution in radar data on hydrological forecast errors was investigated by Cluckie, Tilford & Shepherd (1991). They demonstrated that 8 intensity levels were adequate for the majority of rural and urban catchments in the majority of UK precipitation events. This is because the bulk of the relevant information content is concentrated at the low frequency end of the power spectrum. Nonetheless, in convective precipitation events, a reduction in intensity resolution may have an effect similar to that of the storm smearing described by Ogden and Julian (1994).

6.6 Benefits of precipitation nowcasts to hydrological forecasting

In the absence of precipitation forecasts, the lead time of flood warnings is limited by the catchment response time, a quantity dependent on catchment size, morphology and land use. Skilful precipitation forecasts offer the prospect of some forewarning of flash floods in small, fast responding catchments, and of extending the lead time of flood warnings in other catchments (Roberts et al., 2009).

Although numerous authors have evaluated the impact of QPE algorithms on the utility of radar for hydrological forecasting there have been relatively few investigations of the benefits of precipitation nowcasts in this area. Cluckie and Owens (1987) compared the performance of stream flow forecasts made using a linear transfer function model and radar extrapolation nowcasts from FRONTIERS (Browning, 1979) against similar flow predictions

made using average past rainfall and an assumption of no more rain. In most cases, they found that nowcast driven hydrological forecasts outperformed the alternatives, although on one occasion they showed the former to be poor.

Several decades later, a similar, case study orientated evaluation of the utility of Nimrod (Golding, 1998) extrapolation nowcasts for rainfall-run-off modelling in Scotland (Werner and Cranston, 2009) drew similar conclusions: although errors in nowcast driven predictions of river flows could be substantial, they were smaller than those of flow forecasts made assuming zero future rainfall.

Mecklenburg et al. (2001) found that COTREC-based radar extrapolation nowcasts (Lagrangian persistence) produced superior hydrological forecasts to Eulerian persistence using a lumped conceptual model. In a similar vein, Berenguer et al. (2005) compared hydrological forecasts made with the S-PROG model (Seed, 2003) with those produced using a simpler, extrapolation-based precipitation nowcast in a Mediterranean environment. S-PROG utilizes a scale decomposition framework and associated hierarchy of auto-regressive models to smooth the advected precipitation field at a rate that is consistent with its loss of predictive skill on a hierarchy of scales. This approach is intended to minimize the root mean squared forecast error. Berenguer et al. (2005) concluded that radar-based precipitation nowcasts in general could extend the lead time of useful hydrological forecasts from 10 minutes to over an hour in a fast response responding Mediterranean catchment. However, the results obtained with S-PROG were not significantly better than those obtained with a simpler Lagrangian persistence technique.

Since one of the key benefits of radar is its ability to provide contiguous, instantaneous observations of precipitation over a wide area, other studies have focused their efforts on demonstrating the benefits of precipitation nowcasts when input to distributed hydrological models. In these models, the run-off response can vary within a catchment according to the temporal and spatial variability of the rainfall, surface properties and antecedent wetness (Ivanov et al., 2004; Vivoni et al., 2005). Amongst other things, this capability allows time series of run-off to be generated at ungauged sites (Moore et al., 2007).

Sharif et al. (2006) explored the potential of the National Center for Atmospheric Research's Auto-Nowcaster to improve the lead time and accuracy of hydrological forecasts made with a physically-based distributed parameter model. Rain gauge and radar observation driven simulations were used as a baseline. Results confirmed that the use of precipitation nowcasts could significantly improve flood warning in urban catchments, even in the case of short-lived events in small catchments. Similar conclusions were drawn by Vivoni et al. (2006) in relation a set of small, mixed land-use catchments in Oklahoma, in this case using NEXRAD-based extrapolation nowcasts and a distributed hydrological model.

6.7 Treatment of nowcast errors in hydrological forecasts

Vivoni et al. (2007) explored the impact of errors in deterministic precipitation nowcasts on errors in flood forecasts using a distributed hydrological model and a range of catchment sizes. Their investigations showed that increases in nowcast error with lead time produced larger errors in the resulting hydrological forecasts. They demonstrated that the effects of nowcast errors could be simultaneously enhanced or dampened in different locations depending on forecast lead time and precipitation characteristics. Differences in error

propagation between sub-catchments were effectively averaged out over larger catchment areas.

Despite continuing incremental advances in radar technology and performance during the 1970s and 1980s, a number of authors recognized that radar derived estimates of surface precipitation rate and accumulation would remain subject to hydrologically significant errors, particularly in hilly and mountainous areas. Collier and Knowles (1986) concluded that the full benefits of radar to operational hydrology would only be realized when ways could be found of accounting for these errors.

This thinking coincided with a growing awareness of the need to develop operational systems integrating meteorological and hydrological forecast models (Georgakakos and Kavvas, 1987). Early examples of such systems are the Integrated Flood Observing and Warning System (IFLOWS) implemented in the USA (Barrett and Monro, 1981), and the Regional Communication Scheme in north-west England, integrating operational weather radar data with hydrological forecasting and warning under the North-West radar project (Noonan, 1987).

More recently, a number of multi-national initiatives including HEPEx (e.g. Buizza, 2008; Pappenberger et al., 2008), MAP-D-Phase (Zappa et al., 2008; Bogner & Calas, 2008) and COST-731 (Rossa et al., 2011) have supported work to implement integrated flood forecasting systems exploiting weather radar. A number of UK-based research programmes, are relevant in this context, including HYREX (e.g. Mellor et al., 2000a,b; Bell & Moore, 2000a), the Natural Environment Research Council's Flood Risk from Extreme Events (FREE), the Engineering and Physical Sciences Research Council's Flood Risk Management Research Consortium (FRMRC) and FLOODsite.

Until Krzysztofowicz's pioneering work (Krzysztofowicz, 1983, 1993, 1998, 1999, 2001) to develop and implement an integrated hydro-meteorological systems framework, incorporating a Bayesian treatment of uncertainties in data inputs and deterministic model forecasts, errors in the precipitation inputs to operational hydrological models tended to be handled through the use of what-if scenarios (Haggett, 1986; Werner et al., 2009). The derived distribution approach (Seo et al., 2000) developed by Krzysztofowicz exploits the total probability law to derive by quasi-analytic means the conditional probability distribution of river stage given the initial and boundary conditions, including future precipitation parameterized in the form of a probabilistic QPF.

An alternative method for accounting for data input uncertainty entails the ingestion of ensemble precipitation forecasts into a hydrological model, whilst taking separate account of other sources of uncertainty contributing to the total uncertainty in the hydrological forecast variable of interest (Krzysztofowicz, 2001). Probabilities of exceeding specific river stage thresholds can then be estimated from the resulting ensemble of hydrographs (Schaake & Larson, 1998; Pierce et al., 2004). During the past decade, this ensemble approach has gained credence with the widespread implementation of operational ensemble NWP models and the development of stochastic nowcasting and post-processing techniques for the production of ensembles of high resolution precipitation nowcasts (e.g. Bowler et al., 2006).

Carpenter and Georgakakos (2006) investigated the combined effects of radar rainfall errors and catchment size on the uncertainty in predicted river flow with the aid of a distributed hydrological model. Using a parsimonious model to represent the spatial structure and variance of radar errors, they demonstrated that ensemble spread in predicted flow was logarithmically related to catchment scale.

A handful of ensemble-based probabilistic QPN schemes have been developed during the past decade or so. These were described earlier in this Chapter and include the String of Beads Model (Pegram & Clothier, 2001; Berenguer et al., 2011), the Short-Term Ensemble Prediction System (Bowler et al., 2006) and a method recently described by Kober et al. (2011). Here we draw a distinction between ensemble QPN schemes and others such as those described by Andersson and Iverson (1991) and Germann and Zawadzki (2004) which produce forecasts of the probability distribution of precipitation at a point. The latter cannot be used for ensemble-based probabilistic hydrological forecasting because they do not provide a complete description of the joint probability distribution of precipitation, which plays a key role in the hydrological response of a catchment.

In the UK, the Department of the Environment, Fisheries and Rural Affairs and the Environment Agency recently funded an R&D project to explore the benefits of high resolution precipitation forecasts to fluvial flood prediction and warning (Schellekens et al., 2010). The potential for operational use of ensemble rainfall nowcasts from STEPS (Bowler et al., 2006) was investigated in conjunction with lumped and distributed rainfall-run-off models. The evaluation included hydrological configuration issues, data volumes, run times and options for displaying probabilistic forecasts. No quantitative verification of the precipitation ensemble-driven hydrological forecasts was undertaken.

Recently, the Environment Agency has implemented a nationally configured, distributed hydrological model, known as Grid-to-Grid (Bell et al., 2007). In the near future (2012), this model will be driven by ensemble precipitation forecasts integrating STEPS ensemble nowcasts.

7. The future of nowcasting

One of the major changes in the past decade has been the increase in the ability of the general population in developed countries to receive real-time information over a range of mobile platforms. This makes it possible to deliver location specific nowcasts to millions of users. They use this information to make routine decisions regarding leisure and other outdoor activities and very occasionally decisions relating to severe weather events. Mitigating damage due to severe weather has been the motivation for developing nowcasting systems in the past, but the focus is likely to change to providing routine nowcasting services to the general public. The current generation of nowcasting systems are already capable of delivering products that are useful in this context and the focus in the short term should be on developing the ability to customize and disseminate these to a very large number of users.

Improved communications and computer capacity have also made it possible to routinely combine data from a network of weather radars into a single large domain, and to improve the algorithms that are used to provide quantitative radar rainfall estimates. Improvements in the QPE will continue as the radar hardware improves and the density of the radar networks increases. These improvements will allow for improvements in the quality of the nowcasts in the first hour.

There are still incremental gains to be made by improving the accuracy of the tracking algorithms and by combining the cell tracking and field advection paradigms into a single advection scheme. More generally, there is evidence that the cell tracking and field tracking systems are complementary, so rather than viewing them as competitors there should be value in developing a way of optimally combining the forecasts from several nowcasting systems based on an analysis of which system is likely to be providing better nowcasts in any given situation.

Predicting the initiation and decay of convective storms will continue to be a major focus for research because gains in this area will lead to significant improvements in the accuracy of nowcasts beyond 30 minutes. The problem with heuristic and analogue techniques is that they require large data sets for calibration, and the associated conceptual models that are developed tend to be location specific. This can be overcome if a way can be found to allow the algorithms to learn as they go, based on the results of routine real-time verification.

Possibly the major use of radar data in the future will be for assimilation into NWP models of the national weather services that run radar networks. Empirical advection nowcasting will continue to provide nowcasts, but for more limited lead times as the NWP models gain accuracy at shorter lead times. Not all users will be able to afford the costs of a full NWP system that is able to assimilate radar data and there will continue to be a demand for fast and cheap rainfall nowcasts for specific purposes.

Forecast errors, rather like death and taxes, will always be with us and the future lies in using ensembles or other techniques to convey the uncertainty in the current forecast to the users. Further research on quantifying forecast errors and understanding how they depend on location and meteorological situation is required before we are able to demonstrate that the spread in a nowcast ensemble fully represents the uncertainty. There is also a need to develop probabilistic nowcasting systems that do not only forecast rainfall, but are used to forecast end-user impacts, for example the traffic capacity of an air-corridor, or the water level in a river.

8. References

- Anagnostou, E. N., Krajewski, W. F. & Smith, J. A. (1999). Uncertainty quantification of mean-areal radar-rainfall estimates, *Journal of Atmospheric and Oceanic Technology*, Vol. 16, No. 2, (February 1999), pp. 206-215, Available from [http://dx.doi.org/10.1175/1520-0426\(1999\)016<0206:UQOMAR>2.0.CO;2](http://dx.doi.org/10.1175/1520-0426(1999)016<0206:UQOMAR>2.0.CO;2)
- Anderl, B., Attmannspacher, W. & Schultz, G. A. (1976). Accuracy of reservoir inflow forecasts based on radar rainfall measurements, *Water Resources Research*, Vol. 12, No. 2, pp. 217-223, doi:10.1029/WR012i002p00217
- Andersson, T. & Ivarsson, K.-I. (1991). A model for probability nowcasts of accumulated precipitation using radar. *Journal of Applied Meteorology*, Vol. 30, (January 1991), pp. 135-141
- Austin, P. M. (1987). Relation between measured radar reflectivity and surface rainfall. *Monthly Weather Review*, Vol. 115, No. 5, pp. 1053-1070, ISSN 00270644
- Austin, G. L. & Bellon, A. (1974). The use of digital weather records for short-term precipitation forecasting, *Quarterly Journal of the Royal Meteorological Society*, Vol. 100, No. 426, (), pp. 658-664

- Austin, G. L. & Bellon, A. (1982). Very short-range forecasting of precipitation by the objective extrapolation of radar and satellite data, In: *Nowcasting*, K. A. Browning (Ed.), 177-190, Academic Press, London, UK
- Baker, S. E. (1986). The relationship of QPF to the management of hydroelectric power on the Santee River Basin in North and South Carolina, *Proceedings of the Conference on Climate and Water Management: A Critical Era*, pp. 77-82, Asheville, North Carolina, American Meteorological Society, Boston, Massachusetts, 4-7 August 1986
- Ball, J. E. (1994). The influence of storm temporal patterns on catchment response, *Journal of Hydrology*, Vol. 158, NO. 3-4, pp. 285-303, ISSN 0022-1694
- Ballard, S., Zhihong, L., Simonin, D., Buttery, H., Charlton-Perez, C., Gaussiat, N. & Hawkness-Smith, L. (2011). Use of radar data in NWP-based nowcasting in the Met Office, *Proceedings of the eighth International Symposium on Weather Radar and Hydrology*, Exeter, UK, April 2011, to appear in IAHS red book
- Bally, J. (2004). The Thunderstorm Interactive Forecast System: Turning automated thunderstorm tracks into severe weather warnings, *Weather Forecasting*, Vol. 19, No. 1, (February 2004), pp. 64-72
- Barge, B. L., Humphries, R. G., Mah, S. J. & Kuhnke, W. K. (1979). Rainfall measurements by weather radar: applications to hydrology, *Water Resources Research*, Vol. 15, No. 6, pp. 1380-1386, doi:10.1029/WR015i006p01380
- Barker, D.M., Huang, W., Guo, Y.-R. & Xiao, Q. (2004). A three-dimensional variational (3DVAR) data assimilation system for use with MM5: Implementation and initial results, *Monthly Weather Review*, Vol. 132, pp. 897-914
- Barrett, C. B. & Monro, J. C. (1981). National prototype flash flood warning system. Preprint Volume, *4th Conference on Hydrometeorology*, pp. 234-239, Reno, Nevada, 7-9 October 1981
- Battan, L. J. (1953). Observations of the formation and spread of precipitation in cumulus clouds, *Journal of Meteorology*, Vol. 10, pp. 311-324
- Bedient, P. B. & Springer, N. K. (1979). Effect of rainfall timing on design floods, *Journal of Civil Engineering Design*, Vol. 1, No. 4, pp. 311-323
- Bell, V. A., Kay, A. L., Jones, R. G. & Moore, R. J. (2007). Development of a high resolution grid-based river flow model for use with regional climate model output, *Hydrology and Earth System Sciences*, Vol. 11, No. 1, pp. 532-549, doi:10.5194
- Bell, V.A. & Moore, R.J. (2000a). Short period forecasting of catchment-scale precipitation. Part II: a water-balance storm model for short-term rainfall and flood forecasting, *Hydrology and Earth System Sciences*, Vol. 4, No. 4, pp. 635-651
- Bell, V.A. & Moore, R.J. (2000b). The sensitivity of catchment runoff models to rainfall data at different spatial scales, *Hydrology and Earth System Sciences*. Vol. 4, No. 4, pp. 653-667
- Bellon, A. & Austin, G. L. (1978). The evaluation of two years of real time operation of a short-term precipitation forecasting procedure (SHARP), *Journal of Applied Meteorology*, Vol. 17, No. 12, pp. 1778-1787, DOI: 10.1175/1520-0450
- Bellon, A. & Austin, G. L. (1984). The accuracy of short-term radar rainfall forecasts, *Journal of Hydrology*, Vol. 70, Nos. 1-4, (February 1984), pp. 35-49
- Benjamin, S. G., Schwartz, B. E., Szoke, E. J., & Koch, S. E. (2004). The value of wind profiler data in U.S. weather forecasting, *Bulletin of the American Meteorological Society*, Vol. 85, pp. 1871-1886

- Berenguer, M., Corral, C., Sanchez-Diezma, R. & Sempere-Torres, D. (2005). Hydrological validation of a radar-based nowcasting technique, *Journal of Hydrometeorology*, Vol. 6, No. 4, pp. 532-549
- Berenguer, M., Sempere-Torres, D. & Pegram, G. G. S. (2011). SBMcast - An ensemble nowcasting technique to assess the uncertainty in rainfall forecasts by Lagrangian extrapolation, *Journal of Hydrology*, Vol. 404, pp. 226-240
- Blackmer, R. H., Duda, R. O. & Reboh, R. (1973). *Application of pattern recognition to digitized Weather Radar Data*. Final Rep., Contract 1-36072, SRI Project 1287, Stanford Research Institute, Menlo Park, CA, 89 pp., Available from National Information Service, Operations Division, Springfield, VA 22161.
- Bogner, K. & Kalas, M. (2008). Error-correction methods and evaluation of an ensemble based hydrological forecasting system for the Upper Danube catchment. *Atmospheric Science Letters*, Vol. 9, No. 2, (April 2008), pp. 95-102, DOI: 10.1002
- Bowen, E. G. (1951). Radar observations of rain and their relation to mechanisms of rain formation. *Journal of Atmospheric and Terrestrial Physics*, Vol. 1, pp. 125-140
- Bowler, N. E., Pierce, C. E. & Seed, A. W. (2004). Development of a precipitation nowcasting algorithm based upon optical flow techniques, *Journal of Hydrology*, Vol. 288, pp. 74-91
- Bowler, N. E., Pierce, C. E. & Seed, A. W. (2006). STEPS: A probabilistic precipitation forecasting scheme which merges an extrapolation nowcast with downscaled NWP, *Quarterly Journal of the Royal Meteorological Society*, Vol. 132, pp. 2127-2155
- Brewster, K., Thomas, K. W., Gao, J., Brotzgel, J., Xue, M. & Wang, Y. (2010). A nowcasting system using full physics numerical weather prediction initialized with CASA and Nexrad radar data, *Proceedings of the 25th Conference on Severe Local Storms*, pp. 11, American Meteorological Society, Denver, Colorado, October 11-14
- Brousseau, P., Berre, L., Bouttier, F. & Desroziers, G. (2011). Background-error covariances for a convective-scale data-assimilation system : AROME-France 3D-Var, *Quarterly Journal of the Royal Meteorological Society*, Vol. 137, No. 655, pp. 409-422
- Browne, I. C. & Robinson, N. P. (1952). Cross-polarization of the radar melting band, *Nature*, Vol. 170, (December 1952), pp. 1078-1079
- Browning, K. A. (1979). The FRONTIERS plan: a strategy for using radar and satellite imagery for very short-range precipitation forecasting, *Meteorological Magazine*, Vol. 108, pp. 161-184
- Browning, K. A. (1980). Local weather forecasting, *Proceedings of the Royal Society of London, Series A*, Vol. 371, No. 1745, pp. 179-211
- Buizza, R. (2008). The value of probabilistic prediction, *Atmospheric Science Letters*, Vol. 9, No. 2, pp. 36-42
- Byers, H. R. (1948). The use of radar in determining the amount of rain falling over a small area, *Eos Transactions of the American Geophysical Union*, Vol. 29, pp. 187-196
- Byers, H. R. & Braham Jr., R. R. (1949). *The Thunderstorm*. U.S. Govt. Printing Office, 187 pp
- Carpenter, T. M. & Georgakakos, K. P. (2006). Discretization scale dependencies of the ensemble flow range versus catchment area relationship in distributed hydrologic modelling, *Journal of Hydrology*, Vol. 328, pp. 242-257
- Carpenter, T. M., Georgakakos, K. P. & Sperfslage, J. A. (2001). On the parametric and NEXRAD-radar sensitivities of a distributed hydrologic model suitable for operational use, *Journal of Hydrology*, Vol. 253, pp. 169-193

- Caumont, O., Ducrocq, V., Wattrelot, E., Jaubert, G. & Pradie-vabre, S. (2010). 1D+3DVar assimilation of radar reflectivity data: a proof of concept, *Tellus A*, Vol. 62, pp. 173-187
- Caya, A., Sun, J. & Snyder, C. (2005). A comparison between the 4D-Var and the ensemble Kalman filter techniques for radar data assimilation, *Monthly Weather Review*, Vol. 133, No. 11, pp. 3081-3094, ISSN 0027-0644
- Ciach, G. J., Krajewski, W. F. & Villarini, G. (2007). Product-error-driven uncertainty model of probabilistic quantitative precipitation estimation with NEXRAD data, *Journal of Hydrometeorology*, Vol. 8, pp. 1325-1347
- Clark, A. J., Weiss, S. J., Kain, J. S., Jirak, I. L., Coniglio, M., Melick, C. J., Siewert, C., Sobash, R. A., Marsh, P. T., Dean, A. R., Xue, M., Kong, F., Thomas, K. W., Wang, Y., Brewster, K., Gao, J., Wang, X., Du, J., Novak, D. R., Barthold, F. E., Bodner, M. J., Levit, J. J., Entwistle, C. B., Jensen, T. L. & Correia, J. Jn. (2011). An Overview of the 2010 hazardous weather testbed experimental forecast program spring experiment, *Bulletin of the American Meteorological Society*, doi: 10.1175/BAMS-D-11-00040.1
- Cluckie, I.D. & Owens, M. D. (1987). Real-time rainfall-runoff models and use of weather radar information, In: *Weather Radar and Flood Forecasting*, V. Collinge & C. Kirby (Eds.), 171-190, John Wiley & Sons, Chichester
- Cluckie, I. D. & Pessoa, M. A. (1988). Weather radar and dam safety: An evaluation, *Proceedings of the 2nd Anglo/Polish Hydrology Colloquium*, held at the University of Birmingham under the auspices of the Polish Academy of Sciences and the Royal Society of London, August 1988
- Cluckie, I. D., Pessoa, M. L. & Yu, P. S. (1991). Probable maximum flood modelling utilising transposed, maximised radar-derived precipitation data, In: *Hydrological Applications of Weather Radar*, I. D. Cluckie & C. G. Collier (Eds.), 181-191, Ellis Horwood, London
- Cluckie, I. D., Tilford, K. A. & Shepherd, G. W. (1991). Radar signal quantization and its influence on rainfall-runoff models, In: *Hydrological Applications of Weather Radar*, I. D. Cluckie & C. G. Collier (Eds.), 440-451, Ellis Horwood, London
- Cluckie, I. D. & Tyson, J. M. (1989). Weather radar and urban drainage systems. In: *Weather Radar and the Water Industry: Opportunities for the 1990s*, 65-73, BHS Occasional Paper No. 2, British Hydrological Society
- Collier, C. G. (1996). *Applications of Weather Radar Systems: a guide to uses of radar data in meteorology and hydrology*, John Wiley and Sons Ltd
- Collier, C. G. & Hardaker, P. J. (1996). Estimating Probable Maximum Precipitation using a storm model approach, *Journal of Hydrology*, Vol. 183, pp. 277-306
- Collier, C. G. & Knowles, J. M. (1986). Accuracy of rainfall estimates by radar, Part III: Application for short-term flood forecasting, *Journal of Hydrology*, Vol. 83, pp. 237-249
- Cox, D. R. & Isham, V. (1988). A simple spatio-temporal model of rainfall, *Proceedings of the Royal Society of London, Series A*, Vol. 415, No. 1849, pp. 317-328
- Crane, R. K. (1979). Automatic cell detection and tracking, *Institute of Electrical and Electronics Engineers (IEEE) Transactions on Geosciences and Electronics (GE)*, Vol. 17, No. 4, pp. 250-262
- Dance, S., Ebert, E. E. & Scurrah, D. (2010). Thunderstorm strike probability nowcasting, *Journal of Atmospheric and Oceanic Technology*, Vol. 27, pp. 79-93
- Davies, T., Cullen, M. J. P., Malcolm, A. J., Mawson, M. H., Staniforth, A., White, A. A. & Wood, N. (2005). A new dynamical core for the Met Office's global and regional

- modelling of the atmosphere, *Quarterly Journal of the Royal Meteorological Society*, Vol. 131, pp. 1759-1782
- Dixon, M. & Wiener, G. (1993). TITAN: Thunderstorm Identification, Tracking, Analysis and Nowcasting – A radar-based methodology, *Journal of Atmospheric and Oceanic Technology*, Vol. 10, pp. 785–797
- Dixon, M., Li, Z., Lean, H., Roberts, N. & Ballard, S. P. (2009). Impact of data assimilation on forecasting convection over the United Kingdom using a high-resolution version of the Met Office Unified Model, *Monthly Weather Review*, Vol. 137, pp. 1562–1584
- Duda, R. O. & Blackmer, R. H. (1972). *Applications of pattern recognition techniques to digitized weather radar data*, Final Rep. Contract I-36092, SRI Project 1287, Stanford Research Institute, Menlo Park, CA, 135 pp., Available from National Information Service, Operations Division, Springfield, VA 22161
- Ebert, E. E., Wilson, L. J., Brown, B. G., Nurmi, P., Brooks, H. E., Bally, J. & Jaeneke, M. (2004). Verification of nowcasts from WWRP Sydney 2000 Forecast Demonstration Project, *Weather and Forecasting*, Vol. 19, pp. 73 – 96
- Fabry, F. & Seed, A. W. (2009). Quantifying and predicting the accuracy of radar-based quantitative precipitation forecasts, *Advances in Water Resources*, Vol. 32, No. 7, pp. 1043-1049
- Faurès, J. M., Goodrich, D. C., Woodliser, D. A. & Sorooshian, S. (1995). Impact of small-scale spatial rainfall variability on run-off modelling, *Journal of Hydrology*, Vol. 173, pp. 309-326
- Foresti, L. & Pozdnoukhov, A. (2011). Exploration of alpine orographic precipitation patterns with radar image processing and clustering techniques, *Meteorological Applications*, Vol. 18, No. 4, DOI:10.1002/met.272
- Fox, N. I. and Wikle, C. K. (2005). A Bayesian quantitative precipitation nowcasting scheme, *Weather and Forecasting*, Vol. 20, pp. 264-275
- French, M. N. & Krajewski, W. F. (1994) A model for real-time quantitative rainfall forecasting using remote sensing: Part 1 Formulation, *Water Resources Research*, Vol. 30, No. 4, pp. 1075-1083
- Gebremichael, M. & Krajewski, W. (2004). Assessment of the statistical characterisation of small-scale rainfall variability from radar: analysis of TRMM ground validation datasets, *Journal of Applied Meteorology*, Vol. 43, pp. 1180 – 1199
- Georgakakos, K. P. & Bras, R. L. (1984a). A hydrologically useful station precipitation model: 1. Formulation, *Water Resources Research*, Vol. 20, No. 11, pp. 1585-1596
- Georgakakos, K. P. & Bras, R. L. (1984b). A hydrologically useful station precipitation model: 2. Case studies, *Water Resources Research*, Vol. 20, No. 11, pp. 1597-1610
- Georgakakos, K. P. & Kavvas, M. L. (1987). Precipitation analysis, modelling and prediction in hydrology, *Reviews of Geophysics*, Vol. 25, No. 2, pp. 163-178
- Germann, U., Berenguer, M., Sempere-Torres, D. & Zappa, M. (2009). REAL – ensemble radar precipitation estimation for hydrology in a mountainous region, *Quarterly Journal of the Royal Meteorological Society*, Vol. 135, No. 639, pp. 445–456
- Germann, U. & Zawadzki, I. (2002). Scale-dependence of the predictability of precipitation from continental radar images. Part 1: Description of the methodology, *Monthly Weather Review*, Vol. 130, pp. 2859–2873
- Germann, U. & Zawadzki, I. (2004). Scale dependence of the predictability of precipitation from continental radar images. Part II: Probability forecasts, *Journal of Applied Meteorology*, Vol. 43, pp. 74–89

- Germann, U., Zawadzki, I. & Turner, B. (2006). Predictability of precipitation from continental radar images. Part IV: Limits to prediction, *Journal of Atmospheric Science*, Vol. 63, pp. 2092-2108
- Greco, M. & Krajewski, W. F. (2000). A large-sample investigation of statistical procedures for radar-based short-term quantitative precipitation forecasting *Journal of Hydrology*, Vol. 239, pp. 69-84
- Golding, B.W. (1998). Nimrod: a system for generating automated very short range forecasts, *Meteorological Applications*, Vol. 5, pp. 1-16
- Golding, B. (2009). Long lead time flood warnings: reality or fantasy? *Meteorological Applications*, Vol. 16, pp. 3-12
- Gustafsson, N., Berre, L., Hornquist, S., Huang, X. -Y., Lindskog, M., Navascues, B., Mogensen, K. S. and Thorsteinsson, S. (2001). Three-dimensional variational data assimilation for a limited area model. Part I: General formulation and the background error constraint, *Tellus A*, Vol. 53, pp. 425-446
- Haggett, C. M. (1986). The use of weather radar for flood forecasting in London, *Proceedings of Conference of River Engineers 1986*, Cranfield, 15th-17th July 1986, Ministry of Agriculture, Fisheries and Food, London
- Han, L., Fu, S., Zhao, L., Zheng, Y., Wang, H. & Lin, Y. (2009). 3D convective storm identification, tracking, and forecasting—An enhanced TITAN algorithm, *Journal of Atmospheric and Oceanic Technology*, Vol. 26, pp. 719-732
- Handwerker, J. (2002). Cell tracking with TRACE3D - a new algorithm, *Atmospheric Research*, Vol. 61, pp. 15-34
- Harris, D., Foufoula-Georgiou, E., Droegemeier, K. K. & Levit, J. J. (2001). Multiscale statistical properties of a high-resolution precipitation forecast, *Journal of Hydrometeorology*, Vol. 2, pp. 406-418
- Hilst, G. R. & Russo, J. A. (1960). An objective extrapolation technique for semi-conservative fields with an application to radar patterns, *Tech. Memo 3*, The Travelers Research Center, Hartford, CT, 34 pp
- Hitschfeld, W. and Bordan, J. (1954). Errors inherent in the radar measurement of rainfall at attenuating wavelengths, *Journal of Meteorology*, Vol. 11, pp. 58-67
- Hollingsworth A. & Lonnberg P. (1986). The statistical structure of short-range forecast errors as determined from radiosonde data. 1. The wind-field. *Tellus A*, Vol. 38, pp. 111-136
- Honda, Y., Nishijima, M., Koizumi, K., Ohta, Y., Tamiya, K., Kawabata, T. & Tsuyuki, T. (2005). A pre-operational variational data assimilation system for a non-hydrostatic model at the Japan Meteorological Agency: Formulation and preliminary results, *Quarterly Journal of the Royal Meteorological Society*, Vol. 131, pp. 3465-3475
- Horn, B. K. P. & Schunck, B. G. (1981). Determining optical flow, *Artificial Intelligence*, Vol. 17, pp. 185-203
- Huang, X., Xiao, Y. Q., Barker, D. M., Zhang, X., Michalakes, J., Huang, W., Henderson, T., Bray, J., Chen, Y., Ma, Z., Dudhia, J., Guo, Y. R., Zhang, X., Won, D. J., Lin, H. C. & Kuo, Y. H. (2009). Four-dimensional variational data assimilation for WRF: Formulation and preliminary results. *Monthly Weather Review*, Vol. 137, pp. 299-314
- Hudlow, M. D., Farnsworth, R. K. & Green, D. R. (1981). Hydrological forecasting requirements for precipitation data from space measurements, In: *Precipitation Measurement from Space, Workshop Report*, eds D. Atlas and O. W. Thiele, Goddard Space Flight Center, National Aeronautics and Space Administration, pp. D23-D30

- Hunter, I. M. (1954). Polarization of radar echoes from meteorological precipitation, *Nature*, Vol. 173, pp. 165-166
- Ivanov, V. Y., Vivoni, E. R., Bras, R. L. & Entekhabi, D. (2004). Preserving high-resolution surface and rainfall data in operational-scale basin hydrology: A fully-distributed physically-based approach, *Journal of Hydrology*, Vol. 298, pp. 80-111
- Johnson, J. T., MacKeen, P. L., Witt, A., Mitchell, E. D., Stumpf, G. J., Eilts, M. D., & Thomas, K. W. (1998). The Storm Cell Identification and Tracking algorithm: An enhanced WSR-88D algorithm, *Weather and Forecasting*, Vol. 13, pp. 263-276
- Jones, C. D. & Macpherson, B. (1997). A latent heat nudging scheme for the assimilation of precipitation data into an operational mesoscale model, *Meteorological Applications*, Vol. 4, pp. 269-277
- Jordan, P. W., Seed, A. W. & Weinmann, P. E. (2003). A stochastic model of radar measurement errors in rainfall accumulations at catchment scale, *Journal of Hydrometeorology*, Vol. 4, pp. 841 – 855
- Kessler, E. (1966). Computer program for calculating average lengths of weather radar echoes and pattern bandedness, *Journal of Atmospheric Science*, Vol. 23, pp. 569-574
- Kessler, E. & Russo, J. A. (1963). Statistical properties of weather radar echoes, *Proceedings 10th Weather Radar Conference*, pp. 25-33, Washington, D.C., American Meteorological Society, Boston, Massachusetts
- Kober, K., Craig, G. C., Keil, C. & Dörnbrack, A. (2011). Blending a probabilistic nowcasting method with a high-resolution numerical weather prediction ensemble for convective precipitation forecasts, *Quarterly Journal of the Royal Meteorological Society*, DOI:10.1002/qj.939
- Kong, F., Xue, M., Thomas, K. W., Wang, Y., Brewster, K. A., Wang, X., Gao, J., Weiss, S. J., Clark, A. J., Kain, J. S., Coniglio, M. C. & Du, J. (2011). CAPS multi-model storm-scale ensemble forecast for the NOAA HWT 2010 spring experiment, *24th Conference on Weather and Forecasting, 20th Conference on Numerical Weather Prediction*, paper 457, American Meteorological Society
- Krajewski, W. F. & Georgakakos, K. P. (1985). Synthesis of radar rainfall data, *Water Resources Research*, Vol. 21, No. 5, pp. 764-768
- Krajewski, W. F., Venkataraman, L., Georgakakos, K. P. & Jain, S. C. (1991). A Monte Carlo study of rainfall sampling effect on a distributed catchment model, *Water Resources Research*, Vol. 27, pp. 119-128
- Krzysztofowicz, R. (1983). Why should a forecaster and a decision maker use Bayes theorem?, *Water Resources Research*, Vol. 19, No. 2, pp. 327-336
- Krzysztofowicz, R. (1993). A theory of flood warning systems, *Water Resources Research*, Vol. 29, No. 12, pp. 3981-3994
- Krzysztofowicz, R. (1998). Probabilistic hydrometeorological forecasts: Toward a new era in operational forecasting, *Bulletin of the American Meteorological Society*, Vol. 79, No. 2, pp. 243-51
- Krzysztofowicz, R. (1999). Bayesian theory of probabilistic forecasting via deterministic hydrologic model, *Water Resources Research*, Vol. 35, No. 9, pp. 2739-2750
- Krzysztofowicz, R. (2001). The case for probabilistic forecasting in hydrology, *Journal of Hydrology*, Vol. 249, pp. 2-9
- Laroche, S. & Zawadzki, I. (1995). Retrievals of horizontal winds from single-Doppler clear-air data by methods of cross correlation and variational analysis, *Journal of Atmospheric and Oceanic Technology*, Vol. 12, pp. 721-738

- Langille, R.C. & Gunn, K. L. S. (1948). Quantitative analysis of vertical structure in precipitation, *Journal of Meteorology*, Vol. 5, pp. 301-304
- Lean, H. W., Clark, P. A., Dixon, M., Roberts, N. M., Fitch, A., Forbes, R. & Halliwell, C. (2008). Characteristics of high-resolution versions of the Met Office unified model for forecasting convection over the United Kingdom, *Monthly Weather Review*, Vol. 136, pp. 3408-3424
- Lee, G. W. (2006). Sources of errors in rainfall measurements by polarimetric radar: Variability of drop size distributions, observational noise, and variation of relationships between R and polarimetric parameters. *Journal of Atmospheric and Oceanic Technology*, Vol. 23, pp. 1005-1028
- Lee, G. W. & Zawadzki, I. (2005a): Variability of drop size distributions: Time scale dependence of the variability and its effects on rain estimation. *Journal of Applied Meteorology*, Vol. 44, pp. 241-255
- Lee, G. W. & Zawadzki, I. (2005b). Variability of drop size distributions: Noise and noise filtering in disdrometric data, *Journal of Applied Meteorology*, Vol. 44, pp. 634-652
- Lee, G. W. & Zawadzki, I. (2006). Radar calibration by gage, disdrometer and polarimetry: Theoretical limit caused by the variability of drop size distribution and application to fast scanning operational radar data. *Journal of Hydrology*, Vol. 328, pp. 83-97
- Lee, G., Seed, A. W. & Zawadzki, I. (2007). Modeling the variability of drop size distributions in space and time, *Journal of Applied Meteorology and Climatology*, Vol. 46, pp. 742-756
- Lee, T. & Georgakakos, K. P. (1990). A two-dimensional stochastic-dynamical quantitative precipitation forecasting model, *Journal of Geophysical Research*, Vol. 95, pp. 2113-2126
- Lee, H. C., Bellon, A., Kilambi, A. & Zawadzki, I. (2009). McGill Algorithm for Precipitation nowcasting by Lagrangian Extrapolation (MAPLE) applied to the South Korean radar network. Part 1: Sensitivity studies of the Variational Echo Tracking (VET) technique, *Proceedings of the 34th Radar Conference*, American Meteorological Society
- Lewin, J. (1986). The control of spillway gates during floods, *Water Services*, Vol. 90, No. 1081, pp. 93-95
- Li, L., Schmid, W. & Joss, J. (1995). Nowcasting of motion and growth of precipitation with radar over a complex orography, *Journal of Applied Meteorology*, Vol. 34, No. 6, pp. 1286-1300
- Li, P. W., Wong, W. K., Chan, K.Y., & Lai, E. S. T. (2000). SWIRLS - an evolving nowcasting system, *Hong Kong Observatory Technical Note No. 100*, Hong Kong Observatory, 134A Nathan Road, Kowloon, Hong Kong
- Liang, Q., Feng, Y., Deng, W., Hu, S., Huang, Y., Zeng, Q. & Chen, Z. (2010). A composite approach of radar echo extrapolation based on TREC vectors in combination with model-predicted winds, *Advances in Atmospheric Sciences*, Vol. 27, No. 5, pp. 1119-1130
- Ligda, M. G. H. (1951). Radar storm observation, In: *Compendium of Meteorology*, T. F. Malone, (Ed.), 1265-1282, American Meteorological Society
- Ligda, M. G. H. (1953). The horizontal motion of small precipitation areas as observed by radar, *Tech. Rep. 21*, Department of Meteorology, M.I.T., 60 pp., Available from Library, Massachusetts Institute of Technology, 77 Massachusetts Ave., Cambridge, MA 02139
- Lin, Y., Ray, P. & Johnson, K. (1993). Initialization of a modelled convective storm using Doppler radar derived fields, *Monthly Weather Review*, Vol. 121, pp. 2757-2775

- Llort, X., Velasco-Forero, C., Roca-Sancho, J. & Sempere-Torres, D. (2008) Characterization of uncertainty in radar-based precipitation estimates and ensemble generation, *Proceedings of the Fifth European conference on radar in meteorology and hydrology (ERAD 2008)*
- Lorenc, A. C. (1981). A global three-dimensional multivariate statistical interpolation scheme, *Monthly Weather Review*, Vol. 109, pp. 701-721
- Lorenc, A. C., Ballard, S. P., Bell, R. S., Ingleby, N. B., Andrews, P. L. F., Barker, D. M., Bray, J. R., Clayton, A. M., Dalby, T., Li, D., Payne, T. J., & Saunders, F. W. (2000). The Met. Office global 3-Dimensional variational data assimilation scheme, *Quarterly Journal of the Royal Meteorological Society*, Vol. 126, pp. 2991-3012
- Lorenz, E. N. (1963). Deterministic nonperiodic flow, *Journal of Atmospheric Sciences*, Vol. 20, pp. 120-141
- Lorenz, E. N. (1973). On the existence of extended range predictability, *Journal of Applied Meteorology*, Vol. 12, pp. 543-546
- Lovejoy, S. & Schertzer, D. (1985). Generalized Scale Invariance in the Atmosphere and Fractal Models of Rain, *Water Resources Research*, Vol. 21, pp. 1233-1250
- Lovejoy, S. & Schertzer, D. (1986). Scale Invariance, Symmetries, Fractals and Stochastic Simulation of Atmospheric Phenomena, *Bulletin of the American Meteorological Society*, Vol. 67, pp. 21-32
- Macpherson, B., Wright, B. J., Hand, W. H., & Maycock, A. J. (1996). The impact of MOPS moisture data in the UK Meteorological Office mesoscale data assimilation scheme, *Monthly Weather Review*, Vol. 124, No. 8, pp. 1746-1766
- Marsan, D., Schertzer, D. & Lovejoy, S. (1996). Causal space-time multifractal processes: predictability and forecasting rain fields, *Journal of Geophysical Research*, 101, 21D, pp. 26333-26346
- Marshall, J. S. & Palmer, W. McK. (1948). The distribution of rain-drops with size, *Journal of Meteorology*, Vol. 5, pp. 165-166
- Mecklenburg, S., Joss, J. & Schmid, W. (2000). Improving the nowcasting of precipitation in an Alpine region with an enhanced radar echo tracking algorithm, *Journal of Hydrology*, Vol. 239, pp. 46-68
- Mecklenburg, S., Bell, V. A., Carrington, D. S., Cooper, A. M., Moore, R. J., & Pierce, C. E. (2001). Applying COTREC-derived rainfall forecasts to the rainfall-runoff model PDM—estimating error sources, *Proceedings of the 30th International Conference on Radar Meteorology*, Munich, Germany, 19-24 July 2001, American Meteorological Society
- Megenhardt, D. L., Mueller, C., Trier, S., Ahijevych, D. & Rehak, N. (2004). NCWF-2 Probabilistic Forecasts, Preprints, 11th Conference on Aviation, Range, and Aerospace Meteorology, 5.2, American Meteorological Society, Available online at <http://ams.confex.com/ams/pdfpapers/81993.pdf>
- Mellor, D., Sheffield, J., O'Connell, P. E. & Metcalfe, A. V. (2000a). A stochastic space-time rainfall forecasting system for real time flow forecasting, I: development of MTB conditional rainfall scenario generator, *Hydrology and Earth Systems Science*, Vol. 4, No. 4, pp. 603-615
- Mellor, D., Sheffield, J., O'Connell, P.E. & Metcalfe, A.V. (2000b). A stochastic space-time rainfall forecasting system for real time flow forecasting, II: application of SHETRAN and ARNO rainfall runoff models to the Brue catchment, *Hydrology and Earth Systems Science*, Vol. 4, No. 4, pp. 617-626

- Mittermaier, M. P. (2007). Improving short-range high-resolution model precipitation forecast skill using time-lagged ensembles, *Quarterly Journal of the Royal Meteorological Society*, Vol. 133, No. 627, pp. 1487-1500
- Montmerle, T. & Faccani, C. (2009). Mesoscale assimilation of radial velocities from Doppler radars in a pre-operational framework, *Monthly Weather Review*, Vol. 137, pp. 1939-1953
- Moore, R. J. (1987). Towards more effective use of radar data for flood forecasting, In: *Weather Radar and Flood Forecasting*, V. K. Collinge and C. Kirby (Eds.), 223-238, John Wiley & Sons Ltd., Chichester
- Moore, R. J., Bell, V. A., Cole, S. J. & Jones, D. A. (2007). Rainfall-runoff and other modelling for ungauged/low-benefit locations. *Science Report - SC030227/SR1*, Research Contractor: CEH Wallingford, Environment Agency, Bristol, UK, 249pp.
- Morcette, C., Lean, H., Browning, K., Nicol, J., Roberts, N., Clark, P., Russell, A. & Blyth, A. (2007). Combination of mesoscale and synoptic mechanisms for triggering an isolated thunderstorm: Observational case study of CSPIOP 1, *Monthly Weather Review*, Vol. 135, pp. 3728-3749, DOI: 10.1175/2007MWR2067.1
- Murphy, A. H. & Carter, G. M. (1980). On the comparative evaluation of objective and subjective precipitation probability forecasts in terms of economic value. *Preprints, Eighth Conference on Weather Forecasting and Analysis*, pp. 478-487, American Meteorological Society, Denver, Colorado, 10-13 June
- Newell, R. E., Geotis, S. G., Stone, M. L. & Fleisher, A. (1955). How round are raindrops? *Proceedings of the Fifth Conference on Radar Meteorology*, pp. 261-268, American Meteorological Society, Asbury Park, New Jersey
- Noel, T. M. & Fleisher, A. (1960). *The linear predictability of weather radar signals*, Research Rep. 34, Department of Meteorology, M.I.T., 46 pp., Available from Library, Massachusetts Institute of Technology, 77 Massachusetts Ave., Cambridge, MA 02139
- Noonan, G. A. (1987). An operational flood warning system, In: *Weather Radar and Flood Forecasting*, 109-126, V. K. Collinge and C. Kirby (Eds.), Wiley, Chichester
- Norman, K., Seed, A. & Pierce, C. (2010) A comparison of two radar rainfall ensemble generators, *Proceedings of the Sixth European Conference on Radar in Meteorology and Hydrology (ERAD 2010)*
- Novak, P. (2007). The Czech Hydrometeorological Institute's severe storm nowcasting system, *Atmospheric Research*, Vol. 83, pp. 450-457
- Obled, C., Wendling, J. & Bevin, K. (1994). The sensitivity of hydrological models to spatial rainfall patterns: an evaluation using observed data, *Journal of Hydrology*, Vol. 159, pp. 305-333
- Ogden, F. L. & Julien, P. Y. (1994). Runoff model sensitivity to radar rainfall resolution, *Journal of Hydrology*, Vol. 158, pp. 1-18
- Ott, E., Hunt, B. R., Szunyogh, I., Zimin, A. V., Kostelich, E. J., Corazza, M., Kalnay, E., Patil, D. J. & Yorke, J. A. (2004). A Local ensemble Kalman filter for atmospheric data assimilation, *Tellus A*, Vol. 56, 415-428
- Pappenberger, F., Scipal, K. & Buizza, R. (2008). Hydrological aspects of meteorological verification, *Atmospheric Science Letters*, Vol. 9, No. 2, pp. 43-52
- Panziera, L., Germann, U., Gabella, M. & Mandapaka, P.V. (2011). NORA-Nowcasting of Orographic Rainfall by means of Analogues, *Quarterly Journal of the Royal Meteorological Society*, Vol. 137, pp. 2106-2123

- Pegram, G. G. S. & Clothier, A. N. (2001). Downscaling rainfields in space and time, using the String of Beads in time series mode, *Hydrology and Earth Systems Science*, Vol. 5, No. 2, pp. 175-186, doi:10.5194/hess-5-175-2001
- Pessoa, M. L., Raael, L. B. & Earle, R. W. (1993). Use of weather radar for flood forecasting in the Sieve river basin: A sensitivity analysis, *Journal of Applied Meteorology*, Vol. 32, pp. 462-475
- Peura, M. & Hohti, H. (2004). Optical flow in radar images, *Proceedings of the Third European Conference on Radar Meteorology (ERAD)*, pp. 454-458, Visby, Island of Gotland, Sweden, 6-10 September 2004
- Pierce, C. E., Norman, K. and Seed, A. (2011). Use of ensemble radar estimates of precipitation rate within a stochastic, quantitative precipitation nowcasting algorithm, *Proceedings of the eighth International Symposium on Weather Radar and Hydrology*, Exeter, UK, April 2011, to appear in IAHS red book
- Pierce, C. E., Bowler, N., Seed, A., Jones, A., Jones, D. & Moore, R. J. (2004). Use of a stochastic precipitation nowcast scheme for fluvial flood forecasting and warning. *Proceedings of the Sixth International Symposium on Hydrological Applications of Weather Radar*, 2-4 February 2004, Melbourne, Australia
- Poli, V., Alberoni, P.P. & Cesari, D. (2008). Intercomparison of two nowcasting methods: preliminary analysis, *Meteorology and Atmospheric Physics*, Vol. 101, pp. 229-244, doi: 10.1007/s00703-007-0282-3
- Rawlins, F. R., Ballard, S. P., Bovis, K. R., Clayton, A. M., Li, D., Inverarity, G. W., Lorenc, A. C., & Payne, T. J. (2007). The Met Office global four-dimensional data assimilation system, *Quarterly Journal of the Royal Meteorological Society*, Vol. 133, pp. 347-362
- Rennie, S. J., Dance, S. L., Illingworth, A. J., Ballard, S. P. & Simonin, D. (2010). 3D-Var assimilation of insect-derived Doppler radar radial winds in convective cases using a high-resolution model, *Monthly Weather Review*, Vol. 139, pp. 1148-1163
- Rigo, T., Pineda, N. & Bech, J. (2010). Analysis of warm season thunderstorms using an object-oriented tracking method based on radar and total lightning data, *Natural Hazards and Earth System Sciences*, Vol. 10, pp. 1881-1893
- Rinehart, R. E. & Garvey, E. T. (1978). Three-dimensional storm motion detection by conventional weather radar, *Nature*, Vol. 273, pp. 287-289
- Rinehart, R. E. (1981). A pattern-recognition technique for use with conventional weather radar to determine internal storm motions, In: *Recent Progress in Radar Meteorology*, R. Carbone (Ed.), 105-118, National Center for Atmospheric Research
- Roberts, N. M. & Lean, H. W. (2008). Scale-selective verification of rainfall accumulations from high-resolution forecasts of convective events, *Monthly Weather Review*, Vol. 136, pp. 78-97
- Roberts, N. M., Cole, S. J., Forbes, R. M., Moore, R. J. & Boswell, D. (2009). Use of high-resolution NWP rainfall and river flow forecasts for advance warning of the Carlisle flood, north-west England, *Meteorological Applications*, Vol. 16, pp. 23-34
- Roca-Sancho, J., Berenguer, M., Zawadzki, I., & Sempere-Torres, D. (2009). Characterization of the error structure of precipitation nowcasts, *Proceedings of the 34th AMS Radar Conference*, American Meteorological Society
- Rossa, A. M., Liechti, K., Zappa, M., Bruen, M., Germann, U., Haase, G., Keil, C. & Krahe, P. (2011). COST 731 Action: A review on uncertainty propagation in advanced hydro-meteorological forecast systems, *Atmospheric Research*, Vol. 100, pp. 150-167

- Russo, J. A. & Bowne, N. E. (1962). Linear extrapolation as a meteorological forecast tool when applied to radar and cloud ceiling patterns, *Proceedings of the ninth weather radar conference*, Kansas City, Mo., October 23-26, 1961
- Ruzanski, E., Chandrasekar, V., & Wang, Y. (2011). The CASA nowcasting system, *Journal of Atmospheric and Oceanic Technology*, Vol. 28, pp. 640-655
- Ryde, J. W. (1946). The attenuation and radar echoes produced at centimetre wave-lengths by various meteorological phenomena, *Meteorological Factors in Radio-Wave Propagation*, Physical Society of London, pp. 169-189
- Saito, K., Fujita, T., Yamada, Y., Ishida, J., Kumagai, Y., Aranami, K., Ohmori, S., Nagasawa, R., Kumagai, S., Muroi, C., Kato, T., Eito, H. & Yamazaki, Y. (2006). The operational JMA nonhydrostatic mesoscale model, *Monthly Weather Review*, Vol. 134, pp. 1266-1298
- Schaake, J. C. & Larson, L. (1998). Ensemble streamflow prediction (ESP): Progress and research needs, *Special Symposium on Hydrology*, J1.3, 410-413, American Meteorological Society, Phoenix, Arizona
- Schellart, A. N. A., Rico-Ramirez, M. A., Liguori, S. & Saul, A.J. (2009). Quantitative precipitation forecasting for a small urban area: use of radar nowcasting, *8th International Workshop on precipitation in urban areas, Rainfall in the urban context: Forecasting, Risk and Climate Change*, 10-13 December, 2009, St. Moritz, Switzerland
- Schellekens, J., Minett, A. R. J., Reggiani, P., Weerts A. H., Moore, R. J., Cole, S. J., Robson, A. J., Bell, V. A. (2010). *Hydrological modelling using convective scale rainfall modelling – phase 3*. Project: SC060087/R3, Authors. Research Contractor: Deltares and CEH Wallingford, Environment Agency, Bristol, UK, 231pp. <http://publications.environment-agency.gov.uk/pdf/SCHO0210BRYT-e-e.pdf>
- Schenkman, A., Xue, M., Shapiro, A., Brewster, K. & Gao, J. (2011a). The analysis and prediction of the 8-9 May 2007 Oklahoma tornadic mesoscale convective system by assimilating WSR-88D and CASA radar data using 3DVAR, *Monthly Weather Review*, Vol. 139, pp. 224-246
- Schenkman, A., Xue, M., Shapiro, A., Brewster, K. & Gao, J. (2011b). Impact of CASA radar and Oklahoma mesonet data assimilation on the analysis and prediction of tornadic mesovortices in a MCS, *Monthly Weather Review*, Vol. 139, pp. 3422-3445
- Schertzer, D., Lovejoy, S., Schmitt, F., Chigirinskaya, Y. & Marsan, D. (1997). Multifractal cascade dynamics and turbulent intermittency, *Fractals*, Vol. 5, No. 3, pp. 427-471
- Schmid, W., Mecklenburg, S. & Joss, J. (2000). Short-term risk forecasts of severe weather, *Physics and Chemistry of the Earth, Part B*, Vol. 25, pp. 1335-1338
- Seed, A. W., Srikanthan, R. & Menabde, M. (1999). A space and time model for design storm rainfall, *Journal of Geophysical Research*, Vol. 104, No. D24, pp. 31623-31630
- Seed, A. W. (2003). A dynamic and spatial scaling approach to advection forecasting, *Journal of Applied Meteorology*, Vol. 42, pp. 381-388
- Seity, Y., Brousseau, P., Malardel, S., Hello, G., Benard, P., Bouttier, F., Lac, C. & Mason, V. (2011). The AROME-France convective scale operational model, *Monthly Weather Review*, Vol. 139, pp. 976-991
- Seo, D.-J., Perica, S., Welles, E., & Schaake, J. C. (2000). Simulation of precipitation fields from probabilistic quantitative precipitation forecast, *Journal of Hydrology*, Vol. 239, No. 1, pp. 203-229
- Shah, S. M. S., O'Connell, P. E., & Hosking, J. R. M. (1996). Modelling the effects of spatial variability in rainfall on catchment response. II. Experiments with distributed and lumped models, *Journal of Hydrology*, Vol. 175, pp. 89-111

- Sharif, H. O., Yates, D., Roberts, R. & Mueller, C. (2006). The use of an automated nowcasting system to forecast flash floods in an urban watershed, *Journal of Hydrometeorology*, Vol. 7, pp. 190–202
- Smith, T. L., Benjamin, S. G., Brown, J. M., Weygandt, S. S., Smirnova, T. & Schwartz, B. E. (2008). Convection forecasts from the hourly updated, 3-km high resolution Rapid Refresh Model, *Preprints, 24th Conference on severe local storms*, Savannah, GA, American Meteorological Society, Available online at http://ams.confex.com/ams/24SLS/techprogram/paper_142055.htm
- Snook, N., Xue, M. & Jung, J. (2011). Analysis of a tornadic mesoscale convective vortex based on ensemble Kalman filter assimilation of CASA X-band and WSR-88D radar data, *Monthly Weather Review*, Vol. 139, pp. 3446–3468
- Snook, N., Xue, M. & Jung, J. (2012). Ensemble probabilistic forecasts of a tornadic mesoscale convective system from ensemble Kalman filter analyses using WSR-88D and CASA radar data, to appear in *Monthly Weather Review*
- Stensrud, D. J., Xue, M., Wicker, L. J., Kelleher, K. E., Foster, M. P., Schaefer, J. T., Schneider, R. S., Benjamin, S. G., Weygandt, S. S., Ferree, J. T. & Tuell, J. P. (2009). Convective-scale warn-on-forecast system. A vision for 2020, *Bulletin of the American Meteorological Society*, Vol. 90, pp. 1487–1499
- Stephan, K., Klink, S. & Schraff, C. (2008). Assimilation of radar-derived rain rates into the convective-scale model COSMO-DE at DWD, *Quarterly Journal of the Royal Meteorological Society*, Vol. 134, pp. 1315–1326
- Stout, G. E. & Neill, J. C. (1953). Utility of radar in measuring areal rainfall, *Bulletin of the American Meteorological Society*, Vol. 34, No. 1, pp. 21–27
- Sun, J. (2005a). Initialization and numerical forecasting of a supercell storm observed during STEPS, *Monthly Weather Review*, Vol. 133, pp. 793–164
- Sun, J. (2005b). Convective-scale assimilation of radar data: progress and challenges, *Quarterly Journal of the Royal Meteorological Society*, Vol. 31, pp. 3439–3463
- Sun, J., Chen, M. & Wang, Y. (2010). A frequent-updating analysis system based on radar, surface, and mesoscale model data for the Beijing 2008 Forecast Demonstration Project, *Weather and Forecasting*, Vol. 25, pp. 1715–1735
- Sun, J. & Crook, A. (1994). Wind and thermodynamic retrievals from single-Doppler measurements of a gust front observed during Phoenix II, *Monthly Weather Review*, Vol. 122, pp. 1075–1091
- Sun, J. & Crook, N. A. (1997). Dynamical and microphysical retrieval from Doppler radar observations using a cloud model and its adjoint: I. Model development and simulated data experiments, *Journal of Atmospheric Science*, Vol. 54, pp. 1642–1661
- Sun, J. & Crook, N. A. (1998). Dynamical and microphysical retrieval from Doppler radar observations using a cloud model and its adjoint: II. Retrieval experiments of an observed Florida convective storm, *Journal of Atmospheric Science*, Vol. 55, pp. 835–852
- Sun, J. & Crook, N. A. (2001). Real-time low-level wind and temperature analysis using single WSR-88D data, *Weather Forecasting*, Vol. 16, pp. 117–132
- Sun, J., Flicker, D. W. & Lilly, D. K. (1991). Recovery of three-dimensional wind and temperature fields from single-Doppler radar data, *Journal of Atmospheric Science*, Vol. 48, pp. 876–890
- Sun, J. & Zhang, Y. (2008). Analysis and prediction of a squall line observed during IHOP using multiple WSR-88D observations, *Monthly Weather Review*, Vol. 136, pp. 2364–2388

- Sun, J., Xiao, Q., Trier, S., Weisman, M., Wang, H., Ying, Z., Xu, M. & Zhang, Y. (2012). Sensitivity of 0-12 hour warm-season precipitation forecast over the central United States to model initialization and parameterizations, submitted to *Weather and Forecasting*
- Tsonis, A. A. & Austin, G. L. (1981). An evaluation of extrapolation techniques for the short-term prediction of rain amounts, *Atmosphere-Ocean*, Vol. 19, pp. 54-65
- Tsonis, A. A. (1989). Chaos and unpredictability of weather, *Weather*, Vol. 44, No. 6, pp. 258-263
- Twomey, S. (1953). On the measurement of precipitation by radar, *Journal of Meteorology*, Vol. 10, pp. 601-620
- Turner, B. J., Zawadzki, I. & Germann, U. (2004). Predictability of precipitation from continental radar images. Part III: Operational nowcasting implementation (MAPLE), *Journal of Applied Meteorology*, Vol. 43, pp. 231-248
- Velasco-Forero, C. A., Sempere-Torres, D., Cassiraga, E. F. & Gómez-Hernández, J. J. (2009). A non-parametric automatic blending methodology to estimate rainfall fields from rain gauge and radar data. *Advances in Water Resources*, Vol. 32, pp. 986-1002
- Vivoni, E. R., Ivanov, V. Y., Bras, R. L. & Entekhabi, D. (2005). On the effects of triangulated terrain resolution on distributed hydrologic model response, *Hydrological Processes*, Vol. 19, pp. 2101-2122
- Vivoni, E. R., Entekhabi, D., Bras, R. L., Ivanov, V. Y. & Van Horn, M. P. (2006). Extending the predictability of hydrometeorological flood events using radar rainfall nowcasting, *Journal of Hydrometeorology*, Vol. 7, pp. 660-677
- Vivoni, E. R., Entekhabi, D. & Hoffman, R. N. (2007). Error propagation of radar rainfall nowcasting fields through a fully distributed flood forecasting model, *Journal of Applied Meteorology And Climatology*, Vol. 46, pp. 932-940
- Wang, J. and contributing authors (2009). *Overview of the Beijing 2008 Olympics project. Part I; Forecast Demonstration Project*, A report to the WMO World Weather Research Programme
- Werner, M. & Cranston, M. (2009). Understanding the value of radar rainfall nowcasts in flood forecasting and warning in flashy catchments, *Meteorological Applications*, Vol. 16, No. 1, pp. 41-55
- Werner, M., Cranston, M., Harrison, T., Whitfield, D. & Schellekens, J. (2009). Recent developments in operational flood forecasting in England, Wales and Scotland, *Meteorological Applications*, Vol. 16, No. 1, pp. 13-22
- Wexler, R. (1951). Theory and observation of radar storm detection, *Compendium of Meteorology*, T. F. Malone, (Ed.), 1283-1289, American Meteorological Society
- Wexler, R. & Swingle, D. M. (1947). Radar storm detection, *Bulletin of the American Meteorological Society*, Vol. 28, pp. 159-167
- Weygandt, S. S., Benjamin, S. G., Smirnova, T. G. & Brown, J. M. (2008). Assimilation of radar reflectivity data using a diabatic digital filter within the Rapid Update Cycle., *Preprints, 12th Conference on IOAS-AOLS, 8.4.*, New Orleans, LA, American Meteorological Society, Available online at http://ams.confex.com/ams/88Annual/techprogram/paper_134081.htm
- Winchell, W., Gupta, H. V. & Sorooshian, S. (1998). On the simulation of infiltration- and saturation-excess runoff using radar-based rainfall estimates: Effects of algorithm uncertainty and pixel aggregation, *Water Resources Research*, Vol. 34, pp. 2655-2670

- Wilk, K. E. & Gray, K. C. (1970). Processing and analysis techniques used with the NSSL weather radar system, *Preprints, 14th Conference on Radar Meteorology*, pp. 369–374, Tucson, AZ, American Meteorological Society
- Wilson, J. W. (1966). Movement and predictability of radar echoes, *Tech. Memo ERTM-NSSL-28*, National Severe Storms Laboratory, 30 pp., Available from National Information Service, Operations Division, Springfield, VA 22161
- Wilson, C. B., Valdes, J. B., & Rodriguez-Iturbe, I. (1979). On the influence of the spatial distribution of rainfall on storm runoff, *Water Resources Research*, Vol. 15, No. 2, pp. 321–328
- Wilson, J. W., Crook, N. A., Mueller, C. K., Sun, J. & Dixon, M. (1998). Nowcasting thunderstorms : a status report, *Bulletin of the American Meteorological Society*, Vol. 79, pp. 2079–2099
- Wilson, J. W., Feng, Y., Chen, M., & Roberts, R. (2010). Nowcasting challenges during the Beijing Olympics; Successes, failures, and implications for future nowcasting systems, *Weather Forecasting*, Vol. 25, pp. 1691–1714
- Witt, A. & Johnson, J. T. (1993). An enhanced storm cell identification and tracking algorithm, *Preprints, 26th International Conference on Radar Meteorology*, pp. 514–521, Norman, OK, American Meteorological Society
- Xiao, Q., Kuo, Y. -H., Sun, J., Lee, W. -C., Lim, E., Guo, Y., & Barker, D. M. (2005). Assimilation of Doppler radar observations with a regional 3D-VAR system: Impact of Doppler velocities on forecasts of a heavy rainfall case, *Journal of Applied Meteorology*, Vol. 44, pp. 768–788
- Xiao, Q., Lim, E., Won D. -J, Sun, J., Lee, W. -C., Lee, M. -S., Lee, W. -J., Cho, J. -Y., Kuo, Y. -H., Barker, D. M., Lee, D. -K., Lee, H. -S. (2008). Doppler radar data assimilation in KMA's operational forecasting, *Bulletin of the American Meteorological Society*, Vol. 89, pp. 39–43
- Xue, M., Kong, F., Thomas, K. W., Wang, Y., Brewster, K., Gao, J., Wang, X., Weiss, S. J., Clark, A. J., Kain, J. S., Coniglio, M. C., Du, J., Jensen, T. L. & Kuo, Y. H. (2011). CAPS Real time storm scale ensemble and high resolution forecasts for the NOAA hazardous weather testbed 2010 spring experiment, *24th Conference on Weather and Forecasting, 20th Conference on Numerical Weather Prediction*, paper 9A.2, American Meteorological Society
- Yeung, H.-Y, Man, C., Chan, S. -T. & Seed, A. W. (2011). Application of radar-raingauge co-Kriging to improve QPE and quality control of real-time rainfall data, *Proceedings of the eighth International Symposium on Weather Radar and Hydrology*, Exeter, UK, April 2011, to appear in IAHS red book
- Zappa, M., Rotach, M. W., Arpagaus, M., Dorninger, M., Hegg, C., Montani, A., Ranzi, R., Ament, F., Germann, U., Grossi, G., Jaun, S., Rossa, A., Vogt, S., Walser, A., Wehrhan, J. & Wunram, C. (2008). MAP D-PHASE: real-time demonstration of hydrological ensemble prediction systems, *Atmos. Science Letters*, Vol. 9, No. 2, pp. 80–87
- Zawadzki, I. (1973). Statistical properties of precipitation patterns, *Journal of Applied Meteorology*, Vol. 12, pp. 459–472
- Zawadzki, I., Morneau, J. & Laprise, R. (1994). Predictability of precipitation patterns: an operational approach, *Journal of Applied Meteorology*, Vol. 33, pp. 1562 – 1571
- Zittel, W. D. (1976). Computer applications and techniques for storm tracking and warning, *Preprints, 17th Conference on Radar Meteorology*, pp. 514–521, Seattle, WA, American Meteorological Society

Use of Radar Precipitation Estimates in Urban Areas: A Case Study of Mexico City

Ernesto Caetano¹, Baldemar Méndez-Antonio² and Víctor Magaña¹

¹*Instituto de Geografía, National Autonomous University of Mexico,*

²*Energy Department, Metropolitan Autonomous University, Mexico*

1. Introduction

Storm events have long been a menace to Mexico City. The main reason is related to the fact that in summer, many showers can reach intensities of more than 20 mm/hour, which makes difficult the management of the drainage system in various areas of the city. As instance discharges of large magnitudes in the western part of the city are an element of danger, as they lead to flash flood that inundate populated areas downstream in a matter of minutes. Recent flooding events in Mexico City have revealed its vulnerability to severe weather conditions. Although regularization programs and new urban land policies are been implemented by the council government, there are still many families living in high risk areas. These areas over hillsides, and irregular human settlements still proliferate. Usually, severe storms can cause hazard landslides because unstable landfills and deforested hill slopes. On the other hand in the flat parts of the city, faulty drainage systems usually cause sewage flooding after continuous rain events. The urban sprawl undergone in the last half century, has not kept pace with urban services such as drainage. In the rainy season, puddles arise, sometimes caused by the presence of silt and debris in the ducts and the drainage system capacity is exceeded, and in other cases there are no absorption wells in areas with problems in the drainage network. Additionally, the lack of maintenance of dams and channels can also result in severe flooding problems. In most cases, the intense rainfall events produce merely an emergency response of fire departments.

In the last three decades there have been major advances in remote sensing techniques for estimation of rain, mainly in the use of meteorological radar and weather satellites, increasing the availability of rainfall data for operational meteorological and hydrological applications. Precipitation estimates derived from meteorological radar are useful in runoff simulation in urban drainage. Spatial distribution of radar rainfall used as input to a distributed hydrological model permit to characterize the performance of drainage infrastructure at local and regional scale. Radar data used in this analysis are obtained from C-band radar deployed at western Mexico Valley basin and derived rainfall estimates provides the input to a distributed hydrologic model applied to the Mixcoac microwatershed located at western Mexico basin. Radar and distributed hydrologic model are capable to provide accurate rainfall and runoff data supporting specific-site flood information and, also provides a baseline for comparison and guides design of radar network as one component of an early warning system for the region.

The international practice aims at a comprehensive approach to flood management in response not only to the consequences of a specific event, but measures that starting from the prediction of extreme events and monitoring for early warning purposes to establishment of civil protection measures for those affected by the occurrence of such events and the hazard remediation, including infrastructure development and non-structural measures to reduce the vulnerability.

The structure of this work is as follows. Section 2 presents the summer precipitation regime over Mexico Valley. Section 3 a brief description the meteorological radar deployed in Cerro Catedral at western of Mexico Valley. In Section 4 a case study for the microwatershed of the Mixcoac River is discussed. In Section 5 new design of a weather information system is proposed. Concluding remarks are found in Section 6.

2. Mexico valley precipitation climatology

The México Valley is located at 2240 m altitude and at a latitude of approximately 19°N and is characterized by well-defined rainy season from late May to early October which can be classified as a monsoon climate type.

The orography of region plays an important role on the precipitation patterns (intensity, timing, spatial distribution and, extreme events occurrence). On northeastern area, region nearly flat, the average precipitation is around 500 mm/year and at southwestern mountainous region part of the México Valley, the average reaches almost 1200 mm/year (Fig. 1). The occurrence of extreme events follows the same patterns as shown by Magaña et al. (2003) by establishing a criterion to determine when intense precipitation should be considered an extreme event based on a Gamma distribution of the observed amount of daily rainfall, for each station of the rain gauge network (Fig. 2). The similarity of spatial variability of severe weather and average precipitation becomes apparent. An extreme precipitation event to occur in the western or southern part of the basin, rainfall in 24 hours should exceed 25 or 30 mm, while in the eastern part of the city, more than 15 mm in 24 hours already constitute an extreme event. To a large extent the interaction of the mountains with the summer easterly winds determines, the characteristics of precipitation (Barros 1994).

The summer precipitation diurnal cycle indicates the intense precipitation begins in the afternoon (Fig. 3), around 16:00 h local time, generally in the eastern part of the valley, and propagate to the western part during the evening, reaching the other extreme of the valley by late evening and midnight (Mendez et al., 2006).

3. The Cerro Catedral radar

The radar network operated by Mexico's National Water Commission is focalized mainly in monitoring of the tropical cyclone activity and consists of thirteen C-band radars (manufactured by Ericsson Inc., Enterprise Electronics Corporation and Vaisala). There is also a weather radar deployed at Cerro Catedral which cover almost all Mexico Basin (located 40 km and altitude 3785 m, approximately 1500 meter above México City), to monitor severe weather over this region (Fig. 4). This radar measures reflectivity and has a Doppler and dual polarization and, is configured as follows (Table 1):

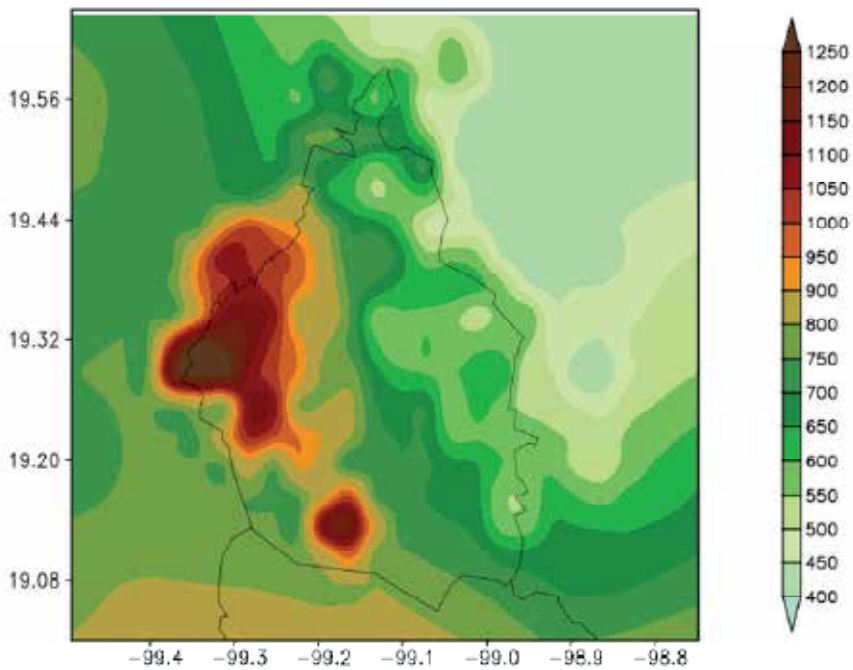


Fig. 1. Summer (May-October) climatology (2003-2008) accumulated (mm) precipitation distribution over Mexico Valley.

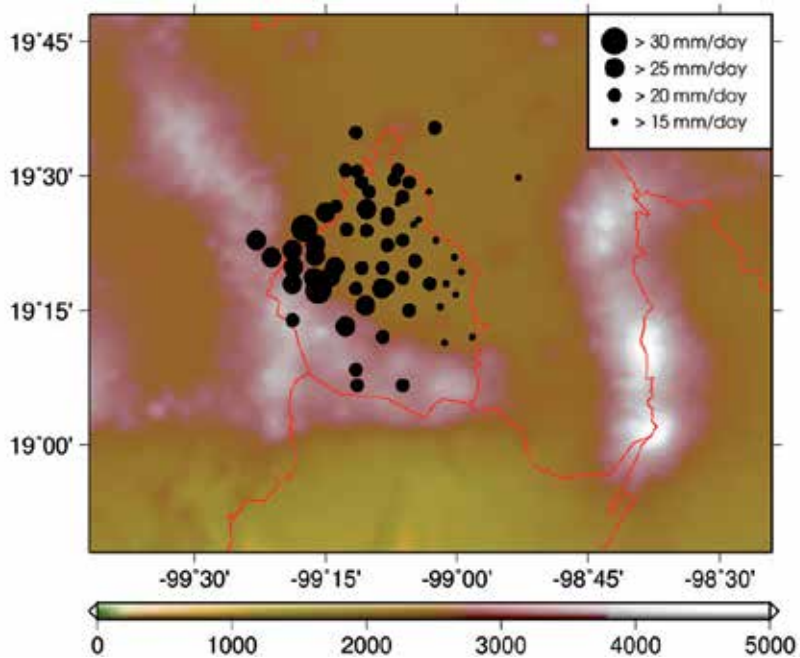
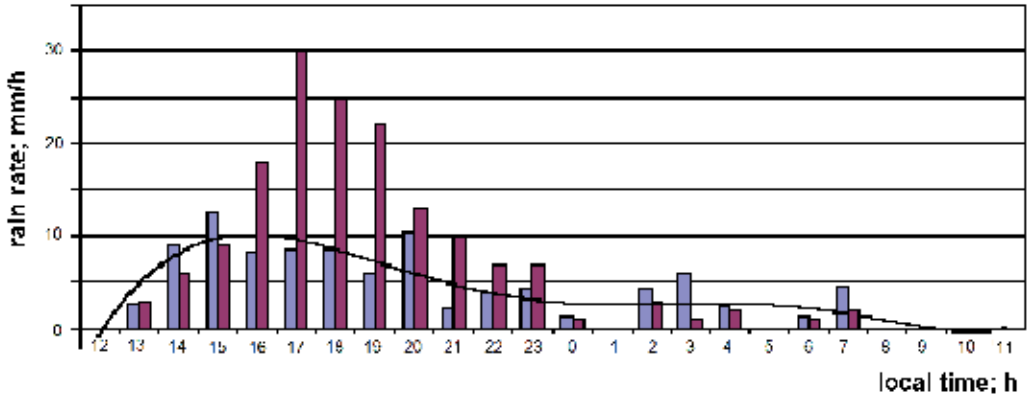
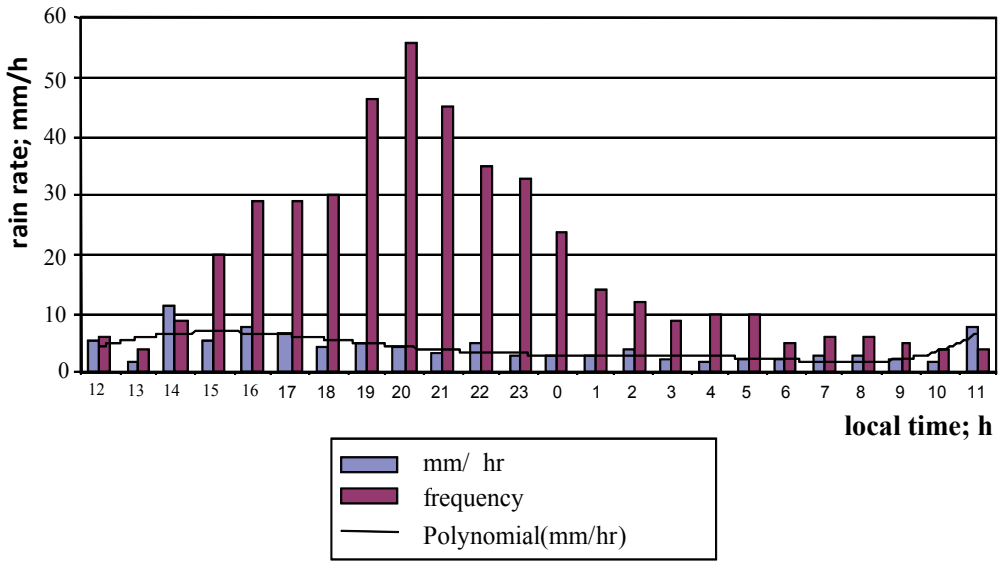


Fig. 2. Threshold values to determine daily extreme precipitation event. Topography (m) is shown in color.



(a)



(b)

Fig. 3. Precipitation intensity, frequency and occurrence time histograms; (a) northern and (b) southern Mexico basin; (1993-2001).

Antenna diameter (m)	4.2.
Antenna Gain (dB)	44.7
Beamwith (")	0.9
Polarization	Linear hor/vert
Frequency (GHz)	5.60-5.65
Wavelength (cm)	5.30-5.35
Peak power (kW)	250
Pulse length (μ s)	0.5 - 2.0
PRF (Hz)	250, 900, 1200
MDS (dBm)	-114, -110, -109

Table 1. Cerro Catedral weather radar (Ericsson UBS 103 04, upgraded by Sigmat/Vaisala technology) technical characteristics.

Such elevation has effects over the precipitation estimated at low level on Mexico Valley Watershed. In order to get a good coverage of shallow rain, originating close to ground, it is necessary to settle the elevation angles to negative value of around -1.5 degree. This has the inconvenience of blockage, clutter and loss of signal. The weather radar usually suffers partial or total blockade operating in mountain zones due to the complex topography around it. This effect can limit the coverage of the radar when it use negative degrees and affect the precipitation measurements (Joss & Waldvogel, 1990; Sauvageot, 1994; Collier, 1996 and Smith, 1998). The application of some blockage corrections to the observations radar is worthwhile, in order to get quantitative estimation of the precipitation and it can be combined with elimination of spurious echoes by two and three-dimensional analysis of the topography and the storm (Krajewski & Vignal, 2001; Steiner & Smith, 2002). A promising development in this field is related to the gradual change of weather radar concept, from a tool for qualitative rainfall estimation to a tool for more quantitative rainfall measurement (Borga et al., 1997).

Despite the drawback of the radar height site (1500 m above Mexico City) to follow stratiform precipitation system, convective systems are adequately monitored. In fact, the radar is capable of doing the full scan within convective clouds but no precipitation estimates in clouds with a base height of less than 3500 m (Fig. 5).

Figure 6 shows the monitoring of three storm events within range of radar coverage. In addition to tracking the storms, which would support decision makers in a warning system in these figures one can see the fixed echoes caused by the presence of volcanoes on the eastern side of Mexico City. This represents a serious problem in estimating precipitation, both qualitatively and in its distribution and location, as it provides information on areas where there is rain. Considering that the fixed echoes, whether caused by the interception of the land or effect of the lateral lobes, they can be largely eliminated with the Doppler radar function. However, despite all the Mexican radar, including that of Cerro Catedral, have this feature is not used to remove these echoes.

The Doppler radar function is a great help to eliminate this kind of echo and it is important for a better estimation of rainfall fields for hydrological or/and alert purposes. The cost of sending false warning alerts to users, when these echoes are not removed, is high, because once lost confidence in warnings of severe storms is difficult to recover it.

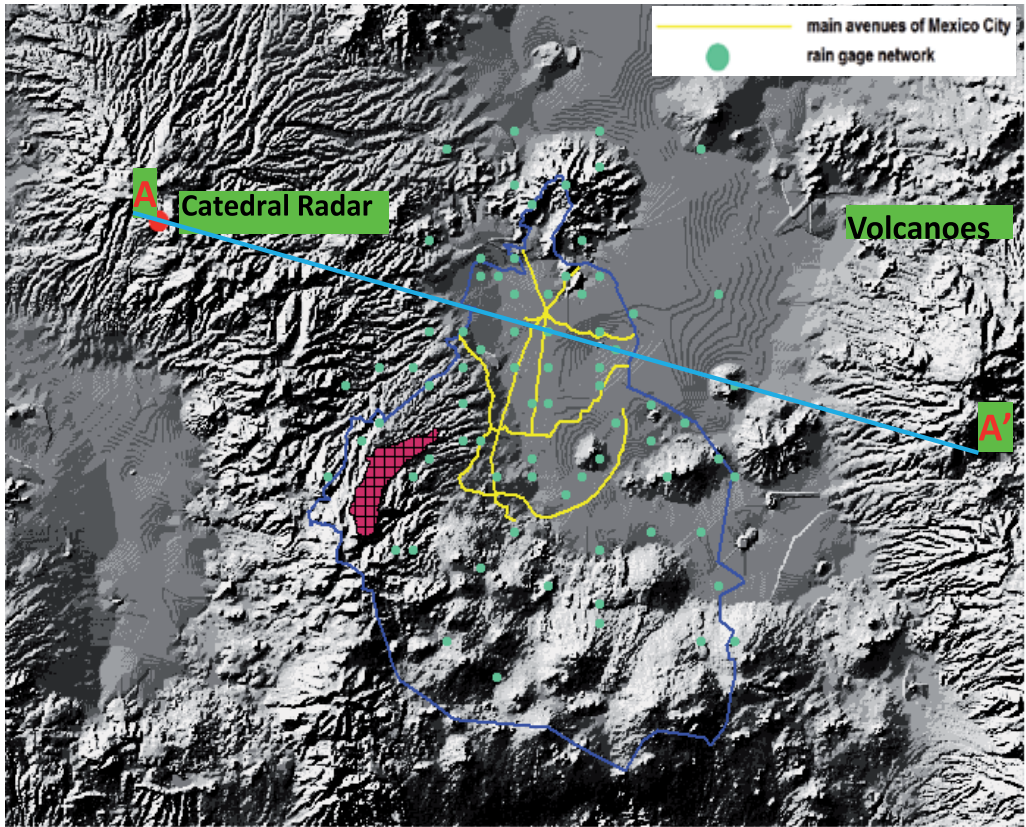


Fig. 4. Mixcoac River Basin (pink shaded area), Cathedral radar site and main avenues of Mexico City and rain gauges network.

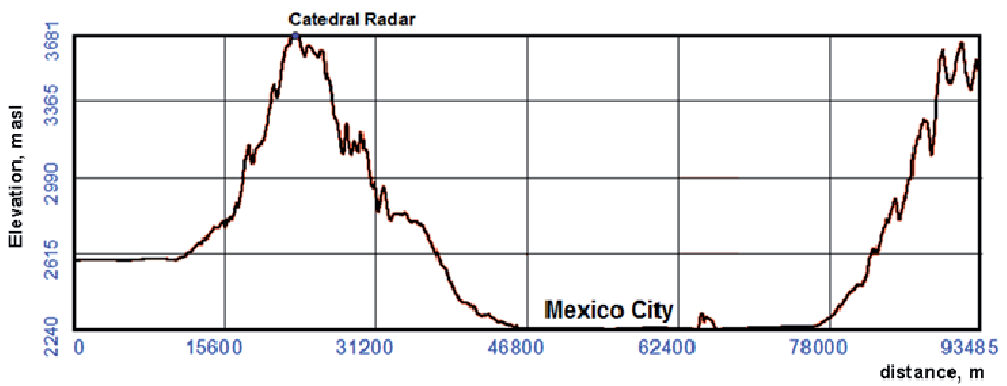
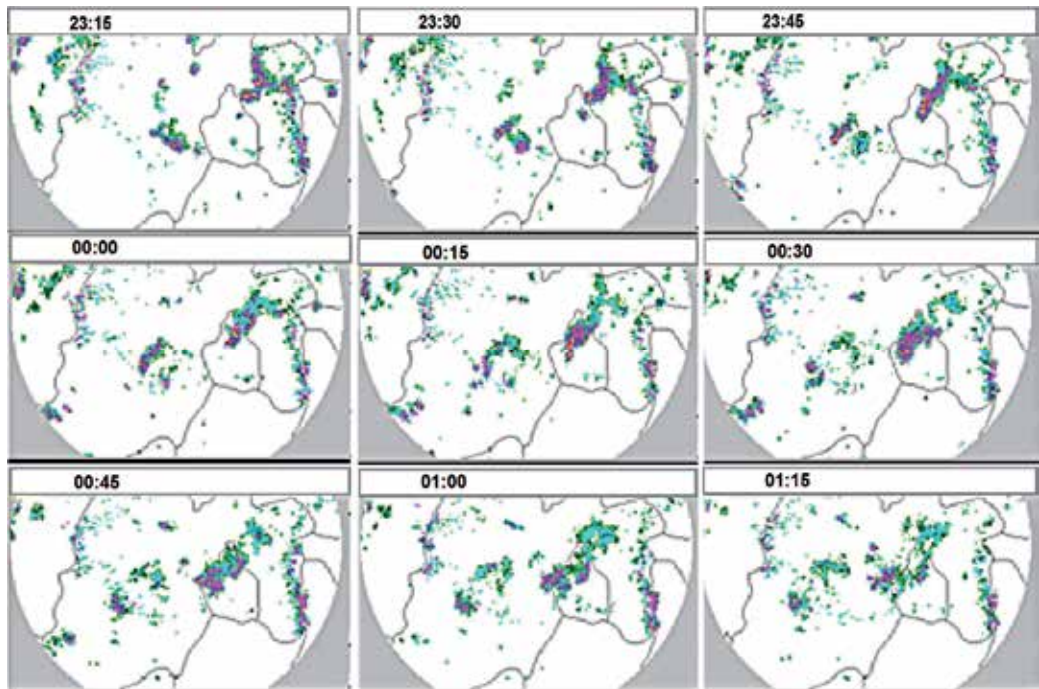
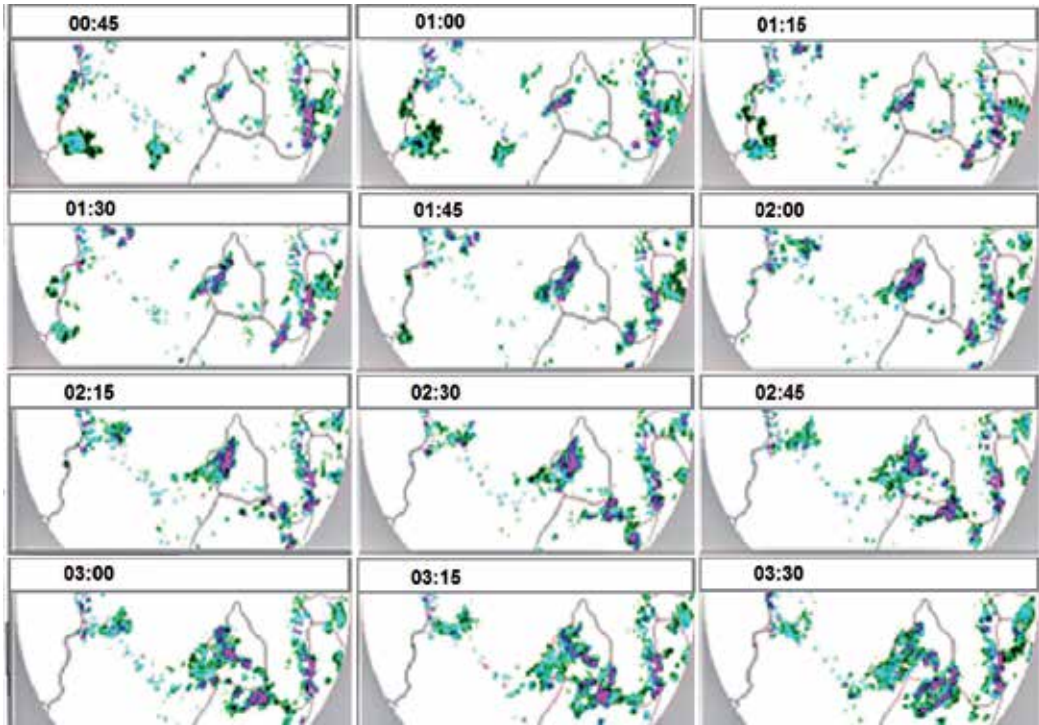
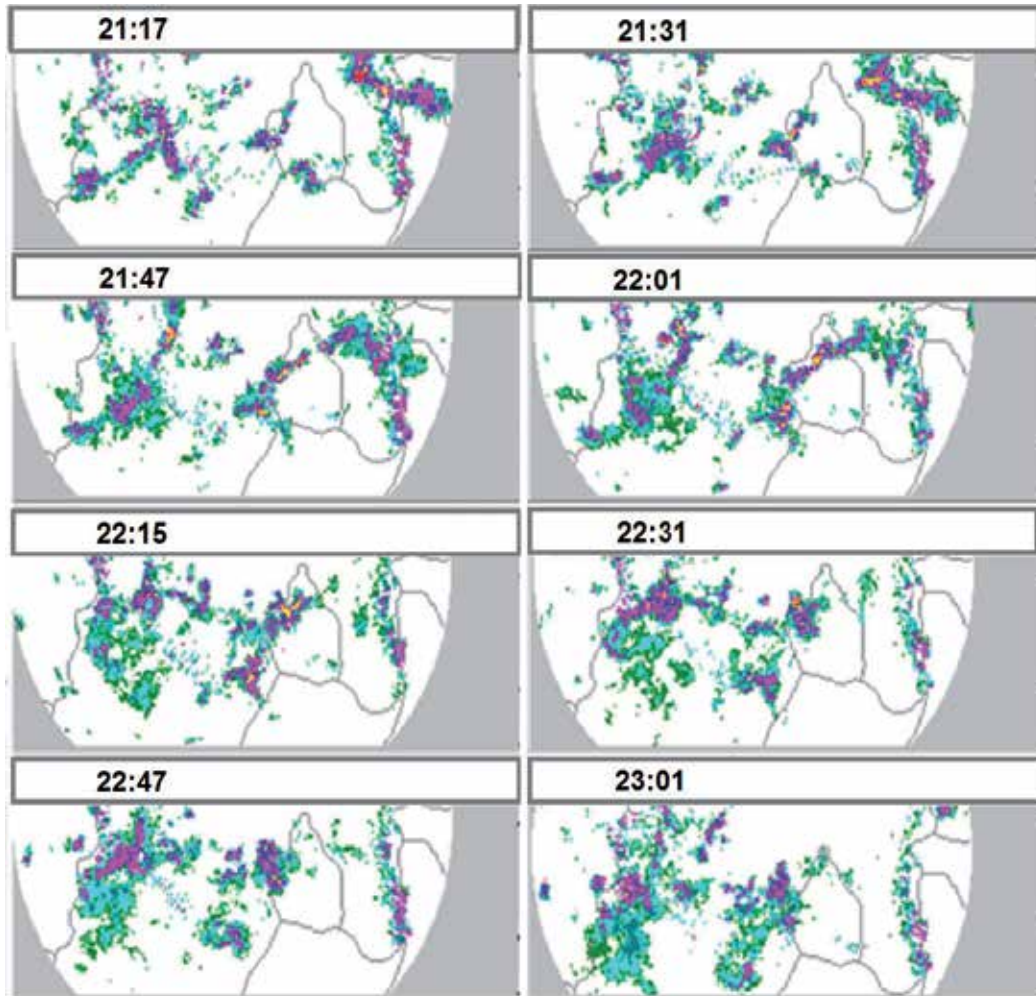


Fig. 5. Relief cross section A-A' of the Mexico Valley basin (see Fig. 4).





(c)



Fig. 6. Examples of storm radar monitoring over the Valley of Mexico basin and identification of fixed echoes caused by the interception of the radar beam with volcanoes located eastern Mexico City: a) 15 June; b) 13 July and; c) 19 September 1998.

4. Case study

Mendez (2005) and Mendez et al. (2009) using reflectivity radar data for the period of 1995-1998, selected 13 intense precipitation events to examine the rainfall patterns over México City, determined by the Cerro Catedral radar, by looking at spatial characteristics (shape, position and magnitude) of precipitation across the valley. The analysis also constitutes a

first step towards an improved understanding of storms over urban areas, particularly during the summer rainy season.

Méndez et al. (2011) developed a lumped model of the rainfall-runoff type with input from radar and pluviograph (rain gauge network of Mexico City water management system) data for calibration, applied to the microwatershed of Mixcoac River located at western Valley of Mexico basin, over an area of 31.5 km² (Fig. 4).

Currently all Mexican radar precipitation estimatives use the Marshall-Palmer equation (Marshall and Palmer, 1948), which presents certain discrepancy for tropical regions (Fig. 7). However, the precipitation underestimation could also be associated to beam overshooting, attenuation or hardware calibration issues. A local calibration was performed in order to improve the rainfall estimation taking into account characteristics of precipitation system over Mexico (Mendez et al., 2006). The resulting local calibration improves the estimation of rain (Fig. 7). Although false echoes treatment is not yet done, one might think that it can improve even more if they are removed.

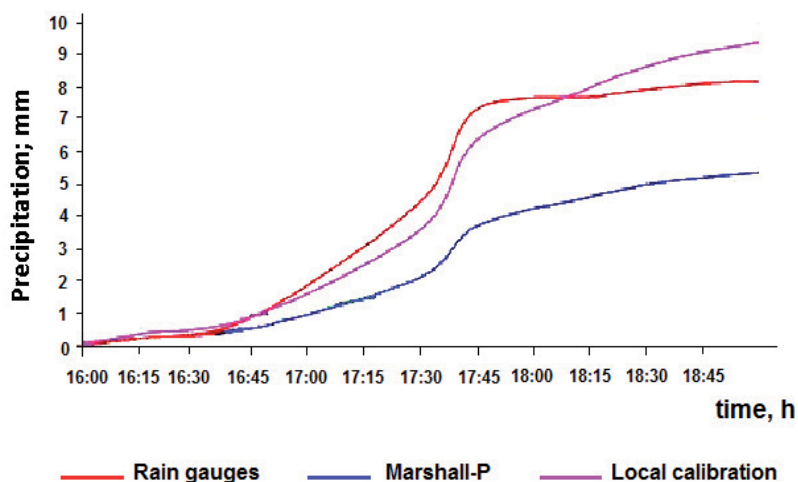


Fig. 7. Storm rainfall of 27 September 1998.

It should be mentioned the radar estimates reproduce well the precipitation patterns in time but not quantitative ones. This new calibration distribution improves this estimate.

4.1 Hydrological analysis

The improvement in the unitary hydrograph of the basin is clear (Fig 8). This is an expected result if one notices that the radar initially reproduce the temporal variability of rainfall and subsequently, after calibration hydrology, quantitative estimate improves. It is obvious that the radar properties would be underused in aggregated hydrological models because the ability to detect the precipitation spatial variability usually are not take into account in these models and, thus the analysis of the hydrological processes within the basin. However, an analysis of the aggregated model applied here is performed to detect the advantage of the radar data for hydrological model in an experimental urban catchment.

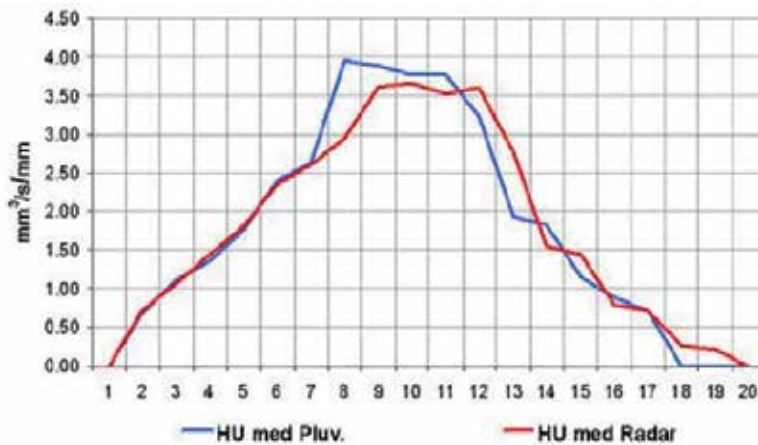


Fig. 8. The unit hydrograph estimated from radar data and pluviographs.

Additionally, in order to obtain a methodology to determine the distributed parameter hydrologic model in other watersheds, the experimental basin of the river Mixcoac and the technique Distributed Unit Hydrograph (Clark, 1943) is used. The conceptual model obtained (Fig. 9) is similar to Maidment model (Maidment, 1993). The model obtains the isochrones to Mixcoac River Basin (Fig. 10), which is then used to estimate the outflow hydrograph of the basin. The comparison between the observed and estimated with the distributed hydrological model fed with precipitation data obtained from the radar is showed in the figure 11.

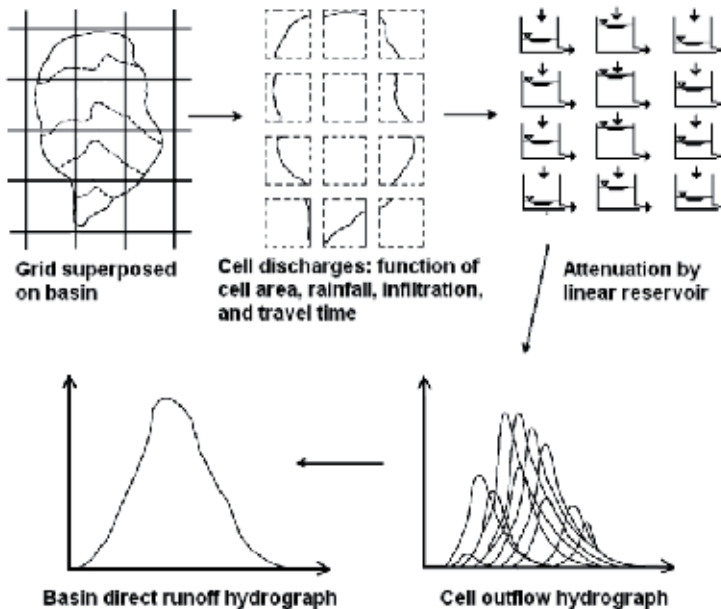


Fig. 9. Conceptual model of the distributed hydrologic model known as the Modified Clark (Source: Kull & Feldman, 1998).

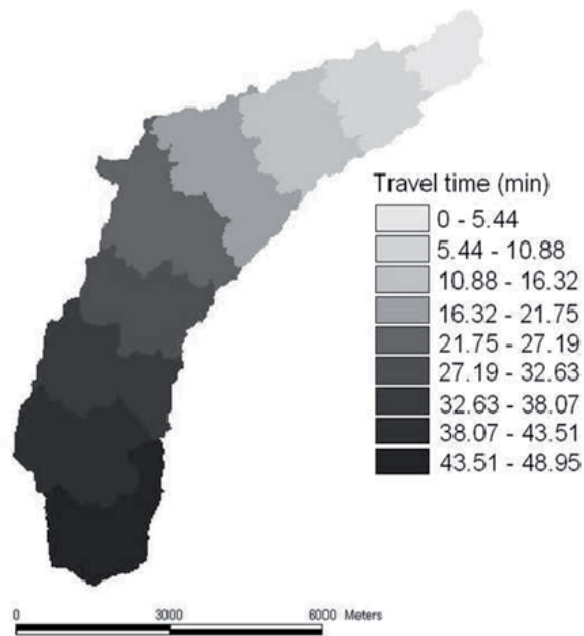


Fig. 10. Mixcoac watershed Isochronous.

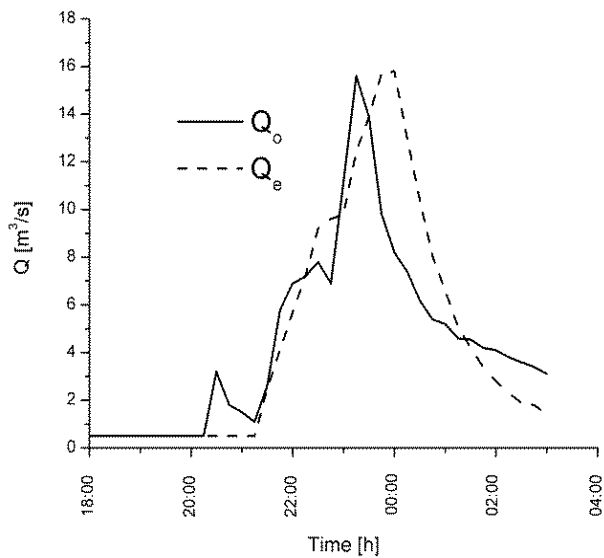


Fig. 11. Hydrological response of Mixcoac river basin, observed (Q_o) and estimated (Q_e) with radar rainfall data.

The observed and estimated response using radar rainfall data demonstrate a fairly agreement and creates the confidence to apply the methodology used in this analysis, in other watersheds. It is important to establish how to estimate correctly the radar rainfall

data by eliminating false echoes, using Doppler mode techniques to filter those echoes caused by the interception beam (principal and/or secondary lobes) with the terrain. This will give greater confidence to hydrologists that the data used were carefully treated before feeding to their models.

Aiming to use the radar hydrological information with operational purposes, a short hydrological forecast system should include the following components integrated components: a) Automatic meteorological stations network (pluviographs); b) Weather Radar; c) Satellite products and; d) Mesoscale numerical weather prediction model. The main feature of each of these components is to provide real time and hours/days in advance (forecast) rainfall data, which is a necessary condition for implementing an operational hydrological system.

5. Weather forecast system

In most cases, the fire department response facing intense rainfall events over Mexico basin is a merely emergency procedure. Its work would be greatly improved and lead to more efficient use of human and material resources available by the city government by taking advantage of weather information that is, diagnoses and forecasts of weather and climate. Unfortunately, the information prepared by the National Weather Service lacks the detail and quality required for making decisions as presented in general terms, without data, in order to one can acquire confidence in the forecast. This problem is particularly severe when it comes to prediction of severe storms considered as a danger to the water system in Mexico City. Requirements to take the first steps in the right direction are the improvement of surface measurement networks, radar and satellite information, forecasting deadlines to produce hydrometeorological information useful in decision making for disaster prevention and development of an early warning system that includes not just the danger or threat, but also the vulnerability facing to severe weather.

Any centre that generates meteorological information for decision making is based on the following required elements (Fig. 12):

1. Data Collection
2. Assimilation and display of information. Very short-term prognosis based on radar and satellite estimates of rainfall and rain gauge information.
3. Weather Forecast Systems
4. Post-processing of weather forecasting in the short term to prepare products tailored to user needs
5. Scheme for submission of information to the user or decision maker, including an early warning system useful for the Water System of Mexico City
6. Seasonal climate forecasts for water management in the long run

Although all components are equally important, the main focus to be discussed here is the radar network to be implemented in the system. Méndez et al. (2009) presented a proposal for a new radar system for Mexico Valley based on precipitation analysis estimated by the existing Cerro Catedral radar. They found an underestimation in the amount of precipitation over the western mountains of the valley, at the foothills, while rainfall rates tend to be overestimated over the eastern parts, resulting of the blockage

effect of mountains between the current radar position and the basin. The weather radar usually suffers partial or total blockade when it is located in mountainous regions. The current location of the Cerro Catedral radar can limit the coverage of the radar when it requires negative angles in the vertical measurements to monitor the valley, affecting the precipitation estimates (Joss and Waldvogel, 1990; Sauvageot, 1994; Collier, 1996; Smith, 1998).

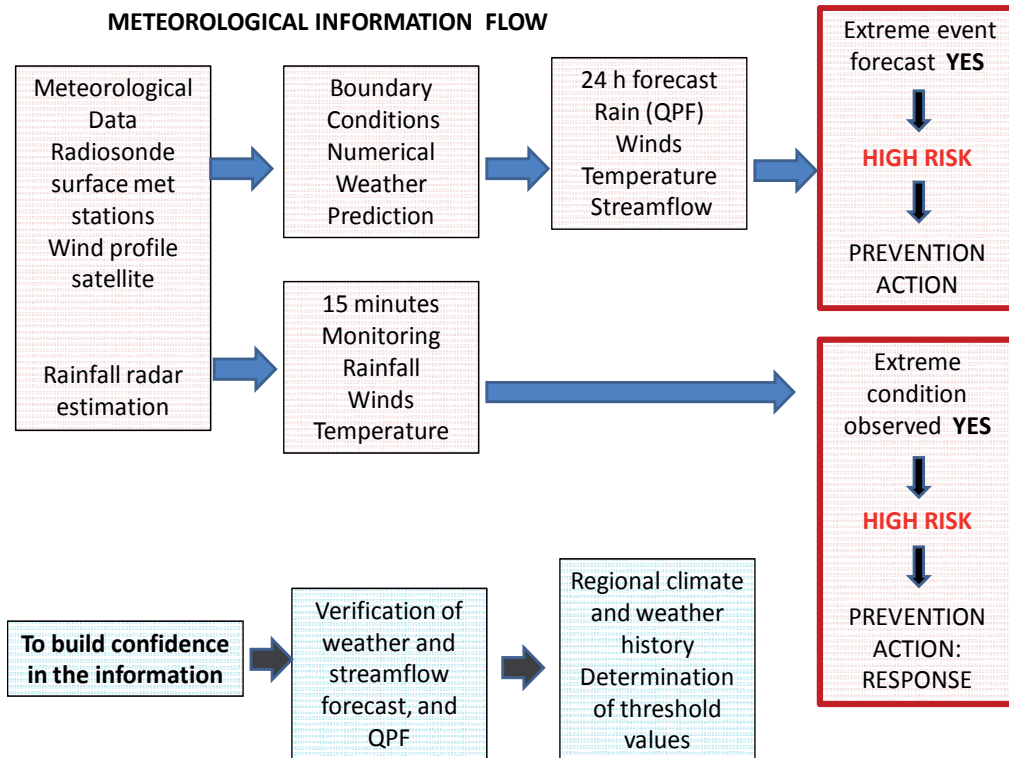


Fig. 12. Meteorological information flow of Early Warning System.

In order to achieve a complete three-dimensional coverage of México City a second radar deployment in the opposite extreme of the basin is required. Several conditions of propagation either from the present radar or from others possible positions (Fig. 13a) were attempted to get the greater coverage area (Méndez et al., 2009). The site selected was the Cerro de la Estrella located at the central eastern of Mexico Valley (Fig. 13b) had shown more adequate. The Cerro de la Estrella is at an approximate elevation of 300 m above the City of Mexico and therefore is able to scan both stratiform and convective precipitation (Fig. 14). The radar coverage was obtained from a Geographic Information System.



Fig. 13. a) Proposed sites in Mexico Basin for the new radar deployment. Black line is the political boundary of Mexico City; b) View of the Valley of Mexico basin from the Cerro de la Estrella.

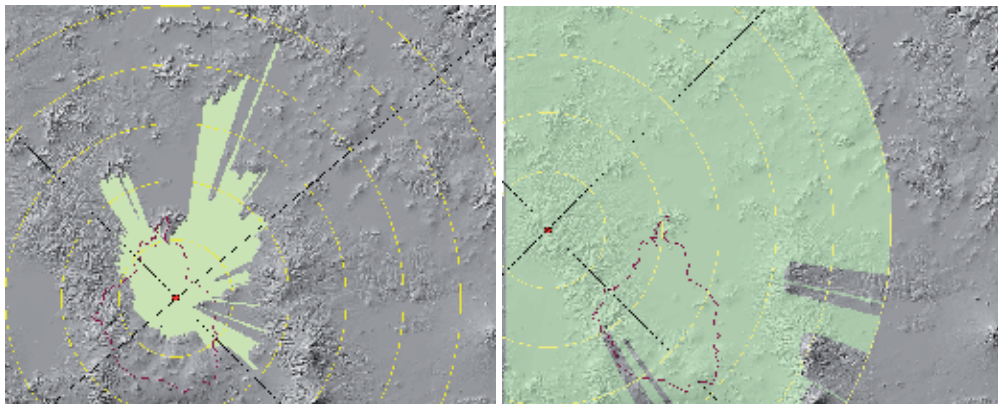


Fig. 14. Radar scan at 0 deg.: Left, The Cerro de La Estrella (2450 msl) and; right the Cerro Catedral site (3785 msl). Red line is the political boundary of Mexico City.

The Mexico Basin rain gauge network (Méndez et al. 2009) is very dense (Fig. 4) and the new Mexico Valley radar system should take advantage of this to implement quantitative precipitation estimation schemes as one of main products generated by the early warning system. To achieve this, a proper processing of radar data must be implemented in order to develop methodology to prevent beam blockage due to orography (Bech et al. 2003), ground clutter (Fornasiero et al., 2006), which can produce frequent false alarms and affect the precipitation estimative. These effects can be mitigated through the application of the decision-tree method proposed by Lee et al. (1995) for a dual-polarized system, which is able to provide additional parameters such as differential reflectivity, correlation coefficient (and their texture) that can be used to further reinforce the traditional techniques.

All products generated by the early warning system (graphic, data image, text, bulletin) will be integrated into a display system based in GIS system. This will permit produce better quality graphic resolution and generate tailor made products for specific needs to stakeholders and general public.

6. Conclusion

Hydrological applications of meteorological radars have become an important branch of remote sensing in meteorology and disaster preparedness activities. The high temporal and spatial resolution precipitation fields generated by meteorological radars meet the requirements of the hydrological modeling (Sempere-Torres et al., 2004). Furthermore the radar covers large areas and is of rapid access for real time hydrological applications and, therefore an adequate blending of radar and rain gauge data results in better estimates of real time precipitation (Collier, 1996; Joss & Waldvogel, 1990). Méndez et al. (2009) has pointed the capacity of the Doppler radars to scan storm gives a big advantage for runoff and precipitation prediction and may be fundamental to understand the physics of storm intensification in complex orography as México Valley.

The system of weather/hydrological forecasting and monitoring storms enable user and stake holders to have information of more severe events in advance and establish risk management policies for their mitigation. The scheme for dissemination of information must contemplate to present the results of diagnostic scheme and weather forecasting as clearly as possible in order that users and stake holders have relevant elements to incorporate objective vulnerability assessments to more closely meet the facing risks. To achieve this the continuous results display in a color system associated with critical values of risk, using a Geographic Information System, is a powerful tool for prevention and response prevention or emergency in accordance with the Mexico City government interests. Further improvements in the short term precipitation forecast, or quantitative precipitation forecast (QPF), can be achieved by blending Doppler radar products and output of numerical weather prediction models (Atencia et al. 2010)

The results of this study and Méndez et al. (2011) assess the value of using weather radar data as input distributed hydrological models. These models are adequate for applications in regions of strong slopes and heavy rainfall with complex draining networks for which reason it would be very useful in early warning systems.

Early warning systems, widely used in the world, aim to provide relevant information for making decisions within a framework of prevention. This type of action has proved to be much more helpful, even under weather forecasts uncertainties, than a system based only an emergency response.

7. References

- Atencia, A.; Rigo, T., Sairouni, A., Moré, J., Bech, J., Vilaclara, E., Cunillera, J., Llasat, M. C., & Garrote, L. (2010). Improving QPF by blending techniques at the Meteorological Service of Catalonia. *Nat. Hazards Earth Syst. Sci.*, 10, 1443–1455.
- Barros, A. P. (1994). Dynamic modeling of orographically induced precipitation. *Rev. Geophys.*, 32, 265–284.
- Bech, J.; Codina, B., Lorente, J., & Bebbington, D. (2003). The Sensitivity of Single Polarization Weather Radar Beam Blockage Correction to Variability in the Vertical Refractivity Gradient. *J. Atmos. Ocean. Technol.*, 20, 845–855.
- Borga, M.; Da Ros, D., Fattorelli, S., & Vizzaccaro, A. (1997). Influence of various weather radar correction procedures on mean areal rainfall estimation and rainfall-runoff simulation. *Weather radar technologies for water resources management*. Braga, B. J. and

- Massambani, O. (Eds.), IRTCUD/University of Sao Paulo, Brazil and IHP-UNESCO, 73-86.
- Clark, C. O. (1943). Storage and the Unit Hydrograph. *Transactions of the American Society of Civil Engineers*, 110, 1419-1446.
- Collier, C. G. (1996). *Applications of weather radar systems*. John Wiley and Sons, 2nd Ed., New York, 390 pp.
- Fornasiero, A.; Alberoni, P. P., & J. Bech (2006). Statistical analysis and modelling of weather radar beam propagation conditions in the Po Valley (Italy). *Nat. Hazards Earth Syst. Sci.*, 6, 303-314.
- Joss, J., & Waldvogel, A. (1990). Precipitation Measurement and Hydrology. *Radar in Meteorology*, D. Atlas, Ed.. Amer. Meteor. Soc., 577-597.
- Krajewski, W. F., & Vignal, B. (2001). Evaluation of anomalous propagation echo detection in WSR-88D data: a large sample case study. *J. Atmos. Ocean. Tech.*, 18, 807-814.
- Kull D. W. & Feldman A. D., (1998) Evolution of Clark's Unit Graphs Method to Spatially Distributed Runoff. *Journal Hydrology Engineering*, ASCE 3 (1), 9-19.
- Lee, R.; Della Bruna, G., & Joss, J., (1995). Intensity of ground clutter and echoes of anomalous propagation and its elimination. *Proc. On the 27th Conference on Radar Meteorology*, the Amer. Meteor. Soc., Vail, Colorado, 651-652.
- Magaña, V.; Pérez, J., & Méndez, M. (2003). Diagnosis and prognosis of extreme precipitation events in the México City watershed. *Geofísica Int.*, 41, 247-259.
- Maidment, D.R. (1993). GIS and Hydrologic Modeling. *Environmental Modeling with GIS*, ed. by M.F. Goodchild, B.O. Parks, and L.T. Steyaert, Oxford University Press, New York, pp. 147-167.
- Marshall, J.S., & Palmer, W.M. (1948). The distribution of raindrops with size. *Journal of Meteorology*, 5, 165-166.
- Méndez, B. (2005). *Aplicación hidrológica de los radares meteorológicos*. PhD. Thesis, Faculty of Engineering - UNAM, 186 pp. (in Spanish).
- Méndez, B.; Domínguez, R., Magaña, V., Caetano, E., & Carrizosa, E. (2006). Calibración hidrológica de radares meteorológicos. *Ing. Hidrául. Méx.*, 21, 43-64. (in Spanish).
- Méndez, B.; Magaña, V., Caetano, E., Silveira, R., & Domínguez, R. (2009): Analysis of daily precipitation based on weather radar information in México City. *Atmosfera*, 22(3), 299-313.
- Méndez, B.; Domínguez, R., Rivera-Trejo, F., Soto-Cortés, G., Magaña, V., & E. Caetano, (2011). Radars, an alternative in hydrologic modeling. *Aggregate Model. Atmosfera*, 24(2), 157-171.
- Sauvageot, H. (1994): Rainfall measurement by radar: A review. *Atmos. Res.*, 35, 27-54.
- Sempere-Torres, D.; Corral, C., Sánchez-Diezma, R., Berenguer, M., Velasco, C., Franco, M., Llorca, X., Velasco, E., & Pastor, J. (2004). Are radar rainfall estimates ready for hydrological applications? Some reflections from the experience in Catalunya. *European Conference on Radar in Meteorology and Hydrology (ERAD) – COST 717. Final Seminar. Abstracts Book*, 30 p.
- Smith, P. L., Jr. (1998): On the minimum useful elevation angle for weather surveillance radar scans. *J. Atmos. Oceanic Technol.*, 15, 841-843.
- Steiner, M.; & Smith, J. A. (2002). Use of three-dimensional reflectivity structure for automated detection and removal of nonprecipitating echoes in radar data. *J. Atmos. Ocean. Tech.*, 19, 673-686.

Measuring Snow with Weather Radar

Elena Saltikoff
*Finnish Meteorological Institute
 Finland*

1. Introduction

People of warm climate tend to think of snow as something rather rare and exotic. However, most weather radars operating at mid-latitudes measure snow every day, at some altitude. Even at relatively low elevation angles the edges of a PPI image are often measured above the freezing level. Fig. 1 shows radar measurements from a night when surface minimum temperature was +13 °C – still, the majority of radar measurement volume was filled with snow.

In many meteorological classifications hydrometeors are divided in two or three classes (rain, wet snow and dry snow, see Fig. 1.). On the other hand, we have been told that there are not two identical snowflakes. Between these extremes are the snowflake type classifications such as those by Ukichiro Nakaya (Nakaya, 1954). From his work we can learn how, based on temperature and humidity, snow crystals can take the shape of needles, columns, plates, stars, rosettes and dendrites, only to name a few. They can also join each other in a process called aggregation, and they can be covered in icing in a process called riming.

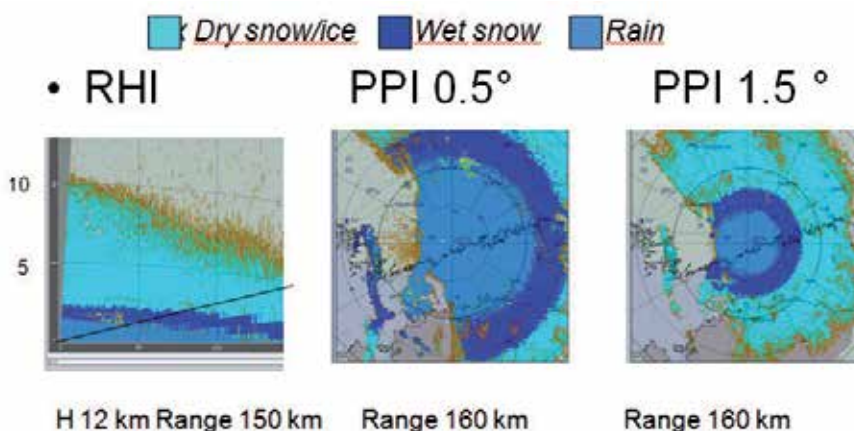


Fig. 1. Hydrometeor classification 30 August 2009 00:45 UTC in Vantaa, Finland. RHI to 150 km in range, 12 km in height (left). PPI to 160 km in range, 0.5 degrees in elevation (middle) and 1.5 degrees in elevation (right). Cyan for dry snow, dark blue for melting snow, light blue for rain.

Measuring snowfall with short wavelengths can bring us to the edge of assumption of the radar equation for Rayleigh scattering: are the particles much smaller than the radar wavelength ?

In this chapter, snow will be discussed from viewpoint of a radar meteorologist. Many topics are relevant for operational weather service, others more for the researcher. Increasing use of polarimetric radars is bringing new perspectives to measuring snow with radars.

2. Vertical structure of snowfall

With the usual measuring geometry of a scanning weather radar we have to take into account the vertical structure of precipitation. In warm weather, we measure rain near ground, wet snow above it and dry snow on the top, as can be seen in Fig. 1. A typical reflectivity structure is related to the temperature structure so that we have a maximum just below 0 °C isotherm. Above it, in the snowfall area, reflectivity decreases with an even gradient of approximately 7.5 dBZ/km. This decrease is related to four factors:

- at higher altitudes, it is colder and snow crystals are typically smaller in diameter
- at higher altitudes, the absolute humidity is smaller so the mass of snow per cubic kilometer of cloud is smaller there
- crystals fall down while they grow, so older crystals which have had time to grow large are more likely to be located at lower altitudes
- near the cloud top there may be effects of partial beam overshooting

In the precipitation system of a warm front, the two first factors create also horizontal gradients: the leading edge is in colder and drier air.

When the snowflakes melt, the surface gets wet first while the inner parts are still of dry snow. The partially-melted, wet snowflakes have approximately the size and fallspeed of snowflakes, but the dielectric properties of water surfaces. Hence the radar reflectivity peaks in the melting layer, a phenomenon also known as the bright band. In the hands of an inexperienced user of radar data, this could lead to an overestimation of precipitation intensity. In a modern weather radar service, the overestimation is corrected using knowledge of the vertical profile of reflectivity (Koistinen et al., 2003). Recently, Giangrande et al. (2005) and Boodoo et al. (2010) have shown, that the parameters of dual-polarization radars can be used effectively to follow the temporal and spatial variation of the melting layer height and thickness. This is especially important in cold and temperate climates, where much of precipitation is associated with fronts, because in frontal situations the temperature gradients are sharp.

In Fig. 2 we see RHI and PPI images in a snowstorm in Finland 2 February 2010. Cloud tops are observed between 6 and 8 km, and reflectivity is growing downwards from there. No bright band is observed, as there is no melting. Temperatures in cloud tops are near -35..-40 °C, at ground -5..-7 °C (based on Tallinn and Jokioinen 00 UTC soundings). The effect of vertical gradient is obvious in the RHI image, but the gradient in PPI is related to two factors: the vertical gradient and the horizontal variation of intensity.

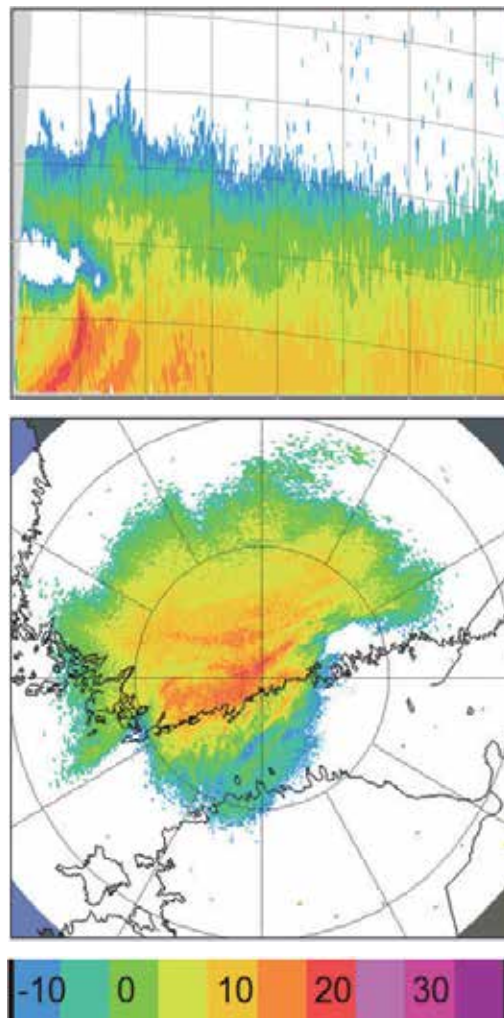


Fig. 2. Radar measurements in a snowstorm in Finland 2 Feb 2010. RHI north of radar to range of 150 km, horizontal lines at every 2 km (upper panel) and PPI with elevation of 1.5 degrees, rings at each 100 km (lower panel). Reflectivity values are between -15 and +25 dBZ.

3. Fallspeeds of solid hydrometeors

Terminal fallspeeds of hydrometeors are influenced by their type and size, and hence Doppler spectra measured with vertically pointing radar can be used for hydrometeor classification. Barthazy and Schefold (2006) showed that the fall velocity of snowflakes consisting of needles or plates is strongly dependent on the riming degree. The average fall velocity of any type of snowflakes of diameter of 1 mm or larger is typically between 1 and 2 m s^{-1} . In cases when hydrometeor types change, or two types of hydrometeors coexist in same measurement volume, Doppler spectra can provide valuable information of cloud physical processes such as riming and aggregation. In addition of academical interest they may provide value in aviation weather services.

4. Clutter cancellation and clear air echoes

One of the main reasons why operational weather services started to use Doppler radars was the use of Doppler signal for clutter cancellation of reflectivity fields. The principle is simple: precipitation has velocity (at least fallspeed and turbulence), while ground clutter does not, and Doppler radar can measure the velocity (or absence thereof). However, when the precipitation is in form of snow, there are some complicating details, and we have to study the filtering process in depth.

A Doppler radar does not measure the true speed of the particles, just the component parallel to the radar beam. When the real wind is nearly perpendicular to the beam (e.g. for northerly winds in east and west of radar), this component is near zero. We can not set the threshold to censor only the bins with exactly zero speed, because even clutter targets have apparent speeds due to different viewing angle of the rotating antenna, trees and masts waving in wind and trucks and lorries in an urban environment. On the other hand, if the threshold of censorship is too high, Doppler filter removes data with near-zero Doppler velocities in areas where wind is perpendicular to beam. Because there is wind shear and measurement is made at different heights at different distances, the direction of missing data is undulating, and hence the gap in reflectivity PPIs is sometimes called *Doppler snake*.

In Fig. 3, it is relatively easy to see the underestimation of reflectivity on a line coiling from west-southwest through the radar and to the opposite side. In this case, there is also a “secondary snake” south of the radar, where the near-zero-velocities are related to folding.

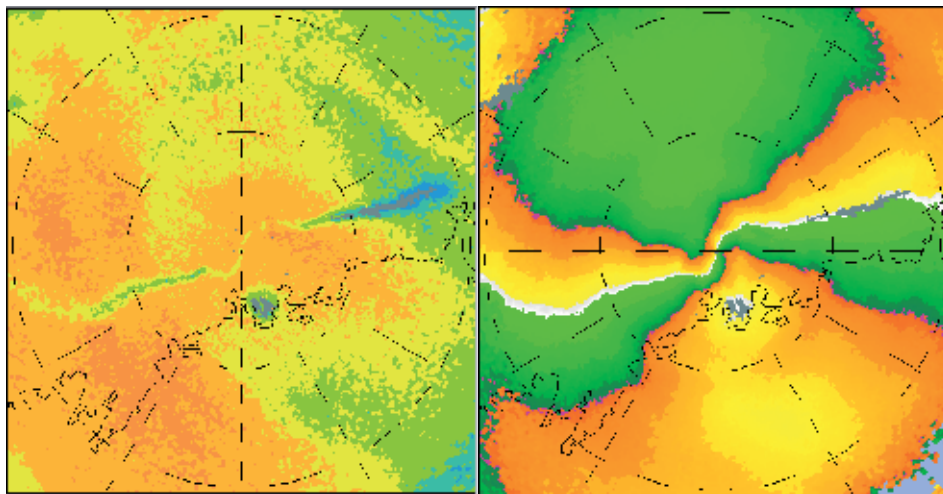


Fig. 3. A Doppler snake case 17 March 2005 03:00 UTC. PPIs of reflectivity (left) and Doppler velocity (right). Wind is from south-southeast, warm colours indicate echoes moving away from the radar and cold colours towards the radar. The velocity field is folded, unambiguous speed 7.6 m/s. A band of weaker reflectivities cutting through the image from southwest to east, at same location as zero Doppler speeds (white). Reflectivity colour scale as in Fig. 2.

It is tempting to try to get rid of the Doppler snake by using a less aggressive Doppler filter. However, amount of residual clutter may increase. Finding the compromise between too aggressive and too weak filter is threading on a fine line, and the selection should be tested in different wind and temperature conditions. Temperature inversions (typical for cloudfree winter days or nights) affect amount of clutter by causing anomalous propagation, which then leads to the increase of ground or sea clutter. Wind affects sea clutter but may also cause blowing snow. Especially the blowing snow falling from trees in hilly areas may give false alarms of ground clutter – it is real snow flying in real wind and hence immune to most clutter cancellation techniques, even though it is not precipitation falling from clouds.

Case of sea clutter is especially annoying. In summer we have nocturnal inversions and anomalous propagation mainly when it is not raining. In winter it is very likely to have on continent cold weather and inversion, and simultaneously rigorous lake effect snow (see section 6.2) over the water areas. This is possible, because the propagation is affected by temperature near the radar, not at the measurement location. Sea clutter is immune to Doppler filtering, but dual polarization measurements can reveal it, as is seen in Fig. 4.

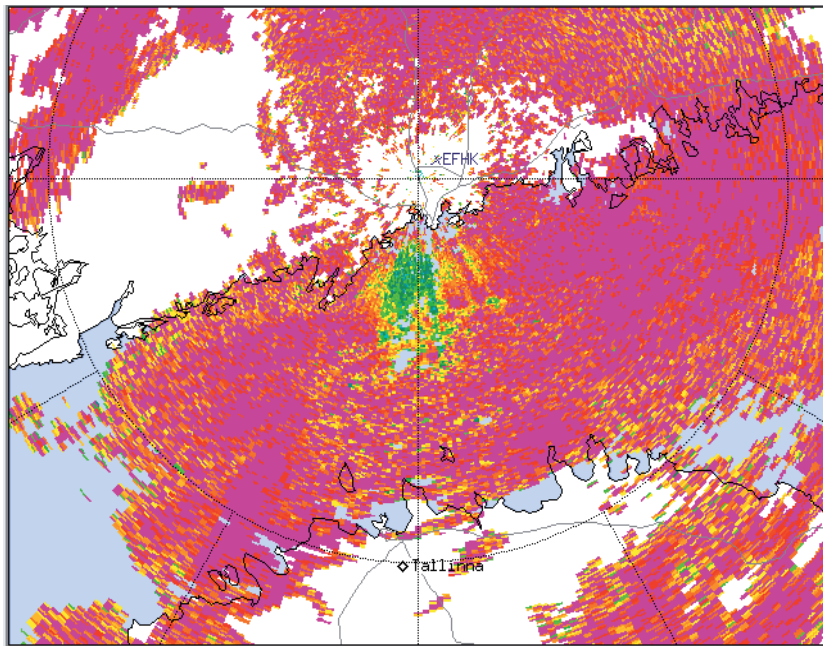


Fig. 4. Sea clutter and lake effect snow seen with polarimetric parameter RhoHV. RhoHV over 0.98 in snow, less than 0.8 in sea clutter. The range ring indicates 100 km from the radar.

5. Dual polarization

While one of the most popular applications of dual-polarisation technology enables one to distinguish the types of the hydrometeors measured (Straka et al., 2000), dual polarization can be used for much more. On the other hand, some applications developed for rain, such as KDP-based algorithms for quantitative precipitation estimates do not work in snow.

When implementing published algorithms to new environments, it is wise to compare the hardware used in the original development work to the platform where it will be implemented. Research community has used S-band radars a lot, while the operational weather services in cold climates use mainly C-band. There may be also difference between simultaneous and alternating transmission of the dual polarization channels.

5.1 Hydrometeor classification

Polarimetric properties of wet snow and single snow crystals are very different from the ones in rain. Hence, these two snow categories are easily distinguishable from rain. However, discrimination between stratiform rain and dry snowflakes (aggregates) is challenging, as relatively low Z and ZDR , and high $RhoHV$ are typical for both (Ryzhkov & Zrnica, 1998). A typical solution in this case is to use the information of height of melting layer, either from sounding, NWP model or radar measurements.

Decision boundaries for dense snow, dry snow, wet snow, rain, dry graupel, wet graupel rain and hail co-existing and hail alone using Z , ZDR , $RhoHV$, LDR and KDP have been published by e.g. Straka and Zrnica (1993). In many of the parameters, the selected classes overlap, which has encouraged researchers to try fuzzy logic (Bringi & Chandrasekar, 2001). In Fig. 5 we see RHI scans in the same situation as in Fig. 1. The 0 °C isotherm is at 2 km, and a layer of melting snow can be seen below it.

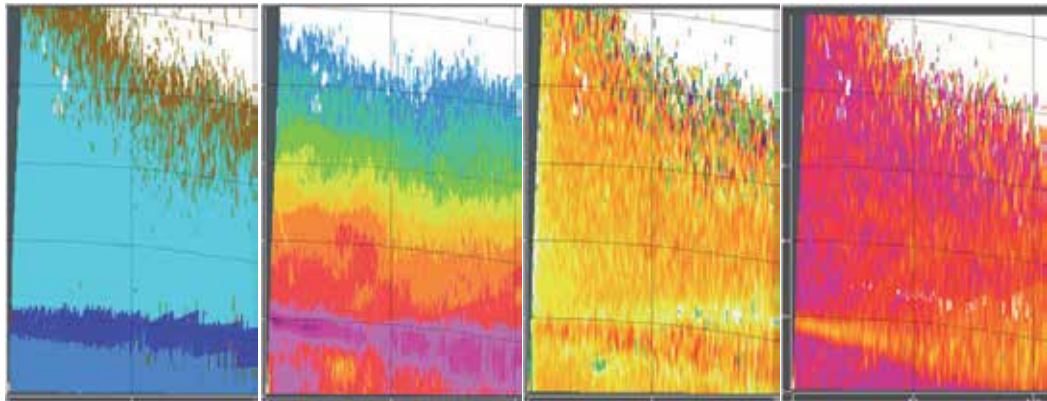


Fig. 5. RHI scans north of Vantaa radar 30 August 2009 00:45 UTC. . Range 100 km, height 10 km, parameters from left to right: Hydrometeor classification, reflectivity Z , differential reflectivity ZDR and copolar correlation factor $RhoHV$.

5.2 Snow types

In the JPOLE classifier for cold season Ryzhkov et al. (2005) distinguished between Dry aggregated snow: DS and Wet snow: WS, and single crystals. In some cases, this distinction can be made using reflectivity and differential reflectivity alone: wet snow has typically larger reflectivities, and individual crystals larger differential reflectivities. However, the variability of both parameters for both classes is large, and the definitions tend to overlap.

Developing a universal method for snow type classification is even more challenging than finding a representative ZR relation: reliable surface observations of snowflake type are rare, and if they are performed at longer distances from the radar, the snowflakes can change between the radar measurement and the surface observation. Correction for vertical profile of reflectivity is a standard procedure, but correction for vertical profile of snow type is still strongly hypothetical.

6. Characteristic properties of typical snowfall situations

In general, precipitation events can be split to orographic, frontal and convective precipitation. Especially snowfall is often related to warm fronts and lake effect induced convection.

6.1 Warm fronts

Much of snowfall is related to frontal systems of extratropical systems. In their analysis and forecasting, the value of weather radar data lies primarily in the mesoscale structure: detection of the mesoscale bands of heavy snowfall is needed for accurate short term forecasting. The banded structure leads to rapid changes in visibility, and areal differences of accumulated snowfall. Their dynamical structure is complicated, related to negative equivalent potential vorticity (EPV) mainly associated with conditional symmetric instability (CSI), and not always perfectly forecasted by numerical weather prediction models. Hence, identification and extrapolation of movement of these bands using a radar can improve short-range forecasts of extreme events significantly (Nicosia and Grumm, 1999).

Snowfall from warm fronts is also a challenge for a radar meteorologist: forgetting the three-dimensional structure of the frontal system can lead to embarrassing misinterpretation.

In satellite images, we can see the leading edge of frontal system (“warm front shield”) and educated meteorologists already know, that arrival of this edge does not mean onset of precipitation. In Fig. 6 the shield at 2 km extends 70 km ahead the surface precipitation. I sincerely hope that everyone using different radar products remembers this, too: the leading edge in products like TOPS, MAX, VIL or even medium-level CAPPI does not indicate the precipitation on ground level. See Fig. 7.

The sloping edge of precipitation area can also be seen in PPIs. In upper panels of Fig. 8, the gap in the centre of the image indicates area where radar beam was below the warm front shield. The gap gets smaller when the surface front approaches the radar. Also, the gap is not a circle but an oval, also indicating the slope of the cloud base.

Warm fronts are ideal for producing Doppler wind profiles (VAD and VVP), because the wind field is usually uniform. In lower right panel of Fig. 8 we have a time series of VVP wind and reflectivity. In this case, the wind shear related to the warm advection is not very strong, and it is hard to distinguish it from wind shear related to friction in the boundary layer. Sharper turning of wind is of interest to aviation weather service. We can also see the shield of overhanging precipitation with approaching front (05-06 UTC) from “+”-signs indicating missing wind barbs. Warm advection can also be seen indirectly: part of the increase of reflectivity at low altitudes around 08 UTC is probably related to temperatures rising to near zero, and snowflakes growing larger.

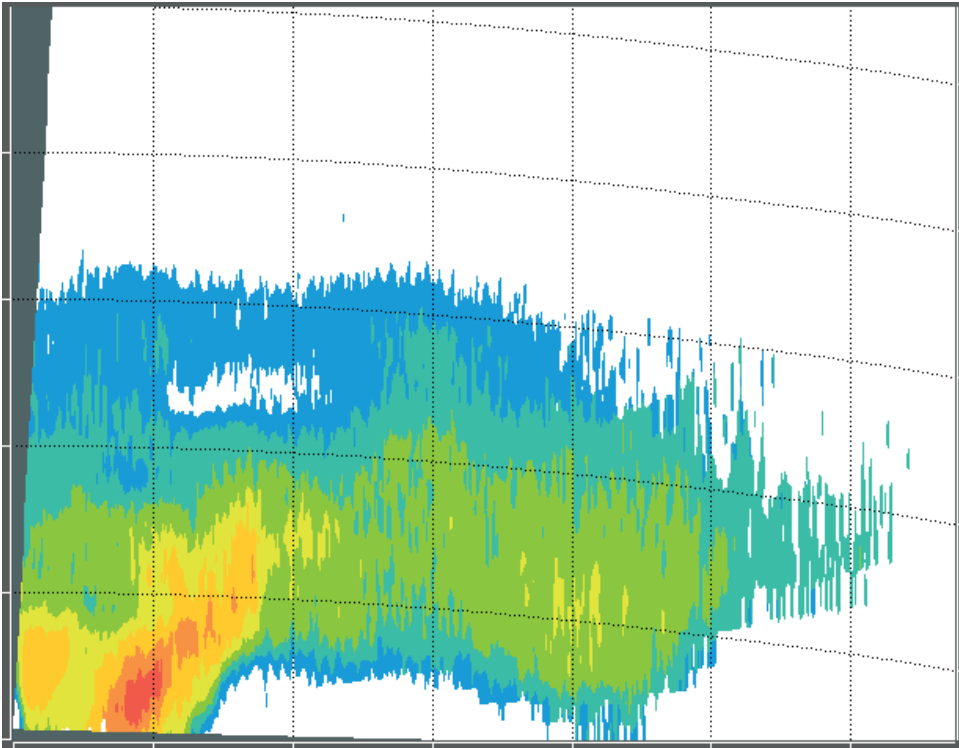


Fig. 6. RHI north of Anjalankoski radar 17 December 2011 12 UTC, warm front approaching from south. Vertical lines at 20 km, horizontal lines at 2 km intervals. Colour scale from -10 dBZ (blue) to 20 dBZ (red) as in Fig. 2.

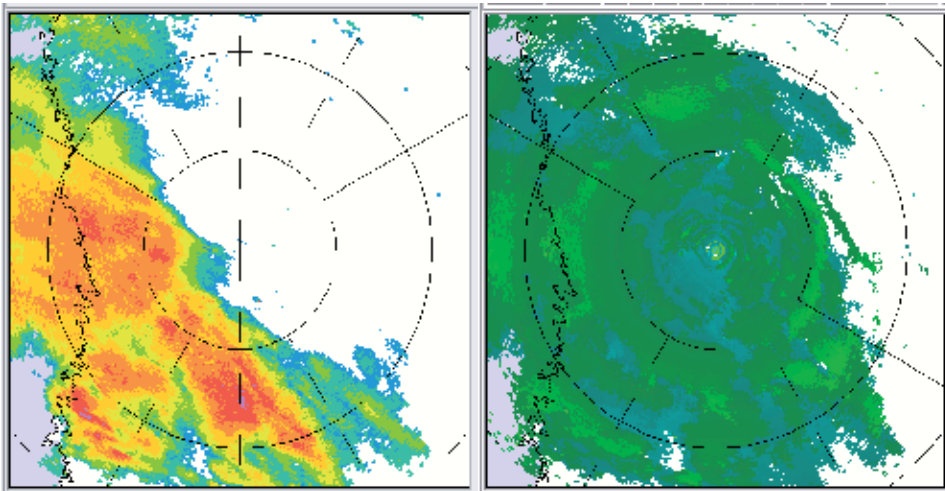


Fig. 7. CAPPI at 500 m height on left, TOPS with threshold -10 dBZ on right. 14 January 2008 05:30 UTC, precipitation on the surface had not yet reached the radar location. Range rings at 50 and 100 km from radar, reflectivity scale as in Fig. 2., green shades for tops in steps of 2 km.

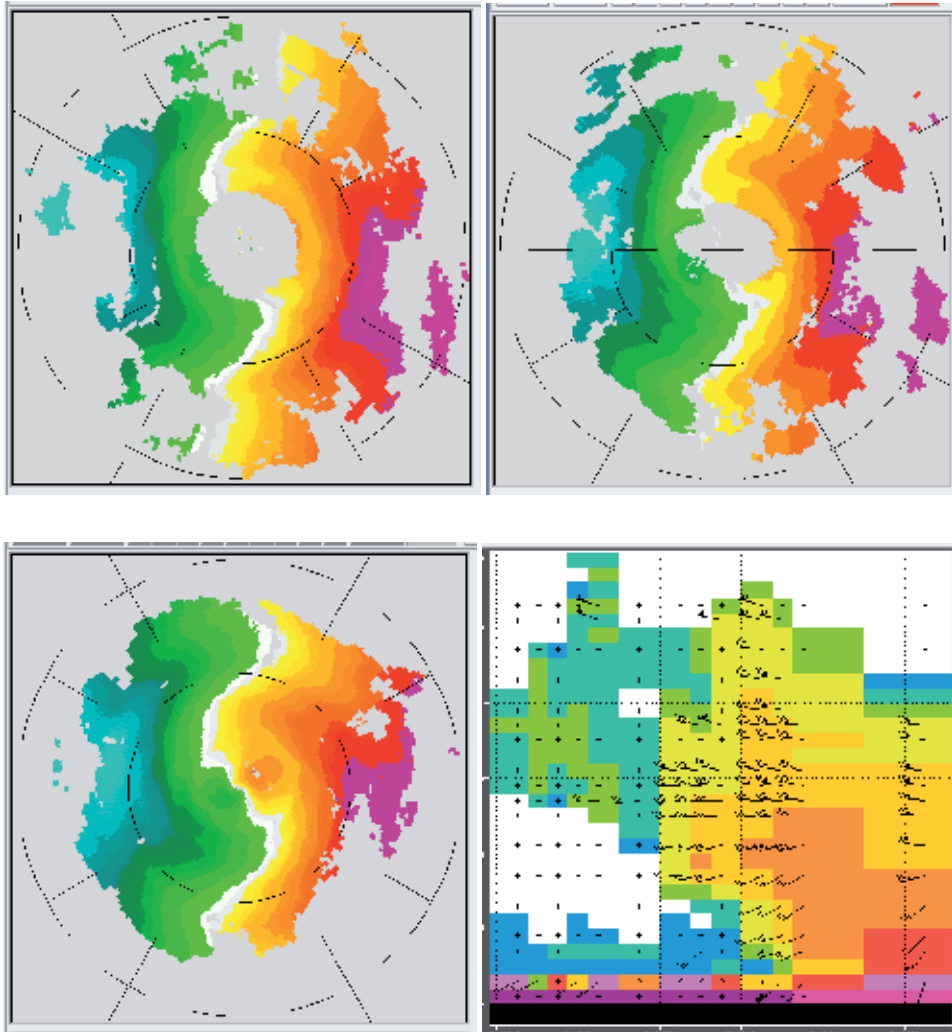


Fig. 8. PPI images of Doppler velocity 30 minutes apart (5:00, 5:30 and 6:00) and time series of wind and reflectivity profiles 02:00 to 07:00 UTC 14 January 2008. Green colours towards radar, reds and yellows away. Reflectivity from -20 dBZ (blue) to +20 dBZ (purple)

In Fig. 9 we see another scale of shear. There is a small wind maximum below 1 km. In this case it lasted for less than 45 minutes. This is an indicator of low level jet related to conveyor belt in the frontal structure. In the real atmosphere, the wind shear related to that is probably larger, as the VVP is averaged over a cylinder of 30 km.

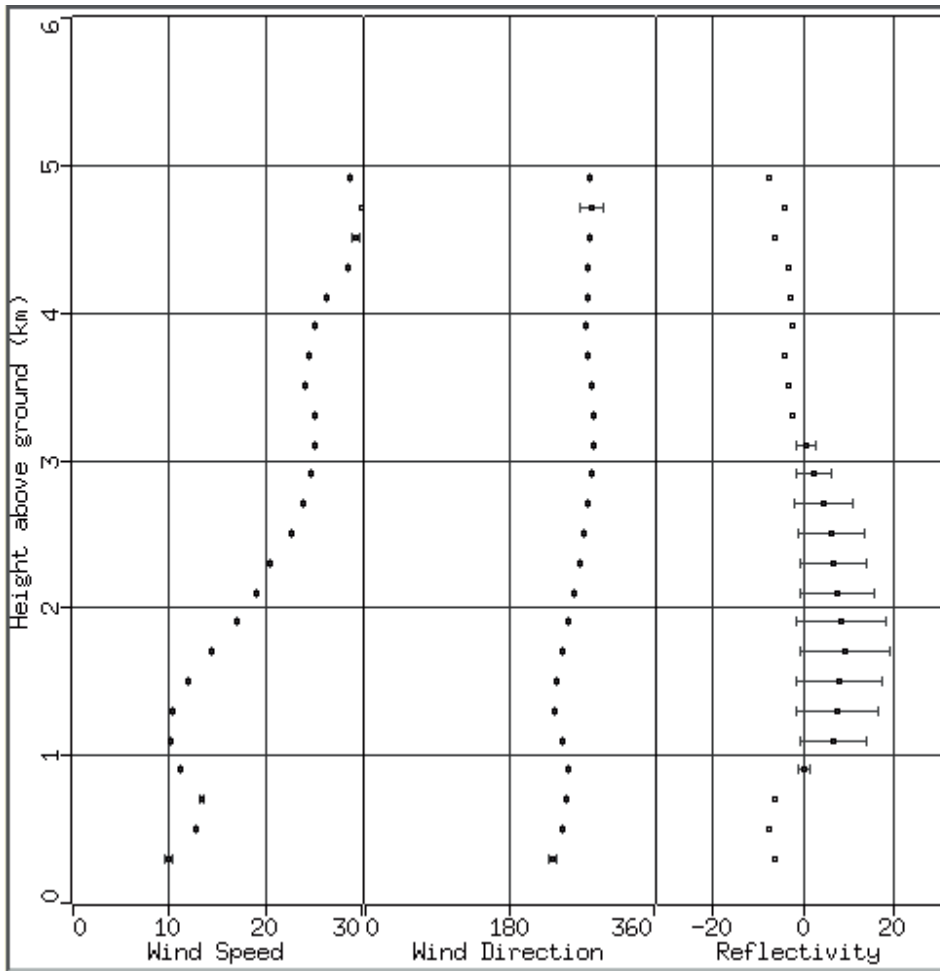


Fig. 9. VVP sounding. Windspeed on left, wind direction in middle and reflectivity on right.

6.2 Lake effect snow

Lake effect snow is a phenomenon observed regularly around open water surfaces in cold weather. The name originated from weather phenomena around the Great Lakes of North America, but it is also observed around bays and straits of sea and great rivers. Lake-effect snowstorms get their energy from the temperature difference between the relatively warm open water and very cold, continental air blowing over the water. These provide the most spectacular outbreaks of boundary layer convection in winter (Markowski & Richardson, 2010).

Markowski and Richardson (2010) mention that the convective clouds associated with lake-effect precipitation can be several kilometres deep. However, even shallower lake-effect clouds can produce significant amounts of snowfall (see Fig. 10), and these shallow yet intense clouds present challenges to the design of a radar network in coastal areas in a cold climate.

The organization of convection in a lake-effect snowstorm depends on the ratio of the wind speed to the maximum fetch distance. When the wind is strong, offshore convection is rapidly organized into horizontal convective rolls. When the wind is weaker, it is more likely that bands parallel to the shoreline (and perpendicular to the mean wind) are formed in the land-breeze convergence zone. With very weak winds, convection can be organized into vortices that stay over the sea and have the structure of a miniature hurricane (Laird et al., 2003). These vortices provide another example of mesoscale weather systems which can only be observed with remote sensing instruments.

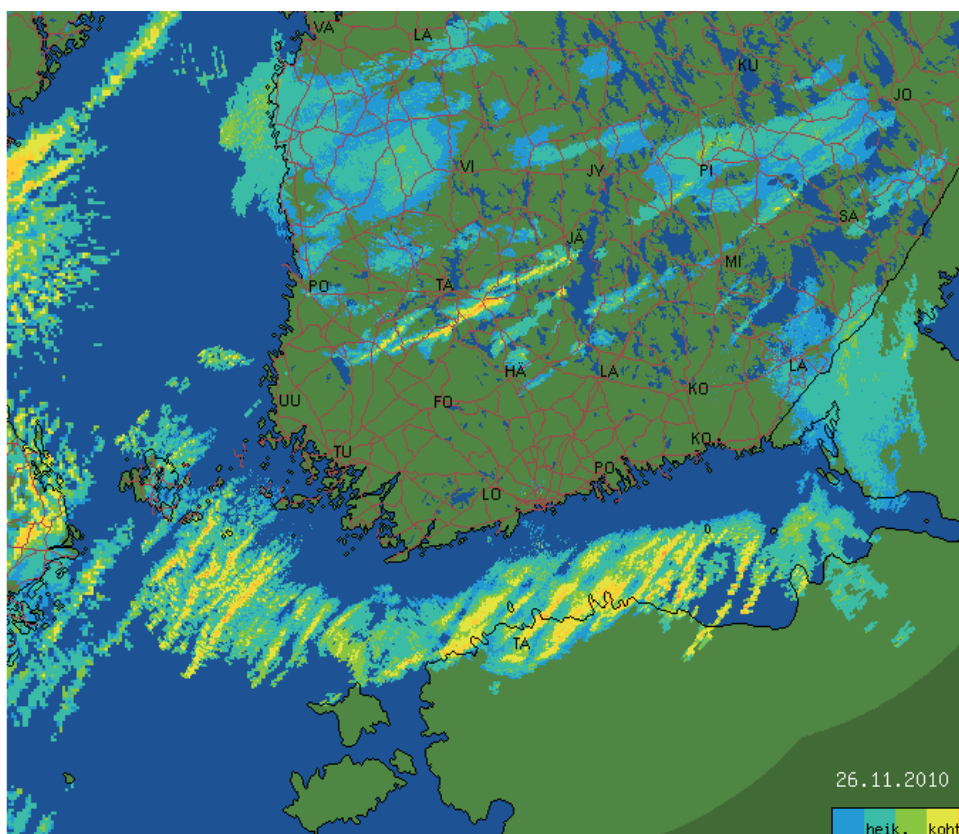


Fig. 10. Lake effect snow 26.11. 2010 10 UTC. Pseudo-CAPPI reflectivity composite of 5 Finnish and 2 Swedish radars at nominal height of 500 m.

For radar-based nowcasting applications, lake effect snow is a challenge firstly, because the snow storms do not move, thus motion vectors can be misleading, and secondly because their shallow and intense nature can cause beam overshooting problems..

7. Operational applications

Snowflakes are beautiful and interesting, but most people who buy radars want also to do something useful with the data. The most frequently asked questions are when, where and how much. These have been solved with more and less advanced accuracies over the years. Advanced questions to be still researched are related to properties of snow, most of all its density.

7.1 Accumulated snowfall, Z/S

When we talk of precipitation, we often think about rainfall, and ignore snow. There are two main approaches to accumulated snow: 1) snow water equivalent (SWE): how large is the mass of snow per unit area and 2) the (increase of) thickness of snow layer (TSL). SWE is important for hydrological applications, and it is also usually the parameters measured at surface station rain gauges (in manual gauges, the snow is melted and volume of resulting water is measured). SWE has also applications in estimates of snowload of buildings and tree crowns. Thickness of snow layer has applications in road maintenance, biology and recreational activities, and it is a tricky thing to estimate for everyone, not just radar meteorologists. A bulk equation $TSL=10*SWE$ (both TSL and SWE expressed in mm), is often used, even though we all know that the density of snow on ground varies a lot. Matters are further complicated if we try to accumulate TSL over a longer period, because snow on ground is changing shape, density and even location (by blowing snow).

The radar equation (see Zrníc, this volume, for details) includes the parameter $|K|$, dielectricity of scattering particles, which has different values for ice and water. In operational signal processing, this is assumed to be always the water-value, so we should call the measured parameter Z_e (where the “e” stands for “equivalent”). The error caused by assuming the same dielectricity is compensated in using a different ZS relation for snow, and including the effect of dielectricity there.

The density of snow crystals and aggregates varies as a function of structure from 50 to 900 kg m³, with higher values expected for solid ice structures and wetted particles. The size distributions of ice crystals and snow aggregates can be represented by exponential and gamma functions, and the total number of concentrations is on the order of 1-10⁴ m⁻³ for aggregates, 10-10⁹ m³ for individual crystals at colder temperatures ($T < -20$ °C), and often as high as 10⁴ m⁻³ at warmer temperatures (Pruppacher & Klett, 1996). The diameter of large crystals can be up to 1-5 mm, while the diameter of aggregates can grow to 20-50 mm, occasionally even more. The shapes of aggregates vary from approximately spherical to extremely oblate, and the approximate shapes of crystals can vary from extreme prolates and oblates to essentially spheres (Pruppacher & Klett, 1996). Most individual crystals tend to fall with their largest dimension horizontally oriented unless there are pronounced electric fields. Aggregates also can fall in a horizontally oriented manner or may tumble (Straka, 2005).

Radar estimates of ice water content of crystals and aggregates are greatly complicated by the multitude of crystal sizes and shapes, various crystal and aggregate densities, and dielectric constants, among others. Of all the snow types, the determination of the amount of wet aggregates is probably the most difficult (Straka, 2005).

For liquid precipitation, the classical ZR relation was published by Marshall and Palmer 1948. For snow, similar classical paper is probably that of Sekhon and Srivastava (1970). However, when dropsize distributions are known to vary a lot, snow particle distributions vary even more. Applying correction for vertical profile of reflectivity before the ZR relation is crucial, but does not eliminate all uncertainties.

7.2 Nowcasting snow

The simplest application of radar images for nowcasting is to display a time series as an animation, and visually follow its speed and direction of movement. Second level of complication is to estimate the future movement with some vector field, which can be derived from observed movement, NWP, or even Doppler velocity field (note this is not recommended but some people do it). Compared to summertime convective precipitation, snow has some advantages and some disadvantages in this respect. Because snow is seldom related to convection, it has less diurnal variation, and hence frontal snowstorms can sometimes be tracked and extrapolated for several hours with fairly good accuracy. On the other hand, snowstorms tend to be shallow, and hence the geometrical factors can cause error in speed estimates, and even causes of total miss (snowstorms hiding under the lowest radar measurement).

Because snowflakes fall slowly, they can advect remarkable distances after the radar measurement. If we measure at height of 800 m, and the snowflakes fall 1 m/s, they reach the ground 800 seconds later, and if wind blows 10 m/s, the location can be 8 km downwind from the radar measurement. From height of 1800 m, the flakes fall for half an hour, and from height of 4 km more than an hour, and for a distance in order of 40 to 60 km. This affects all studies comparing radar measurements to “ground truth”, and it can be annoying for nowcasting, too. On the other hand, for an optimist it is a source of information: basically, we have already measured the snowflakes which will fall e.g. to the runway half an hour later. Lauri et al. (2012) have discussed the effect of advection in snowfall measurement.

7.3 Visibility in snow

Aviation meteorology uses abbreviation LVP (low visibility procedure) and we often read this as “fog and stratus”). However, even snowfall reduces visibility in significant amounts. Unlike in fog, the visibility in snowfall often fluctuates rapidly and significantly, and hence use of radar data to aid nowcasting would be beneficial.

Visibility is related to scattering of visible light, radar reflectivity is related to scattering of microwaves. In case of particles in typical sizes of snowflakes and snow crystals, these two behave differently: if the amount of snow in air stays same, but crystals join to larger aggregates, radar reflectivity grows (following the ND^6 equation) while the optical visibility

improves (scattering gets smaller). Hence, any reflectivity-to-visibility –equations depend heavily on particle size distribution.

Rasmussen and Cole (2002) have given to visibility the equation $Vis = k / ND^2$, where k is a constant related to snow type. Having the two equations available, it would be tempting to “just solve the k ” and get a reflectivity – visibility equation. However, the “constant” k can get plethora of values depending on the crystal type, the degree of riming, the degree of aggregation, and the degree of wetness of the crystals. Rasmussen et al (1999) derived ratios of visibility and liquid equivalent snowfall rate for 27 crystal types and two aggregate types. In their study, typical variations in visibility for a given liquid equivalent snowfall rate ranged from a factor of 3 to a factor of 10, depending on the storm.

After this, the next attempt would be try to “calibrate” the factor k for each storm. However, Rasmussen et al. (1999) also noted that k has a wide degree of scatter also during a given storm. As we know from other studies, the type of snow crystals depends on temperature and humidity it has experienced during its growth time. Snowstorms are often related to weather situations (such as warm fronts) with strong gradients of temperature and humidity. Hence, changes of crystal type during a storm are natural.

Another factor making comparison of reflectivity and visibility is the illumination. In same snowfall intensity, visibility in night (how far can you see a light source) can be twice as good as in daylight.

8. Conclusion

The four main properties a radar meteorologist should remember about snow are:

- It falls from shallow clouds, so you can't see it from far.
- It falls slowly, so it may advect after we measure it.
- It has different scattering properties from rain, so your precipitation estimates may be inaccurate if ZR relations are applied for snowfall
- Snowflakes come in many sizes and shapes, and their scattering properties may vary, so more information may be acquired using dual polarization.

9. Acknowledgment

The author wishes to thank Aulikki Lehkonen for finding the illustrative weather situations for examples, and Tuomo Lauri and Pekka Rossi for their constructive comments to the manuscript.

10. References

Barthazy E. & Schefold, R. (2006). Fall velocity of snowflakes of different riming degree and crystal types. *Atm. Res.*, 391-398

- Boodoo, S., Hudak, D., Donaldson, N. & Leduc, M. (2010). Application of dual polarization radar melting-layer detection algorithm. *J. Appl. Meteor. Clim.*, 49, 1779–1793.
- Bringi V. N. & Chandrasekar, V. (2001). *Polarimetric Doppler weather radar: principles and applications*, Cambridge University Press. ISBN 978-0521623841
- Giangrande, S., Ryzhkov, A.V. & Krause J. (2005). Automatic detection of the melting layer with a polarimetric prototype of the WSR-88D radar. 32nd Conference on Radar Meteorology, Amer. Meteor. Soc., Albuquerque, NM, available online via <http://ams.confex.com/ams/32Rad11Meso/techprogram/paper/95894.htm>.
- Koistinen, J., Michelson, D.B., Hohti, H. & Peura, M. (2003). Operational measurement of precipitation in cold climates. *Weather Radar: Principles and Advanced Applications*, pp. 78–110. P. Meischner, Ed., Springer, ISBN 978-3540003281 Berlin Heidelberg.
- Laird, N. F., Walsh, J. E. & D. R. Kristovich, D.R. (2003). Model simulations examining the relationship of lake-effect morphology to lake shape, wind direction, and wind speed. *Mon. Wea. Rev.*, 131, 2102–2111.
- Lauri, T., Koistinen, J. & Moisseev, D. (2012). Advection based Adjustment of Radar Measurements *Mon. Wea. Rev.*, 140, 1014–1022.
- Markowski, P. & Richardson, Y. (2010). *Mesoscale Meteorology in Midlatitudes*. John Wiley and Sons, ISBN 978-1119966678, Chichester, UK.
- Nakaya U. (1954). *Snow Crystals: Natural and Artificial*. Harvard University Press. ISBN 978-0674811515. Cambridge, UK.
- Nicosia, D. J. & Grumm R. H. (1999). Mesoscale Band Formation in Three Major Northeastern United States Snowstorms. *Wea. Forecasting*, 14, 346–368.
- Pruppacher, H. R. & Klett J.D. (1996). *Microphysics of Clouds and Precipitation*. Second ed., Springer, ISBN 978-0792342113. Heidelberg London New York.
- Rasmussen, R. & Cole, J.A (2002). How Snow Can Fool Pilots. National Center for Atmospheric Research, Boulder, CO, USA. Available online at <http://www.rap.ucar.edu/projects/wsddm/SNOFOOL.pdf>
- Rasmussen, R. M., Vivekanandan, J., Cole, J. Myers, B. & Masters, C (1999): The Estimation of Snowfall Rate Using Visibility. *J. Appl. Meteor.*, 38, 1542–1563.
- Ryzhkov, A.V. & Zrnica, D.S. (1998). Discrimination between rain and snow with a polarimetric radar, *J. Appl. Meteor.*, 37, 1228–1240.
- Ryzhkov, A. V., Schuur T.J., Burgess, D.W., Heinselman, P.L., Giangrande, S.E. & Zrnica, D.S. (2005). The Joint Polarization Experiment: Polarimetric Rainfall Measurements and Hydrometeor Classification. *Bull. Amer. Meteor. Soc.*, 86, 809–824.
- Sekhon, R. S., & Srivastava, R. C. (1970). Snow size spectra and radar reflectivity. *J. Atmos. Sci.*, 27, 299–307.
- Straka, J., Zrnica, D.S. & Ryzhkov, A. (2000). Bulk hydrometeor classification and quantification using polarimetric radar data: Synthesis of relations. *J. Appl. Meteor.*, 29, 1341–1372.

Straka J., & Zrnic, D.S. (1993). An algorithm to deduce hydrometeor types and contents from multiparameter radar data. *Preprints, 26th Conf. on Radar Meteorology, Norman, OK, Amer. Meteor. Soc.*, 513–516.

A Network of Portable, Low-Cost, X-Band Radars

Marco Gabella^{1,2}, Riccardo Notarpietro², Silvano Bertoldo³, Andrea Prato²,
Claudio Lucianaz³, Oscar Rorato³, Marco Allegretti³ and Giovanni Perona³

¹*Meteoswiss*

²*Politecnico di Torino – Electronics Department,*

³*Consorzio Interuniversitario per la Fisica delle Atmosfere (CINFAI) – Sede di Torino*

¹*Switzerland*

^{2,3}*Italy*

1. Introduction

1.1 Excellent qualitative overview of the weather in space and time

Radar is a unique tool to get an overview on the weather situation, given its high spatio-temporal resolution. Over 60 years, researchers have been investigating ways for obtaining the best use of radar. As a result we often find assurances on how much radar is a useful tool, and it is! After this initial statement, however, regularly comes a long list on how to increase the accuracy of radar or in what direction to move for improving it. Perhaps we should rather ask: is the resulting data good enough for our application? The answers are often more complicated than desired. At first, some people expect miracles. Then, when their wishes are disappointed, they discard radar as a tool: both attitudes are wrong; radar is a unique tool to obtain an excellent overview on what is happening: when and where it is happening. At short ranges, we may even get good quantitative data. But at longer ranges it may be impossible to obtain the desired precision, e.g. the precision needed to alert people living in small catchments in mountainous terrain. We would have to set the critical limit for an alert so low that this limit would lead to an unacceptable rate of false alarms.

1.2 Range dependence of the results (range degradation)

Perhaps accurate quantitative precipitation estimation (QPE) can only be achieved at short ranges from the radar. This is not because we miss careful investigations, but simply, because radar can only see the hydrometeors aloft, while we would need to know what is arriving at ground level. Obstacles as well as earth curvature lead to a limited horizon, allowing us to see precipitation at variable height, often too far from the ground. All these difficulties increase rapidly with range from the radar location. The situation becomes obviously much more difficult in mountainous terrain, where weather echoes can only be detected at high altitudes because of beam shielding by relieves: there, terrain blockage combined with the shallow depth of precipitation during cold seasons and low melting levels causes inadequate radar coverage to support QPE, especially in narrow valleys.

Furthermore, precipitation is too variable for the “coarse” resolution of long-range ground-based radars (GR). The variability of natural precipitation is so large that the radar beam often does not resolve it. As a result we find aloft different types of particles and non-homogeneous reflectivity in the pulse volume, to be compared with rain rate at the ground level. The under-sampling problem becomes increasingly severe with increasing ranges because the radar backscattering volume increases with the square of the range; therefore, at longer ranges, small but intense features of the precipitation system are blurred (non-homogeneous beam filling). Furthermore, it is more likely to include different types of hydrometeors (e.g., snow, ice, and rain drops), especially in the vertical dimension. We know that, on average, the radar backscattered echo from liquid, mixed phase, and frozen hydrometeors decreases with height. Using several TRMM overpasses, the comparison between the TRMM radar and linearly averaged GR radar reflectivity, carried out in circular rings around the GR site, has clearly confirmed a significant range dependence of the TRMM/GR ratio (*Gabella et al.* [2006], *Gabella et al.* [2011a], *Gabella et al.* [2011b]). This well-known problem is caused mainly by the increasing sampling volume of the long-range GR with range, combined with non-homogeneous beam filling: e.g., at longer ranges of GR, the lower part of the volume could be in rain, whereas the upper part of the same pulse can be filled with snow, ice, and mixed phase particles. Quite often it can be even characterized by an echo weaker than the radar sensitivity itself (apparently, no backscattered echo). This phenomenon (called “beam overshooting” by radar meteorologists) is also caused by the decrease of vertical resolution with range, thus amplifying the influence of the horizon and Earth’s curvature. Because of beam overshooting, strong range degradation has been noticed in several parts of the world when analyzing weather radar data over a long time period. The reader can refer, for instance, to the 2-year analysis by *Young et al.* [1999] in the United States or by *Gabella et al.* [2005] in the Swiss Alps.

In mountainous terrain, precipitation is even more variable both in space and time because of orographic effects and interactions of mountains with wind fields. This variability within the scattering volume is in contradiction with the homogeneously filled pulse volume assumption usually made when considering the meteorological radar equation. Fulfilling the assumption of homogeneous beam filling, however, is a prerequisite for a precise estimate of reflectivity, attenuation and phase shift along the beam.

1.3 Type and width of the distribution of precipitation

Another fundamental problem is the asymmetry and the large variability of precipitation rates in time and space. In other words, distributions are wide and skewed-to-the-high-end at the same time. This statement concerns particle type, particle size, number density of particles as well as derived integral parameters such as reflectivity, rain- and snow-rate. As a consequence of the distributions in time and space, we find that a small area (say 1/10 of the “rainy” area, which in turn can be 1/20 of the surveillance area ...) during a “short” time (i.e. smaller than the rainy/cloudy period) contributes a large fraction of the total precipitation amount. As a direct consequence of this (small “time/space” of significant and heavy rain rate), the chance of detecting weak rain rate is much larger than high rain rate. Without careful thinking and without having analyzed large data sets, we may be tempted to extrapolate the rules of weak rain into strong one. This extrapolation will involve large errors, because mechanisms producing rain vary with its intensity. In other words, different mechanisms produce weak and large rain rates.

1.4 Difficulties with conventional long-range radar: Inability to observe the lower part of the troposphere combined with non-homogeneous beam filling

We may wonder: why is it so difficult to grasp a realistic precision out of “long-range” (say two hundred kilometers) weather radar? Perhaps, the main reason can be found in the difficulty of reproducing the results verified with large effort at close ranges. We cannot extrapolate them to the full range displayed by our operational, meteorological radars. At short ranges problems caused by shielding, inhomogeneous beam filling, attenuation and vertical profile may be dealt with. This is not possible at longer ranges. This statement does not exclude the use for weather forecasting in full range of our radars. The radar tells us where and when something is coming; radar data are helpful to validate the forecasts of the Numerical Weather Prediction models. Here, combining the information of many radars into a network may help a lot. The combination of data from many radars may also mitigate the effects caused by the range-dependence of each single radar.

Long-range radar networks remain an essential part of the weather forecasting and warning infrastructures used by many nations worldwide. Despite significant capability and continuous improvement, one fundamental limitation of today’s weather radar networks is the inability to observe the lower part of the atmosphere and detect fine-scale weather features. Designed for long-range coverage through precipitation, these radars must operate at radar wavelengths not subject to attenuation. This implies the use of large antennas (to achieve narrow beam width) and high-power transmitters (to meet sensitivity requirements at long ranges); up to now, such large antennas are mechanically scanned, hence requiring dedicated land, towers and other support infrastructures. Consequently, the installation and acquisition cost of each site is usually much larger than the cost of the sensor itself.

1.5 Proposed solution: Distributed networks of many, inexpensive, redundant, low-cost, high temporal resolution, short-range, small radars

How to tackle the emerging need for improved low-altitude coverage, high temporal-resolution meteorological radars? Many low-cost, fast-scanning, short-range X-band radars for rain monitoring can be a valid solution for complementing long-range radars. Long range radars have proved to be useful for weather forecasting and qualitative surveillance. As already discussed in Sec. 1.2, the results, verified with large effort at close ranges, cannot be generalized. Because of range degradation (non uniform beam filling and overshooting, see Sec. 1.2), it seems impossible to reproduce the results easily obtained close to the radar for quantitative applications at far ranges. This is especially true in mountainous terrain. Therefore, an interesting solution could be to combine the data of many, small, low-cost and short-range X-band radar for rain estimates within valleys.

2. The potential for distributed networks of small low-cost weather radars

2.1 The work of the remote sensing group at the Politecnico di Torino

The European INTERREG IIIB Alpine Space Programme started in 2004 the FORALPS Project (“Meteo-hydrological Forecast and Observations for improved water Resource management in the ALPS”). One of the aims of FORALPS was the design and development of a portable, low-cost, small radar for weather monitoring. The Remote Sensing Group at

the Politecnico di Torino was involved in the development activities of this new network starting from its early ideation stages (Notarpietro *et al.* [2005]).

The first designed scenario was specifically intended to cover narrow valleys within the Alps. This was initially achieved by adopting a non-conventional vertical plane scanning strategy with a fan beam slot waveguide antenna (1° beam width in the vertical plane, 25° beam width along the valley). The initial implementation was simply designed to collect two low elevation acquisitions with opposite directions along the valley plus a vertical sounding to evaluate the vertical reflectivity profile (Gabella *et al.* [2008]). Then, this initial approach was extended to collect radar sounding coming from the entire vertical plane. This kind of small low-cost radar has been patented and is now sold with the name “wind-mill” mini-radar.

In a second stage, the more conventional horizontal scanning strategy was implemented to cover wide planar areas with very high temporal resolution at a fixed, optimized elevation. This suggested combining a number of short-range, low-cost radars into a network concept, to obtain a set of similar small unattended units, tightly connected within a unified environment. The result of the above approaches and suggestions is an unmaned, low-consumption, network of low-cost, small, X-band radars. Adding up, the first prototypes, running since October 2006, were installed on the Politecnico di Torino roof, sensing either the horizontal or the vertical planes. During these years several progresses and modifications were made, leading to a network of mini radars: one operated by the Aosta Valley Civil Protection (since March 2007) and a vertical scanner unit (wind-mill) installed next to the glide path of the “Sandro Pertini” Turin International Airport. Recently (autumn 2010), four horizontal scanners units were installed in different areas of Sicily (see the web site <http://meteoradar.polito.it/>). At present, seven small radars have been installed on the Italian territory and are successfully running. In our approach, such network is capable of mapping storms with temporal resolution better than 1 min and focusing on the low-troposphere “gap” region. Such network has the potential to complement the long-range radar networks in use today. In Chapters 3 and 4 the deployment of small, low-cost, X-band radars will be presented for the following environments:

- heavily populated areas (e.g. Palermo town and harbor, see Sec. 3.2 and 4.2; Turin town, see Sec. 4.4);
- specific dry and semi-arid regions where it is crucial to improve observation of low-level meteorological phenomena (e.g. western Sicily, Sec 4.3)
- deep valleys surrounded by high mountains region (e.g. Valle d’Aosta, see Sec. 3.1).

2.2 X-band, “short” wavelength technology for short-range monitoring

Cost, radiation safety issues and aesthetic issues motivate the use of small antennas and low-power transmitters that could be installed on either low-cost towers or existing infrastructures such as rooftops of existing buildings or telecommunication poles. This requires that the radars are physically small and that the radiated power levels are low enough so as not to pose an actual or perceived radiation safety hazard. We have opted for a very small parabolic antenna ($D = 0.6$ m) which corresponds to a 3 dB cross-range spatial resolution of 1 km at 20 km range (two third of the used range, which is 30 km). The antenna is hidden below a 1 m diameter radome (Fig. 1, left picture) and rotates at $\sim 120^\circ$ per second using a single elevation.

One precipitation map is made available every minute by averaging 16 rotations (out of the 22 available) 9 consecutive rays and 2 range-bins, hence resulting in a total of 144 samples.

Table 1 summarizes main characteristics of our low-cost weather radars for both configurations described in Sec. 2.1 and 2.2: the innovative “wind-mill” (tailored to narrow valleys in mountainous terrain) and the more conventional horizontal scanner (also called “super-gauge”). More details on the temporal sampling scheme and averaging process are given in the next Section 2.3.

Frequency	X-Band (9.4 GHz)
Range	up to 30 km
Power	10 kW
Pulse duration for long (short) pulse	400 (80) ns
Pulse Repetition Frequency	800 (3200) Hz; for long (short) pulse, respectively
1] Super-Gauge	Single elevation, 3.6° beam width, horizontal plane
2] Wind-mill	1.2° along valley, 25° across valley, vertical plane
Antenna (depending on scanning)	1] 0.6 m paraboloid; 2] slotted waveguide
Cost of a mini radar	< 30 kEuro (within a network of, say, 6 radars)

Table 1. Main characteristics of the low-cost weather radar.

2.3 High temporal resolution

The use of precipitation estimates from weather radar has been limited not only by the quantitative accuracy but also by the spatio-temporal resolution: firstly, there is a significant number of sources of uncertainty in the process of converting the reflectivity volume data measured by a radar to an estimate of falling precipitation close to the ground. The factors that contribute to this uncertainty have been introduced and summarized in Section 1. Secondly, the spatio-temporal resolution of radar-based QPE products from weather radar networks was generally insufficient, especially for small-scale hydrological applications. Hence, one important advantage of our mini-radar with small antenna approach is also the high temporal resolution.



Fig. 1. The portable, low-cost weather radar with (left picture) and without (right picture) the 1-meter Diameter radome. The configuration shown here is the so-called “super-gauge”, which is a single-elevation scanning in the horizontal plane with a 3.6° beam width paraboloid (Diameter of the paraboloid is 0.6 m).

As described in Sec. 2.2, both kinds of mini radar, the “wind-mill” (vertical plane scanning along valley) and the “super-gauge” (which implements the traditional horizontal scan) currently deliver an image of precipitation every minute; furthermore, the temporal resolution can easily be reduced to 30 or even 15 s.

We here describe in more details how the time-averaged (1-minute-sampled) radar reflectivity measurements are acquired. For each of the 9 consecutive shots, 2 contiguous pulses have been acquired: the 2 contiguous pulses are separated by the pulse width, which is 400 ns; the 9 consecutive shots are separated by the pulse repetition interval, which is 1.25 ms. Every minute, the antenna performs 22 revolutions; however only data from the first 16 revolutions (out of 22) were averaged on a linear power scale (algebraic average: dBm values are antilog transformed, then averaged, then again transformed on a decibel logarithmic scale). This means a total of 288 (18 times 16) samples; among them, at least 2×16 are independent, if we assume a decorrelation time of ~ 10 ms (Fig. 1.14, *Sauvageot* [1992]): sample #1 and # 9 of the 9 consecutive rays are in fact separated by $9 \times 1.25 = 11.25$ ms.

3. A few qualitative examples

3.1 An hostile environment: Detecting precipitation even inside a narrow valley

At the beginning of November 2011 (from 3 to 9 November around noon) six days of continuous, wide-spread precipitation hit the north-western part of Italy (see Fig. 2). In the south-western Alps and in the surrounding flatlands and hills, in fact, autumn is the season in which the longest and heaviest rainfalls occur. This fact has long been known: a description of these “late-summer” Mediterranean storms can already be found in the works by the old-Roman author, Plinius. It can be explained in simple terms as follows: in autumn the Mediterranean Sea surface temperature is still high, while cold air is already forming over the central-northern part of Europe. This has two effects: first of all, the thermal contrast facilitates the deepening of pressure low over the north-western part of the Mediterranean Sea; secondly, the warm air that arrives from the south, flowing over the Mediterranean, provides a ready source of moisture.

The enforced rising of this warm-humid convectively unstable air, thanks to the Alpine barrier, causes extensive and heavy rainfall. One has the impression of being subject to a long storm, but, in reality, it is the continuous formation of stormy cells over the same place.

The first study site here presented is located in north-western Italy in the “Aosta Valley”, which is the smallest region in Italy. It is set between the Graian and Pennine Alps, which are very steep. Among the more than “four-thousand” massifs, the most famous are: Mont Blanc, Monte Rosa, the Matterhorn and Gran Paradiso. The Dora Baltea river together with its tributaries have formed the tree-leaf-shape veining of the Valley. A Digital Elevation map of the investigated area is shown in Fig. 2.

Being surrounded by such high relieves (> 4000 m MSL), the deep Aosta Valley (< 500 m MSL) cannot be effectively monitored by any of the surrounding weather radars (Dole, close to Geneva; Bric, close to Torino; Monte Lema, close to Maggiore Lake). Among these

three radars, the one with “less worse” visibility is certainly Monte Lema, which was the only one able to detect some weak echoes during the 24-hour period shown in Fig. 3a (from 12 UTC of November 4 to 12 UTC of November 5). However, because of beam shielding by relieves combined with overshooting, the 24-hour radar-derived rainfall amounts above the central-western part of the Aosta Valley are heavily underestimated: for instance, above Aosta town, the Swiss weather radar network (see Fig. 3a) shows amounts smaller than 2 mm in 24 hours.

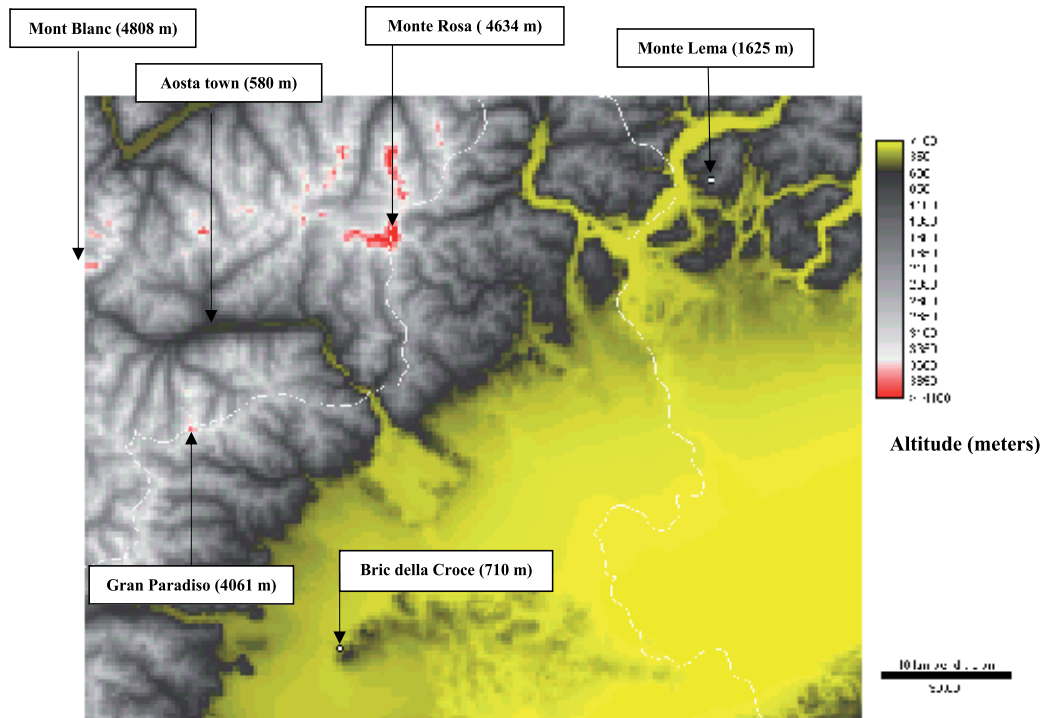


Fig. 2. Digital Elevation map of the north-western part of Italy.

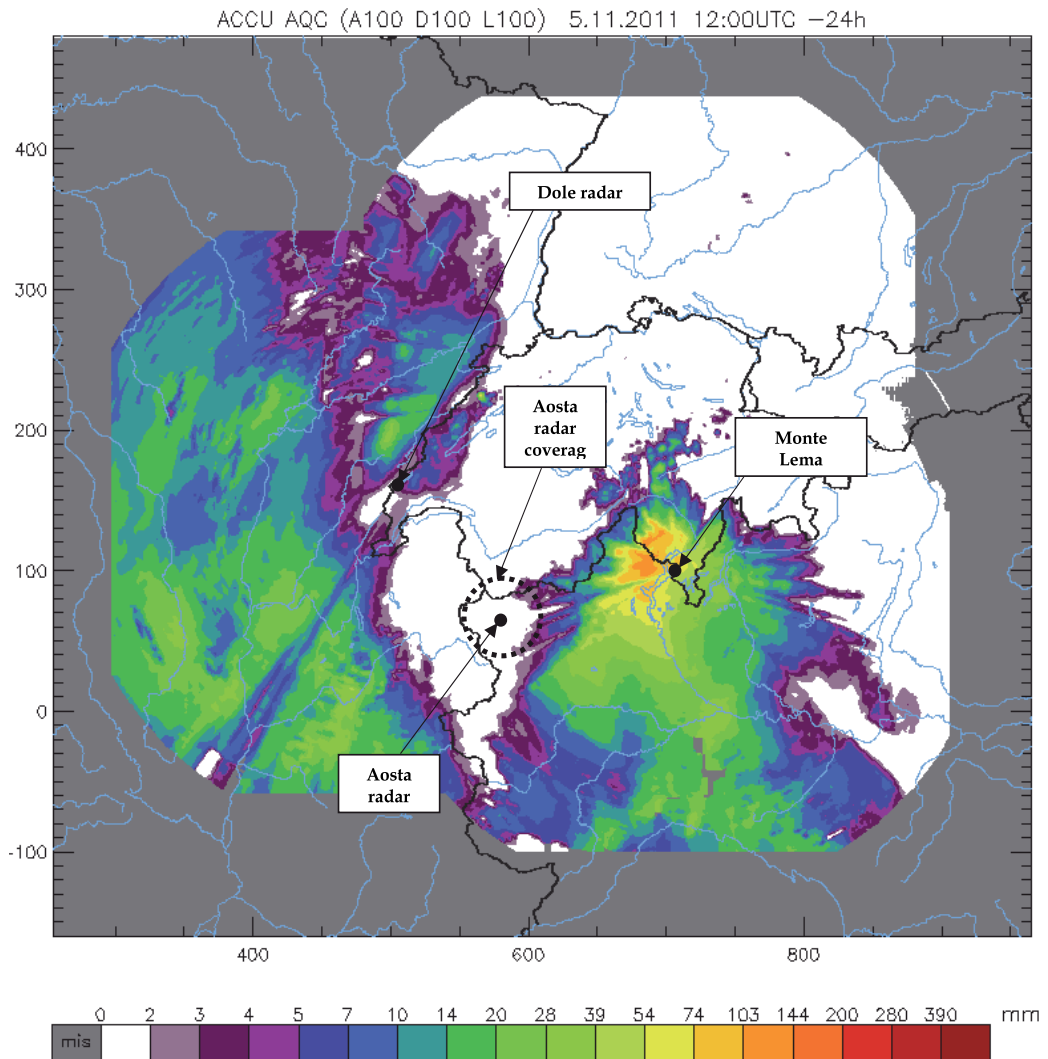


Fig. 3a. 24-hour cumulative rainfall amounts in the western Alps as seen by the Swiss weather radar network (from 12 UTC of November 4 to 12 UTC of November 5, 2011). North and East axes map units are in km.

What if we supplement long-range weather radar information with precipitation fields derived at high spatio-temporal resolution by portable, low-cost X-band radars? The answer is given in Fig. 3b, which shows what the low-cost X-band radar can detect, despite being deployed down deeply into the valley. As it can be seen, the 24-hour cumulative

precipitation amounts surrounding Aosta town indicate values between 16 and 25 mm in 24 hours (yellow patch). According to rain gauges, such amount still represent ~ 2 dB radar underestimation: from 12 UTC of November 4 to 12 UTC of November 5, in fact, the gauges “Aosta Piazza Plouves” (580 m MSL) and “Aosta St. Christophe” (550 m MSL) respectively measured 44.2 mm and 40.2 mm.

Finally, it is worth noting that the very complex orography causes severe beam shielding: the radar is practically blind at all ranges in the northern part of the circular surveillance area while in the southern half-circle weather echoes are only detected in approximately 10% of the 30 km range.

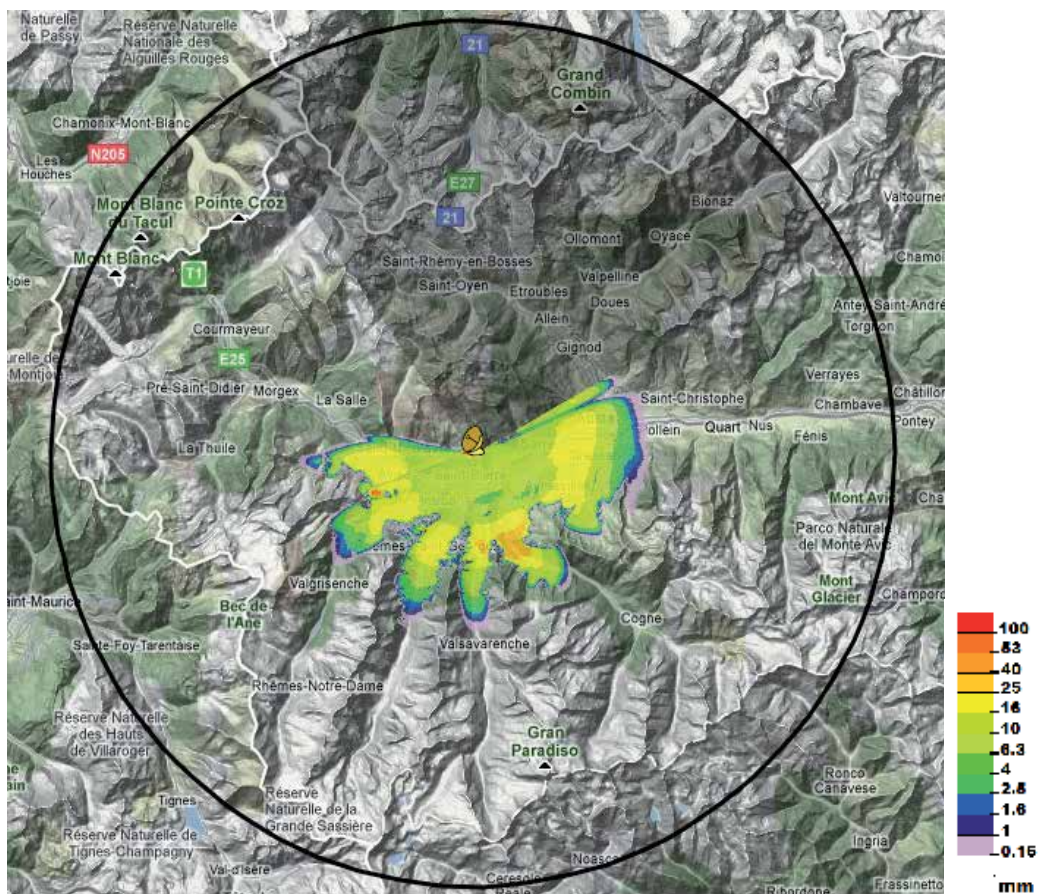


Fig. 3b. 24-hour cumulative rainfall amounts in the north-western part of Italy as seen by the low-cost X-band radar located near the town of Aosta (from 12 UTC of November 4 to 12 UTC of November 5, 2011). The circular range ring is at 30 km range from the site of the mini-radar.

3.2 The extreme spatio-temporal variability of the precipitation field in semi-arid regions

In this section, a typical Mediterranean thunderstorm hitting the Palermo town in Sicily is presented. More details are given in the caption of Fig. 4 below, while QPE performances of the Palermo mini radar are thoroughly discussed in Sec. 4.2.1 and 4.2.2.

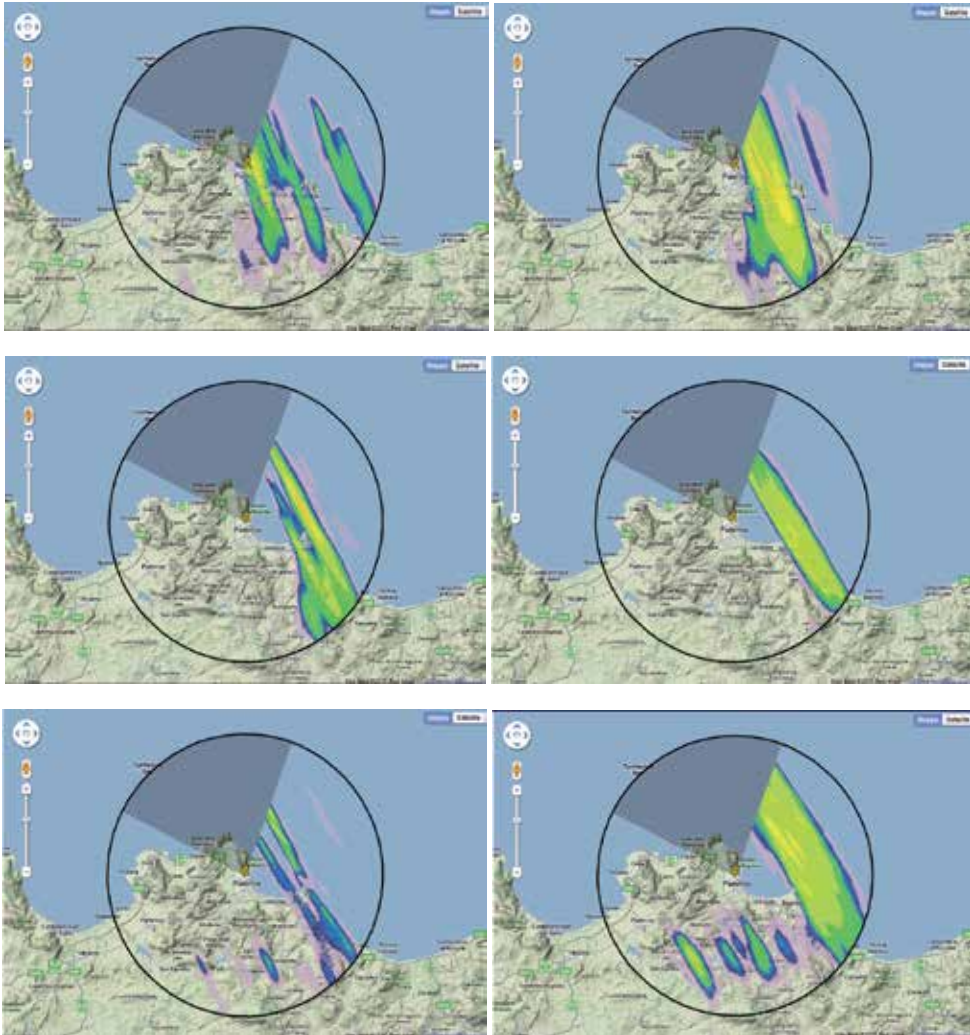


Fig. 4. Average hourly precipitation field on the evening of February 18, 2011 in the northern part of a dry Mediterranean island (Sicily); it is worth noting the “wide precipitation band” shape and the high spatial variability of the field despite the averaging process used to derive hourly cumulated rainfall amounts. Each of the 6 consecutive pictures shows the average of 60 instantaneous maps of radar reflectivity (one per minute) transformed into equivalent rain rate using a fixed Z-R relationship. The first picture shows hourly accumulation rainfall amounts from 16 to 17 UTC; the last one from 21 to 22 UTC. The circular range ring is at 30 km range from the site of the mini-radar.

4. Some quantitative examples in Sicily and Piedmont

4.1 Quantitative precipitation estimation (QPE)

While Section 3 dealt with qualitative examples, in the present Section 4 we will present hourly radar-derived precipitation amounts as obtained from weather echoes aloft to be compared with point rainfall measurements acquired at the ground by rain gauges.

4.1.1 From instantaneous radar reflectivity to hourly rain rate amounts

We have seen in Sec. 2.3 that the mini-radar finally provides an instantaneous radar reflectivity value once per minute for each radar bin of 3° by 120 m. This value is in turn the average of 288 samples (among them, at least 32 samples are independent, see Sec. 2.3).

It is well known that the backscattered power caused by rain drops is, unfortunately, only indirectly linked to the rain rate, R ($[R] = \text{mm/h}$). The backscattered power caused by the hydrometeors and detected by the radar is, in fact, directly proportional to the radar reflectivity factor, Z . A fundamental quantity for precise assessment of both Z and R is the drop size distribution (DSD), $N(D)$, which is defined as the number of rain drops per unit volume in the diameter interval δD , i.e. between the diameter D and $D+\delta D$. The radar reflectivity factor, Z , is defined as the 6th moment of the DSD, namely:

$$Z = \int_0^{\infty} N(D)D^6 dD. \quad (1)$$

In radar meteorology, it is common to use the dimensions of mm for drop diameter, D , and to consider the summation (integral) to take place over a unit volume of 1 m^3 . Therefore, the conventional unit of Z is in mm^6/m^3 . For the assessment of rain rate, another fundamental quantity is needed: the terminal drops fall velocity as a function of the diameter, $v(D)$. Since it is common to use $[v] = \text{m/s}$, then the relationship is

$$R = 6 \cdot 10^{-4} \cdot \pi \int_0^{\infty} N(D)D^3 v(D) dD. \quad (2)$$

If precipitating hydrometeors in the radar backscattering volume were all spherical raindrops (which is almost never the case!) and the DSD could be described to a good approximation by an exponential DSD, then a simple power-law would relate Z to R . The first ever exponential DSD presented in a peer-reviewed paper and probably the most quoted is the Marshall-Palmer (M-P) distribution. The power law derived using the exponential fit proposed in Eq. (1) and (3) of the famous paper by *Marshall and Palmer* [1948] is $Z=296 \cdot R^{1.47}$.

Here we have used the following Z-R relationship $Z = 316 \cdot R^{1.5}$ to derive the variable of interest, R , from the geophysical observable, Z , which is detected by the meteorological radar. Such values have been retrieved by *Doelling et al.* [1998] using seven years of measurements in central Europe. It is also worth noting that for the 2 radars in Sicily prior to any processing, the radar reflectivity values were increased by 4 dB to compensate system losses not properly compensated in the "traditional" radar equation.

For each radar bin, a maximum of 60 clutter-free radar reflectivity values are then transformed into R using $R = (Z / 316)^{2/3}$ and then averaged to derive the corresponding hourly rain rate used in this study.

4.1.2 QPE evaluation based on the comparison between hourly radar and gauge rainfall amounts

The evaluation is based by looking at the average value and the dispersion of the errors (we call error the disagreement between radar and gauge amounts). For such characterization, we define the two following parameters:

1. *Bias* (in dB). The bias in dB is defined as the ratio between radar and gauge total precipitation amounts on a logarithmic (decibel) scale. It describes the overall agreement between radar estimates and ground point measurements. It is averaged over the whole space-time window of the sample. A positive (negative) bias in dB denotes an overall radar overestimation (underestimation).
2. *Scatter* (in dB). The definition of scatter is strictly connected to the selected error distribution from a hydrological (end-user) and radar-meteorological (operational remotely sensed samples of the spatio-temporal variability of the precipitation field) perspective. The error distribution is expressed as the cumulative contribution to total rainfall (hydrologist point of view, y axis) as a function of the radar-gauge ratio (radar-meteorologist point of view, x axis). Most of the sources of error in radar precipitation estimates, in fact, have a multiplicative (rather than an additive) nature. An example of the error distribution is shown in Fig. 2 and 3 of *Germann et al.* [2004]. The scatter is defined as half the distance between the 16% and 84% percentiles of the error distribution. The scatter refers to the spread of radar-gauge ratios when pooling together all volumetric radar estimates aloft and point measurements at the ground.

From our radar-meteorological point of view the multiplicative nature of the error prevails with respect to the additive one. For example, water on the radome, a wrong calibration radar constant, or a bad estimate of the profile all result in a multiplicative error (i.e. a factor) rather than an additive error (i.e. a difference). This is why bias, error distribution and scatter are expressed as ratios in dB. A 3 dB scatter, for instance, means that radar-gauge ratios vary by a factor of 2. If bias is zero, it is interpreted as follows: the radar-derived estimate lies within a factor of 2 of the gauge estimate for 68% of rainfall while for the remaining 32% the uncertainty is larger. The scatter as defined above is a robust measure of the spread. It is insensitive to outliers for two reasons. First, each radar-gauge pair is weighted by its contribution to total rainfall (y axis of the cumulative error distribution). An ill-defined large ratio that results from two small values, e.g. 0.4 mm/2 mm \sim -7 dB, describes an irrelevant event from a hydrological point of view, and only gets little weight. Second, by taking the distance between the 16% and the 84% percentiles, the tails of the error distribution are not overrated. Another important advantage of the spread measure is that it is unaffected by the bias error, hence providing a complementary view of the error in the estimates. The above definition of the scatter is thus a better measure of the spread than the less resilient standard deviation.

4.2 Quantitative precipitation estimation for the Palermo radar

The Palermo radar is located on a small hill next to the harbor of the capital of Sicily (blue triangle, Fig. 5): its latitude is 38°.1139; its longitude is 13°.358; its altitude is 45 m above Mean Sea Level (MSL). The radar has been installed in autumn 2010.

For the quantitative evaluation of the radar estimates, the most reasonable available rain gauge in terms of range and radar visibility is the one located in Altofonte. It is run by the Servizio Informativo Agrometeorologico Siciliano (SIAS). Its location (red triangle) is shown in Fig. 5, which represents a 90 m resolution Digital Elevation Model of the region at two different scales: left picture domain is ~ 540 by 540 km²; right picture is 90 by 90 km².

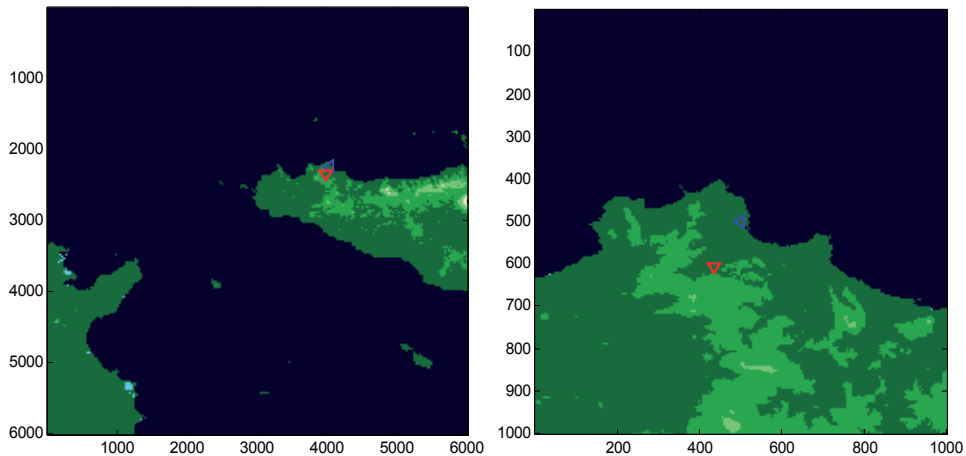


Fig. 5. Digital Elevation Map of Sicily showing two different domains (pixel size is 90 m); the blue triangle shows the site of the mini radar next to Palermo downtown. The red triangle shows the location of the most reasonable rain gauge in terms of range and radar visibility (see Fig. 6); this gauge (Altofonte) has been used for the QPE evaluation. Axes map units are 90-m pixels.

The radar-gauge distance is 11.1 km; the rain gauge altitude is 370 m above MSL. Fig. 6 shows the radar-gauge profile as derived using the DEM shown in Fig. 5. In addition to the terrain profile (black curve), the picture shows the mini-radar 3.6° Half Power Beam Width (HPBW, often called “3 dB beamwidth” in radar meteorology) by means of two blue lines. The radar beam axis, which divides such angular sector in two equal parts of 1.8°, has an angle of elevation equal to +3°. As it can be seen from Fig. 6, the gauge location is not optimal: in the last kilometer before the gauge, the 3 dB portion of the primary lobe hits the hilly terrain, hence causing some beam shielding (power loss) and ground clutter contamination. However, regarding this last problem, it is worth noting that the rain gauge location is behind the top of the hill: this means that Palermo radar echoes above the Altofonte gauge are practically ground-clutter-free; nevertheless, as stated, because of beam shielding, some (radar) underestimation above the gauge can be expected.

For what concerns QPE, 6 rainy days (144 hours) during the first 4 months of 2011 have been analyzed; these days are February 1, 23 and 28, March 5, April 26 and 27. During these 144 hours the Gauge (Radar) total amounts was 77.4 (62.7) mm, which corresponds to an “overall Bias” of -0.9 dB (radar underestimation). Out of 144 analyzed hours, in 48 (42) cases the Gauge (Radar) derived hourly rainfall amount was larger than 0.4 mm/h, which is the hydrological threshold adopted in this Chapter for discriminating between “hydrologically speaking” wet and dry hours (see also Table 2).

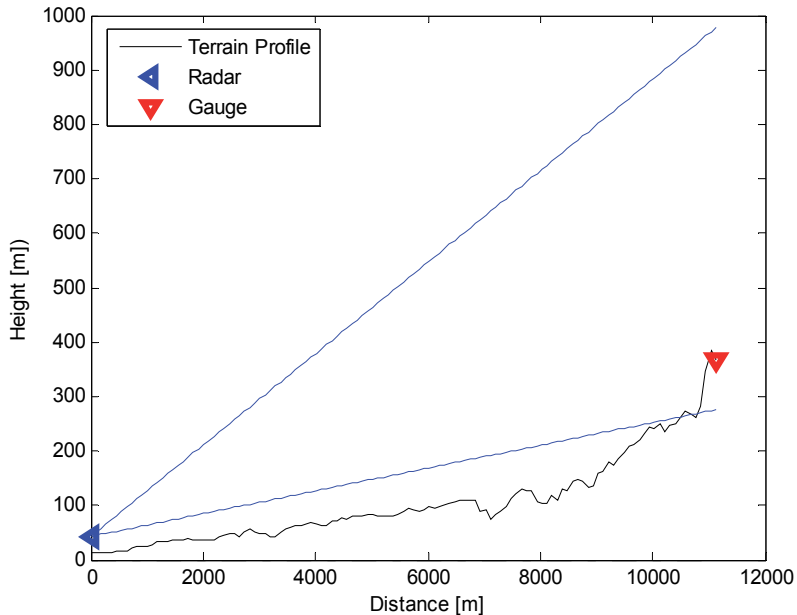


Fig. 6. Vertical section of the terrain profile from the Palermo radar site to the Altofonte gauge derived from the Digital Elevation Model shown in Fig. 5. The blue lines indicate the boundaries of the radar antenna Half Power Beam Width.

The scope of our QPE analysis is twofold:

- to evaluate from an hydrological point of view the radar ability in discriminating wet versus dry hours;
- to assess quantitatively the radar accuracy in estimating hourly rain rates.

As introduced in the methodological Section 4.1.2, the latter quantitative assessment will be based on the Scatter in dB and thoroughly described in Sec. 4.2.2; the former evaluation will be presented in the Sec. 4.2.1.

4.2.1 Wet versus dry hours discrimination according to radar echoes using the gauge as reference

The history of applying contingency tables (also called error matrices in the remote sensing field) for the verification of one set of observations against a reference set is a quite long one. The history of categorical statistics based on such tables is rather fascinating and an interesting account is given by Murphy (1996). Most of the scores were first derived nearly a century ago and have been rediscovered several times (with different names in different branches of science, see for instance the bullet list below).

The dimension of the contingency tables can be as small as 2×2 (tetrachoric) or larger (polychoric) depending on the number of thresholds used in the classification scheme. Obviously, in our wet-versus-dry hourly values discrimination, we are dealing with tetrachoric tables, since just one discrete value (namely 0.4 mm/h) is used to divide the two categories. On the one hand, the properties of a set of observations can be condensed and clearly displayed through such tables; on the other hand, to satisfy needs of specific users, even for a simple tetrachoric table, several different scores have been introduced. Here, we will use two scores that can be applied to both tetrachoric and polychoric tables:

- the Heidke Skill Score (HSS), also known as Kappa Index of Agreement (KIA), Khat, ...
- the Hanssen-Kuipers (HK) score also known as True Skill Score (TSS), ...

Details regarding these two scores can be found in literature; the interested reader may refer, among others, to the paper by *Tartaglione* [2010] regarding HK and to the work by *Hogan et al.* [2009] regarding HSS. In particular, the Appendix of this last paper interestingly aims at estimating confidence intervals in the HSS.

	G ≥ 0.4 mm/h	G < 0.4 mm/h	
R ≥ 0.4 mm/h	38	4	42
R < 0.4 mm/h	10	92	102
	48	96	144

Table 2. Contingency table between the Palermo radar estimates and the Altofonte rain gauge measurements.

From Table 2, it is straightforward to derive the Probability Of Detection (POD), which is $38/48 = 0.79$ and the False Alarm Ratio (FAR), which is $4/42 = 0.095$.

Regarding the two above mentioned multi-categorical scores selected, **HSS** results to be **0.774**; HK is slightly smaller: 0.750.

4.2.2 Quantitative agreement between gauge and radar-derived hourly rain rates

During the 48 “Wet-Gauge” hours, the total rainfall amount according to the Altofonte Gauge was 72.4 mm. According the Palermo Radar, the total rainfall amount was 55.9 mm, which means a residual “Wet-Gauge Mean Field Bias” of -1.1 dB (radar underestimation). Based on these 48 “**Wet-Gauge**” hourly amounts, which are shown in Fig. 7, the **Scatter** results to be **2.38 dB**, as can also be seen from the 48 values displayed in Fig. 8.

Using only the 38 hours where BOTH the Radar AND the Gauge amounts were larger or equal to 0.4 mm/h, the total Gauge (Radar) amount was 64.6 (54.7) mm. Consequently, the “wet-wet” Mean Field Bias is -0.7 dB. As expected, also the “wet-wet” Scatter improves: based on such 38 “wet-wet” hourly amounts, it results to be 1.97 dB, as can be seen from Fig. 9. The 0.4 dB decrease in the value of the Scatter is a clue of the not-negligible rain amount missed by the radar during the 10 “Missing Detection hours”.

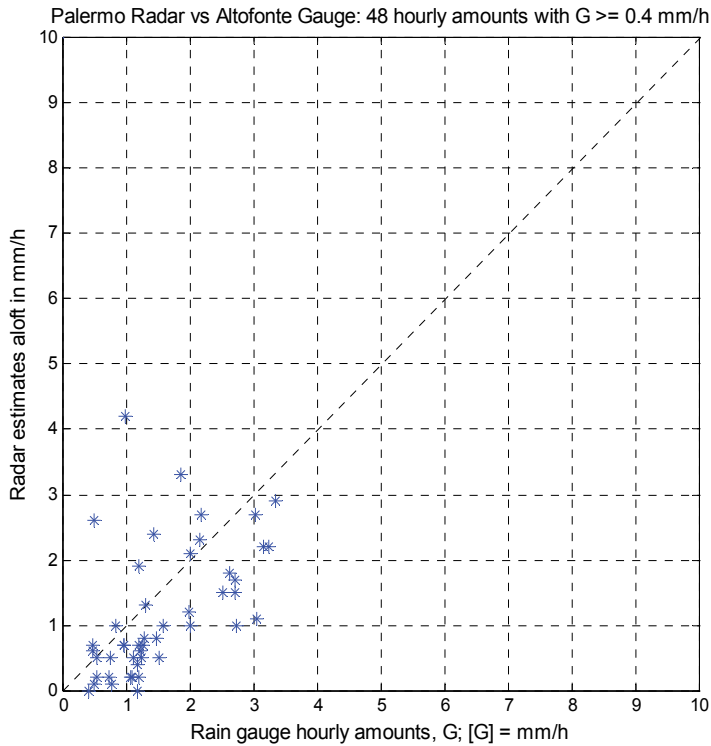


Fig. 7. Scatter plot of 48 hours with Altofonte gauge amounts larger or equal than 0.4 mm/h and the corresponding Palermo radar estimates. The scale is linear and the maximum value is set to 10 mm/h (as in Fig. 16 for the Torino site).

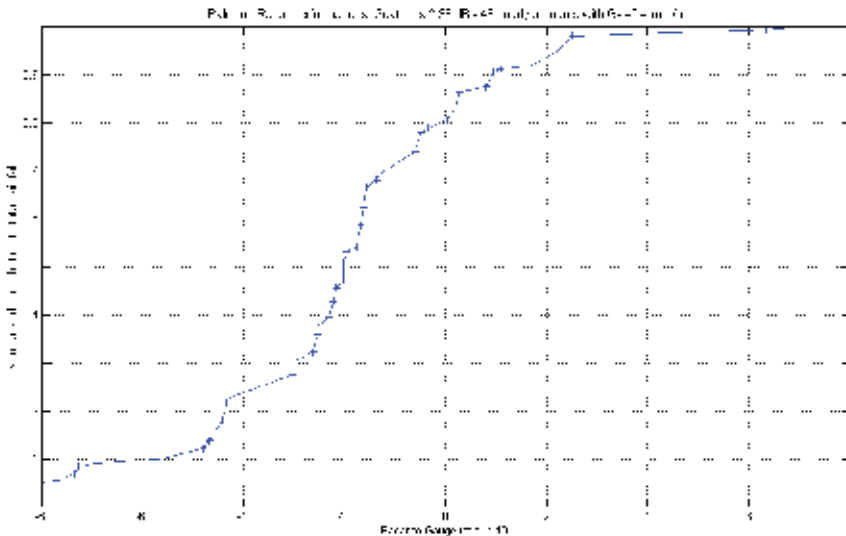


Fig. 8. Cumulative contribution to total rainfall as a function of Radar-Gauge ratio for hourly precipitation with $G \geq 0.4$ mm/h (48 samples).

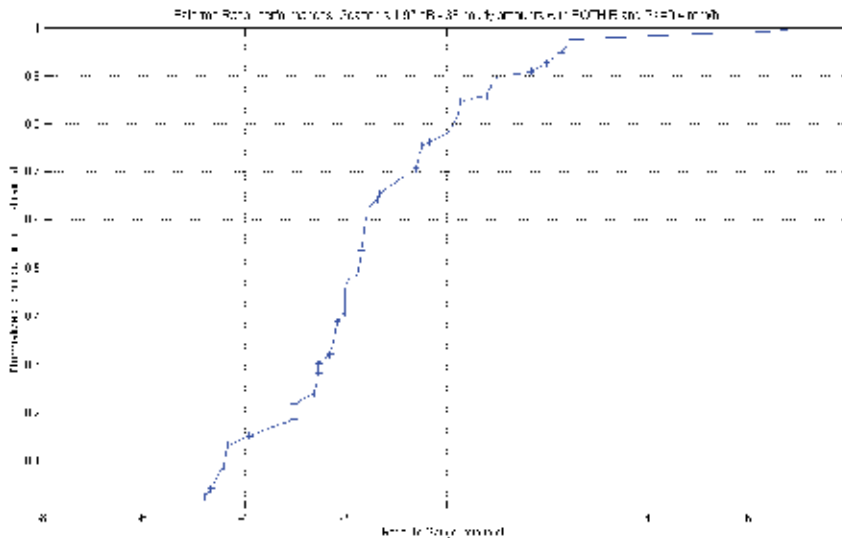


Fig. 9. Cumulative contribution to total rainfall as a function of Radar-Gauge ratio for hourly precipitation with both R and G ≥ 0.4 mm/h (38 samples).

4.3 Quantitative precipitation estimation for the Bisacchino radar

The Bisacchino radar is located in the central-western part of Sicily: latitude is $37^{\circ}.707$; longitude is $13^{\circ}.262$; altitude is 780 m above Mean Sea Level (MSL). As for the Palermo radar (Sec. 4.2), it has been installed in autumn 2010.

For the quantitative evaluation of the radar estimates there is an optimal rain gauge run by the Servizio Informativo Agrometeorologico Siciliano (SIAS) and installed in the municipality of Giuliana (località Castellana). Its location (red triangle) with respect to the radar (blue triangle) is shown in Fig. 10 together with the DEM of the area.

The radar-gauge distance is 8.7 km; the rain gauge altitude is 250 m above MSL. As can be seen from Fig. 11, the gauge location is optimal not only in terms of range, but most of all in terms of radar visibility: no partial beam shielding by relieves affects the mini radar 3.6° Half Power Beam Width (HPBW), which is delimited by the two blue lines in Fig. 11 (the radar beam axis has an angle of elevation set to 1°).

Furthermore, the hill located at 3 km range from the radar, causes partial beam shielding of the remaining part of the primary lobe and total shielding of the secondary lobes in elevation; consequently, we can conclude that residual ground clutter contamination affecting radar echoes above the Giuliana rain gauge is negligible.

For what concerns QPE, 4 rainy days (96 hours) during the first 5 months of 2011 have been analyzed; these days are February 23, March 13, April 26 and May 22. During these 96 hours the Gauge (Radar) total amounts was 98.2 (77.7) mm, which corresponds to an “overall Bias” of -1.0 dB (radar underestimation).

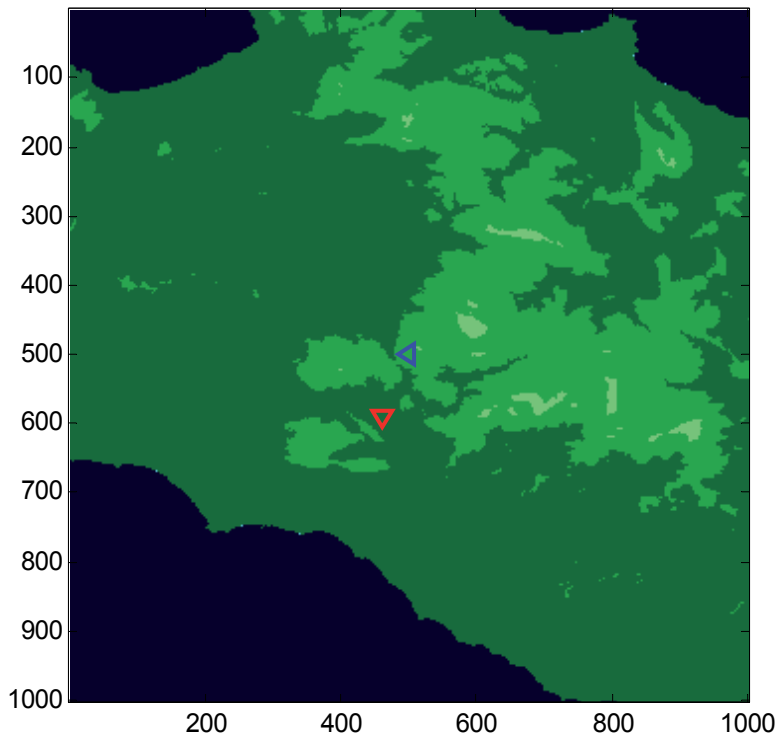


Fig. 10. Digital Elevation Map of the western part of Sicily showing the Bisacquino radar site (red triangle) and the Giuliana rain gauge location (blue triangle). Axes map units are 90-m pixels.

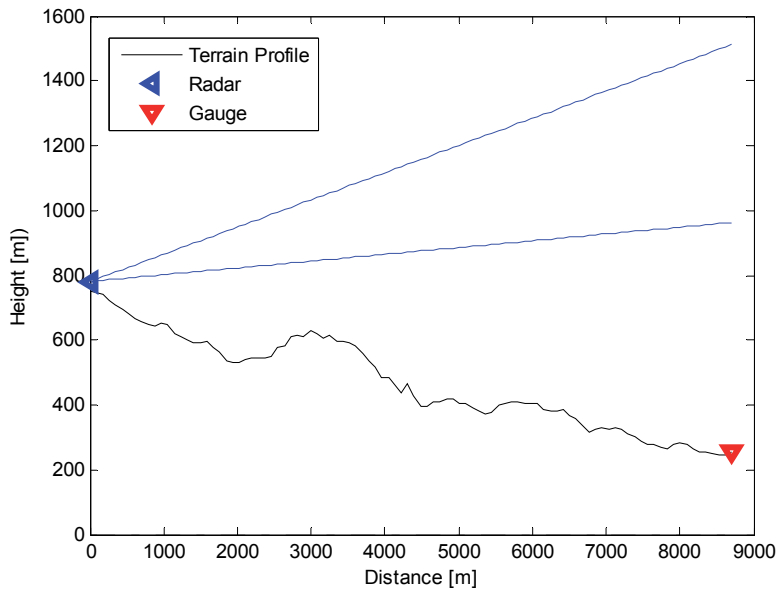


Fig. 11. As in Fig. 6, but for the Bisacquino radar and the Giuliana rain gauge.

Out of 96 analyzed hours, in 37 (34) cases the Gauge (Radar) derived hourly rainfall amount was larger than 0.4 mm/h (see the next Sec. 4.3.1 and Table 3 for more details).

4.3.1 Wet versus dry hours discrimination

From Table 3, it is easy to see that in this case the POD is (29/37) 0.78 while the FAR is relatively high: (5/34) 0.15. If we consider scores that deal with all the elements of the table, then HSS results to be **0.710** while HK is quite similar: 0.699.

	$G \geq 0.4$ mm/h	$G < 0.4$ mm/h	
$R \geq 0.4$ mm/h	29	5	34
$R < 0.4$ mm/h	8	54	62
	37	59	96

Table 3. Contingency table between the Bisacquino radar observations and the Giuliana rain gauge measurements during the 96-hour observation period.

4.3.2 Quantitative agreement between gauge and radar-derived hourly rain rates

During the 37 “Wet-Gauge hours”, the total rainfall amount according to the Giuliana Gauge was 97.4 mm. According to the Palermo Radar, the total rainfall amount was 74.6 mm, which means a residual “Wet-Gauge Mean Field Bias” of -1.2 dB (radar underestimation). Based on these 37 “Wet-Gauge” hourly amounts, the **Scatter** results to be **1.47 dB**. (as can be seen in Fig. 12). Such 37 Radar-Gauge data pairs are shown in Fig. 13.

Bisacquino Radar performances. Scatter is 1.47 dB - 37 hourly amounts with $G \geq 0.4$ mm/h

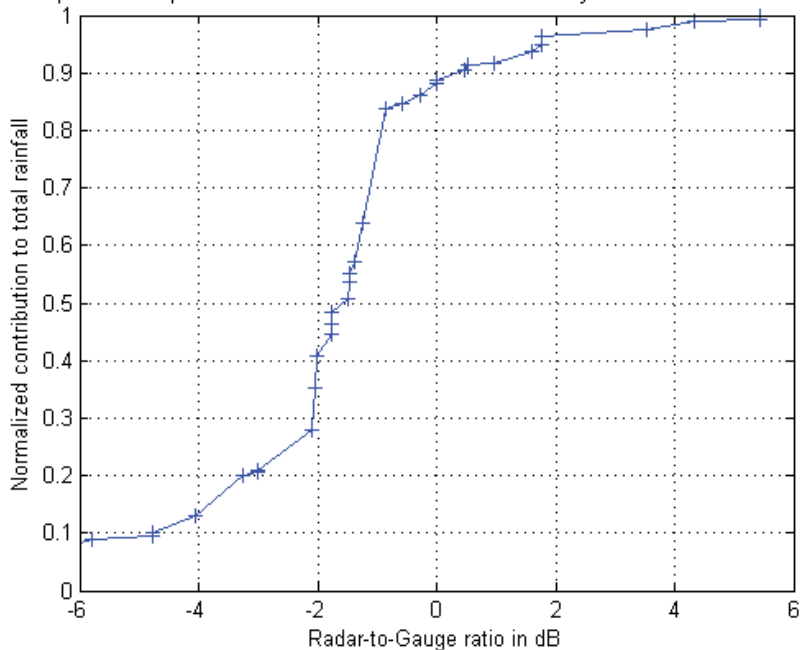


Fig. 12. As for Fig. 8, but for the 37 samples ($G \geq 0.4$ mm/h) of the Giuliana rain gauge.

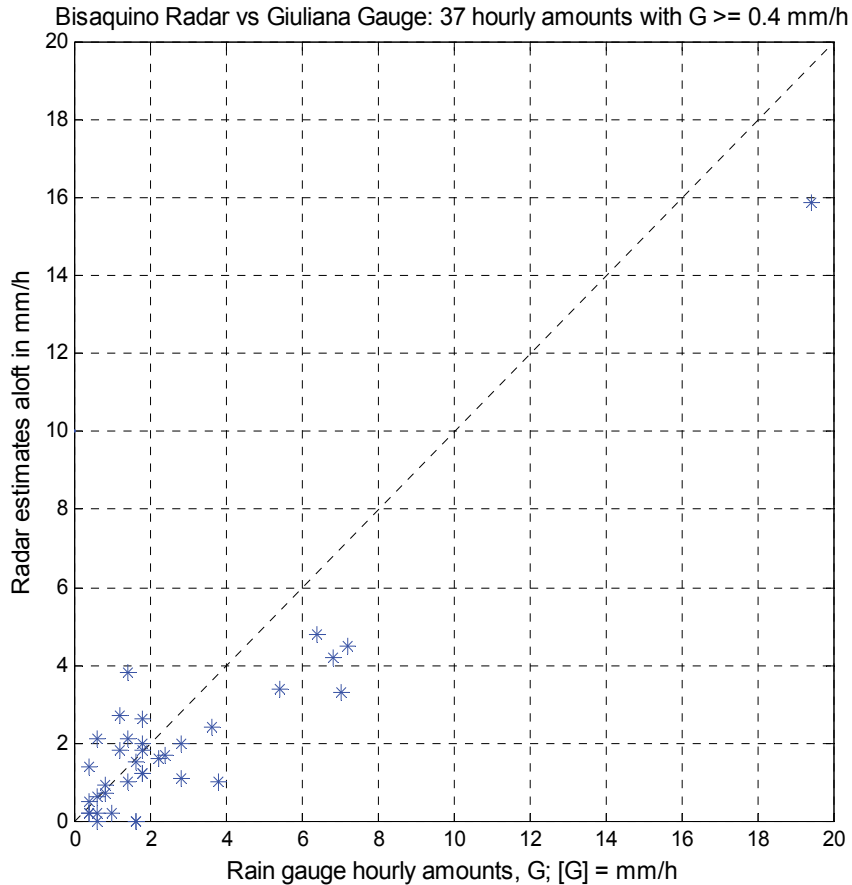


Fig. 13. Scatter plot of 37 hours with Giuliana gauge amounts larger or equal than 0.4 mm/h and the corresponding Bisacquino radar estimates. It is worth noting that in this case the maximum value of the linear scale for the scatter plot is 20 mm/h.

Using only the 29 hours where BOTH the Radar AND the Gauge amounts were larger or equal to 0.4 mm/h, the total Gauge (Radar) amount was 90.6 (73.5) mm. Consequently, the “wet-wet” Mean Field Bias is -0.9 dB. Also the “wet-wet” Scatter improves slightly: based on such 29 “wet-wet” hours, it results to be 1.31 dB, as it can be seen from Fig. 14. The 0.16 dB decrease in the value of the Scatter is a clue of the almost marginal rain amount missed by the radar during the 8 “Missing Detection hours” (6.8/97.4).

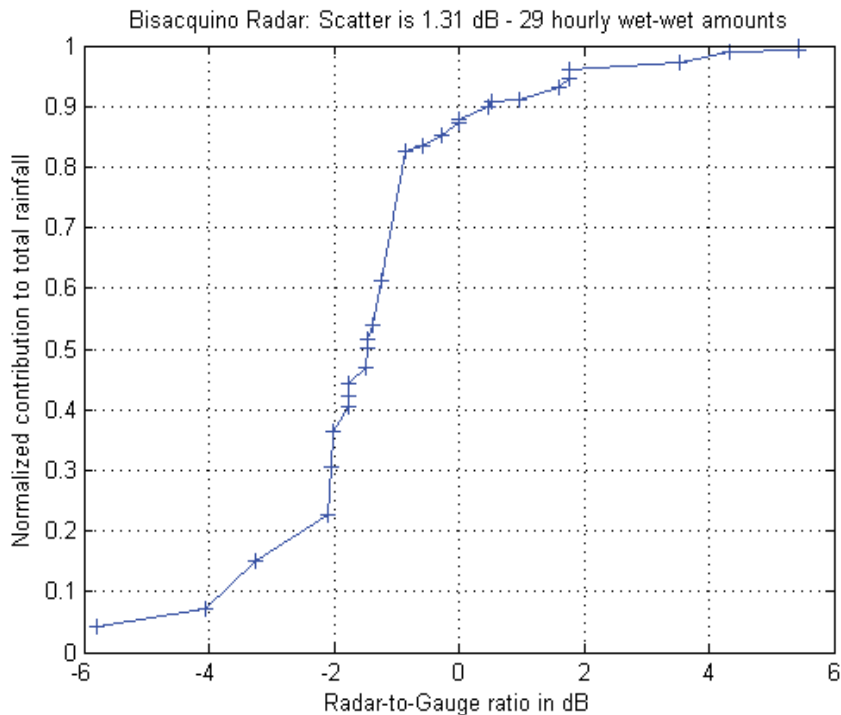


Fig. 14. As for Fig. 12, but for 29 samples with both R and G ≥ 0.4 mm/h.

4.4 Quantitative precipitation estimation for the Torino radar

The Torino radar is located on the roof of the Politecnico di Torino (Electronics and Telecommunications Department): its latitude is $45^{\circ}.063$; the longitude is $7^{\circ}.660$; the altitude is 275 m above Mean Sea Level (MSL).

For the quantitative evaluation of the radar estimates we have been using three rain gauges: Castagneto Po, Ciriè and Nichelino. The observation period is based on 42 hours.

For the rain gauge of Castagneto Po, the radar visibility is similar to that of Palermo radar versus Altofonte gauge, although the range is considerably longer: 21.1 km. As it can be seen from Fig. 15 (left picture), which shows the radar-gauge profile, the ground clutter contamination at the gauge location should be negligible since the device is luckily just behind the top of the hill: this means that Torino radar echoes above the gauge are at least ground-clutter-free. For the rain gauge in Ciriè, the range is 18.7 km, while the situation is worse in terms of ground clutter: the gauge location (Fig. 15, right) is, in fact, visible from the radar site. For the Nichelino gauges the situation is similar.

For what concerns QPE, we have at our disposal data from the 3 gauges during the same 42 hours (April 2011). During these 126 hours the Gauge (Radar) total amounts was 121.7 (114.2) mm, which corresponds to an "overall Bias" of -0.3 dB (radar underestimation).

Out of 126 analyzed hours, in 63 (45) cases the Gauge (Radar) derived hourly rainfall amount was larger than 0.4 mm/h (see the next Sec. 4.4.1 and Table 4 for more details).

4.4.1 Wet versus dry hours discrimination

From Table 4, we can see that on the one hand the number of Missing Detections (22) is relatively high: hence POD is relatively small 0.65; FAR is relatively small: 0.089. Finally, HSS results to be **0.587**, which is by chance exactly the same as HK .

	$G \geq 0.4 \text{ mm/h}$	$G < 0.4 \text{ mm/h}$	
$R \geq 0.4 \text{ mm/h}$	41	4	45
$R < 0.4 \text{ mm/h}$	22	59	81
	63	63	126

Table 4. Contingency table for the Torino radar and 3 gauges (42-hour observation period).

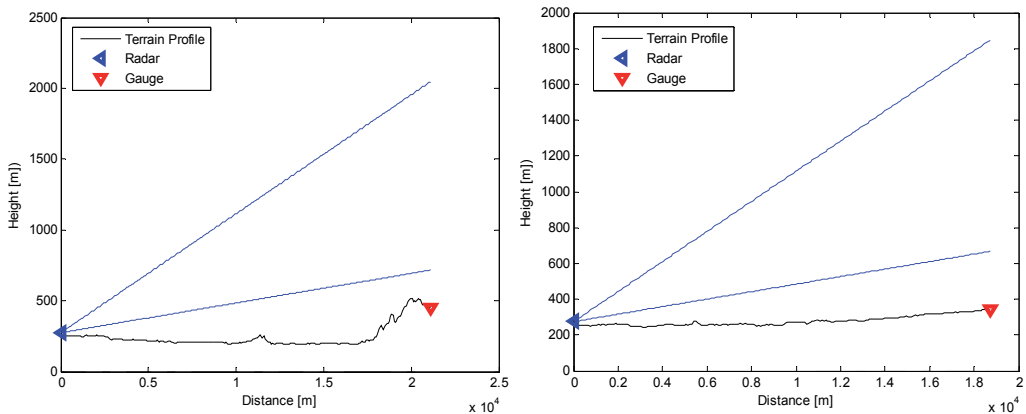


Fig. 15. As in Fig. 6, but for the Torino radar. Left: Castagneto Po-Torino Radar profile; right: Ciriè-Torino Radar profile.

4.4.2 Quantitative agreement between gauge and radar-derived hourly rain rates

During the 63 “Wet-Gauge hours”, the total rainfall amount measured by the three gauges was 119.7 mm. The corresponding radar-derived amount was 108.0 mm. Based on these “Wet-Gauge” 63-hourly amounts the Bias is -0.4 dB . As can be clearly seen from Fig. 16, the agreement between the radar and the 3 gauges is quite poor. This fact is obviously reflected in the amazingly large value of the Scatter, which is as bad as $5.38! \text{ dB}$.

Fig. 17 shows the 63 “Wet-Gauge hours” hourly amounts as measured by the gauges at the ground and as derived from radar echoes aloft: the large scatter between such different devices and their different sampling modes is again evident.

Using only the 41 hours where BOTH the Radar AND the Gauge amounts were larger or equal to 0.4 mm/h , the total rainfall amount measured by the three gauges is reduced to 94.5 mm. The corresponding radar-derived amount remains instead almost the same: 106.2 mm. Consequently, the “wet-wet” Mean Field Bias increases and becomes even positive: $+0.5 \text{ dB}$ (radar overestimation). Also the “wet-wet” Scatter improves remarkably: based on such 41 “wet-wet” hours, it results to be 3.73 dB , which is still a figure much worse than the one obtained for the 2 radars in Sicily. Such huge Scatter value decrease (high sensitivity to different radar thresholds) is again a clue of the poor QPE agreement for the Torino radar.

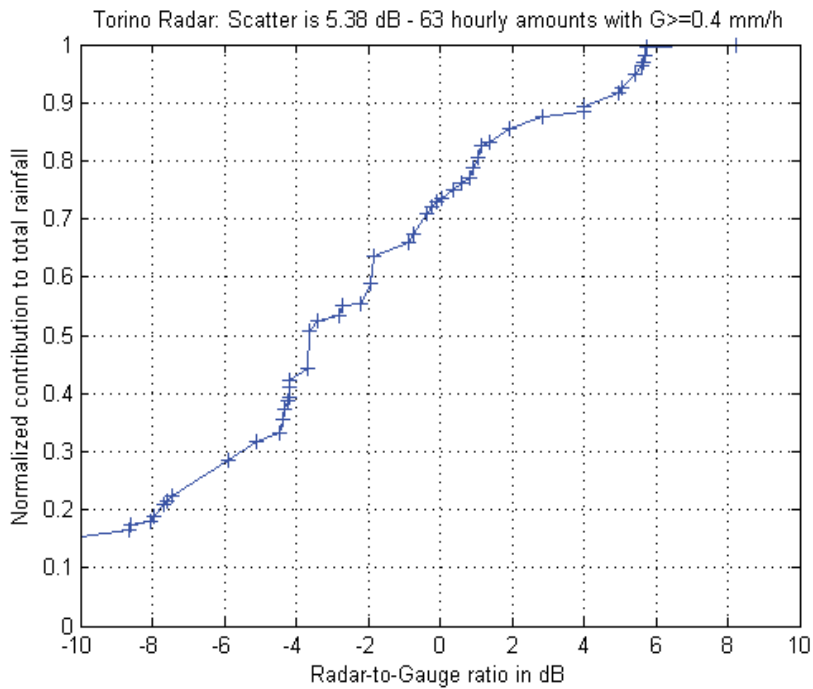


Fig. 16. As for Fig. 8, but for 63 samples with $G \geq 0.4$ mm/h.

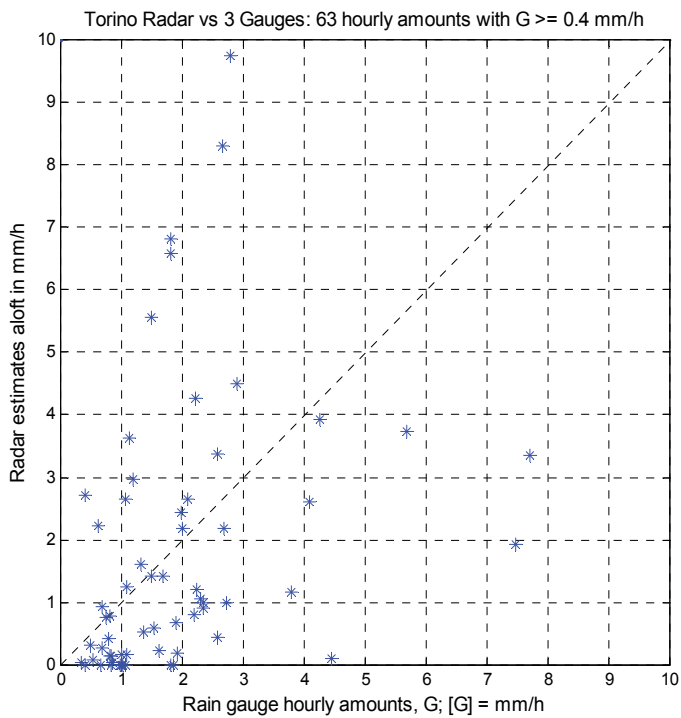


Fig. 17. Same as Fig. 7, but for the Torino radar (63 hours with $G \geq 0.4$ mm/h).

4.5 QPE Summary in terms of bias and scatter in dB

For the three mini-radar sites discussed in the previous paragraphs, Table 5 provides a summary of the QPE evaluation in terms of Bias in dB (as a function of the number of considered hours). When all the wet and dry hours are considered, we have the so-called “overall” Bias: it includes False Alarm events (mainly caused by ground clutter contamination) and Missing Detection (caused by beam overshooting, see Sec. 1.2 and, in some cases, attenuation) events; it is certainly the most resistant and complete definition of Bias. It is obviously a measure of the mean error and says nothing about the error dispersion around the mean. For this purpose, there is the Scatter, which will be presented in the Table 6.

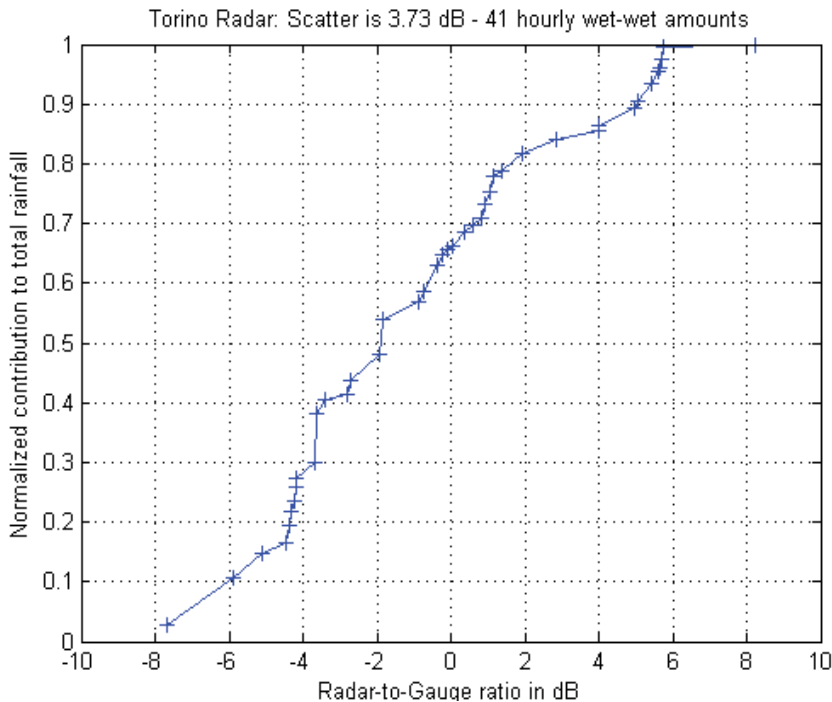


Fig. 18. As for Fig. 16, but for but for 41 samples with both R and G ≥ 0.4 mm/h.

While the “overall” Bias (1st column) includes both wet and dry periods, the other two Bias (2nd and 3rd column) are conditional upon rain: the “Wet-Gauge” Bias considers only hours where the gauge amounts are larger than 0.4 mm/h; finally, the definition of “wet-wet” Bias reduces further the number of hours used in the calculus: in such case, only hours with both radar and gauge amounts larger than 0.4 mm/h are used.

Site	“Overall” Bias	“Wet-Gauge” Bias	“Wet-Wet” Bias
Palermo radar	-0.9 dB (144 h)	-1.1 dB (48 h)	-0.7 dB (38 h)
Bisacquino radar	-1.0 dB (96 h)	-1.2 dB (37 h)	-0.9 dB (29 h)
Torino radar	-0.3 dB (126 h)	-0.4 dB (63 h)	+0.5 dB (41 h)

Table 5. QPE evaluation summary in terms of Bias for three mini-radar sites. The number of hours of each data set are given in parentheses.

Table 6 summarizes the dispersion of the radar-gauge errors using the hydrological-oriented score called **Scatter** (see Sec. 4.1.2). Since, as discussed previously, in the radar detection process (see for instance the “multiplicative” nature of the meteorological radar equation derived by *Probert-Jones* [1962]), the multiplicative nature of error prevails, the Scatter is defined as a ratio between the Radar (the device under test) and the Gauge (the reference). Hence, dry hours cannot be considered in evaluating the Scatter (unless using some trick, like for instance adding a negligible amount...) Consequently, only “Wet-Gauge” hours or “wet-wet” hours are considered in Table 6.

It can be concluded that the three-presented X-band radars are less reliable at low rain rates. By limiting the observations to hours with both Radar and Gauge amounts larger than 0.4 mm/h, the agreement improves not only in terms of Bias, but most of all in terms of Scatter. Finally, in the interpretation of these values of Bias and Scatter, it is important to bear in mind the large intrinsically different sampling modes as well as mismatches in time of the radar and gauge devices (e.g. *Zawadzki* [1975]).

Site	“Wet-Gauge” Scatter	“Wet-Wet” Scatter
Palermo radar	2.38 dB (48 h)	1.97 dB (38 h)
Bisacquino radar	1.47 dB (37 h)	1.31 dB (29 h)
Torino radar	5.38 dB (63 h)	3.73 dB (41 h)

Table 6. QPE evaluation summary in terms of Scatter for three mini-radar sites. The number of hours of each data set are given in parentheses.

5. Open issues and limitations

Short-wavelength (X-band) radar has the benefit of attaining high spatial resolution with a smaller antenna. However, there is a clear disadvantage compared to longer wavelengths: an increased attenuation in the presence of precipitation. Imagine three 2-km convective cells with instantaneous rain rate of 20, 40 and 100 mm/h respectively: at X-band frequencies these cells would cause two-way attenuation in radar reflectivity values of approximately 1.5, 3.6! and 11!! dB. Such figures preclude not only the use of X-band radar for long-range monitoring but also an accurate QPE, even at short-range. A partial remedy could be the use of polarimetric information, but this would remarkably increase the cost of the system: in the interesting work by *Mc Laughlin et. al* [2009], the cost of a Doppler, fully Polarimetric advanced X-band system developed within the framework of the CASA project is estimated in approximately 180 kEuro, which is almost 8 dB more expensive than our low-cost, semi-quantitative approach.

6. Summary: Filling the gap, which is observing the lowest part of the troposphere at short-range with portable, low-cost radars

Radar sampling volume increases with the square of the range (beam broadening) therefore, at longer ranges, small but intense features of the precipitation system are blurred (non-homogeneous beam filling). Furthermore, it is more likely to include different types of hydrometeors (e.g. snow, ice, rain drops), especially in the vertical dimension. At long-range, because of the decreased vertical resolution, the lower part of the sampling volume can be in rain whereas the upper part can be even characterized by an echo weaker than the radar sensitivity itself (beam overshooting).

By the term “range degradation” we mean several important sources of uncertainty regarding radar-based estimates of rainfall: beam broadening, non-homogeneous beam filling, partial beam occultation, overshooting and, depending on the operating frequency, attenuation. Such sources of uncertainty in general increase with increasing range. Current approaches to operational weather observation are based on the use of physically large, high-power, long-range radars, which are blocked from viewing the lower part of the troposphere by the Earth’s curvature combined with orography. Hence, range degradation is one of the main problems in QPE and certainly a key factor in the underestimation of rainfall accumulation at far ranges with conventional long-range radars (e.g. *Kitchen and Jackson* [1993], *Smith et al.* [1996], *Meischner et al.* [1997], *Seo et al.* [2000], *Gabella et al.* [2000], *Chumechean et al.* [2004], *Joss et al.* [2006]).

This Chapter describes an alternate approach based on networks of large number of small, low-cost, X-band radars. Spacing these radars twenty kilometers apart defeats the Earth’s curvature problem and enables the sampling of the lowest part of the troposphere using small antennas and low-power transmitters. Such networks can provide observing capabilities which supplement the operational state of the art radar network satisfying at the same time the needs of multiple users. Improved capabilities associated with this technology include low-altitude coverage and high temporal resolution. This technology has the potential to supplement the widely spaced networks of physically large high-power radars in use today.

Indeed, short-wavelength low-cost radar is able to fill a remarkable gap in observational meteorology: small, low-cost, radars can be used to supplement conventional, long-range radar networks in complex orography regions (e.g. the Alps and the Apennines), in highly populated areas (improving urban hydrology in major towns), in sensitive regions (areas prone to hydro-geological hazards) and along technological networks (e.g. highways, gas pipelines, ...) New important spatio-temporal scales (see Table 7), which characterize the highly variable precipitation field can now be investigated at affordable costs thanks to portable, low-cost, X-band weather radar developed, among others, by the Remote Sensing Group at Politecnico di Torino.

Type of device	Band	Cost	Coverage	Sampling vol.	Temporal res.
TRMM (or future GPM) spaceborne radar	Ku (Ka)		global	$5 \cdot 10^9 - 10^{10} \text{ m}^3$	Once per day
Long-range, Doppler, dual-pol radar	S (C)	1000 to 2000 k€	200 000 km ²	$10^5 - 10^9 \text{ m}^3$	300 s
Medium-range dual-pol radar	X	200 to 500 k€	5000 km ²	$10^4 - 10^8 \text{ m}^3$	120 s
Short-range radar	X	30 k€	2000 km²	$10^4 - 10^7 \text{ m}^3$	30 s
Rain Gauge	---		point	50 m ³	600 s
Disdrometer	---		point	10 m ³	1800 s

Table 7. The observational gap filled by the new portable, low-cost X-band weather radar network.

7. Acknowledgements

Gauge data were provided by the Regione Autonoma Valle d'Aosta - Ufficio Meteorologico della Protezione Civile, the Servizio Informativo Agrometeorologico Siciliano and Weather Underground. The mini radar development was possible thanks to the financial and technical support by Consorzio Interuniversitario per le Fisiche della Atmosfera (CINFAI).

8. References

- Chumchean, S., Seed, A., and A. Sharma, 2004: Application of scaling in radar reflectivity for correcting range dependent bias in climatological radar rainfall estimates, *J. Atmos. Ocean. Technol.*, 21, 1545-1556.
- Doelling, I. G., J. Joss, and J. Riedl, Systematic variations of Z-R relationships from drop size distributions measured in Northern Germany during seven years, *Atmos. Res.*, 48, 635-649, 1998.
- Gabella, M., M. Bolliger, U. Germann, and G. Perona, 2005: Large sample evaluation of cumulative rainfall amounts in the Alps using a network of three radars, *Atmos. Res.*, 77, 256-268.
- Gabella, M., J. Joss, and G. Perona, 2000: Optimizing quantitative precipitation estimates using a non-coherent and a coherent radar operating on the same area, *J. Geophys. Res.*, 105, 2237-2245.
- Gabella M., Joss J., Michaelides S., Perona G., 2006: Range adjustment for Ground-based Radar, derived with the spaceborne TRMM Precipitation Radar, *IEEE Trans. on Geosci. Rem. Sens.*, 44, 126-133, doi: 10.1109/ TGRS.2005.858436
- Gabella M., Orione F., Zambotto M., Turso S., 2008: A Portable Low-Cost X-Band Radar For Rainfall Estimation In Alpine Valleys - Analysis of radar reflectivities and comparison between remotely sensed and in situ measurements, FORALPS Final Meeting Report, ISBN 978-88-8443-235-3, pp. 39.
- Gabella M., Morin E., Notarpietro R., 2011a: Using TRMM spaceborne radar as a reference for compensating ground-based radar range degradation: Methodology verification based on rain gauges in Israel, *J. Geophys. Res.*, 116, D02114, doi: 10.1029/2010JD014496
- Gabella M., Morin E., Notarpietro R., Michaelides S., 2011b: Precipitation field in the Southeastern Mediterranean area as seen by the Ku-band spaceborne weather radar and two C-band ground-based radars, *Atmos. Res.*, doi: 10.1016/j.atmosres2011.06.001.
- Germann U., Galli G., Boscacci M., Bolliger M., Gabella M., 2004: Quantitative precipitation estimation in the Alps: where do we stand?, *Third European Conference on Radar meteorology ERAD2004*, Visby, Sweden, 2-6.
- Hogan, R. J., O'Connor E. J. and A. J. Illingworth 2009: Verification of cloud-fraction forecasts, *Q. J. Royal Meteorol. Soc.*, 135, 1494-1511.
- Joss J., Gabella M., Michaelides S., and G. Perona, 2006: Variation of weather radar sensitivity at ground level and from space: case studies and possible causes, *Meteorol. Z.*, 15, 485-496, doi: 10.1127/0941-2948/2006/0150.
- Kitchen, M., and P.M. Jackson, 1993: Weather radar performance at long range simulated and observed, *J. Appl. Meteor.*, 32, 975-985.

- Marshall, J. S. and W. M. Palmer, 1948: The distribution of raindrops with size, *J. Meteor.*, 5, 165-166.
- Mc Laughlin and other 28 coauthors, 2009: Short-wavelength technology and the potential for distributed networks of small radar systems, *Bull. Am. Meteorol. Soc.*, 90, 1797-1817.
- Meischner, P., Collier, C., Illingworth, A., Joss J., and W. Randeu, 1997: Advanced weather radar systems in Europe: the COST 75 action, *Bull. Am. Meteorol. Soc.*, 78, 1411-1430.
- Murphy, A. H., 1996: The Finley affair: A signal event in the history of forecast verification, *Weather Forecast.*, 11, 3-20.
- Notarpietro R., Zambotto M., Gabella M., Turso S., Perona G., 2005: The radar-ombrometer: a portable, low-cost, short-range X-band radar for rain estimation within valleys, VOLTAIRE final conference joint with the 7th European Conference on Applications of Meteorology (ECAM7) and the European Meteorological Society meeting (EMS05), September 12-16, Utrecht, The Netherlands, 19.
- Probert-Jones, J. R., 1962: The radar equation in meteorology, *Quart. J. Royal Meteorol. Soc.*, 88, 485-495.
- Seo, D. J., Breidenbach J., Fulton R., Miller D., and T. O'Bannon, 2000: Real-time adjustment of range-dependent biases in WSR-88D rainfall estimates due to non-uniform vertical profile of reflectivity. *J. Hydrometeorol*, 1, 222-240.
- Smith, J. A., Seo D. J., Baeck M. L., Hudlow M. D., 1996: An inter-comparison study of NEXRAD precipitation estimates, *Water Resour. Res.*, 32, 2035-2045.
- Tartaglione N., 2010: Relationship between precipitation forecast errors and skill scores of dichotomous forecasts, *Weath. Forec.*, 25, 355-364.
- Young C. B., Nelson B. R., Bradley A. A., Smith J.A., Peters-Lidard C. D., Kruger A., Baeck M. L., 1999: An evaluation of NEXRAD precipitation estimates in complex terrain, *J. Geophys. Res. Atmos.*, 104, 19691-19703.
- Sauvageot, H., 1992: *Radar Meteorology*, Boston, Artech House.
- Zawadzki I., 1975: On radar-raingage comparison, *J. Appl. Meteorol.*, 14, 1430-1436.

Part 3

Tropospheric Wind and Turbulence Observations

Retrieving High Resolution 3-D Wind Vector Fields from Operational Radar Networks

Olivier Bousquet

*Météo-France, Centre National de Recherches Météorologiques
France*

1. Introduction

The ability to retrieve 3-D wind vector fields in a fully operational framework has a potentially wide-ranging impact on a variety of meteorological research and operational meteorological applications. This capability was recently evaluated by the French Weather Service in the course of an upgrade program aiming to introduce Doppler and dual-polarimetric technologies within its radar network. Starting in November 2006, real-time multiple-Doppler wind fields have been produced routinely every 15 minutes for 2 years within a 320x320 km² domain centered on Paris city (Bousquet et al. 2007, 2008a). The evaluation of wind fields synthesized in this framework was carried out from observations collected in a variety of weather situations including low-level cyclones, frontal systems and squall lines. Wind vectors retrieved in the greater Paris area were generally proved very realistic and have been found reliable enough to be used for research applications (mesoscale meteorology, statistical analysis) and numerical model verification (Bousquet et al. 2008b). In order to prepare for the field phase of the international Hydrological Mediterranean Experiment (HyMeX¹), which will be conducted in 2012-2013, this analysis has later been successfully extended to regions of complex terrain located in the southern part of the country (Bousquet, 2009). The ability to perform operational wind retrieval in mountainous areas is an important step to improve our understanding of orographic precipitation developing in these usually poorly instrumented regions, and also demonstrates that operational real-time wind retrieval could potentially be carried out over the entire French territory - ground elevation exceeds 500 m over ~ 1 fifth of mainland France - which was the initial objective of the French Weather Service when this experiment was started. In 2009, the wind retrieval analysis was therefore extended to the full metropolitan radar network with the goal to implement an operational, nationwide, three-dimensional reflectivity and wind field mosaic to be ultimately delivered to forecasters and modelers, as well as automatic nowcasting systems for air traffic management purposes. In this composite analysis, which is expected to become operational in 2013, data collected by all 24 radars of the French radar network are concentrated, pre-processed and combined in real-time at a frequency of 15 minutes to retrieve the complete wind vector (u,v,w) and

¹ HyMeX is an international program that aims at a better understanding and quantification of the hydrological cycle and related processes in the Mediterranean, with emphasis on high-impact orographic weather events. Information about this program can be found on <http://www.hymex.org>

reflectivity fields at a horizontal resolution of 2.5 km within a domain of approximately 1000 x 1000 x 12 km³. This achievement, through the size of the retrieval domain, the number of Doppler radars (24) involved in the analysis, and the fact that retrieved three-dimensional winds rely exclusively on an operational infrastructure, represents an unprecedented breakthrough in operational applications of the Doppler information, which are so far generally limited to clutter filtering and Velocity Azimuth Display analysis (VAD, Browning and Wexler 1968).

The present study aims at examining the technical requirements needed to achieve real-time operational multiple-Doppler analysis in an operational framework, as well as to evaluate the performance and usefulness of three-dimensional wind composite retrieved from operational radar systems. After a recall of the principle of dual-Doppler wind retrieval and a description of the French radar network characteristics winds retrieved in this operational framework are evaluated using outputs produced during various high impact weather events that recently occurred over mainland France. This includes the extratropical storm Klaus, already referred to as the storm of the decade by many European forecasters, which stroke France with hurricane strength winds on 24 January 2009, as well as a heavy orographic precipitation event that occurred over the Massif Central Mountains in September 2010. The potential value of these unique datasets for both operational and a research application is also discussed with emphasis on the upcoming HyMeX program.

2. Wind retrieval

2.1 Principle of dual-Doppler wind retrieval

All current **dual-Doppler** analysis techniques originate from the seminal work of Armijo (1969) who demonstrates that it was possible to retrieve the three components of the wind field in precipitating area using i) the precipitation radial velocity data collected by 2 Doppler radars, ii) the anelastic air mass continuity equation and iii) empirical relationships between radar reflectivity and precipitation fallspeed (Z-R relationships). Among the numerous methods based on Armijo's methodology, three groups can be identified: i) analytical approaches (e.g. Scialom and Lemaitre 1990), which aim at retrieving the wind field under its analytical form, ii) coplane techniques (Lhermitte and Miller 1970, Chong and Testud 1996), which allow resolving the wind field in a cylindrical space and, iii) Cartesian methods, which aim to resolve the wind field in a Cartesian space by the mean of an iterative process between the radial velocity equations and the continuity equation (Heymsfield 1978). Among those 3 families, the latter is the most computationally efficient and the easiest to implement, making it by far the most popular method with researchers.

Despite its relative simplicity, the Cartesian method has nevertheless been an inexhaustible source of inspiration for radar scientists and led to more than 50 peer-reviewed publications over the last 30 years. Although highlighting a particular method among all available Cartesian techniques is difficult, one could mention the approaches proposed by Gamache (1995) – detailed information about this technique can be found in the appendix of Reasor et al. (2009) – Bousquet and Chong (1998) and Gao et al. (1999). All three techniques significantly improved the Cartesian approach by suppressing the iterative process traditionally associated with Cartesian retrieval algorithm (see below).

2.2 The MUSCAT analysis

The wind retrieval technique used by the French Weather Service is the Multiple-Doppler Synthesis and Continuity Adjustment Technique (MUSCAT), which is a variational algorithm allowing for a simultaneous and computationally efficient solution of the three Cartesian wind components (u, v, w). This method was originally proposed by Bousquet and Chong (1998) to overcome the drawbacks of iterative analysis techniques used to process data collected by airborne Doppler radars. It was later adapted to ground-based radars (Chong and Bousquet 2001) in order to analyze observations collected during the field phase of Mesoscale Alpine Programme (Bougeault et al. 2001) during which it was used in a semi-operational mode to guide research aircrafts in the field (Chong et al., 2000). The MUSCAT algorithm has been used successfully for more than 10 years in order to synthesize data collected by ground-based and mobile research radars (e.g. Bousquet and Chong 2000, Georgis al. 2003, Bousquet and Smull 2006), and has even been applied to wind lidars (Drechsel et al. 2009). In order to use this algorithm in an operational framework a modification of the initial MUSCAT formalism was proposed by Bousquet et al. (2008a) to take into account extensive radar separation distances prevailing in operational radar networks.

The current form of the MUSCAT algorithm is given hereafter. It consists in a global minimization, in a least-squares sense, of the function F :

$$F(u, v, w) = \int_S [A(u, v, w) + B(u, v, w) + C(u, v, w) + D(u, v)] dx dy \quad (1)$$

such that,

$$\frac{\partial F}{\partial u} \approx 0, \quad \frac{\partial F}{\partial v} \approx 0 \quad \text{and} \quad \frac{\partial F}{\partial w} \approx 0. \quad (2)$$

The expression of term A is given by:

$$A_{i,j}(u, v, w) = \frac{1}{N} \sum_{p=1}^{n_p} \sum_{q=1}^{n_q(p)} \omega_q [\alpha_q u + \beta_q v + \gamma_q (w + v_T) - V_q]^2 \quad (3)$$

where u, v, w , are the components of the wind field at grid point (i, j) ; V_T is the terminal particle fallspeed at grid point (i, j) evaluated from empirical relationships with pre-interpolated radar reflectivity, subscript q defines the q^{th} measurement of a total number n_q that is observed from the p^{th} radar and that falls inside an ellipsoid of influence centered on the grid point (i, j) ; N is the total number of n_q 's over the considered domain; ω_q is the Cressman weighting function depending on the distance between measurement q within the ellipsoid and the considered grid point; and n_p is the total number of radars covering grid point (i, j) (≥ 2).

This term represents the optimal least-squares fit of the observed radial Doppler velocities to the derived wind component. The Cressman distance-dependent weighting function accounts for non-collocated data and grid point values, and allows the interpolation of the radar data onto the Cartesian grid of interest, in the data fit. In the current framework, the interpolation is performed using a fixed horizontal influence radius of the Cressman

weighting function R_H of 3 km and a variable vertical radius of influence R_V that matches the beamwidth of ARAMIS radars.

Term B is given by:

$$B(u, v, w) = \mu_1 \left(\frac{\partial u}{\partial x} + \frac{\partial v}{\partial y} + \frac{1}{\rho} \frac{\partial \rho w}{\partial z} \right)^2 \quad (4)$$

where ρ is the air density and μ_1 is a normalized weighting parameter that controls the relative importance of this term with respect to term A .

This term represents the least-squares adjustment with respect to mass continuity. It is formulated for each individual grid box in terms of mass flux throughout the faces of the considered box, which allows solving the wind field over both flat and complex terrains (Chong and Cosma 2000). In this formalism the wind components estimated at the previously investigated plane are used as input values to solve the wind at the current level. In order to initialize the wind synthesis, horizontal components are assumed constant between the surface and the first plane for which the solution for the wind components is searched.

Term C is given by:

$$C(u, v, w) = \mu_2 [J(u) + J(v) + J(w)]^2 \quad (5)$$

where J is a differential operator based on 2nd and 3rd derivatives of the wind components [see Bousquet and Chong (1998) for the detailed expression of this term].

It is a constraint that acts as a low pass filter. Term C allows decreasing small-scale wind variations through the minimization of the second- and third order derivatives. It is controlled by a weighting factor μ_2 , which is a function of the cutoff wavelength of the filter. In addition to provide more regular fields, this term is also essential to obtain an objective solution in regions of ill-conditioned analysis through realizing a regular extrapolation in these regions from surrounding properly conditioned areas.

Finally, D is given by:

$$D(u, v) = \mu_3 \left(\frac{\partial (u \sin^2 \alpha_i - v \sin \alpha_i \cos \alpha_i)^2}{\partial x} + \frac{\partial (-u \sin \alpha_i \cos \alpha_i + v \cos^2 \alpha_i)}{\partial y} \right)^2 \quad (6)$$

where μ_3 is given by:

$$\mu_3 = \cos^4 \beta_m \quad (7)$$

and β_m defines the angle between the horizontal projection of the two radar beam axes.

Term D is a constraint that is applied in regions covered by only 2 radars. It allows minimizing the variation of the cross-baseline component of the wind. Its effect is maximum close to the radar baseline and weak in properly conditioned areas (the reader is referred to Bousquet et al. 2008b for more details about this specific term).

According to Equations 3-6, the three-dimensional wind field reconstructed by MUSCAT represents a least squares fit to the available observations and does not perfectly satisfy the mass continuity equation. In order to obtain a wind field that truly verifies this equation, a posteriori upward integration is needed to limit the errors in the vertical component. Many integration methods can be found in the literature to accomplish this last step. For operational applications the basic adjustment technique proposed by O'Brien (1970) was chosen. This method consists in adjusting the vertical velocity by forcing w to be zero at the bottom and top of any column and to linearly distribute the error throughout the column.

3. Operational radar data

3.1 Overview of the French radar network

The French metropolitan operational radar network ARAMIS (Application Radar a la Météorologie Infra-Synoptique) is composed of 16 C-band and 8 S-band Doppler radars. 10 of these radars are equipped with dual-polarization capabilities and we expect the network to be fully polarimetric by 2016. The ARAMIS network covers about 95 % of mainland France with radar baselines fluctuating from ~ 200 km in the northern part of the country to ~ 60 km in Southeastern France (Fig. 1). It is composed of 5 different types of radars ranging from 25-year old facilities, with limited workload and scanning capabilities, to state of the art dual-polarimetric radar systems. All systems are however equipped with the same radar processor, which allows producing harmonized products despite different hardware characteristics. The French Weather Service, Météo-France, also operates 8 S-band Doppler radars overseas, as well as 2 "gap filling" polarimetric X-band radars in the French Alps. Those 10 additional radars are not considered in this paper.

3.2 The triple PRT Doppler scheme

Doppler capabilities have been introduced in 2002 in the frame of an 8-year upgrade program aiming to modernize the network and fill some gaps in the radar coverage. During this period, all radars have been progressively equipped with the triple pulse rise time (PRT) Doppler scheme proposed by Tabary et al. (2006). This scheme, which is based on the approach proposed by Zrníc and Mahapatra (1985), consists in operating the radars at different pulse repetition frequencies (PRF) in order to mitigate the effect of the "Doppler dilemma" ensuing from the inverse relationship between the unambiguous range and the unambiguous velocity (Doviak and Zrníc 1993). The French scheme yields an extended Nyquist velocity of 60 m s^{-1} up to a range of ~ 250 km. Its particularity lies in the fact that interleaved frequencies are rather low (379, 321, and 305 Hz). This allows this scheme to be indifferently implemented on old and new radars, but also to get rid of potential second trip returns.

The capacity to retrieve multiple-Doppler winds in an operational framework directly arises from the mitigation of the Doppler dilemma. Indeed, one of the main consequences of this long lasting issue is to limit operational Doppler measurements to short range (~ 100 km) so as to mitigate velocity ambiguities resulting from the aliasing of radial velocities outside of the Nyquist interval. Because operational Doppler radars are generally separated by hundreds of kilometers, this limitation in range dramatically impedes overlapping areas where airflow can be successfully reconstructed, and does not allow for adequate dual- or multiple-Doppler wind synthesis.

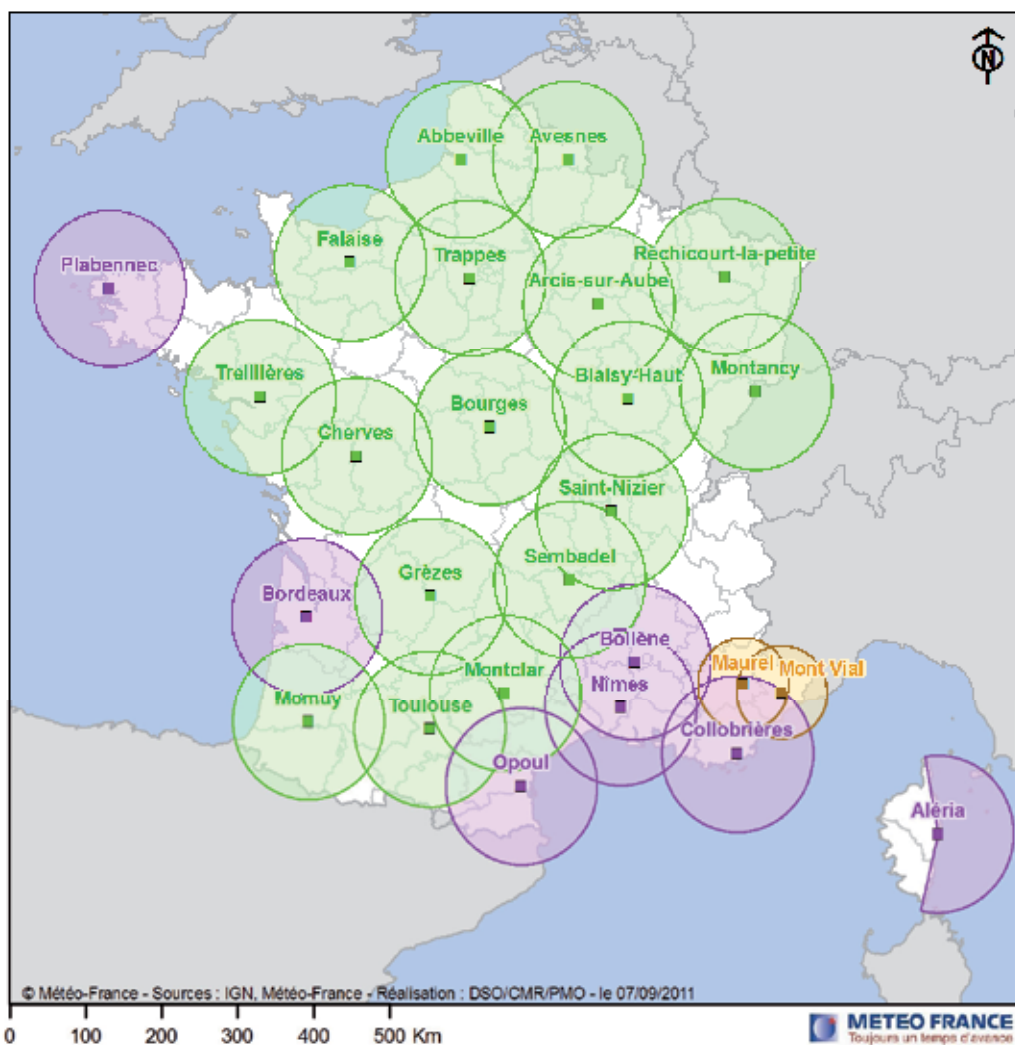


Fig. 1. Map of the French operational radar network ARAMIS. The 100 km (50 km for X-band) ranges of measurement associated with each radar are shown by circles. Green, purple and yellow colors correspond to C-, S-, and X-band radars, respectively.

In France, the ability to measure Doppler velocities at long range allows for a significant dual- and multiple-Doppler coverage over a large part of the country. The resulting coverage is quite heterogeneous due to the principle of ground-based radar measurements and is slightly superior in southern France due to the higher network density in this region. Between a height of 2 and 10 km (Fig. 2a) ~90% of the country is covered by at least 2 radar systems. Multiple-Doppler coverage (3 radars or more) is maximized between 2.5 and 9 km altitude, where ~80% of the French territory being covered by at least 3 radars. The radar overlapping near the surface is however quite limited due to both extensive radar baselines and beam blocking by terrain. The detailed maps of radar coverage at 2.5 and 5 km are shown in Fig. 2b-c.

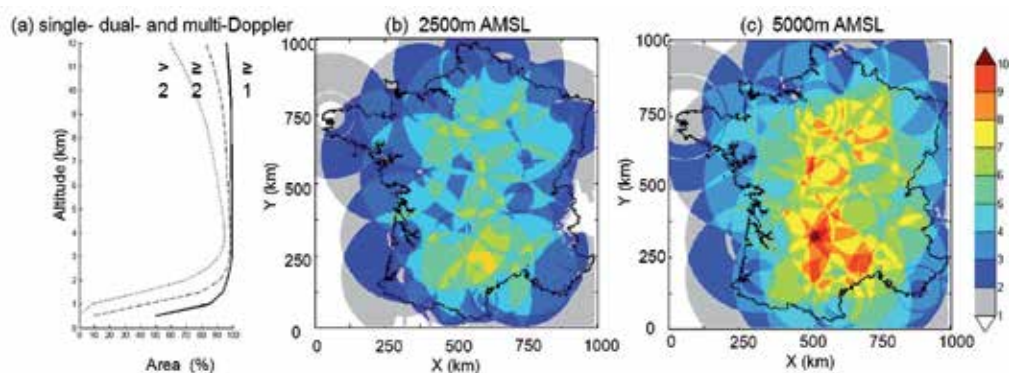


Fig. 2. (a) Radar overlapping within mainland France as a function of height and detailed overlapping map at (b) 2.5 and (c) 5 km AMSL.

3.3 Data processing

Reflectivity and radial velocity observations collected by all (24) ARAMIS radars are concentrated at the national center, in Toulouse, and automatically processed every 15'. Data consist in Cartesian, 512 km x 512 km, 1 km² in resolution, sweeps of radar observations, which are already exploited for current operational applications such as VAD analysis, quantitative precipitation estimates (Tabary et al. 2011) or data assimilation (Montmerle and Faccani 2009). Spurious reflectivity echoes are removed by the mean of a threshold on the pulse-to-pulse fluctuation of the reflectivity based on the work of Sugier et al. (2002). A 5x5 km² median filter is then applied to radial velocity measurements to discard potential spurious velocities resulting from dealiasing failures (Tabary et al. 2006). Finally, data are synchronized with respect to the ending time of the 15' sampling period to account for the non-simultaneity of the measurements following the approach of Tuttle and Foote (1990). Once pre-processed, data are ingested in the MUSCAT analysis described in Section 2.

4. Examples of retrieved wind fields

A qualitative evaluation of the multiple-Doppler winds reconstructed in this framework is provided through the analysis of radar data collected during various rain events that occurred over mainland France between 2008 and 2010. This includes the extratropical cyclone Klaus, which stroke France on 24 January 2009 with hurricane force gusts, and a number of orographic convective precipitation events that produced large amount of rain over the Massif Central Mountains.

4.1 Extratropical cyclone "Klaus"

4.1.1 Overview

On 24 January 2009, an extratropical cyclone called "Klaus" made landfall over southwestern Europe with hurricane force gusts, causing widespread damage and many fatalities, especially across France and Spain. This event is considered the most intense storm affecting Western Europe since the infamous extratropical cyclones "Lothar"

(Wernli et al., 2002) and “Martin” in 1999. The heaviest damages occurred in southern France where millions of homes and commercial properties experienced power cuts and heavy damages due to falling trees. In Northern Spain and Southwestern France some of the most productive European forests have been profoundly impacted by the storm and will likely take decades to recover. In the French Landes department for instance, one estimates that 70 % of the pine forest – this forest, the largest of this kind in Europe, was accounting for about one third of France's lumber production - has been completely wiped in just a few hours.

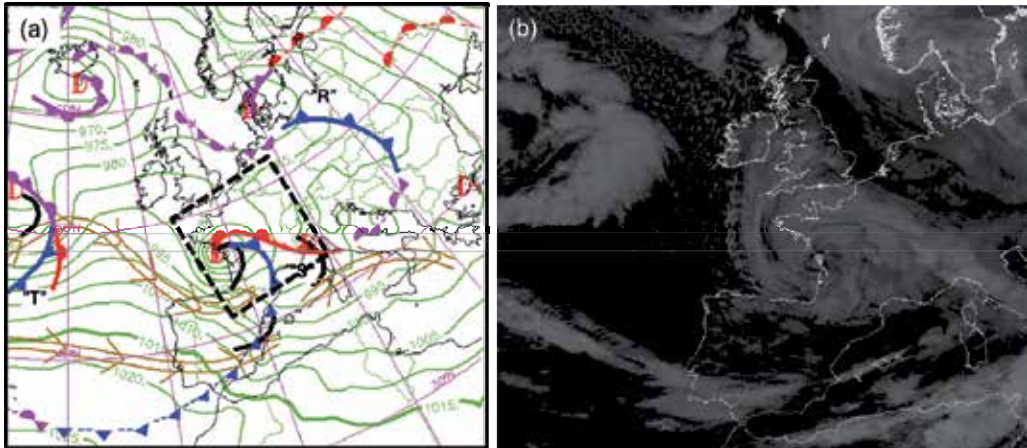


Fig. 3. (a) Surface analysis and satellite imagery over Western Europe valid 24 January 2009 at 6 UTC. The black square in (a) shows the area where wind retrieval is performed.

Klaus formed west of the Azores islands on 23 January 2009 near 00 UTC and made landfall about 30 hours later after crossing the Atlantic Ocean at a mean speed of $27 \text{ m}\cdot\text{s}^{-1}$. The life cycle of this system approximately follows the conceptual model proposed by Shapiro and Keyser (SK, 1990). It is characterized by an explosive intensification period, during which the sea level pressure (SLP) at the cyclone center deepened by $\sim 36 \text{ hPa}$ in 24 hours, ending up with a warm seclusion phase and a rapid decay. The SLP minimum (964 hPa) was reached at 00 UTC, 24 January, as the low-level vortex was located ~ 400 kilometers off the French coasts. Klaus made landfall slightly before 6 UTC on 24 January near Bordeaux, France (Fig. 3) with a minimum pressure of $\sim 967 \text{ hPa}$ (Fig. 4). The corresponding surface analysis (Fig. 3a) shows a warm frontal zone to the North of the cyclone center and a cold front extending far southward across the Pyrenees and Northern Spain. According to satellite images (Fig. 3b) the storm was elongated in the west-east direction along the warm front, which is in good agreement with the SK model theory (Schultz et al. 1998). After landfall, the system progressed eastward at a mean speed of about $15 \text{ m}\cdot\text{s}^{-1}$ and reached Italy near 18UTC (Fig. 4). At this time the associated minimum pressure has already increased to 988 hPa . Maximum surface winds occurred in a region located approximately 300 to 350 km south of the cyclone center, along a 100 km swath oriented in a direction almost parallel to the cyclone trajectory. In France, wind gusts peaked at $\sim 184 \text{ km}\cdot\text{h}^{-1}$ near Opoul (Fig. 1), a value corresponding to category 3 hurricane winds on the Saffir-Simpson scale. The situation was even more impressive in Northern Spain where surface wind gusts over $200 \text{ km}\cdot\text{h}^{-1}$ have been recorded at several locations.

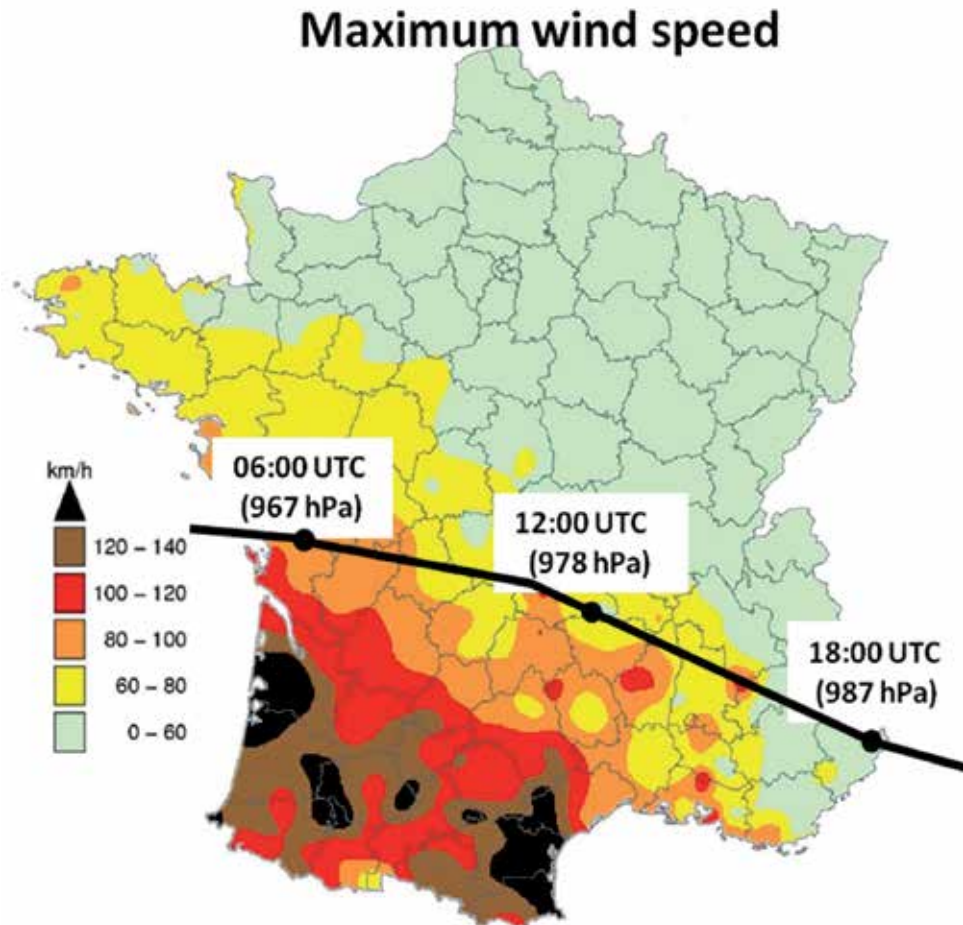


Fig. 4. Recorded maximum surface wind speed during the passage of Klaus over France. The trajectory and central pressure of the cyclone are also indicated.

4.1.2 Radar-derived wind and reflectivity fields

Observations collected between 03 and 9 UTC on 24 January 2009 are shown in Fig. 5. All radars performed nominally during this period with the exception of the Momuy radar, which was forced to cease operations near 05UTC due to heavy wind damages. Velocity data recorded just before the radar failure were in excess of 60 m.s^{-1} (216 km.h^{-1}) at 2000m MSL and $\sim 45 \text{ m.s}^{-1}$ (160 km.h^{-1}) close to the ground. Also note that the French radar network was not yet completely Doppler-ized at this time resulting in some gaps in the dual-Doppler radar coverage over northwestern and southern France.

Figure 5 presents horizontal cross-sections of wind and reflectivity fields over France at 2 km MSL and different stages of the storm evolution. At 3 UTC (Fig. 5a-b), a large part of the country was already affected by weak to moderate precipitation. The most intense rainfall occurred approximately 300-400 km in advance of the cyclone center along a SW-to-NE oriented rainband that marks the location of the cyclone associated cold front. Another area of intense precipitation associated with the cloud head (Browning 1999) could also be identified farther west. Both regions of intense precipitation were separated by an area of weaker precipitation associated with the dry intrusion identified in Fig.5a. Relatively intense winds in the range of 25- 30 m.s⁻¹ could already be observed in the southeastern France (east of the cold front) and within the cloud head.

According to radar data, Klaus made landfall ~ 3 hours later near the city of Nantes (Fig. 5c-d). The closed circulation associated with the cyclone center can be clearly identified in Fig 5c. The diameter of the vortex deduced from radar observations was about 350 km. Severe winds reaching up to 50 m.s⁻¹ have already penetrated deeply over land as seen by the patch of very intense winds located ~400 km of the cyclone center from each side of the dry slot. The location of this area of particularly strong winds is in good agreement with surface observations (Fig. 4). One can also notice the presence of several thin rainbands located to the west of the wind maximum, within the cloud head. This banded structure is consistent with that described by Browning (2004) and suggests the existence of multiple mesoscale slantwise circulations, which may have played an active role in strengthening the damaging winds (the investigation of processes at play during this event is outside the scope of this study). After landfall the patch of strong winds stretched out along a NW-SE axis more or less parallel to the orientation of the Pyrenees mountain chain and slowly progressed southeastward towards the Mediterranean coast. Strong winds remained active during the entire period. A wind maximum of up to 55 m.s⁻¹ could be observed west of the Toulouse radar at 09UTC ($x \sim 400$ km, $y \sim 200$ km) in good agreement with surface observations (Fig. 4).

As there is currently no way to collect wind measurements at the space-time resolution achieved by ground-based Doppler radars, the validation of such operational wind data is extremely difficult. In order to evaluate these results, we propose to compare retrieved radar winds with those analyzed by the French operational numerical weather prediction system ALADIN (Aire Limitée Adaptation Dynamique Développement International; Radnóti et al. 1995). ALADIN is a limited area regional model that covers France and part of Western Europe at the horizontal resolution of 10 km. The comparison between radar-derived and analyzed horizontal winds at 1.5 km MSL at 6 UTC is shown in Fig. 7. Overall, the location of the cyclone center, the dimension of the vortex, and the intensity and direction of the winds at mid-level appear quite similar in both analyses. Some discrepancies can yet be seen along frontal boundaries (the wind shift associated with the cold front is for instance slightly more marked in the radar analysis) and to the North of the Massif Central Mountains, about 500 km east of the cyclone center. In the latter area the model produces a pronounced zonal wind component that is apparently not resolved in the radar analysis. This pronounced southerly component was nevertheless missing in all 15' analyses produced between 4 and 8 UTC. Although no strong conclusions can be inferred from this observation, this temporal consistency of the wind field may plead for an error in the analysis rather than in the retrieved winds.

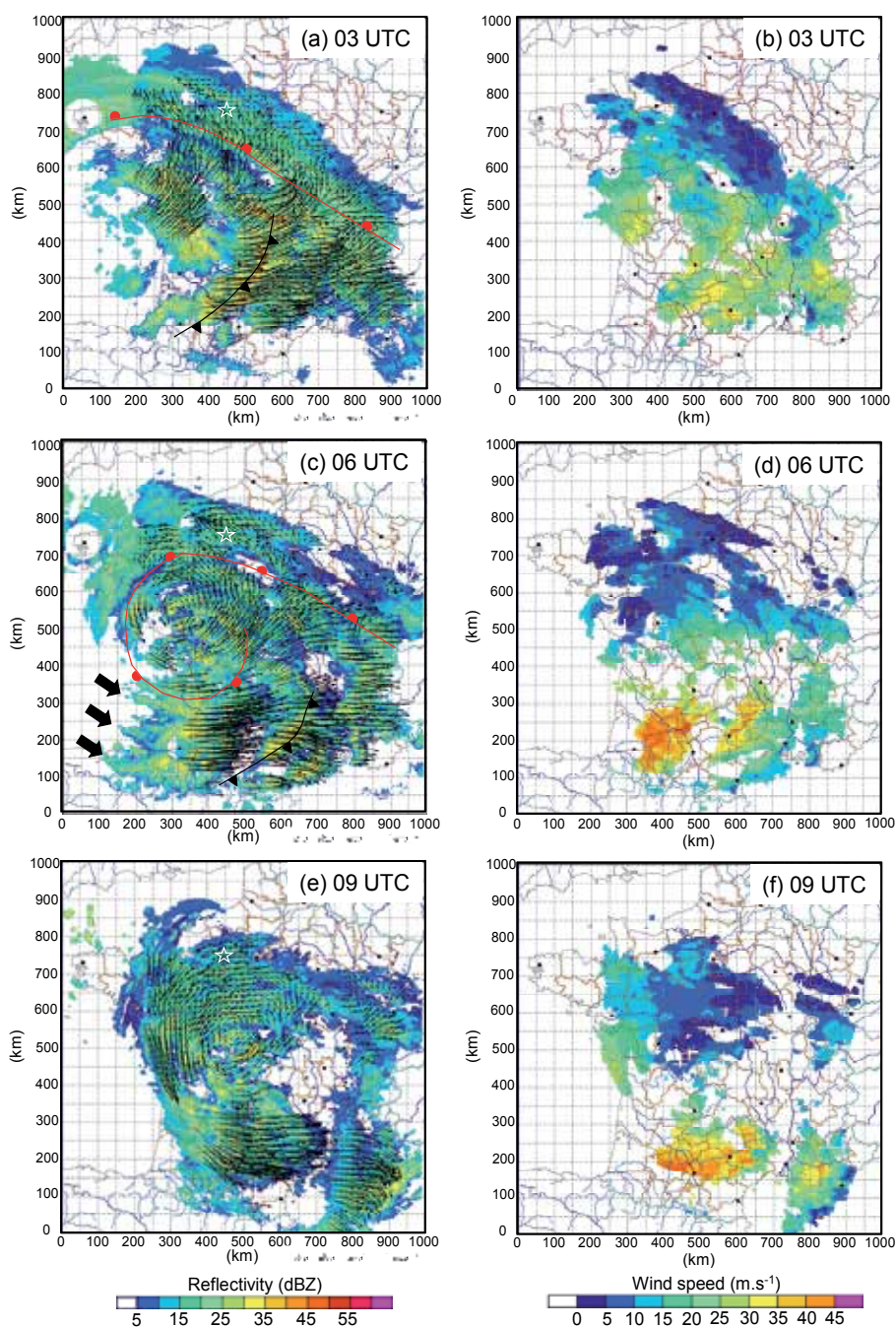


Fig. 5. 3-hourly multiple-Doppler analysis of radar data over France starting at 03 UTC on 24 January 2009. Left panel shows reflectivity (dBZ) superimposed on horizontal wind vector at 2.5 km AMSL. Right panel shows horizontal wind speed (m/s). One every sixth vector is plotted. Frontal boundaries deduced from surface analysis are shown in (a) and (c).

4.2 The 7 September 2010 “Cevenol” event

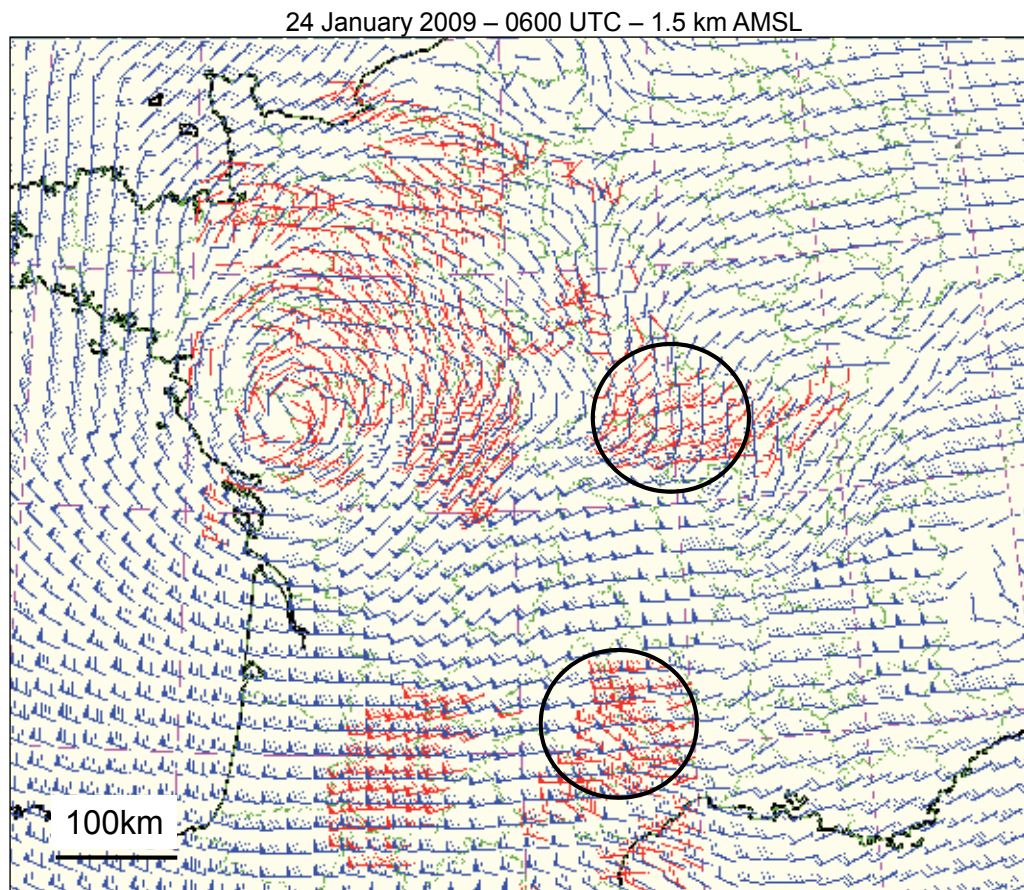


Fig. 6. Comparison between ALADIN operational (blue) and radar-derived winds (red) at 1500 AMSL on 24 January at 6 UTC. Black circles show area where the 2 analyses significantly differ.

4.2.1 Overview

During the fall season, the southeastern region of France is often affected by intense flash-flooding episodes ensuing from the formation of quasi-stationary mesoscale convective systems along the south-eastern flank of the Massif Central Mountains (Cevennes region). These systems can generate considerable amount of precipitation in relatively short periods of time. A well-known example of such systems is the so called “Gard case” (Delrieu et al. 2005) during which ~ 800 mm of rain fell down in less than 24 hours over the French Gard department, resulting in many fatalities and total damage amount of about 1.2 billion US dollars. Observing and understanding the dynamical and to some extent microphysical processes at play during these high impact weather events is critical to develop effective flood warnings systems and to improve their forecast. In the following we present examples of radar analyses produced during a heavy precipitation event that

occurred in the Nîmes area on 7 September 2010. Although this storm did not generate major damage, it locally produced rainfall accumulation in excess of 300 mm in just a few hours.

The 500 hPa analysis at 12 UTC, 7 September 2010 is shown in Fig. 7. Note that at this time convection over the Gard department has already started and was already well established. The upper level analysis indicates the presence of an upper-level cold low centered over the British Islands with an associated trough extending southward toward the Iberian Peninsula. This synoptic pattern generates a mid-to-upper level southwesterly flow over France and a low-level southerly flow over the Mediterranean Sea veering slightly southeasterly near the French coast.

The corresponding Deutscher Wetterdienst (DWD) low-level analysis (Fig. 8b) shows a surface low centered over Ireland and a main front extending meridionally through central France ahead of the trough which attained France on the 6 September (Fig. 8a). A secondary front can also be noticed a few hundred kilometers west of the main front, over the Atlantic Ocean. The latter is associated with a low-pressure anomaly located slightly north of the Spanish coast. In the following hours (Fig. 8c-d), this front and its associated surface low propagated rapidly eastwards to ultimately catch up with the leading front. The low surface pressure anomaly reached Western France by 18 UTC (Fig. 8c) and rapidly extended over a large part of the country (Fig. 8d).

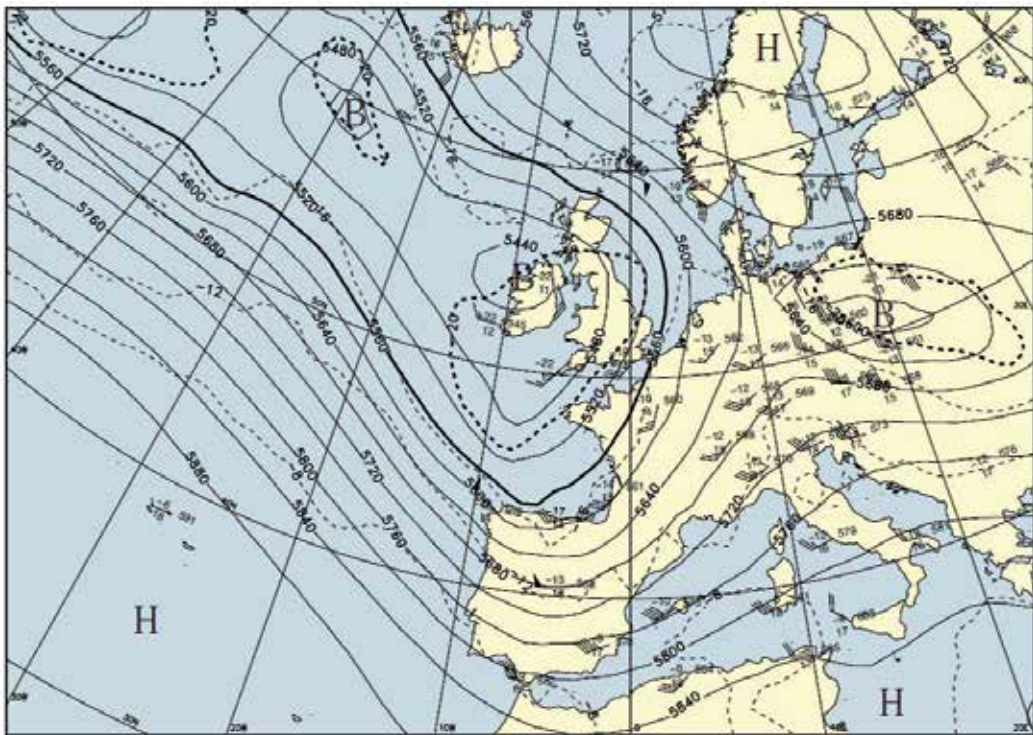


Fig. 7. Operational analysis of geopotential height at 500 hPa valid on 7 Sept 2010 at 12 UTC.

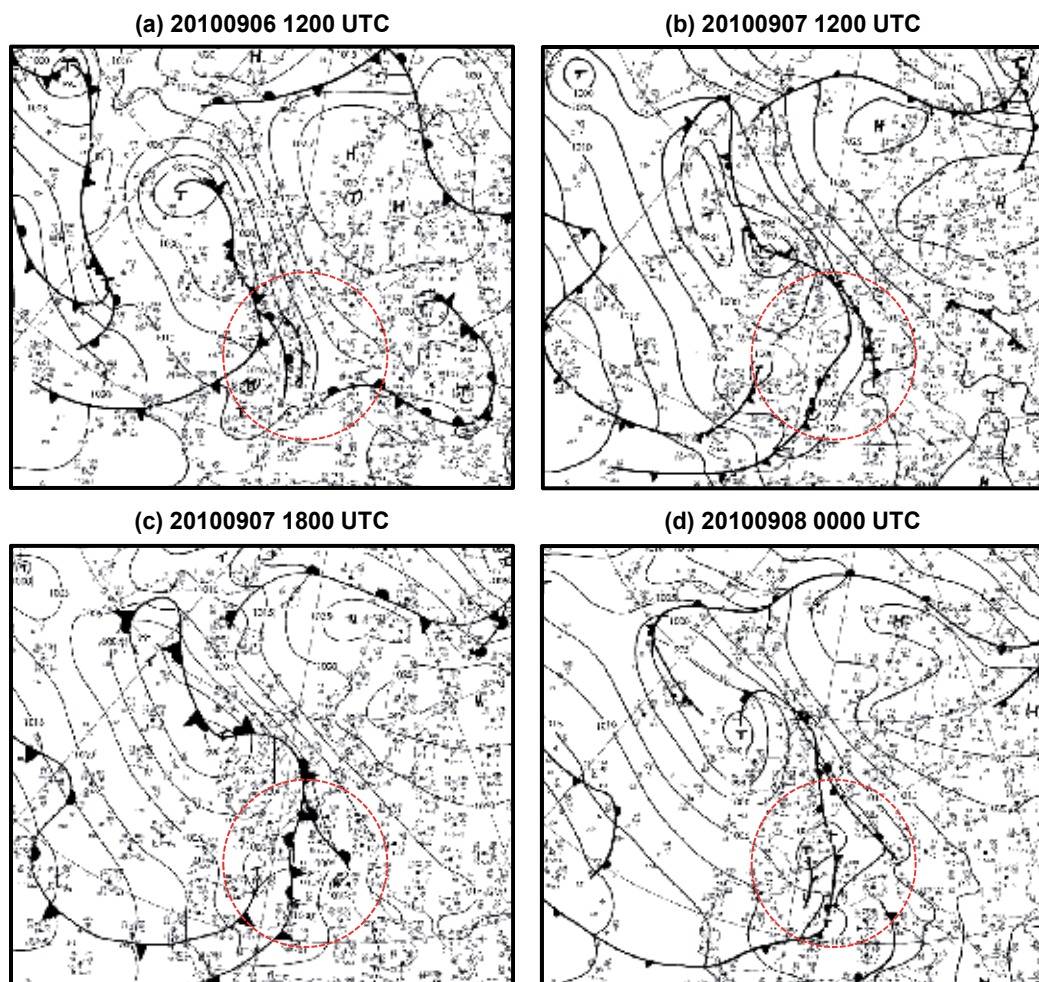


Fig. 8. DWD operational surface analyses valid at (a) 12 UTC 06 Sept 2010, (b) 12 UTC 07 Sept 2010, (c) 18 UTC 07 Sept 2010, and (d) 00 UTC 08 Sept 2010. The red circle indicates the area where multiple-Doppler wind retrieval is performed.

The 24-hour accumulated precipitation pattern (Fig. 9) shows a pronounced maximum of ~300 mm over the Gard department. The maximum rainfall amount was recorded close to the foothills of the Massif Central in the city of Conqueyrac where 308 mm of precipitation fell in 7 hours. Significant rainfall also occurred over the Massif Central as indicated by a well-defined band of accumulated precipitation in the range of 75-150 mm. This pattern is consistent with the slow propagation of the leading surface front noticed in Fig. 8 and suggests that frontal perturbations have been slowed-down and possibly enhanced by the Massif Central Mountains.

4.2.2 Radar-derived wind and reflectivity fields

Figure 10 presents multiple-Doppler analysis of radar data produced every 6 hours from 12 UTC, Sept 6 to 00 UTC, Sept 8 at a height of 2.5 km (left panel) and 6 km (right panel). The composite reflectivity patterns (right panel) show extensive frontal rainbands propagating eastwards in good agreement with the surface analyses shown in Fig. 8. Starting from 18 UTC, 6 September (Fig. 10c), one can notice the presence of widespread convective cells over southeastern France and northern Spain that seem to be triggered by the pronounced relief of the Pyrenees. These cells, which develop in a southwesterly midlevel level flow, are advected northeastwards towards the Massif Central Mountains before eventually aggregating into a stationary mesoscale convective system (MCS) along the flank of the mountains. The retrieved wind circulation at both 2.5 and 6 km altitude shows relatively uniform southwesterly wind, except near the Massif Central where the mid-level flow exhibits a more pronounced southerly component. This southerly flow, which tends to advect warm and moist air masses from the Mediterranean Sea toward the coast, impinges on the Massif Central Mountains and is responsible for the enhancement of convection over

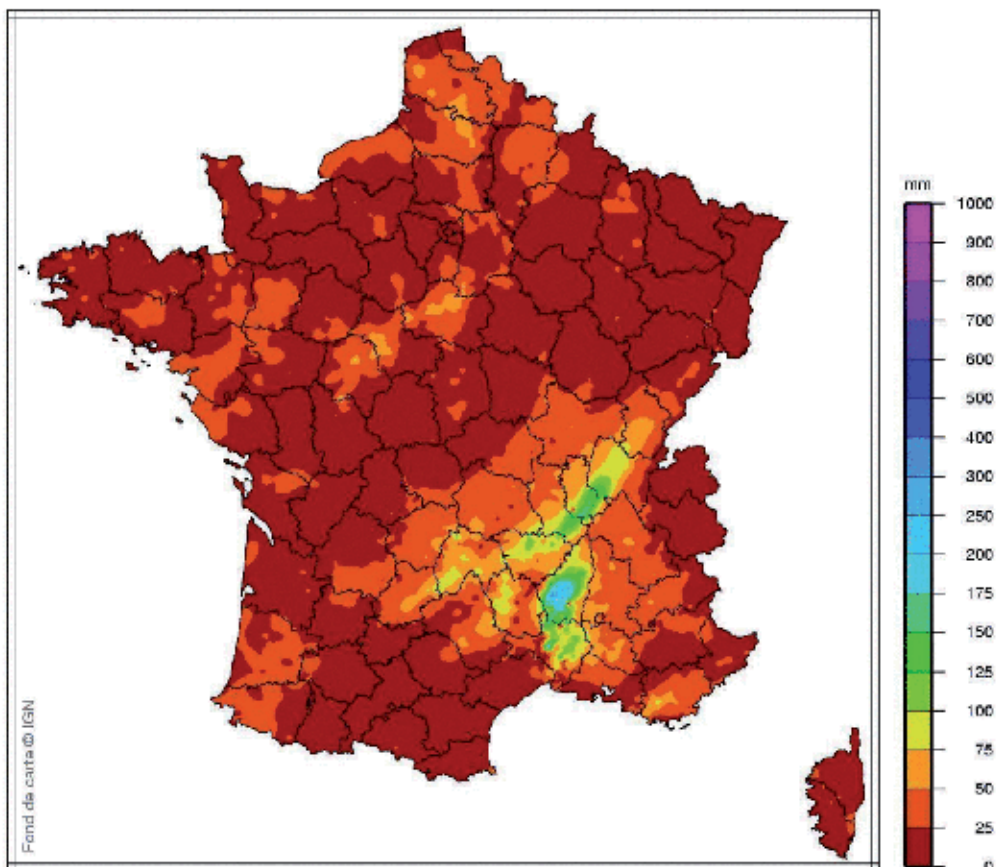
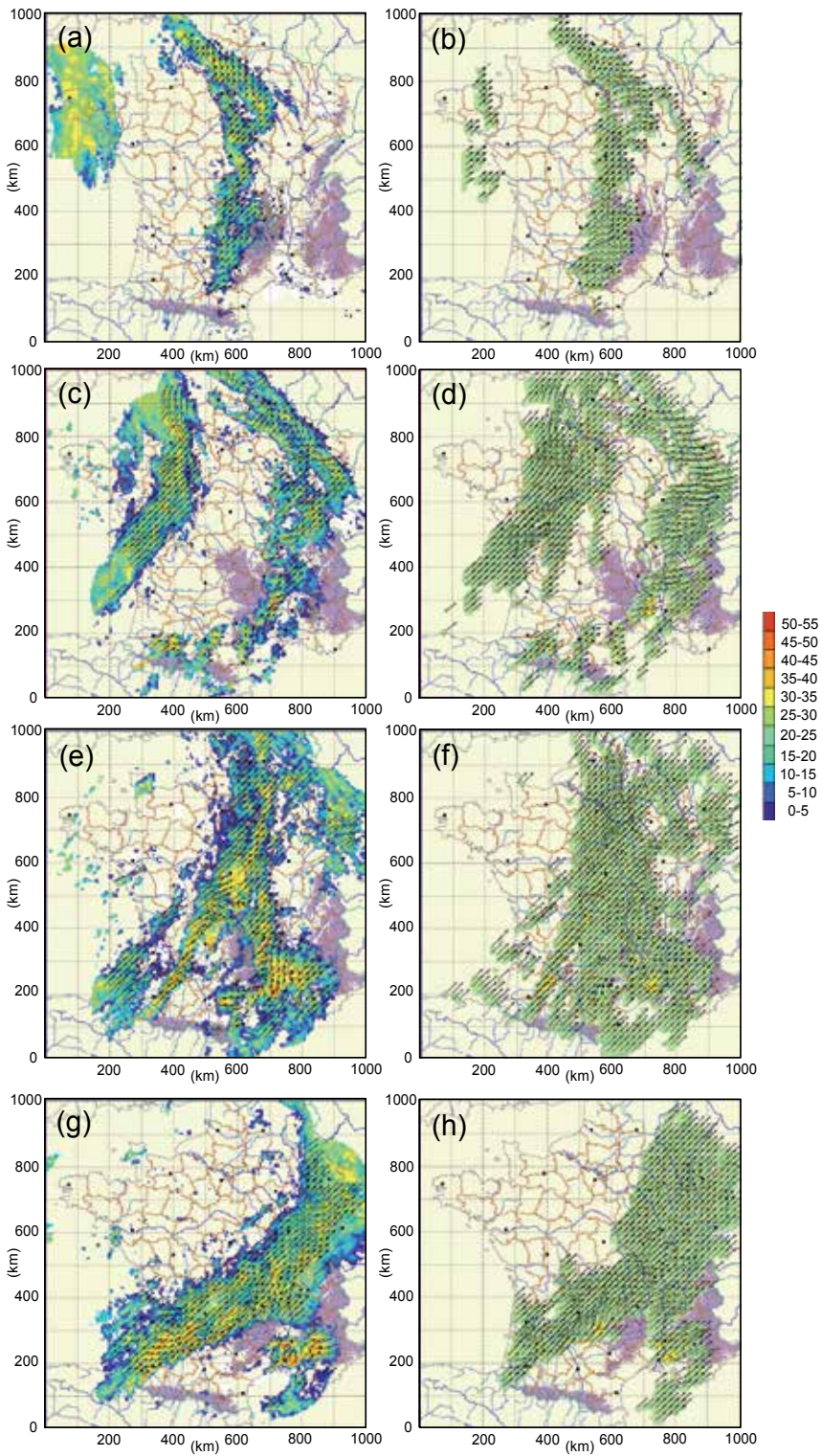


Fig. 9. 24-h accumulated precipitation (mm) over France starting at 00 UTC, 7 Sept 2010



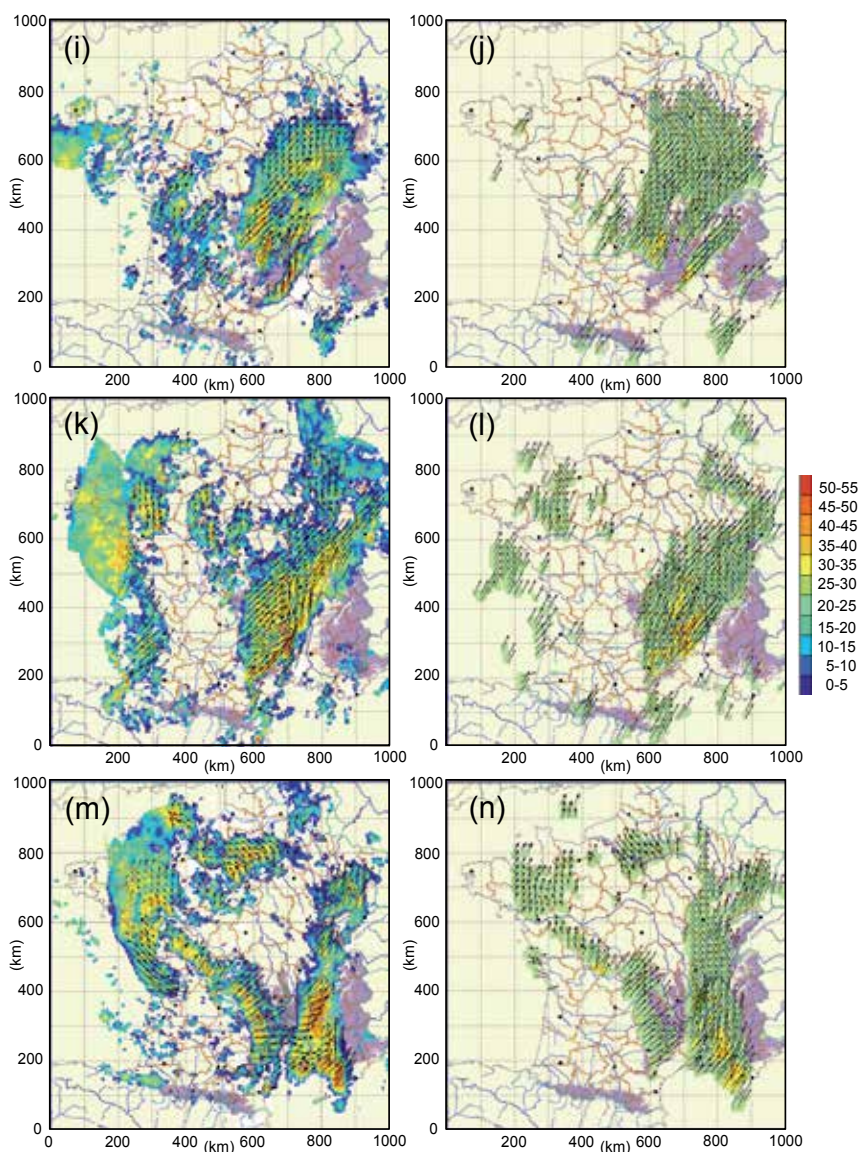


Fig. 10. 6-hourly multiple-Doppler analysis of radar data over France starting at 12 UTC on 6 Sept 2010. Left panel shows reflectivity (dBZ) superimposed on horizontal wind vector at 2.5 km AMSL. Right panel shows vertical velocity (m/s) and horizontal wind vectors at 6 km AMSL. Vertical velocity values (m/s): dark green ($w < -1$), green ($-1 \leq w < 1$), yellow ($1 \leq w < 2$), orange ($w \geq 2$). One every sixth vector is plotted.

the Cevennes area. The convective activity in this region significantly intensified in the following 12 hours (Fig. 10e and g), as shown by radar reflectivity values increasing up to 55 dBZ. During this period, the MCS also became more organized and developed a well-defined stratiform region. At 12 UTC, 7 September, the MCS was absorbed by the frontal

rainband associated with the cold front that had been moving across France for ~ 24 hours (Fig. 10i). The various interactions between air masses occurring during the merging process seemed to reinforce the convective activity along the southern flank of the Massif Central. The most intense convection was hence observed around 18 UTC (Fig. 10k).

In order to better understand the processes at play in the Cevennes region, Fig. 11 presents a zoomed view of low and midlevel flow at 00 and 21 UTC, 7 September within a 400 x 400 km² domain centered on Nimes. At 00 UTC (Fig. 11c), the low-level flow impinging on the Massif Central was from the SE and was oriented in a direction almost perpendicular to the mountains. The maximum convection was observed slightly off the slopes. This is likely due to the presence of a cold pool below the system, which acted to displace the triggering effect of the mountains farther south (cold dome effect; Reeves and Lin 2005).

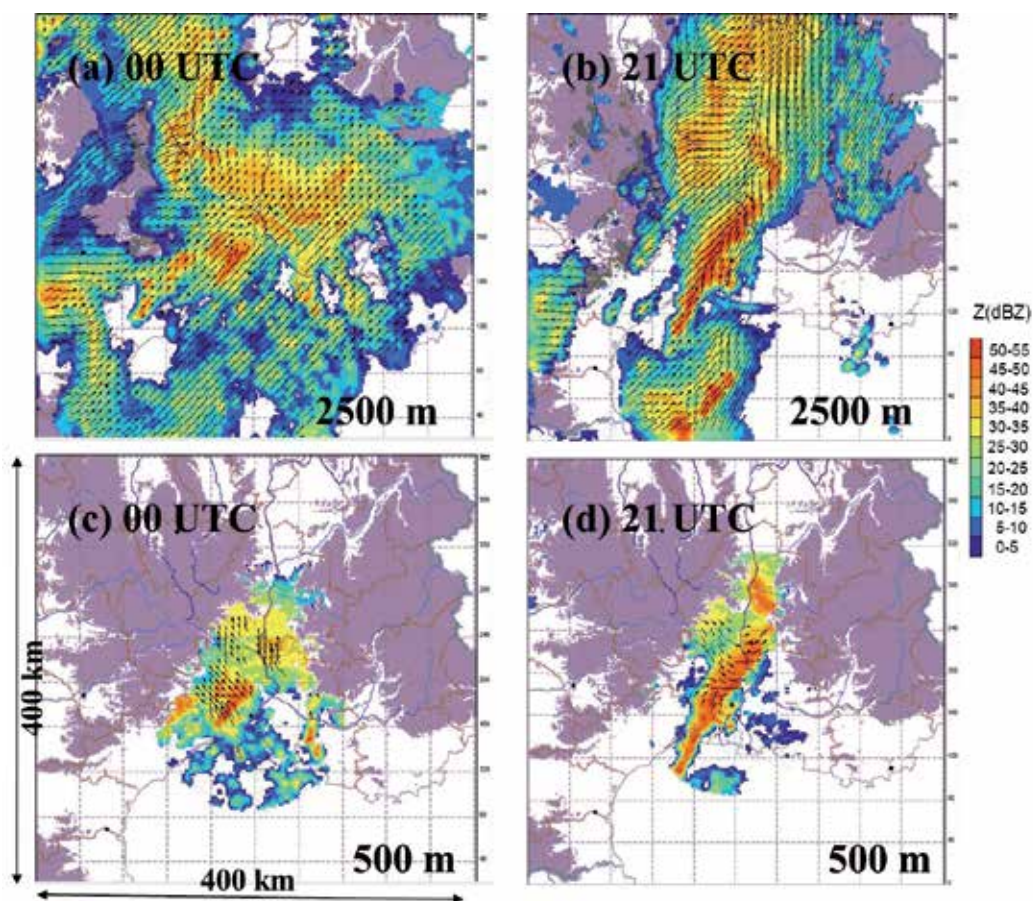


Fig. 11. Multiple-Doppler analysis of radar data within a domain of 400 km x 400 km centered near Nimes, France valid at 00 UTC and 21 UTC, 7 Sept 2010. Upper panels shows reflectivity (dBZ) superimposed on horizontal wind vector at 2.5 km AMSL. Lower panels shows panel shows reflectivity (dBZ) and horizontal wind vectors at 500m AMSL. Grey shading indicates Massif Central (left) and Alps (right) mountain chains. One every fourth vector is plotted.

At 21 UTC, one can note a profound reversal of the incident upslope-oriented flow, resulting in the formation of a northwesterly flow over the slopes of the Massif Central. Such pronounced return flow has already been observed over the Alps in the frame of the MAP experiment from airborne and mobile radar systems in response to negative buoyancy generated by both melting and evaporation of precipitation particles below the 0° C isotherm (Bousquet and Smull 2003, Steiner et al. 2003). The process generating the observed downslope flow by cooling from melting and evaporation of precipitation particles in the Massif Central is likely similar to that observed over the Alps in the late nineties. This is supported by the fact that stratiform precipitation lasted for several hours over the mountains before the formation of this downslope circulation (Fig. 10g,i,k). In this particular case, however, it seems that the downslope flow has had a strong impact on the convective activity by triggering new cells in the Rhone valley (Fig. 11d), whereas its effect was not found significant in previous studies.

After the merging, the frontal system remained blocked over the Massif Central and the eastern part of France for about 12 hours during which another 100 mm of rain fell over the Cevennes area. It finally passed the Cevennes near 00 UTC, 8 September as it was swept away by another frontal system approaching from the West. At this time, the low surface pressure anomaly identified in Fig. 8c had reached the French territory and had started to extend over a large part of the country. The associated cyclonic circulation (Fig. 10m) was well captured by the French radar network.

More information about the vertical structure of precipitation can be inferred from Fig. 12, which presents 6-hourly meridional cross-sections of the retrieved 3D composite reflectivity pattern along a 1000 km line ranging from the Golfe du Lion, in the Mediterranean Sea, to Belgium. These cross-sections provide a unique picture of the structure and evolution of precipitation over the entire country and can be very useful to quickly identify regions of intense rainfall, as well as to segregate between frontal and more convective precipitation. This time series, extending from 00 UTC to 18 UTC on 7 September, thus confirms that convection became significantly more intense after the frontal system reached the Massif Central Mountains. At 12 UTC (Fig. 12c) and 18 UTC (Fig. 12d) one can see that very deep convection was thus occurring over the Cevennes and the Rhone valley with convective cells reaching up to 35 dBZ at a height of 11 km.

In addition to horizontal wind fields, the MUSCAT analysis used by the French weather service also allows to retrieve accurate vertical velocities in the whole precipitating area within the 1000 km x 1000 km domain of analysis. Retrieved vertical motion fields at a height of 6 km, which is the altitude at which maximum vertical motion was observed, are displayed in Fig. 10. Overall, one can note a very good consistency between the location/intensity of updrafts and the position of the most active convective cells (left panel). Upward vertical motions are the most intense after the MCS has merged with the frontal rainband that is the moment when low level convergence was the most important. This observation is consistent with the vertical structure of precipitation deduced from Fig. 12 that indicates the presence of deep convection and shows a particularly impressive vertical extension of the convective cells.

During the Klaus storm, getting real-time or quasi real-time information about wind intensity would have been particularly useful to forecasters in order to trigger or cancel alerts, as well as to precisely monitor the propagation of the strong wind swath. On September 7 2010, a watch was ongoing for heavy precipitation and flash flood in the Cevennes area but forecasters were more interested in getting high resolution radar quantitative precipitation estimates in order to assess the hydrological risks.

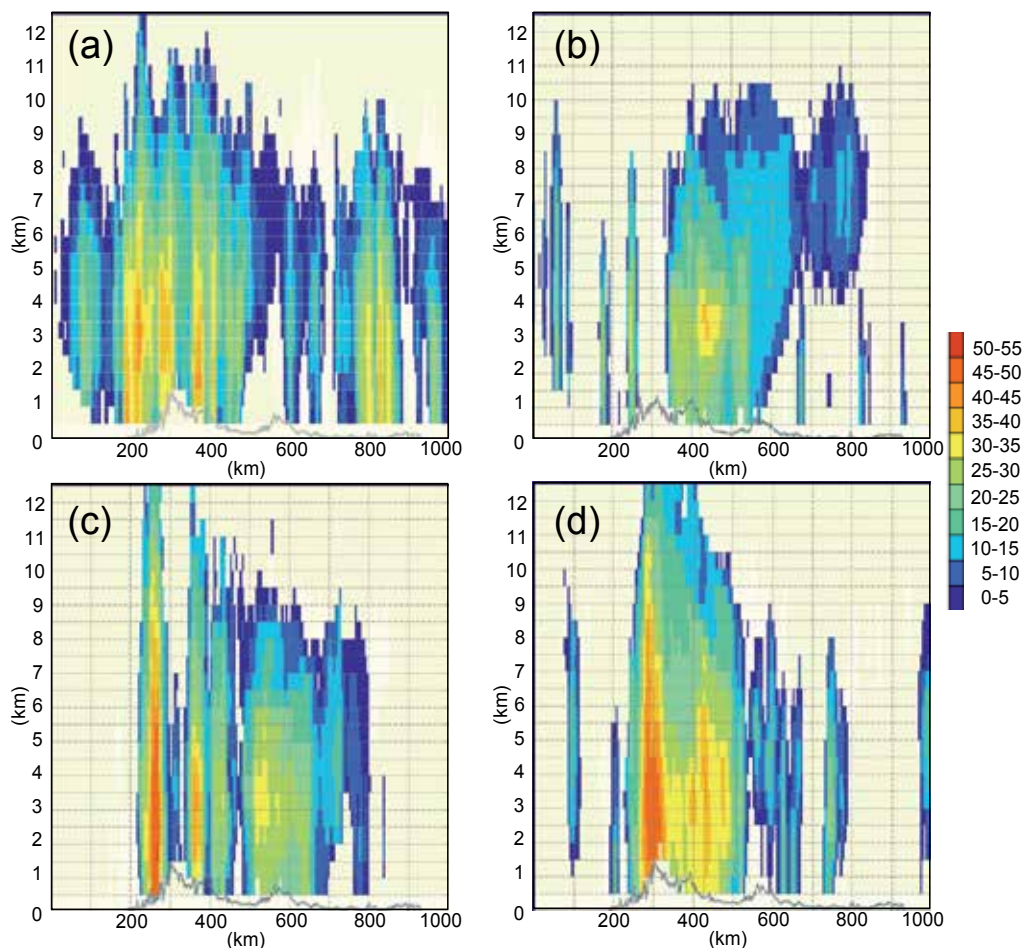


Fig. 12. Vertical cross-section of radar reflectivity (dBZ) at $x=700$ km (Fig. 10) at (a) 00 UTC, (b) 6 UTC, (c) 12 UTC and (d) 18 UTC on 7 Sept 2010.

Wind observations would nevertheless have been quite useful to anticipate the behavior of convective cells, especially in the Rhone valley where the intensity of the convection seemed directly related to the direction and strength of the wind. On the other hand, the benefit inferred from such products for research purposes is priceless. These wind fields could be used to develop new methods for model verification as well as more efficient nowcasting tools. Radar-derived wind information produced in a fully operational framework (i.e., in real time and automatically) could also be relied upon to evaluate numerical model output in real time (through identifying possible temporal or spatial phase shift in model output), as well as to build a weather database that would be used for statistical analysis purposes or more traditional case studies. Such capabilities, for instance, are at the heart of the upcoming HyMeX field phase, which will be held in Sept-Nov 2012.

4.3 20-22 October 2008 MCS Cevenol precipitation event

The last example consists in an isolated MCS (Fig. 13a) that developed along the south-eastern flank of the Massif Central Mountains on October 20th and remained stationary for about 15 hours. Again, this storm did not generate any significant damage, but it locally produced rainfall accumulation in excess of 250 mm in a just a few hours.

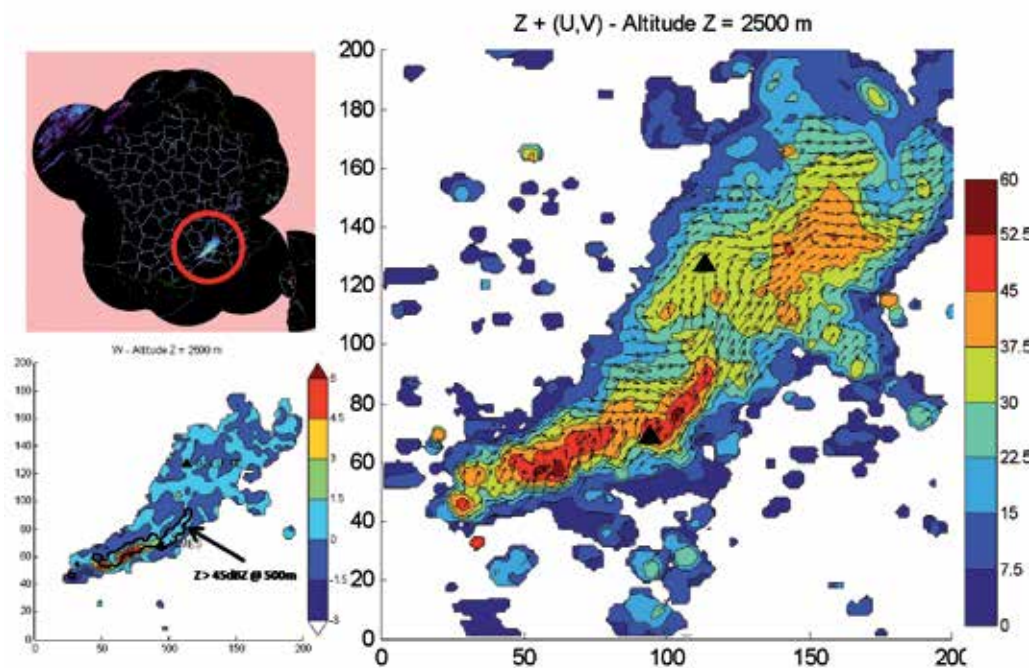


Fig. 13. Stationary mesoscale convective system observed on 20 October 2008 at 14 UTC. (Left, top): French operational radar reflectivity mosaic output. (Right): Horizontal wind vectors superimposed on radar reflectivity (shaded) at 2.5 km MSL within the 200 km x 200 km experimental domain, as derived from multiple-Doppler analysis of radar data. (Left, bottom): Associated retrieved vertical velocity. Triangles show the location of Nimes and Bollène radars. One every sixth vector is plotted.

The retrieved wind and reflectivity fields associated with this MCS at 14 UTC are shown in Fig. 13b within a domain of 200 x 200 km centered between the Nimes and Bollene radars (black triangles) at a horizontal resolution of 1 km. Note that only 4 radars (Bollene, Nimes, Montclar and Collobrieres, see Fig. 1) are used in this analysis. This setup will be used to produce high resolution wind fields in real-time during the first phase of the HyMeX program in fall 2012. Radar-derived wind and reflectivity fields will be used to guide both research aircraft and ground-based mobile radars systems towards the most interesting areas. Overall, the radar analysis shows a rather complex wind circulation resulting from the interactions between the incident flow originating from the Mediterranean Sea and the terrain. A region of strong convergence was observed near Nimes due to the interactions of westerly flow in the southern part of the massif with southerly-to-southwesterly flow to the east. As a consequence, strong convection could be observed in this region while more

stratiform precipitation, associated with older cells, could be seen to the North. The vertical velocity field (Fig. 13, bottom right) in the convective region also shows intense updraft up to 8 m/s, which is consistent with observed reflectivity cores up to 60 dBZ. Note that retrieved vertical velocities were significantly higher than those retrieved within the 7 September 2010 system due to the much higher horizontal resolution of the wind field (1 km vs. 2.5 km).

A new precipitation event occurred over the same area the day after as a new stationary MCS formed at about the same location, along the southern flank of the Massif Central Mountains (Fig. 14). This time, however, the situation was quite different as a rainband associated with a southeastward propagating cold front merged with the isolated MCS at the end of the day and eventually swept it away. In essence, this new event is thus relatively similar to the 7 Sept 2010 case described previously. Figure 15 shows the evolution of the MCS between 0 UTC and 8 UTC on the 22nd of October. This time series begins slightly after the frontal system reached the Massif Central. The location of the cold front can be identified by the wind shift seen at both low and mid-levels. Note that the strong low-level southerly flow impinging on the barrier at 0 UTC quickly weakened as the front approached the eastern flank of the Massif, which acted to cut the feed of moisture originating from the Mediterranean Sea and prevented the formation of new convective cells. Convection over the area thus died very quickly and the MCS was rapidly swept away by the cold front. A major difference with the 2010 case is that the frontal system did not remain blocked over the relief and stratiform precipitation over the slopes thus only lasted for a short period of time. This is likely the reason why no reversal flow could be observed over the slopes of the Massif Central on this day as the cooling resulting from melting and evaporation of precipitation particles, which is responsible for the formation of the downslope flow, was not sufficient for this phenomenon to occur.

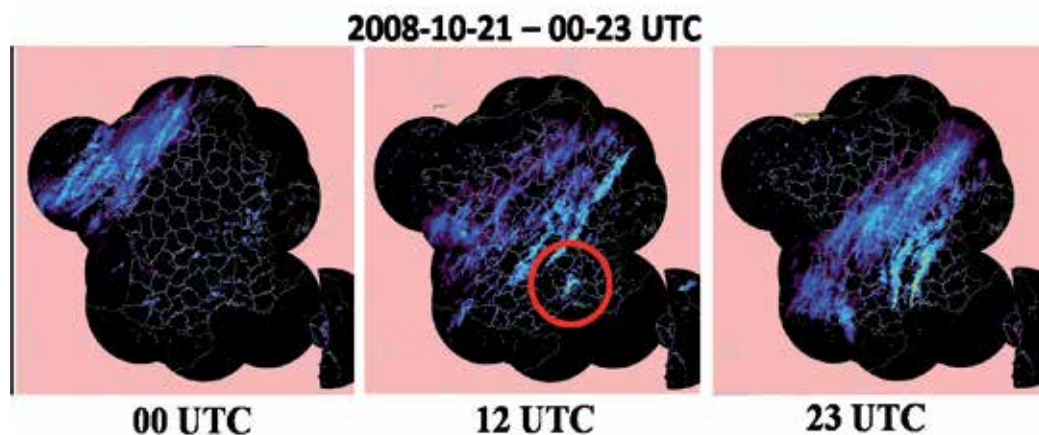


Fig. 14. French operational radar reflectivity mosaic outputs on 21 October 2008 at 00, 12, and 23 UTC. Red circle indicate the location of the isolated MCS.

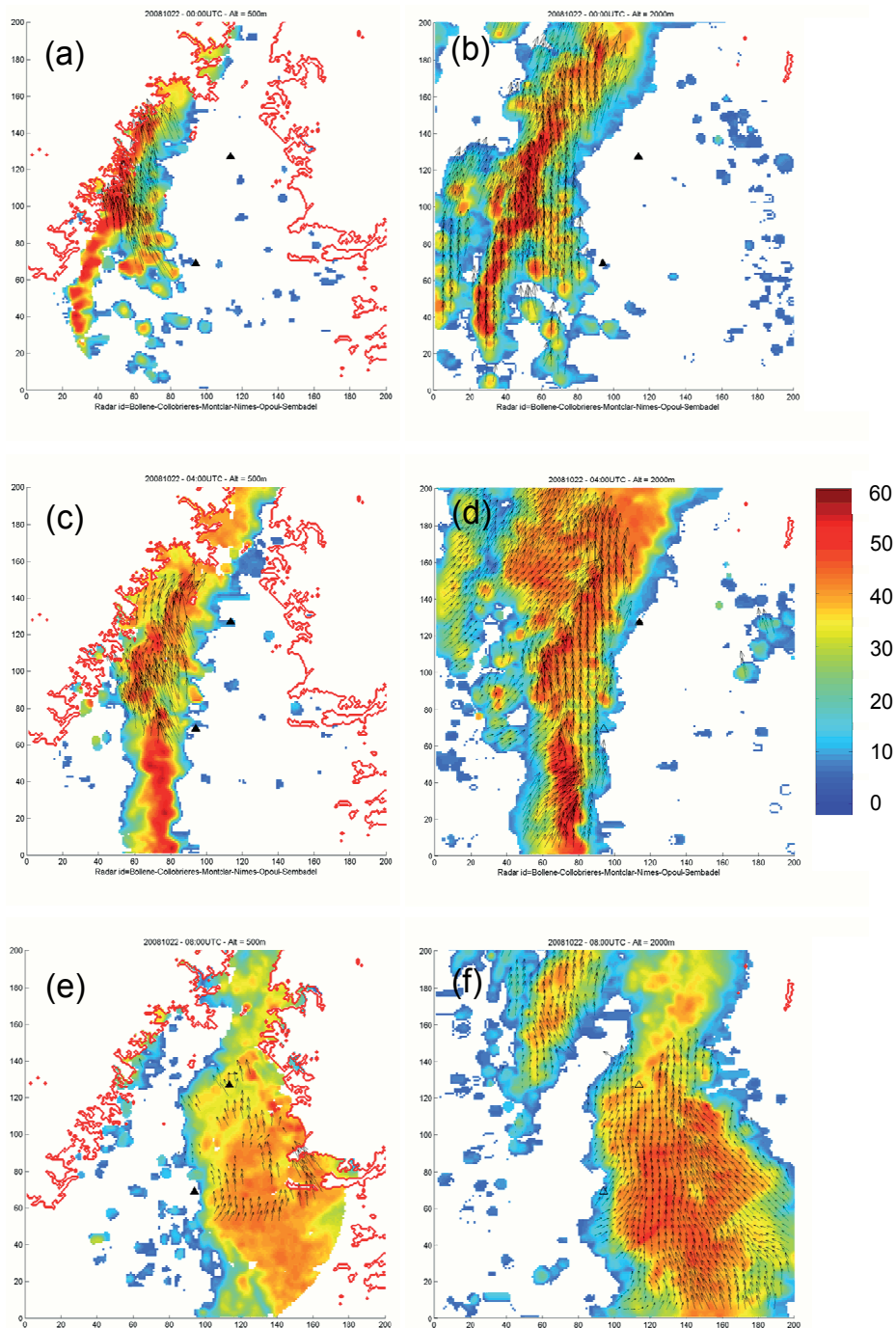


Fig. 15. Horizontal wind vectors superimposed on radar reflectivity (shaded) at 0.5 km (left panel) and 2.0 km (right panel) AMSL within a 200 km x 200 km experimental domain, as derived from multiple-Doppler analysis of radar data at (a,b) 00 UTC, (c,d) 04 UTC and (e,f) 08 UTC on 22 October 2008. One every sixth vector is plotted.

5. Conclusion

The ability to collect Doppler measurements up to long range resulting from the recent deployment of a new triple-PRT scheme within the French radar network ARAMIS allows to mitigate the Doppler dilemma and to achieve extensive multiple-Doppler coverage while collecting high quality radial velocities. This achievement brings new perspectives in terms of exploitation of operational Doppler measurements such as the ability to perform multiple-Doppler wind synthesis in a fully operational framework. In this context the French weather service has started to produce a new mosaic of wind and reflectivity covering the entire French territory. Reflectivity and radial velocity observations collected by the 24 ARAMIS radars, which are concentrated at the national center in Toulouse, are synthesized every 15' to produce a nationwide, three dimensional, wind and reflectivity composite.

An evaluation of multiple-Doppler wind fields synthesized in this framework was carried out from data collected during several weather situations characterized by fundamentally different airflow and precipitation regimes that is, the extratropical cyclone Klaus that struck France with hurricane strength winds on 24 January 2009, as well as several heavy orographic precipitation events that occurred over the Massif Central Mountains in 2008 and 2010. Airflows retrieved at different horizontal resolutions ranging from 2.5 to 1 km are highly consistent with those documented earlier from high resolution research radar data, which suggests that multiple-Doppler winds retrieved in this operational framework are definitely reliable. Wind and reflectivity fields produced routinely in this framework are archived since about a year and are already available to researchers from many countries. This product will be used in a quasi-operational mode (real-time) to guide mobile research systems and evaluate numerical model outputs during the field phase of the Hydrometeorological Cycle in the Mediterranean Experiment (HyMeX) to be held in southern France in fall 2012. It should become fully operational near year 2013 after having been thoroughly evaluated by the forecasters of the French Weather Service.

6. References

- Armijo, L., 1969: A Theory for the Determination of Wind and Precipitation Velocities with Doppler Radars. *J. Atmos. Sci.*, 26, pp. 570-573
- Bougeault, P., P. Binder, A. Buzzi, R. Dirks, R. A. Houze Jr, R. Kuettnner, R. B. Smith, R. Steinacker and H. Volkert, 2001: The MAP special observing period. *Bull. Am. Meteorol. Soc.*, 82, 433-462.
- Bousquet, O., and M. Chong, 1998: A multiple Doppler and continuity adjustment technique (MUSCAT) to recover wind components from Doppler radar measurements. *J. Atmos. Oceanic Technol.*, 15, 343-359.
- Bousquet, O., and M. Chong, 2000: The oceanic mesoscale convective system and associated mesovortex observed on 12 December 1992 during TOGA COARE. *Quart. J. Roy. Meteor. Soc.*, 126, 189-212.
- Bousquet, O., and B. F. Smull, 2003: Airflow and precipitation fields within deep Alpine valleys observed by airborne radar. *J. of Appl. Meteorol.*, 42, 1497-1513
- Bousquet, O., and B. F. Smull, 2006: Observed mass transports accompanying upstream orographic blocking during MAP IOP8, *Quart. J. Roy. Meteor. Soc.*, 132, 2393-2413.

- Bousquet, O., P. Tabary, and J. Parent du Châtelet, 2007: On the value of operationally synthesized multiple-Doppler wind fields, *Geophys. Res. Lett.*, *34*, L22813, doi:10.1029/2007GL030464.
- Bousquet, O., P. Tabary, and J. Parent du Châtelet, 2008a: Operational multiple-Doppler wind retrieval inferred from long range radar velocity measurements, *J. Appl. Meteorol. Clim.*, *47*, 2929–2945.
- Bousquet, O., T. Montmerle, and P. Tabary, 2008b: Using operationally synthesized multiple-Doppler winds for high resolution NWP model horizontal wind verification. *Geophys. Res. Lett.*, *35*, L10803, doi:10.1029/2008GL033975.
- Bousquet, O., 2009: Dynamical and microphysical properties of high impact orographic mesoscale convective systems from high resolution operational multiple-Doppler and polarimetric radar data. *Preprints*, 34th Conference on Radar Meteorology, Williamsburg, USA
- Browning, K.A., and R. Wexler, 1968: The determination of kinematic properties of a wind field using Doppler radar, *J. Appl. Meteorol.*, *7*, 105–113.
- Browning, K.A., 1999: Mesoscale aspects of extratropical cyclones: An observational perspective. in *Life Cycles of Extratropical Cyclones*, American Meteorological Society, Boston, 265-283.
- Browning, K.A., 2004: The sting at the end of the tail: Damaging winds associated with extratropical cyclones. *Quart. J. Roy. Meteor. Soc.*, *130*, 375-399.
- Chong, M., and J. Testud, 1996: Three-Dimensional Air Circulation in a Squall Line from Airborne Dual-Beam Doppler Radar Data: A Test of Coplane Methodology Software. *J. Atmos. Oceanic Technol.*, *13*, 36-53.
- Chong, M., and O. Bousquet, 2001: On the application of Muscat to a ground-based dual-Doppler radar system., *Meteorol. Atmos. Phys.*, *78*, 133-139.
- Chong, M., J.-F. Georgis, O. Bousquet, S. R. Brodzik, C. Burghart, S. Cosma, U. Germann, V. Gouget, R. A. Houze Jr., C. N. James, S. Prieur, R. Rotunno, F. Roux, J. Vivekanandan, Z.-X. Zeng, 2000: Real-Time Wind Synthesis from Doppler Radar Observations during the Mesoscale Alpine Programme. *Bull. Amer. Meteor. Soc.*, *81*, 2953–2962.
- Delrieu, G., and co-authors, 2005: The Catastrophic Flash-Flood Event of 8–9 September 2002 in the Gard Region, France: A First Case Study for the Cévennes–Vivarais Mediterranean Hydrometeorological Observatory. *Journal of Hydrometeorology*, *6*, 34-52.
- Doviak, R. J., and D. S. Zrnic, 1993: Doppler radar and weather observations (second edition), Academic Press, Inc.
- Drechsel, S., G. J. Mayr, M. Chong, M. Weissmann, A. Dörnbrack, and R. Calhoun, 2009: Three-dimensional wind retrieval: application of MUSCAT to dual-doppler lidar. *J. Atmos. Oceanic Technol.*, *26*, 635–646.
- Gamache, J. F., 1995: A three-dimensional variational method for determining wind velocities from Doppler data as applied to the TOGA COARE test case. Summary Report, TOGA COARE Int. Data Workshop TOGA, COARE International Project Office, UCAR, Boulder, CO, 106 pp.
- Gao, J., M. Xue, A. Shapiro and K. K. Droegemeier, 1999: A Variational Method for the Analysis of Three-Dimensional Wind Fields from Two Doppler Radars. *Mon. Wea. Rev.*, *127*, 2128-2142.

- Heymsfield, G. M., 1978: Kinematic and Dynamic aspects of the Harrah tornadic storm analyzed from dual-Doppler radar data. *Mon. Wea. Rev.*, 106, 253-264.
- Lhermitte, R. M., and L. J. Miller, 1970: Doppler radar methodology for the observation of convective storms. *Preprints, 14th Radar Meteorology Conf*, Tucson, Arizona, Amer. Meteorol. Soc, pp 133-138.
- Georgis, J-F., F. Roux, M. Chong and S. Pradier, 2003: Triple-Doppler analysis of the heavy rain event observed in the Lago Maggiore region during MAP IOP 2b. *Quart. J. Roy. Meteor. Soc.*, 129, 495-522.
- Montmerle, T., and C. Faccani, 2009: Mesoscale assimilation of radial velocities from Doppler radar in a pre-operational framework. *Mon. Wea. Rev.*, 137, 1939-1953.
- O'Brien, J. J., 1970: Alternative solutions to the classical vertical velocity problem., *J. Appl. Meteor.*, 9, 197-203.
- Radnóti, G., R. Ajjaji, R. Bubnovà, M. Caian, E. Cordoneanu, K. von der Emde, J.-D. Gril, J. Hoffman, A. Horányi, S. Issara, V. Ivanovici, M. Janousek, A. Joly, P. Le Moigne, S. Malardel, 1995 : The spectral limited area model Arpege/Aladin. *PWPR Report Series n° 7*, WMO T.D. N. 799, 111-118.
- Reasor, P. D., M. D. Eastin, and J. F. Gamache, 2009: Rapidly intensifying Hurricane Guillermo (1997). Part I: Low-wavenumber structure and evolution. *Mon. Wea. Rev.*, 137, 603-631.
- Reeves, H. D., and Y-L Lin, 2005: Effect of stable layer formation over the Po Valley on the development of convection during MAP IOP-8. *J. Atmos. Sci.*, 63, 2567-2584.
- Scialom, G., and Y. Lemaître, 1990 : A New Analysis for the Retrieval of Three-Dimensional Mesoscale Wind Fields from Multiple Doppler Radar. *J. Atmos. Oceanic Technol.*, 7, 640-665
- Shapiro, M. A., and D. Keyser, 1990: Fronts, jet streams and the tropopause. *Extratropical Cyclones, The Erik Palmén Memorial Volume*, C. W. Newton and E. O. Holopainen, Eds., Amer. Meteor. Soc., 167-191.
- Schultz, D. M., D. Keyser and L. Bosart, 1998: The Effect of Large-Scale Flow on Low-Level Frontal Structure and Evolution in Midlatitude Cyclones. *Mon. Wea. Rev.*, 126, pp. 1767-1791
- Steiner, M., O. Bousquet, R. A. Houze Jr, B. F. Smull, and M. Mancini, 2003: Airflow within major Alpine river valleys under heavy rainfall. *Quart. J. Roy. Meteor. Soc.*, 129, 411-432.
- Sugier, J., J. Parent-du-Châtelet, P. Roquain, and A. Smith, 2002: Detection and removal of clutter and anaprop in radar data using a statistical scheme based on echo fluctuation. *Proc. Second European Radar Conf.*, Delft, Netherlands, Copernicus GmbH, 17-24.
- Tabary, P., F. Guibert, L. Perier, and J. Parent-du-chatelet, 2006: An operational triple-PRT scheme for the French radar network. *J. Atmos. Oceanic Technol.*, 23, 1645-1656.
- Tabary, P., A.A. Boumahmoud, H. Andrieu, R. J. Thompson, A. J. Illingworth, E. Le Bouar and J. Testud, 2011: Evaluation of two "integrated" polarimetric Quantitative Precipitation Estimation (QPE) algorithms at C-band, *Journal of Hydrology*, 405., 248,260.
- Tuttle, J. D., and G. B. Foote, 1990: Determination of boundary layer airflow from a single Doppler radar. *J. Atmos. Oceanic Technol.*, 7, 218-232.
- Wernli, H., Dirren, S., Liniger, M. A. and Zillig, M., 2002, Dynamical aspects of the life cycle of the winter storm 'Lothar' (24-26 December 1999). *Quart. J. Roy. Meteor. Soc*, 128, 405-429
- Zrnica, D. S., and P. Mahapatra, 1985: Two methods of ambiguity resolution in pulsed Doppler weather radars., *IEEE Trans. Aerosp. Electron. Syst.*, 21, 470-483.

Multiple Doppler Radar Analysis for Retrieving the Three-Dimensional Wind Field Within Thunderstorms

Shingo Shimizu

*National Research Institute for Earth Science and Disaster Prevention/ Storm,
Flood, and Land-Slide Research Department
Japan*

1. Introduction

Multiple Doppler radar analysis has been widely used to retrieve three-dimensional wind fields within thunderstorms and meso-scale convective systems (MCS) since the late 1960s. A number of countries have constructed dense operational radar networks, such as the Operational Programme for the Exchange of Weather Radar Information (OPERA; Köck et al., 2000), to monitor and forecast severe weather in metropolitan regions. Multiple Doppler radar analysis using such operational radar networks improves 1) understanding of the physical mechanisms behind heavy rainfall and severe wind, 2) detection and forecasting of hazardous weather phenomena, and 3) planning for mitigation of human and socioeconomic losses in metropolitan regions.

Early single Doppler radar measurements provided a basic understanding of storm morphologies and their three-dimensional structures, including concepts for single-cell, multicell, and supercell storms (Browning, 1964, 1965). Single Doppler radar observations can only provide information on the radial component of wind (i.e., velocity which is directed toward or away from the radar), rather than the full three-dimensional structure. Armijo (1969) formulated a method that allowed the deduction of the three-dimensional wind structure by combining the data from several Doppler radars. Improvements in this multiple Doppler radar analysis method were reported during the 1970s and 1980s, including the design of optimal radar networks (Ray et al., 1979, 1983), the development of alternative analysis schemes for solving the mass continuity equation (Ray et al., 1980), and the introduction of floating boundary conditions (Chong & Testud, 1983). These improvements were primarily motivated by the need to overcome errors in the estimation of vertical velocity using upward integration of the mass continuity equation (Doviak et al., 1976). Errors in estimates of vertical velocity tend to amplify during such upward integration because of the stratification of density in the atmosphere (Doviak et al., 1976; Ray et al., 1980). Theoretical demonstrations indicate that downward integration of the mass continuity equation could yield more accurate estimates of vertical velocity than those that can be obtained from upward integration (Ray et al., 1980). Many subsequent studies have therefore applied downward integration schemes to determine the three-dimensional structure of winds within severe storms (Kessinger et al., 1987; Biggerstaff & Houze, 1991; Dowell & Bluestein, 1997).

Downward integration requires observations at the storm top; however, typical radar scan geometries are configured for operational monitoring of low-level precipitation and severe low-level wind phenomena (e.g., downburst and tornado). Such configurations do not often provide detailed observations of the storm top, where the vertical velocities may be significantly different from zero during storm development (Mewes & Shapiro, 2002). Several studies have used low pass filters, such as the Leise filter (Leise, 1981), to apply high wavenumber adjustments to the lower boundary conditions prior to upward integration of the mass continuity equation. Such adjustments reduce noise in estimates of upper-level winds (Parsons & Kropfli, 1990, Wakimoto et al., 2003).

One alternative is to apply the anelastic mass conservation equation as a weak constraint (Gao et al., 1999, hereafter G99; Gao et al., 2004, hereafter G04). This method is based on a three-dimensional variational approach, and removes the need to explicitly integrate the anelastic continuity equation. This prevents the accumulation of severe errors in the vertical velocity and ensures that uncertainties in the upper and lower boundary conditions do not propagate vertically. Furthermore, multiple Doppler radar analysis is usually performed in a Cartesian coordinate system; Doppler velocity data are often interpolated into this Cartesian coordinate system using a Cressman filter (Cressman, 1959). The scheme introduced by G99 bypasses this step by allowing reverse linear interpolation (from the regularly spaced Cartesian grid to the irregularly spaced radar observation points) during calculation of the cost function. This reverse interpolation procedure preserves the radial nature of radar observations; however, as noted above, operational radar networks are often incapable of providing dense observations, especially at upper levels. In such cases, the G99 scheme requires accurate background information, such as sounding data, to fill in the data-void regions between successive elevation angles. It is frequently difficult to obtain accurate background information in these cases, due in part to the coarse temporal resolution of sounding data. If spatially continuous Doppler velocity data could be obtained in Cartesian coordinates through the careful use of Cressman filters, accurate vertical velocity could be obtained from operational radar scans without the need for additional information. Otherwise, additional information regarding upper-level winds is necessary to reduce errors in estimates of vertical velocity near the storm top.

This chapter presents a simplified version of the G99 scheme that applies a three-dimensional variational approach on a regular Cartesian grid. The accuracy of calculated winds and the dependence of this accuracy on the density of upper-level radar observations are investigated using a set of idealized data sampled from a simulated supercell storm. A detailed description of the structure of this simulated supercell has been provided by Shimizu et al. (2008). The objective of this chapter is to propose an optimal method for analyzing severe thunderstorms using typical configurations of current operational radar data (less than 20 Plan Position Indicators, or PPIs, within 5–6 minutes).

2. Analysis method and variational scheme

This section briefly reviews the variational scheme for multiple Doppler radar analysis; a detailed description has been provided by Gao et al. (1999). The variational technique minimizes a cost function (J), which is defined as the sum of squared errors due to discrepancies between observations and analyses and additional constraint terms:

$$J = J_o + J_d + J_s + J_b \quad (1)$$

J_o represents the difference between the analysed radial velocity and the observed radial velocity, J_d is the mass continuity equation constraint term, J_s is the smoothness constraint term, and J_b is the background constraint term. The definition of J_o used here differs from that used by G99. J_o is defined as

$$J_o = \frac{1}{N} \sum_{i,j,k,m} C_o (Vr^{i,j,k,m} - Vr_{obs})^2 \quad (2)$$

Vr is the analysed radial velocity on a specified Cartesian grid, where i , j , and k indicate spatial location in the x , y , and z directions, respectively, and m indicates the m^{th} radar in the network. N is the total number of observations, which is equal to the product of the number of grid cells and the number of radars in the network. C_o is the reciprocal of the mean squared error in the observations. Vr_{obs} is the radial velocity interpolated to the regular Cartesian grid. The cost function is evaluated at each grid point in the Cartesian coordinates, rather than in spherical coordinates.

Each constraint is weighted by a factor that accounts for its respective proportion of the reciprocal of the mean squared error. As noted by G99, it is usually difficult to obtain appropriate values for the weighting coefficients. In particular, the value of the weighting coefficient for the anelastic mass conservation constraint plays an important role in determining the vertical wind component. This study uses the coefficient value used by G99, although G04 introduced a more objective method for estimating this coefficient.

The variational method uses the derivative of J with respect to the analysis variables to obtain an optimal solution. The gradient of the cost function is derived with respect to the control variables, namely the two horizontal wind components (u , v) and the vertical wind component (w). The form of the gradient used here differs slightly from that used by G99 because the form of the observational constraint differs. The gradient of the observational constraint with respect to u is given by

$$\frac{\partial J_o}{\partial u} = C_o \frac{x}{r} (Vr^{i,j,k,m} - Vr_{obs}) \quad (3)$$

where r is the distance between the radar and the grid point and x is the component of r in the x direction.

After the cost function is evaluated and its gradients are obtained, a quasi-Newton-type optimization scheme is used to update the control variables. This analysis uses a limited-memory Broyden-Fletcher-Goldfarb-Shanno (L-BFGS) method (Liu & Nocedal, 1989). For most meteorological applications, the L-BFGS method is more efficient than the conjugate gradient method (Navon & Legler, 1987). L-BFGS uses an approximation of the second-order derivative, so that an iteration of the L-BFGS method typically requires less computation than an iteration of the CG method. L-BFGS is therefore a better choice for optimizing a computationally expensive cost function.

3. Observational system simulation experiment and model description

The performance of the variational technique is evaluated in the context of an observational system simulation experiment (OSSE). This OSSE is conducted using numerical simulations

of a supercell thunderstorm observed near Tokyo on 24 May 2000 (Shimizu et al., 2008). The numerical simulations are generated using the Cloud-Resolving Storm Simulator (CReSS; Tsuboki & Sakakibara, 2002). CReSS is a three-dimensional nonhydrostatic model. The microphysical and other parameterization schemes used in CReSS have been described in detail by Tsuboki & Sakakibara (2002). The model grid comprises $300 \times 300 \times 70$ grid points, with grid intervals of 1 km in the horizontal directions. The vertical grid interval increases with height from 0.2 km near the surface to 0.37 km at the model top. The OSSE focuses on the three-dimensional distribution of wind within a 50×50 km domain around the simulated supercell at 1206 local standard time (LST), assuming that four Doppler radars are observing the storm (Fig. 1).

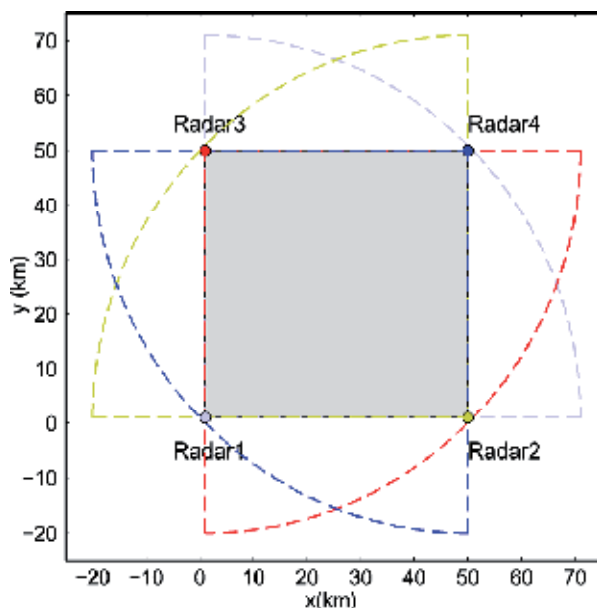


Fig. 1. Four radar locations around a simulated supercell storm. The simulated winds are compared with those derived from radar observations within the shaded region (50×50 km). The detection range of the radars is 70 km.

Updrafts associated with the simulated storm reached approximately 12 km above sea level (ASL). The locations of the four radars are chosen so that the distance between each radar and the storm is approximately 30–40 km (the supercell is located in the center of the shaded domain shown in Fig. 1). High elevation angle ($\sim 20^\circ$) radar scans are required to observe the storm top. Figure 2 shows the heights of the simulated radar beams. Three different volume scan strategies are considered in this chapter. The first strategy assumes that one volume scan consists of 17 PPIs. This strategy corresponds to X-band radar surveillance of a thunderstorm with echo top below 10 km ASL during an interval of 5–6 minutes. The elevation angles used in this strategy are 0.7° , 1.2° , 1.7° , 2.2° , 2.8° , 3.3° , 3.9° , 4.7° , 5.6° , 6.5° , 7.4° , 8.3° , 9.3° , 10.3° , 11.8° , 13.5° , and 15.6° . The second strategy adds three high elevation angles (16.7° , 17.8° , and 18.9°) to the previous volume scan (blue lines in Fig. 2). This strategy corresponds to a sector- or adaptive-scanning mode (Junyent et al., 2010) for a tall thunderstorm located near the radar. The third strategy adds nine additional high elevation angles (20.0° – 32.0° spaced at 1.5° intervals) to the preceding volume scan (red lines in Fig. 2).

This corresponds to an ideal observing mode. The third scanning strategy appears to be impossible to implement at a rate of one volume scan every 5–6 minutes using current technology, but it may be possible using the high temporal resolution capabilities of next-generation phased array radars (Heinselman & Torres, 2011).

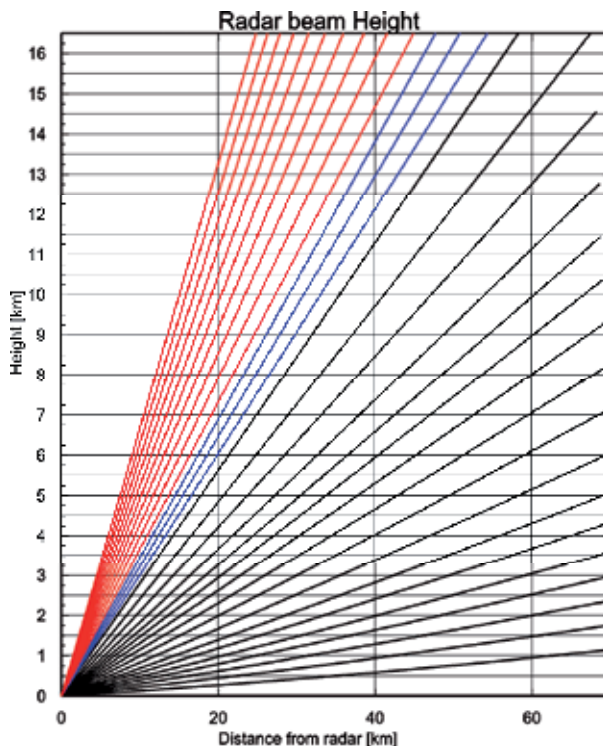


Fig. 2. Radar beam heights for the three analysed scanning strategies. Radar beam paths with elevation angles between 0.7° and 15.6° (17 PPIs) are shown as black lines, those with elevation angles between 16.7° and 18.9° are shown as blue lines, and those with elevation angles between 20.1° and 32° are shown as red lines.

4. Results

Figure 3 shows the mixing ratio of rain and the distribution of horizontal and vertical winds at an altitude of 4 km ASL. The Weak Echo Region (WER) within the strong updraft region was well simulated (the maximum updraft was 25 m s^{-1}). These strong updrafts were fed by southeasterly inflow below 1.5 km ASL (data not shown). Northwestern wind was dominant at 4 km ASL, and advected the area of heavy precipitation toward the southeast (Fig. 3). Three downdraft cores were simulated at 4 km ASL. The first of these was located in the heavy rain region to the east of updraft, and was associated with precipitation loading. The second downdraft core was located in the light rain region to the southeast of the updraft, and was related to the melting and sublimation cooling of ice-phase precipitation (Shimizu et al., 2008). The third downdraft core was located in the non-precipitating region to the south of the updraft, and was associated with compensation for the nearby strong updraft. The strong updraft, first downdraft, and second downdraft cores were also simulated at 2 km ASL (Fig. 4). The maximum updraft speed exceeded 18 m s^{-1} at 2 km ASL. Anticlockwise wind

rotation with a vertical vorticity of 0.08 s^{-1} was simulated along with this strong vertical velocity (Fig. 4). At 2 km ASL, the downdraft in the heavy precipitation region (maximum velocity -3 m s^{-1}) covered a broad area to the northeast of the updraft at 2 km ASL.

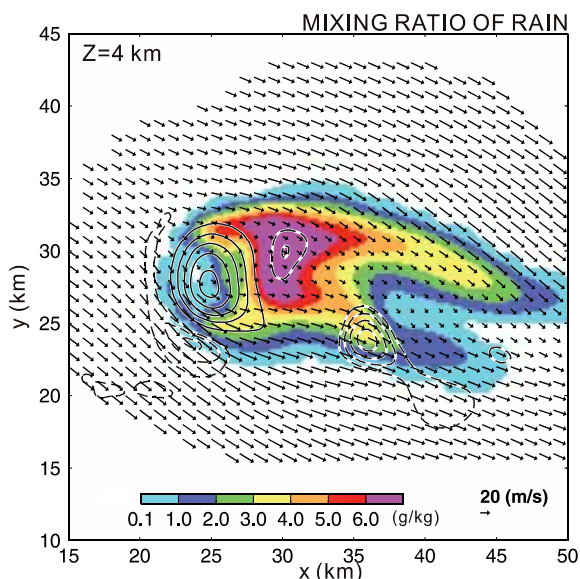


Fig. 3. CReSS model-simulated mixing ratio of rain at 4 km ASL. Updraft speeds are shown as solid contours with a contour interval of 5 m s^{-1} . Downdraft speeds are shown as dashed contours with a contour interval of 1 m s^{-1} . Winds are shown for all grid points where the vertically integrated mixing ratio of rain exceeded 0.0 kg kg^{-1} .

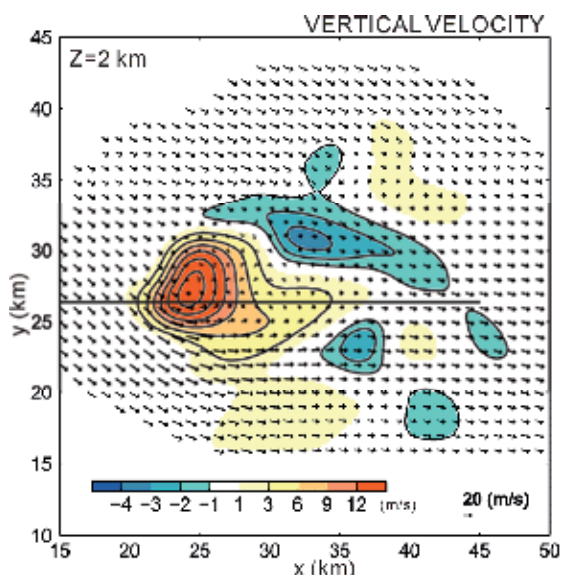


Fig. 4. CReSS model-simulated horizontal winds (vectors) and vertical velocity (shading) at 2 km ASL. Solid contours indicate updrafts at 3 m s^{-1} contour intervals and downdrafts at 1 m s^{-1} contour intervals. A vertical cross-section along the thick horizontal line is shown in Fig. 5.

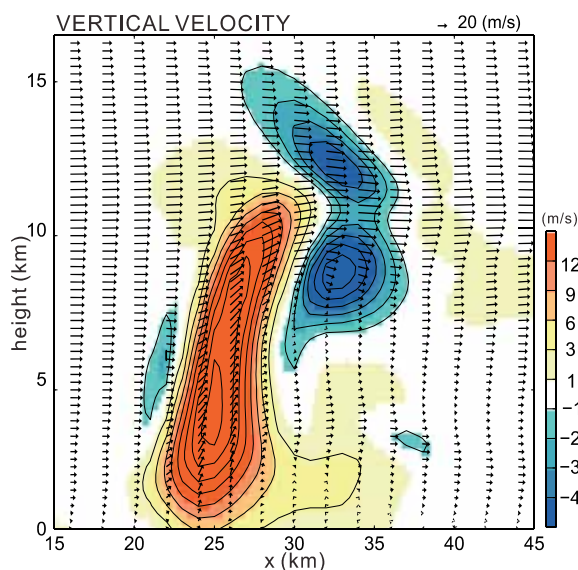


Fig. 5. Vertical cross-section of CRESS model-simulated vertical velocity at $y = 26$ km in Fig. 4. Contours are as in Fig. 4. Vectors indicate the speed and direction of wind flow along the vertical cross-section.

Figure 5 shows a vertical cross-section of the simulated storm along the $y = 26$ km transect in Fig. 4. The strong updraft extended upward to 12 km ASL, with a maximum updraft speed of 24 m s^{-1} at 4 km ASL. Three downdraft cores flanked the strong updraft core. A weak compensating downdraft was located to the west of the strong updraft at approximately 6 km ASL. A second strong downdraft (6 m s^{-1}) formed at 8 km ASL, and was associated with a high graupel mixing ratio (data not shown). A third strong downdraft was simulated at heights above 11 km ASL in the non-precipitating region. This downdraft was likely related to gravity wave dynamics.

Four pseudo-radars are assumed to observe this simulated three-dimensional wind field (the locations of these pseudo-radars are shown in Fig. 1). The wind components are bilinearly interpolated from the model grid to sampling locations along the radar beams. Radial velocity is calculated from the three wind components interpolated to each radar grid point. The maximum range of detection is set to 70 km for all four pseudo-radars, as shown in Fig. 1. Each radar sweep observes a total of 90 azimuthal angles, with a gate spacing of 100 m and an azimuthal resolution of 1° . The radial velocities along each radar beam in the volume scan (see Fig. 2) are interpolated back onto the Cartesian coordinate system using a Cressman scheme with an influence radius R of 1.0 km. Some upper-level velocities will be lost because the highest elevation angle was less than 30° (Fig. 2). The robustness of the variational analysis method to noise is shown by adding random errors (mean 0 m s^{-1} , variance $1 \text{ m}^2 \text{ s}^{-2}$) to the radial velocities after interpolation back to the Cartesian coordinate system.

The accuracy of the multiple Doppler radar analysis is evaluated using root-mean-square errors in retrieved radial velocity (RMSE_VR) and vertical velocity (RMSE_W), defined as follows:

$$\text{RMSE_VR}(k) = \frac{1}{N} \sum_{i,j,m} (Vr^{i,j,k,m} - Vr_{obs})^2 \quad (4)$$

$$\text{RMSE_W}(k) = \frac{1}{N2} \sum_{i,j} (W^{i,j,k} - W^{true})^2 \quad (5)$$

Average values of RMSE_VR and RMSE_W are computed at each vertical level after L-BFGS optimization. W^{true} is the vertical velocity output by the CReSS model. N and $N2$ are the number of individual samples used to compute the averages at a given layer.

The L-BFGS optimization scheme is able to successfully minimize the cost function. Figure 6 shows the relationship between the value of the cost function and the number of iterations performed. The value of the cost function is effectively constant after 20 iterations.

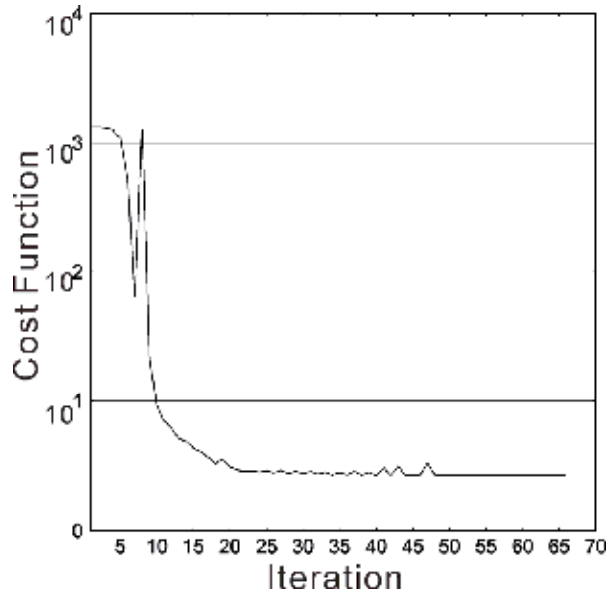


Fig. 6. Value of the cost function according to the number of iterations.

The results of the variational multiple Doppler radar analysis using volume scans with 30 PPIs (experiment name: EL30) is shown in Fig. 7 and Fig. 8. Figure 7 shows that the EL30 experimental setup successfully retrieves the strong updraft core shown in the original model output (Fig. 4). The EL30 results indicate a maximum updraft speed at 2 km ASL of 12 m s⁻¹, and successfully reproduce the anticlockwise rotation at this level. The downdraft region located in the area of heavy precipitation to the east of the strong updraft is retrieved by EL30, although the size of this downdraft region is too small (Fig. 4). The horizontal wind field retrieved by EL30 is similar to the original model output (Fig. 4), but there are two major discrepancies in vertical velocity. First, the strength of the updraft speed at 2 km ASL is underestimated by 3 m s⁻¹. Second, a spurious downdraft is identified to the southwest of the

strong updraft. The estimated northwesterly winds are much stronger in this spurious downdraft region than in the original model output (Fig. 4). This stronger northwesterly wind causes stronger divergence, which in turn induces the spurious strong downdraft. The strength of the enhanced northwesterly winds at 2 km ASL is similar to the strong northwesterly winds at 3–4 km ASL (cf. Fig. 2). Vertical smoothing of the radial velocity field by the Cressman interpolation procedure likely plays a major role in the erroneous vertical velocity field. Errors in radial velocity from vertical interpolation tend to occur near the boundaries of the storm, as shown in Fig. 7. This concentration of errors near the storm boundaries occurs because the number of radial velocity samples measured at neighboring grid cells is limited, so that the relative influence of radial velocities measured at distant grid cells grows.

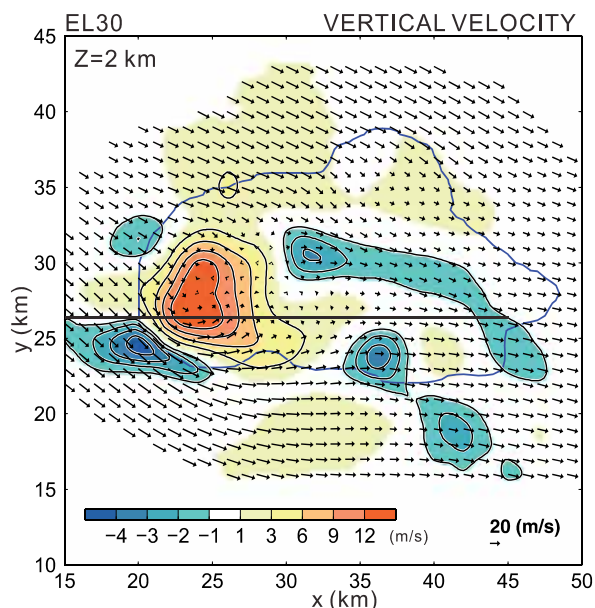


Fig. 7. Horizontal (vectors) and vertical wind velocity (shading) deduced by variational multiple Doppler radar analysis using 30 PPIs (EL30) at 2 km ASL. Solid contours indicate updrafts at 3 m s⁻¹ contour intervals and downdrafts at 1 m s⁻¹ contour intervals. The blue contour line outlines the region where the mixing ratio of rain exceeds 0.1 g kg⁻¹. A vertical cross-section along the thick horizontal line is shown in Fig. 8.

Figure 8 shows a vertical cross-section of the wind fields retrieved by EL30 along the $y = 26$ km transect in Fig. 7. Compared with the original model output (Fig. 5), the strong updraft and downdraft cores in the heavy precipitation region (at 8 km ASL) and the downdraft core associated with gravity wave dynamics (at 11 km ASL) are well retrieved. The maximum retrieved updraft speed is 21 m s⁻¹, and occurred at approximately 4 km ASL. The maximum retrieved downdraft speed is 7 m s⁻¹. The maximum updraft speed was underestimated by 3 m s⁻¹, while the maximum downdraft speed was overestimated by 1 m s⁻¹. The speed of the downdraft associated with gravity wave dynamics was underestimated by 1 m s⁻¹ relative to the original model output (Fig. 5). Several spurious updrafts and downdrafts can be identified in the EL30 retrieval, especially at 7–12 km ASL. Figure 7 and Fig. 8 indicate that the EL30 pseudo-radar configuration provides a good estimation of vertical velocity. Errors in the retrieved vertical velocity are uniformly less than 3 m s⁻¹.

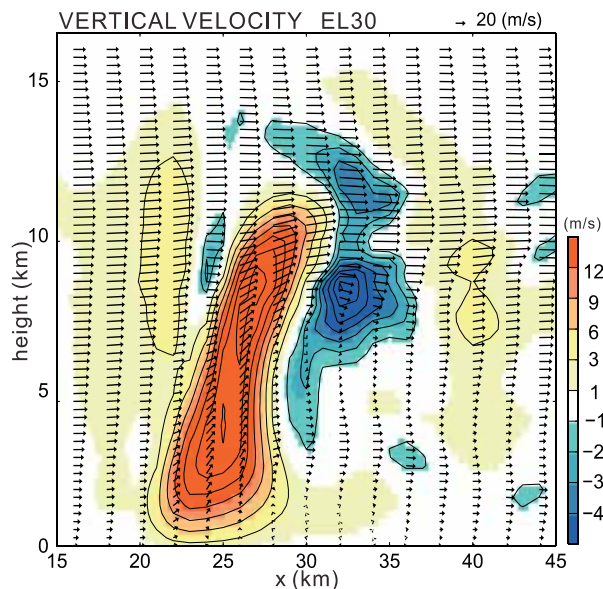


Fig. 8. Vertical cross-section of vertical velocity (shading) in EL30 at $y = 26$ km in Fig. 7. Contours are as in Fig. 5.

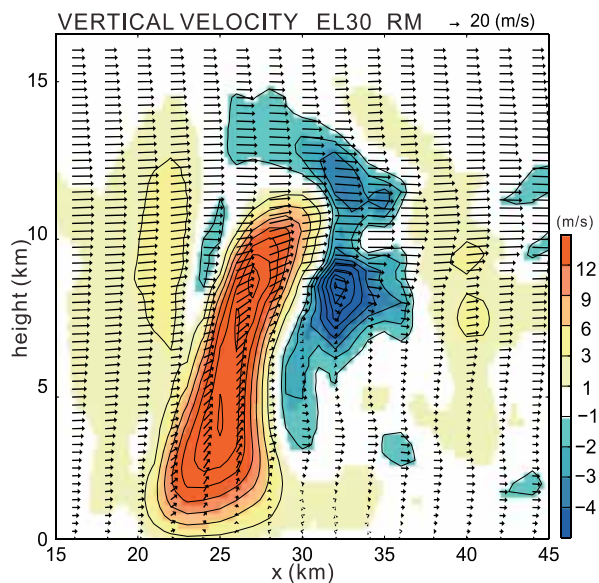


Fig. 9. As in Fig. 8 but with radial velocity observations contaminated by random noise.

As noted above, the use of the variational scheme removes the need to explicitly integrate the mass continuity equation, thus eradicating the vertical propagation of errors in the estimated wind field. Figure 9 shows the same vertical cross-section as in Fig. 8, but with random errors added to the input radial velocities. The distribution of retrieved vertical velocity is nearly identical in the cases with and without random errors. By contrast, the use of an upward integration scheme without random noise generates an erroneous vertical

velocity field (too strong), especially at upper levels (Fig. 10). The addition of random noise to the upward integration method exacerbated these errors (data not shown).

These experiments reveal 1) that the variational approach provides more realistic estimates of vertical velocity than the upward integration method, and 2) that observational noise does not propagate upward when the variational method is used. These results have been obtained using a volume scan with 30 PPIs (experiment EL30). This choice of volume scan is currently unrealistic because it would take more than 10 minutes using typical current antenna rotation speeds (a few rotations per minute). For operational use, volume scans with 15–20 PPIs are realistic given the need for rapid updates (less than 400 seconds). Two further experiments are performed to mimic volume scan data with 20 PPIs (experiment name: EL20) and 17 PPIs (experiment name: EL17). The analysis method is the same for the EL20 and EL17 experiments as for the EL30 experiment. In EL20, the highest elevation angle is 18.9° (Fig. 2). A beam at this elevation angle reaches 14 km ASL 40 km away from radar. This is sufficient to ensure a valid upper boundary condition ($w = 0$) in this case, because the storm top is located at 12 km ASL. In EL17, however, the highest elevation angle is 15.7° (Fig. 2). This beam does not reach 12 km ASL within the detection range of the radar.

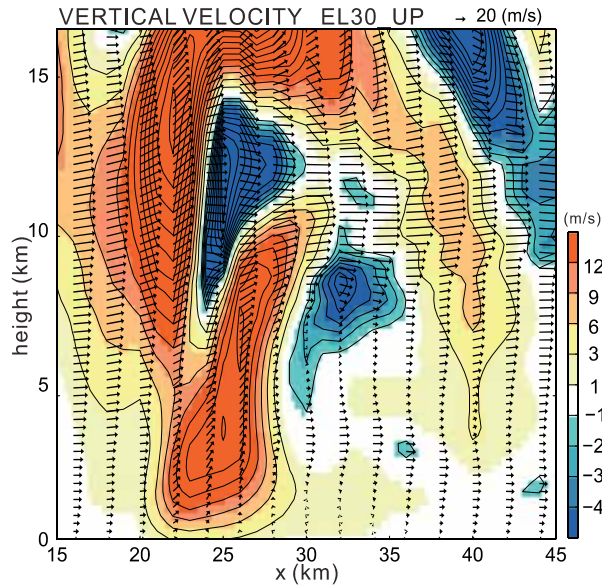


Fig. 10. As in Fig. 8 but using an upward integration scheme.

Figure 11 is the same as Fig. 8 but for EL20 rather than EL30. Vertical velocities retrieved by EL20 are similar to those retrieved by EL30 (Fig. 8) below 8 km ASL; however, the downdraft associated with gravity wave dynamics is not retrieved by EL20 because the pseudo-radar configuration does not observe that location. The maximum updraft was 20 m s^{-1} , a 1 m s^{-1} underestimate of the EL30 retrieval. As with EL30 (Fig. 8), a spurious updraft and downdraft are retrieved near 8–12 km ASL to the west of the strong updraft (Fig. 11). The area of this spurious downdraft is larger in EL20 than in EL30. This implies that EL20 is not capable of fully observing the storm top, so that erroneous upper boundary conditions induced the spurious downdraft.

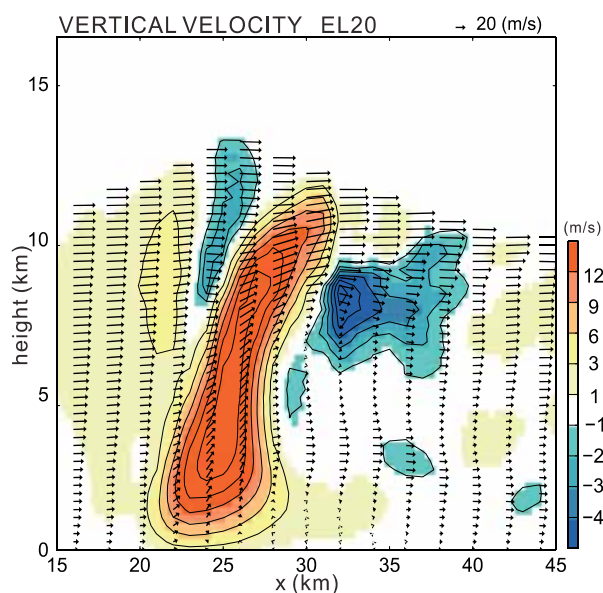


Fig. 11. As in Fig. 8 but with a volume scan of 20 PPIs.

Figure 12 is the same as Fig. 11 but for EL17 rather than EL20. The downdraft region associated with heavy precipitation to the east of the strong updraft is extended further downward in EL17. The maximum retrieved downdraft speed exceeds 9 m s^{-1} , a 3 m s^{-1} overestimate of the original model output (Fig. 5). These results indicate that even with the use of the variational approach, incomplete upper boundary conditions may lead to incorrect estimates of vertical velocity, especially near the storm top.

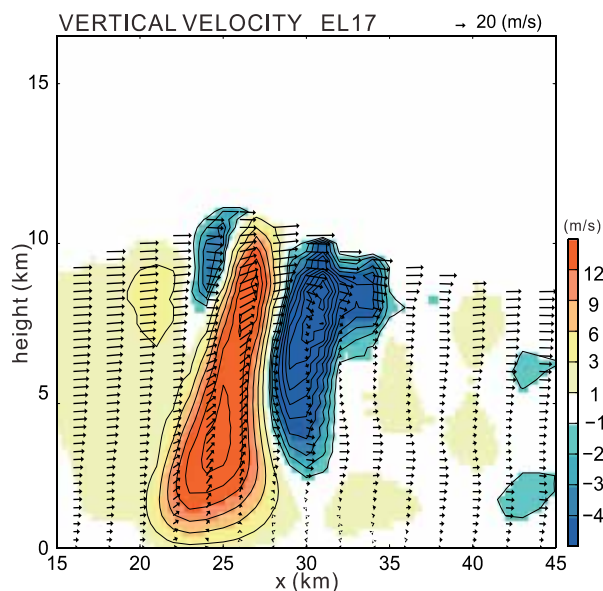


Fig. 12. As in Fig. 8 but with a volume scan of 17 PPIs.

Figure 13 shows root-mean-square errors in radial velocity (RMSE_VR) for the three experiments (EL30, EL20, and EL17). The EL30 RMSE_VR (black line in Fig. 13) was the smallest among the three experiments. The EL20 (red line) and EL17 (blue line) RMSE_VR both increased with height, while the RMSE_VR for all three experiments was small below 5 km ASL. The RMSE_VR and the root-mean-square error of the retrieved vertical velocity (RMSE_W) are closely related (Fig. 14). Differences in RMSE_W among the three experiments are relatively small below 5 km ASL and relatively large above 7 km ASL.

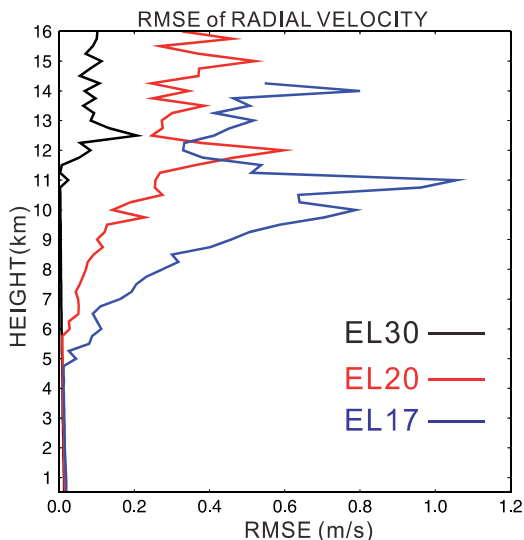


Fig. 13. Vertical profile of RMSE_VR for the EL30 (black), EL20 (red), and EL17 (blue) scanning strategies.

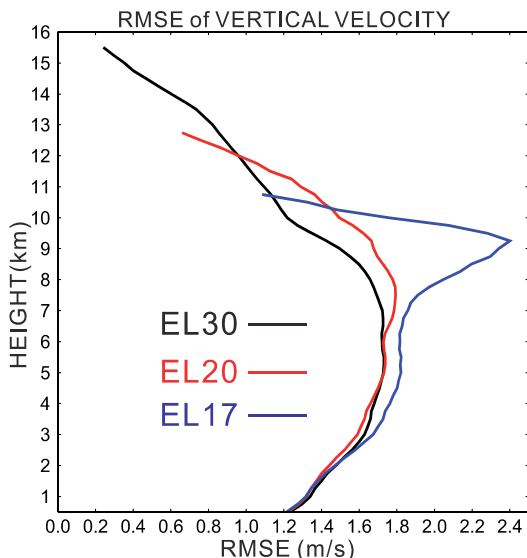


Fig. 14. Vertical profile of RMSE_W for the EL30 (black), EL20 (red), and EL17 (blue) scanning strategies.

For analyses of real thunderstorms the true value of vertical velocity is unknown, rendering the calculation of RMSE_W impossible; however, RMSE_VR can be calculated. Therefore, users could apply the variational multiple Doppler radar analysis approach to operational scans if the vertical profile of RMSE_VR is used to validate upper-level vertical velocities. The variational approach is a useful tool even for operational volume scans (less than 20 PPIs) because accurate three-dimensional winds can be retrieved at lower levels without contamination from sampling error in upper level or uncertainty in the upper boundary condition. These errors do not propagate vertically under the variational approach. Future work should examine the dependence of the retrieved wind field on scan strategy using observational datasets generated from real radar networks.

5. Conclusions

This chapter has introduced a variational multiple Doppler radar analysis for retrieving three-dimensional wind fields in a severe thunderstorm. A simplified version of the method presented by Gao et al. (1999) has been used to investigate the dependence of retrieved vertical velocity on scan strategy. Three volume scan strategies have been considered in this chapter: 1) a typical operational volume scan (17 PPIs), 2) a dense operational volume scan (20 PPIs), and 3) an extremely dense volume scan (30 PPIs). The variational approach has notable advantages over the upward integration method, particularly the avoidance of error accumulation during the upward integration; however, incomplete observations of the upper boundary condition can cause errors in estimates of vertical velocity near the storm top even when the variational approach is used. Users should limit their use of upper-level wind retrievals according to the root-mean-square error of radial wind, as described in this chapter. The variational method provides accurate estimates of the three-dimensional wind field at lower altitudes regardless of the upper boundary conditions. The density of operational radar networks in metropolitan regions has been increased in recent years to better monitor and forecast severe weather. Together with this increase in operational radar network density, the variational analysis method presented in this chapter will provide new information on the three-dimensional structure of wind within thunderstorms, and advance understanding of the physical mechanisms underlying heavy rainfall and severe winds.

6. Acknowledgment

The author thanks Dr. K. Iwanami of the National Research Institute for Earth Science and Disaster Prevention (NIED) for providing useful suggestions regarding multiple Doppler radar analysis. The model simulation was conducted at NIED using an SGI Altix 4700.

7. References

- Armijo L. (1969). A theory for the determination of wind and precipitation velocities with Doppler radars, *J. Atmos. Sci.*, 26, 570-573
- Byre, H. R. & Braham, R. R. (1949). *Thunderstorms*, , U.S. Government Printing Office, Washington D. C., 287 pp, USA.
- Biggerstaff M. I. & R. A. Houze (1991). Kinematic and precipitation structure of the 10-11 June 1985 squall line, *Mon. Wea. Rev.*, 119, 3034-3065

- Browning K. A. (1964). Airflow and precipitation trajectories within severe local storms which travel to the right of the winds, *J. Atmos. Sci.*, 21, 634-639
- Browning K. A. (1965). The evolution of tornadic storm, *J. Atmos. Sci.*, 22, 664-668
- Chong M. J & J. Testud. (1983). Three-dimensional wind field analysis from dual-Doppler radar data. Part III : the boundary condition : an optimal determination based on a variational concept, *J. Climate Appl. Meteor.*, 22, 1227-1241
- Cressman G.(1959). An operational objective analysis system, *Mon. Wea. Rev.*, 87, 367-374
- Doviak R. J. ; P. S. Ray ; R. G. Strauch & L. J. Miller (1976). Error estimation in wind fields derived from dual-Doppler radar measurement. *J. Appl. Meteor.*, 15, 868-878
- Dowell D. C & H. B. Bluestein. (1997). The Arcadia, Oklahoma, storm of 17 May 1981 : Analysis of a supercell during tornadogenesis, *Mon. Wea. Rev.*, 125, 2562-2582
- Gao J. ; M. Xue ; A. Shapiro & K. K. Droegemeier (1999). A variational method for the analysis of three-dimensional wind fields from two Doppler radars, *Mon. Wea. Rev.*, 127, 2128-2142
- Gao J. ; M. Xue ; K. Brewster & K. K. Droegemeier (2004). A three-dimensional variational data analysis with recursive filter for Doppler radars, *J. Atmos. Oceanic Technol.*, 21, 457-469
- Heinselman P. L. & S. M. Torres (2011). High-temporal-resolution capabilities of the national weather radar Testbed phased-array radar. *J. Appl. Meteor. Climatol.*, 50, 579-593
- Junyent F. ; V. Chandrasekar ; D. McLaughlin ; E. Insanic & N. Bharadwaj (2010). The CASA Integrated Project I : Network radar system, *J. Atmos. Oceanic Technol.*, 27, 61-78
- Kessinger C. J. ; P. S. Ray & C. E. Hane (1987). The Oklahoma squall line of 19 May 1977. Part I : a multiple Doppler analysis of convective and stratiform structure, *J. Atmos. Sci.*, 44, 2840-2865
- Köck K. ; T. Leitner ; W. L. Randeu ; M. Divjak & K. J. Schreiber (2000). OPERA: Operational Programme for the Exchange of Weather Radar information: First results and outlook for the future. *Phys. Chem. Earth*, 25B, 1147-1151
- Leise J. E. ; E. F. Blick & R. R. Bensch (1981). A multidimensional scale-telescoped filter and data extrapolation package, NOAA Tech. Memo ERL. WPL-82, Wave Propagation Laboratory, 20 pp
- Mewes J. J & A. Shapiro (2002). Use of the vorticity equation in dual-Doppler analysis of the vertical velocity field, *J. Atmos. Oceanic Technol.*, 19,543-567
- Parsons D. B & R. A. Kropfli (1990). Dynamics and fine structure of a microburst, *J. Atmos. Sci.*, 47, 1674-1692
- Ray P. S; K. W. Johnson & J. J. Stephens. (1979). Multiple Doppler network design, *J. Appl. Meteor.*, 18, 706-710
- Ray P. S & K. L. Sangren. (1983). On multiple-Doppler radar network design, *J. Climate. Appl. Meteor.*, 22, 1444-1453
- Ray P. S ; C. L. Ziegler ; W. C. Bumgarner & R. J. Serafin. (1980). Single and multiple Doppler radar observations of tornadic storms, *Mon. Wea. Rev.*, 108,1607-1625
- Shimizu S ; H. Uyeda ; Q. Moteki ; T. Maesaka ; Y. Takaya ; K. Akaeda & M. Yoshizaki (2008). Structure and formation mechanism on the 24 May 2000 supercell-like storm developing in a moist environment over the Kanto Plain, Japan, *Mon. Wea. Rev.*, 136, 2389-2407

Wakimoto R.; M. Hane; V. Murphey; D. C. Dowell & H. B. Bluestein (2003). The Kellerville Tornado during VORTEX : Damage survey and Doppler radar analyses, *Mon. Wea. Rev.*, 131, 2187-2221

New Observations by Wind Profiling Radars

Masayuki K. Yamamoto

*Research Institute for Sustainable Humanosphere (RISH), Kyoto University,
Japan*

1. Introduction

Wind profiling radar, also referred to as “radar wind profiler”, “wind profiler”, and “clear-air Doppler radar”, is used to measure height profiles of vertical and horizontal winds in the troposphere. It receives signals scattered by radio refractive index irregularities (clear-air echo) and measures the Doppler shift of the scattered signals (Gage, 1990). Wind profiling radar measures wind velocities by steering its beam directions or using spaced receiving antennas (e.g., Larsen & Röttger 1989; May, 1990). The two methods are referred to as the Doppler beam swinging (DBS) technique and spaced antenna (SA) technique, respectively. Owing to its capability to measure wind velocities in the clear air with high height and time resolutions (typically a hundred to several hundreds of meters and less than several minutes, respectively), it is used for atmospheric research such as radio wave scattering, gravity waves, turbulence, temperature and humidity profiling, precipitation system, and stratosphere-troposphere exchange (STE) processes (Fukao, 2007; Hocking, 2011). Wind profiling radar is also utilized for monitoring wind variations routinely. In USA and Japan, a nationwide ultrahigh frequency (UHF) wind-profiling radar network is operated in order to provide upper-air wind data to numerical weather prediction (Ishihara et al., 2006; Stanley et al., 2004). In Europe, Cost Wind Initiative for a Network Demonstration in Europe (CWINDE), now renamed as the Co-Ordinated Wind Profiler Network in Europe, is also operated (Met Office, 2011).

For wind profiling radars, frequency range of 30-3000 MHz (i.e., very high frequency (VHF) and UHF bands) is generally used because the energy spectrum of atmospheric turbulence falls off rapidly with decreasing eddy size in the inertia subrange, and radar radio waves are scattered only from turbulent eddies at the Bragg scale (i.e., half the radar wavelength). For measurements from the ground to several thousand meters, UHF wind profiling radars are widely used because their small antenna size enables their easy installation and their quick switching time from transmission to reception is necessary for measurements near the ground. Such UHF wind profiling radars are referred to as the boundary layer radars. Because the minimum size of turbulent eddies increases exponentially with increasing altitude (e.g., Hocking, 1985), frequencies near 50 MHz are used for clear-air radars which measure the mesosphere, stratosphere and troposphere (MST radars) and those which measure the stratosphere and troposphere (ST radars). In the chapter, measurement results of VHF and UHF radars are presented.

Recent development in radar interferometry techniques provides means for enhancing radar resolution and improving data quality. In radar interferometry, spaced receiver antennas are used to improve angular resolution, and multiple carrier frequencies are used to improve range resolution. The former is referred to as coherent radar imaging (CRI) or spatial domain interferometric imaging (SDI; Palmer et al., 1998; Hassenpflug et al., 2008), and the latter is referred to as range imaging (RIM; Palmer et al., 1999) or frequency-domain interferometric imaging (FII; Luce et al., 2001). Hereafter the abbreviations CRI and RIM are used. Though development of the radar interferometry technique have decades of history (Hocking, 2011), CRI and RIM, which have been intensively developed for the last decade, are presented in section 2.

Wind profiling radars operated at approximately 50 MHz frequency (50-MHz wind profiling radars) are not sensitive for small-sized cloud particles. Therefore 50-MHz wind profiling radars are able to measure vertical and horizontal wind velocities in both the clear air and cloudy regions. Millimeter-wave radars, which use near 35-GHz or 95-GHz frequency (i.e., 8-mm or 3-mm wavelength) and hence are able to detect echoes scattered by small-sized cloud particles, are an indispensable means to measure microphysical properties of clouds (Kollias et al., 2007). Laser radars (lidars), which transmit laser light and receive echoes scattered by atmospheric molecules, aerosols, and hydrometeors, are useful to measure not only various physical quantities in the clear air but also particles and hydrometeors in the atmosphere (Wandinger, 2005). Recent measurements using collocated wind profiling radars and millimeter-wave radars/lidars have gained new insights of turbulence and cloud processes. The measurement results are presented in section 3.

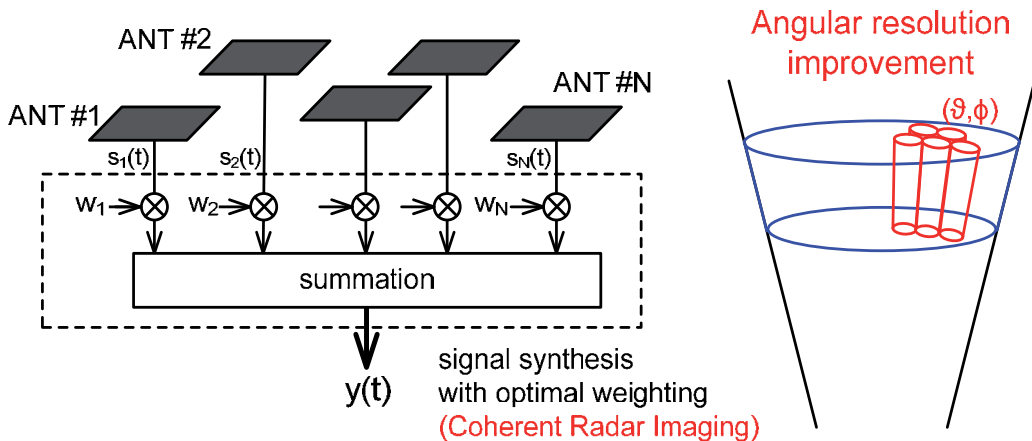


Fig. 1. Conceptual drawing of CRI. The blue-colored volume on the right shows the resolution without CRI (i.e., the angular resolution is determined by the antenna beam width), and the red-colored volumes show the angular resolution improvement attained by CRI.

2. Imaging techniques to enhance radar resolutions

Though development of the radar interferometry techniques have decades of history, CRI and RIM, which have been intensively developed for the last decade, are presented

in section 2.1 and 2.2, respectively. The readers are recommended to refer Hocking (2011) for the thorough development history of the radar interferometry techniques. Further applications aiming at advanced probing of the atmosphere are presented in section 2.3.

2.1 Angular resolution enhancement using spaced receivers

2.1.1 Signal processing

Fig. 1. shows a conceptual drawing of CRI. In CRI, signals from the spaced receivers are synthesized with appropriate weights in order to steer the radar beam in certain directions with improved angular resolution. For CRI, the Capon method (Capon, 1969) is widely used because it satisfies both high angular resolution and simple calculation. Hereafter signal processing of CRI using the Capon method is described. The Capon method is described as the problem of finding optimal weights. The optimal weights used in order to calculate the weighted sum of signals which are received by the spaced receivers. \mathbf{s} denotes a set of signals associated with the N spaced receivers at an arbitrary range gate and expressed by

$$\mathbf{s}(t) = (s_1(t), s_2(t), \dots, s_N(t))^T, \quad (1)$$

where t is the sampled time and T is the transpose operator. \mathbf{w} denotes a set of weights for summation and is expressed by

$$\mathbf{w} = (w_1, w_2, \dots, w_N)^T. \quad (2)$$

The optimal weight vector is given by a solution that minimizes the resulting average power B . B is expressed by

$$B = \mathbf{w}^H \mathbf{R} \mathbf{w}, \quad (3)$$

where H represents the Hermitian operator (conjugate transpose) and \mathbf{R} is a covariance matrix given by

$$\mathbf{R} = \begin{pmatrix} R_{11} & R_{12} & \dots & R_{1N} \\ R_{21} & R_{22} & \dots & R_{2N} \\ \vdots & \vdots & \dots & \vdots \\ R_{N1} & R_{N2} & \dots & R_{NN} \end{pmatrix}, \quad (4)$$

R_{ij} is a covariance between s_i and s_j . The length of time used for calculating \mathbf{R} should be determined by considering the accuracy of covariance value and the time resolution. \mathbf{w} is constrained by the condition of constant gain to waves coming from the target volume, and the constraint is given by

$$\mathbf{e}^H \mathbf{w} = 1, \quad (5)$$

where

$$\mathbf{e} = (e^{jk \cdot \mathbf{D}_1}, e^{jk \cdot \mathbf{D}_2}, \dots, e^{jk \cdot \mathbf{D}_N})^T, \quad (6)$$

\mathbf{k} represents the wavenumber vector of the focused direction with the zenith and azimuth angle of θ and ϕ , respectively ($\mathbf{k} = \frac{2\pi}{\lambda}[\sin\theta\sin\phi, \sin\theta\cos\phi, \cos\theta]$), and the vectors which represent the center of each receiving receiver are denoted by \mathbf{D}_m for the m th receiver. \mathbf{e} is referred to as the steering vector. The constrained minimization problem can be solved using the Lagrange method, and Palmer et al. (1998) describe details of solving the constrained minimization problem (see their appendix). As the solution of the constrained minimization problem, the optimal weight $\mathbf{w}_C(\mathbf{k})$ is given by

$$\mathbf{w}_C(\mathbf{k}) = \frac{\mathbf{R}^{-1}\mathbf{e}}{\mathbf{e}^H\mathbf{R}^{-1}\mathbf{e}}. \quad (7)$$

Using Equations (1) and (7), scalar output of the filter $y(t)$ is given by

$$y(t) = \mathbf{w}_C^H(\mathbf{k})\mathbf{s}(t). \quad (8)$$

By calculating the Doppler spectrum of $y(t)$, brightness B_C (i.e., power density), radial Doppler velocity, and spectral width are able to be computed with improved angular resolution. B_C is able to be obtained without calculating \mathbf{w}_C and given by

$$B_C(\mathbf{k}) = \frac{1}{\mathbf{e}^H\mathbf{R}^{-1}\mathbf{e}}. \quad (9)$$

When the brightness at arbitrary Doppler velocity needs to be calculated, \mathbf{R} is replaced by the cross-spectral matrix of the N receiver signals. Palmer et al. (1998) showed a clear difference in angular distribution of brightness between positive and negative Doppler velocities (see their Plate 2). Brightness at the arbitrary Doppler velocity of received data is also able to be calculated by applying band-pass filtering to \mathbf{s} .

In the Fourier-based method, in which all the signals from receivers were synthesized with equal weight, a weight vector $\mathbf{w}_F(\mathbf{k})$ which steers the beam in the direction \mathbf{k} is given by

$$\mathbf{w}_F(\mathbf{k}) = (e^{j\mathbf{k}\cdot\mathbf{D}_1}, e^{j\mathbf{k}\cdot\mathbf{D}_2}, \dots, e^{j\mathbf{k}\cdot\mathbf{D}_N})^T. \quad (10)$$

Scalar output of the filter is calculated by replacing $\mathbf{w}_C(\mathbf{k})$ in Equation (8) with $\mathbf{w}_F(\mathbf{k})$.

Other methods are able to be used for CRI. Details of multiple signal classification (MUSIC) method and maximum entropy method (MEM) are explained by H elal et al. (2001) and Yu et al. (2000), respectively. For more general review of CRI, see Woodman (1997).

There are factors that affect the performance of CRI. Using numerical simulation, effects of receiver noise and turbulence distribution were evaluated by Yu et al. (2000) and Cheong et al. (2004). Further, Yu et al. (2000) evaluated relation between CRI performance and receiver arrangement. Effects of uncertainty of receiver gain and phase were evaluated for the case of turbulent Eddy Profiler (TEP), which was developed by the University of Massachusetts in order to carry out CRI measurement in the boundary layer (Mead et al. 1998).

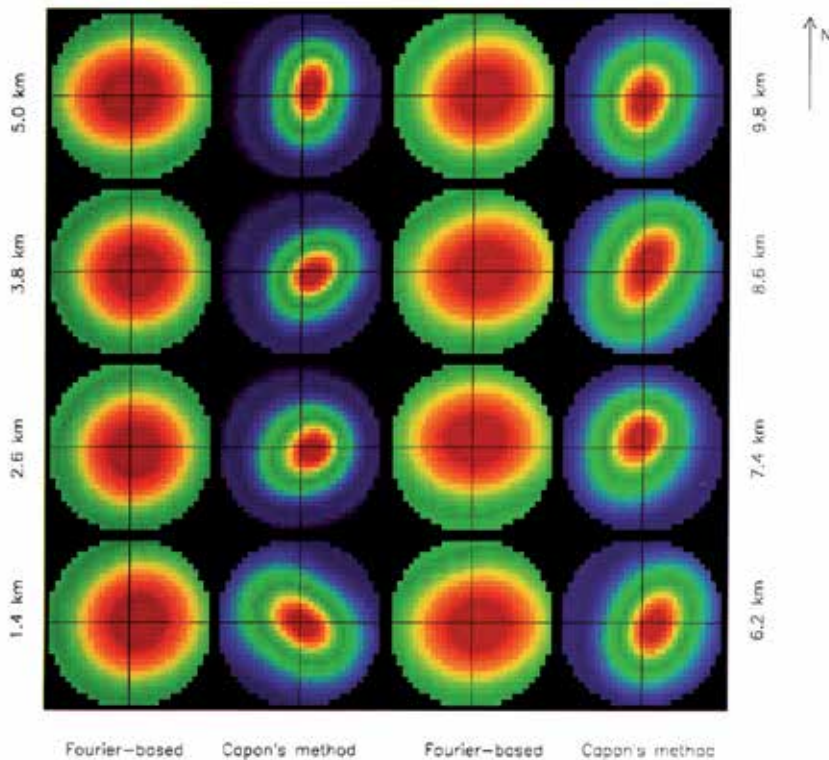


Fig. 2. Brightness distributions within $\pm 4^\circ$ from the center of beam direction at the altitudes from 1.4 km to 9.8 km (Palmer et al., 1998). Red color corresponds to highest brightness. Images on the left and right of each pair were obtained with the Fourier-based method and the Capon method, respectively.

2.1.2 Measurement results

An example of high-angle-resolution measurement using CRI is presented. Fig. 2 shows brightness distributions within $\pm 4^\circ$ from the center of beam direction measured by the Middle and Upper Atmosphere radar (MU radar). MU radar is a MST radar installed at Shigaraki MU Observatory, Japan (34.85°N , 136.10°E ; Fukao et al., 1990). CRI successfully produces fine-scale angular distributions of backscattered clear-air echo power within the two-way half-power full beam width of 2.5° . Such high angular resolution cannot be attained without CRI. It is noted that the Capon method exhibits better resolution than the Fourier-based method. Using data collected by a VHF radar installed at Tourris, France (43.08°N , 6.01°E), H elal et al. (2001) showed a fine-scale angular distribution of backscattered clear-air echo power using the Capon and MUSIC methods. Chau and Woodman (2001) also showed the angular distribution using the Fourier-based method, Capon method, MEM, and the fitting technique. Using the characteristic that raindrop fall velocity is much greater than vertical wind velocity, Palmer et al (2005) demonstrated that fine-scale angular distributions of backscattered power from clear air and that from raindrops are able to be obtained separately. From a CRI measurement by TEP, Pollard et al. (2000) demonstrated that horizontal distribution of refractive index structure function is able to be measured.

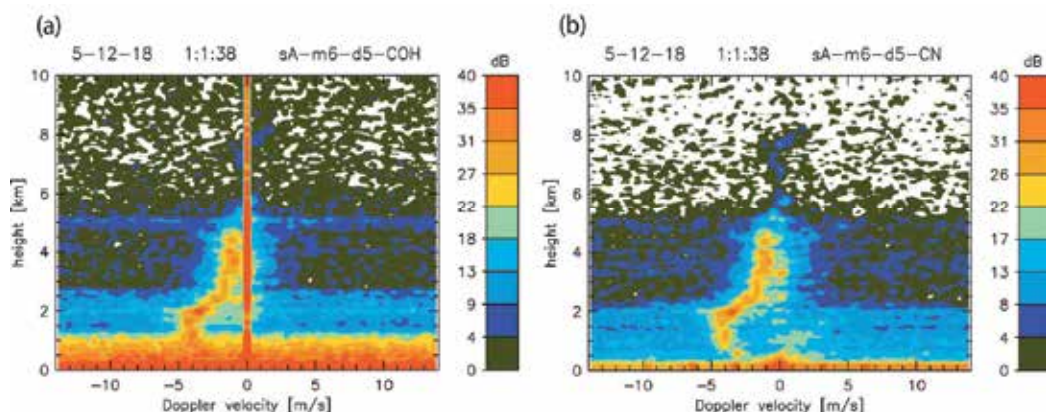


Fig. 3. Altitude profile of Doppler spectra (a) before and (b) after applying clutter mitigation algorithm (Nishimura et al., 2010). Colors show the backscattered power in an arbitrary unit.

CRI is also able to be used for clutter mitigation. Fig. 3 is an example of clutter mitigation. Measurement data were collected by the receiving antenna array of the Equatorial Atmosphere Radar (EAR), which were temporally installed for multistatic radar observations. The EAR is installed at West Sumatra, Indonesia and is operated with a center frequency of 47-MHz and peak output power of 100 kW (Fukao et al., 2003). Strong returns centered at 0 m s^{-1} in Fig. 3a are signals returned from the ground (i.e., ground clutter), and have to be removed in order to estimate spectral moments correctly. By applying the clutter mitigation algorithm developed by Nishimura et al (2010), the clutter signals are successfully removed (Fig. 3b). Nishimura et al. (2010) attained the clutter mitigation by combining the directional-constrained minimization of power with constrained norm (DCMP-CN; see Kamio et al. (2004) for details) and an algorithm that compensates electromagnetic coupling between antennas and the ground. The compensation was carried out because the electromagnetic coupling can cause a phase error of atmospheric echoes received by antenna arrays, and the phase error can lead to degradation of desired atmospheric echoes in the output of the adaptive clutter mitigation process.

In the case shown by Nishimura et al. (2010), each antenna element has an identical antenna gain. When a high-gain antenna is used for transmission and reception of scattering from atmospheric targets, using auxiliary antennas which are used only for receiving ground clutters is effective for clutter mitigation. In order to realize clutter mitigation using the main antenna of the MU radar and auxiliary antennas, Kamio et al. (2004) modified the DCMP-CN method. In the modified method, the weight of main antenna is kept to 1 in order to keep the main lobe pattern, and the weights of auxiliary antennas are optimized in order to minimize the received power from side lobes.

Moving biological targets like birds and insects can cause a large error of wind velocity measured by wind profiling radars (e.g., Vaughn, 1985; Wilczak et al., 1995). Using CRI, moving clutter is able to be suppressed. From the CRI measurement using TEP, Cheong et al. (2006) succeeded in separating clear-air echoes and the biological scattering which was moving in the grating-lobe region, and demonstrated that the separation of biological scattering greatly reduced the error of wind velocity estimates. Chen et al. (2007) also applied CRI to data measured by multiple antenna profiler radar (MAPR) of National

Center for Atmospheric Research (NCAR) in order to mitigate effects of bird contamination in wind velocity estimates.

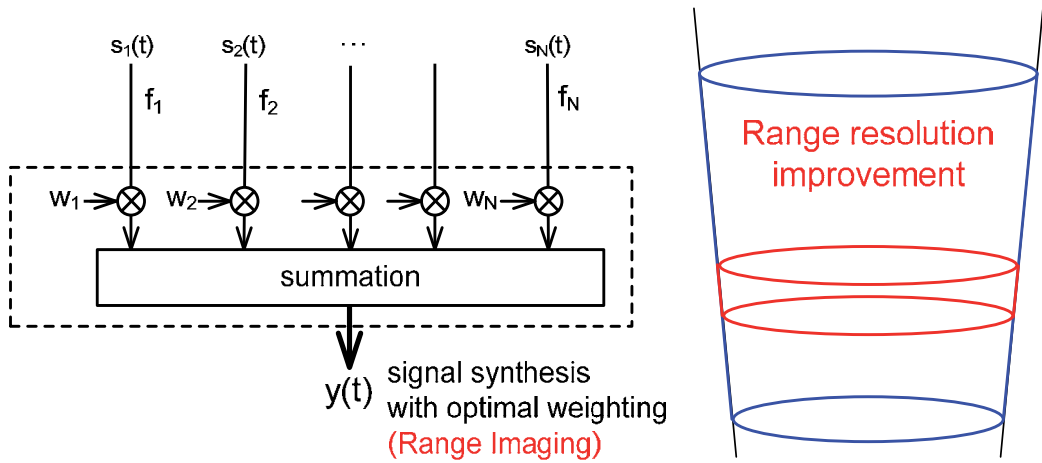


Fig. 4. Conceptual drawing of RIM. The blue-colored volume shows the resolution without RIM (i.e., range resolution is determined by the transmitted pulse width), and the red-colored volume shows the range resolution improvement attained by RIM.

2.2 Range resolution enhancement using multiple frequencies

2.2.1 Signal processing

Figure 4 shows a conceptual drawing of RIM. The width of range gate is determined by the sampling interval of analog-to-digital converter, and the range resolution without RIM is determined by the transmitted pulse width. In RIM, signals sampled from multiple frequencies are synthesized with appropriate weights in the subranges within a range gate. Using the synthesized signal, the first three spectral moments (brightness, Doppler velocity, and spectral width) at the subranges are estimated in order to attain range resolution improvement. Among various methods which can be used for RIM processing (Luce et al., 2001; Palmer, et al., 1998; Smaïni et al., 2002), the Capon method (Capon, 1969) is widely used because it satisfies both high range resolution and simple calculation. Hereafter signal processing of RIM using the Capon method is described. \mathbf{s} denotes a set of signals collected by N carrier frequencies at an arbitrary range gate and is expressed by

$$\mathbf{s}(t) = (s_1(t), s_2(t), \dots, s_N(t))^T. \tag{11}$$

Frequencies are switched on a pulse-to-pulse basis in order to maximize the correlation of signals sampled by different frequencies. Using numerical simulation, Palmer et al. (1999) showed that using 3 or more frequencies are required for RIM measurements. For field measurements, four or five frequencies are used typically (e.g., Fukao et al., 2011; Palmer et al., 2001; Yu & Brown, 2004). The optimal weight vector is given as a solution that minimizes the resulting average power B_r . B_r is expressed by

$$B_r = \mathbf{w}^H \mathbf{R} \mathbf{w}, \tag{12}$$

where \mathbf{w} denotes a set of weights for summation as expressed by Equation (2) and \mathbf{R} is a covariance matrix as expressed by Equation (4). \mathbf{w} is constrained by the condition of constant gain to waves coming from the target range, and the constraint is given by

$$\mathbf{e}^H \mathbf{w} = 1, \quad (13)$$

where \mathbf{e} is a range steering vector and given by

$$\mathbf{e} = (e^{-j(2k_1 r_1 - \phi_1)}, e^{-j(2k_2 r_1 - \phi_2)}, \dots, e^{-j(2k_N r_1 - \phi_N)})^T, \quad (14)$$

where k_m denotes the wavenumber of m th frequency, r_1 represents the range between the target and radar, and ϕ_m is the initial phase of m th frequency.

Because ϕ_m is determined not only by the total system delay throughout the transmitter and receiver chains but also by k_m , the values of ϕ_1, \dots, ϕ_N are different. Therefore the total system delay, from which the values of ϕ_1, \dots, ϕ_N are computed, needs to be known in order to determine \mathbf{e} correctly. Chilson et al. (2004) and Palmer et al. (2001) measured the total system delay by leaking the transmitted signal back to the receiver through an ultrasonic delay line. In a practical manner, only the relative phase differences among the frequencies are necessary to correct the effects of system delay. Therefore, the correction is able to be attained by calculating the phase term of cross correlation between the two time series of received signals measured at different frequencies (Chen, 2004). Measurement results of phase correction using the clear-air echoes are shown by Chen et al. (2009, 2010) and Chen & Zecha (2009).

The optimal weight \mathbf{w}_{rC} is given by

$$\mathbf{w}_{\text{rC}} = \frac{\mathbf{R}^{-1} \mathbf{e}}{\mathbf{e}^H \mathbf{R}^{-1} \mathbf{e}}. \quad (15)$$

Using Equations (11) and (15), scalar output of the filter $y(t)$ is given by

$$y(t) = \mathbf{w}_{\text{rC}}^H \mathbf{s}(t). \quad (16)$$

By calculating Doppler spectrum of $y(t)$, brightness B_{rC} (i.e., power density) and other spectral parameters are able to be computed with improved range resolution. B_{rC} is given by

$$B_{\text{rC}} = \frac{1}{\mathbf{e}^H \mathbf{R}^{-1} \mathbf{e}}. \quad (17)$$

Brightness at arbitrary Doppler velocity is also able to be calculated in the same manner as described in section 2.1.1.

Because of the limited width of transmitted pulse (i.e., wave form of transmitted pulse), received signal power within the range gate has range dependency (i.e., the received signal power decreases near the edge of range gate). Chen and Zecha (2009) proposed a practical method in order to correct the range weighting, and the correction results are also presented by Chen et al. (2009, 2010) and Chen & Zecha (2009).

Recently, Le et al. (2010) proposed a technique that improves received signal power by exploiting the temporal correlation difference between the desired signal and system noise. Le et al. (2010) showed that the technique has better performance of radar echo production than RIM in the low SNR regions.

2.2.2 Measurement results

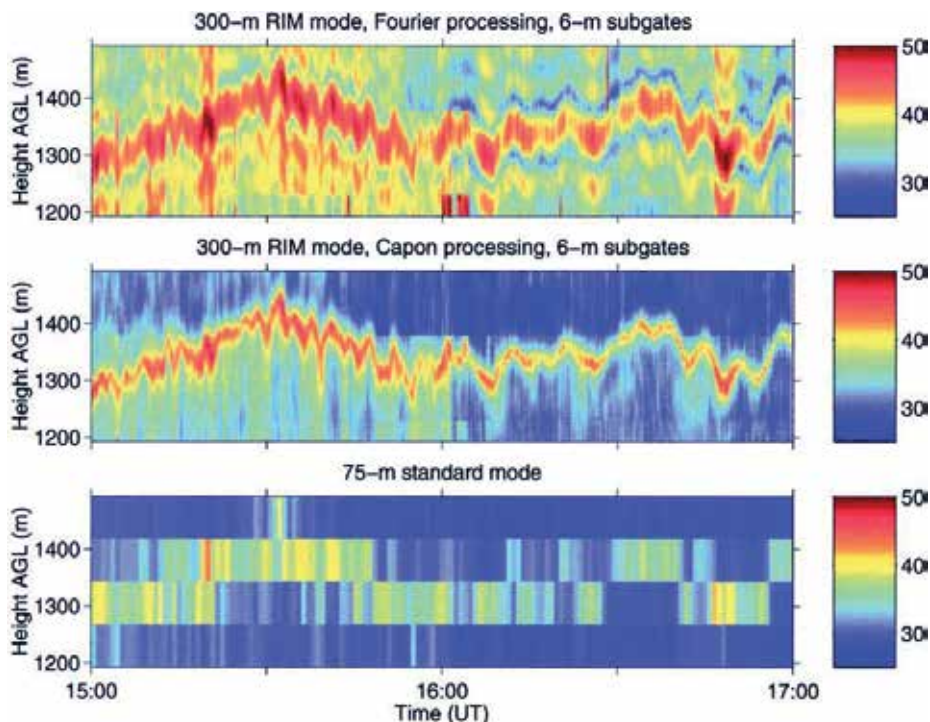
In order to demonstrate that RIM is useful for improving range resolution, measurement results are presented. Fig. 5 shows an example of RIM measurement. The brightness profiles were produced with 6-m range intervals by applying RIM to received signals measured with the 2- μ s transmitted pulse and four transmitted frequencies (914.0, 914.33, 915.33, and 916 MHz). The bandwidth of the RIM measurement was 2.5-MHz (2 MHz for the actual frequency spread and 0.5 MHz for the 2- μ s transmitted pulse). During the experiment, the RIM measurement and single frequency measurement using the 0.5- μ s transmitted pulse (i.e., corresponding to 75-m range resolution and 2-MHz bandwidth) were carried out alternatively. Although the frequency bandwidth difference between the two observation modes was as small as 500 kHz, it is clear that both the brightness produced by the Fourier-based method and by the Capon method show finer height variations than the backscattered power measured with the 75-m range resolution. Further, it is clear that the Capon method attains finer range resolution than the Fourier-based method. By applying RIM to the same dataset, Chilson et al. (2004) produced Doppler velocity with 15-m range intervals and showed that the Doppler velocity produced by RIM agreed well with that measured with the 0.5- μ s transmitted pulse.

Fig. 6 shows an example of Kelvin-Helmholtz (KH) instability (i.e., shear instability) measured by the MU radar operated with a RIM observation mode (Fukao et al., 2011). The measurement was carried out using the new MU radar system upgraded in 2004 (Hassenpflug et al., 2008). Structure of KH billows is clearly seen in the brightness around 1.5 km from 00:35 to 00:53 (Fig. 6a). The resemblance to the evolution of KH vortices measured in the laboratory experiment (Patterson et al., 2006) is striking. Vertical wind velocity shows perturbations with magnitudes of 1 m s⁻¹ or more. Because accurate high-resolution vertical wind measurement is quite difficult for instruments other than clear-air Doppler radars (e.g., Fukao, 2007; Hocking 2011), measurements by wind profiling radars are indispensable to understand turbulence processes in the atmosphere. RIM measurements have revealed a fine structure of KH billows in the jet stream in the mid-latitudes (Luce et al., 2008) and upper-tropospheric easterly jet in the tropical region (Mega et al., 2010). Fukao et al (2011) carried out a statistical analysis of KH billows in order to quantify their occurrence frequency, spatial scales, energy dissipation rate, and vertical eddy diffusivity.

2.2.3 Advantage of range resolution enhancement using multiple frequencies

In the section, advantages of RIM over other methods are described. Radar range resolution is determined by the transmitted pulse width, and ranges typically a hundred to several hundreds of meters. However, for UHF wind profilers, a range resolution down to approximately 30 m is able to be attained by transmitting shorter pulses (e.g., Wilson et al., 2005). Although the range resolution is able to be improved by transmitting shorter pulses, it requires not only wider bandwidth but also more transmitted power in order to keep the

receiver sensitivity constant. RIM also contributes to efficient usage of frequencies. Chilson et al. (2003) pointed out that for the RIM measurement shown in Fig. 5, the spurious intensity of frequency power spectrum of transmitted pulses was smaller than the 0.4- μ s transmitted pulse width which also uses 2.5-MHz bandwidth (see their Fig. 2). RIM is especially useful for VHF wind profiling radars because their frequency bandwidth allowed by license and that determined by antenna are limited.



©American Meteorological Society. Reprinted with permission.

Fig. 5. Time-range plot of (top) brightness produced by the Fourier-based method, (center) brightness produced by the Capon method, and (bottom) backscattered power expressed in decibels (Chilson et al., 2003). The data was collected with the Platville 915-MHz tropospheric wind profiler. See text for details of the measurement.

Pulse compression using frequency-modulated continuous wave (FMCW) is also useful for UHF clear-air radars to improve their range resolution down to several meters or less (Eaton et al., 1995; Richter, 1969). However, a use of the FMCW pulse compression causes deterioration in data quality by range aliasing and by range ambiguity caused by Doppler shift of scatterers. Though range resolution in RIM depends on range distribution of scatterers, signal-to-noise ratio, and signal processing method used for RIM (e.g., Palmer et al., 1999; Luce et al., 2001; Smaïni et al., 2002), RIM does not suffer the drawbacks of using short transmitted pulse or FMCW pulse compression.

RIM contributes to reduce amount of on-line data size and computational complexity. In the case shown in Fig. 5, although the on-line sampling interval of the RIM measurement was 2 μ s (i.e., 300-m range spacing), brightness data are able to be processed with finer (6-m) range

spacing by off-line signal processing. On the other hand, on-line sampling interval in cases of short pulse transmission must be equivalent or shorter compared with the range resolution determined by transmitted pulse width. On-line sampling interval in cases of FMCW transmission also must be equivalent or shorter compared with the range resolution determined by sweep range of transmitted frequency.

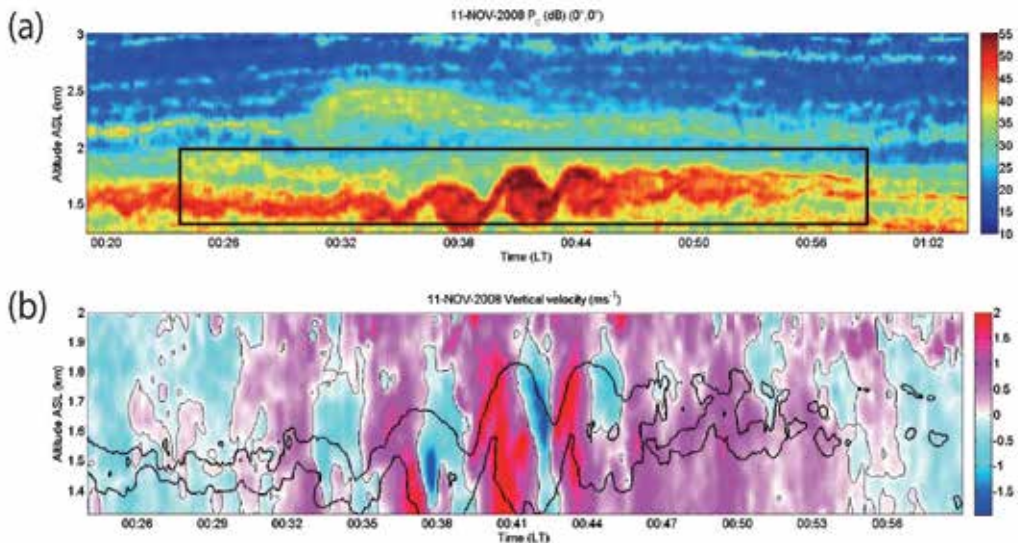


Fig. 6. Time-altitude plots of (a) brightness and (b) vertical wind velocity. Data were collected using vertically-pointing beam of the MU radar operated with the RIM observation mode (Fukao et al., 2011). The region within the black rectangular is plotted in panel (b). The thick black contours in panel (b) show 46 dB brightness level. The figure is reproduced with permission from the Royal Meteorological Society.

2.3 Further applications

2.3.1 High-resolution measurement using both spaced antennas and multiple frequencies

By using spaced receivers and multiple frequencies simultaneously, radar resolution is able to be improved both in angle and range, which leads to realize a three-dimensional (3-D) imaging. Signal processing procedures of the 3-D imaging are described by Yu & Palmer (2001). In 2004, the MU radar was upgraded for the 3-D imaging capability with 5 frequencies across a 1 MHz bandwidth and 25 intermediate frequency (IF) digital receivers (Hassenpflug et al., 2008). Using the 3-D imaging with the Capon method, Hassenpflug et al. (2008) showed a 3-D structure of radar echoes associated with billows of KH instability. Chen et al. (2008) applied the 3-D imaging to data collected by the MU radar in order to investigate relations between the angular distribution of clear-air echo power and tilted refractive-index layers caused by KH instability. The 3-D imaging technique is also able to be used for clutter mitigation. Using the MU radar, Yu et al. (2010) showed that the 3-D imaging provides comparable or better performance of both echo layer reconstruction and clutter mitigation compared to RIM.

The 3-D imaging technique is able to contribute to high-range-resolution wind measurement. Yu and Brown (2004) proposed a technique named RIM-SA that calculates wind velocity using both spaced antennas and multiple frequencies. In RIM-SA, first, RIM was separately applied to signals received by each of spaced antennas in order to produce high-range-resolution received signals. Next, SA technique was applied to the received signals produced by RIM in order to calculate horizontal wind velocity with high range resolution. Using data measured by MAPR, Yu and Brown (2004) produced profiles of horizontal wind velocity with 100-m intervals from a RIM-SA measurement using 2- μ s transmitted pulse and four frequencies (914.667, 915.000, 916.000, and 916.667 MHz). Yu and Brown (2004) showed that the horizontal wind produced by RIM-SA agrees well with both wind velocity measured by a radiosonde and that measured by MAPR using the 0.67- μ s transmitted pulse (i.e., 100-m range resolution).

2.3.2 Assessment of wind velocity measurement

Because DBS has been widely used for wind profiling radars, accuracy of wind velocity measured by DBS needs to be assessed. High resolution measurements using CRI and RIM provide the opportunity to assess the accuracy of wind velocity measured by DBS.

Wind field inhomogeneity within the scanning area of radar beams is a significant factor that produces errors of wind velocity measured by DBS. Cheong et al. (2008) carried out CRI measurement using TEP in order to obtain radial Doppler velocities from 490 beam directions, and used the radial Doppler velocity data in order to estimate how the wind field inhomogeneity affects the error of wind velocity measured by DBS. Cheong et al. (2008) concluded that optimal zenith angle of off-vertical radar beams is approximately 9-10° for minimizing the root-mean square (RMS) error in wind velocity measured by DBS, and that increasing number of off-vertical radar beams significantly reduces the RMS error in wind velocity measured by DBS.

Tilted refractive-index layers caused by KH instability deteriorate the measurement accuracy of vertical wind velocity because the tilted refractive-index layers cause contamination of horizontal wind velocity to the Doppler velocity of vertically-pointed radar beam, from which vertical wind is calculated in DBS (Muschinski, 1996; Yamamoto et al., 2003). Chen et al. (2008) applied the 3-D imaging to data collected by the MU radar in order to investigate relations between angular distribution of clear-air echo power and Doppler velocity measured by the vertically-pointed radar beam with improved range resolution. Chen et al. (2008) successfully showed the clear relation between the Doppler velocity bias measured by the vertically-pointed radar beam and the tilt of radar echo layers.

Though multistatic radar technique is not CRI, it is useful for measuring 3-D distribution of wind velocities. By installing two receiver arrays at approximately 1 km away from the westward and southward of the main antenna of the EAR, Nishimura et al. (2006) and (2010) realized the multistatic radar measurement of wind velocities. Their measurement results revealed 3-D wind perturbations down to the horizontal scale of 500 m.

2.3.3 High-resolution temperature measurement

Radio acoustic sounding system (RASS) is a radar remote sensing system for measuring profiles of temperature¹ with high time and height resolutions (e.g., May et al., 1990; Tsuda et al., 1989). RASS is also able to be used for monitoring humidity profiles (e.g., Furumoto et al., 2005; Tsuda et al., 2001). Using the MU radar, Furumoto et al. (2011) applied RIM to RASS measurement (RIM-RASS) in order to demonstrate that range resolution of temperature is improved down to approximately 60 m compared with the nominal range gate width of 150 m determined by the transmitted pulse width. Furumoto et al. (2011) pointed out that (1) sample time difference at an arbitrary range among data on different operational frequencies and (2) the Doppler shift bias due to the shape of range-gate weighting have to be corrected for RIM-RASS measurement, and developed an iteration algorithm that corrects (1) and (2). By applying CRI to temperature profiles measured by TEP with RASS, Dekker & Frasier (2004) retrieved virtual temperature structure function from horizontal distribution of temperature. The study by Dekker & Frasier (2004) indicates a usefulness of CRI to quantify turbulence intensity in the atmosphere.

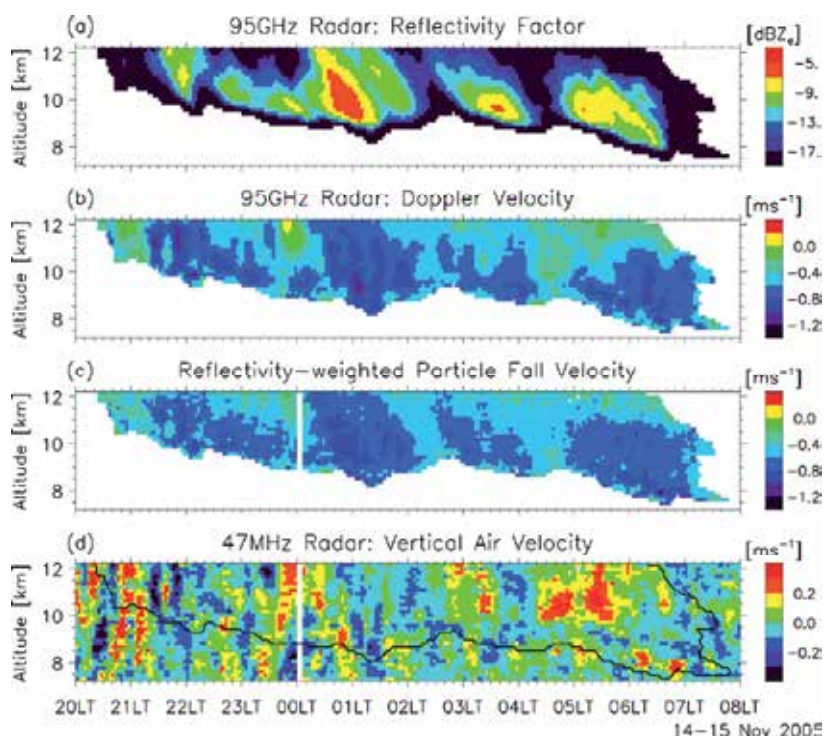


Fig. 7. Time-altitude plot of (a) equivalent radar reflectivity factor, (b) reflectivity-weighted particle fall velocity relative to the ground, (c) reflectivity-weighted particle fall velocity relative to the air, and (d) vertical wind velocity (Yamamoto et al., 2008). Equivalent radar reflectivity factor and reflectivity-weighted particle fall velocity relative to the ground were measured by a millimeter-wave radar. Vertical wind velocity was measured by the EAR. Horie et al. (2000) describe details of the millimeter-wave radar.

¹To be exact, RASS measures a virtual temperature expressed by $T_v = T(1 + 0.61q)$, where T_v , T , and q are virtual temperature in K, temperature in K, and water vapor mixing ratio in kg kg⁻¹, respectively.

3. Multi-instrument measurements

Measurements using collocated wind profiling radar and millimeter-wave radar/lidar have been carried out in the last decade. In section 3, we focus on measurement results of vertical wind in and around clouds due to the following reasons. First, measurement of vertical wind in cloudy region with high resolution and accuracy is difficult by means other than wind profiling radars (e.g., Nishi et al., 2007). Though wind profiling radars measure only the area right above the radars, they are suitable for measuring wind motions with high time and vertical resolutions. Second, observations aiming at clarifying generation and maintenance mechanisms of clouds are indispensable. Clouds reflect a fraction of the solar radiation that would otherwise be absorbed at the Earth's surface. On the other hand, clouds also contribute to the blocking of outgoing radiation by the atmosphere (Wallace and Hobbs, 2006). However, the effects of clouds on the radiation budget of the earth-atmosphere system are not sufficiently quantified (Stephens, 2005). Measurements using collocated wind profiling radar and millimeter-wave radar/lidar provide an opportunity to observe dynamical and microphysical processes of clouds simultaneously.

3.1 Particle fall velocity

Fall velocity of cloud particles (hereafter particle fall velocity) is one of crucial factors that determine life time of clouds (e.g., Petch et al., 1997; Starr and Cox, 1985), and particle fall velocity relative to the air has been modeled in order to relate particle fall velocity to the size and shape of particles [e.g., Heymsfield & Iaquinta, 2000; Mitchell 1996; Mitchell and Heymsfield, 2005]. However, because fall velocity of cloud particles relative to the ground (i.e., a sum of particle fall velocity relative to the air and vertical wind velocity) is measured by millimeter-wave radars or lidars, measurement of vertical wind velocity is required to retrieve particle fall velocity relative to the air. Fig. 7 shows a measurement example. Reflectivity-weighted particle fall velocity relative to the ground, which was measured by a millimeter-wave radar, showed small-scale perturbations with a time scale less than several ten minutes (Fig. 7b). The small-scale perturbations were caused by vertical wind motions (Fig. 7d). By subtracting vertical wind velocity from the reflectivity-weighted particle fall velocity relative to the ground, reflectivity-weighted particle fall velocity relative to the air was retrieved (Fig. 7c). The small-scale perturbations caused by the vertical wind motions were not observed in the retrieved reflectivity-weighted particle fall velocity relative to the air. The results clearly demonstrate that vertical wind measurement by wind profiling radar is useful for measuring particle fall velocity accurately. Retrieval of particle fall velocity leads to data analysis to clarify cloud properties. Using data shown by Figs. 7a and c, Yamamoto et al. (2008) related particle fall velocity to cloud particle size. The collected data were also used to assess an algorithm that retrieves vertical wind velocity, effective diameter of cloud particles, and ice water content from millimeter-wave radar and lidar measurements (Sato et al., 2009). Using the MU radar and an X-band Doppler weather radar (Yamamoto et al., 2011a), Luce et al. (2010a) showed a similar retrieval result of particle fall velocity (see their Fig. 15).

3.2 Turbulence measurements in and around clouds

Fig. 8 presents a measurement result around the cloud bottom. Cloud bottom altitude estimated by the equivalent radar reflectivity factor showed protuberance structure. Such

protuberances are referred to as mammatus cloud, whose generation mechanisms still remain to be discussed (Schultz et al., 2006). Brightness showed an increase around the cloud border due to the turbulence generation by KH instability. Vertical wind velocity showed oscillations exceeding $\pm 3 \text{ m s}^{-1}$ in magnitude due to KH instability, and played a role in producing protuberances of clouds through its downward motions. Luce et al. (2010a) suggested that the reduction of static stability at the interface between the clear air and cloud provided the favorable condition for triggering KH instabilities. Using the MU radar and a lidar (Behrendt et al., 2004), Luce et al. (2010b) also showed a correspondence between protuberances of clouds and vertical wind disturbances caused by atmospheric instability. Using the MU radar and a scanning millimeter-wave radar (Hamazu et al., 2003), Wada et al. (2005) showed a 3-D cell structure of cirrus clouds generated by KH instability, and the cell structures have greater vertical extension in the presence of upward vertical wind.

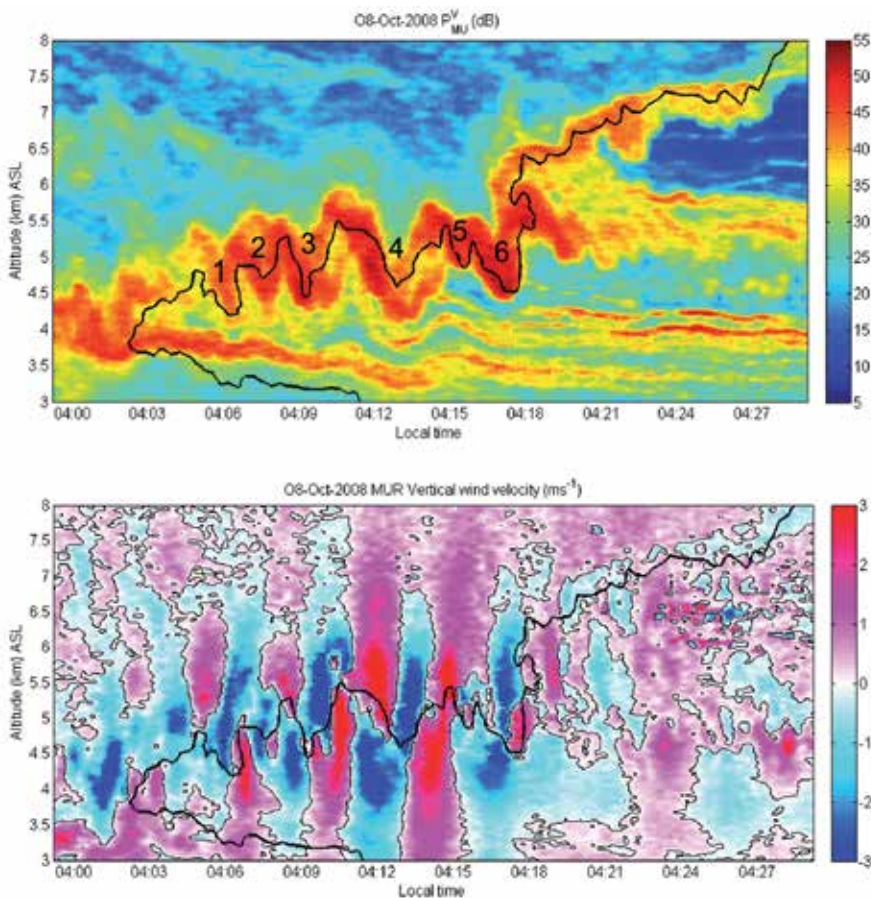


Fig. 8. Time-altitude plot of (upper) brightness and (lower) vertical wind velocity measured by the vertical beam of the MU radar operated with the RIM measurement mode (Luce et al., 2010a). Thick black curve shows a contour of -6 dBZ_e equivalent radar reflectivity factor measured by a millimeter-wave radar. Numbers 1-6 shown in the upper panel indicate protuberances of clouds. Yamamoto et al. (2011b) describe details of the millimeter-wave radar.

Fig. 9 shows a measurement result around the cloud top. In the upper part of clouds, an increase of spectral width up to 0.5–0.7 m s⁻¹, which indicates the presence of small-scale turbulence triggered by convective instabilities, is observed (Fig. 9c). Further, in the top part of clouds (0–500 m below the cloud tops), downward wind up to 0.2–0.3 m s⁻¹, which was caused by radiative cooling, was observed. For further discussion on the generation mechanism of turbulence, see Yamamoto et al. (2009a). From a case study using data measured by the MU radar and Raman/Mie lidar, Yamamoto et al. (2009b) showed a clear relation between the cloud-top altitude of mid-latitude cirrus and the bottom altitude of subtropical jet with high time and altitude resolutions (12 min and 150 m, respectively).

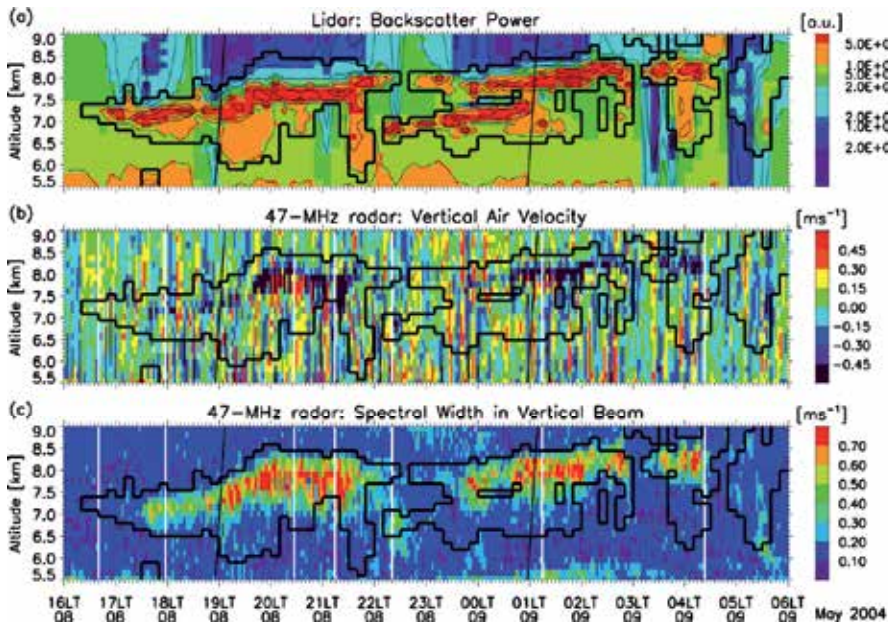


Fig. 9. Time-altitude plots of (a) backscattered power measured by a 532-nm Mie lidar, and (b) vertical wind velocity and (c) spectral width measured by the vertical beam of the EAR (Yamamoto et al., 2009a). Thick black curves in each panel indicate cloud boundaries estimated by the lidar backscattered power.

3.3 Other measurements

Measurements using wind profiling radars and other instruments are not limited to cloud researches. Measurement results of stratosphere-troposphere exchange (STE) processes have been reported in the last decade. Using observation network of wind profiling radar and lidar, Bertin et al. (2001) showed details of turbulent generation above and below the jet axis associated with a tropopause folding in the middle latitude. Using measurement data collected by the MU radar and ozonesonde, Gavrilov et al. (2006) compared distribution of turbulent diffusivity with vertical ozone flux. It is well known that clear-air echo power showed a vertical increase around the tropopause due to the increase of static stability or turbulence intensity (see section 14 of Hocking, 2011). Using data collected by the intensive observation of wind profiling radars and ozonesonde at Canada, Hocking et al. (2007) showed that stratospheric ozone has impacts on tropospheric ozone by its downward

transportation to the ground, and demonstrated that tropopause altitude determined by wind profiling radar with high time resolution can be used to infer the possibility of ozone intrusions, as well as to represent tropopause motions in association with stratosphere-troposphere transport. Using the EAR and radiosondes, Fujiwara et al. (2003) showed the turbulence generation around the tropical tropopause caused by the Kelvin wave breaking.

Using results of RIM measurement by the MU radar and water vapor measurement by the Raman lidar (Behrendt, et al., 2004), Luce et al. (2010c) demonstrated that vertical gradient of humidity causes enhancement of backscattered intensity of radar echo by generating refractive index irregularities at the Bragg scale. Further coordinated observations would lead to clarify the radio scattering and propagation mechanisms in the clear air.

4. Conclusion

In the Chapter, new observations by wind profiling radars in the last decade were reviewed. In section 2, the signal processing and measurement results of radar interferometry techniques (CRI and RIM) were described. Resolution enhancements attained by CRI and RIM will be useful not only for scientific researches aiming at clarifying atmospheric processes but also practical radar utilization through improvement in data quality (i.e., clutter mitigation) and early detection of turbulence associated with storm or wind shear. Further assessments aiming at quantifying their usefulness under various weather conditions are desirable.

In section 3, it was demonstrated that multi-instrument measurement using wind profiling radar and millimeter-wave radar/lidar is useful to clarify phenomena related to cloud processes. In order to clarify interactions among dynamics, cloud physics, and radiation, simultaneous remote sensing and in-situ measurements are highly desirable. In-situ measurements of cloud particles, temperature, humidity, and radiation using balloons and/or aircrafts will contribute to quantify phenomena measured by wind profiling radar, millimeter-wave radar, and lidar. Numerical simulation is also important to assess the interactions. The author hopes that efforts to realize further coordinated studies are executed continuously.

5. Acknowledgment

This work was supported by the research grant for Exploratory Research on Sustainable Humanosphere Science from Research Institute for Sustainable Humanosphere (RISH), Kyoto University.

6. References

- Behrendt, A., Nakamura, T. & Tsuda, T. (2004). Combined Temperature Lidar for Measurements in the Troposphere, Stratosphere, and Mesosphere, *Applied Optics*, Vol. 43, No.14, pp.2930-2939, doi:10.1364/AO.43.002930.
- Bertin, F., Campistron, B., Caccia, J.L. & Wilson, R. (2001). Mixing Processes in a Tropopause Folding Observed by a Network of ST Radar and Lidar, *Annales Geophysicae*, Vol.19, No.8, pp.953-963, doi:10.5194/angeo-19-953-2001.

- Capon, J. (1969). High-Resolution Frequency-Wavenumber Spectrum Analysis, *Proceedings of the IEEE*, Vol.57, No.8, pp.1408-1418, doi:10.1109/PROC.1969.7278.
- Chau, J.L. & Woodman, R.F. (2001). Three-Dimensional Coherent Radar Imaging at Jicamarca: Comparison of Different Inversion Techniques, *Journal of Atmospheric and Solar-Terrestrial Physics*, Vol.63, No.2-3, pp.253-261, doi:10.1016/S1364-6826(00)00142-5.
- Chen, J.-S. (2004). On the Phase Biases of Multiple-frequency Radar Returns of Mesosphere-Stratosphere-Troposphere Radar, *Radio Science*, Vol.39, Art.no.RS5013, doi:10.1029/2003RS002885.
- Chen, J.-S., Hassenpflug, G. & Yamamoto, M. (2008). Tilted Refractive-index Layers Possibly Caused by Kelvin-Helmholtz Instability and Their Effects on the Mean Vertical Wind Observed with Multiple-receiver and Multiple-frequency Imaging Techniques, *Radio Science*, Vol.43, Art.no.RS4020, doi:10.1029/2007RS003816.
- Chen, J.-S., Su, C.-L., Chu, Y.-H., Hassenpflug, G. & Zecha, M. (2009). Extended Application of a Novel Phase Calibration Approach of Multiple-Frequency Range Imaging to the Chung-Li and MU VHF Radars. *Journal of Atmospheric and Oceanic Technology*, Vol.26, No.11, pp.2488-2500, doi:10.1175/2009JTECHA1295.1.
- Chen, J.-S. & Zecha, M. (2009). Multiple-Frequency Range Imaging Using the OSWIN VHF Radar: Phase Calibration and First Results, *Radio Science*, Vol.44, Art.No.RS1010, doi:10.1029/2008RS003916.
- Chen, J.-S., Furumoto, J.-I. & Nakamura, T. (2010). Effects of Radar Beam Width and Scatterer Anisotropy on Multiple-Frequency Range Imaging Using VHF Atmospheric Radar, *Radio Science*, Vol.45, Art.no.RS5001, doi:10.1029/2009RS004267.
- Chen, M.-Y., Yu, T.-Y., Chu, Y.-H., Brown, W.O.J. & Cohn, S.A. (2007). Application of Capon Technique to Mitigate Bird Contamination on a Spaced Antenna Wind Profiler, *Radio Science*, Vol.42, Art.no.RS6005, doi:10.1029/2006RS003604.
- Cheong, B.L., Hoffman, M.W., Palmer, R.D., Frasier, S. J. & López-Dekker, F.J. (2004). Pulse Pair Beamforming and the Effects of Reflectivity Field Variations on Imaging Radars, *Radio Science*, Vol.39, RS3014, doi:10.1029/2002RS002843.
- Cheong, B.L., Hoffman, M.W., Palmer, R.D., Frasier, S.J. & López-Dekker, F.J. (2006). Phased-Array Design for Biological Clutter Rejection: Simulation and Experimental Validation, *Journal of Atmospheric and Oceanic Technology*, Vol.23, No.4, pp.585-598, doi:10.1175/JTECH1867.1.
- Cheong, B.L., Palmer, R.D., Yu, T.-Y., Yang, K-F., Hoffman, M.W., Frasier, S.J. & Lopez-Dekker F.J. (2008). Effects of Wind Field Inhomogeneities on Doppler Beam Swinging Revealed by an Imaging Radar, *Journal of Atmospheric and Oceanic Technology*, Vol.25, No.8, pp.1414-1422, doi:10.1175/2007JTECHA969.1.
- Chilson, P.B., Yu, T.-Y., Strauch, R.G., Muschinski, A. & Palmer, R.D. (2003). Implementation and Validation of Range Imaging on a UHF Radar Wind Profiler, *Journal of Atmospheric and Oceanic Technology*, Vol.20, No.7, pp.987-996, doi:10.1175/1520-0426(2003)20<987:IAVORI>2.0.CO;2.
- Chilson, P.B. (2004). The Retrieval and Validation of Doppler Velocity Estimates from Range Imaging. *Journal of Atmospheric and Oceanic Technology*, Vol.21, No.7, pp.1033-1043, doi:10.1175/1520-0426(2004)021<1033:TRAVOD>2.0.CO;2.

- Dekker, P.L. & Frasier, S.J. (2004). Radio Acoustic Sounding with a UHF Volume Imaging Radar. *Journal of Atmospheric and Oceanic Technology*, Vol.21, No.5, pp.766-776, doi:10.1175/1520-0426(2004)021<0766:RASWAU>2.0.CO;2.
- Eaton, F.D., McLaughlin, S.A. & J. R. Hines (1995). A New Frequency-Modulated Continuous Wave Radar for Studying Planetary Boundary Layer Morphology, *Radio Science*, Vol.30, No.1, pp.75-88, doi:10.1029/94RS01937.
- Fujiwara, M., Yamamoto, M.K., Hashiguchi, H., Horinouchi, T. & Fukao, S. (2003). Turbulence at the Tropopause due to Breaking Kelvin Waves Observed by the Equatorial Atmosphere Radar, *Geophysical Research Letters*, Vol.30, No.4, 1171, doi:10.1029/2002GL016278.
- Fukao, S., Sato, T., Tsuda, T., Yamamoto, M., Yamanaka, M.D. & Kato, S. (1990). MU radar: New Capabilities and System Calibrations, *Radio Science*, Vol.25, No.4, doi:10.1029/RS025i004p00477.
- Fukao, S., Hashiguchi, H., Yamamoto, M., Tsuda, T., Nakamura, T., Yamamoto, M. K. , Sato, T. , Hagio, M. & Yabugaki, Y. (2003). Equatorial Atmosphere Radar (EAR): System Description and First Results, *Radio Science*, Vol.38, Art.No.1053, doi:10.1029/2002RS002767.
- Fukao, S. (2007) Recent Advances in Atmospheric Radar Study, *Journal of the Meteorological Society of Japan*, Vol.85B, pp.215-239, doi:10.2151/jmsj.85B.215.
- Fukao, S., Luce, H., Mega, T. & Yamamoto, M.K. (2011), Extensive Studies of Large-Amplitude Kelvin-Helmholtz Billows in the Lower Atmosphere with the VHF Middle and Upper Atmosphere radar (MUR), *Quarterly Journal of the Royal Meteorological Society*, Vol.137, No.657, 1019-1041, doi:10.1002/qj.807.
- Furumoto, J.-I., Iwai, S., Fujii, H., Tsuda, T., Xin, W., Koike, T. & Bian L. (2005). Estimation of Humidity Profiles with the L-Band Boundary Layer Radar-RASS Measurements, *Journal of the Meteorological Society of Japan*, Vol.83, No.5, pp.895-908, doi:10.2151/jmsj.83.895.
- Furumoto, J.-I., Shinoda, T., Matsugatani, A. & Tsuda T (2011). Measurements of Detailed Temperature Profiles within the Radar Range Gate Using the Range Imaging Technique, *Journal of Atmospheric and Oceanic Technology*, Vol.28, No.1, pp.22-36, doi:10.1175/2010JTECHA1506.1.
- Gage, K.S. (1990). Radar Observations of the Free Atmosphere: Structure and Dynamics, In : *Radar in Meteorology*, D. Atlas, (Ed.), pp.534-565, American Meteorological Society, ISBN-10: 0933876866, Boston, Massachusetts, USA.
- Gavrilov, N. M., Fukao, S., Hashiguchi, H., Kita, K., Sato, K., Tomikawa, Y. & Fujiwara, M. (2006), Combined MU Radar and Ozoneprobe Measurements of Turbulence and Ozone Fluxes in the Tropo-stratosphere over Shigaraki, Japan, *Geophysical Research Letters*, Vol.33, Art.no.L09803, doi:10.1029/2005GL024002.
- Hamazu, K., Hashiguchi H., Wakayama T., Matsuda T., Doviak R. J. & Fukao, S. (2003). A 35-GHz Scanning Doppler Radar for Fog Observations. *Journal of Atmospheric and Oceanic Technology*, Vol.20, No.7, pp.972-986, doi:10.1175/1520-0426(2003)20<972:AGSDRF>2.0.CO;2.
- Hassenpflug, G., Yamamoto, M., Luce, H. & Fukao, S. (2008). Description and Demonstration of the New Middle and Upper Atmosphere Radar Imaging System: 1-D, 2-D, and 3-D Imaging of Troposphere and Stratosphere, *Radio Science*, Vol.43, Art.no.RS2013, doi:10.1029/2006RS003603.

- Hélat, D., Crochet, M., Luce, H. & Spano, E. (2001). Radar Imaging and High-Resolution Array Processing Applied to a Classical VHF-ST Profiler, *Journal of Atmospheric and Solar-Terrestrial Physics*, Vol.63, No.2-3, doi:10.1016/S1364-6826(00)00135-8.
- Heymsfield, A.J. & Jaquinta, J. (2000). Cirrus Crystal Terminal Velocities, *Journal of the Atmospheric Sciences*, Vol.57, No.7, pp.916–938, doi:10.1175/1520-0469(2000)057<0916:CCTV>2.0.CO;2.
- Hocking, W.K. (1985). Measurement of Turbulent Energy Dissipation Rates in the Middle Atmosphere by Radar Techniques: A Review, *Radio Science*, Vol.20, No.6, pp.1403–1422, doi:10.1029/RS020i006p01403.
- Hocking, W.K., Carey-Smith T., Tarasick, D.W., Argall P.S., Strong, K., Rochon, Y., Zawadzki, I. & P. A. Taylor (2007). Detection of Stratospheric Ozone Intrusions by Windprofiler Radars, *Nature*, Vol.450, No.7167, pp.281-284, doi:10.1038/nature06312.
- Hocking, W.K. (2011). A Review of Mesosphere–Stratosphere–Troposphere (MST) Radar Developments and Studies, Circa 1997–2008, *Journal of Atmospheric and Solar-Terrestrial Physics*, Vol.73, No.9, pp.848-882, doi:10.1016/j.jastp.2010.12.009.
- Horie, H., Iguchi, T., Hanado, H., Kuroiwa, H., Okamoto, H. & Kumagai, H. (2000). Development of a 95-GHz Airborne Cloud Profiling Radar (SPIDER) - Technical aspects -, *IEICE Transactions on Communications*, Vol.E83-B, No.9, pp.2010-2020.
- Ishihara, M., Kato, Y., Abo, T., Kobayashi, K. & Izumikawa, Y. (2006). Characteristics and Performance of the Operational Wind Profiler Network of the Japan Meteorological Agency, *Journal of the Meteorological Society of Japan*, Vol.84, No.6, pp.1085-1096, doi:10.2151/jmsj.84.1085.
- Kamio, K., Nishimura, K. & Sato, T. (2004). Adaptive Sidelobe Control for Clutter Rejection of Atmospheric Radars, *Annales Geophysicae*, Vol.22, No.11, pp.4005-4012, doi:10.5194/angeo-22-4005-2004.
- Kollias, P., Clothiaux, E.E., Miller, M.A., Albrecht, B.A., Stephens, G.L. & Ackerman T. P. (2007). Millimeter-Wavelength Radars: New Frontier in Atmospheric Cloud and Precipitation Research, *Bulletin of the American Meteorological Society*, Vol.88, No.10, pp.1608-1624, doi:10.1175/BAMS-88-10-1608.
- Larsen, M.F. & Röttger, J. (1989). The Spaced Antenna Technique for Radar Wind Profiling, *Journal of Atmospheric and Oceanic Technology*, Vol.6, No.6, 920–938, doi:10.1175/1520-0426(1989)006<0920:TSATFR>2.0.CO;2.
- Le, K.D., Palmer, R.D., Cheong, B.L., Yu, T.-Y., Zhang, G. & Torres, S.M. (2010). Reducing the Effects of Noise on Atmospheric Imaging Radars Using Multilag Correlation, *Radio Science*, Vol.45, RS1008, doi:10.1029/2008RS003989.
- Luce, H., Yamamoto, M., Fukao, S., Helal, D. & Crochet M. (2001). A Frequency Domain Radar Interferometric Imaging (FI) Technique Based on High-Resolution Methods, *Journal of Atmospheric and Solar-Terrestrial Physics*, Vol.63, No.2-3, pp.221-234, doi:10.1016/S1364-6826(00)00147-4.
- Luce, H., Hassenpflug, G., Yamamoto, M., Fukao, S. & Sato, K. (2008). High-Resolution Observations with MU Radar of a KH Instability Triggered by an Inertia–Gravity Wave in the Upper Part of a Jet Stream, *Journal of the Atmospheric Sciences*, Vol.65, No.5, pp.1711–1718, doi:10.1175/2007JAS2346.1.
- Luce, H., Mega, T., Yamamoto, M.K., Yamamoto, M., Hashiguchi, H., Fukao, S., Nishi, N., Tajiri, T. & Nakazato, M. (2010a). Observations of Kelvin-Helmholtz Instability at a

- Cloud Base with the Middle and Upper Atmosphere (MU) and Weather Radars, *Journal of Geophysical Research*, Vol.115, Art.no.D19116, doi:10.1029/2009JD013519.
- Luce, H., Nakamura, T., Yamamoto, M. K., Yamamoto, M. & Fukao, S. (2010b). MU Radar and Lidar Observations of Clear-Air Turbulence Underneath Cirrus, *Monthly Weather Review*, Vol.138, No.2, pp.438-452, doi:10.1175/2009MWR2927.1.
- Luce, H., Takai, T., Nakamura, T., Yamamoto, M., Fukao, S. (2010c). Simultaneous Observations of Thin Humidity Gradients in the Lower Troposphere with a Raman Lidar and the Very High-Frequency Middle- and Upper-Atmosphere Radar, *Journal of Atmospheric and Oceanic Technology*, Vol.27, No. 5, pp.950-956, doi:10.1175/2010JTECHA1372.1.
- May, P.T. (1990). Spaced antenna versus Doppler Radars: A Comparison of Techniques Revisited, *Radio Science*, Vol.25, No.6, pp.1111-1119, doi:10.1029/RS025i006p01111.
- May, P.T., Strauch, R.G., Moran, K.P. & Ecklund, W.L. (1990). Temperature Sounding by RASS with Wind Profiler Radars: A Preliminary Study, *IEEE Transactions on Geoscience and Remote Sensing*, Vol.28, No.1, pp.19-28, doi:10.1109/36.45742.
- Mead, J.B., Hopcraft, G., Frasier, S.J., Pollard, B.D., Cherry, C.D., Schaubert, D.H. & McIntosh, R.E. (1998). A Volume-Imaging Radar Wind Profiler for Atmospheric Boundary Layer Turbulence Studies, *Journal of Atmospheric and Oceanic Technology*, Vol.15, No.4, pp.849-859, doi:10.1175/1520-0426(1998)015<0849:AVIRWP>2.0.CO;2.
- Mega, T., Yamamoto, M.K., Luce, H., Tabata, Y., Hashiguchi, H., Yamamoto, M., Yamanaka, M. D. & Fukao, S. (2010). Turbulence Generation by Kelvin-Helmholtz Instability in the Tropical Tropopause Layer Observed with a 47 MHz Range Imaging Radar, *Journal of Geophysical Research*, Vol.115, Art.no.D18115, doi:10.1029/2010JD013864.
- Met Office (2011), CWINDE Network, Available from <http://www.metoffice.gov.uk/science/specialist/cwinde/>.
- Mitchell, D.L. (1996). Use of Mass- and Area-Dimensional Power Laws for Determining Precipitation Particle Terminal Velocities. *Journal of the Atmospheric Sciences*, Vol.53, No.12, pp.1710-1723, doi:10.1175/1520-0469(1996)053<1710:UOMAAD>2.0.CO;2.
- Mitchell, D.L. & Heymsfield, A.J. (2005). Refinements in the Treatment of Ice Particle Terminal Velocities, Highlighting Aggregates. *Journal of the Atmospheric Sciences*, Vol.62, No.5, pp.1637-1644, doi:10.1175/JAS3413.1.
- Muschinski, A. (1996). Possible Effect of Kelvin-Helmholtz Instability on VHF Radar Observations of the Mean Vertical Wind, *Journal of Applied Meteorology*, Vol.35, No.12, pp.2210-2217, doi:10.1175/1520-0450(1996)035<2210:PEOKHI>2.0.CO;2.
- Nishi, N., Yamamoto, M. K., Shimomai, T., Hamada, A. & Fukao, S. (2007). Fine Structure of Vertical Motion in the Stratiform Precipitation Region Observed by a VHF Doppler Radar Installed in Sumatra, Indonesia, *Journal of Applied Meteorology and Climatology*, Vol.46, No.4, pp.522-537, doi:10.1175/JAM2480.1.
- Nishimura, K., Gotoh, E. & Sato, T. (2006). Fine Scale 3D Wind Field Observation with a Multistatic Equatorial Atmosphere Radar, *Journal of the Meteorological Society of Japan*, Vol.84A, pp.227-238, doi:10.2151/jmsj.84A.227.
- Nishimura, K., Harada, T. & Sato, T. (2010). Multistatic Radar Observation of a Fine-Scale Wind Field with a Coupling-Compensated Adaptive Array Technique, *Journal of the Meteorological Society of Japan*, Vol.88, No.3, pp.409-424, doi:10.2151/jmsj.2010-309.

- Palmer, R.D., Gopalam, S., Yu, T.-Y. & Fukao S. (1998). Coherent Radar Imaging Using Capon's Method, *Radio Science*, Vol.33, No.6, pp.1585–1598, doi:10.1029/98RS02200.
- Palmer, R.D., Yu, T.-Y. & Chilson, P. B. (1999). Range Imaging Using Frequency Diversity, *Radio Science*, Vol.34, No.6, pp.1485–1496, doi:10.1029/1999RS900089.
- Palmer, R.D., Chilson, P.B., Muschinski, A., Schmidt, G., Yu, T.-Y. & Steinhagen H. (2001). SOMARE-99: Observations of Tropospheric Scattering Layers Using Multiple-Frequency Range Imaging, *Radio Science*, Vol.36, No.4, pp.681–693, doi:10.1029/1999RS002307.
- Palmer, R.D., Cheong, B.L., Hoffman, M.W., Frasier, S.J., López-Dekker, F.J. (2005). Observations of the Small-Scale Variability of Precipitation Using an Imaging Radar. *Journal of Atmospheric and Oceanic Technology*, Vol.22, No.8, pp.1122–1137, doi:10.1175/JTECH1775.1.
- Patterson, M.D., Caulfield, C.P., McElwaine, J.N. & Dalziel, S.B. (2006). Time-dependent Mixing in Stratified Kelvin-Helmholtz Billows: Experimental Observations, *Geophysical Research Letters*, Vol.33, Art.no.L15608, doi:10.1029/2006GL026949.
- Petch, J.C., Craig, G.C. & Shine, K.P. (1997). A Comparison of Two Bulk Microphysical Schemes and Their Effects on Radiative Transfer Using a Single column Model, *Quarterly Journal of the Royal Meteorological Society*, Vol.123, No.542, pp.1561–1580, doi:10.1002/qj.49712354206.
- Pollard, B.D., Khanna, S., Frasier, S.J., Wyngaard, J.C., Thomson, D.W., & McIntosh, R.E. (2000). Local Structure of the Convective Boundary Layer from a Volume-Imaging Radar, *Journal of the Atmospheric Sciences*, Vol.57, No.15, pp.2281–2296, doi:10.1175/1520-0469(2000)057<2281:LSOTCB>2.0.CO;2.
- Richter, J.H. (1969). High Resolution Tropospheric Radar Sounding, *Radio Science*, Vol.4, No.12, pp.1261–1268, doi :10.1029/RS004i012p01261.
- Sato, K. & Coauthors (2009). 95-GHz Doppler Radar and Lidar Synergy for Simultaneous Ice Microphysics and in-cloud Vertical Air Motion Retrieval, *Journal of Geophysical Research*, Vol.114, Art.no.D03203, doi:10.1029/2008JD010222.
- Schultz, D. M. & Coauthors (2006). The Mysteries of Mammatus Clouds: Observations and Formation Mechanisms. *Journal of the Atmospheric Sciences*, Vol.63, No.10, pp.2409–2435, doi:10.1175/JAS3758.1.
- Smaïni, L., Luce, H., Crochet, M. & Fukao, S. (2002). An Improved High-Resolution Processing Method for a Frequency Domain Interferometric Imaging (FII) Technique. *Journal of Atmospheric and Oceanic Technology*, Vol.19, No.6, pp.954–966, doi:10.1175/1520-0426(2002)019<0954:AIHRPM>2.0.CO;2.
- Stanley G.B., Schwartz, B.E., Koch, S.E., & Szoke, E.J. (2004). The Value of Wind Profiler Data in U.S. Weather Forecasting, *Bulletin of the American Meteorological Society*, Vol.85, No.12, pp.1871–1886, doi:10.1175/BAMS-85-12-1871.
- Starr, D. O'C. & Cox, S.K. (1985). Cirrus Clouds. Part II: Numerical Experiments on the Formation and Maintenance of Cirrus, *Journal of the Atmospheric Sciences*, Vol.42, No.23, pp.2682–2694, doi:10.1175/1520-0469(1985)042<2682:CCPINE>2.0.CO;2.
- Stephens, G.L. (2005). Cloud Feedbacks in the Climate System: A Critical Review, *Journal of Climate*, Vol.18, No.2, pp.237–273, doi:10.1175/JCLI-3243.1.
- Tsuda, T. and Coauthors (1989). High Time Resolution Monitoring of Tropospheric Temperature with a Radio Acoustic Sounding System (RASS), *Pure and Applied Geophysics*, Vol.130, No.2-3, pp.497–507, doi:10.1007/BF00874471.

- Tsuda, T., Miyamoto, M. & Furumoto, J.-I. (2001). Estimation of a Humidity Profile Using Turbulence Echo Characteristics, *Journal of Atmospheric and Oceanic Technology*, Vol.18, No.7, pp.1214-1222, doi:10.1175/1520-0426(2001)018<1214:EOAHPU>2.0.CO;2.
- Vaughn, C.R. (1985). Birds and Insects as Radar Targets: A Review, *Proceedings of the IEEE*, Vol.73, No.2, pp. 205 -227, doi:10.1109/PROC.1985.13134.
- Wallace, J.M. & Hobbs P.V. (2006). *Atmospheric Science: An Introductory Survey, 2nd Edition*, pp.447-450, Academic Press, ISBN-10: 012732951X, San diego, California, USA.
- Wada, E., Hashiguchi, H., Yamamoto, M.K., Teshiba, M. & Fukao, S. (2005). Simultaneous Observations of Cirrus Clouds with a Millimeter-Wave Radar and the MU Radar, *Journal of Applied Meteorology*, Vol.44, No.3, pp.313-323, doi:10.1175/JAM2191.1.
- Wandinger, U. (2005). Introduction to Lidar, In : *Lidar : Range-Resolved Optical Remote Sensing of the Atmosphere*, C. Weitkamp, (Ed.), pp.1-18, Springer, ISBN-10: 0387400753, New York, USA.
- Wilson, R., Dalaudier, F. & Bertin, F. (2005). Estimation of the Turbulent Fraction in the Free Atmosphere from MST Radar Measurements, *Journal of Atmospheric and Oceanic Technology*, Vol.22, No.9, pp.1326-1339, doi:10.1175/JTECH1783.1.
- Wilczak, J. M. & Coauthors (1995). Contamination of Wind Profiler Data by Migrating Birds: Characteristics of Corrupted Data and Potential Solutions. *Journal of Atmospheric and Oceanic Technology*, Vol.12, No.3, pp.449-467, doi:10.1175/1520-0426(1995)012<0449:COWPDB>2.0.CO;2.
- Woodman, R. (1997). Coherent Radar Imaging: Signal Processing and Statistical Properties, *Radio Science*, Vol.32, No.6, pp.2373-2391, doi:10.1029/97RS02017.
- Yamamoto, M.K., Fujiwara M., Horinouchi, T., Hashiguchi, H. & Fukao S. (2003). Kelvin-Helmholtz Instability around the Tropical Tropopause Observed with the Equatorial Atmosphere Radar, *Geophysical Research Letters*, Vol.30, No.9, Art.no.1476, doi:10.1029/2002GL016685.
- Yamamoto, M.K. & Coauthors (2008). Observation of Particle Fall Velocity in Cirriform Cloud by VHF and Millimeter-Wave Doppler radars, *Journal of Geophysical Research*, Vol.113, Art.no.D12210, doi:10.1029/2007JD009125.
- Yamamoto, M.K. & Coauthors (2009a). Vertical Air Motion in Midlevel Shallow-Layer Clouds Observed by 47-MHz Wind Profiler and 532-nm Mie lidar: Initial Results, *Radio Science*, Vol.44, Art.no.RS4014, doi:10.1029/2008RS004017.
- Yamamoto, M.K. & Coauthors (2009b). Wind Observation around the Tops of the Midlatitude Cirrus by the MU radar and Raman/Mie lidar, *Earth Planets Space*, Vol.61, e33-e36 (Available from <http://www.terrapub.co.jp/journals/EPS/abstract/6107/6107e033.html>).
- Yamamoto, M.K. & Coauthors (2011a). Doppler Velocity Measurement of Portable X-band Weather Radar Equipped with Magnetron Transmitter and IF Digital Receiver, *IEICE Transactions on Communications*, Vol.E94-B, No.6, pp.1716-1724, doi:10.1587/transcom.E94.B.1716.
- Yamamoto, M.K. & Coauthors (2011b). Assessment of Radar Reflectivity and Doppler Velocity Measured by Ka-band FMCW Doppler Weather Radar, *Journal of Atmospheric Electricity*, Vol.31, No.2, pp.85-94.
- Yu, T.-Y., Palmer, R.D. & Hysell, D.L. (2000). A Simulation Study of Coherent Radar Imaging, *Radio Science*, Vol.35, No.5, pp.1129-1141, doi:10.1029/1999RS002236.

- Yu, T.-Y. & Palmer, R.D. (2001). Atmospheric Radar Imaging Using Multiple-Receiver and Multiple-frequency Techniques, *Radio Science*, Vol.36, No.6, pp.1493-1503, doi:10.1029/2000RS002622.
- Yu, T.-Y. & Brown, W.O.J. (2004). High-Resolution Atmospheric Profiling Using Combined Spaced Antenna and Range Imaging Techniques, *Radio Science*, Vol.39, Art.no.RS1011, doi:10.1029/2003RS002907.
- Yu, T.-Y., Furumoto, J.-I. & Yamamoto M. (2010). Clutter Suppression for High-Resolution Atmospheric Observations Using Multiple Receivers and Multiple Frequencies, *Radio Science*, Vol.45, Art.no.RS4011, doi:10.1029/2009RS004330.

Synergy Between Doppler Radar and Lidar for Atmospheric Boundary Layer Research

Chris G. Collier

*National Centre for Atmospheric Science, University of Leeds
United Kingdom*

1. Introduction

The principle of operation of radar and lidar is similar in that pulses of energy at wavelengths ranging from millimetres to metres for radar and 0.5 to 10 microns for lidar are transmitted into the atmosphere; the energy scattered back to the transceiver is collected and measured as a time-resolved signal. From the time delay between each outgoing transmitted pulse and the backscattered signal, the distance to the scatterer is inferred. The radial or line-of-sight velocity of the scatterers is determined from the Doppler frequency shift of the backscattered radiation. The systems use a heterodyne detection technique in which the return signal is mixed with a reference beam (i.e. local oscillator) of known frequency. A signal processing computer then determines the Doppler frequency shift from the spectra of the heterodyne signal. The energy content of the Doppler spectra can also be used to determine boundary layer eddy characteristics.

2. Characteristics of radar

The atmospheric boundary layer has been studied using weather radar extensively over the last forty years or so, such that networks of radars comprise systems sometimes operating unmanned in remote locations (see for example Atlas, 1990). Doppler radar operating at X, C or S-band (3cm, 5cm and 10cm wavelength respectively) has provided the opportunity to measure the reflectivity of target hydrometeors and the three dimensional wind structure of the lower parts of the atmosphere inferred from their motion (see for example Doviak and Zrnica, 1984). Typical parameters for a C-band radar are listed in Table 1. In addition, high power radar systems, such as the Oklahoma University Polarimetric radar for Innovations in Meteorology and Engineering (OU-PRIME) which operates at C-band and has a peak power of 1000 kW and a beamwidth of 0.45 degree (Palmer et al., 2011), provide information on the clear air structure of wind fields, and sometimes lower power systems may do the same at close range to the radar site. The detailed principle of operation has been described elsewhere in this book.

Millimetre-wave cloud radars exploit the fact that the echo intensity of Rayleigh scatterers increases with the inverse fourth power of the wavelength. These radars normally operate at 35 GHz and 94 GHz. UHF and VHF Doppler radar systems measure both wind speed and direction by detecting small irregularities in back scattered signals due to refractive index

inhomogeneities caused by turbulence. In the lower troposphere the refractive index inhomogeneities are mainly produced by humidity fluctuations. The clear air Doppler shift provides a direct measurement of the mean radial velocity along the radar beam. Typically a UHF wind profiler operates at 1290 MHz or 915 MHz with a peak power of 3.5 kW and a beamwidth of 8.5 degrees.

Wavelength/ frequency	5 cm (C-band)/ 5430-5800 MHz
Pulse repetition frequency	250-1200 Hz selectable
Bandwidth single PRF dual PRF	± 15.9 m s ⁻¹ ± 63.8 m s ⁻¹
Sampling frequency - IF	60 MHz
Peak power	250 kW
Minimum Detectable Signal	-111 dBm
Beamwidth	1 degree
Down range resolution/ Maximum range	75 m 200 km
Transmitter type	Coaxial magnetron

Table 1. Typical parameters of a C-band radar (from Selex Gematronik)

Generally radars used for weather forecasting other than wind profilers have a resolution of about 100 m with an antenna having a diameter of about 4 m. Some research radars, such as the Chilbolton radar in the UK, provide measurements with a resolution at 100 km range using a 0.25 degree beamwidth (25 m diameter antenna) of 0.4 km. These resolutions certainly improve our understanding of the structure and behaviour of boundary layer phenomena, and examples will be described in this chapter. Nevertheless, boundary layer turbulent eddies may exist with characteristic length scales from tens of metres to fractions of a metre close to the ground. Such length scales require different instrumentation. Doppler lidar is an instrument providing high resolution, clear air measurements with resolutions of around 30 m, albeit over much shorter ranges than available from radar systems.

3. Characteristics of lidar

Lidar has been developed which operate in various atmospheric windows, namely the 10, 2, 1.5 and 1 micron spectral regions. Hardesty et al. (1992) compared the transmission, backscatter, refractive turbulence and Doppler estimation characteristics of a 2 and a 10 micron Doppler lidar system. Whilst backscatter at 2 microns in the free atmosphere is 4-10 times higher than for a 10 micron Doppler lidar, the effects of turbulence on the 2 micron system beyond a few kilometres range are significant, with the signal to noise ratio being reduced by about 6 dB at 5 km range. However, early equipment operated with CO₂ lasers at 10.6 micron wavelength, but involved delicate optical systems (Post and Cupp, 1990; Mayor et al., 1997; Pearson and Collier, 1999). The advent of fibre optic technology has enabled compact, robust equipment to be developed and operated remotely at wavelengths of 1.5 microns (Pearson et al., 2002, 2009). Table 2 shows the parameters of this type of Doppler lidar. The range resolution of 30 m is considerably smaller than that used in CO₂ lidars of about 112 m.

Wavelength	1.5 μm
Pulse repetition rate	20 kHz
Bandwidth	$\pm 14 \text{ m s}^{-1}$
Sampling frequency	30 MHz
Points per range gate	6
Number of pulses averaged	20 000
Δr	18 m
Δp	30 m
Averaging time	1 s

Table 2. Parameters of 1.5 micron Doppler lidar. Range gate parameters: Δr relates to pulse length and Δp is the down range extent of the range gate used in the signal processing (from Pearson et al., 2009).

4. Advantages and disadvantages of radar and lidar

Both radars and lidars have advantages and disadvantages, and in this chapter a review of the accuracy with which measurements of boundary layer winds from both instruments is given. However both instruments offer complimentary information. Lidar backscatter is from widely dispersed aerosol particles in the clear air, but their concentration decreases away from the surface. Although thin clouds also provide backscatter, hydrometeors strongly attenuate the lidar signal. Radar backscatter is generally from hydrometeors, and therefore the operating range is much greater than that of lidar although this depends upon the wavelength used as short wavelength signals are attenuated.

Topography strongly controls the flux of momentum and energy between the terrain surface and the boundary layer. In-situ instruments have minimum spatial coverage, and radar cannot make measurements very close to the ground due to beam side lobes which produce ground clutter. With beamwidths of 0.1-1 m. rad., lidar transverse resolution is 20-200 times finer than the one degree (17.5 m. rad.) of weather radars (Drechsel et al., 2009). Lidar provides wide area coverage, although not as extensive as radar, but does not suffer from ground clutter problems. Hence lidar offers the opportunity to improve our knowledge of flow over complex terrain close to the ground surface (Barkwith and Collier, 2011). However radar can provide detailed information in the boundary layer over very wide areas, particularly related to the development of convective systems.

5. Wind profiling

5.1 Single instrument measurements

Measurements of the vertical profile of wind may be made using Doppler lidar and both weather radars and UHF / VHF profilers. There are two modes that can be utilised for this. The beam can be scanned in a cone at fixed elevation and the resulting data fitted to a sine wave. This is known as the velocity-azimuth display (VAD) approach as described by Browning and Wexler (1968). This has been the preferred technique for radar systems although it has also been used with lidar systems. An alternative approach uses three fixed line of sights from which a vector analysis provides the three components of the wind (u , v and w) as described by Werner (2005).

Using the VAD technique Bozier et al. (2004) compared the average horizontal wind velocity difference and average standard deviation between a CO₂ Doppler lidar and tethered balloon borne turbulence probe measurements at a site in Eastern England as shown in Table 3. The in situ sensor captures a higher frequency turbulence component in the wind velocity data due to the higher measurement rate, 4 Hz, compared to the lidar data sampling rate of 0.1 Hz.

Measurement run	Height range (m)	Wind velocity difference (m s ⁻¹)	Lidar standard deviation (m s ⁻¹)	Balloon standard deviation (m s ⁻¹)
L1, B1	350–750	0.53	1.04	0.80
L2, B2	180–530	0.38	1.50	0.78
L3, B3	210–530	0.34	1.39	1.14
L4, B4	350–900	0.19	1.28	0.67

Table 3. Comparison of lidar and balloon borne instrument probe derived horizontal wind profiles (from Bozier et al., 2004)

Pearson et al. (2009) suggests that the three-beam technique may offer a better option in regions where the flow is not constant and laminar over the disc swept out by the VAD scan for example where topography influences the flow field. They showed examples of both approaches in a study of the performance of a 1.5 micron Doppler lidar. Based on 51 days continuous, unattended operation at a site in southern England, Figure 1 shows the results of an inter-comparison carried out on 13 September 2007 between a UHF radar and lidar data. There is no cloud cover. The wind speed data are less well correlated possibly due to ground clutter contamination of the radar velocity data, or a reduction in the Signal-to-Noise (SNR) leading to a larger degree of uncertainty in the sine-wave fit procedure. Similar results have been found using a 10.6 micron CO₂ Doppler lidar by Mayor et al. (1997), who compared vertical velocities derived from a 915 MHz radar profiler. A difference between the two instruments of -0.81 cm s⁻¹ was found. It was noted that the difference may be due to the different sizes of the sampling volumes, the spatial separation of the two measurements and the different SNRs. Comparisons of VAD winds derived from Doppler lidar reported by Drechsel et al. (2009) deviated from wind profiler measurements by less than 1.0 m sec⁻¹ and -1 degree, and only 0.1 m sec⁻¹ and 2 degrees from radiosonde data.

5.2 Dual-doppler systems

A single Doppler radar or lidar measures the field of wind velocities that are directed towards or away from the instrument. Doviak and Zrnic (1984) describe how a second Doppler radar spaced far from the first produces a field of different radial velocities which can be vectorially synthesized to retrieve the two dimensional velocities in the plane containing the radials.

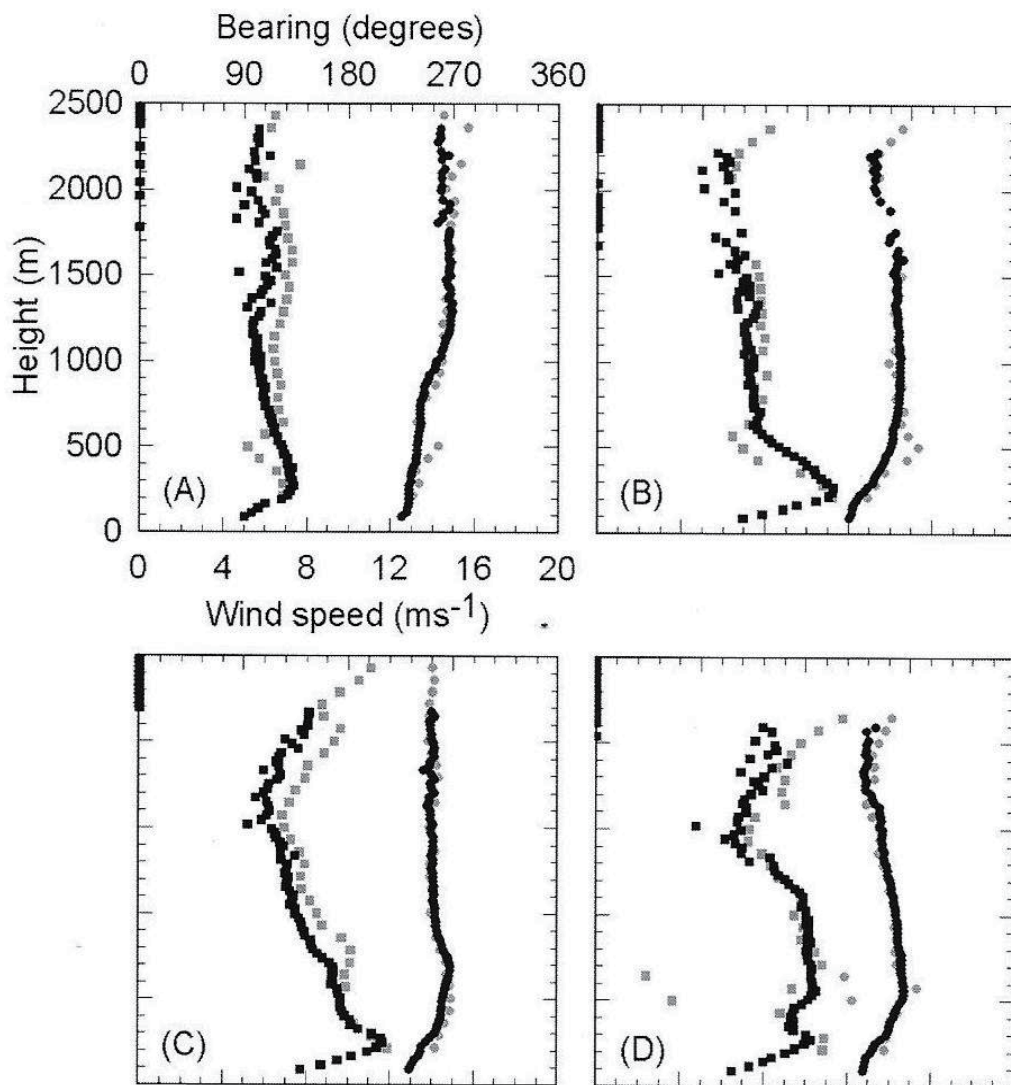


Fig. 1. Radar and lidar profiles from the evening of 13 Sept. 2007. The lidar scan took 9 min and the radar data are for a 10-min average. (A)-(D) Start times of 1900, 2100, 2200 and 2300 UTC respectively. The circles and squares show the bearing and speed data respectively (grey radar and black lidar) (from Pearson et al., 2009)

This is greatly simplified if this operation is performed in cylindrical coordinates with axis chosen to be in the line connecting the two radars 1 and 2, referred to as the baseline. The mean Doppler velocity is corrected for the reflectivity-weighted mean terminal velocity of the scatterers w_t . Hence the estimate of the radial component of air motion is:

$$v_{1,2} = v_{1,2}' + \overline{w_t} \sin \Theta_{e1,2}$$

where $v_{1,2}'$ are the mean Doppler target velocities measured by radars 1,2 at data points and w_t is positive. To estimate w_t an empirical expression such as that given by Atlas et al. (1973) can be used. The estimated radial velocities $v_{1,2}$ of the air can be interpolated to uniformly spaced grid points in planes at an angle α to the horizontal surface containing the baseline. The wind component w_α normal to the plane is obtained by solving the continuity equation in cylindrical coordinates:

$$1/r \partial/\partial r (r\rho w_r) + 1/r \partial/\partial x (\rho w_\alpha) + \partial/\partial s (\rho w_s) = 0$$

with the boundary condition $w = 0$ at the ground. Generally this approach covers a smaller area compared to the full dual-Doppler coverage and may contain residual errors.

An improved albeit similar approach has been developed by Bousquet and Chong (1998) for three dimensional wind retrieval from multiple airborne Doppler radars, called the Multiple Doppler Synthesis and Continuity Adjustment Technique (MUSCAT). It was extended for application over both flat or complex terrain by Chong and Cosma (2000), and for ground-based radar systems by Chong and Bousquet (2001). An alternative computationally inexpensive plane-to-plane solution known as the Multiple Analytical Doppler (MANDOP) system has been described by Tabary and Scialom (2001).

In 2003 two mobile Doppler lidars were sited at either end of a disused runway approximately 1.6 km apart at RAF Northolt in West London (Collier et al., 2005). The aim was to investigate the optimal lidar configuration to measure wind flow turbulence characteristics. Three dual-lidar configurations are shown in Figure 2. Figures 2a and 2c show data taken with the two lidars where the beams cross at a point, which is in the vertical plane defined by the line joining the two lidar positions. With each lidar system the radial velocities along the beams were measured every five seconds. The two radar computer clocks were first synchronised, and then for the different configurations, the time series of data were taken. Table 4 gives statistics derived from operating the lidar systems as in configuration 2c. The data were taken for a period of 700 seconds, and for different heights over a period of approximately 50 minutes. The errors in the vertical velocities from this dual-Doppler lidar deployment were analysed by Davies et al. (2005). It was found that the spread in vertical velocities due to the combined effects from instrumental errors of the two lidars can in some cases act to cancel each other out, although on other occasions this was not the case. We discuss the implications of this in the next section.

Drechsel et al. (2009) applied the MUSCAT processing system to dual-Doppler lidar data collected during the Terrain - induced Experiment (T-REX) in the spring of 2006. The flow pattern derived from 19 three dimensional wind fields revealed differences of wind speed and direction of less than 1.1 m sec⁻¹ and 3 degrees on average compared to radiosonde and wind profiler data. The average vertical motion from MUSCAT was -0.24 m sec⁻¹ compared to -0.52 m sec⁻¹ from wind profiler data and -0.32 m sec⁻¹ from radiosonde data.

Height (m)	Mean horizontal wind in direction of the lidar axis (m/s)	Mean vertical Wind (m/s)	Std. dev. of wind in direction of the lidar axis (m/s)	Std. Dev. of vertical wind (m/s)
100	-0.05	1.1	0.50	3.43
200	1.52	-0.90	0.59	1.45
400	0.77	-0.66	0.59	1.78
709	0.68	-0.83	1.49	1.13

Table 4. Means and standard deviations of the horizontal and vertical winds. The horizontal wind is the wind in the direction of the axis joining the two lidars. The heights of the data are determined by the crossing points of the two lidar beams as shown in the configuration of Figure 2c. The lidar data were taken from 1134-1224 UTC 23 July 2003 (from Collier et al. (2005))

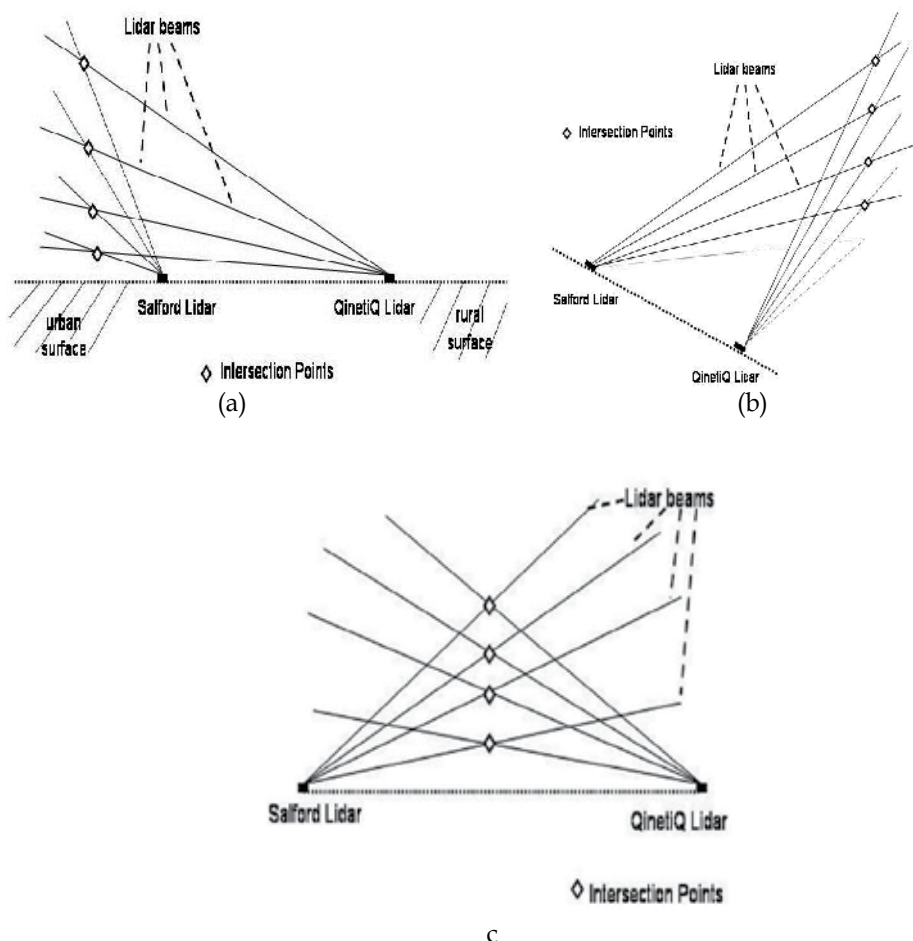


Fig. 2. Dual-lidar configurations. Diamonds denote beam intersection points (from Collier et al., 2005)

6. Measuring turbulent structure

A comprehensive review of the use of radar to measure the morphology of the boundary layer is provided by Gossard (1990), who also provides a review of the use of Doppler radar to measure turbulent velocity variance and covariance. VAD scans do not produce perfect sinusoids, and their derived time series are perturbed by random turbulent fluctuations at scales larger than the radar pulse volume, but much smaller than the diameter of the VAD. Wilson (1970) and Wilson and Miller (1972) developed a procedure for extracting quantitatively the variances and covariances of u , v and w . This was developed further by Kropfli (1984) who measured profiles of vertical momentum flux through the convective boundary layer as shown in Figure 3.

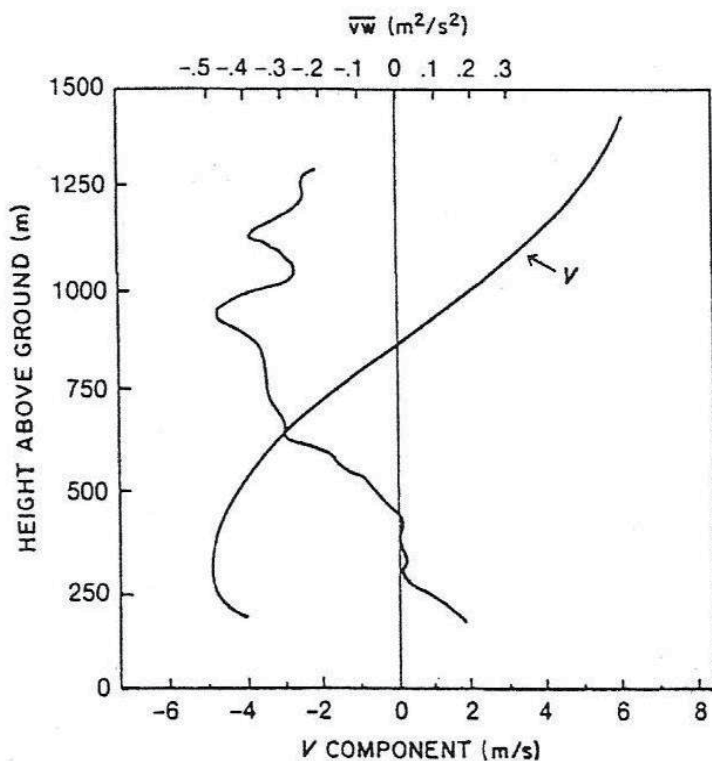


Fig. 3. Single radar measurement of vertical profile of momentum flux through the boundary layer by the method of Wilson (1970). Data are from a 100-min period beginning at 12-3 MDT during the PHOENIX experiment (from Kropfli, 1984)

The radar Doppler spectral width has also been used to extract small-scale turbulence information from spectral broadening due to wind shear, the radar antenna properties and the variance of the velocity component in the radial direction due to turbulence. In particular, the eddy dissipation rate can be measured, the first attempt to do this being by Gorelik and Mel' nichuk (1963). Table 5 is a summary of the literature on the measurement of turbulent energy dissipation (ϵ). Note that both radar and lidar have been used to measure this quantity.

Type	Typical Values of $\epsilon \times 10^3$ ($\text{m}^2 \text{sec}^{-3}$)	Typical estimate	Reference
D_N	0.2	Model	Simmons and Hoskins, (1978)
D_{GW}	6 (Over major mountains)	Model	Shutts (2005)
D_C	1-10	Radar and aircraft observations	Meischner et al (2001)
D_F	1000 (within the surface layer)	Hot-wire anemometer at 3m Radar observations	Piper and Lundquist (2004) Chapman and Browning (2001); Chapman and Browning (2001);
	2 (in shallow sloping frontal layers); 3 (close to the ground before surface front passes);		
	20 (jet stream level; clear air turbulence)	Aircraft observations	Kennedy and Shapiro (1975, 1980) Gage et al (1980)
	30 (jet stream level; clear air turbulence)	Radar observations	
D_B (Urban areas)	Up to 4 (urban areas)	Lidar observations at several hundred metres	Davies et al (2004);
	0.2 - 6.2 (urban areas)	Lidar observations	Davis et al (2008)

Table 5. Energy dissipation rates, ϵ ($\text{m}^2 \text{sec}^{-3}$) (from Collier and Davies, 2009)

Generally the vertical velocity in the turbulent boundary layer is very small, and difficult to measure. It is clear that significant temporal averaging is necessary. Kropfli (1984) suggested averaging over 20 minutes for VAD radar data, whereas Davies et al. (2005) averaged lidar data over 10 to about 50 minutes. However, the errors in the wind velocity, particularly those in w were thought by Sathe et al. (2011) to prelude the use of Doppler lidar with the VAD technique from measuring boundary layer turbulence precisely. This conclusion is not necessarily appropriate when two lidars are used as demonstrated by Davies et al. (2005) and Pearson et al. (2009).

In order to investigate the detailed structure of the turbulent motion above the Urban Canopy Layer (UCL), Davies et al. (2004) compared Doppler lidar-measured turbulent structure functions with those derived using the Von Karman model of isotropic turbulence in the inertial sub-range. Making allowance for the spatial averaging of the lidar pulse volume, the correspondence is comforting (Fig. 4). Hence, estimates of the integral length-scale, the dominant spatial scale of the turbulence above the UCL, can be made from the fit of the model to the observations, giving a range from 250–400 m. In addition, measurements were made of the velocity covariance power spectra, and the corresponding eddy dissipation rates are shown in Fig. 5. The slope of the spectra within the inertial sublayer is usually $-5/3$, although this depends upon the presence of inversion layers and the strength of the turbulence. The fact that the spectrum falls off faster than $-5/3$ may indicate that the turbulence approaches isotropy locally in the inertial range (Lumley, 1965). However, in the

case of the lidar measurements the fall off at less negative wave numbers is more likely to be due to the spatial averaging of the data over the beam. Climatologies of urban and rural eddy dissipation rates are needed to evaluate the urban effects.

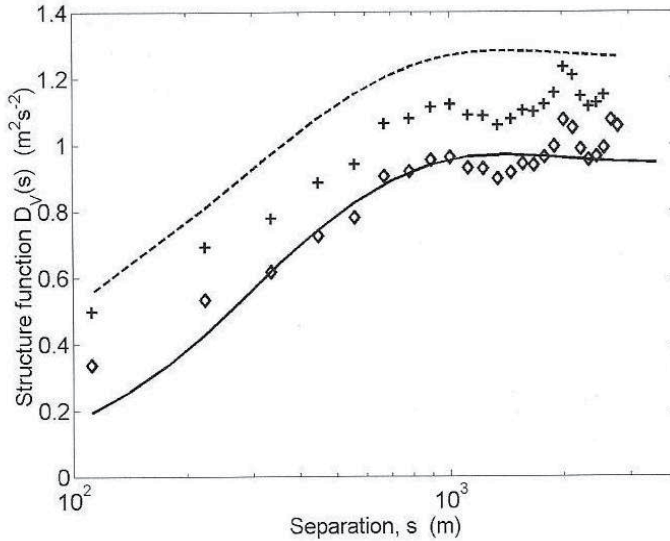


Fig. 4. Comparison of lidar measurements of structure function with the Von Karman model over Salford, Greater Manchester at 1317 UTC 2 May 2002. The upper dashed line represents the uncorrected model and the lower thick line the corrected model; crosses are uncorrected lidar measurements and diamonds are the corrected lidar measurements. (From Davies et al. 2004.)

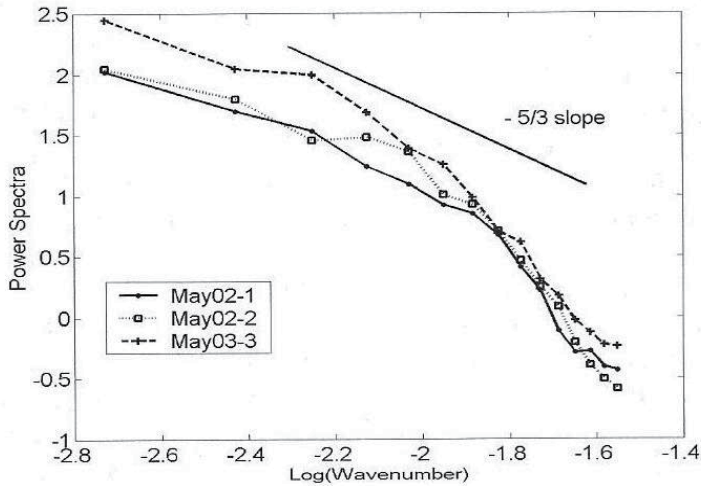


Fig. 5. Covariance power spectra and eddy dissipation rates, ϵ , over Salford, Greater Manchester, derived from line-of-sight measurements made during the SALFEX experiment for three datasets as indicated. The values of ϵ for the three curves range from 1.1 to $4.3 \times 10^{-3} \text{ m}^2 \text{ sec}^{-3}$. (From Davies et al. 2004.)

Recently Krishnamurthy et al. (2011) reported Doppler lidar measurements of turbulent kinetic energy dissipation rate, integral length scale and velocity variance assuming a theoretical model of isotropic wind fields during the T-REX Project. Corrections to address the complications inherent in volumetric averaging of radial velocity over each range gate, noise in the data and the assumption made regarding the effects of smaller scales of motion were considered and tested. Comparisons between the lidar and tower measurements supported the soundness of the lidar measurements of boundary layer turbulence.

7. Doppler radar and lidar measurements of boundary layer phenomena

7.1 Storm outflows

One of the most difficult forecasting problems remains the identification of when and where convective cells develop. Two facets of this problem are (a) how first-generation convective cells are triggered in an environment which has been previously quiescent for a period, but which becomes more and more unstable; and (b) for convective cells that persist, how and where subsequent generations of cells are triggered by the propagation of cold outflows from existing cells. Over the years there have been many studies addressing these issues using radar data (see for example Bader et al., 1995). Indeed, it is well known that first generation convective cells may be triggered by orographic uplift, and by land surface heterogeneity caused by variations in the temperature and moisture fields.

Collier and Davies (2004) describe a study of the pre-storm environment for a case study using a Doppler lidar located at Northolt, North West London, a C-band weather radar sited at Chemies north of London and the S-band Chilbolton radar. It was noted that the Doppler lidar and the weather radar data complement each other. Figure 6 shows Chemies and Chilbolton radar images, a PPI from the Doppler lidar and a LDR PPI from the Chilbolton radar. An outflow boundary is evident in all the images. A reversal of the wind direction at low levels is shown near the lidar site. The Chemies radar shows a thin line of broken echoes about 12 km to the north and north west of the main area of convective rain. The Chilbolton radar Linear Depolarisation Ratio (LDR) suggests that the radar targets in the outflow region are probably not raindrops, but may be particulate matter (straw, dust). The Doppler radial velocities observed by Chilbolton are consistent with the lidar measurements in the figure.

Similar measurements of an outflow have been reported by Collier et al. (2008). This study illustrates the difficulty of measuring an outflow using a radar, in this case the DLR C-band radar. In Figure 7a an outflow from a thunderstorm over the Rhine Valley is partially observed by the radar, but the details are not clear as there is some confusion with ground clutter. Figure 7b shows Doppler lidar measurements of the vertical velocities made from Achern in the Rhine Valley. Here the outflow is clear. It is about 800 m deep, and a cap cloud is observed near the leading edge. The peak kinetic energy dissipation rate was calculated to be $0.18 \text{ m}^2 \text{ sec}^{-3}$.

7.2 Observing smoke plumes

Combined observations of smoke plumes using lidar and radar have not been extensively reported. Such plumes may be generated from wild fires, or from prescribed (planned) burns. The plumes may contain lofted debris as the primary source of targets, although smoke and condensed water droplets may also be evident. Banta et al. (1992) used Doppler radar and

lidar to observe both prescribed and wild fires. Figure 8 shows Doppler lidar measurements of plumes over Helsinki produced from forest fires in North West Russia. The correlation between the lidar backscatter data and the retrieved vertical velocities shows convective updrafts containing the particulate-laden air from the cleaner air contained in downdrafts.

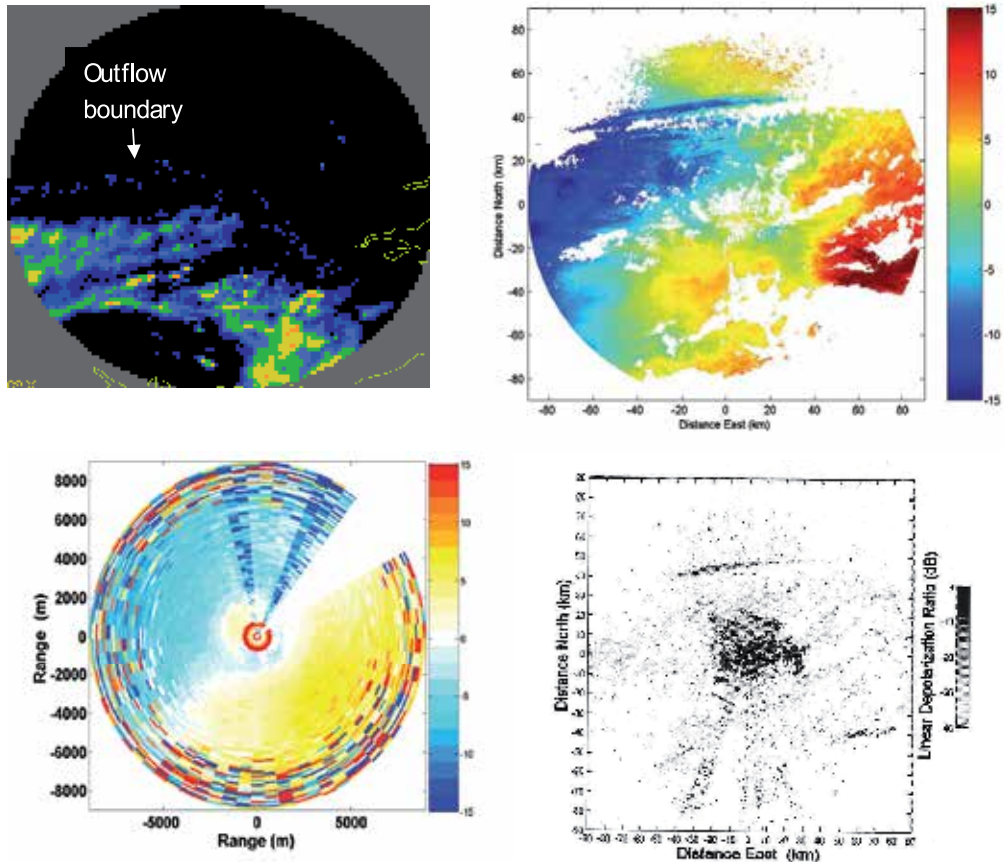


Fig. 6. (a) (top left) Chemies radar images on 16 July 2003 [Blue less than 1 mm h^{-1} ; yellow $2\text{--}4 \text{ mm h}^{-1}$; grid $2 \text{ km} \times 2 \text{ km}$ maximum range 75 km]; (b) (top right) Chilbolton unfolded radial velocities 16 July 0903 UTC in m sec^{-1} [negative away from the radar]; (c) (bottom left) Doppler lidar PPI [10 deg.] radial velocities [m sec^{-1}] 16 July 2003.0850 UTC [negative towards the lidar]. Note the wind reversal at low levels; (d) (bottom right) Chilbolton radar Linear Depolarisation Ratio (LDR) 16 July 0903 UTC (from Collier and Davies, 2004).

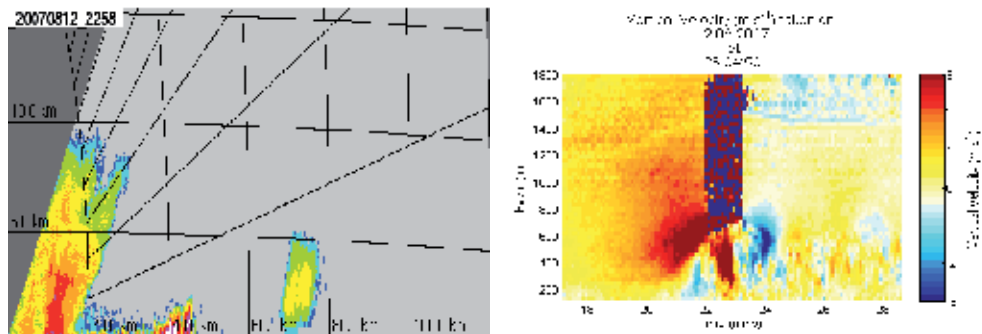


Fig. 7. Illustrating (a) RHI from the DLR Poldirad radar located at Waltenheim-sur-zorn towards the Supersites Achern (36 km), Hornisgrinde (46 km) and AMF (62 km) at 22.58 UTC 12 August 2007; and (b) vertical velocity measured at 23.04 UTC by Doppler lidar located at Achern on 12 August 2007 (from Collier et al., 2008).

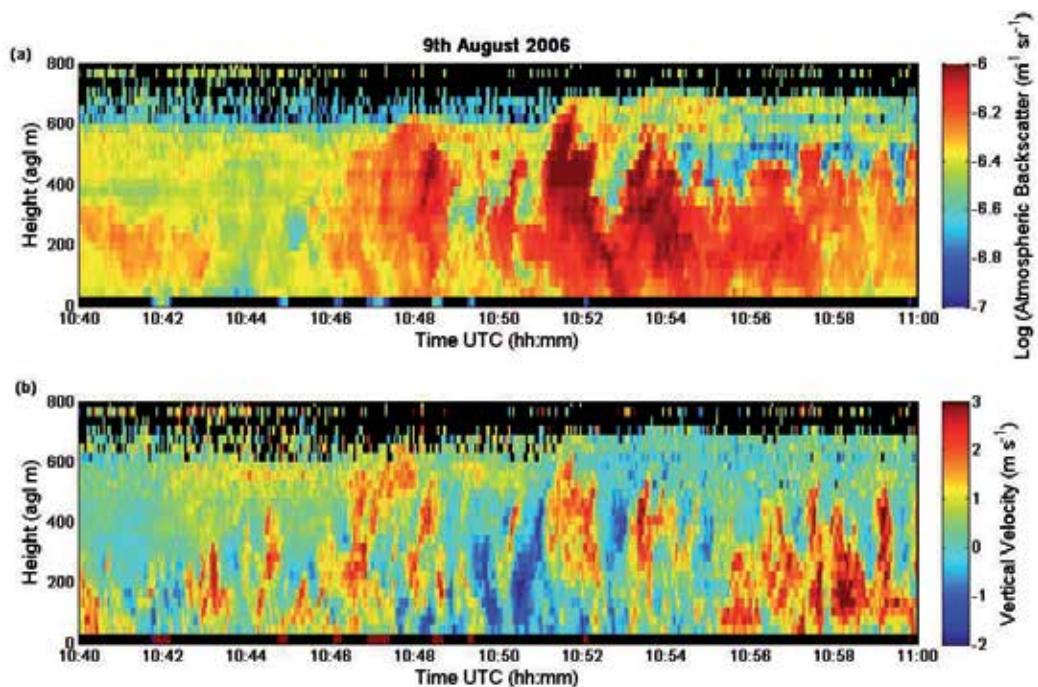


Fig. 8. Time series of lidar atmospheric backscatter and vertical velocity measurements taken on 9 August 2006 1040-1100 UTC in Helsinki, Finland. The log of the atmospheric backscatter is shown in (a) with the vertical velocity data from the lidar shown in (b). The vertical axis shows height above ground level (m) and the horizontal axis is time (UTC) (from Bozier et al., 2007).

7.3 Understanding convection

Skewness is a measure of asymmetry in the distribution of vertical velocity perturbations. Positive skewness at the surface suggests narrow intense updrafts from the surface and broad downdrafts (fair weather, clear). Negative skewness suggests sharp, narrow downdrafts and larger areas of weaker updraft, rather like “upside down” surface heating driven by turbulence on a cloudy day. Skewness may be calculated using,

$$S = w^3 / (w'^2)^{3/2}$$

Both Doppler radar and Doppler lidar are capable of measuring vertical velocity and they can measure skewness throughout the boundary layer. Knowing the skewness can help understand the structure of convection (see for example Hogan et al., 2009).

Although weather radars are available around the edges of tropical rain forests, there have as yet been only a few studies combining radar wind profilers and lidar (ceilometers) data (Grimsdell and Angevine, 1998). Vila-Guerau de Arellano et al. (2009) studied the isoprene fluxes in the tropical rain forest environment, but recommended the continued use of a radar wind profiler or Doppler lidar. Pearson et al. (2010) used a Doppler lidar to measure the diurnal cycle of the wind field in the tropical boundary layer, Sabah, Borneo.

8. Concluding remarks

Since radar and lidar provide measurements of backscatter and atmospheric motion based upon different targets, it is clear that much useful complementary information on atmospheric phenomena and processes can be obtained. Used together these instruments provide a powerful mechanism by which to enhance our knowledge of the atmosphere and develop improved forecasting procedures of a wide range of phenomena. Both technologies offer instrumentation capable of continuous unattended operation.

9. References

- Atlas, D. (ED) (1990) *Radar in Meteorology*, Am. Met. Soc., 806pp
- Atlas, D., Srivastava, R.C. and Sekhon, A.S. (1973). Doppler radar characteristics of precipitation at vertical incidence, *Rev. Geophys. Space Phys.*, 2, pp 1-35
- Bader, M.J., Forbes, G.S., Grant, J.R., Lilley, R.B.E. and Waters, A.J. (1995). *Images in Weather Forecasting. A practical guide for interpreting satellite and radar imagery*, Cambridge University Press, 499pp
- Banta, R.M., Olivier, L.D., Holloway, E.T., Kropfli, R.A., Bartram, B.W., Cupp, R.E. and Post, M.J. (1992). Smoke-column observations from two forest fires using Doppler lidar and Doppler radar, *J. Appl. Met.*, 31, 1328-1349
- Barkwith, A. and Collier, C.G. (2011). Lidar observations of flow variability over complex terrain, *Meteor. Appl.*, 18, 372-382
- Bousquet, O. and Chong, M. (1998). A Multiple-Doppler Synthesis and Continuity Adjustment Technique (MUSCAT) to recover wind components from Doppler radar measurements, *J. Atmos. Ocean. Tech.*, 15, pp 343-359
- Bozier, K.E., Pearson, G.N. and Collier, C.G. (2007). Doppler lidar observations of Russian forest fire plumes over Helsinki, *Weather*, 62, no 8, pp 203-208

- Browning, K.A. and Wexler, R. (1968). The determination of kinematic properties of a wind field using Doppler radar, *J. Appl. Met.*, 7, pp 105-113
- Chong, M. and Cosma, S. (2000). A formulation of the continuity equation of MUSCAT for either flat or complex terrain, *J. Atmos. Ocean. Tech.*, 17, pp 1556-1565
- Chapman, D. and Browning, K.A. (2001). Measurements of dissipation rate in frontal zones, *Quart. J. R. Met. Soc.*, 127, pp 1939-1959
- Collier, C.G. and Davies, F. (2004). Observations of the development of the convective boundary layer using radar and Doppler lidar, *Proc. European Radar Conf. (ERAD)*, Copernicus GmbH, Visby, Gotland, Sweden, 6-10 Sept. 2004, ISBN 3-936586-29-2
- Collier, C.G. and Davies, F. (2009). "Representing energy drain in Numerical Weather Prediction models induced by boundary layer sub-grid scale processes", *Atmos. Sci. Letters*, 10, Issue 3, DOI: 10.1002/asl.222, 146-151
- Collier, C.G., Davies, F., Bozier, K.E., Holt, A., Middleton, D.R., Pearson, G.N., Siemen, S., Willetts, D.V., Upton, G.J.G. and Young, R.I. (2005). Dual Doppler lidar measurements for improving dispersion models, *Bull. Am. Met. Soc.*, 86, pp 825-838
- Collier, C.G., Davies, F., Davis J.C., Pearson, G.N. and Hagen, M. (2008). Doppler radar and lidar observations of a thunderstorm outflow, *Proc. 5th European Conf. on Radar Met. and Hydrology (ERAD)*, Copernicus GmbH, June, Helsinki, ISSN 978-951-697-676-4
- Davies, F., Collier, C.G., Pearson, G.N. and Bozier, K.E. (2004). Doppler lidar measurements of turbulent structure function over an urban area, *J. Atmos. Ocean. Tech.*, 21, pp 753-761
- Davies, F., Collier, C.G. and Bozier, K.E. (2005). Errors associated with dual Doppler-lidar turbulence measurements, *J. Opt. A: Pure Appl. Opt.*, 7, pp S280-S289
- Davis, J.C. Collier, C.G., Davies, F. and Bozier, K.E. (2008). Spatial variations of sensible heat flux over an urban area measured using Doppler lidar, *Meteor. Appl.*, 15, pp 367-380
- Doviak, R.J. and Zrnich, D.S. (1984). *Doppler Radar and Weather Observations*, 2nd Ed., Academic Press, 562pp
- Drechsel, S., Chong, M., Mayr, G.J., Weissmann, M., Calhoun, R. and Dornbrack, A. (2009). Three-dimensional wind retrieval: application of MUSCAT to dual-Doppler lidar, *J. Atmos. Ocean. Tech.*, 26, pp 635-646
- Gage, K.S., Green, J.L. and Van Zandt, T.E. (1980). Use of a Doppler radar for the measurement of atmospheric turbulence parameters from the intensity of clear-air echoes, *Radio Sci.*, 15, pp 407-416
- Gorelik, A.G. and Mel'nichuk, Yu.V. (1963). Radar study of dynamic process in the atmosphere, Tr. Vses. Nov. Meteor. Souesh. No5
- Gossard, E.E. (1990). Radar research on the atmospheric boundary layer, in *Radar in Meteorology*, ed. D. Atlas, Am. Met. Soc., Boston, pp 477-527
- Grimsdell, R.W. and Angevine, W.M. (1998). Convective boundary layer height measurement with wind profilers and comparison to cloud base, *J. Atmos. Ocean. Tech.*, 15, pp 1331-1338
- Hardesty, R.M., Grund, C.J., Post, M.J., Rye, B.J. and Pearson, G.N. (1992). Measurements of winds and cloud characteristics: a comparison of Doppler lidar systems, *Int. Geoscience & Remote Sensing (Houston, IX, 1992) Session TA-P, Paper 2*
- Hogan, R.J., Grant, A.L.M., Illingworth, A.J., Pearson, G.N. and O'Connor, E.J. (2009). Vertical velocity variance and skewness in clear and cloud-topped boundary layers as revealed by Doppler lidar, *Quart. J. R. Met. Soc.*, 135, pp 635-643

- Kennedy, P.J. and Shapiro, M.A. (1975). The energy budget in a clear air turbulence zone as observed by aircraft, *Mon. Wea. Rev.*, 103, pp 650-654
- Kennedy, P.J. and Shapiro, M.A. (1980). Further encounters with clear air turbulence in research aircraft, *J. Atmos. Sci.*, 37, pp 986-993
- Krishnamurthy, A., Calhoun, R., Billings, B. and Doyle, J. (2011). Wind turbulence estimates in a valley by coherent Doppler lidar, *Meteor. Appl.*, 18, pp 361-371
- Kropfli, R.A. (1984). Radar probing and measurement of the planetary boundary layer. Part II Scattering from particulates, in *Probing the Atmospheric Boundary Layer*, ed. D.H. Lenschow, Am. Met. Soc./NCAR, Chapters 27a, 27b, pp 183-199
- Mayor, S.D., Lenschow, D.H., Schwiesow, R.L., Mann, J., Frush, C.L. and Simon, M.K. (1997). Validation of NCAR 10.6 μ m CO₂ Doppler lidar radial velocity measurements and comparison with a 915 MHz profiler, *J. Atmos. Ocean. Tech.*, 14, pp 1110-1126
- Meischner, P.F., Baumann, R., Holler, H. And Jank, T. (2001). Eddy dissipation rates in thunderstorms estimated by Doppler radar in relation to aircraft in situ measurements, *J. Atmos. Ocean. Tech.*, 18, pp 1609-1627
- Palmer, R.D., Bodine, D., Kiemjian, M., Cheong, B., Zhang, G., Cao, Q., Bluestein, B., Ryzhkov, A., Yu, T-Y. and Wang, Y. (2011). Observations of the 10 May 2010 tornado outbreak using OU-PRIME, *Bull. Am. Met. Soc.*, 92, no7, pp 871-891
- Pearson G.N. and Collier, C.G. (1999). A compact pulsed coherent CO₂ laser radar for boundary layer meteorology, *Quart J. R. Met. Soc.*, 125, 2703-2721
- Pearson, G.N., Roberts, P.J., Eacock, J.R. and Harris, M. (2002). Analysis of the performance of a coherent pulsed fiber lidar for aerosol backscatter applications, *Appl. Opt.*, 41, pp 6442-6450
- Pearson, G., Davies, F. and Collier, C. (2009). An analysis of the performance of the UFAM pulsed Doppler lidar for observing the boundary layer, *J. Atmos. Ocean. Tech.*, 26, pp 240-250
- Pearson, G., Davies, F. and Collier, C. (2010). Remote sensing of the tropical rain forest boundary layer using pulsed Doppler lidar, *Atmos. Chem. Phys. Discuss.*, 10, pp 5021-5049
- Piper, M. and Lundquist, J.K. (2004). Surface layer turbulence measurements during a frontal passage, *J. Atmos. Sci.*, 61, pp 1768-1780
- Post, M.J. and Cupp, R.E. (1990). Optimising a pulsed Doppler lidar, *Appl. Opt.*, 29, pp 4145-4158
- Shutts, G. (2005). A kinetic energy backscatter algorithm for use in ensemble prediction systems, *Quart. J. R. Met. Soc.*, 131, pp 3079-3102
- Simmons, A. and Hoskins, B.J. (1978). The life cycles of some nonlinear baroclinic waves, *J. Atmos. Sci.*, 35, pp 414-432
- Vila-Guerau de Arellano, J., Van den Dries, K. And Pino, D. (2009). On inferring isoprene emission surface flux from atmospheric boundary layer concentration measurements, *Atmos. Chem. Phys.*, 9, pp 3629-3640
- Werner, C. (2005). Doppler wind lidar, in *Lidar: Range-Resolved Optical Remote Sensing of the Atmosphere*, ed. C. Weitkamp, Series in Optical Sciences, Vol. 102, Springer, pp 339-342
- Wilson, J.W. (1970). Integration of radar and gage data for improved rainfall measurement, *J. Appl. Met.*, 9, pp 489-497
- Wilson, J.W. and Miller, L.J. (1972). Atmospheric motion by Doppler radar, in *Remote Sensing of the Atmosphere*, ed. V. E. Derr, Chapters 21a, 27a, 27pp

Part 4

Weather Radar Quality Control and Related Applications

Quality Control Algorithms Applied on Weather Radar Reflectivity Data

Jan Szturc, Katarzyna Ośródka and Anna Jurczyk
*Institute of Meteorology and Water Management – National Research Institute
Poland*

1. Introduction

Quality related issues are becoming more and more often one of the main research fields nowadays. This trend affects weather radar data as well. Radar-derived precipitation data are burdened with a number of errors from different sources (meteorological and technical). Due to the complexity of radar measurement and processing it is practically impossible to eliminate these errors completely or at least to evaluate each error separately (Villarini & Krajewski, 2010). On the other hand, precise information about the data reliability is important for the end user.

The estimation of radar data quality even as global quantity for single radar provides very useful and important information (e.g. Peura et al., 2006). However for some applications, such as flash flood prediction, more detailed quality information is expected by hydrologists (Sharif et al., 2004; Vivoni et al., 2007, Collier, 2009). A quality index approach for each radar pixel seems to be an appropriate way of quality characterization (Michelson et al., 2005; Friedrich et al., 2006; Szturc et al., 2006, 2008a, 2011). As a consequence a map of the quality index can be attached to the radar-based product.

2. Sources of radar data uncertainty

There are numerous sources of errors that affect radar measurements of reflectivity volumes or surface precipitation, which have been comprehensively discussed by many authors (e.g. Collier, 1996; Meischner 2004; Šálek et al., 2004; Michelson et al., 2005).

Hardware sources of errors are related to electronics stability, antenna accuracy, and signal processing accuracy (Gekat et al., 2004). Other non-meteorological errors are results of electromagnetic interference with the sun and other microwave emitters, attenuation due to a wet or snow (ice) covered radome, ground clutter (Germann & Joss, 2004), anomalous propagation of radar beam due to specific atmosphere temperature or moisture gradient (Bebbington et al., 2007), and biological echoes from birds, insects, etc. Next group of errors is associated with scan strategy, radar beam geometry and interpolation between sampling points, as well as the broadening of the beam width with increasing distance from the radar site. Moreover the beam may be blocked due to topography (Bech et al., 2007) and by nearby objects like trees and buildings, or not fully filled when the size of precipitation echo is relatively small or the precipitation is at low altitude in relation to the antenna elevation (so called overshooting).

Apart from the above-mentioned non-precipitation errors, meteorologically related factors influence precipitation estimation from weather radar measurements. Attenuation by hydrometeors, which depends on precipitation phase (rain, snow, melting snow, graupel or hail), intensity, and radar wavelength, particularly C and X-band, may cause the strong underestimation in precipitation, especially in case of hail. Another source of error is Z - R relation which expresses the dependence of precipitation intensity R on radar reflectivity Z . This empirical formula is influenced by drop size distribution, which varies for different precipitation phases, intensities, and types of precipitation: convective or non-convective (Šálek et al., 2004). The melting layer located at the altitude where ice melts to rain additionally introduces uncertainty into precipitation estimation. Since water is much more conductive than ice, a thin layer of water covering melting snowflakes causes strong overestimation in radar reflectivity. This effect is known as the bright band (Battan, 1973; Goltz et al., 2006). Moreover the non-uniform vertical profile of precipitation leads to problems with the estimation of surface precipitation from radar measurement (e.g. Franco et al., 2002; Germann & Joss, 2004; Einfalt & Michaelides, 2008), and these vertical profiles may strongly vary in space and time (Zawadzki, 2006).

Dual-polarization radars have the potential to provide additional information to overcome many of the uncertainties in contrast to situation when only the conventional reflectivity Z and Doppler information is available (Illingworth, 2004).

3. Methods for data quality characterization

3.1 Introduction

Characterization of the radar data quality is necessary to describe uncertainty in the data taking into account potential errors that can be quantified as well as the ones that can be estimated only qualitatively. Generally, values of many detailed “physical” quality descriptors are not readable for end users, so the following quality metrics are used as more suitable:

- total error level, i.e. measured value \pm standard deviation expressed as measured physical quantity (radar reflectivity in dBZ, precipitation in mm h⁻¹, etc.),
- quality flag taking discrete value, in the simplest form 0 or 1 that means “bad” or “excellent” data,
- quality index as unitless quantity related to the data errors, which is expressed by numbers e.g. from 0 to 1.

Many national meteorological services provide quality information in form of flags to indicate where radar data is burdened with specific errors and if it is corrected by dedicated algorithms (Michelson et al., 2005; Norman et al., 2010). The flags are expressed as discrete numbers.

The quality index (QI) is a measure of data quality that gives a more detailed characteristic than a flag, providing quantitative assessment, for instance using numbers in a range from 0 (for bad data) to some value (e.g. 1, 100, or 255 for excellent data). The quality index concept is operationally applied to surface precipitation data in some national meteorological services (see review in Einfalt et al., 2010).

3.2 General description of QI scheme

An idea of quality index (QI) scheme is often employed to evaluate radar data quality. In this scheme the following quantities must be determined (Szturc et. al., 2011):

1. Quality factors, X_i (where $i = 1, \dots, n$) – quantities that have impact on weather radar-based data quality. Their set should include the most important factors that can be measured or assessed.
2. Quality functions, f_i – formulas for transformation of each individual quality factor X_i into relevant quality index QI_i . The formulas can be linear, sigmoidal, etc.
3. Quality indices, QI_i – quantities that express the quality of data in terms of a specific quality factors X_i :

$$QI_i = \begin{cases} 0 & \text{bad data} \\ 1 & \text{good data} \\ f_i(X_i) \in (0,1) & \text{other cases} \end{cases} \quad (1)$$

4. Weights, W_i – weights of the QI_i s. The optimal way of the weight determination seems to be an analysis of experimental relationships between proper quality factors X_i and radar data errors calculated from comparison with benchmark data (on historical data set).
5. Final quality index, QI – quantity that expresses quality of data in total, calculated using one of the formulae:
 - minimum value:

$$QI = \min(QI_i), \quad (2a)$$

- additive scheme (weighted average):

$$QI = \sum_{i=1}^n (QI_i \cdot W_i), \quad (2b)$$

- multiplicative scheme (multiplication):

$$QI = \prod_{i=1}^n (QI_i \cdot W_i) \text{ or } QI = \prod_{i=1}^n QI_i. \quad (2c)$$

The latter seems to be the most appropriate and its form is open (e.g. changes in set of quality indicators do not require the scheme parameterization).

4. Quality control algorithms for radar reflectivity volumes

Starting point in dealing with weather radar reflectivity data should be quality control of 3-D raw radar data. There are not many papers focused on quality characterization of such data. Fornasiero et al. (2005) presented a scheme employed in ARPA Bologna (Italy) for quality evaluation of radar data both raw and processed. The scheme developed in Institute of Meteorology and Water Management in Poland (IMGW) in the frame of BALTRAD project (Michelson et al., 2010) was described by Ośródk et al. (2010, 2012). Commonly employed groups of quality control algorithms are listed in Table 1.

Task	Correction algorithm	Quality factor	QC	QI
Evaluation of technical radar parameters	-	Set of technical radar parameters		x
Assessment of effects related to distance to radar site	-	Horizontal and vertical beam broadening		x
Ground clutter removal	Using Doppler filter or 3-D clutter map	Presence of ground clutter	x*	x
Removal of non-meteorological echoes	Analysis of 3-D reflectivity structure. Using dual-polarization parameters	Presence of the non-meteorological echoes	x	x
Beam blockage correction	Using topography map	Presence of beam blockage	x	x
Correction for attenuation in rain	Based on attenuation coefficient. Using dual-polarization parameters	Attenuation in rain along the beam path	x	x
Spatial variability evaluation	Analysis of 3-D reflectivity structure	Spatial variability of reflectivity field		x

* commonly the correction is made by built-in radar software.

Table 1. Groups of quality control algorithms (correction QC and characterization QI) for 3-D reflectivity (Z) data.

4.1 Technical radar parameters

This algorithm aims to deliver data quality metric only. A set of technical radar parameters that impact on data quality can be selected as quality factors. The parameters are for instance: operating frequency, beam width, pointing accuracy in elevation and azimuth, minimal detectable signal at 1000 m, antenna speed, date of last electronic calibration, etc. (Holleman et al., 2006). All the factors are static within the whole radar range and characterize quality of each particular radar so different radars can be compared in terms of their quality. The threshold values for which the quality index becomes lower than one should be set for all parameters according to the common standards.

4.2 Horizontal and vertical broadening of a radar beam

Radar measurements are performed along each beam at successive gates (measurement points in 3-D data space), which represent certain surrounding areas determined by the beam width and pulse length. Since the radar beam broadens with the distance to the radar site, the measurement comes from a larger volume and related errors increase as well. There is no possibility to correct this effect, however it can be quantitatively determined and taken into account in the total quality index.

The horizontal and vertical broadening of radar beam for each gate can be geometrically computed knowing its polar coordinates: elevation, azimuth, and radial distance to radar site,

and two parameters of radar beam: beam width and radar pulse length. Related quality index may be determined from broadenings of the both beam cross section (Ośródko et al., 2012).

4.3 Ground clutter removal

The correction of radar data due to contamination by ground clutter is commonly made at a level of radar system software which uses statistical or Doppler filtering (e.g. Selex, 2010). In such situation the information about the correction is not available so generation of a ground clutter map for the lowest (and higher if necessary) scan elevation must be employed, e.g. using a digital terrain map (DTM). In order to determine areas contaminated by ground clutter a diagram of partial beam blockage values (*PBB*) is analysed. The *PBB* is defined as a ratio of blocked beam cross section area to the whole one.

Gates where ground clutter was detected should be characterized by lowered quality index. A simple formula for quality index QI_{GC} related to ground clutter presence can be written as:

$$QI_{GC} = \begin{cases} a & \text{ground clutter is detected} \\ 1 & \text{no clutter} \end{cases} \quad (3)$$

where a is the constant, e.g. between 0 and 1 in the case of $QI_i \in (0, 1)$. The quality index decreases in each gate with detected clutter even if it was removed.

4.4 Removal of non-meteorological echoes

Apart from ground clutter other phenomena like: specks, external interference signals (e.g. from sun and Wi-Fi emitters), biometeors (flock of birds, swarm of insects), anomalous propagation echoes (so called anaprop), sea clutter, clear-air echoes, chaff, etc., are considered as non-meteorological clutter. Since various types of non-precipitation echoes can be found in radar observations, in practice individual subalgorithms must be developed to address each of them. More effective removal of such echoes is possible using dual-polarization radars and relevant algorithms for echo classification.

Removal of external interference signals. Signals coming from external sources that interfere with radar signal have become source of non-meteorological echoes in radar data more and more often. Their effect is similar to a spike generated by sun, but they are observed in any azimuth at any time, mainly at lower elevations, and may reach very high reflectivity. The spurious spike-type echoes are characterized by their very specific spatial structure that clearly differs from precipitation field pattern (Peura, 2002; Ośródko et al., 2012): they are observed along the whole or large part of a single or a few neighbouring radar beams. Commonly reflectivity field structure is investigated to detect such echo on radar image (Zejdlik & Novak, 2010). Recognition of such echo is not very difficult task unless it interferes with a precipitation field: its variability is low along the beam and high across it. The algorithm removes it from the precipitation field and replaces by proper (e.g. interpolated) reflectivity values. In the algorithm of Ośródko et al. (2012) two stages of spike removal are introduced: for "wide" and "narrow" types of spikes.

Removal of "high" spurious echoes. "High" spurious echoes, not only spikes, are echoes detected at altitudes higher than 20 km where any meteorological echo is not possible to exist. All the "high" echoes are removed.

Removal of “low” spurious echoes. “Low” spurious echoes are all low-reflectivity echoes detected at low altitudes only. No meteorological echo can exist here. All the “low” echoes are removed. The algorithm can be treated as a simple method to deal with biometeor echoes (Peura, 2002).

Meteosat filtering. As a preliminary method for non-meteorological echo removal the filtering by Meteosat data on cloudiness can be used. A Cloud Type product, which is provided by EUMETSAT, distinguishes twenty classes of cloud type with the classes from 1 to 4 assigned to areas not covered by any cloud. All echoes within not clouded areas are treated as spurious ones and removed. Such simple technique can turn out to be quite efficient in the cases of anomalous propagation echoes (anaprop) over bigger areas without clouds (Michelson, 2006).

Speck removal. Generally, the specks are isolated radar gates with echo surrounded by non-precipitation gates. Number of echo gates in a grid around the given gate (e.g. of 3×3 gates) is calculated (Michelson et al., 2000). If a certain threshold is not achieved then the gate is classified as a speck, i.e. measurement noise, and the echo is removed. Algorithm of the reverse specks (i.e. isolated radar gates with no echo surrounded by precipitation gates) removal is analogous to the one used for specks.

Using artificial intelligence techniques. Artificial intelligence algorithms, such as neural network (NN), are based on analysis of reflectivity structure (Lakshmanan et al., 2007). The difference is that similarity of the given object pattern to non-meteorological one, on which the model was learned, is a criterion of spurious echo detection. For this reason NN-based algorithms are difficult to parameterize and control their running.

Using dual-polarization observations. The basis is the fact that different types of targets are characterized by different size, shape, fall mode and dielectric constant distribution. In general, different combinations of polarimetric parameters can be used to categorize the given echo into one of different types (classes). The fuzzy logic scheme is mostly employed for the combination. Such methods consider the overlap of the boundaries between meteorological and non-meteorological objects. For each polarimetric radar observable and for each class a membership function is identified basing on careful analysis of data. Finally, an object is assigned to the class with the highest value of membership function.

The most often horizontal reflectivity (Z_H), differential reflectivity (Z_{DR}), differential phase shift (Φ_{DP}), correlation coefficient (ρ_{HV}), and analyses of spatial pattern (by means of standard deviation) of the parameters are employed in fuzzy logic schemes. Radars operating in different frequencies (S-, C-, and X-band) may provide different values of polarimetric parameters as they are frequency-dependent. For that reason, different algorithms are developed for identification of non-meteorological echoes using different radar frequencies, see e.g. algorithms proposed by Schuur et al. (2003) for S-band radars and by Gourley et al. (2007b) for C-band. A significant disadvantage of such techniques is that they are parameterized on local data and conditions so they are not transportable to other locations.

Quality index. Quality index for the gates in which non-meteorological echoes are detected is decreased to a constant value using formula similar to Equation (3).

An example of algorithms running for spike- and speck-type echoes removal is depicted in Figure 2b (for Legionowo radar).

4.5 Beam blockage

Radar beam can be blocked by ground targets, i.e. places where the beam hits terrain. A geometrical approach is applied to calculate the degree of the beam blockage. This approach is based on calculation what part of radar beam cross section is blocked by any topographical object. For this purpose a degree of partial beam blocking (*PBB*) is computed from a digital terrain map (DTM). According to Bech et al. (2003, 2007), the *PBB* is calculated from the formula:

$$PBB = \frac{y\sqrt{a^2 - y^2} + a^2 \arcsin \frac{y}{a} + \frac{\pi a^2}{2}}{\pi a^2} \quad (4)$$

where a is the radius of radar beam cross section at the given distance from radar, y is the difference between the height of the terrain and the height of the radar beam centre. The partial blockage takes place when $-a < y < a$, and varies from 0 to 1 (see Figure 1).

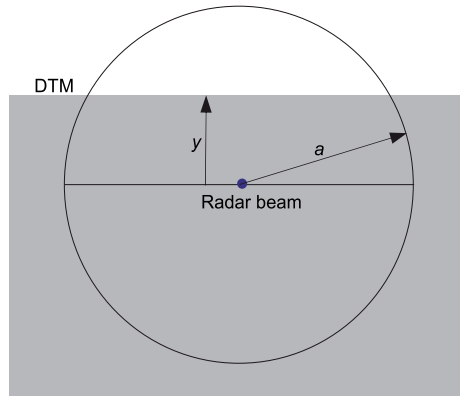


Fig. 1. Scheme of partial beam blockage *PBB* calculation using Bech et al. (2007) algorithm.

Quantity y in Equation 4 and Figure 1 is calculated as an altitude obtained from DTM for pixel located in radar beam centre taking into account altitude of radar antenna, the Earth curvature, and antenna elevation. Then the correction of partial beam blocking is made according to the formula (Bech et al., 2007):

$$Z_{cor} = Z + 10 \cdot \lg_{10}(1 - PBB)^{-1} \quad (5)$$

The correction is introduced if the *PBB* value is lower than 0.7. For higher *PBB* values “no data” (Bech et al., 2007) or reflectivity from neighbouring higher elevation (Ośródka et al., 2012) may be taken. A quality of blocked measurement dramatically decreases and can be expressed by:

$$QI_{PBB} = \begin{cases} 1 - PBB & PBB \leq a \\ 0 & PBB > a \end{cases} \quad (6)$$

where coefficient a can be set as 0.5 (Fornasiero et al., 2005) or 0.7 (Bech et al., 2007; Ośródka et al., 2012). If reflectivity in a specific gate has been replaced by reflectivity from higher

elevation then QI_{PBB} is taken from the higher one multiplied by factor b set as e.g. 0.3 (Ośródką et al., 2012). An example of the algorithm running is presented in Fig. 2 for Pastewnik radar which is located near mountains.

4.6 Attenuation in rain

Attenuation is defined as decrease in radar signal power after passing a meteorological object, that results in underestimation of the measured rain:

$$A = 10 \cdot \log_{10} \frac{Z_{corr}}{Z} \quad (7)$$

where A is the specific attenuation (dB km^{-1}), Z_{corr} is the non-attenuated rain and Z is the measured one ($\text{mm}^6 \text{ m}^{-3}$). Especially at C- and X-band wavelength the attenuation can considerably degrade radar measurements. The aim of the algorithm is to calculate the non-attenuated rain. Empirical formulae for determination of specific attenuation can be found in literature. Using 5.7-cm radar wavelength (C-band radar) for rain rate the two-way attenuation A in 18°C can be estimated from the formula (Battan, 1973):

$$A = 0.0044 \cdot R^{1.17} \quad (8)$$

Reflectivity-based correction made iteratively (“gate by gate”) is a common technique of correction for attenuation in rain (Friedrich et al., 2006; Ośródką et al., 2012). For a given gate i the attenuation at distance between gate $i-1$ and gate i can be calculated taking into account underestimations calculated for all gates along the beam from the radar site up to the $i-1$ gate (based on Equation 8). Finally, corrected rain rate in the gate i is computed from the attenuation and underestimations in all previous gates.

In case of dual-polarization radars specific attenuation for horizontal polarization A_H and specific differential attenuation A_{DP} (in dB km^{-1}) can be calculated using different methods. For C-band radar typically specific differential phase K_{DP} is applied using a nearly linear relation between the attenuation and K_{DP} , e.g. (Paulitsch et al., 2009):

$$A_H = 0.073 K_{DP}^{0.99}, \quad A_{DP} = 0.013 K_{DP}^{1.23} \quad (9)$$

or a linear one.

The iterative approach can lead to unstable results because it is very sensitive to small errors in both measurement and specific attenuation. Therefore, in order to avoid the instability in the algorithm, certain threshold values must be set to limit the corrections. For dual-polarization radar a ZPHI algorithm is recommended, in which specific attenuation is stabilized by differential phase shift Φ_{DP} (Testud et al., 2000; Gourley et al., 2007a).

Magnitude of the correction in precipitation rate can be considered as a measure of quality due to radar beam attenuation (Ośródką et al., 2012).

4.7 Spatial variability of reflectivity field

Small-scale variability of precipitation field is directly connected with uncertainty because heavy precipitation is more variable in space and time, as it can be especially observed in

the case of small-scale convective phenomena. Moreover non-precipitation echoes, such as ground clutter, are often characterized by high variability that differs from that for stratiform precipitation echoes. Spatial variability can be quantified as 3-D reflectivity gradient (Friedrich & Hagen, 2004) or standard deviation in a certain spatial grid (Szturc et al., 2011) and should be taken into account in quality index determination.

4.8 Total quality index

Computation of the total quality index QI is the final step in estimation of radar volume data quality. If the individual quality indices QI_i characterizing data quality are quantitatively determined, then the total quality index QI is a result of all the individual values QI_i employing one of the formulas 2a – 2c.

Each elevation of raw reflectivity volume can be compared with final corrected field. A set of such data for the lowest elevation is presented in Fig. 2. In this Figure a strong impact of spike echoes is observed for Legionowo radar whereas ground clutter and related blockage on data from Pastewnik radar is evident. Both radars are included in Polish radar network POLRAD (Szturc & Dziewit, 2005).

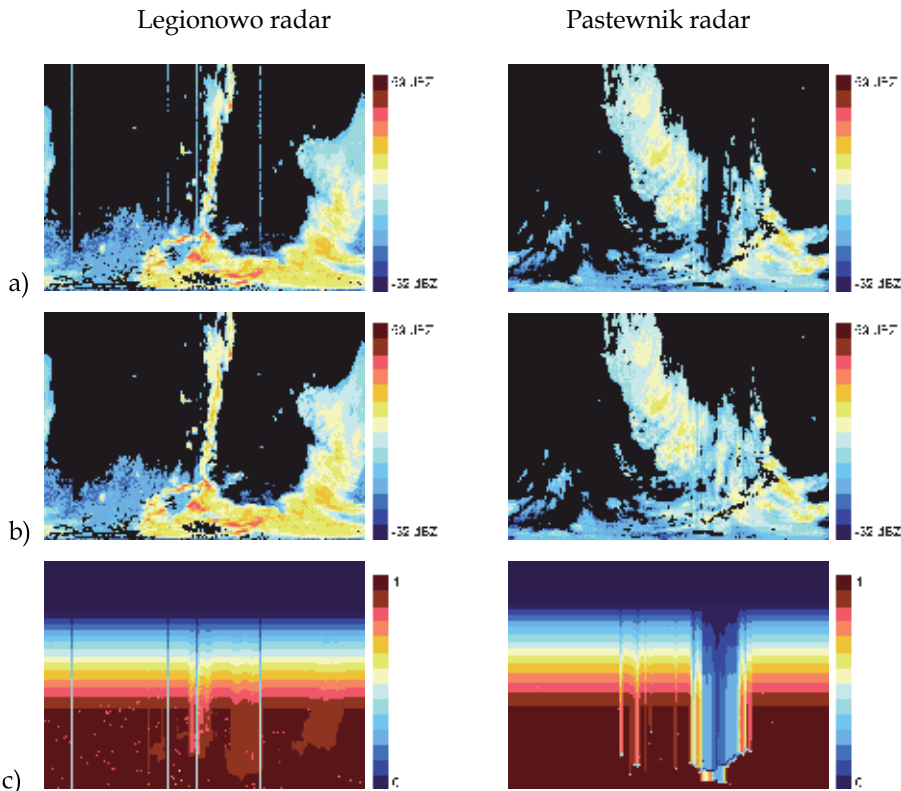


Fig. 2. Example of influence of all correction algorithms for the lowest elevation (0.5°): a) raw data Z (in dBZ); b) corrected data Z; c) total quality index QI (the left image for Legionowo radar, 10.05.2010, 15:30 UTC, the right for Pastewnik radar, 5.05.2010, 18:00 UTC; distance to radar up to 250 km). The panels represent range (y -axis) vs. azimuth (x -axis) displays.

5. Quality control algorithms for surface precipitation products

Corrections of 2-D radar data should constitute consecutive stages in radar data processing in order to get the best final radar products. These corrections include algorithms related to specific needs of the given product. The particular quality factors employed for calculating quality indices for 3-D data which also influence quality of 2-D data are not described here.

Many algorithms for surface precipitation field estimation from weather radar measurements applied in operational practice (e.g. Michelson et al., 2005) are described in this Section. For precipitation accumulation a different group of quality factors is applied. More common quality control algorithms employed in the practice are listed in Table 2.

Task	Correction algorithm	Quality factor	QC	QI
Z-R relationship estimation	Changeable Z-R relationship used	-	x	
Bright band (melting layer) effect correction	VPR-based correction	Presence of melting layer	x	x
Data extrapolation onto the Earth surface	VPR-based correction	Height of the lowest radar beam	x	x
Orographic enhancement	Physical model	Magnitude of the enhancement	x	x
Adjustment with rain gauge data	Correction using rain gauge data	Radar precipitation – rain gauge differences	x	x
For accumulation: number of rate data	-	Temporal continuity of data (number of the products)		x
For accumulation: averaged QI for rate data	-	Quality of included data (averaged QI)		x

Table 2. Quality control algorithms (correction and characterization) for 2-D surface precipitation data (in order of implementation into the chain).

5.1 Estimation of Z-R relationship

The Z-R relationship ($Z = aR^b$) variability is one of the most significant error sources in precipitation estimation. Each hydrometeor contributes to the precipitation intensity roughly to 3.7th power of its diameter, thus assumption on the drop size distribution is needed as the integral intensity is measured. Nowadays, for a single polarization radar it is a common practice to apply a single (usually Marshall and Palmer formula $Z = 200 \cdot R^{1.6}$) or seasonally-dependent Z-R relationship. However, use of a fixed Z-R relation can lead to significant errors in the precipitation estimation, as it depends on precipitation type (stratiform or convective), its kind (rain, snow, hail), etc. There are approaches that use tuned Z-R relationships for different meteorological situations. It requires the different types of precipitation to be identified on the basis of dedicated algorithms, which is easier if disdrometer measurements are available (Tenório et al., 2010).

Improvement in precipitation rate R estimation is noticeable using dual-polarization parameters, especially for heavy rainfall. In addition to the horizontal reflectivity Z_H available for single polarization radar, the specific differential phase K_{DP} and the differential reflectivity Z_{DR} can be applied (Bringi & Chandrasekhar, 2001). Typical forms of relationships for precipitation estimation are as follows: $R = f(K_{DP})$, $R = f(Z_H, Z_{DR})$, $R = f(K_{DP}, Z_{DR})$, and $R = f(Z_H, K_{DP}, Z_{DR})$. These approaches for precipitation rate estimation are potentially unaffected by radar calibration errors and attenuation, unbiased by presence of hail, etc.

5.2 Bright band phenomenon

Vertical profile of reflectivity (VPR) provides very useful information for radar data quality control. An averaged VPR is suggested to be taken from radar pixels lying at distance between about from 30 to 80 km from radar site to obtain the profile valid for the whole range of heights (Franco et al., 2002; Germann & Joss, 2004; Einfalt & Michealides, 2008). The bright band is a phenomenon connected with the presence of the melting layer. It is assumed that the melting layer is placed in range from the 0°C isotherm down to 400 m below (Friedrich et al., 2006). The melting of ice precipitation into water drops and related overestimation of precipitation rate results in errors of ground precipitation estimation. The phenomenon is clearly visible in vertically pointing radar observations. For dual-polarization radar a vertical profile of correlation coefficient (ρ_{HV}) is investigated instead of reflectivity profile analysis (Tabary et al., 2006).

It is proposed that the relevant quality index equals 0 inside the melting layer due to bright band, and equals 0.5 for measurement gates above the layer (Friedrich et al., 2006). In the case when the melting layer does not exist (in winter season or within convective phenomena) the quality index equals 1.

5.3 Data extrapolation onto the Earth surface

Information available from VPR can be used for another quality correction algorithm, which is extrapolation of precipitation data from the lowest beam to the Earth surface, especially at longer distances over 80 km. The averaged VPR is estimated for distance to radar site in range from 30 to 80 km and then employed to extrapolate radar data from the lowest beam to the Earth surface (Šálek et al., 2004). A quality factor which describes the relevant quality index is the height of the lowest radar calculated from radar scan strategy, digital terrain map (DTM), and the radar coordinates. It strongly depends on terrain complexity and related radar beam blocking and is defined as a minimum height for which radar measurement over a given pixel is feasible.

5.4 Orographic enhancement (seeder-feeder effect)

Orographic enhancement is a result of so called seeder–feeder mechanism which is observed when ascent of air is forced by hills or mountains. The low-level clouds formed in this way (feeder clouds) provide a moisture source that is collected by drops falling from higher clouds (seeder clouds). Radar is not able to capture the enhancement, which occurs close to the ground, as the measurement is performed at certain height over the hill. This effect can be estimated by 3-D physical model taking account of information from numerical weather

prediction model: wind speed, wind direction, relative humidity, temperature, as well as the topography of the region (Alpert & Shafir, 1989). Magnitude of such correction can be taken to determine related quality index.

5.5 Adjustment with rain gauge data

Weather radar-based precipitation may differ from “ground truth”, which can be locally estimated from rain gauge measurements, especially in close vicinity of the gauge. It is assumed that rain gauge measures precipitation exactly as its correction can be calculated (Førland et al., 1996), whereas radar provides information about space distribution. The idea is to use rain gauge information to improve radar data, as so called adjustment. The following solutions are proposed (Gjertsen et al., 2004):

- Mean field correction is a simple method to make the radar measurements unbiased. The correction factor is calculated from comparison of the averaged radar observations over the whole considered area, and the analogical averaged rain gauge measurements. The mean field bias can be calculated from historical data set or dynamic time-window. The last method allows to take into consideration variability in precipitation characteristics with time, but the time-period of the dynamic window cannot be too short due to requirement of data representativeness.
- Other methods of radar precipitation correction employ the distance to radar site L as the predictor apart from rain gauge information. Correction factor C can be expressed as e.g. polynomial relationship in form proposed by Michelson et al. (2000):

$$C = aL^2 + bL + c \quad (10)$$

where a , b , and c are the empirically estimated parameters of the equation.

- More advanced methods based on multiple regression involve more predictors which play significant role in precipitation estimation. Especially in mountainous terrain the distance to radar site turned out not sufficient because of strong influence of beam blockage and shielding. Additional predictors can be height of the lowest radar beam, height above sea level, etc.

Quality index related to the adjustment with rain gauge data can be determined from magnitude of the correction.

5.6 Quality factors for precipitation accumulation

The following quality factors for precipitation accumulation can be considered:

- *Number of precipitation rate products.* Accumulated precipitation field is composed from a certain number of discrete radar measurements. The number of precipitation rate products included into the given precipitation accumulation can be used to calculate a related quality index. Lack of one or more products during the accumulation period results in a significant decrease of quality. Moreover lack of the products one after the other results in much lower quality.
- *Averaged quality index from precipitation rate products* is computed as a mean from all values of quality indices for precipitation rates (e.g. maximally seven for 10-minute time resolution and 1-hour period of accumulation) that are aggregated into the accumulation.

5.7 Combination: weather radar precipitation – rain gauges

The combination of radar precipitation and rain gauge data is treated as the next stage in precipitation field estimation: the adjustment is considered as the radar data correction, whereas the result of combination is not corrected radar data, but precipitation estimated from larger number of data sources.

The measurement techniques such as rain gauges, weather radar, and satellite are considered as independent ones, which provide rainfall information with different error characteristics. Rain gauges are assumed to measure precipitation directly with good point accuracy. However in the case of rather sparse network density, the number of rain gauges might not be sufficient to successfully reproduce spatial variability of precipitation. On the other hand weather radar is capable of reflecting the spatial pattern of rainfall with high resolution in time and space over a large area almost in the real-time. Nevertheless radar data are burdened with non-negligible errors: both non-meteorological and meteorological. Therefore, merging these two sources of information could lead to improvement in precipitation estimation. As a consequence, several methods have been developed to estimate rainfall field from radar- and raingauge-driven data.

One of them is a geostatistical approach, where spatially interpolated rain gauge data and radar field are combined employing the Cokriging technique (Krajewski, 1987). However the need for estimation of required empirical parameters might be crucial and may lead to significant errors. Velasco-Forero et al. (2004) tested different Kriging estimators (ordinary Kriging, Kriging with External Drift, Cokriging and Collocated Cokriging) to produce merged field from raingauge observations and radar data. Kriging with External Drift technique turned out to give the best final field.

In another approach (Todini, 2001) Kalman filtering is applied to optimally combine data from the two sensors (rain gauge network and weather radar) in a Bayesian sense. Radar field taken as the *a priori* estimate and the block Kriging of the raingauge observations treated as the measurement vector enable to find the *a posteriori* estimate of precipitation.

As it was pointed out, radar data is considered to be better than rain gauge network in reproduction of spatial distribution, whereas rain gauges measure precipitation accurately in their locations. This observation is a starting point in a technique proposed by Sinclair & Pegram (2005) in which the radar information is used to obtain the correct spatial structure of the precipitation field, while the field values are fitted to the raingauge observations.

5.8 Example of *QI* data

An example of the *QI* scheme application implemented in Institute of Meteorology and Water Management (IMGW) is presented below. Polish weather radar network POLRAD consists of eight C-Band Doppler radars of Gematronik with Rainbow software for basic processing of data. In Figure 3 an example of precipitation composite for selected event is presented together with quality index *QI* obtained from the aforementioned quality factors (Table 2) using additive scheme (Equation 2b).

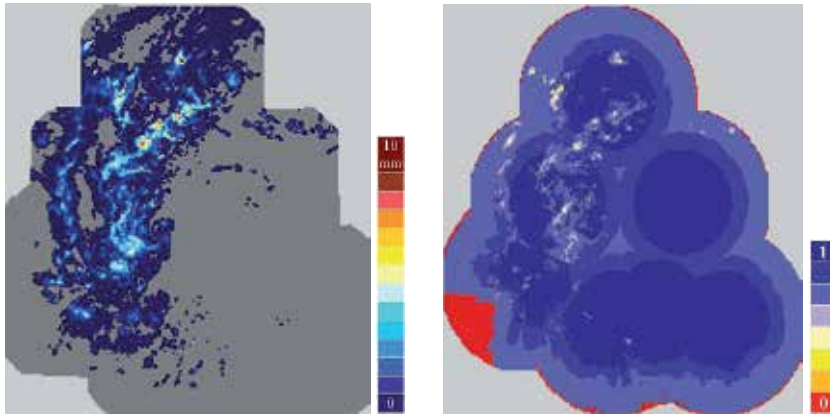


Fig. 3. Example of corrected field of precipitation rate (on the left) (composite from 5 August 2006, 03 UTC, when 7 from 8 weather radars were running) and resulting averaged quality index QI (on the right) (Szturc et. al., 2011).

The final quality index QI field depends on all quality factors included in the scheme. The most significant ones are height of the lowest radar beam, especially for places at longer distances to the nearest radar site and in mountainous areas (the zero-quality area south-west of the right map), and precipitation field variability (calculated analogically to the related 3-D algorithm) that follows the pattern of the precipitation field to some degree. It is noticeable that some quality factors are related to the precipitation field, whereas other fields are static if the set of running radars is constant, as they depend on radar locations only.

6. Conclusions

Weather radar data before being applied by the end-users must be quality controlled at all data processing stages. The main stages are generation of 3-D data (volumes) and then specialized 2-D data (products) dedicated to certain groups of the end-users. At first, the 3-D data should be corrected as they constitute the information source for generation of radar products. The corrections that are related to specific products should be made at the next stage – 2-D data processing. Due to numerous radar errors various correction techniques must be employed, moreover radar hardware limitations determine application of particular corrections. First of all dual-polarization radars, which will be a standard in the near future, open up new possibilities.

In quality control of radar data apart from the data correction, information about the data uncertainty plays also a key role. The high importance of radar data quality characterization is appreciated not only by radar people (meteorologists, hydrologists, etc.) but by end-user communities as well. Dealing with such quality information is a difficult task, however it is crucial for risk management and decision-making support.

For these reasons the quality control of radar data is becoming an essential task in weather radar data generation and processing. It has been a main subject of many international programmes, especially: the COST Action 731 (“Propagation of uncertainty in advanced meteo-hydrological forecast systems”, 2005-2010), the EUMETNET OPERA (“Operational Programme for the Exchange of Weather Radar Information”, from 1999), the BALTRAD

("An advanced weather radar network for the Baltic Sea Region: BALTRAD", Baltic Sea Region Programme, 2009-2014), the WMO programme RQOI ("Radar Quality Control and Quantitative Precipitation Intercomparisons", from 2011), etc. In the frame of the projects some recommendations are being developed, that will ensure harmonisation of practices in particular national meteorological services.

7. Acknowledgement

This paper contains outcomes from the BALTRAD and BALTRAD+ research projects ("An advanced weather radar network for the Baltic Sea Region: BALTRAD", Baltic Sea Region Programme) and the COST Action 731 "Propagation of uncertainty in advanced meteorological forecast systems".

8. References

- Alpert, P. & Shafir, H. (1989). A physical model to complement rainfall normals over complex terrain. *Journal of Hydrology*, Vol. 110, pp. 51-62, ISSN 0022-1694
- Battan, L. J. (1973). *Radar observation of the atmosphere*. University of Chicago Press, ISBN 9780226039190, Chicago - London, UK
- Bebbington, D.; Rae, S.; Bech, J.; Codina, B. & Picanyol, M. (2007). Modelling of weather radar echoes from anomalous propagation using a hybrid parabolic equation method and NWP model data. *Natural Hazards and Earth System Sciences*, Vol. 7, pp. 391-398, ISSN 1561-8633
- Bech, J.; Codina, B.; Lorente, J. & Bebbington, J. (2003). The sensitivity of single polarization weather radar beam blockage correction to variability in the vertical refractivity gradient. *Journal of Atmospheric and Oceanic Technology*, Vol. 20, pp. 845-855, ISSN 1520-0426
- Bech, J.; Gjertsen, U. & Haase, G. (2007). Modelling weather radar beam propagation and topographical blockage at northern high latitudes. *Quarterly Journal of the Royal Meteorological Society*, Vol. 133, pp. 1191-1204, ISSN 0035-9009
- Bringi, V. N. & Chandrasekar, V. (2001). *Polarimetric Doppler weather radar. Principles and applications*. Cambridge University Press, ISBN 9780521623841, Cambridge, UK
- Collier, C. G. (1996). *Applications of weather radar systems. A guide to uses of radar data in meteorology and hydrology*. Wiley-Praxis, ISBN 0-7458-0510-8, Chichester, UK
- Collier, C. G. (2009). On the propagation of uncertainty in weather radar estimates of rainfall through hydrological models. *Meteorological Applications*, Vol. 16, pp. 35-40, ISSN 1469-8080
- Einfalt, T. & Michaelides, S. (2008). Quality control of precipitation data. In: *Precipitation: Advances in measurement, estimation and prediction*, S. Michaelides, (Ed.), 101-126, Springer-Verlag, Berlin - Heidelberg, Germany
- Einfalt, T.; Szturc, J. & Ośródka, K. (2010). The quality index for radar precipitation data: a tower of Babel? *Atmospheric Science Letters*, Vol. 11, pp. 139-144, ISSN 1530-261X
- Førland, E. J.; Allerup, P.; Dahlström, B.; Elomaa, E.; Jónsson, T.; Madsen, H.; Perälä, J.; Rissanen, P.; Vedin, H. & Vejen, F. (1996). *Manual for operational correction of Nordic precipitation data*. DNMI Report Nr. 24/96, Oslo, Norway, ISSN 0805-9918

- Fornasiero, A.; Alberoni, P. P.; Amorati, R.; Ferraris, L. & Taramasso, A. C. (2005). Effects of propagation conditions on radar beam-ground interaction: impact on data quality. *Advances in Geosciences*, Vol. 2, pp. 201–208, ISSN 1680-7340
- Franco, M.; Sempere-Torres, D.; Sánchez-Diezma, R. & Andrieu, H. (2002). A methodology to identify the vertical profile of reflectivity from radar scans and to estimate the rainrate at ground at different distances. *Proc. ERAD 2002*, 299–304.
- Friedrich, K. & Hagen, M. (2004). Wind synthesis and quality control of multiple-Doppler-derived horizontal wind fields. *Journal of Applied Meteorology*, Vol. 43, pp. 38–57, ISSN 1520-0450
- Friedrich, K.; Hagen, M. & Einfalt, T. (2006). A quality control concept for radar reflectivity, polarimetric parameters, and Doppler velocity. *Journal of Atmospheric and Oceanic Technology*, Vol. 23, pp. 865–887, ISSN 1520-0426
- Gekat, F.; Meischner, P.; Friedrich, K.; Hagen, M.; Koistinen, J.; Michelson, D. B. & Huuskonen, A. (2004). The state of weather radar operations, networks and products. In: *Weather radar. Principles and advanced applications*, P. Meischner, (Ed.), 1–51, Springer-Verlag, ISBN 3-540-000328-2, Berlin – Heidelberg, Germany
- Germann, U. & Joss, J. (2004). Operational measurement of precipitation in mountainous terrain. In: *Weather radar. Principles and advanced applications*, P. Meischner, (Ed.), 52–77, Springer-Verlag, ISBN 3-540-000328-2, Berlin – Heidelberg, Germany
- Gjertsen, U.; Šálek, M. & Michelson, D.B. (2004). *Gauge-adjustment of radar-based precipitation estimates*. COST Action 717, ISBN 92-898-0000-3, Luxembourg
- Goltz, C.; Einfalt, T. & Galli, G. (2006). Radar data quality control methods in VOLTAIRE. *Meteorologische Zeitschrift*, Vol. 15, pp. 497–504, ISSN 1610-1227
- Gourley, J. J.; Tabary, P. & Parent-du-Châtelet, J. (2007a). Empirical estimation of attenuation from differential propagation phase measurements at C-band. *Journal of Applied Meteorology*, Vol. 46, pp. 306–317, ISSN 1520-0450
- Gourley, J. J.; Tabary, P. & Parent-du-Châtelet, J. (2007b). A fuzzy logic algorithm for the separation of precipitating from nonprecipitating echoes using polarimetric radar observations. *Journal of Atmospheric and Oceanic Technology*, Vol. 24, pp. 1439–1451, ISSN 1520-0426
- Holleman, I.; Michelson, D.; Galli, G.; Germann, U. & Peura, M. (2006). Quality information for radars and radar data. OPERA workpackage 1.2 (OPERA_2005_19 document).
- Illingworth, A. (2004). Improved precipitation rates and data quality by using polarimetric measurements. In: *Weather radar. Principles and advanced application*, P. Meischner, (Ed.), 130–166, Springer-Verlag, ISBN 3-540-000328-2, Berlin – Heidelberg, Germany
- Krajewski, W. F. (1987). Cokriging radar-rainfall and rain gage data. *Journal of Geophysical Research*, Vol. 92, pp. 9571–9580, ISSN 0148-0227
- Lakshmanan, V.; Fritz, A.; Smith, T.; Hondl, K. & Stumpf, G. J. (2007). An automated technique to quality control radar reflectivity data. *Journal of Applied Meteorology and Climatology*, 46, 288–305, ISSN 1558-8424
- Meischner, P. (ed.) (2004). *Weather radar. Principles and advanced applications*. Springer-Verlag, ISBN 3-540-000328-2, Berlin – Heidelberg, Germany
- Michelson, D. B.; Andersson, T.; Koistinen, J.; Collier, C. G.; Riedl, J.; Szturc, J.; Gjersten, U.; Nielsen, A. & Overgaard, S. (2000). *BALTEX Radar Data Centre products and their methodologies*, SMHI Reports Meteorology and Climatology, No. 90, Norrköping.

- Michelson, D.; Einfalt, T.; Holleman, I.; Gjertsen, U.; Friedrich, K.; Haase, G.; Lindskog, M. & Jurczyk, A. (2005). *Weather radar data quality in Europe – quality control and characterization. Review*. COST Action 717, ISBN 92-898-0018-6, Luxembourg
- Michelson, D. (2006). The Swedish weather radar production chain. *Proceedings of ERAD 2006: 4th European Conference on Radar in Meteorology and Hydrology*, pp. 382–385, ISBN 978-84-8181-227-5, Barcelona, Spain, September 18-22, 2006
- Michelson, D.; Szturc, J.; Gill, R. S. & Peura, M. (2010). Community-based weather radar networking with BALTRAD. *Proceedings of ERAD 2010: 6th European Conference on Radar in Meteorology and Hydrology*, pp. 337-342, ISBN 978-973-0-09057-4, Sibiu, Romania, September 6-10, 2010
- Norman, K.; Gaussiat, N.; Harrison, D.; Scovell, R. & Boscaci, M. (2010). A quality index scheme to support the exchange of volume radar reflectivity in Europe. *Proceedings of ERAD 2010: 6th European Conference on Radar in Meteorology and Hydrology*, ISBN 978-973-0-09057-4, Sibiu, Romania, September 6-10, 2010 (http://www.erad2010.org/pdf/oral/wednesday/dataex/07_ERAD2010_0259.pdf)
- Ośródką, K.; Szturc, J.; Jurczyk, A.; Michelson, D.B.; Haase, G. & Peura, M. (2010). Data quality in the BALTRAD processing chain. *Proceedings of ERAD 2010: 6th European Conference on Radar in Meteorology and Hydrology, Advances in radar technology*, pp. 355–361, ISBN 978-973-0-09057-4, Sibiu, Romania, September 6-10, 2010
- Ośródką, K.; Szturc, J. & Jurczyk, A. (2012). Chain of data quality algorithms for 3-D single-polarization radar reflectivity (RADVOL-QC system). *Meteorological Applications* (submitted).
- Paulitsch, H.; Teschl, F. & Randeu W. L. (2009). Dual-polarization C-band weather radar algorithms for rain rate estimation and hydrometeor classification in an alpine region. *Advances in Geosciences*, Vol. 20, pp. 3-8, ISSN 1680-7340
- Peura, M. (2002). Computer vision methods for anomaly removal. *Proc. ERAD 2002*, 312–317.
- Peura, M.; Koistinen, J. & Hohti, H. (2006). Quality information in processing weather radar data for varying user needs. *Proceedings of ERAD 2006: 4th European Conference on Radar in Meteorology and Hydrology*, pp. 563–566, ISBN 978-84-8181-227-5, Barcelona, Spain, September 18-22, 2006
- Šálek, M.; Cheze, J.-L.; Handwerker, J.; Delobbe, L. & Uijlenhoet, R. (2004). *Radar techniques for identifying precipitation type and estimating quantity of precipitation*. COST Action 717. Luxembourg.
- Schuur, T.; Ryzhkov, A. & Heinselman, P. (2003). *Observations and classification of echoes with the polarimetric WSR-88D radar*. NSSL Tech. Report, Norman, OK, USA.
- Sharif, H. O.; Ogden, F. L.; Krajewski, W. F. & Xue, M. (2004). Statistical analysis of radar rainfall error propagation. *Journal of Hydrometeorology*, Vol. 5, pp. 199–212, ISSN 1525-7541
- Selex (2010). *Rainbow 5. Products and algorithms*. Selex SI GmbH, Neuss, Germany
- Sinclair, S. & Pegram, G. (2005). Combining radar and rain gauge rainfall estimates using conditional merging. *Atmospheric Science Letters*, Vol. 6, pp. 19–22, ISSN 1530-261X
- Szturc, J. & Dziewit Z. (2005). Status and perspectives on using radar data: Poland. In: *Use of radar observations in hydrological and NWP models*. COST Action 717, Final report, pp. 218–221, ISBN 92-898-0017-8, Luxembourg
- Szturc, J.; Ośródką, K. & Jurczyk, A. (2006). Scheme of quality index for radar-derived estimated and nowcasted precipitation. *Proceedings of ERAD 2006: 4th European*

- Conference on Radar in Meteorology and Hydrology*, pp. 583–586, ISBN 978-84-8181-227-5, Barcelona, Spain, September 18-22, 2006
- Szturc, J.; Ośródką, K. & Jurczyk, A. (2008a). Parameterization of QI scheme for radar-based precipitation data. *Proceedings of ERAD 2008: 5th European Conference on Radar in Meteorology and Hydrology*, Helsinki, Finland, June 30 – July 4, 2008 (CD).
- Szturc, J.; Ośródką, K.; Jurczyk, A. & Jelonek, L. (2008b). Concept of dealing with uncertainty in radar-based data for hydrological purpose. *Natural Hazards and Earth System Sciences*, Vol. 8, pp. 267–279, ISSN 1561-8633
- Szturc, J.; Ośródką, K. & Jurczyk, A. (2011). Quality index scheme for quantitative uncertainty characterisation of radar-based precipitation. *Meteorological Applications*, Vol. 18, pp. 407-420, ISSN 1469-8080
- Tabary, P.; Le Henaff, A.; Vulpiani, G.; Parent-du-Châtelet, J.; Gourley, J.J. (2006), Melting layer characterization and identification with a C-band dual-polarization radar: a long-term analysis. *Proceedings of ERAD 2006: 4th European Conference on Radar in Meteorology and Hydrology*, pp. 17–20, ISBN 978-84-8181-227-5, Barcelona, Spain, September 18-22, 2006
- Tenório, R. S.; Moraes, M. C. S. & Kwon, B. H. (2010). Raindrop distribution in the eastern coast of northeastern Brazil using disdrometer data. *Revista Brasileira de Meteorologia*, Vol. 25, pp. 415-426, ISSN 1982-4351
- Testud, J.; Le Bouar, E.; Obligis, E. & Ali-Mehenni, M. (2000). The rain profiling algorithm applied to the polarimetric weather radar, *Journal of Atmospheric and Oceanic Technology*, Vol. 17, pp. 332–356, ISSN 1520-0426
- Todini, E. (2001). A Bayesian technique for conditioning radar precipitation estimates to rain-gauge measurements. *Hydrology and Earth System Sciences*, Vol. 5, pp. 187-199, ISSN 1027-5606
- Velasco-Forero, C. A.; Cassiraga, E. F.; Sempere-Torres, D.; Sanchez-Diezma, R. & Gomez-Hernandez, J. J. (2004). Merging radar and raingauge data to estimate rainfall fields: An improved geostatistical approach using non-parametric spatial models. *Proceedings of 6th International Symposium on Hydrological Applications of Weather Radar “Success stories in radar hydrology”*, ISBN 3-936586-29-2, Visby, Sweden, September 6-10, 2004 (CD).
- Villarini, G. & Krajewski, W. F. (2010). Review of the different sources of uncertainty in single polarization radar-based estimates of rainfall. *Surveys in Geophysics*, Vol. 31, pp. 107–129, ISSN 1573-0956
- Vivoni, E. R.; Entekhabi, D. & Hoffman R. N. (2007). Error propagation of radar rainfall nowcasting fields through a fully distributed flood forecasting model. *Journal of Applied Meteorology and Climatology*, Vol. 46, pp. 932–940, ISSN 1558-8424
- Zawadzki, I. (2006). Sense and nonsense in radar QPE. *Proceedings of ERAD 2006: 4th European Conference on Radar in Meteorology and Hydrology*, pp. 121–124, ISBN 978-84-8181-227-5, Barcelona, Spain, September 18-22, 2006
- Zejdlik, T. & Novak, P. (2010). Frequency protection of the Czech weather radar Network. *Proceedings of ERAD 2010: 6th European Conference on Radar in Meteorology and Hydrology, Advances in radar technology*, pp. 319–321, ISBN 978-973-0-09057-4, Sibiu, Romania, September 6-10, 2010

Effects of Anomalous Propagation Conditions on Weather Radar Observations

Joan Bech¹, Adolfo Magaldi², Bernat Codina¹ and Jeroni Lorente¹

¹*Dep. Astronomy and Meteorology, University of Barcelona*

²*Institute of Space Sciences, Spanish National Research Council (CSIC), Bellaterra Spain*

1. Introduction

The effect of atmospheric propagation on radar observations is an important topic both for radar application developers and end-users of radar products, particularly of weather radar systems. An excellent review of this subject is given by Patterson (2008), and most general books about weather radars have a chapter on the topic –see for example Battan (1973), Collier (1996), Doviak and Zrníc (2006), Rinehart (2001) or Sauvageot (1991).

In this chapter our objective is to provide an overview of the effects of anomalous propagation conditions on weather radar observations, based mostly on studies performed by the authors during the last decade, summarizing results from recent publications, presentations, or unpublished material. We believe this chapter may be useful as an introductory text for graduate students, or researchers and practitioners dealing with this topic. Throughout the text a spherical symmetric atmosphere is assumed and the focus is on the occurrence of ground and sea clutter and subsequent problems for weather radar applications. Other related topics such as long-path, over-the-horizon propagation and detection of radar targets (either clutter or weather systems) at long ranges is not considered here; however readers should be aware of the potential problems these phenomena may have as range aliasing may cause these echoes appear nearer than they are – for more details see the discussion about second trip echoes by Zrníc, this volume.

Despite the motivation and results shown here are focused on ground-based weather radar systems (typically X, C or S band radars, i.e. cm-radars), a large part of these results are applicable to other types of radar, in fact also to micro-wave links or, in general terms, for propagation of electromagnetic waves in the atmosphere. As discussed in detail below, the main effect of anomalous propagation on weather radar observation is a lower height of the observed echoes than expected in normal conditions. This may imply an increase of ground clutter or, for radars operating near the coast, an increase of sea clutter, which will be hardly corrected by the standard Doppler filtering, affecting inevitably precipitation estimates.

This chapter is organized as follows. Section 2 introduces the fundamental concepts of refractivity and modified refractivity and the various propagation conditions associated with refractivity profiles. Section 3 presents some results on propagation condition variability, and Section 4 focuses specifically upon the impact of that variability on radar beam blockage

corrections and subsequent precipitation estimates. Section 5 deals with the topic of propagation conditions forecasting and Section 6 presents a method to correct the effects of intense anomalous propagation conditions on weather radar precipitation estimates using satellite observations. Finally Section 7 provides a summary and concluding remarks.

2. Weather radar beam propagation conditions

This section presents qualitatively the different propagation regimes affecting the radar beam refraction. By radar beam we mean the energy emitted (and received) by the radar, limited by the half-power (3 dB) antenna main lobe (see Zrnic, this volume, for more details). In the vacuum, as in any media with constant index of refraction, a radar beam follows a straight trajectory. But in the atmosphere the index of refraction changes and therefore the variation of the air refractive index plays a key role when characterizing the propagation conditions of a radar beam in the troposphere, i.e. the lowest part of the atmosphere. In particular, the vertical profiles of the air temperature, moisture and pressure are mostly responsible for the way the radar energy will propagate in a given air layer. A number of assumptions on these vertical profiles are usually made, assuming the so-called "standard" or normal propagation conditions which are associated with the average state of the atmosphere accepted as the most representative, as discussed below. Under those conditions, the radar beam bends downward with a radius of curvature greater than that of the Earth surface. Consequently, the net effect is an increase of the height of the centre of the beam with respect to the ground as the distance from the radar increases (in Section 4 the equation for the radar beam height is given).

However, due to the inherent variability of the atmosphere, it is a well-known fact that propagation conditions may differ, sometimes significantly, from those considered standard resulting in anomalous propagation (AP). As illustrated schematically in Fig. 1, subrefraction causes the radar beam to bend less than usual, and therefore follows a higher trajectory than in normal conditions. Super refraction of a weather radar beam produces more bending towards the ground surface than expected for standard conditions and therefore increases and intensifies ground clutter echoes (AP or anaprop echoes). An extreme case of superrefraction, known as ducting, occurs when the beam has a curvature smaller than that of the Earth surface.

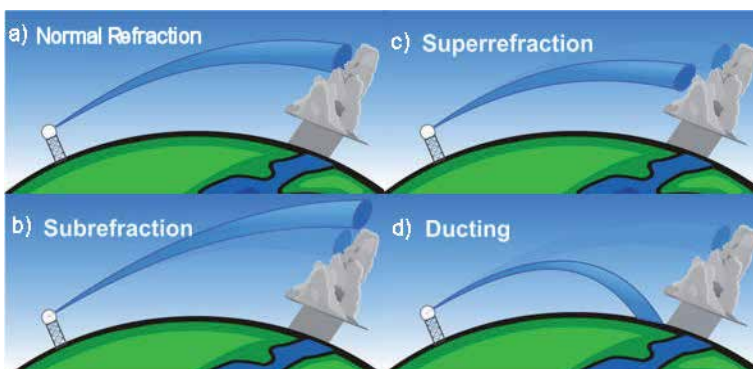


Fig. 1. Radar beam propagation conditions (adapted from US NOAA National Weather Service, introductory radar tutorial, "Doppler radar beams", http://www.srh.noaa.gov/jetstream/doppler/beam_max.htm).

Note that the term AP literally means “anomalous propagation” but AP echoes are associated with superrefraction and ducting, not to subrefraction. The occurrence of AP echoes may be particularly negative for automated quantitative precipitation estimates (QPE) such as those required for operational weather surveillance and hydrological flood warning. On the other hand, it should be noted that ducting may occur not only in the lowest air layer (surface ducting) as represented in Fig. 1d, but also on an elevated layer above which there is normal refraction. In that case, the duct (known as elevated duct), may trap the radar energy for a long distance without producing evident signs – AP echoes.

Figure 2 illustrates the effect of AP echoes on weather radar observations. It shows two radar reflectivity Plan Position Indicator (PPI) images recorded by the weather radar of the Meteorological Service of Catalonia located in Vallirana (41°22'N, 1°52'E, about 20 km west of Barcelona). The PPIs were obtained in two different days, one with normal propagation conditions, and the other under superrefraction conditions; none on those images show real precipitation, only ground and sea clutter. To see more clearly the change in AP echoes no Doppler filtering was applied to these images. In Fig. 2b arrows indicate some of the new or intensified AP echoes, either ground clutter (southernmost arrow pointing to the coast, or easternmost arrow pointing to the small island of Minorca), or sea clutter (around the centre of the image). PPI images corresponding to Fig. 2b where Doppler filtering was applied reduced largely AP ground clutter but not sea clutter, or other moving targets such as wind turbines, which may yield spurious hourly accumulations exceeding 50 mm.

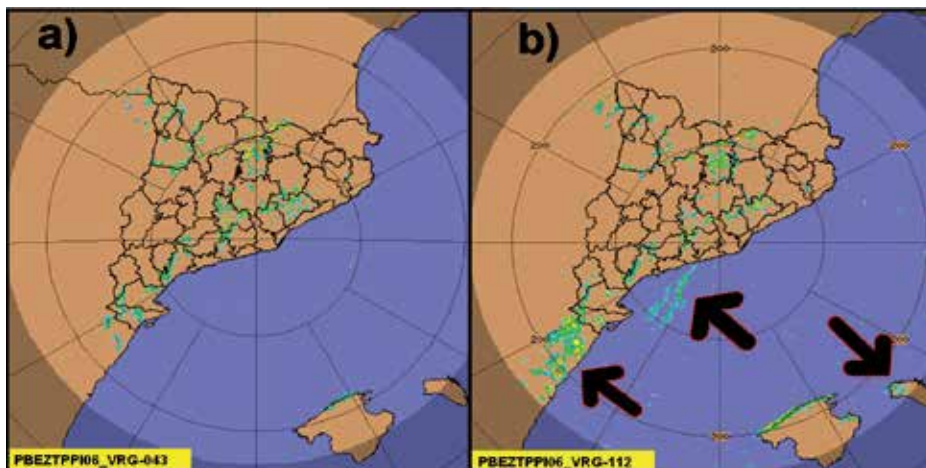


Fig. 2. Radar reflectivity base PPI images (0.6°) with no Doppler filtering showing ground and sea clutter on a normal propagation day (a) and a superrefractive day (b). Arrows indicate new or more intense AP echoes.

Despite the fact that AP echoes may be detected and cleaned with several techniques, this does not prevent that radar observations may be affected because of the difference between their real height and that expected assuming standard conditions. If this difference is important enough for a given application, any procedure which requires a precise knowledge of the echo altitude may be potentially affected by AP. For example, if radar data (either echo intensity or Doppler winds) are to be assimilated in a NWP model or if the radar echo intensity is corrected for beam blockage due to mountain sheltering (Bech et al., 2003), the effect may be relevant.

2.1 Refractivity N

As anomalous propagation is due to relatively small variations of the air refractive index n , the magnitude known as refractivity N , defined as one million times $n-1$, is commonly used in anaprop studies. As shown by Bean and Dutton (1968), or more recently in ITU (2003), N can be written as:

$$N = (n - 1)10^6 = \frac{77.6}{T} \left(p + \frac{4810 \cdot e}{T} \right), \quad (1)$$

where T is the air temperature (K), p atmospheric pressure (hPa), and e is the water vapour pressure (hPa). According to ITU (2003), this expression may be used for all radio frequencies; for frequencies up to 100 GHz, the error is less than 0.5%. This formula takes into account only air gases and does not consider liquid water content (usually with negligible effects), or free electron density (important for high atmospheric altitudes, typically above 60 km).

Note that N is a dimensionless magnitude, though quite often the term “ N units” is employed. N is sometimes considered the sum of two different terms of (1): the dry term, N_d , which depends only on p and T , and the wet term, N_w , which is also function of e , i.e. is related to moisture content. Typical values of N of air at ground level are within the range 250 to 450.

2.2 Modified refractivity M

A magnitude related to N is the modified refractivity M , which is defined as:

$$M = N + \frac{z}{10^{-6} r}, \quad (2)$$

where z is altitude and r is the radius of the Earth, expressed in meters (m). Modified refractivity is very useful to characterize propagation conditions as for constant M the curvature of the ray path is that of the Earth's surface and, therefore, when there are negative M vertical gradients the ray path may be bent towards the surface and then radio waves get trapped like in a wave guide (ducting). Based on M gradients, Johnson et al. (1999) suggested the use of a ducting index, with positive values proportional to the probability of occurrence of ducting.

2.3 Propagation conditions

Propagation characteristics may vary largely, depending for instance on the type of air mass (Gossard, 1977). When characterizing the radio propagation environment it is usual to consider the vertical refractivity gradient (VRG) of the air of the first kilometre above ground level to estimate propagation effects such as ducting, surface reflection and multipath on terrestrial line-of-sight links. However, the effect on weather radar beam refraction not only depends on the refractivity gradient of a layer but also on the angle of incidence between the beam and the trapping layer considered or the frequency of the electromagnetic wave (ITU, 2003). In the following paragraph, specific VRG values are given for the propagation conditions described earlier qualitatively.

For weather radar applications, if the vertical refractivity gradient of the first kilometre (VRG) of the atmosphere is around $-1/4r$ (i.e. -39 N units km^{-1} or 118 M units km^{-1} , where r is the Earth's radius) then standard propagation will occur for any angle of incidence (Doviak and Zrnic, 2006). An increase in VRG bends the radar beam more slowly than normal (subrefraction) and reduces the microwave radar horizon. With regard to ground clutter echoes, subrefraction implies a decrease in their frequency and intensity. On the other hand, a decrease in VRG generates the opposite effect, bending the beam faster than normal (super refraction) for the interval between (typically) -78.7 km^{-1} and -157 km^{-1} (the threshold to distinguish between standard propagation and superrefraction varies in the literature around 80 km^{-1}). Trapping, or ducting, the most extreme case of anomalous propagation, occurs for values lower than -157 km^{-1} , and in this case the microwave energy may travel for long distances before intercepting ground targets producing anomalous propagation (i.e., anaprop or AP) echoes. In fact the exact threshold for ducting depends on the precise local value of the Earth radius, which means that it is not a constant value (for example varies with latitude) – see Table 1 for a summary of ranges of refractivity and modified refractivity gradients for different propagation conditions. As a reference, the two examples of radar images shown in Fig. 2 were recorded with VRGs of -43 and -112 km^{-1} .

Characteristic	dN/dZ (km^{-1})	dM/dZ (km^{-1})
Subrefraction	$(0, +\infty)$	$[157, +\infty)$
Normal	$(-79, 0]$	$(157, 79)$
Superrefraction	$[-79, -157)$	$[79, 0)$
Ducting	$[-157, -\infty)$	$[0, -\infty)$

Table 1. Effects upon propagation under different ranges of dN/dZ and dM/dZ (adapted from Bech et al. 2007a).

On the other hand, a careful analysis of the fluctuation of target reflectivity may be a way to monitor variations in atmospheric conditions (changes in moisture content, etc.) as shown by Fabry et al. (1997). Subsequent research from that work triggered new interest in the analysis and characterization of refractivity profiles near ground level – see for example Park & Fabry (2011).

Superrefraction and ducting in particular, is usually associated with temperature inversions or sharp water vapour vertical gradients. During cloudless nights, radiation cooling over land favours the formation of ducts which disappear as soon as the sun heats the soil surface destroying the temperature inversion. This process may be sometimes clearly observed in the daily evolution of clutter echoes, as reported by Moszkowicz et al. (1994) and others.

3. Propagation condition variability

As radiosoundings have been traditionally the only source of upper air information available on a routine basis, they have been used for years to calculate long term averages of propagation conditions –see, for example, Gossard (1977) or Low and Huddak (1997)–. Since 1997, radiosonde observations have been made in Barcelona to support the operations of the regional government's Subdirectorate of Air Quality and Meteorology, which later became the Meteorological Service of Catalonia.

Results presented below were derived from observations collected from Vaisala RS-80 sondes (from 41.38°N, 2.12°E and 98 m asl) which sampled every 10 s providing much higher vertical resolution than the usual standard operational radiosounding observations. This allowed better characterization of the air refractive index variability and the detection of thinner super refractive layers that may not be detected by standard radiosounding observations but may have significant effects in the propagation of the radar beam. Most results presented in this and the next section, are based on data collected between 1997 and 2002, at 00 and 12 UTC in Barcelona (Bech et al., 1998, 2000, 2002). From the original 2485 radiosoundings available, 86% passed the quality control process (based both in data format and content analysis, adapted from Météo-France, 1997).

3.1 Surface refractivity

Surface refractivity is an important factor in radiometeorology; it appears in the refractivity exponential model and is one of the terms used in the standard computation of the VRG (ITU, 2003). Table 2 shows Barcelona N_s statistics.

00Z							
MONTH	Mean	St_dev	Min	P25	P50	P75	Max
J	315	8	291	310	315	320	335
F	317	10	293	309	318	325	334
M	316	10	296	310	319	323	334
A	320	10	292	314	322	329	335
M	329	13	294	319	332	339	351
J	341	13	297	334	343	350	366
J	347	15	302	336	351	357	372
A	354	15	303	346	355	364	382
S	344	13	309	338	345	354	371
O	336	14	305	326	335	347	367
N	316	13	286	309	314	321	367
D	313	11	284	305	312	318	339
Total 00Z	330	19	284	315	328	346	382
12Z							
MONTH	Mean	St_dev	Min	P25	P50	P75	Max
J	312	10	286	305	311	317	340
F	309	11	284	302	310	317	331
M	316	12	292	306	316	324	342
A	313	13	268	306	315	324	336
M	326	13	300	316	328	336	352
J	335	13	285	326	338	344	367
J	341	16	265	332	341	352	388
A	344	16	298	331	345	356	369
S	337	17	300	322	340	350	368
O	328	15	299	316	327	340	359
N	312	12	283	305	311	319	348
D	311	11	278	303	310	318	338
Total 12Z	325	18	265	312	324	339	388
Total							
00Z & 12Z	327	19	265	313	325	341	388

Table 2. N_s statistics for Barcelona calculated from 00Z and 12Z data.

It may be noted that nocturnal N_s values were lower than noon values (about 5 N units in the monthly means) and also the existence of a marked seasonal pattern with a peak in August and a minimum in December. This yearly cycle may be explained by examining the behaviour of the magnitudes considered in the computation of refractivity and also by considering separately the dry and wet terms (Fig. 3).

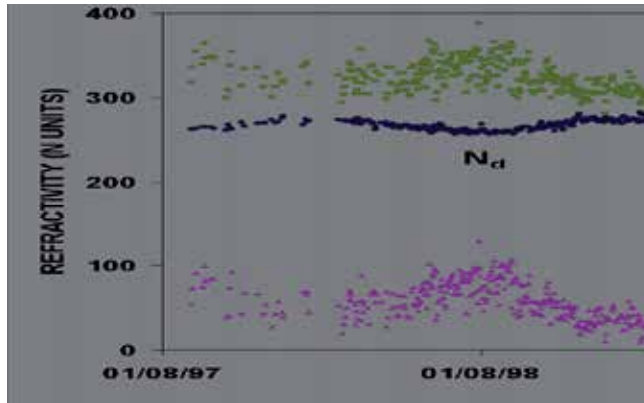


Fig. 3. Evolution of surface refractivity (N_s) and the wet (N_w) and dry terms (N_d) over Barcelona (Bech, 2003).

Monthly variations of these magnitudes show different behaviours. While the temperature follows a very clear seasonal pattern (high in summer and low in winter, as expected), in the case of the pressure it is much weaker (approximately winter maxima and summer minima). The humidity, changing constantly throughout the year, exhibits no apparent pattern. These behaviours are reflected in the evolution of N_d and N_w . The first one, proportional to pT^{-1} , is nearly constant with maxima in summer and minima in winter; the second, proportional to eT^{-2} , is much more variable (because of e) but maxima and minima are swapped with respect to N_d (because of T^{-2}). Therefore, N_w , which represents about 30% of N , contributes mostly to its variation: at short scale, it adds variability and also, at monthly scale, modulates the summer maximum and winter minimum cycle which is slightly compensated by the opposite cycle shown by N_d .

Surface refractivity distributions in Barcelona are shown in Fig. 4, exhibiting larger variations at 12 UTC (approx. 265 – 385) than at 00 UTC.

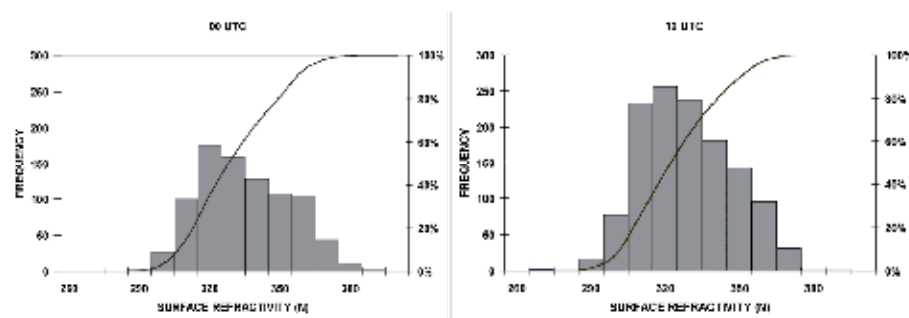


Fig. 4. Surface refractivity distributions at 00 and 12 UTC in Barcelona.

3.2 Vertical refractivity gradient

Vertical refractivity gradient in the first 1000 m (VRG) exhibits, like N_s , lower values for night conditions and a similar seasonal pattern both in the 00 Z & 12 Z data (Fig. 5).

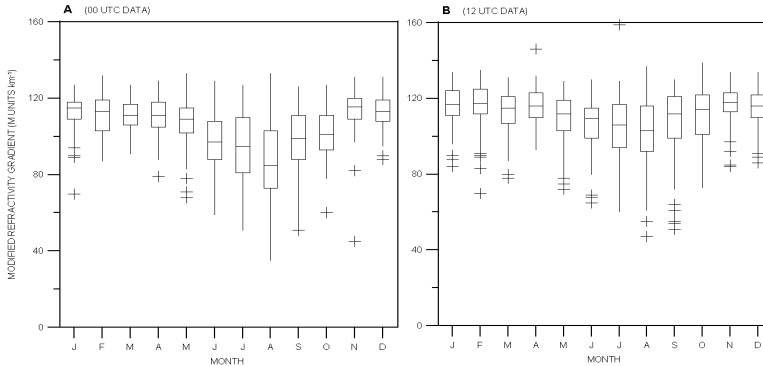


Fig. 5. Box-whisker plots of VRG in Barcelona for 00 Z and 12 Z data.

These box plots show that in summer not only there is a minimum monthly median value (August), but also that the interquartile range (IQR) is increased compared to cold months. Another significant feature is that outliers seldom represent subrefractive events but are quite common for superrefraction; besides, they appear almost at any month, in particular for 12Z data. A similar behaviour is observed using 2 years of radiosonde data recorded at several northern latitude observatories (Fig. 6).

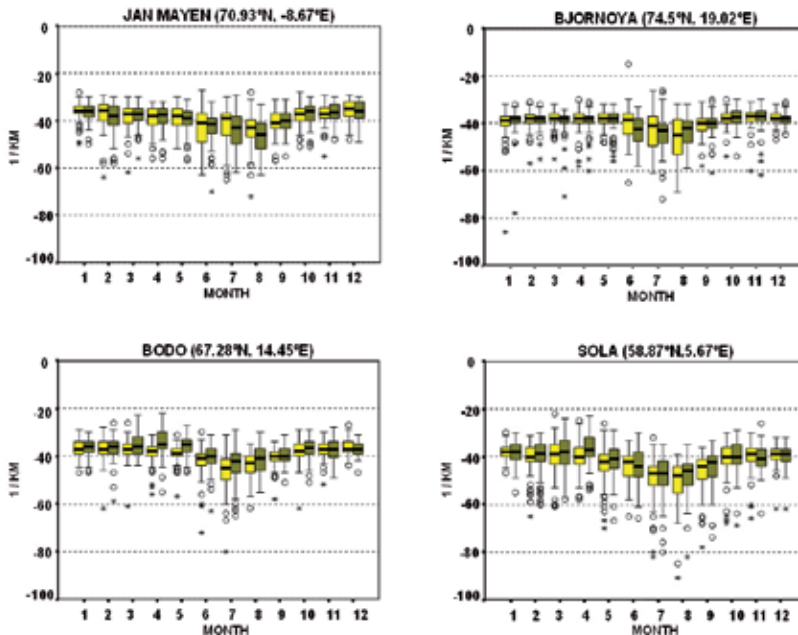


Fig. 6. Box-whisker plots for several Norwegian radiosonde sites showing 00 Z (clear boxes) and 12 Z (dark boxes) data. Adapted from Bech et al. (2007b).

The yearly minima of VRG, below -80 km^{-1} sometimes reaching -120 km^{-1} (maximum superrefraction), at the end of the warm season is also appreciated in the VRG time series plot of Barcelona shown in Fig. 7.

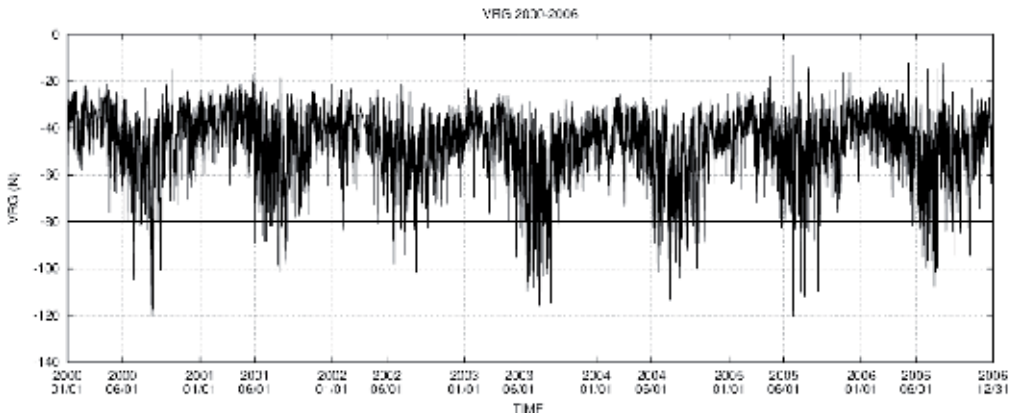


Fig. 7. Time series plot of VRG (N units km^{-1}) for the period 2000-2006 in Barcelona.

The seasonal pattern noted in Barcelona is already indicated in the VRG World Wide maps prepared by the International Telecommunications Union (ITU, 2003). In particular, in August, an area of maximum superrefraction affects the Western Mediterranean region, comparable in intensity to the maximum above the SW Pacific coast of N. America, and somewhat weaker than the Arabian Peninsula –where the world maximum is located for that month–. Using the Historical Electromagnetic Propagation Condition Data Base from the US Naval Systems Ocean Center (Patterson, 1987) a comparison with ten radiosonde stations located in the area was performed. Median monthly values allowed to check similar patterns both in N_s and VRG. A related study was carried out recently by Lopez (2009) using global analysis data from the European Centre for Medium-range Weather Forecasts (ECMWF) to assess the occurrence of superrefraction, or with a similar approach, but at a local scale, by Mentés and Kaymaz (2007) in Turkey, or Mesnard and Sauvageot (2010) in France.

The frequency and cumulative probability distributions for Barcelona VRG are shown in Fig. 8. A similar unimodal left skewed pattern, with steeper slopes for higher VRG values (tending to super refraction), is shown for both 00 and 12 Z data. However, modal values are very near the nominal standard propagation value of -40 N units/km (-49 N units/km at night and -42 N/km units at noon).

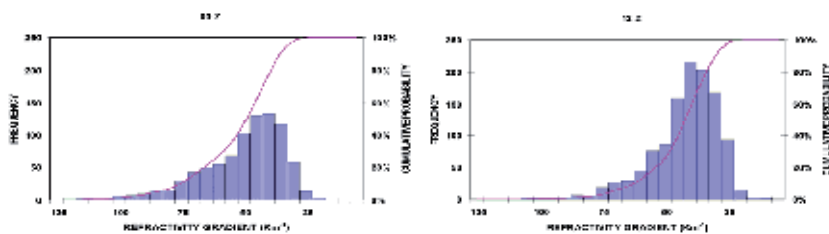


Fig. 8. Frequency and cumulative probability distributions for the Barcelona VRG.

The relationship between surface refractivity and the vertical refractivity gradient for the first kilometre was investigated during the sixties for data collected in the UK (Lane, 1961) and the US (Bean and Dutton, 1968). In both cases a high correlation was found for monthly averages of both magnitudes. For the data set collected in Barcelona, a correlation of 0.9745 was found.

3.3 Anaprop echo variability

Quality control procedures for QPE have traditionally dealt with anaprop and, in general, clutter echoes (see, for example, Anderson et al., 1997; Archibald, 2000; da Silveira and Holt, 1997; Fulton et al., 1998; Joss and Lee, 1995; Kitchen et al., 1994; Sánchez-Diezma et al., 2001, Steiner and Smith, 2002; Szturc et al., in this volume; and Villarini and Krajewski, 2010, among others).

Fornasiero et al. (2006a, 2006b), studied AP echoes occurrence in two radars in the Po Valley, Italy, with a methodology developed by Alberoni et al. (2001). With a three year dataset, they examined the seasonal variability of AP echoes in the diurnal cycle (Fig. 9).

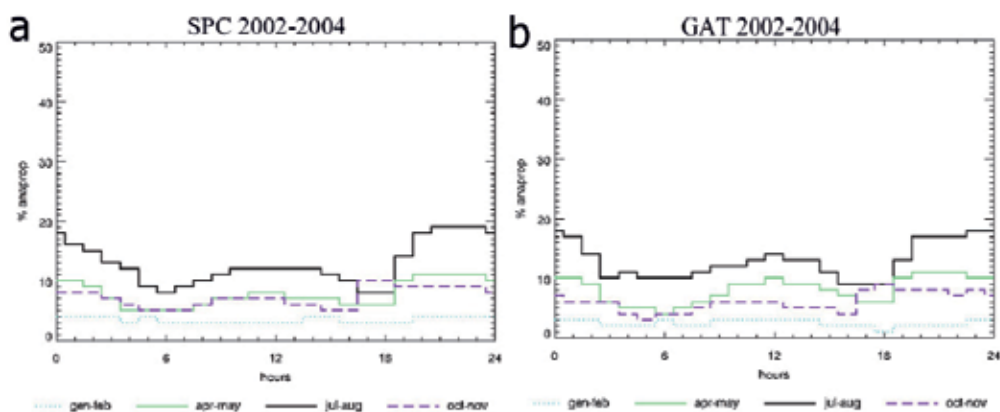


Fig. 9. Mean percentage of anaprop clutter detected. The average is calculated for each hour during the time range 1 January 2002–31 December 2004 for San Pietro Capofiume (a) and for Gattatico radar (b) in the Po Valley, Italy (adapted from Fornasiero et al. 2006a).

They found that in the warm season there were more AP echoes (reaching nearly 20% of the time) with a maximum in the late evening and a secondary maximum at noon, probably associated with local circulations such as sea breeze. In winter the variability was much lower and AP echoes were generally below 5%. These results were helpful to characterize the incidence of AP in precipitation estimates and to design an adequate quality control procedure.

4. Radar beam blockage and propagation conditions

In this section the effect of propagation conditions on beam blockage corrections is described. This type of correction is a classical post-processing step applied to radar reflectivity measurements in order to obtain quantitative precipitation estimates in hilly terrain. A particular implementation of this correction developed during the COST 717 action (Rossa 2000) is described.

4.1 Radar beam blockage

Weather radars installed in complex orographic areas may suffer from partial or total beam blockage caused by surrounding mountains. This effect can restrict seriously the use of the lowest antenna elevation angles which typically provide the most useful information for precipitation estimation at ground level – see for example Joss and Waldvogel (1990), Sauvageot (1994), Collier (1996), or Smith (1998) among others. Therefore, in hilly terrain, beam blockage correction schemes are needed to minimize the effect of topography if quantitative precipitation estimations (QPE) are required. Such corrections are usually included in operational QPE procedures as can be seen in, for example, Crochet (2009), Harrold et al. (1974), Kitchen et al. (1994), Joss and Lee (1995), or Fulton et al. (1998) and may be combined with correction techniques based in the analysis of the 3-D echo structure (Krajewski and Vignal, 2001; or Steiner and Smith, 2002).

The idea that assuming normal propagation conditions for radar observations may not always be a good choice and the use of local climatological refractive data for a specific radar site was already proposed, for example, in the COST 73 Project (Newsome, 1992) and, in a different context, evaluated by Pittman (1999) to improve radar height measurements. In this section the effect of changing the radar beam propagation conditions upon an ordinary single polarization reflectivity blockage correction is described – note that polarimetric radars allow other type of corrections (Giangrande and Ryzhkov 2005; Lang et al. 2009). A simplified interception function is proposed to simulate beam blockage and particular results for the Vallirana weather radar, located at 650 m above sea level near Barcelona (NE Spain) in a complex orography zone are obtained considering real atmospheric propagation conditions.

4.2 Beam blockage simulation

To describe in full detail the interception of the energy transmitted by the radar with the surrounding topography, a precise description of the antenna radiation pattern is required. As this pattern is rather complex, it is common to assume the usual geometric-optics approach and consider that the radar energy is concentrated in the main lobe of the radar antenna pattern (Skolnik, 1980). Then, when a radar beam intercepts a mountain, two situations are possible: 1) only part of the beam cross section illuminates the intercepted topography (partial blockage) or 2) the radar beam is completely blocked (total blockage). The percentage area of the radar beam cross section blocked by topography may be expressed as a function of the radius of the beam cross section, a , and the difference of the average height of the terrain and the centre of the radar beam, y (Fig. 10).

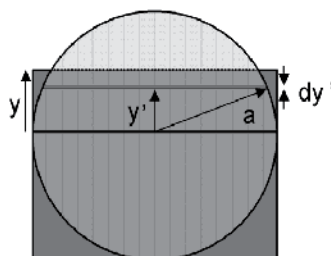


Fig. 10. Elements considered in the radar beam blockage function: a , radius of the radar beam cross section, y , difference between the centre of the radar beam and the topography, dy' differential part of blocked beam section and y' the distance from the center to dy' .

$$P_{BB} = \frac{y\sqrt{a^2 - y^2} + a^2 \arcsin \frac{y}{a} + \frac{\pi}{2} a^2}{\pi a^2} . \quad (3)$$

Depending on the relative position of the beam height respect to topography, y may be either positive or negative. According to these definitions, partial beam blockage occurs when $-a < y < a$, total beam blockage means that $y \geq a$, and finally, $y \leq -a$ implies there is no blockage at all. Using the notation introduced above, it can be seen that integrating dy' partial beam blockage, PBB, may be written as an analytical expression (Bech et al. 2003):

On the other hand, the height of the centre of the radar beam, h , is given at a distance r by the expression (see, for example, Doviak and Zrnica, 2006):

$$h = \sqrt{r^2 + (k_e R)^2 + 2 r k_e R \sin \theta} - k_e R + H_0 , \quad (4)$$

where R is the Earth's radius, k_e is the ratio between R and the equivalent Earth's radius, θ the antenna elevation angle and H_0 the antenna height. Information about atmospheric propagation conditions is contained in k_e , which may be written in terms of the refractivity gradient as:

$$k_e = \frac{1}{1 + R \left(\frac{dN}{dh} \right)} \quad (5)$$

The usual value for k_e in the first kilometre of the troposphere, assuming the normal VRG value of 40 km^{-1} , is approximately $4/3$. Substituting (5) and (4) in (3), an expression of the beam blockage in terms of the propagation conditions is obtained (Bech et al. 2003).

Three clutter targets (MNT, LML and MNY), which presented partial beam blockage under normal propagation conditions, were chosen to examine the effects of changing the VRG. The Vallirana radar (41 22' 28" N, 1 52' 52" E) is a C band Doppler system with a 1.3° beam width antenna at 3 dB. The targets chosen are normally used to check the radar antenna alignment on a routine basis and are located within the region of interest of radar QPE.

The targets were located at different ranges, had different heights and showed different degrees of blockage, in order to be representative of the topography surrounding the radar. They are located in the so called Pre-coastal Range sharing a similar propagation environment and comparable to that obtained by the Barcelona radiosonde. For example the area considered is usually influenced by a marked sea-breeze circulation pattern, just like the city of Barcelona (Redaño et al., 1991).

4.3 Beam blockage correction

To evaluate the effects of anomalous propagation, the partial beam blocking correction scheme used in the NEXRAD Precipitation Processing System has been considered. This scheme (Fulton et. al, 1998) is applied to radar beams partially shielded. In particular, this type of beam blockage correction is applied to radar pixels (or radar bins) whose shielding ranges between 10% and 60% and it consists of modifying radar equivalent reflectivity

factor measurements by adding 1 to 4 dB depending on the degree of occultation. The correction is also applied to all pixels further out in range of the same blocked radar ray, neglecting diffraction below shadow boundary. The correction depends only on the percentage of beam cross section shielded and, in the description provided by Fulton et al. (1998), no specific mention is made about which part of the beam is shielded. This approach allows consideration of a simple interception function, as the one proposed in the previous section, assuming that the correction additive factors contain considerations about interception details such as the beam power distribution. This beam blockage procedure is used with other corrections such as a test on the vertical echo continuity and a sectorized hybrid scan (Shedd et al., 1991). Other approaches to this question with different degrees of sophistication have been used in the past (see for example Delrieu et al. 1995, Gabella and Perona 1998, Michelson et al. 2000, Park et al. 2009). All of them have in common the assumption of standard propagation conditions of the radar beam.

4.4 Refractivity gradient vs beam blockage

The radar beam blockage under a particular VRG can be simulated considering both the observed propagation conditions and the interception function described in the previous sections. This may be achieved by assuming an homogeneous VRG for the whole radar beam and calculating the associated beam blockage for each selected target for a given initial antenna elevation angle.

In Fig. 11 a set of beam blockages vs VRG plots is shown for different antenna elevation angles. The refractivity gradient values considered contain the observed extreme VRG values (-119 km^{-1} and -15 km^{-1}) and are also extended to include pure subrefraction (0 km^{-1}) and almost ducting conditions (-156 km^{-1}) to illustrate their effects. These extreme cases seem realistic taking into account the presence of thin ducting layers that may have high VRG embedded in others with lower VRG and considering the fact that the bending of the ray path is an additive process throughout the whole layer crossed by the radar beam.

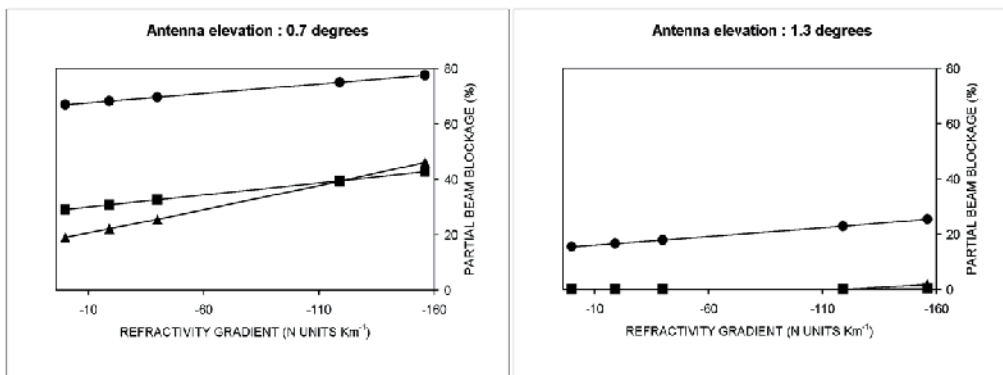


Fig. 11. Simulated beam blockage vs vertical refractivity gradient for targets MNT, (circle), LML (square) and MNY (triangle) at different antenna elevation angles.

As expected, as the antenna angle increases, beam blockage is reduced. For example, for an antenna elevation of 0.7° a relatively high beam blockage rate is expected as the lowest part of the main lobe in a 1.3° beam width antenna is pointing to the surrounding hills,

producing values of blockage ranging mostly between 30% and 80%. On the other hand, the 1.3° elevation beam blockage values are mostly below 20% and for some targets are always null (no blockage at all) except for the most super refractive situations.

In Fig. 12, target MNT, shows moderate (around 40%) to low (10%) rate of beam blockage, respectively (similar results were obtained for LML). On the other hand, we found that the most distant target, MNY, intercepted the radar beam mostly between 8% and 14%. The range of variations in the beam blockage observed in the above mentioned histograms oscillates from 8% (LML) and 10% (MNT) to 18% (MNY). From the cumulative probability plots obtained it may be noted that MNT and LML show single classes representing more than 50% while a more smoothed distribution is found for MNY.

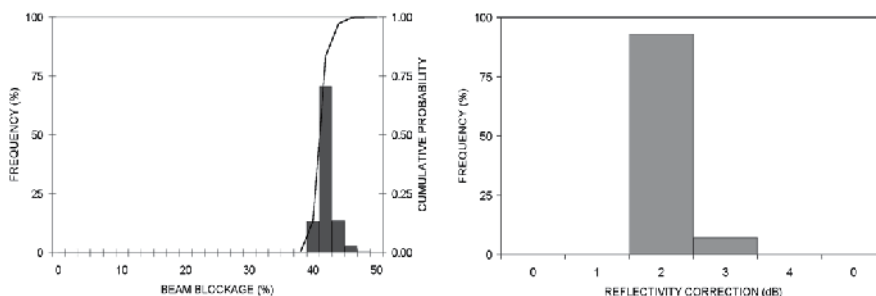


Fig. 12. Simulated beam blockage frequency and cumulative probability distributions (left) and the corresponding correction histograms (right) for 1° antenna elevation for target MNT.

The corresponding correction histogram is also shown. Should the beam blockage correction have been a continuous function, where for a particular value of blockage a different correction factor would be applied, then the spread of the beam blockage histograms would have been reflected in the spread of the correction histograms. However, this is not the case for the particular type of correction considered where only four different correction values are possible depending on the beam blockage. Therefore, a big variability in the beam blockage occurrence does not necessarily produce the same variability in the blockage correction. An additional conclusion of this analysis (Bech et al. 2003) was that errors in beam blockage corrections derived from propagation variability were comparable to antenna pointing errors of 0.1°, which is a typical value for operational systems. This confirms the need for hardware calibration control and monitoring, particularly if quantitative precipitation estimates are required.

4.5 Improved quantitative precipitation estimates

The methodology proposed in the previous section to simulate the radar beam blockage by topography has been implemented to derive correction factors which were applied to improve precipitation estimates. For example Fornasiero et al. (2006b) performed corrections in different events, calculating specific corrections assuming both standard and non-standard propagation conditions and finding some improvement with the corrections. In Bech et al. (2007b, 2010a) results reported were carried out in the framework of the COST-731 action (Rossa et al. 2010) using the so-called BPM model (which implements the blockage function presented above. Larger data sets were considered for blockage corrections under standard

conditions and individual ducting events were examined in detail. Here we illustrate some of the results obtained assuming standard propagation conditions.

Figure 13 shows details of Bømlo radar (59.5°N, 5.1°E) from the Norwegian Meteorological Service (met.no). A panorama from the radar site shows some of the hills which block the radar coverage (three of them are numbered). One year of precipitation, illustrating the blocked areas is also shown, as well as the correction factors computed with the BPM model. The improvement in the bias, defined here as 10 times the decimal logarithm of the ratio of gauge to radar derived precipitation amounts, is shown in Table 3. At all ranges the correction reduced the bias.

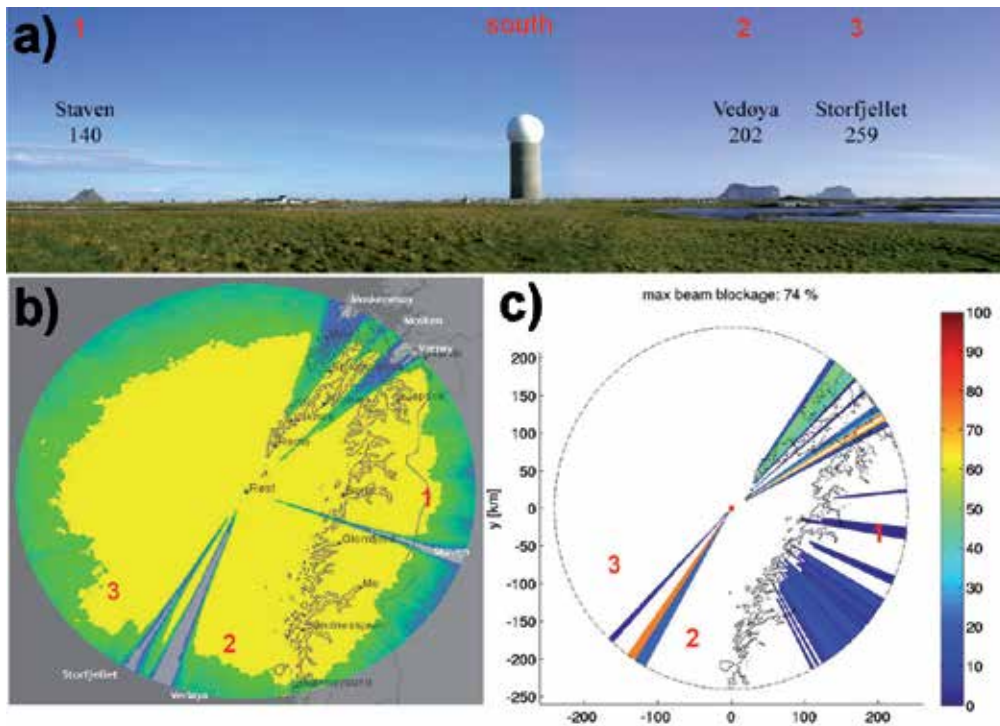


Fig. 13. a). Southern view from the Bømlo radar in Norway; three of the surrounding hills are numbered and indicated on the other panels. b). One year of radar precipitation estimates, illustrating clearly the blocked sectors with less (or no) precipitation. c). Modelled blockage with the BPM system. Figure courtesy of Dr. Uta Gjertsen (met.no).

Blockage (%)	Range (km)								
	40-100			100-160			160-240		
0	2.3		(12)	5.2		(19)	11.2		(16)
1-50	4.2	3.1	(16)	9.3	8.5	(26)	15.0	14.1	(70)
50-70	8.6	6.0	(5)	14.4	11.8	(15)	21.4	18.2	(29)

Table 3. Bias (dB) of uncorrected and blockage-corrected (bold) radar estimates from the Bømlo radar for 2004 grouped in different ranges. Sample size is in parentheses. Adapted from Bech et al. (2007b).

5. Radar propagation condition forecasting

This section deals with anomalous propagation forecasting using mesoscale numerical weather prediction models. It is illustrated with several examples, discussing capabilities and limitations found in this application.

5.1 VRG forecasts

Anticipating the occurrence of AP may be an advantage for monitoring purposes of radar quality control or to obtain a deeper understanding of processes related to anomalous propagation. Numerical Weather Prediction (NWP) systems provide the capability to obtain forecasts of propagation conditions from temperature and humidity forecast profiles in a similar way as they are obtained from radiosonde observations. Despite NWP systems allow to study anomalous propagation events with more spatial detail than that given by the synoptic radiosonde network, they have a number of accuracy limitations that may hamper the operational production of AP forecasts. For example Bech et al. (2007a) compared 4 months of vertical refractivity gradient forecasts over Barcelona retrieved from numerical model output of the MASS system (Codina et al. 1997a, 1997b; Koch et al. 1985) with actual radiosonde observations and found a systematic bias of the model towards subrefraction (Fig. 14).

In order to reduce the bias, a simple heuristic approach was suggested combining linearly model output and previous radiosonde observations. As illustrated in the Taylor diagram (Taylor, 2001) shown in Fig. 15, the modified forecasts, labelled here as H2b, H4b, H6b and H8b, produced better results in terms of RMS and correlation compared to the original forecasts (MASS).

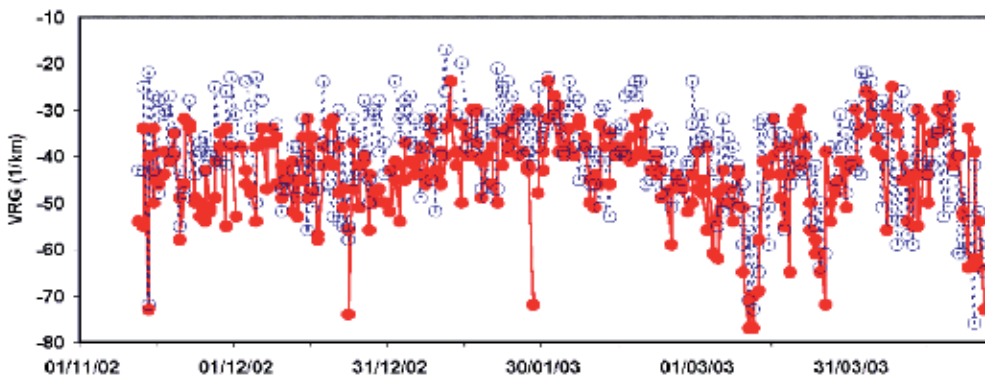


Fig. 14. Time series of Vertical Refractivity Gradient (VRG) over Barcelona from NWP-derived forecasts (dashed line) and radiosonde-based diagnostics (solid line).

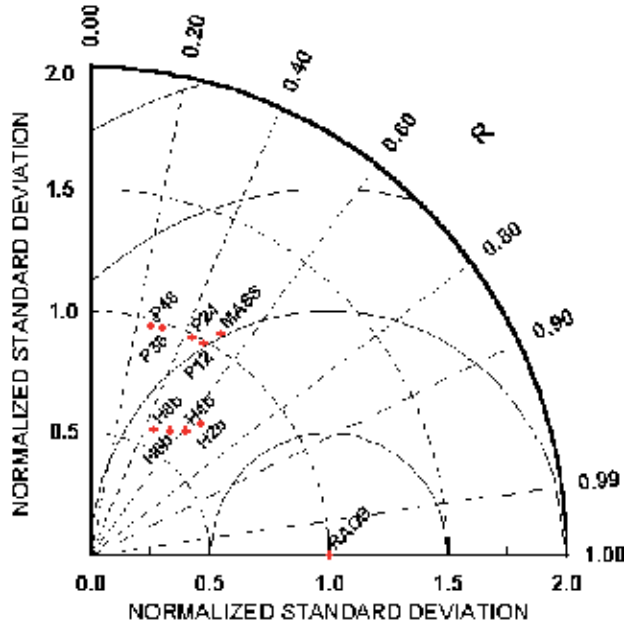


Fig. 15. Taylor Diagram of Vertical Refractivity Gradient VRG radiosonde observations (RAOB), original MASS forecasts, persistence of the observations and modified forecasts.

5.2 AP case studies

A number of anomalous propagation case studies examined with an electromagnetic propagation model with different degrees of sophistication and NWP data or simply with a radiosonde profile can be found in the literature, covering different geographic areas, such as Burk and Thompson (1997) in California, Atkinson et al (2001) over the Persian Gulf, or Bebbington et al. (2007) in the Mediterranean. Applications of this type of modelling tool include radar coverage computation (Haase et al. 2006), or even correction or improvement of radar data in NWP assimilation systems (Haase et al. 2007).

Fig. 16 shows an example of AP case study for the Røst radar (met.no), where NWP data provided by the HIRLAM system provided better results, even 24 h forecasts, than actual radiosonde data, which in this case was not representative of the radar coverage environment. In Bech et al. (2007b) this and two other case studies were discussed, highlighting the quality of HIRLAM forecasts for examining and anticipating AP cases with the BPM model.

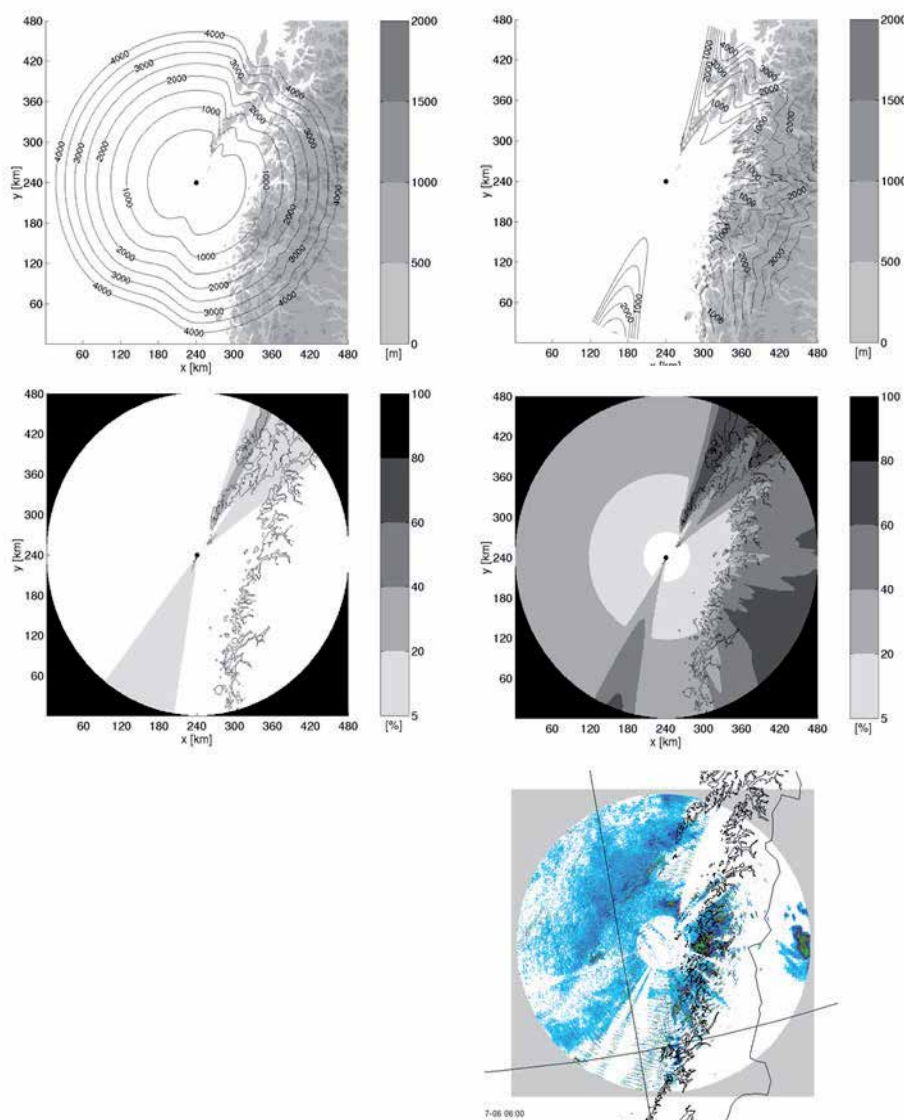


Fig. 16. Lowest unblocked radar coverage (top row) and beam blockage (middle) computed with radiosonde data (left column) and NWP-derived profiles (right column). The bottom panel shows actual radar observations, 6 July 2005 00 UTC (Røst radar, met.no). Adapted from Bech et al. (2007a).

6. Detection and correction of AP echoes with satellite data

Several studies have been reported regarding the use of satellite images to detect AP echoes, based on the simple approach of removing echoes in cloudless conditions. However, in practice this procedure is not as straight forward as might seem and requires substantial fine tuning to obtain a reasonable balance between false alarms and detection, particularly in

cloudy, and most importantly, rainy conditions. Some correction procedures to remove non-precipitating echoes rely only on radar data (e.g. Berenguer et al. 2006, Sánchez-Diezma et al. 2001, Steiner & Smith, 2002) but others consider as well the use of satellite observations – see for example Michelson and Sunhede (2004), Bøvith et al. (2006) or Magaldi et al. (2009). In any case, quantitative applications of radar data such as thunderstorm tracking (Rigo et al., 2010), precipitation estimates (Trapero et al. 2009), or radar-based precipitation forecasts (Atencia et al., 2010), or even qualitative use of radar images by a non-specialized audience (as discussed in Bech et al. 2010b), clearly require the use of proper clutter filtering, particularly considering anomalous propagation.

6.1 Methodology

We summarize in this section the methodology proposed by Magaldi et al. (2009) to detect and remove AP echoes in radar images using satellite observations and NWP model data. They took advantage of the improved temporal and spatial resolution of the Meteosat Second Generation (MSG) satellite to update the procedure developed by Michelson and Sunhede (2004), based on the first generation of Meteosat satellites, and incorporated the use of enhanced precipitating cloud masks. Fig. 17 illustrates the basic idea behind the proposed methodology, showing a radar reflectivity image with real precipitation and clutter (in this case sea clutter, near the coast), the precipitating cloud mask associated, and the new image where clutter has been removed.

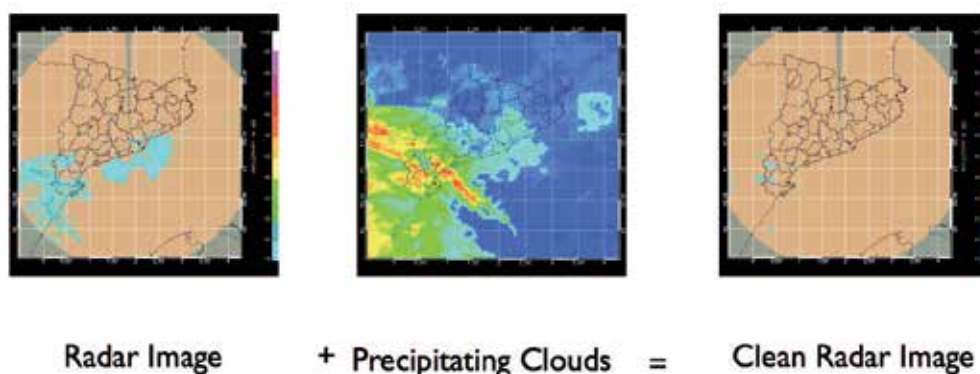


Fig. 17. Illustration of the correction procedure of radar reflectivity echoes affected by clutter (left panel) with a precipitating cloud mask (centre panel) and the resulting cleaned radar image (Vallirana radar, 1 January 2004 14 UTC).

The basic algorithm is shown on Fig. 18, where a data flow diagram showing the different processes involved is displayed. Analysis of radio propagation conditions with radiosonde (RAOB) data (vertical refractivity gradients below -80 km^{-1} or ducting index above 20) was used to select AP events. For those events, MSG satellite and NWP MASS model data were used to build precipitating cloud masks based on the SAF (SAF 2004, 2007; hereafter S) and Michelson and Sunhede (2004) algorithms (hereafter M). These masks were compared pixel by pixel with radar data, and non-precipitating pixels were removed in the final corrected radar data.

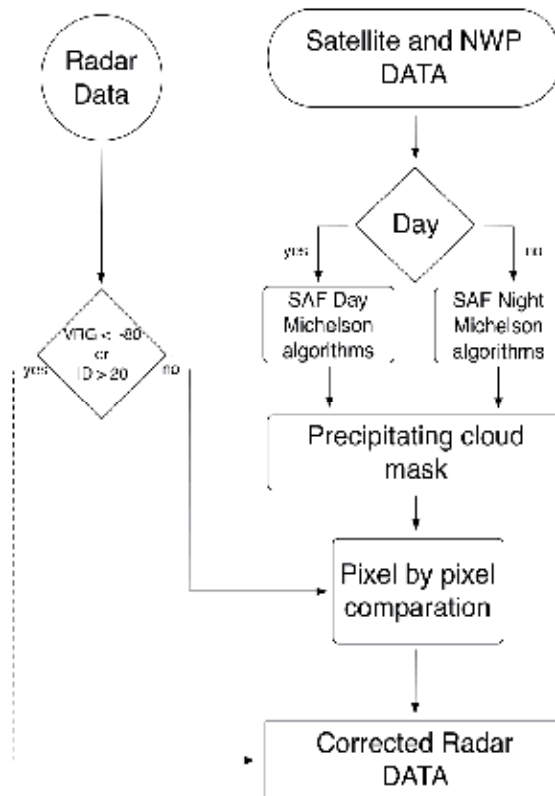


Fig. 18. Flow diagram showing the main processes involved in the algorithm to detect radar AP echoes with precipitating cloud masks derived from satellite images. Adapted from Magaldi et al. (2009).

6.2 Results

Using the SMC Vallirana radar (Fig. 17) and a network of 155 raingauges and manually edited radar data as verification data sets, Magaldi et al. (2009) tested the performance of this procedure for several case studies, considering the original uncorrected data (UC), and data corrected with the M and S algorithms, all compared against manually corrected data. They obtained statistics considering Percentage Correct (PC), False Alarm Rate (FAR), and Hanssen-Kuipers skill (HKS) scores - see Wilks (1995) for details. The HKS suggested that S performed better, despite for strong echoes M yielded lower false alarms (Table 4).

Echo class	Mean sample	FAR			PC			HKS		
		UC	M	S	UC	M	S	UC	M	S
Weak	883713	0.34	0.28	0.21	78.12	92.65	96.59	0.80	0.74	0.96
Strong	769162	0.25	0.07	0.37	73.12	94.21	95.81	0.88	0.87	0.80
All	929055	0.30	0.22	0.27	75.55	93.16	96.35	0.83	0.78	0.90

Table 4. Verification scores for different echo intensities (strong echoes are higher than 15 dBZ; weak, the rest).

A larger data set of six months (January to July 2007) using the SMC Vallirana radar provided additional insight to the performance of this correction technique of AP echoes. It also allowed to evaluate the performance of the technique applied by Bøvith et al. (2006) which made use of cloud type information (SAF, 2011) as precipitating echo mask. A parallax correction (Vicente et al., 2002) was introduced in the mask in order to improve the matching between the two data types and, as seen in Table 5, substantial changes were found for some of the cloud types.

Uncorrected

Cloud type	Precipitation frequency(%)
01.- Cloud free land	0.64
02.- Cloud free sea	0.62
03.- Snow/ice land	0.41
06.- Very low Cu.	0.77
08.- Low St.	3.60
10.- Medium St.	15.30
12.-High & opaque St.	29.18
14.-Very High & opaque St.	31.90
15.- Thin Ci.	0.79
16.-Moderate thick Ci.	1.53
17. Ci. above lower cloud	6.80
19.- Fractional cloud	1.40
20.-Holes	0.00

Corrected

Cloud type	Precipitation frequency(%)
01.- Cloud free land	0.30
02.- Cloud free sea	0.40
03.- Snow/ice land	0.40
06.- Very low Cu.	0.60
08.- Low St.	3.48
10.- Medium St.	16.38
12.-High & opaque St.	30.85
14.- Very High & opaque St.	32.76
15.- Thin Ci.	0.99
16.-Moderate thick Ci.	1.68
17. Ci. above lower cloud	6.62
19.- Fractional cloud	0.63
20.-Holes	0.85

Table 5. Precipitation frequency for Cloud type product using the parallax corrected (left) and uncorrected products (right), both generated using six months of SMC radar data (January-July 2007).

7. Final remarks

In this chapter, an overview of the effects of radio propagation conditions upon radar observations has been given. Though we have focused in ground-based weather radar systems, many of the concepts presented apply as well to other types of radar and applications. Particular emphasis has been given to aspects with potential impact on radar quantitative precipitation estimates, considering beam blockage corrections or anomalous propagation echoes detection and removal. These items should be considered in quality control for weather radars, particularly those operating in complex topography environments and located near the coast where anomalous propagation may affect dramatically radar observations.

8. Acknowledgments

Part of the results presented here were obtained by the authors in research projects made in collaboration with a number of individuals including Uta Gjertsen (formerly at met.no and now at the Norwegian Defence Research Establishment, Norway), Günther Haase and Anke

Toss (Swedish Meteorological and Hydrological Institute, SMHI, Sweden), Pier Paolo Alberoni and Anna Fornasiero (ARPA, Italy), and David Bebbington (Essex University, UK). Weather radar observations, and radiosonde and surface automated observations data were provided by ARPA, SMHI, met.no and the Meteorological Service of Catalonia (SMC). This chapter was produced in the framework of the ProFEWS project (CGL2010-15892) and the Hymex project (Hymex.es CGL2010-11757-E).

9. References

- Alberoni, P. P.; Anderson, T.; Mezzasalma, P.; Michelson, D. B. & Nanni, S. (2001). Use of the vertical reflectivity profile for identification of anomalous propagation, *Meteorological Applications*, Vol. 8, pp. 257–266
- Anderson, T.; Alberoni, P. P.; Mezzasalma, P.; Michelson, D. & Nanni, S. (1997). Anomalous propagation identification from terrain and sea waves using vertical reflectivity profile analysis, *Proceedings of 28th International Conference On Radar Meteorology*, pp. 93–94, American Meteorological Society, Austin, Texas, USA
- Archibald, E. (2000). Enhanced clutter processing for the UK weather radar network. *Physics and Chemistry of the Earth. Part B-Hydrology, Oceans and Atmosphere*, Vol. 25, No.10-12, pp. 823–828
- Atencia, A.; Rigo, T.; Sairouni, A.; Moré, J.; Bech, J.; Vilaclara, E.; Cunillera, J.; Llasat, M.C. & Garrote, L. (2010). Improving QPF by blending techniques at the Meteorological Service of Catalonia. *Natural Hazards and Earth System Science*, Vol.10, No.7, pp. 1443–1455
- Atkinson, B.W.; Li, J.G. & Plant, R.S. (2001). Numerical modelling of the propagation environment in the atmospheric boundary layer over the Persian Gulf. *Journal of Applied Meteorology*, Vol.40, pp. 586–603
- Battan, L. J. (1973). *Radar Observation of the atmosphere*. University of Chicago Press, Chicago, USA, 324 pp.
- Bean, B. R. & Dutton, E. J. (1968). *Radio meteorology*. 435 pp., Dover Publications, New York USA
- Bebbington, D.; Rae, S.; Bech, J.; Codina B. & Picanyol, M. (2007). Modelling of weather radar echoes from anomalous propagation using a hybrid parabolic equation method and NWP model data. *Natural Hazards and Earth System Science*, Vol.7, No.3, pp. 391–398
- Bech, J. (2003). *Observational analysis and numerical modelling of weather radar anomalous propagation echoes*. PhD Thesis, ISBN 8468854506, University of Barcelona, Barcelona, Spain
- Bech, J.; Bebbington, D.; Codina, B., Sairouni, A. & Lorente, J. (1998). Evaluation of atmospheric anomalous propagation conditions: an application for weather radars. *EUROPTO Conference on Remote Sensing for Agriculture, Ecosystems, and Hydrology*. SPIE Vol. 3499, pp. 111–115, Barcelona, Spain.
- Bech, J.; Codina, B. & Lorente, J. (2007a). Forecasting weather radar propagation conditions. *Meteorology and Atmospheric Physics*, Vol.96, No.3–4, pp. 229–243
- Bech, J.; Codina, B.; Lorente, J. & Bebbington, D. (2002). Monthly and daily variations of radar anomalous propagation conditions: How “normal” is normal propagation?”. *Proceedings 2nd European Conference on Radar Meteorology*, pp. 35–39. Copernicus GmbH © 2002, Delft, Netherlands

- Bech, J.; Codina, B.; Lorente, J. & Bebbington, D. (2003). The sensitivity of single polarization weather radar beam blockage correction to variability in the vertical refractivity gradient. *Journal of Atmospheric and Oceanic Technology*, Vol. 20, No.6, pp. 845-855
- Bech, J.; Gjertsen, U. & Haase, G. (2007b). Modelling weather radar beam propagation and topographical blockage at northern high latitudes. *Quarterly Journal of the Royal Meteorological Society*, Vol.133, No.626, pp. 1191-1204
- Bech, J.; Gjertsen, U. & Haase, G. (2010a). Reply to comment of J.I. Dahl on DOI: 10.1002/qj.98. *Quarterly Journal of the Royal Meteorological Society*, Vol.136, No.648, pp. 817-818
- Bech, J.; Molina, T.; Vilaclara, E. & Lorente, J. (2010b). Improving TV weather broadcasts with technological advancements. *Meteorological Applications*, Vol.17, No.2, pp. 142-148
- Bech, J.; Sairouni, A.; Codina, B.; Lorente, J. & Bebbington, D. (2000). Weather radar anaprop conditions at a Mediterranean coastal site. *Physics and Chemistry of the Earth. Part B-Hydrology, Oceans and Atmosphere*, Vol.25, No.10-12, pp. 829-832
- Berenguer, M.; Sempere-Torres, D.; Corral, D. & Sánchez-Diezma, R. (2006). A Fuzzy Logic Technique for Identifying Nonprecipitating Echoes in Radar Scans. *Journal of Atmospheric and Oceanic Technology*, Vol.23, No.9, pp. 1157-1180
- Bøvith, T.; Gill, R.S.; Overgaard, S; Nielsen, A.A. & Hansen, L.K. (2006). Detecting weather radar clutter using satellite-based nowcasting products. Proc fourth European conference on radar meteorology (ERAD), pp 153-156, Barcelona, Spain
- Burk, S.D. & Thompson, W.T. (1997). Mesoscale modelling of summertime refractive conditions in the southern California night. *Journal of Applied Meteorology*, Vol. 36, pp. 22-31
- Codina, B.; Aran, M.; Young, S. & Redaño, A. (1997a). Prediction of a mesoscale convective system over Catalonia (Northeastern Spain) with a nested numerical model. *Meteorology and Atmospheric Physics*, Vol.62, pp. 9-22
- Codina, B.; Sairouni, A.; Bech, J. & Redaño, A. (1997b). Operational application of a nested mesoscale numerical model in Catalonia (Meteo'96 Project). *Proceedings of the INM/WMO International Symposium of Cyclones and Hazardous Weather in the Mediterranean*, pp. 657-667, ISBN 84-7632-329-8, Palma de Mallorca, Spain
- Collier, C.G. (1996). *Applications of Weather Radar Systems. A Guide to Uses of Radar Data in Meteorology and Hydrology*. pp 390, 2d ed. John Wiley & Sons., ISBN 0471960136, Chichester, UK
- Crochet, P. (2009) Enhancing radar estimates of precipitation over complex terrain using information derived from an orographic precipitation model. *Journal of Hydrology*, 377:3-4, 417-433
- da Silveira, R. B. & Holt, A.R. (1997). A neural network application to discriminate between clutter and precipitation using polarisation information as feature space. *Proceedings of the 28th Internat. Conf. on Radar Meteor.*, pp. 57-58, Amer. Meteor. Soc., Austin, Texas
- Delrieu, G.; Creutin, J.D. & Andrieu, H. (1995). Simulation of radar mountain returns using a digitized terrain model. *Journal of Atmospheric and Oceanic Technology*, Vol.12, pp.
- Doviak, R.J. & Zrnic, D.S. (2006). *Doppler radar and weather observations*, 2nd edition. Academic Press, ISBN 0122214226, London, UK
- Fabry, F.; Frush, C.; Zawadki, I. & Kilambi, A. (1997). On the extraction of near-surface index of refraction using radar phase measurements from ground targets. *Journal of Atmospheric and Oceanic Technology*, Vol.14, No.4, pp. 978-897

- Fornasiero, A.; Alberoni, P.P. & Bech, J. (2006a). Statistical analysis and modelling of weather radar beam propagation conditions in the Po Valley (Italy). *Natural Hazards and Earth System Science*, Vol.6, No.2, pp. 303-314
- Fornasiero, A.; Bech, J. & Alberoni, P.P. (2006b). Enhanced radar precipitation estimates using a combined clutter and beam blockage correction technique. *Natural Hazards and Earth System Science*, Vol.6, No.5, pp. 697-710
- Fulton, R.A.; Breidenbach, J.P.; Seo, D.; Miller, D. & O'Bannon, T. (1998). The WSR-88D Rainfall Algorithm. *Weather and Forecasting*, Vol.13, No.2, 377-395
- Gabella, M. & Perona, G. (1998). Simulation of the orographic influence on weather radar using a geometric-optics approach. *Journal of Atmospheric and Oceanic Technology*, Vol.15, No.6, pp. 1486-1495
- Giangrande, S.E. & Ryzhkov, A.V. (2005). Calibration of Dual-Polarization Radar in the Presence of Partial Beam Blockage. *Journal of Atmospheric and Oceanic Technology*, Vol.22, No.8, pp. 1156-1166
- Gossard, E.E. (1977). Refractive index variance and its height distribution in different air masses. *Radio Science*, Vol. 12, No.1, pp. 89-105
- Haase, G.; Bech, J.; Wattrelot, E.; Gjertsen, U.; Jurasek, M. (2007). *Towards the assimilation of radar reflectivities: improving the observation operator by applying beam blockage information*, 33rd Conference on Radar Meteorology, AMS, Cairns, Australia.
- Haase, G.; Gjertsen, U.; Bech, J.; Granström, Å. (2006). *Assessment of potential radar locations using a beam propagation model*. 4th European Conf. Radar Meteorol. Hydrol., Barcelona, Spain
- Harrold, T.; English, E. & Nicholass, C. (1974). The accuracy of radar-derived rainfall measurements in hilly terrain. *Quarterly Journal of the Royal Meteorological Society*, Vol. 100, No.425, pp. 331-350
- ITU (2003). ITU-R P.453-9 Recommendation, *The Radio Refractive Index: Its Formula and Refractivity data*, ITU Radiocommunication Assembly, ITU-R P-Series, 2003)
- Johnson, C.; Harrison, D. & Golding, B. (1999). *Use of atmospheric profile information in the identification of anaprop in weather radar images*. Observation Based Products Technical Report No. 17, Forecasting Systems, UK Meteorological Office, 30 pp. [Available from the National Meteorological Library, London Road, Bracknell, RG12, 2SZ, UK]
- Joss, J. & Lee, R. (1995). The application of radar-gauge comparisons to operational precipitation profile corrections. *Journal of Applied Meteorology*, Vol.4, No.12, pp. 2612-2630
- Joss, J. & Waldvogel, A. (1990). *Precipitation measurement and hydrology, a review*. In: Radar in Meteorology, D. Atlas (Ed.), Chapter 29a, pp. 577-606. American Meteorological Society, Boston, USA
- Kitchen, M.; Brown, R. & Davies, A.G. (1994). Real-time correction of weather radar data for the effects of bright band, range and orographic growth in widespread precipitation. *Quarterly Journal of the Royal Meteorological Society*, Vol.120, No.519, pp. 1231-1254
- Koch, S.E.; Skillman, W.C.; Kocin, P.J.; Wetzell, P.J.; Brill, K.F.; Keyser, D.A. & McCumber, M.C. (1985). Synoptic scale forecast skill and systematic errors in the MASS 2.0 model. *Monthly Weather Review*, Vol.113, No. 10, pp. 1714-1737
- Krajewski, W. F. & Vignal, B. (2001). Evaluation of anomalous propagation echo detection in WSR-88D Data: a large sample case study. *Journal of Atmospheric and Oceanic Technology*, Vol. 18, No.5, pp. 807-814

- Lane, J.A (1961). The radio refractive index gradient over the British Isles. *Journal of Atmospheric and Terrestrial Physics*, Vol.21, No.2-3, pp. 157-166
- Lang, T.J.; Nesbitt, S.W. & Carey, L.D. (2009). On the Correction of Partial Beam Blockage in Polarimetric Radar Data. *Journal of Atmospheric and Oceanic Technology*, Vol.26, No.5, pp. 943-957
- Lopez, P. (2009). A 5-yr 40-km-Resolution Global Climatology of Superrefraction for Ground-Based Weather Radars. *Journal of Applied Meteorology and Climatology*, Vol. 48, pp. 89-110
- Low, T.B. & Hudak, D.R. (1997). Development of Air Mass Climatology Analysis for the Determination of Characteristic Marine Atmospheres. Part I: North Atlantic. *Theoretical and Applied Climatology*, Vol.57, No.3-4, pp. 135-153
- Magaldi, A.V.; Bech, J. & Lorente, J. (2009). A multisource scheme based on NWP and MSG data to correct non-precipitating weather radar echoes. *Meteorology and Atmospheric Physics*, Vol.105, No.3-4, pp. 121-132
- Mentes, Ş., & Kaymaz, Z. (2007). Investigation of Surface Duct Conditions over Istanbul, Turkey. *Journal of Applied Meteorology and Climatology*, Vol. 46, pp. 318-337
- Mesnard, F., Sauvageot, H. (2010). Climatology of Anomalous Propagation Radar Echoes in a Coastal Area. *Journal of Applied Meteorology and Climatology*, Vol. 49, pp. 2285-230
- Météo-France (1997). *Quality control on GTS data at Météo-France*. Météo-France, Service Centrale d'Exploitation de la Météorologie. 42, Av. Coriolis, 31057 Toulouse Cedex 1, France
- Michelson, D. B.; Andersson, T.; Koistinnen, J.; Collier, C. G.; Riedl, J.; Szturc, J. ; Gjertsen, U.; Nielsen, A. & Overgaard, S. (2000). *BALTEX radar data centre products and their methodologies*. RMK 90. Swedish Meteorological and Hydrological Institute, Norrköpping, Sweden
- Michelson, D.B. & Sunhede, D. (2004). Spurious weather radar echo identification and removal using multisource temperature information. *Meteorological Applications*, Vol.11, pp. 1-14
- Moszkowicz, S.; Ciach, G.J. & Krajewski, W.F. (1994). Statistical detection of anomalous propagation in radar reflectivity patterns. *Journal of Atmospheric and Oceanic Technology*, Vol.11, No.4, pp. 1026-1034
- Newsome, D.H. (1992). *Weather Radar Networking COST Project 73 Final Report*. Kluwer Academic Publishers, Dordrecht, Netherlands, 254 pp., ISBN 0792319397
- Park, S. & Fabry, F. (2011). Estimation of Near-Ground Propagation Conditions Using Radar Ground Echo Coverage. *Journal of Atmospheric and Oceanic Technology*, Vol.28, No.2, pp. 165-180
- Park, S.; Jung, S.; Lee, J. & Kim, K. (2009) Correction of Radar Reflectivity over Beam Blocking Area by Accumulated Radar Reflectivity. *Journal of Korea Water Resources Association*, Vol.42, No.8, pp. 607-617
- Patterson, W.L. (1987). *Historical Electromagnetic Propagation Condition Database Description*. Technical Document 1149, ADA-A189 157, NOSC 1149, 71 pp., US NAVY, USA
- Patterson, W.L. (2008). The Propagation Factor, F_p , in the radar equation, In: *Radar Handbook*, 3rd edition, M. Skolnik (Ed.), Ch. 26, ISBN 0071485473. McGraw Hill, New York, USA.
- Pittman, T.S. (1999). *A climatology-based model for long-term prediction of radar beam refraction*. Master's Thesis, 184 pp., US Air Force Institute of Technology, USA
- Redaño, A.; Cruz, J. & Lorente, J. (1991). Main features of sea breeze in Barcelona. *Meteorology and Atmospheric Physics*, Vol.46, No.3-4, pp. 175-179
- Rigo, T.; Pineda, N. & Bech, J. (2010). Analysis of warm season thunderstorms using an object-oriented tracking method based on radar and total lightning data. *Natural Hazards and Earth System Science*, Vol.10, No.9, pp. 1881-1893

- Rinehart, R. (2001). *Radar for Meteorologists*. 3rd edition. Rinehart Publications, ISBN 0-9658002-0-2, 428 pp., P.O. Box 30800, MO, USA
- Rossa, A.; Haase, G; Keil, C.; Alberoni, P.P; Ballard, S.; Bech, J.; Germann, U.; Pfeifer, M. & Salonen, K. (2010). Propagation of uncertainty from observing systems into NWP. *Atmospheric Science Letters*, Vol.11, No.2, pp. 145-152
- Rossa, A.M. (2000). The COST 717 action: use of radar observations in hydrological and NWP models. *Physics and Chemistry of the Earth. Part B-Hydrology, Oceans and Atmosphere*, Vol.25, No.10-12, pp. 1221-1224
- SAF (2004) Software user manual for PGE04 of the NWCSAF/MSG: scientific part. EUMETSAT Satellite Application Facility to Nowcasting and Very Short Range Forecasting, 31 pp
- SAF (2007) Validation report for "Precipitating Clouds" (PC-PGE04 v1.4). EUMETSAT Satellite Application Facility to Nowcasting and Very Short Range Forecasting, 29 pp
- SAF (2011) Algorithm Theoretical Basis Document for "Cloud Products" (CMA-PGE01v3.1, CT-PGE02 v2.1 & CTH-PGE03 v2.2). EUMETSAT Satellite Application Facility to Nowcasting and Very Short Range Forecasting, 87 pp
- Sánchez-Diezma, R.; Sempere-Torres, D.; Delrieu, G. & Zawadki, I. (2001). An improved methodology for ground clutter substitution based on a pre-classification of precipitation types. *Proceedings of the 30th Internat. Conf. on Radar Meteor.*, pp. 271-273, Amer. Meteor. Soc., München, Germany
- Sauvageot, H. (1991). *Radar Meteorology*, Artech House, ISBN 978-0-89006-318-7, 366 pp., London, UK
- Sauvageot, H. (1994). Rainfall measurement by radar: a review. *Atmospheric Research*, Vol.35, No.1, pp. 27-54
- Shedd, R.; Smith, J. & Walton, M. (1991). Sectorized hybrid scan strategy of the NEXRAD precipitation-processing system. In *Hydrological Applications of Weather Radar*, I. Cluckie & C. Collier, Eds., pp. 151-159, ISBN 0134414780, Ellis Horwood Limited, New York, USA
- Skolnik, M. (1980). *Introduction to radar systems*. 581 pp., ISBN 0070665729, McGraw-Hill, New York, USA
- Smith, P.L., Jr. (1998). On the minimum useful elevation angle for weather surveillance radar scans. *Journal of Atmospheric Oceanic Technology*, Vol.15, No.3, pp. 841-843
- Steiner, M. & Smith, J.A. (2002). Use of three-dimensional reflectivity structure for automated detection and removal of non-precipitating echoes in radar data. *Journal of Atmospheric and Oceanic Technology*, Vol.19, No.5, pp. 673-686
- Taylor, K.E. (2001). Summarizing multiple aspects of model performance in single diagram. *Journal of Geophysical Research*, Vol. 106, D7, pp. 7183-7192.
- Trapero, L.; Bech, J.; Rigo, T.; Pineda, N. & Forcadell, D. (2009). Uncertainty of precipitation estimates in convective events by the Meteorological Service of Catalonia radar network. *Atmospheric Research*, Vol. 93, No.1-3, pp. 408-418
- Vicente, G.; Davenport, J C. & Scofield, R. A. (2002). The role of orographic and parallax corrections on real time high resolution satellite rainfall rate distribution. *International Journal of Remote Sensing*, Vol.23, pp.221-230
- Villarini, G. & Krajewski, W.F. (2010). Review of the Different Sources of Uncertainty in Single Polarization Radar-Based Estimates of Rainfall. *Surveys in Geophysics*, Vol.31, No.1, pp. 107-129, ISBN 0169-3298
- Wilks, D.S. (1995). *Statistical Methods in the Atmospheric Sciences*. Academic Press, ISBN , 467 pp., London, UK

Doppler Weather Radars and Wind Turbines

Lars Norin and Günther Haase
Swedish Meteorological and Hydrological Institute
Sweden

1. Introduction

In many countries the number of wind turbines is growing rapidly as a response to the increasing demand for renewable energy. The cumulative capacity of wind turbines worldwide has shown a near 10-fold increase in the last decade (Global Wind Energy Council, 2011) and in the coming years many more wind turbines are expected to be built. Existing, older wind turbines are likely to be replaced by larger, next generation, turbines.

Modern wind turbines are large structures, many reach more than 150 m above the ground. Clusters of densely spaced wind turbines, so called wind farms, are being built both on- and offshore.

The continued deployment of wind turbines and wind farms is, however, not unproblematic. Radar systems, for example, are easily disturbed by wind turbines. Interference caused by wind turbines is more severe for many radar systems than interference caused by, for example, masts or towers. This is due to the rotating blades of the wind turbines. Many Doppler radars use a filter that removes echoes originating from objects with no or little radial velocity. However, these filters do not work for moving objects such as the rotating blades of wind turbines. Wind turbines located in line of sight of Doppler radars can cause clutter, blockage, and erroneous velocity measurements, affecting the performance of both military- and civilian radar systems.

Even though both radars and wind turbines have been in use for many decades it is only in the last few years that the interference problem has received substantial attention. The reason for this is simple; in recent years wind turbines have increased in number and size and at the same time radar systems have become increasingly sensitive.

In this chapter we present a brief review of some of the work made to investigate the impact of wind turbines on Doppler weather radars. Starting with a historical overview we outline the evolution of wind turbines and early studies about their impact on Doppler radars in general and Doppler weather radars in particular. Three major interference types for Doppler weather radars are identified: clutter, blockage, and erroneous velocity measurements. Observations, models, and mitigation concepts for all three interference types are discussed.

In particular, we present results from a study on average wind turbine clutter, based on long time series of data. We show that modelling wind turbine clutter using the radar cross section of a wind turbine can lead to erroneous results. We further argue that blockage due to wind turbines is difficult to analyse using operational reflectivity data. An alternative way

of studying blockage is discussed and results are presented. A simple blockage model is described and its results are shown to agree with observations. Finally, examples of erroneous wind measurements are shown and mitigation measures are discussed.

2. Background

2.1 Wind turbine development

Wind power technology dates back many centuries. In the 1st century A.D. Hero of Alexandria described a simple wind wheel that could power an altar organ (Woodcroft, 1851). It is, however, not clear whether this invention was ever constructed or put to use. The first documented description of windmills that were used to perform irrigation and grinding grain comes from the region of Sistan, Persia, in the 9th century (Shepard, 1990). By the 12th century windmills were in use in Europe and in the following centuries they became increasingly important for grinding grain and pumping water. It was only after the industrial revolution their importance receded (Manwell et al., 2009).

Near the end of the 19th century the first wind turbines, used for the production of electricity, were developed. James Blyth built a 10 m high, cloth-sailed wind turbine in Scotland in 1887 (Price, 2005) and Charles Brush constructed a 25 m high wind turbine in Cleveland, Ohio, in 1887–1888 (Anon., 1890). A few years later, in the 1890s, Poul la Cour constructed over 100 wind turbines to generate electricity in Denmark (Manwell et al., 2009). In the 1970s the rising oil prices generated a renewed interest in wind power which led to serial production of wind turbines.

The increasing demand for renewable energy sources in the 21st century led to a further upswing for wind power. The pursuit of ever more powerful wind turbines lead to an increase in rotor blade diameter. A large wind turbine in the early 1980s could have a rotor diameter of 15 m and produce 55 kW whereas a large wind turbine in 2011 could have a rotor diameter larger than 150 m and produce 7 MW. Figure 1 shows the rotor diameter and the corresponding power produced by large wind turbines introduced on the market during the period 1981–2011.

Since wind turbines not only have become increasingly powerful but also grown more numerous during the last decades the global cumulative installed capacity has increased exponentially (see Fig. 2). With the exception of year 2010 the global annual installed capacity has increased monotonically since at least 1996 (cf. Fig. 2).

2.2 Wind turbine impact on Doppler radars

Wind turbines in the path of electromagnetic transmissions may cause interference by scattering parts of the transmitted signal but also by modulating the transmission's frequency. Initial studies on wind turbine interference focused on television and radio transmissions and showed that wind turbines could indeed cause interference to the reception of such signals (see, e.g., Sengupta (1984); Sengupta & Senior (1979); Senior et al. (1977); Wright & Eng (1992)).

By the end of the 20th century and beginning of the 21st century a large number of wind turbines had been installed and several investigations were conducted to analyse the impact of wind turbines on military surveillance radars and civilian air traffic control radars (see, e.g.,

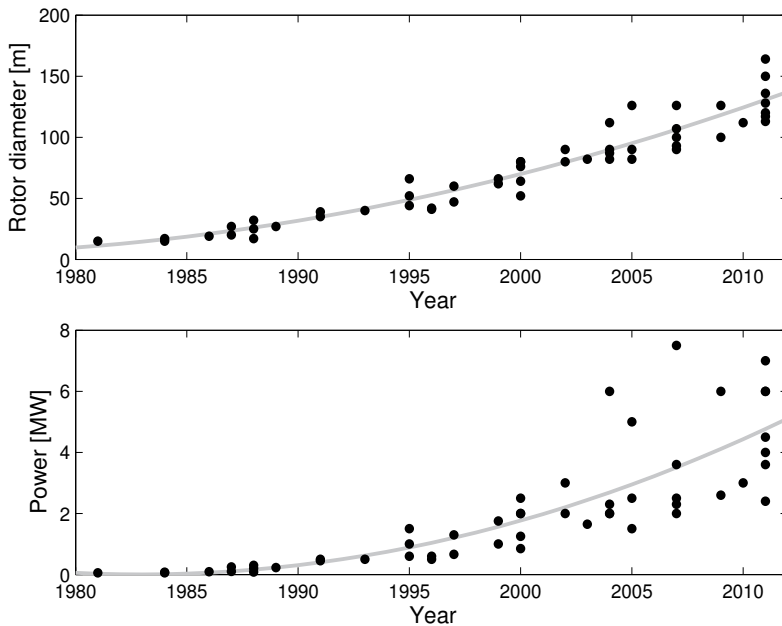


Fig. 1. Rotor diameter (top) and power (bottom) for a selection of large wind turbines introduced on the market during the period 1981–2011. Gray lines show superimposed trends. Data from The Wind Power (www.thewindpower.net) and wind turbine manufacturers' homepages.

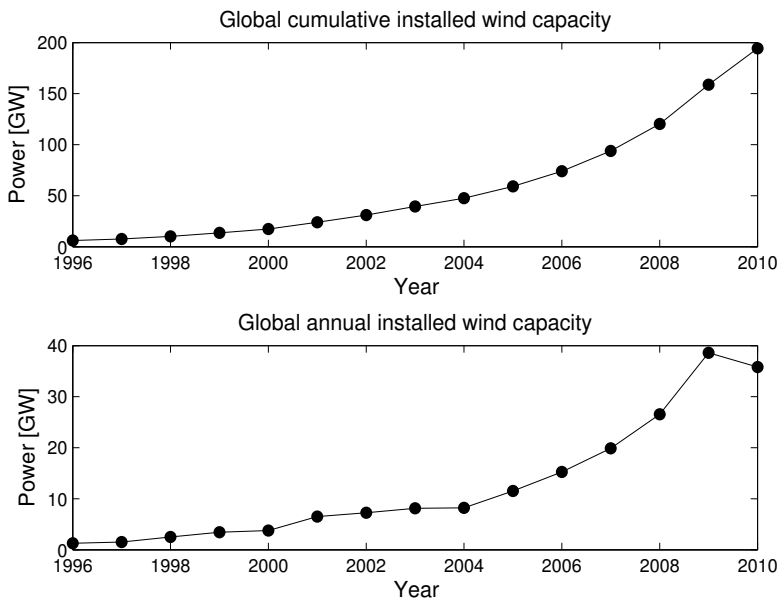


Fig. 2. Global cumulative installed wind capacity (top) and global annual installed wind capacity (bottom). Data from Global Wind Energy Council (2011).

Borely (2010); Butler & Johnson (2003); Davies (1995); Department of Defense (2006); Frye et al. (2009); Jago & Taylor (2002); Lemmon et al. (2008); Ousbäck (1999); Poupart (2003); RABC & CanWEA (2007); Sparven Consulting (2001); Summers (2001); Webster (2005a,b)). From these and other studies it became clear that wind turbines in general cause three types of problems for Doppler radars: clutter, blockage, and erroneous Doppler measurements.

- Clutter consist per definition of unwanted radar echoes. For a military surveillance radar clutter can for example consist of precipitation echoes whereas for a weather radar echoes from, e.g., aircraft are unwanted. Echoes from wind turbines are considered clutter by most radars.
- Blockage occurs when obstacles such as buildings or terrain obscure the radar line of sight. Measurements behind such obstacles become incomplete or non-existing. Wind turbines located near a radar may block a substantial part of the radar's measurement region.
- Doppler radars not only measure the echo strength of their targets but also their radial velocities. The motion of the rotor blades of a wind turbine is detected by the radar and may be interpreted as a moving target.

Clutter originating from the ground or from stationary buildings is often filtered out by built-in clutter filters that remove echoes with zero or low radial velocities. Echoes from the tower of a wind turbine have zero velocity and can therefore easily be removed but the turbine's rotating blades can have very large and variable velocities, escaping the clutter filter. Echoes from rotating wind turbine blades may therefore, for example, be mistaken for aircraft by an air traffic control radar.

Weather radar problems related to wind turbines were recognised early by Hafner et al. (2004) and Agence National des Fréquences (2005). These works have since been followed by many studies (e.g. Brenner et al. (2008); Donaldson et al. (2008); Haase et al. (2010); Hutchinson & Miles (2008); Toth et al. (2011); Tristant (2006a,b); Vogt et al. (2011; 2007a; 2009)). The increased awareness of the problems wind turbines may cause weather radars led both the World Meteorological Organization (WMO) and the Network of European Meteorological Services (EUMETNET) to issue general guidelines for the deployment of wind turbines, based on the distance from the radar (OPERA, 2010; WMO, 2010). These guidelines are summarised in Table 1 and Table 2.

3. Wind turbine interference

In the sections below we examine the three identified problems wind turbines can cause to Doppler weather radars: clutter, blockage, and erroneous wind measurements.

3.1 Clutter

For a weather radar, clutter refers to all non-meteorological radar echoes. Typical examples of clutter include echoes from terrain, buildings, and clear-air targets (e.g. insects, birds, atmospheric turbulence). Clutter can further be divided into two categories: static and dynamic. Static clutter typically originates from terrain and buildings whereas dynamic clutter is caused by moving targets such as clear-air returns. Static clutter has zero or near-zero radial velocity and can be removed by a built-in clutter filter whereas dynamic

Range	Potential impact	Guideline
0–5 km	The wind turbine may completely or partially block the radar and can result in significant loss of data that can not be recovered.	Definite Impact Zone: Wind turbines should not be installed in this zone.
5–20 km	Multiple reflection and multi-path scattering can create false echoes and multiple elevations. Doppler velocity measurements may be compromised by rotating blades.	Moderate Impact Zone: Terrain effects will be a factor. Analysis and consultation is recommended. Re-orientation or re-siting of individual turbines may reduce or mitigate the impact.
20–45 km	Generally visible on the lowest elevation scan; ground-like echoes will be observed in reflectivity; Doppler velocities may be compromised by rotating blades.	Low Impact Zone: Notification is recommended.
> 45 km	Generally not observed in the data but can be visible due to propagation conditions.	Intermittent Impact Zone: Notification is recommended.

Table 1. WMO guidance statement on weather radar/wind turbine siting. (From WMO (2010))

Range	Radar	Statement
0–5 km	C-band	No wind turbine should be deployed within this range
5–20 km	C-band	Wind farm projects should be submitted for an impact study
0–10 km	S-band	No wind turbine should be deployed within this range
10–30 km	S-band	Wind farm projects should be submitted for an impact study

Table 2. Statement of the OPERA group on the cohabitation between weather radars and wind turbines. (From OPERA (2010))

clutter originates from targets having radial velocities larger than the clutter filter limits. Dynamic clutter can therefore not be suppressed by conventional clutter filters.

Operating wind turbines generate both static and dynamic clutter. Since the static clutter from the wind turbines is suppressed by clutter filters the dynamic wind turbine clutter, mainly originating from the rotating blades, has the largest impact on weather radar measurements. Dynamic wind turbine clutter (in the following referred to as wind turbine clutter) is often difficult to separate from precipitation echoes and may therefore incorrectly be interpreted by the weather radar as precipitation.

In addition, wind turbine clutter is highly variable in time since the amplitude of the scattered signal depends sensitively on the wind turbine's yaw- and tilt angle.

3.1.1 Observations

Observations of wind turbine clutter have been presented in numerous works (e.g. Agence National des Fréquences (2005); Burgess et al. (2008); Gallardo et al. (2008); Haase et al. (2010); Isom et al. (2009); Toth et al. (2011); Tristant (2006a); Vogt et al. (2011; 2007a)). The strength

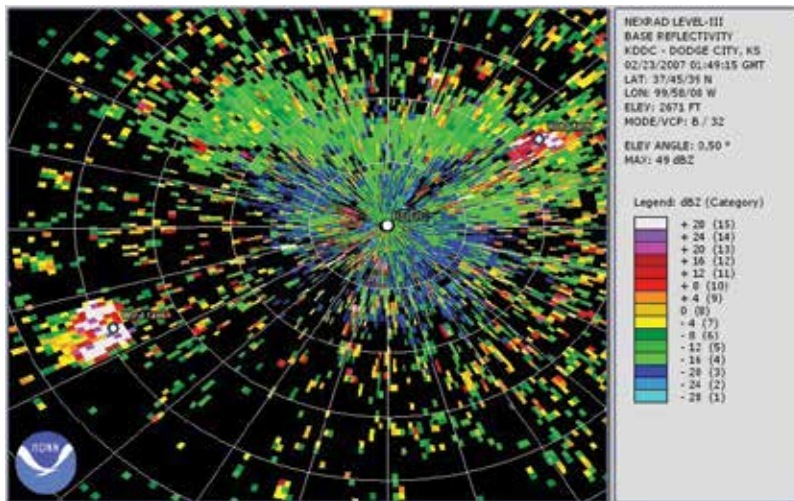


Fig. 3. Wind turbine clutter caused by two wind farms near Dodge City, Kansas, at 0149 GMT on February 23, 2007. One wind farm is located approximately 40 km to the southwest of the radar; the other near 20 km to the northeast. Range rings in white are at 10-km spacing. Adapted from Crum et al. (2008). This image was obtained from NOAA/National Climatic Data Center.

of the observed clutter can range from barely visible (< 0 dBZ) to near saturation levels (> 60 dBZ) (Agence National des Fréquences, 2005; Crum et al., 2008; Toth et al., 2011; Tristant, 2006a).

An example of clutter, originating from two wind farms near Dodge City, Kansas, is shown in Fig. 3. One wind farm consists of 170 wind turbines and is located approximately 40 km southwest of the radar; the other wind farm consists of 72 wind turbines, located approximately 20 km northeast of the radar. On this otherwise clear day reflectivity values close to 30 dBZ can be seen at the location of both wind farms.

Images such as Fig. 3 convincingly demonstrate that wind turbine clutter exists and that it may indeed cause problems for weather radars. However, in order to obtain a quantitative estimate of wind turbine clutter long time series of data should be studied.

In the remainder of this section we present results from a study based on long time series of wind turbine clutter. In the study operational reflectivity data from the four lowest scans of all Swedish weather radars were analysed over a period of more than three years (November 1, 2007 to March 31, 2011). In order to estimate the amount of wind turbine clutter observed by the weather radars, precipitation echoes were filtered out using a custom-designed weather filter. To further increase the quality of the wind turbine clutter, all other clutter — here referred to as background clutter — was removed from the weather-filtered reflectivity data. Finally the wind turbine clutter (z) was converted to rain rate (R) assuming the relation $z = 200R^{1.5}$ (Michelson et al., 2000).

The weather filter removed precipitation echoes from the lowest elevation angle by comparing reflectivity data cellwise to reflectivities from a higher elevation angle. If an echo from a higher

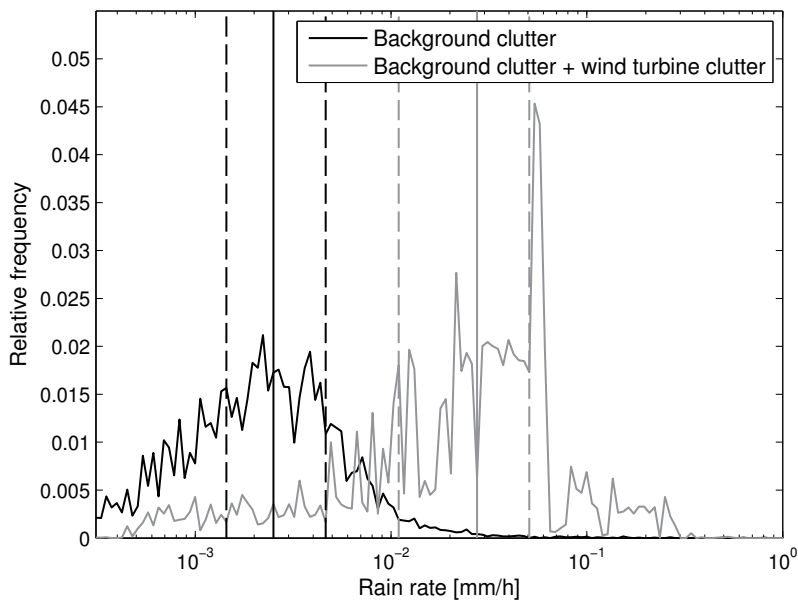


Fig. 4. Distributions of clutter before and after the construction of wind turbines. Solid, vertical lines indicate the median value and dashed, vertical lines show the first and third quartiles.

elevation angle was strong enough to indicate the presence of precipitation the corresponding value from the lowest elevation angle was filtered out.

Approximately 13 km from the weather radar in Karlskrona, Sweden, three wind turbines are located in the same radar cell (i.e., the same range bin and azimuth gate). Weather-filtered clutter distributions from this radar cell before and after the construction of the three wind turbines are shown in Fig. 4. It is seen that the two clutter distributions are easily distinguishable, having similar shapes but very different medians. It is evident that in this radar cell the existence of operational wind turbines has substantially increased the total amount of clutter.

Before the construction of the wind turbines, the reflectivity values remaining after filtering out precipitation echoes were composed of clear-air returns and other, non-identified, moving targets. In a second step of the analysis, this background clutter was removed from the weather-filtered reflectivity values recorded after the construction of the wind turbines. In this way a measure of clutter solely due to wind turbines was obtained.

The median wind turbine clutter was obtained from the difference between clutter after and before the construction of wind turbines. This analysis was carried out for all wind turbines in line-of-sight of a Swedish weather radar. The median wind turbine clutter values of 11 different radar cells, together with the first and third quartiles, are shown in Fig. 5. The median wind turbine clutter is seen to vary from close to zero to more than 0.02 mm h^{-1} . The spread of the clutter is attributed to the fact that the strength of a wind turbine echo depends on the position of the rotor blades and the yaw of the wind turbine, which in turn depends on the direction of the wind.

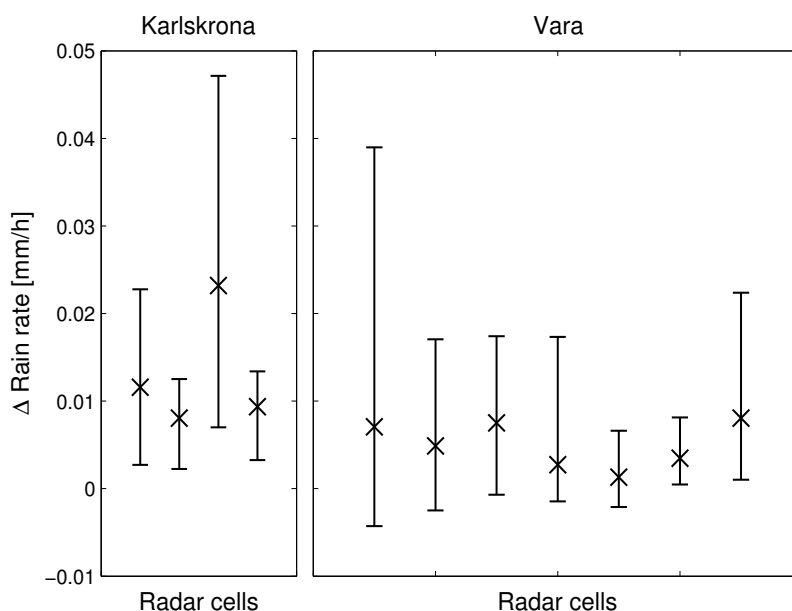


Fig. 5. Median wind turbine clutter together with first and third quartiles observed by two Swedish weather radars (Karlskrona and Vara).

Wind turbine clutter has also been observed from radar cells in which no wind turbines are located. An example of such area effects of wind turbine clutter is shown in Fig. 6. The wind turbine clutter in this figure comes from the same wind farm as in Fig. 4. All together this wind farm consists of five wind turbines with total heights of 150 m above the ground. Three of the five wind turbines are located within the same radar cell, the other two turbines each occupy a different radar cell. In Fig. 6 it is seen that not only the radar cells in which the wind turbines are located show an increase in clutter but also that several radar cells cross- and downrange of the turbines are affected.

Wind turbine clutter downrange from wind turbines (cf. Figs. 6a and b) has been observed in several other works (e.g. Crum et al. (2008); Haase et al. (2010); Isom et al. (2009); Toth et al. (2011); Vogt et al. (2011)). Such clutter tails can be visible for tens of kilometres behind wind turbines. No theoretical model has been put forward to explain this phenomenon but it has been suggested that the tails are caused by multiple scattering effects (scattering between multiple turbines and/or scattering between turbine and ground) (Crum et al., 2008; Isom et al., 2009; Toth et al., 2011). Clutter tails are not considered a problem for wind farms located further than 18 km from the weather radar (Crum & Ciardi, 2010; Vogt et al., 2009).

Cross-range clutter may also occur, as is seen in Figs. 6a and c. For the case shown in Fig. 6, the cross-range clutter is a direct result of the way the reflectivities are stored in the radar data matrix (the azimuthal resolution of the actual radar measurements is lower than the azimuthal spacing of the data matrix). However, for wind turbines generating very strong echoes it has been suggested that clutter may be seen well outside the half-power width of the radar beam, generating cross-range clutter spanning tens of degrees (Agence National des Fréquences, 2005).

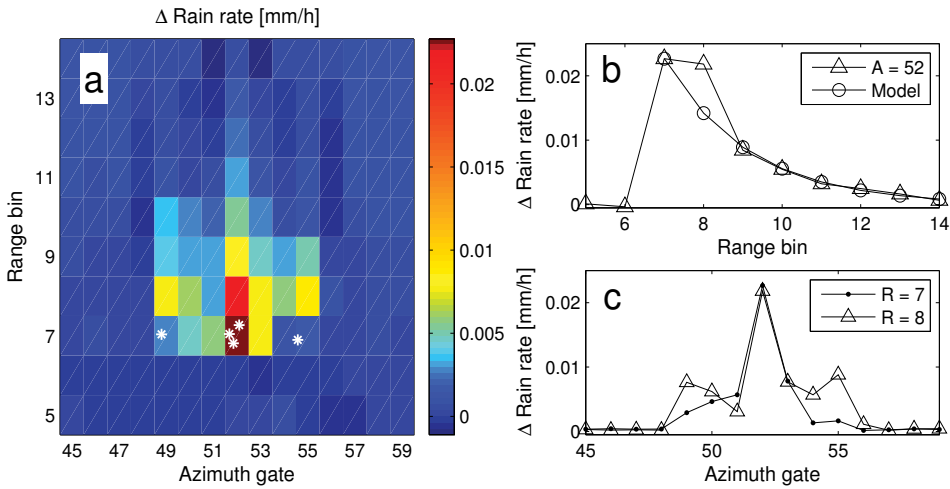


Fig. 6. Wind turbine clutter caused by a wind farm approximately 13 km northeast of the Karlskrona weather radar. a) Clutter from an area containing five wind turbines (shown by white asterisks). One wind turbine is located in radar cell [7,49], three are located in [7,52], and one in [7,55]. b) Clutter from azimuth gate 52 together with model results. c) Clutter from range bins 7 and 8.

3.1.2 Models

Most models of wind turbine clutter rely on the turbines' radar cross section (RCS) as a measure of how efficiently radar pulses are backscattered (Agence National des Fréquences, 2005; Tristant, 2006a). In order to model wind turbine clutter the RCS of a wind turbine must be converted to the equivalent radar reflectivity factor. The radar equation for point targets is given by (see, e.g. Skolnik (2008))

$$P_r = \frac{P_t G^2 \lambda^2 \sigma}{64 \pi^3 D^4} \quad (1)$$

where P_r and P_t are, respectively, the power received and transmitted by the radar, G is the antenna gain, λ is the wavelength, σ is the RCS of the target, and D is the distance from the radar to the target.

For distributed targets, such as rain, the radar equation is written as (see, e.g. Keeler & Serafin (2008))

$$P_r = \frac{P_t G^2 \theta \phi c \tau \pi^3 |K|^2 z}{1024 \ln(2) \lambda^2 D^2} \quad (2)$$

where θ and ϕ are the azimuth and elevation beamwidths, c is the speed of light, τ is the radar pulse width, $|K|^2$ is a parameter related to the complex index of refraction of the material, and z is the linear radar reflectivity factor. For a given RCS the linear radar reflectivity factor can thus be expressed as

$$z = C_1 \frac{\sigma}{D^2} \quad (3)$$

where C_1 is a constant that depends on the parameters of the radar system. For Swedish weather radars, $C_1 = 3 \times 10^{12} \text{ mm}^6 \text{ m}^{-3}$.

Let us use Eq. (3) to calculate what RCS would cause an observed rain rate of $R = 0.1 \text{ mm h}^{-1}$ (cf. Fig. 4) at a distance $D = 13 \text{ km}$ from the radar. Using $z = 200R^{1.5}$ we find that $\sigma = 4 \text{ cm}^2$.

The RCS of wind turbines has been studied both experimentally and numerically (see, e.g., Greiving & Malkomes (2006); Kent et al. (2008); Kong et al. (2011); Ohs et al. (2010); Poupart (2003); Zhang et al. (2011)). These studies have shown that RCSs of wind turbines display a sensitive dependence on yaw- and tilt angle. However, measurements of the RCS of large wind turbines typically range between 20 to 30 dBsm (Kent et al., 2008; Poupart, 2003) which is very far from what we obtained in the calculation. Using the RCS to calculate wind turbine clutter in this simple way may therefore lead to erroneous results.

It has been argued that the RCS is not applicable to wind turbines (Greiving & Biermann, 2008; Greiving et al., 2009; Greiving & Malkomes, 2006; 2008). The reason is that the plane wave condition does not hold for objects on the ground. From the calculation above it is clear that more sophisticated models are needed in order to make a correct simulation of wind turbine clutter.

For downrange clutter a simple, empirical model was constructed using an exponential function to fit the limited amount of data available. The rain rate R behind a wind turbine was modelled as

$$R = R_0 \exp\left(-\frac{C_2 x}{N}\right) \quad (4)$$

where R_0 is the rain rate in mm h^{-1} from the radar cell containing the wind turbine, $C_2 = 0.7$ is an empirically determined constant, x is the distance behind the wind turbine in kilometres, and N is the number of interfering wind turbines present in the radar cell. Observations and model results are shown in Fig. 6b.

3.1.3 Mitigation concepts

Various concepts for mitigating wind turbine clutter have been suggested in different studies. Some of these concepts are listed here.

- Placing wind turbines so that they are not in line of sight of a weather radar. Under normal conditions a radar's measurements will not be affected by objects that are not in the radar line of sight. This method is therefore a certain way of limiting wind turbine clutter. It has also been suggested that wind turbines should be arranged radially from the radar. Such a formation probably does little to mitigate clutter since the blades of the different wind turbines do not move synchronously.
- Reducing the wind turbines' RCS. It has been proposed that stealth materials can be applied to wind turbines as a way of reducing the RCS (Appelton, 2005; Butler & Johnson, 2003). Studies of stealth coating wind turbine blades show that a reduction of more than 10 dB may be possible (Rashid & Brown, 2010), making it an interesting solution. An alternative way of reducing the rotor blades' RCS is to modify their shape, but this is not considered a realistic alternative as the shape of a rotor blade is optimized for efficiency.
- Adaptive clutter filters. Various filter techniques for removing or reducing effects of wind turbine clutter have been suggested. Gallardo et al. (2008) suggested using an image processing technique and Isom et al. (2009) proposed a multiquadratic interpolation technique. Other signal processing techniques have also been proposed (Bachmann et al.,

2010a;b; Gallardo-Hernando & Pérez-Martínez, 2009; Nai et al., 2011). These methods all use raw data as input, i.e., in- and quadrature phase (I/Q) data.

To speed up filtering, only radar cells containing wind turbines should ideally be processed. This may be achieved by keeping maps of all wind turbines near a weather radar or by using automatic detection schemes (Cheong et al., 2011; Gallardo-Hernando et al., 2010; Hood et al., 2009; 2010).

- Gap-filling radars. Areas contaminated by clutter may be covered by a second, nearby radar, a so-called gap-filler (Aarholt & Jackson, 2010; Department of Defense, 2006; Ohs et al., 2010). This alternative may be a convenient solution for specific cases but could also lead to even bigger problems since an introduction of additional radars introduces new sites which also must be protected.
- Adaptation of the radar scan strategy. Changing the radar scan strategy to pass over areas with wind turbines will limit the amount of clutter received. The drawback is that data will be gathered from higher altitudes which may shorten the effective range of the radar.

3.2 Blockage

For a weather radar, blockage manifests itself as a reduction of the expected precipitation echoes downrange from an obstacle. But, as we have seen in Section 3.1, obstacles in line of sight of a radar do not only cause blockage, they also cause clutter. Stationary obstacles cause static clutter which can be removed by a clutter filter. However, dynamic clutter, such as echoes from rotating blades of wind turbines, is not removed by the clutter filter. Downrange from such obstacles both clutter and blockage can appear. For wind turbines in line of sight of a weather radar the increased echo strength from the clutter can often be as large, or larger, than the reduction in echo strength due to blockage. Separating the effects of blockage and clutter is therefore often impossible using data analysis. However, large wind farms may cause substantial blockage and the effect may be visible for tens of kilometres downrange of the farm.

3.2.1 Observations

Blockage caused by wind turbines is not always visible in radar reflectivity images. As explained previously this is partly due to clutter tails but also because precipitation echoes are not always spatially homogeneous.

One example of blockage caused by a wind farm near Dodge City, Kansas, is shown in Fig. 7. In the figure a weak shadow can be seen behind a wind farm to the southwest of the weather radar. Other examples of blockage caused by wind turbines can be found in Vogt et al. (2007a) and Seltmann & Lang (2009).

As mentioned above, making a quantitative analysis of blockage behind wind farms is difficult due to clutter tails and the spatial variation of precipitation echoes. Let us therefore instead examine blockage caused by a stationary structure in line of sight of a weather radar.

The air traffic control tower of Arlanda Airport near Stockholm, Sweden, is located only 0.9 km from the Arlanda weather radar. The full width at half maximum of the radar beam is 0.9° , which at the distance of the tower corresponds to approximately 14 m. The radar beam is

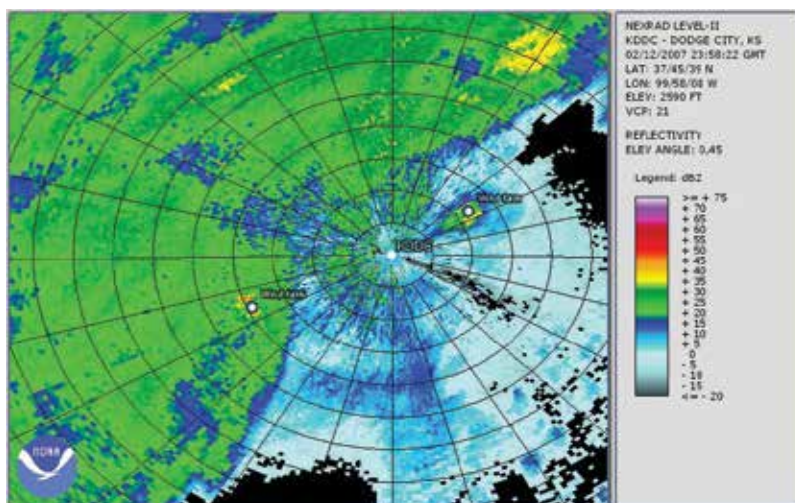


Fig. 7. Reflectivity measurement from the weather radar near Dodge City, Kansas, at 2358 GMT, February 12, 2007. Blockage caused by a wind farm to the southwest results in a reduction of precipitation echoes downrange from the wind farm (most clearly visible at a distance of 70–100 km from the radar). Range rings in black are at 10-km spacing. Adapted from Burgess et al. (2008). This image was obtained from NOAA/National Climatic Data Center.

thus wider than the width of the tower (approximately 8.5 m). For the lowest elevation angle of the radar the tower fills the entire beam height.

The average amount of precipitation per hour, for the period 1 November 2007 to 31 March 2011, is shown in Fig. 8. In this figure it is seen that some azimuth gates have considerably less measured precipitation compared to their neighbours. These gates coincide with the location of the tower.

One way to obtain a quantitative estimate of the reduction in expected precipitation due to blockage is to assume that the precipitation can be considered constant over some neighbouring azimuth gates. To validate this assumption a correlation analysis was performed. The analysis revealed that the correlation between precipitation measurements from neighbouring azimuthal radar cells depends on cross-range distance and accumulation period. The correlation decreases as the cross-range distance increases and for the same cross-range distance, shorter accumulation periods results in lower correlation. Applying the correlation analysis to the precipitation measured by the Arlanda weather radar showed that, for example, precipitation from radar cells with cross-range distances up to 5 km and an accumulation period of 24 h had a correlation over 0.9.

To obtain a measure of how much precipitation varies locally the coefficient of variation of accumulated precipitation from neighbouring azimuthal radar cells was calculated. In the analysis for the Arlanda weather radar it was shown that the coefficient of variation increased with increasing number of neighbouring azimuthal gates (i.e. window size) and decreased with accumulation period.

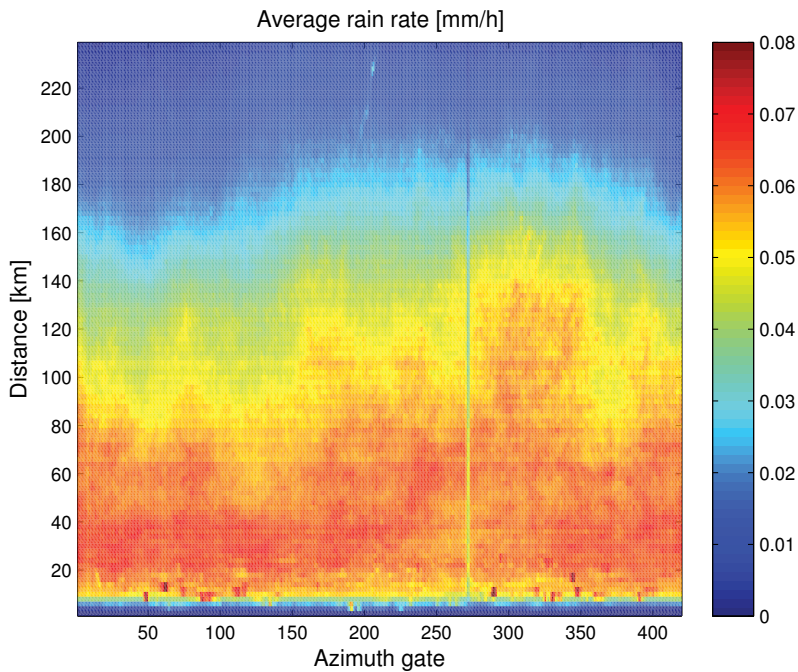


Fig. 8. Average amount of precipitation per hour from the lowest elevation angle (0.5°) for the weather radar at Arlanda airport, Sweden. Blockage caused by a nearby air traffic control tower can be seen near azimuth gate 271.

For example, for an accumulation period of 1 hour and a window size of 13 gates (corresponding to 11.7° in azimuthal angle) the coefficient of variation did not decrease lower than approximately 0.25 at any distance from the radar whereas for an accumulation period of 1 month the coefficient of variation for the same number of gates was lower than 0.05 at 10 km from the radar. The coefficient of variation can be compared with the blockage caused by an obstacle.

To find a quantitative estimate of the reduction in expected precipitation echoes caused by the Arlanda tower a 13-gate wide window was applied to the data, accumulated over the entire three-year-period. The measurements in the window were normalized over azimuth and range to the average value of unaffected gates. In Fig. 9 it is seen that the measured precipitation is reduced by close to 30% in the most severely affected gate.

Comparing the blockage of the Arlanda tower with the coefficient of variation for various accumulation periods it was found that on average between 24 hours and 1 week was needed for the coefficient of variation of the local precipitation to be lower than 30%. On individual radar images it may therefore be difficult to see the effects of the Arlanda tower blockage.

3.2.2 Models

Modelling of electromagnetic shadow effects can be done with varying accuracy and complexity. Methods and results of modelling blockage and shadow effects downrange of wind turbines can be found in, e.g., Belmonte & Fabregas (2010); Greving & Malkomes

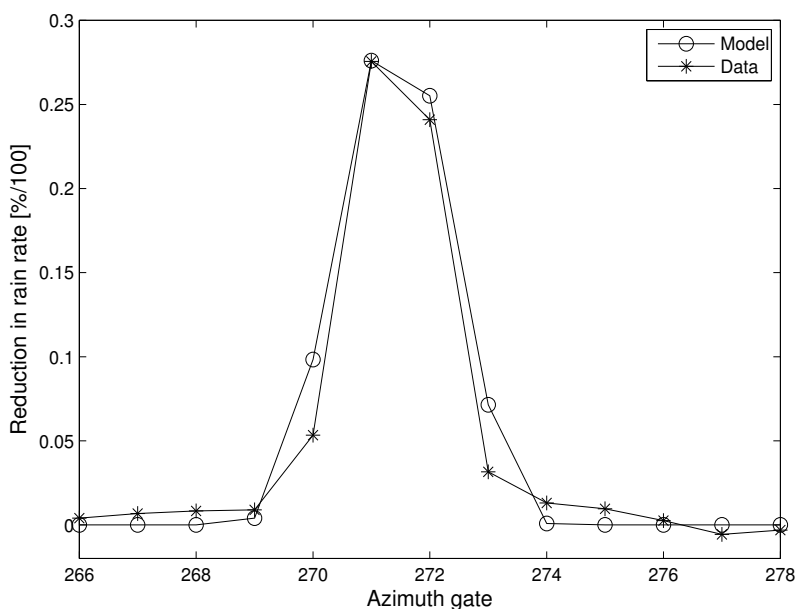


Fig. 9. Blockage caused by an air-traffic control tower at Arlanda Airport. Data and model.

(2008); Høyve (2007). Here we describe a simple and computationally light method to calculate blockage caused by an obstacle.

As a first approximation of the reduction in returned power due to an obstacle we consider the obstacle's geometrical cross section. Convolving the obstacle's cross section with the radar beam's power flux and dividing by the total power from an unperturbed beam we obtain the fraction of power, P_B , blocked by the obstacle. To find the corresponding reduction in rain rate we start by noting that $1 - P_B$ is the amount of power that is unaffected by blockage. The (unaffected) power is proportional to the linear radar reflectivity factor z according to Eq. (2) and z is in turn related to rain rate R by $z \propto R^{1.5}$. Hence the reduction in rain rate, R_B , can be expressed as $R_B = 1 - (1 - P_B)^{1/1.5}$.

Applying this method to the Arlanda air-traffic control tower described in Section 3.2.1 we can estimate the reduction in rain rate it causes. The modelled reduction in rain rate is shown in Fig. 9 together with the observations. The model is seen to capture the magnitude and the cross-range shape of the blockage. This model can be used for estimating blockage caused by wind turbines, but for reasons explained in Section 3.2.1 there are no observations to compare these results with.

3.2.3 Mitigation concepts

Methods proposed to prevent or reduce blockage by wind turbines include:

- Optimising the placement of the wind turbines. Wind turbines should preferably be placed out of the line of sight of the radar. Otherwise it has been suggested that wind turbines should be arranged radially from the radar. In this way the blockage caused by the wind

turbine towers may be reduced, but blockage caused by rotor blades will persist since there is no synchronisation of their movements.

- Use of a gap-filling radar. A way to remove or reduce blockage is to place an additional radar to cover areas affected by blockage.
- Adapting the radar scan strategy so that the radar beam passes over areas with wind turbines. This method ensures that measurements are not affected by blockage but in return data will be gathered from higher altitudes.

3.3 Wind measurements

A Doppler radar measures frequency shifts of the received signals and translates the shifted frequencies to radial velocities. A conventional clutter filter removes echoes with low or zero frequency shifts and thereby prevents static clutter from entering the radar products.

Signals scattered from rotating blades of a wind turbine are shifted in frequency and thereby interpreted by the radar as moving objects, escaping the clutter filter. The tip of a rotor blade can move with a velocity up to 100 m s^{-1} whereas close to the hub the blade velocity is close to zero. The scattered signals will therefore display a broad distribution in frequency space. The wind velocity is normally estimated as the strongest (non-zero) frequency component. Since echoes from wind turbines often are stronger than weather echoes this can lead the weather radar to display erroneous wind measurements.

3.3.1 Observations

There are many observations of wind turbines causing erroneous wind measurements in the literature (see, e.g., Burgess et al. (2008); Cheong et al. (2011); Crum et al. (2008); Haase et al. (2010); Isom et al. (2009); Toth et al. (2011); Vogt et al. (2007a)). One such example from the weather radar in Dodge City, Kansas, is shown in Fig. 10. From this figure it is clear that at the time of the measurements the overall wind direction was to the northwest but signals from radar cells containing a large wind farm, approximately 40 km to the southwest, show up as having close to zero velocity. In Fig. 11 is shown the spectrum width of the velocity measurements and from this figure it is clear that there is a significant broadening of the frequency spectra over the wind farm.

These observations can be understood by examining the raw I/Q data from the radar. Spectrograms of I/Q data, containing echoes from wind turbines, show highly complex and richly structured patterns. Examples of such spectrograms are given by, e.g., Bachmann et al. (2010a); Gallardo et al. (2008); Gallardo-Hernando & Pérez-Martínez (2009); Gallardo-Hernando et al. (2009); Hood et al. (2009); Isom et al. (2009); Nai et al. (2011); Poupart (2003); Vogt et al. (2007a;b). From these and other studies it is clear that echoes from wind turbine rotor blades in different positions result in broad distributions in frequency space even though the average velocity estimate is often close to zero.

As for wind turbine clutter there are observations showing tails of erroneous wind measurements behind the wind turbines (Burgess et al., 2008; Selmann & Lang, 2009; Vogt et al., 2007a; 2009).

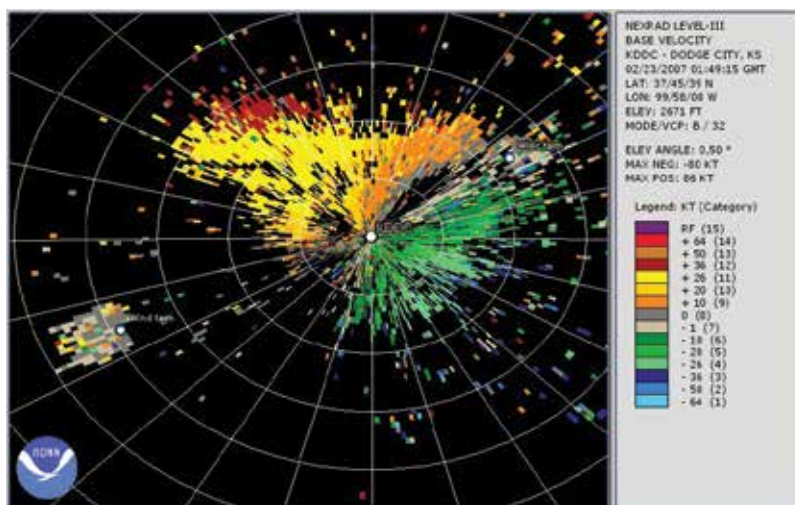


Fig. 10. Wind measurements from the weather radar near Dodge City, Kansas, at 0149 GMT, on February 23, 2007. The general wind direction is to the northwest but measurements near a wind farm to the southwest of the radar show wind velocities close to zero. Range rings in white are at 10-km spacing. Adapted from Vogt et al. (2007a). This image was obtained from NOAA/National Climatic Data Center.

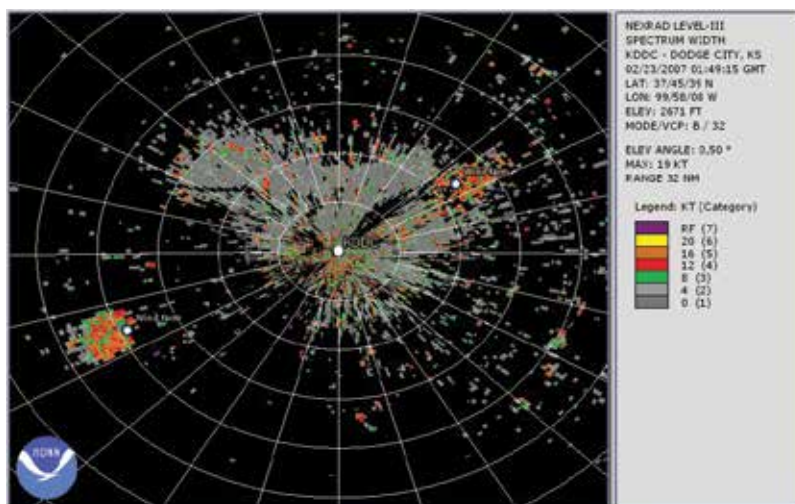


Fig. 11. Measurements of spectrum width from the weather radar near Dodge City, Kansas, at 0149 GMT, on February 23, 2007. The spectrum widths are considerably enhanced near a wind farm to the southwest of the radar. Range rings in white are at 10-km spacing. Adapted from Vogt et al. (2007a). This image was obtained from NOAA/National Climatic Data Center.

3.3.2 Models

A few methods have been proposed to model the frequency spectra generated by wind turbines (Gallardo-Hernando et al., 2010; Hood et al., 2009; 2010; Kong et al., 2011; Zhang et al., 2011). In these models clutter from the tower, hub, and rotor blades are included. The model results show the zero-velocity returns of the tower, near-zero returns of the hub, as well as spectral broadening of the blades.

3.3.3 Mitigation concepts

Most concepts proposed to prevent or reduce clutter (see Section 3.1.3) are also valid for erroneous wind measurements.

Adaptive filters, suggested for removing wind turbine clutter, can also help mitigate erroneous wind measurements. If clutter is removed from the signal, the average wind velocity as well as the spectrum width can easily be estimated. Suggestions for adaptive wind filters can be found in, e.g., Bachmann et al. (2010a;b); Gallardo et al. (2008); Isom et al. (2009); Nai et al. (2011). As for the adaptive clutter filters, all these methods use raw I/Q data as input.

4. Conclusions

In many countries the number of wind turbines is growing rapidly as a response to the increased demand for renewable energy. As wind turbines grow larger and more numerous potential conflicts with other interests are emerging. Doppler radars, for example, are easily disturbed by wind turbines. In this chapter we have presented an overview on wind turbine-related problems experienced by Doppler weather radars. Three main wind turbine-related problems have been identified: clutter, blockage, and erroneous wind measurements.

Clutter — unwanted radar echoes — are generated by all obstacles in line of sight of a radar. Static clutter, i.e., echoes with no or low radial velocities are easily removed by the Doppler radar's built-in clutter filter. However, the moving blades of a wind turbine generate dynamic clutter which displays a wide range of radial velocities that cannot be removed by a conventional clutter filter. In this chapter it has been shown that wind turbine clutter can be problematic for weather radars since such echoes are interpreted as precipitation. Wind turbine clutter can display a large variation in strength, ranging from barely visible to near saturation levels of the radar. Behind wind turbines a tail of clutter can often be seen. This phenomenon is believed to be the result of multiple scattering effects. In an example shown in this chapter, clutter tails were seen to decrease exponentially behind the wind turbines. Cross-range clutter has also been observed. This can be caused by differences in azimuthal resolution of the actual radar measurements and azimuthal spacing of the radar data matrix but it has also been suggested that it may occur as a result of the radar sidelobes.

The magnitude of wind turbine clutter is often estimated by calculating the radar cross section of wind turbines. Such models may lead to results inconsistent with observations. Effects from the ground and terrain should be taken into account, otherwise a calibration of the model may be necessary.

Possible mitigation measures for wind turbine clutter include a) placing wind turbines out of the radar's line of sight b) reducing the wind turbines' radar cross section using stealth material c) development and application of adaptive clutter filters, d) use of gap-filling radars to cover areas contaminated by clutter and e) adapting the radar scan strategy to pass over the wind turbines.

Blockage is caused by any obstacle in line of sight of a radar and is not specific to wind turbines. For a weather radar, blockage leads to an underestimation of the precipitation behind the blocking obstacle. Blockage caused by wind turbines is difficult to analyse using reflectivity data due to spatial variation of precipitation and clutter tails that are generated behind wind turbines. Model results can, however, be compared with observations of blockage caused by stationary obstacles such as towers, masts, or wind turbines that are not in operation.

Concepts for mitigating blockage include a) placing wind turbines radially from the radar b) use of a gap-filling radar to cover affected areas and c) adapting the radar scan strategy to pass over the wind turbines.

The Doppler function of a radar detects movements in echoes such as those from the rotating blades of a wind turbine. Although such measurements are correct, the interpretation by the radar may still be wrong. For example, an air traffic control radar may interpret echoes from rotating wind turbine blades as a moving aircraft and a weather radar may interpret such measurements as an approaching thunderstorm.

A weather radar uses Doppler-shifted echoes to estimate the wind speed. Doppler-shifted echoes from wind turbine blades may therefore lead to erroneous wind measurements. Observations of wind measurements over wind farms occasionally show extremely large wind speeds but most often the wind measurements are close to zero. The non-synchronised movements of the many rotor blades of a wind farm also lead to large spectrum widths.

Mitigation measures for wind measurements are the same as those presented for wind turbine clutter.

5. References

- Aarholt, E. & Jackson, C. A. (2010). Wind farm gapfiller concept solution, *European Radar Conference*, EuRAD, Paris, pp. 236–239.
- Agence National des Fréquences (2005). Perturbations du fonctionnement des radars météorologiques par les éoliennes, *Technical Report Rapport CCE5 No.1*, Commission Consultative de la Compatibilité Electromagnétique. In French.
- Anon. (1890). Mr. Brush's windmill dynamo, *Scientific American* 63(25): 54.
- Appelton, S. (2005). Design & manufacture of radar absorbing wind turbine blades, *Final Report W/44/00636/00/REP*, DTI PUB URN 05/1409, QinetiQ.
- Bachmann, S., Al-Rashid, Y., Bronecke, P., Palmer, R. & Isom, B. (2010a). Suppression of the windfarm contribution from the atmospheric radar returns, *26th Conference on Interactive Information and Processing Systems for Meteorology, Oceanography, and Hydrology*, American Meteorological Society, pp. 81–86.

- Bachmann, S., Al-Rashid, Y., Isom, B. & Palmer, R. (2010b). Radar and windfarms — mitigating negative effects through signal processing, *The Sixth European Conference on Radar in Meteorology and Hydrology*, ERAD, Sibiu, Romania, pp. 81–86.
- Belmonte, A. & Fabregas, X. (2010). Analysis of wind turbines blockage on doppler weather radar beams, *IEEE Antennas and Wireless Propagation Letters* 9: 670–673.
- Borely, M. (2010). Guidelines on how to assess the potential impact of wind turbines on surveillance sensors, *Technical Report EUROCONTROL-GUID-130*, EUROCONTROL.
- Brenner, M., Cazares, S., Cornwall, M. J., Dyson, F., Eardley, D., Horowitz, P., Long, D., Sullivan, J., Vesecky, J. & Weinberger, P. J. (2008). Wind farms and radar, *Technical Report JSR-08-126*, JASON.
- Burgess, D. W., Crum, T. D. & Vogt, R. J. (2008). Impacts of wind farms on WSR-88D radars, *24th International Conference on Interactive Information and Processing Systems for Meteorology, Oceanography, and Hydrology*, American Meteorological Society. Paper 6B.3.
- Butler, M. M. & Johnson, D. A. (2003). Feasibility of mitigating the effects of windfarms on primary radar, *Department of Trade and Industry report ETSU W/14/00623/REP*, Alenia Marconi Systems Limited.
- Cheong, B. L., Palmer, R. & Torres, S. (2011). Automatic wind turbine detection using level-II data, *2nd Conf. on Weather, Climate, and the New Energy Economy*, American Meteorological Society, Seattle, WA. Paper 808.
- Crum, T. & Ciardi, E. (2010). Wind farms and the WSR-88D: An update, *Nexrad Now* 20: 17–22.
- Crum, T., Ciardi, E. & Sandifer, J. (2008). Wind farms: Coming soon to a WSR-88D near you, *Nexrad Now* 18: 1–7.
- Davies, N. G. (1995). Wind farm radar study, *Technical Report ETSU-W-32/00228/49/REP*, Energy Technology Support Unit.
- Department of Defense (2006). The effect of windmill farms on military readiness, *Report to the congressional defense committees*, Office of the Director of Defense Research and Engineering. [Available online at <http://www.defense.gov/pubs/pdfs/windfarmreport.pdf>].
- Donaldson, N., Best, C. & Paterson, B. (2008). Development of wind turbine assessments for Canadian weather radars, *The Fifth European Conference on Radar in Meteorology and Hydrology*, ERAD, Helsinki, Finland.
- Frye, A., Neumann, C. & Müller, A. (2009). The compatibility of wind turbines with radars, *Annual Report 54.7100.035.12*, European Aeronautic Defence and Space Company.
- Gallardo, B., Pérez, F. & Aguado, F. (2008). Characterization approach of wind turbine clutter in the Spanish weather radar network, *The Fifth European Conference on Radar in Meteorology and Hydrology*, ERAD, Helsinki, Finland.
- Gallardo-Hernando, B. & Pérez-Martínez, F. (2009). Wind turbine clutter, in G. Kouemou (ed.), *Radar Technology*, InTech, Croatia.
- Gallardo-Hernando, B., Pérez-Martínez, F. & Aguado-Encabo, F. (2009). Mitigation of wind turbine clutter in C-band weather radars for different rainfall rates, *Proceedings of the 2009 International Radar Conference*, Bordeaux, France.
- Gallardo-Hernando, B., Pérez-Martínez, F. & Aguado-Encabo, F. (2010). Wind turbine clutter detection in scanning weather radar tasks, *The Sixth European Conference on Radar in Meteorology and Hydrology*, ERAD, Sibiu, Romania.

- Global Wind Energy Council (2011). Global wind report – annual market update 2010, *Technical report*, Global Wind Energy Council. [Available online at: http://www.gwec.net/fileadmin/images/Publications/GWEC_annual_market_update_2010_-_2nd_edition_April_2011.pdf].
- Greving, G. & Biermann, W.-D. (2008). Application of the radar cross section RCS for objects on the ground – example of wind turbines, *2008 International Radar Symposium, IRS*, Wroclaw, Poland.
- Greving, G., Biermann, W.-D. & Mundt, R. (2009). RCS – numerical, methodological and conceptual aspects for the analysis of radar distorting objects, *11th International Radar Symposium, IRS*, Vilnius, Lithuania.
- Greving, G. & Malkomes, M. (2006). On the concept of the radar cross section RCS of distorting objects like wind turbines for the weather radar, *The Fourth European Conference on Radar in Meteorology and Hydrology, ERAD*, Barcelona, Spain, pp. 333–336.
- Greving, G. & Malkomes, M. (2008). Weather radar and wind turbines – theoretical and numerical analysis of the shadowing effects and mitigation concepts, *The Fifth European Conference on Radar in Meteorology and Hydrology, ERAD*, Helsinki, Finland.
- Haase, G., Johnson, D. & Eriksson, K.-Å. (2010). Analyzing the impact of wind turbines on operational weather radar products, *The Sixth European Conference on Radar in Meteorology and Hydrology, ERAD*, Sibiu, Romania, pp. 276–281.
- Hafner, S., Reitter, R. & Seltmann, J. (2004). Developments in the DWD radarnetwork, *The Third European Conference on Radar in Meteorology and Hydrology, ERAD*, Visby, Sweden, pp. 425–427.
- Hood, K. T., Torres, S. M. & Palmer, R. D. (2009). Automatic detection of wind turbine clutter using doppler spectral features, *34th Conference on Radar Meteorology*, American Meteorological Society, Williamsburg, VA. Paper P10.1.
- Hood, K., Torres, S. & Palmer, R. (2010). Automatic detection of wind turbine clutter for weather radars, *Journal of Atmospheric and Oceanic Technology* 27: 1868–1880.
- Høyev, G. (2007). Electromagnetic shadow effects behind wind turbines, *FFI Report FFI/RAPPORT-2007/00842*, Norwegian Defence Research Establishment. [Available online at <http://rapporter.ffi.no/rapporter/2007/00842.pdf>].
- Hutchinson, G. & Miles, R. (2008). The protection of weather radar networks. the UK experience, *The Fifth European Conference on Radar in Meteorology and Hydrology, ERAD*, Helsinki, Finland.
- Isom, B. M., Palmer, R. D., Secrest, G. S., Rhoton, R. D., L., D. S. T., Allmon, Reed, J., Crum, T. & Vogt, R. (2009). Detailed observations of wind turbine clutter with scanning weather radars, *Journal of Atmospheric and Oceanic Technology* 26: 894–910.
- Jago, P. & Taylor, N. (2002). Wind turbines and aviation interests — European experience and practice, *Department of Trade and Industry report ETSU W/14/00624/REP*, STASYS Ltd.
- Keeler, R. J. & Serafin, R. J. (2008). Meteorological radar, in M. Skolnik (ed.), *Radar Handbook*, 3 edn, McGraw-Hill.
- Kent, B. M., Hill, K. C., Buterbaugh, A., Zelinski, G., Hawley, R., Cravens, L., Tri-Van, Vogel, C. & Coveyou, T. (2008). Dynamic radar cross section and radar Doppler measurements of commercial general electric windmill power turbines part 1: Predicted and measured radar signatures, *IEEE Antennas Propagation Magazine* 50: 211–219.
- Kong, F., Zhang, Y., Palmer, R. & Bai, Y. (2011). Wind turbine radar signature characterization by laboratory measurements, *Radar Conference (RADAR)*, IEEE.

- Lemmon, J. J., Carroll, J. E., Sanders, F. H. & Turner, D. (2008). Assessment of the effects of wind turbines on air traffic control radars, *NTIA Technical Report TR-08-454*, US Department of Commerce, National Telecommunications & Information Administration.
- Manwell, J., McGowan, J. & Rogers, A. (2009). *Wind Energy Explained: Theory, Design and Application*, 2 edn, John Wiley & Sons, Ltd.
- Michelson, D. B., Andersson, T., Koistinen, J., Collier, C. G., Riedl, J., Szturc, J., Gjertsen, U., Nielsen, A. & Overgaard, S. (2000). BALTEX radar data centre products and their methodologies, *RMK 90*, Swedish Meteorological and Hydrological Institute.
- Nai, F., Palmer, R. & Torres, S. (2011). Wind turbine clutter mitigation using range-Doppler domain signal processing method, *27th Conf. on Interactive Information and Processing Systems*, American Meteorological Society, Seattle, WA. Paper 9.4.
- Ohs, R. R., Skidmore, G. J. & Bedrosian, G. (2010). Modeling the effects of wind turbines on radar returns, *The 2010 Military Communications Conference*, MILCOM, San Jose, CA, pp. 272–276.
- OPERA (2010). Statement of the OPERA group on the cohabitation between weather radars and wind turbines, [Available online at http://www.knmi.nl/opera/opera3/OPERA_2010_14_Statement_on_weather_radars_and_wind_turbines.pdf].
- Ousbäck, J.-O. (1999). Försvaret och vindkraften. Huvudstudie radar, *Slutrappport 99-2936/L*, Försvarets forskningsanstalt (FOA). In Swedish.
- Poupart, G. J. (2003). Wind farms impact on radar aviation interests, *Final Report FES W/14/00614/00/REP, DTI PUB URN 03/1294*, QinetiQ.
- Price, T. J. (2005). James Blyth—Britains first modern wind power pioneer, *Wind Engineering* 29(3): 191–200.
- RABC & CanWEA (2007). Technical information and guidelines of the assessment of the potential impact of wind turbines on radiocommunication, radar and seismoacoustic systems, *Technical report*, Radio Advisory Board and Canadian Wind Energy Association.
- Rashid, L. & Brown, A. (2010). Partial treatment of wind turbine blades with radar absorbing materials (RAM) for RCS reduction, *Proceedings of the Fourth European Conference on Antennas and Propagation*, EuCAP, Barcelona, Spain.
- Seltmann, J. & Lang, P. (2009). Impact of wind turbines on radar measurements and tracking processes. Internal study commissioned by TI.
- Sengupta, D. L. (1984). Electromagnetic interference effects of wind turbines, *The Working Committee on EMI*, International Energy Association, Copenhagen, Denmark.
- Sengupta, D. L. & Senior, T. B. A. (1979). Electromagnetic interference to television reception caused by horizontal axis windmills, *Proceedings of the IEEE* 67: 1133–1142.
- Senior, T. B. L., Sengupta, D. L. & Ferris, J. E. (1977). TV and FM interference by windmills, *Technical Report E(11-1)-2846*, Energy Research and Development Administration.
- Shepard, D. G. (1990). Historical development of the windmill, *Contractor Report 4337 DOE/NASA/5266-1*, NASA.
- Skolnik, M. (2008). An introduction and overview of radar, in M. Skolnik (ed.), *Radar Handbook*, 3 edn, McGraw-Hill.
- Sparven Consulting (2001). Wind turbines and radar: Operational experience and mitigation measures, *Technical report*, Sparven Consulting.

- Summers, E. (2001). The operational effects of wind farm developments on ATC procedures for Glasgow Prestwick international airport, *Technical report*, Glasgow Prestwick International Airport.
- Toth, M., Jones, E., Pittman, D. & Solomon, D. (2011). DOW radar observations of wind farms, *Bulletin of the American Meteorological Society* 92(11): 987–995.
- Tristant, P. (2006a). Impact of wind turbines on weather radars band, *Report to WMO, Commission for Basic Systems Steering Group on Radio Frequency Coordination CBS/SG-RFC 2006/Doc. 3.1(6)*, Météo France. [Available online at [http://www.wmo.int/pages/prog/www/TEM/SG-RFC06/Wind turbine vs weather radars.doc](http://www.wmo.int/pages/prog/www/TEM/SG-RFC06/Wind_turbine_vs_weather_radars.doc)].
- Tristant, P. (2006b). Radio frequency threats on meteorological radar operations, *The Fourth European Conference on Radar in Meteorology and Hydrology*, ERAD, Barcelona, Spain.
- Vogt, R. J., Crum, T. D., Greenwood, W., Ciardi, E. J. & Guenther, R. G. (2011). New criteria for evaluating wind turbine impacts on NEXRAD radars, *WINDPOWER 2011*, American Wind Energy Association Conference and Exhibition, Anaheim, CA.
- Vogt, R. J., Crum, T. D., Reed, J. R., Ray, C. A., Chrisman, J. N., Palmer, R. D., Isom, B., Snow, J. T., Burgess, D. W. & Paese, M. S. (2007a). Weather radars and wind farms — working together for mutual benefit, *WINDPOWER 2007*, American Wind Energy Association Conference and Exhibition, Los Angeles, CA.
- Vogt, R. J., Crum, T. D., Sandifer, J. B., Ciardi, E. J. & Guenther, R. G. (2009). A way forward wind farm — weather radar coexistence, *WINDPOWER 2009*, American Wind Energy Association Conference and Exhibition, Seattle, WA.
- Vogt, R. J., Reed, J., Crum, T., Snow, J. T., Palmer, R., Isom, B. & Burgess, D. W. (2007b). Impacts of wind farms on WSR-88D operations and policy considerations, *23rd International Conference on Interactive Information and Processing Systems for Meteorology, Oceanography, and Hydrology*, American Meteorological Society, San Antonio, TX. Paper 5B.7.
- Webster, D. M. (2005a). The effects of wind turbine farms on air defence radars, *Technical Report AWC/WAD/72/652/TRIALS*, Air Warfare Centre, Waddington, United Kingdom.
- Webster, D. M. (2005b). The effects of wind turbine farms on ATC radar, *Technical Report AWC/WAD/72/665/TRIALS*, Air Warfare Centre, Waddington, United Kingdom.
- WMO (2010). Commission for instruments and methods of observation, *Fifteenth session WMO-No.1046*, World Meteorological Organization. [Available online at http://www.wmo.int/pages/prog/www/CIMO/CIMO15-WMO1064/1064_en.pdf].
- Woodcroft, B. (1851). *The Pneumatics of Hero of Alexandria from the original Greek*, Taylor Walton and Maberly, London. [Available online at <http://www.history.rochester.edu/steam/hero/>].
- Wright, D. T. & Eng, C. (1992). Effects of wind turbines on UHF television reception, *Fifteenth session BBC RD 1992/7*, BBC Research Department.
- Zhang, Y., Huston, A., Palmer, R. D., Albertson, R., Kong, F. & Wang, S. (2011). Using scaled models for wind turbine EM scattering characterization: Techniques and experiments., *IEEE T. Instrumentation and Measurement* 60: 1298–1306.

Part 5

Advanced Techniques for Probing the Ionosphere

Aperture Synthesis Radar Imaging for Upper Atmospheric Research

D. L. Hysell and J. L. Chau

*Earth and Atmospheric Sciences, Cornell University, Ithaca, New York
Jicamarca Radio Observatory, Lima
U.S.A., Peru*

1. Introduction

Radars used for upper-atmospheric applications can be engineered to measure the Doppler spectra of their targets adequately for most intents and purposes, the spectral resolution being limited only by the observing time and the constraints of stationarity. Likewise, they can measure the range to their targets adequately for most intents and purposes, range resolution being limited by system bandwidth, the power budget, and the constraints of stationarity. Problems arise for “overspread” targets, where range and frequency aliasing cannot simultaneously be avoided using pulse-to-pulse methodologies, and more complicated pulse-to-lag or aperiodic pulsing methods are required (see for example (Farley, 1972; Huuskonen et al., 1996; Lehtinen, 1986; Sulzer, 1986; Uppala, 1993)). Important examples of this situation include incoherent scatter experiments (Farley, 1969), observations of meteor head echoes (Chau & Woodman, 2004), and observations of plasma density irregularities present in certain rapid flows, as are found in the equatorial ionosphere during so-called “equatorial spread F ” (Woodman, 2009; Woodman & La Hoz, 1976).

Where capabilities are most limited is in bearing determination and the associated problems of imaging in the directions transverse to the radar beam. Electronic beam steering using phased-array radars offers a means of radar imaging (e.g. Semeter et al. (2009)), but the number of pointing positions that can be used is limited by the incoherent integration time required for each position. If the power budget permits, transmission can be done using a broad beam, and beam forming can be done “after the fact”, such that all pointing positions are examined simultaneously (e.g. Kudeki & Woodman (1990)). Even so, the angular resolution will be limited by the size of the antenna array unless the diffraction limit is removed through numerical deconvolution. The half-power beamwidth of large-aperture radars used for upper atmospheric research is usually of the order of one degree. At ionospheric altitudes, this translates to a transverse resolution of a few to a few tens of kilometers, which may be larger than the scales at which primary plasma waves are excited. The resolution of medium-sized and small research radars with their relatively smaller antenna arrays is relatively poorer still. In applications involving coherent scatter from plasma density irregularities, targets of interest may exhibit backscatter intensities spanning 30 dB or more of dynamic range. For such targets, the 3 dB beamwidth of the antenna is essentially irrelevant, and even targets in the sidelobes of the antenna radiation pattern can contribute to the power assigned to a given

pointing direction. This poses challenges for observing plasma irregularities with important scale sizes of a kilometer or less, which is often the case in ionospheric research.

Aperture synthesis radar imaging utilizes spaced-antenna data to construct true images of the scatterers versus bearing. Some approaches are adaptive, and some achieve “super resolution” by incorporating the effects of diffraction in the analysis. All information about range and Doppler shift can be retained, meaning that the images can be four dimensional, not counting the time axis. As the techniques can synthesize large apertures from small, sparsely-distributed sensors, they may be especially beneficial for small and medium-sized radars, although some of the benefits can only be realized when high signal-to-noise ratios are available.

In this paper, we review the formulation of the radar imaging problem, which is based on concepts and language derived from radar interferometry and radio astronomy. As radar imaging belongs to the class of problems known as inverse problems, some of the ideas from that domain are also reviewed. The factors that govern the resolution achievable in practice will be described, and optimal strategies for sensor placement will be discussed. Error analysis in radar imaging is treated, and some extensions to the basic imaging procedure are outlined. Finally, examples of radar imaging implementations are drawn from upper atmospheric and ionospheric applications. Application in the lower atmosphere exist as well but will not be covered here (Chau & Woodman, 2001; Hassenpflug et al., 2008; Palmer et al., 1998).

2. Imaging problem

The imaging problem has been formulated by (Thompson, 1986), and we follow his treatment below. We consider the far-field problem only and regard the backscatter in a given range gate as a random process constituted by plane waves with sources that are statistically uncorrelated and distributed in space. Imaging data have the form of complex interferometric cross spectra obtained from spaced antenna pairs separated by a vector distance \mathbf{d} . Such “visibility” measurements $V(k\mathbf{d}, f_D)$ are related to the “brightness” distribution $B(\hat{\sigma}, f_D)$, the scattered power density as a function of bearing and Doppler frequency, by

$$V(k\mathbf{d}, f_D) = \int A_N(\hat{\sigma})B(\hat{\sigma}, f_D)e^{jk\mathbf{d}\cdot\hat{\sigma}} d\Omega \quad (1)$$

where k is the wavenumber, f_D is the Doppler frequency, and $\hat{\sigma}$ is a unit vector in the direction of the bearing of interest and where the integration is over all solid angles in the upper half space. As different Doppler spectral components of the data are treated independently, we omit f_D in the formalism that follows.

In (1), A_N is the normalized two-way antenna effective area. In radar imaging, the antennas used for reception are typically much smaller than the antennas used for transmission, and A_N is consequently dominated by the characteristics of the transmitting antenna array. Together, the product $A_N B$ is the effective brightness distribution, B_{eff} , which represents the angular distribution of the received signals. It is this quantity that are interested in recovering from the data, the antenna radiation patterns being known. The radiation pattern need only be treated explicitly when heterogeneous receiving antennas are used (see below).

Equation (1) resembles a Fourier transform between baseline and bearing space. In Cartesian coordinates, (1) is

$$V(kd_x, kd_y, kd_z) = \int \frac{B_{\text{eff}}(\eta, \xi)}{\sqrt{1 - \eta^2 - \xi^2}} e^{jk(d_x\eta + d_y\xi + d_z\sqrt{1 - \eta^2 - \xi^2})} d\eta d\xi \quad (2)$$

where η and ξ are the direction cosines of $\hat{\sigma}$ with respect to the x and y coordinates, which can be oriented arbitrarily. If the field of view of the sky being considered is sufficiently restricted, the radical in the denominator of the integrand can be regarded as a constant. Then, if the spaced receivers are coplanar so that all d_z can be made to be zero, or if the brightness is finite only where η and ψ are small, (2) becomes a two-dimensional Fourier transform. This condition is required for “fringe stopping,” the practice of calibrating the complex gains of the sensor channels so as to remove the fringes in the visibility spectrum of a point calibration target (see phase calibration section below). If B_{eff} is limited by the finite width of the radar radiation pattern, the visibilities can be completely represented by a discrete set of periodic visibility measurements.

3. Inverse methods

Equation (2) shows that the radar imaging problem is actually the linear problem of inverting a Fourier transform. Since visibility data are generally acquired sparsely and incompletely, inversion of (2) by means of a discrete Fourier transform algorithm is generally impossible and would be undesirable in any case unless that algorithm were followed by another one to deconvolve the radar radiation pattern from the resulting image. A number of somewhat ad-hoc approaches to Fourier analysis of sparsely sampled data have emerged, including the Lomb periodogram (Lomb, 1976) and CLEAN (Högbom, 1974), which amount to linear least-squares fitting of representer functions to the data. Performance of such algorithms is uneven and suffers from pathologies inherent in inverse problems that have not been accounted for. The pathologies arise in part from the fact that the measured visibilities contain noise that is not incorporated in (2), which is therefore only an approximation.

As (2) is a linear transformation, the discrete visibility data could be mapped to a discretized version of the brightness distribution through a matrix (G) whose properties would describe the characteristics of the inverse solution. For example, if the column space of G is incomplete, there may be no model brightness that can reproduce the measured visibilities, the problem would be over-determined, and no solution would exist. If the row space of G is incomplete, then it would be possible to add features to the brightness without altering the predicted visibilities, the problem would be under-determined, and solutions to the inverse problem would not be unique.

More generally, both the column and row spaces of G may be incomplete, meaning that the problem is simultaneously over- and under-determined (mixed determined or rank deficient) and that any number of candidate brightness distributions might give acceptably close approximations to the desired solution in terms of a chi-squared prediction error metric. If G is also poorly conditioned, then those candidates could vary widely, and the inversion would be unstable.

Inverse methods are required for mixed-determined, poorly-conditioned problems (see e.g. Aster et al. (2005); Menke (1984); Tarantola (1987) for a review). The strategy generally

amounts to reducing the candidate space of model solutions by imposing a priori information. The information may involve expectations about the variance of the model solution (its “roughness” or regularity) or something more specific, such as the range of admissible numerical values it can assume. A priori information may be incorporated implicitly through the inclusion of damping terms in the inversion algorithm (e.g. damped least squares, Tikhonov regularization, etc.) or explicitly using a Bayesian formalism. Other desirable properties, including model-data consistency, model resolution, and data resolution, can also be optimized.

A common approach to radar imaging is based on the linear constrained minimum variance (LCMV) (or sometimes minimum variance distortionless response (MVDR)) principle and was introduced by Capon (1969). Consider the column vector \mathbf{x} with n entries corresponding to complex voltage samples from n sensors, each at a coordinate \mathbf{r}_n measured from some reference point. Suppose the objective is to discriminate echoes arriving along a wavevector \mathbf{k} from other echoes, noise, interference, etc., by forming an appropriated weighted sum of the voltage samples, $y = \mathbf{w}^\dagger \mathbf{x}$, prior to detection. If the weights are all unity, the signals detected by the sensors from a point source designated by \mathbf{k} would be proportional to the column vector with elements $e^{i\mathbf{k}\cdot\mathbf{r}_1}, e^{i\mathbf{k}\cdot\mathbf{r}_2}, \dots, e^{i\mathbf{k}\cdot\mathbf{r}_n}$. After incoherent integration, the output of the detector with arbitrary weights will be

$$\langle |y|^2 \rangle = \mathbf{w}^\dagger \langle \mathbf{x} \mathbf{x}^\dagger \rangle \mathbf{w} = \mathbf{w}^\dagger R \mathbf{w} \quad (3)$$

where \mathbf{w} is the column vector composed of the weights, R is the signal covariance matrix, constructed from the measured visibilities, and \dagger denotes the complex conjugate transpose.

Capon’s LCMV strategy is to optimize the weights by minimizing the output of the detector while maintaining unity gain in the direction of the point source, viz.

$$\mathbf{w} = \arg \min_{\mathbf{w}, \gamma} : \mathbf{w}^\dagger R \mathbf{w} + \gamma (\mathbf{w}^\dagger \mathbf{e} - 1) \quad (4)$$

where γ is a Lagrange multiplier. The unity-gain constraint is imposed to prevent the trivial solution. The output of the optimal detector using the weights thus found for a given bearing can readily be shown to be $\langle |y|^2 \rangle = (\mathbf{e}^\dagger R^{-1} \mathbf{e})^{-1}$. Imaging then is performed by computing the optimized detector output for all possible bearings. The algorithm is essentially a linear beam former, where nulls are adaptively aligned with sources that are not aligned with the bearing of interest.

Capon’s LCMV method is simple to implement and execute computationally. While there is no provision for error handling in the algorithm posed above, the remedy is to precompute the visibility error covariance matrix (see below) and then transform (3) through similarity transformation into a space where that matrix is the identity. The method is equally well suited for imaging continua and point targets, making it a superior choice for geophysical remote sensing compared to point-targeting algorithms like MUSIC (Schmidt, 1986) or CLEAN. However, there is no guarantee that the brightness distribution found will be consistent with the visibility data within the tolerance of the specified error bounds. The a priori information contained within the method is moreover far from explicit, making it hard to assess its validity.

Any number of alternative imaging methods exist that can minimize or constrain the model prediction error while managing issues arising from the mixed determined or ill conditioned nature of the inverse problem. In the next section of the paper, we turn our attention to the

MaxEnt algorithm, which does not suffer from the limitations of Capon's method and which possesses a number of other desirable features as a consequence of the incorporation of rather informative prior information.

4. MaxEnt formulation

The algorithm described below derives from the MaxEnt spectral analysis method, a Bayesian method based on maximizing the Shannon entropy of the spectrum (Shannon & Weaver, 1949). The method should not be confused with the maximum entropy method (MEM or ME) or similar autoregressive models, with which it has only a remote connection (Jaynes, 1982). MaxEnt was originally applied to spaced-receiver imaging by Gull & Daniell (1978) and also by Wernecke & D'Addario (1977) in a more generalized way. Variations on the technique were published later by Wu (1984), Skilling & Bryan (1984), and Cornwell & Evans (1985). MaxEnt is now applied to a wide array of problems, including natural language processing (NLP), quantum physics, and climate science, to name a few.

Expansive rationales for MaxEnt have been given by Ables (1974), Jaynes (1982; 1985), Skilling (1991), and Daniell (1991), among others. MaxEnt is a Bayesian optimization technique that maximizes the MAP (maximum a posteriori) probability of an image given prior probability rooted in Shannon's entropy and constraints related to the model prediction error, error bounds, image support, certain normalization, and other factors. As entropy admits only globally positive brightness distributions, it rejects the vast majority of candidate solutions in favor of a small, allowable solution subspace. The entropy metric favors uniform images in the absence of contrary information but is nevertheless edge preserving. Moreover, the use of entropy for prior probability makes the algorithm minimally dependent on unknown quantities and, in that sense, bias and artifact free. It is a formalization of Occam's razor.

The algorithm described here is based on one developed by Wilczek & Drapatz (1985) (WD85) for radio astronomy. The real valued brightness will be represented by the symbol $f_i = f(\theta_i)$. The visibility data come from normalized cross-correlation estimates

$$V(k\mathbf{d}_j) = \frac{\langle v_1 v_2^* \rangle}{\sqrt{\langle |v_1|^2 \rangle - N_1} \sqrt{\langle |v_2|^2 \rangle - N_2}} \quad (5)$$

where the $v_{1,2}$ represent quadrature voltage samples from a pair of receivers spaced by a distance \mathbf{d}_j and $N_{1,2}$ are the corresponding noise estimates. The angle brackets above are the expectation. We will represent the visibility data by the symbol $g_j = g(k\mathbf{d}_j)$ and assign two real values for each baseline; one each for the real and imaginary part of (5). Given M interferometry baselines with nonzero length, there will be a total of $2M + 1$ distinct visibility data. (The visibility for the zero baseline is identically unity.)

In matrix notation, (2) may be expressed as

$$g^t + e^t = f^t h \quad (6)$$

where g , e , and f are column vectors and t represents the transpose. Here, the elements of the matrix h (h_{ij}) are the real or the imaginary part of the point spread function $\exp(ik\mathbf{d}_j \cdot \hat{\sigma}_i)$, depending on whether g_j is the real or imaginary part of (5), and e_j represents the corresponding random error arising from the finite number of samples used to estimate (5). The elements f_i of vector f represent the brightness distribution evaluated across the defined image space.

MaxEnt explicitly associates the prior probability of a candidate image with the Shannon entropy of the brightness distribution, $S = -\sum_i f_i \ln(f_i/F)$. Here, $F = f^t \mathbf{1} = g_0 = g(0)$ is the total image brightness (“1” being a column with unity elements). Of all distributions, the uniform one has the highest entropy. In that sense, entropy is a smoothness metric. The entropy of an image is also related to the likelihood of occurrence in a random assembly process. All things being equal, a high-entropy distribution should be favored over a low entropy one. The former represents a broadly accessible class of solutions, while the latter represents an unlikely outcome that should only be considered if the data demand it. Finally, only non-negative brightness distributions are allowed by S . In incorporating it, we reject the vast majority of candidate images in favor of a small subclass of physically obtainable ones.

Neglecting error bounds for the moment, the brightness distribution that maximizes S while being constrained by (6) is the extremum of the functional:

$$E(f(\lambda, L)) = S + (g^t - f^t h)\lambda + L(f^t \mathbf{1} - F) \quad (7)$$

where the λ is a column vector of Lagrange multipliers introduced to enforce the constraints by the principles of variational mechanics and L is another Lagrange multiplier enforcing the normalization of the brightness. Maximizing (7) with respect to the f_i and to L yields a model for the brightness, parametrized by the λ_j :

$$f_i = F \frac{e^{-[h\lambda]_i}}{Z} \quad (8)$$

$$Z = \sum_i e^{-[h\lambda]_i} \quad (9)$$

where we note how Z plays the role of Gibbs’ partition function here.

Statistical errors are accounted for in WD85 by adapting (7) to enforce a constraint on the expectation of χ^2 . The constraint is incorporated with the addition of another Lagrange multiplier (Λ). The constraint regarding the normalization of the brightness is enforced by the form of f resulting from (8) and need not be enforced further.

$$\begin{aligned} E(f(e, \lambda, \Lambda)) &= S + (g^t + e^t - f^t h)\lambda + \Lambda (e^t C e - \Sigma) \\ &= (g^t + e^t)\lambda + F \ln Z + \Lambda (e^t C e - \Sigma) \end{aligned} \quad (10)$$

where the last step was accomplished by substituting (8) and (9) into S . The Σ term constrains the error norm, calculated in terms of theoretical error covariance matrix C , which we take to be diagonal. Rather than finding the brightness with the smallest model prediction error which also has a high entropy, WD85 finds the brightness which deviates from the data in a prescribed way so as to have the highest possible entropy consistent with experimental uncertainties.

Maximizing (10) with respect to the Lagrange multipliers yields $2M + 1$ algebraic equations:

$$g^t + e^t - f^t h = 0 \quad (11)$$

which merely restates (6). Maximizing with respect to the error terms in e yields equations relating them to the elements of λ :

$$\lambda + 2\Lambda C^{-1} e = 0 \quad (12)$$

(no sum implied). Maximizing with respect to Λ yields one more equation relating that term to the others.

$$4\Sigma\Lambda^2 - \lambda^t C\lambda = 0 \quad (13)$$

The resulting system of $2M + 1$ coupled, nonlinear equations for the Lagrange multipliers can be solved numerically. (The algorithm implemented here uses the hybrid method of Powell (1970).) Finally, (8) yields the desired image. The algorithm is robust and converges in practice when provided with data uncontaminated by interference. An analytic form of the required Jacobian matrix can readily be derived from (11).

4.1 Error analysis

Defining ρ_{12} as the normalized cross-correlation of the signals from receivers 1 and 2, an obvious estimator of ρ_{12} is:

$$\hat{\rho}_{12} = \frac{\frac{1}{m} \sum_{i=1}^m v_{1i} v_{2i}^*}{\sqrt{\frac{1}{m} \sum_{i=1}^m |v_{1i}|^2 \frac{1}{m} \sum_{i=1}^m |v_{2i}|^2}} \quad (14)$$

where the numerator and denominator are computed from the same m statistically independent, concurrent samples. The error covariance matrix for interferometric cross-correlation or cross-spectral visibility estimates derived from this estimator was given by Hysell & Chau (2006):

$$\langle e_{r12} e_{r34} \rangle = \Re(\delta^2 + \delta'^2) / 2 \quad (15)$$

$$\langle e_{i12} e_{i34} \rangle = \Re(\delta^2 - \delta'^2) / 2 \quad (16)$$

$$\langle e_{r34} e_{i12} \rangle = \Im(\delta^2 + \delta'^2) / 2 \quad (17)$$

$$\langle e_{r12} e_{i34} \rangle = \Im(\delta'^2 - \delta^2) / 2 \quad (18)$$

where e_{r12} stands for the error in the estimate of the real part of the correlation of the signals from spaced receivers 1 and 2, for example, and where the indices may be repeated depending on the interferometry baselines in question. Also,

$$\begin{aligned} \delta^2 = \frac{1}{m} & \left[\rho_{13} \rho_{24}^* - \frac{1}{2} \rho_{34}^* (\rho_{13} \rho_{23}^* + \rho_{14} \rho_{24}^*) \right. \\ & - \frac{1}{2} \rho_{12} (\rho_{13} \rho_{14}^* + \rho_{23} \rho_{24}^*) \\ & \left. + \frac{1}{4} \rho_{12} \rho_{34}^* (|\rho_{13}|^2 + |\rho_{14}|^2 + |\rho_{23}|^2 + |\rho_{24}|^2) \right] \end{aligned} \quad (19)$$

and

$$\begin{aligned} \delta'^2 = \frac{1}{m} & \left[\rho_{14} \rho_{23}^* - \frac{1}{2} \rho_{34} (\rho_{13} \rho_{23}^* + \rho_{14} \rho_{24}^*) \right. \\ & - \frac{1}{2} \rho_{12} (\rho_{13}^* \rho_{14} + \rho_{23}^* \rho_{24}) \\ & \left. + \frac{1}{4} \rho_{12} \rho_{34} (|\rho_{13}|^2 + |\rho_{14}|^2 + |\rho_{23}|^2 + |\rho_{24}|^2) \right], \end{aligned} \quad (20)$$

ρ_{12} representing the complex correlation of the signals from spaced receivers 1 and 2, for example. In practice, these terms must be based on experimental estimates. The overall stability of error estimators based on data with statistical errors themselves has not been considered.

4.1.1 Added noise

The formulas above were derived in the absence of system noise but can easily be generalized to include noise. The normalized correlation function error covariances for signals in the presence of noise are still given by (19) and (20), only substituting the factor

$$\rho_{Sii} \rightarrow \frac{S + N}{S} \quad (21)$$

wherever correlation terms with repeated indices appear. Here, S and N refer to the signal and noise power, respectively.

On the whole, this analysis shows that the error covariance matrix is diagonally dominant only in cases where either the signal-to-noise ratio or the coherence is small. These limits are seldom applicable to coherent scatter, however. Even the longest interferometry baseline at Jicamarca, nearly 100 wavelengths long, very often exhibits high coherence, and even small, portable coherent scatter radars typically run in the high SNR limit. Since the error covariance is not diagonally dominant in general, neglecting off-diagonal terms misrepresents statistical confidence and could lead to image distortion.

In practice, it is expedient to diagonalize the error covariance matrix computed using the formulas above and to apply the corresponding similarity transformation to forward problem stated in (6) (Hysell & Chau, 2006). We find that the error variances that result fall into two groups with relatively smaller and larger values, respectively. The former correspond roughly to errors associated with measuring interferometric coherence, and the latter to errors associated with interferometric phase.

4.1.2 Error propagation

Error propagation through MaxEnt can be treated as follows (see for example Hysell (2007); Silver et al. (1990)). Using Bayes' theorem, we can cast the MaxEnt optimization problem posed in (10) as one of maximizing the posterior probability of a model image, m , based on visibility data d , which are related linearly through $d = Gm$, in the form

$$p(m|d) \propto e^{S/\Gamma} e^{-\frac{1}{2}d^t C^{-1}d} \quad (22)$$

$$\equiv e^{-E} \quad (23)$$

where the entropy S is the prior probability and the chi-squared model prediction error is transitional probability. The constant Γ weights the two probabilities and must be adjusted according to some criteria. In the variational approach to the optimization problem outlined above, the Lagrange multiplier Λ plays the role of Γ . That variable is controlled by Σ , and so there is always an adjustable free parameter.

Consider small departures δm about the maximum probability (minimum E) solution. In the neighborhood of a maximum, the gradient of the argument E vanishes, and we can always

expand

$$p(m|d) \propto e^{-\frac{1}{2}\delta m^t H \delta m} \quad (24)$$

$$H = \frac{\partial^2 E(m)}{\partial \delta m \partial \delta m}$$

with H the Hessian matrix. Now, (24) has the form of a probability density function (PDF) for normally distributed model errors δm which we maximize through the minimization of E . We can consequently identify the Hessian matrix with the inverse model covariance matrix C_m^{-1} . Taking the necessary derivatives gives the error bounds on the image:

$$C_m^{-1} = G^t C^{-1} G + [\Gamma I m]^{-1} \quad (25)$$

The Γ term in (12) represents the influence of the data on the final MaxEnt model. The greater the influence, the smaller the uncertainties. The other term comes from the entropy prior and ensures that the model variances will be very small where the model values themselves are small. This is obviously significant in view of the importance of suppressing spurious artifacts.

4.2 Extensions

Hysell & Chau (2006) introduced two improvements to WD85 important for upper atmospheric radar research. The first involves incorporating the overall two-way antenna radiation pattern in the imaging analysis. Rather than attempting to remove the two-way pattern from the effective brightness distribution through division, with the attendant conditioning problems, we just acknowledge the influence of the pattern on the effective brightness and modify the entropy metric accordingly to anticipate it. If Shannon's expression favors a uniform brightness distribution, the expression that favors distributions that resemble the beam shape is (Skilling, 1989)

$$S' = - \sum_i f_i \ln(f_i / p_i F)$$

where p_i represents the two-way radiation power pattern. Propagating this expression through the preceding analysis alters only the brightness model:

$$f_i = F p_i \frac{e^{-[h\lambda]_i}}{Z} \quad (26)$$

$$Z = \sum_i p_i e^{-[h\lambda]_i} \quad (27)$$

The remaining formalism is unchanged. The only restriction is that p_i should be positive. In practice, the effect of the modification is to suppress spurious brightness outside in regions where the radiation pattern is depressed.

The second improvement applies when heterogeneous antennas are used for reception. In that case, the p_i in (26) can be made to match the radiation pattern of the transmitting antenna array, which is common to all the received signals. The radiation patterns of the receiving antennas are then explicitly incorporated into the expressions for the effective brightness, B_{eff} , associated with each baseline. In view of (1) or (6), this is done by modifying the point

spread function for the given baseline j such that $h_{ij} \rightarrow h_{ij}\varphi_{1i}\varphi_{2i}$, where $\varphi_{1,2i}$ are the radiation amplitude patterns for the antennas at either end of the baseline. Given the principle of pattern multiplication, characteristics of the radiation pattern common to all the receiving antennas can equally well be incorporated in p_i instead of $\varphi_{1,2i}$.

4.3 Super-resolution

That radar imaging resolution does not need to be diffraction limited can be appreciated by considering coherence (normalized visibility) measurements made with a single interferometry baseline in the high signal-to-noise ratio, high coherence limit. As shown by Farley & Hysell (1996), the mean-squared error for the coherence estimate in this limit is

$$\delta^2 = \frac{1}{m} \left[\frac{N}{S} + \frac{1}{2}\epsilon + \mathcal{O} \left(\epsilon^2, \frac{N^2}{S^2}, \epsilon \frac{N}{S}, \dots \right) \right] \quad (28)$$

where $\epsilon \equiv 1 - |V|^2$, m is the number of statistically independent samples used, and where S and N are the signal and noise powers, respectively. Even given a finite number of samples, the coherence estimate for a highly coherent target can be arbitrarily accurate given a high enough signal-to-noise ratio. This means that the angular width of narrow targets can be measured arbitrarily well, regardless of the baseline spacing, if S/N is sufficiently high. Insofar as imaging, an inverse method that accounts for the effects of diffraction in the forward model (i.e. the point spread function) need not be diffraction limited.

On the basis of information theory pertaining to the rate of information transmission through a noisy channel, Kosarev (1990) investigated the resolution limit for spectral analysis, deriving Shannon's resolution limit:

$$SR = \frac{1}{3} \log_2(1 + S/N) \quad (29)$$

This metric represents the maximum achievable resolution improvement over the diffraction-limited, noise-free case for non-parametric signal processing methods. Kosarev (1990) argued that there is no contradiction between this limit and the Heisenberg uncertainty principle. Kosarev (1990) furthermore performed numerical tests, comparing a spectral recovery algorithm based on maximum likelihood with entropy prior probability. Over the S/N range from 10–50 dB, the algorithm was able to achieve the Shannon limit. At Jicamarca, the longest interferometry baseline is nearly 100 wavelengths long, and the diffraction limited resolution is consequently about 0.5° . In practice, useful resolution at about the 0.1° -level can be obtained with strong backscatter.

4.4 Optimal sensor placement

The placement of sensors (receiving antennas or antenna groups) on the ground is typically constrained by practical consideration. If the sensors are subarrays of a fixed phased array, as in the case of the Jicamarca Radio Observatory in Peru or the MU Radar in Japan, a number of modules set by the number of receivers available will be selected from the total available in such a way as to avoid redundant baselines. To avoid ambiguity, baseline lengths can be selected such that the interferometry sidelobes are not illuminated by the transmitting antenna. Baseline orientations may be selected to accommodate anisotropies in the scatterers. As a rule, uniform sampling of visibility space seems to be conducive to artifact reduction, although there may be good reasons to deviate from it.

Sharif & Kamalabadi (2008) studies the optimal placement of sensors for different remote sensing applications, including aperture synthesis imaging. They considered data inversion through Tikhonov regularization, which is similar to the methodology discussed here except with Gaussian model statistics replacing model entropy as the prior probability. This permitted an entirely linear formulation of the problem. Included in the imaging problem were allowances for constraints on image smoothness and support. Optimization was in terms of minimizing different variations on the model prediction error as well as some detection performance metrics and the informativeness of the sensors with respect to the image (mutual information). Computationally expedient means of performing the different optimizations were also found. Sharif & Kamalabadi (2008) demonstrated that rather different results could be obtained depending on the criteria for which the array was optimized.

There are generally good reasons, however, for confining all of the sensors to a plane if possible. If the antennas are above imperfect earth, then their vertical phase centers may not be well known, but at least they will be identical if the antennas are at the same height and the dielectric constant of the earth is homogeneous. Moreover, with $d_z = 0$ for all interferometry baselines and with the radical in the denominator incorporated into the effective brightness, (2) becomes a two-dimensional Fourier transform. Translations in the brightness consequently map to phase shifts in the visibilities which further map to linear phase progressions of received signals across the aperture plane. This simple relationship can be useful in establishing the absolute phases of signals from different sensors.

4.5 Phase calibration

Sensor phase biases associated with differential cable lengths and other systemic issues must be removed through calibration in order for visibilities to be estimated and inverted. While a number of calibration methods exist, calibration remains one of the most challenging aspects of aperture synthesis imaging in practice (see for example Chau et al. (2008)). The “gold standard” for calibration involves observing point targets with known bearings, i.e. radio stars, and adjusting the complex gains of the receiver channels until the measured visibilities match a model based on the known source locations. However, this is only possible for large-aperture radars with adequate sensitivity, and the infrequency of radio star conjunctions may pose practical problems. Feeding common signals through the entire signal chain is another effective calibration strategy, but this too may be possible only infrequently.

Specular meteor echoes are quasi point-targets that can be observed frequently, even by small radars. While their bearings are not known individually, they can be estimated collectively. If the antenna array lies in a plane, phase biases can be estimated such that the bearings of all meteor echoes are consistent across all interferometry baselines (e.g. Holdsworth et al. (2004)). Corrections to the phase bias estimated can then be made such that the center of gravity of the echoes is aligned with the effective two-way radar radiation pattern, with allowances made for the expected anticipated altitude distribution of the specular meteor echoes. Other radar targets may be used to fine-tune the calibration. For example, that echoes from plasma irregularities arise from the locus of magnetic perpendicularity affords accurate knowledge of their elevation along a given azimuth.

While not widely used in upper atmospheric research, closure phase measurements offer additional information for phase calibration (Cornwall, 1989; Jennison, 1958). The idea is that the sum of the visibility phases from a triad of sensors, calculated for instance using bispectral

(triple-product) analysis, is bias free. If the baseline of the triad are suitably arranged, this can afford some information about sensor phase bias.

A promising class of calibration techniques involves finding the phase biases on the basis of image characteristics through optimization. Uncompensated sensor phase biases tend to degrade images and introduce artifacts that increase the image variance (decrease the smoothness) as well as the overall image entropy. Holding the phase biases of three non-collinear sensors to be arbitrary, the remaining phases could be adjusted to minimize the image entropy, global variance, or some other cost function. Afterward, the phase offsets could be readjusted to “rotate” the artifact-free image into its proper place, taking into account known characteristics of the radar and the target. This optimization can take place outside of the main imaging computation or possibly within it, adopting some of the principles followed by Sharif & Kamalabadi (2008) for optimizing sensor placement. Their smoothness and support metrics, respectively, could be imposed to accomplish the first and second steps of the aforementioned calibration, respectively, only within a unified imaging framework. Since the brightness/visibility mapping is not linear in the phase biases, the procedure would necessarily be iterative.

5. Examples from the upper atmosphere

Here, we present examples of ionospheric phenomena that have been revealed or clarified using aperture synthesis radar imaging. The examples are taken from observations of the Jicamarca Radio Observatory, a 50-MHz phased array radar operated outside Lima, Peru. Aperture synthesis radar imaging was introduced to upper atmospheric research at Jicamarca in 1991 (Kudeki & Sürücü, 1991), and MaxEnt was applied there first five years later (Hysell, 1996). The number of sensors sampled has grown from four to eight in the intervening years. Twelve-sensor experiments are being planned. The longest interferometry baseline available is nearly 100 wavelengths long in the direction perpendicular to the geomagnetic field. A subset of the main antenna array is used for transmission, and a phase taper is applied to broaden the main beam and reduce the sidelobe level. Images are normally computed over a $\approx 13^\circ$ -wide azimuth sector. In practice, only the central part of the sector contains echoes and need be plotted.

At Jicamarca, imaging has mainly been applied to coherent scatter from field-aligned plasma density irregularities. Different varieties of irregularities occupy altitudes between about 95–2500 km at the geomagnetic equator and can be detected by the strong, spectrally narrow radar echoes that arise from them. While imaging is generally performed in two dimensions, the echoes arrive from bearings very close to the locus of perpendicularity to the geomagnetic field, and the images in each range gate can consequently be collapsed into a single dimension. Alternatively, the imaging problem can be formulated in one dimension from the start. Two dimensional images in range and azimuth are produced finally. Sequences of sequential images can also be animated. Imaging in three dimensions has been applied in lower atmospheric applications (Palmer et al., 1998). We have plans to apply it to mesospheric echoes as well.

Images are formed for each Doppler bin, and each image pixel or voxel consequently represents a complete Doppler spectrum. Spectral information is conveyed through color according to the example legend shown in Figure 1. Pixel colors represent the first three moments of the spectrum, with the brightness, hue, and saturation specifying the

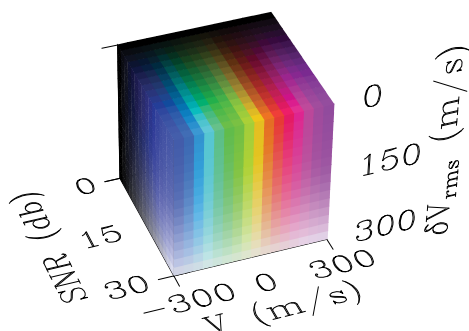


Fig. 1. Scale for interpreting the image pixel coloration. Pixel brightness, hue, and saturation are proportional to the echo signal-to-noise ratio in dB, Doppler shift in m/s, and spectral width in m/s, respectively. Different axes ranges apply to the different images that follow.

signal-to-noise ratio, Doppler shift, and spectral width, respectively. In this example, signal-to-noise ratios between 0–30 dB are represented. The range of Doppler velocities evaluated is controlled by the radar interpulse period and is 300 m/s in this example. By convention, RMS spectral widths between zero and the maximum Doppler shift are portrayed. Incoherent integration times for imaging are typically on the order of a few seconds.

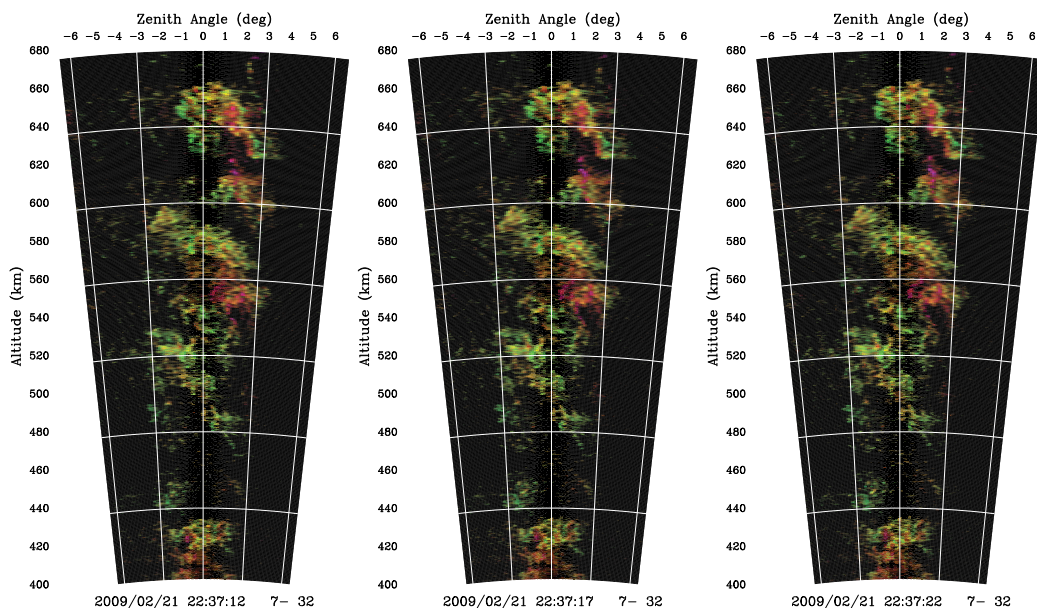


Fig. 2. Coherent scatter from *F* region plasma density irregularities associated with equatorial spread *F* depletions on Feb. 21, 2009. The maximum unaliased Doppler velocity is 300 m/s. Signal-to-noise ratios shown span 7–32 dB.

Figure 2 shows radar images of field-aligned plasma density irregularities associated with equatorial spread *F* (ESF), a nighttime phenomenon characterized by plasma interchange instability and the rapid ascent of depleted plasma wedges from the *F* region bottomside

into the topside. The depletions appear as tilted plumes in the equatorial plane. Here, five plumes between 480–660 km altitude and separated horizontally by about 40 km subtend the Jicamarca beam. No other instrument can provide two-dimensional imagery of ESF plumes with details in the crucial intermediate-scale regime (kilometers to tens of kilometers). Animated sequences of images provide dynamical information with the same detail.

Conventional range-time-intensity (RTI) representations of coherent scatter from ESF demonstrate tremendous qualitative variability from event to event, whereas different plumes generally appear to be similar in radar imagery. RTI plots have been likened to slit-camera images from a “photo finish,” which may produce spurious evidence of horses with three or five legs from time to time, for example (Woodman, 1997). Aperture synthesis imaging reduces instrumental distortion, revealing the salient features of the phenomena under study.

Comparisons with in situ observations of ESF have shown that the bright patches in Figure 2 correspond to localized plasma depletions (Hysell et al., 2009). Moreover, the Doppler shifts of those patches correspond closely to the vertical components of the local $\mathbf{E} \times \mathbf{B}$ drifts. However, since the coherent scatter is spatially intermittent and not homogeneous, the Doppler spectrum representing an entire range gate (without imaging) will not be indicative of the average line-of-sight speed of the plasma in that gate. We know this intuitively; even though the Doppler shifts from active ESF predominantly denote ascent, by mass and by volume, the action of interchange instability is to push ionospheric plasma downward.

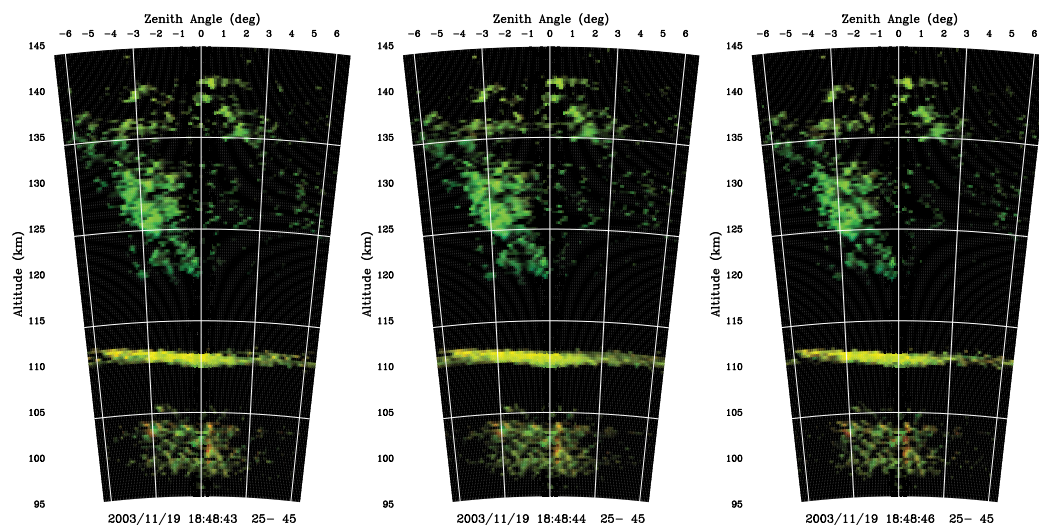


Fig. 3. Coherent scatter from the *E* and valley regions near twilight on Nov. 19, 2003. The maximum unaliased Doppler velocity is 120 m/s. Signal-to-noise ratios shown span 25–45 dB.

Figure 3 shows coherent scatter imagery from around twilight when strong echoes were observed between about 120–145 km in the equatorial valley region (Chau & Hysell, 2004). The echoes do not appear to be directly connected with the equatorial electrojet, which is also producing irregularities below about 112 km here. The valley echoes are organized into waves with wavelengths of about 10 km which propagate downward and westward. The Doppler shifts are mainly positive (downward) and vary systematically with height. It would have

been difficult to distinguish this phenomenon from electrojet-related plasma waves on the basis of RTI information alone.

The cause of the echoes and the underlying source of free energy have not been identified. Recent simulations suggest that the marginal magnetization of the ions at these altitudes is significant and that the irregularities may be due to a class of collisional drift waves. Radar imaging will play a key role in the ongoing investigation of these irregularities.

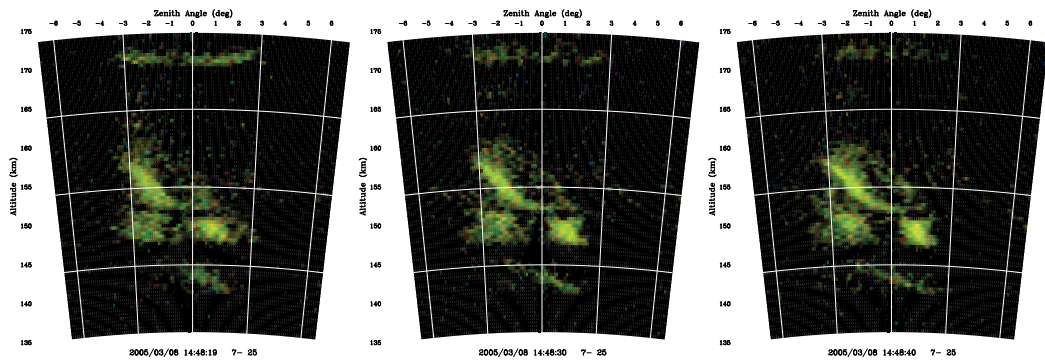


Fig. 4. Radar images of so-called “150-km echoes” observed in the afternoon of Mar. 8, 2005. The maximum unaliased Doppler velocity is 780 m/s. Signal-to-noise ratios shown span 7–25 dB.

Figure 4 presents radar images associated with the so-called “150-km” echoes (Chau, 2004; Kudeki & Fawcett, 1993; Royrvik & Miller, 1981). These daytime echoes are enigmatic, having regular and striking but unexplained patterns in RTI representations. The Doppler shifts of the echoes are known to match the background line-of-sight $E \times B$ drift, implying that dielectric plasma polarization probably does not play a significant role in irregularity production. The spectra, in fact, conform in many ways to expectation for incoherent scatter, both looking perpendicular to B and obliquely to B , and part of the 150-km echoes constitute an ion-line enhancement Chau et al. (2009). The most obvious source of free energy for the irregularities is photoelectron production, which peaks nearby, but the mechanisms at work have yet to be articulated.

The 150-km echoes are weak compared to echoes from other equatorial plasma density irregularities. The image in Figure 4 reveals that the echoes are not homogeneous or beam filling but are instead spatially (and temporally) intermittent. Over time, the spatial organization of the echoes in the imagery varies abruptly in a way that does not convey the sense of proper motion.

Lastly, Figure 5 shows images of large-scale waves in the daytime equatorial electrojet (Farley, 1985; Farley & Balsley, 1973; Kudeki et al., 1982). Coherent scatter from the electrojet is the strongest radar target in the upper atmosphere at VHF frequencies and is produced by a combination of gradient-drift and Farley-Buneman instability. Here, large-scale gradient drift waves with wavelengths of 1–2 km can be seen propagating westward under the influence of a sheared zonal electron $E \times B$ flow associated with a Cowling conductivity. Echoes come from gradient drift wave turbulence and from small-scale, secondary Farley-Buneman waves, with large-telltale Doppler shifts. At night, the flow and the propagation direction reverse, and the wavelength of the dominant large-scale waves increases.

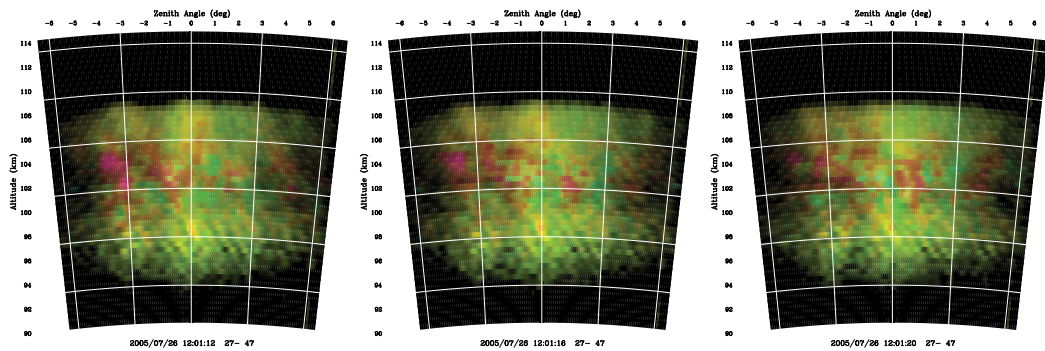


Fig. 5. Coherent scatter from large-scale gradient drift waves in the daytime equatorial electrojet on July 26, 2005. The maximum unaliased Doppler velocity is 600 m/s. Signal-to-noise ratios shown span 27–47 dB.

The dominant wavelength of the waves, their phase speeds, and their dynamical behavior are controlled by a surprisingly complex combination of quasilinear, nonlocal, and nonlinear effects which have been described and simulated by Ronchi et al. (1989) and Hu & Bhattacharjee (1998). Those results could be validated with an unusually high degree of detail using radar imaging experiments (Hysell & Chau, 2002).

6. Summary and future work

Aperture synthesis radar imaging is applied routinely in observations of field-aligned plasma density irregularities at low, middle, and high geomagnetic latitudes, and applications in the lower and middle atmospheres are gradually emerging. Imaging discriminates targets in bearing with resolution limited by the longest interferometry baseline length (rather than by the size of the main antenna) and by the signal-to-noise ratio. It is well suited for heterogeneous sensor arrays with regular or pseudo-random distributions and works alongside other radar modalities like pulse compression and methods for spectral estimation of overspread targets.

We have found the MaxEnt algorithm to be suitable for radar applications in upper atmospheric research. It is an edge-preserving technique, equally applicable to point and continuous targets, and is the embodiment of Occam's razor, suppressing image features for which there is no support in the data. While it was once considered computationally expensive, ongoing improvements in computer performance have made real-time application practical on multi-core systems.

Whereas the example imagery shown above was rendered in two dimensions, imaging is generally performed in three. In the case of scatter from field-aligned plasma density irregularities, information in the direction parallel to the geomagnetic field is limited and is often ignored. However, the magnetic aspect sensitivity of the irregularities, the concentration of the echoes near the locus of perpendicularity, can give insights into the underlying generation mechanism (e.g. Kudeki et al. (1981)). Radar imaging could be used to measure magnetic aspect sensitivity under different conditions in the different regions in the radar field of view. This could be particularly revealing in the auroral electrojet, for example, where different irregularity-producing instabilities may be excited inside, outside, and at the edges of discrete auroral arcs.

An obvious extension of the algorithms described in this paper involves radar imaging of moderately overspread targets, ESF being a good example. Such targets can be investigated using aperiodic or incremental-lag pulses (e.g. Chau et al. (2004); Uppala & Sahr (1994); Virtanen et al. (2009)). This produces temporal lagged-products with nonuniform spacing which can be spectrally analyzed using the same methodologies developed for imaging (Hysell et al., 2008). Moreover, the spatio-temporal lagged products arising from aperiodic aperture synthesis imaging experiments can be analyzed together in one operation, yielding images in range, bearing, and the added dimension of Doppler frequency seamlessly. The total number of distinct lagged products will be given by $N(N - 1)/2$, N being the product of the number of sensors and the number of aperiodic pulses considered at a time. Compromises in spectral and angular resolution will be required if the inverse problem is to remain tractable.

Finally, it has been our observation that the backscatter from ionospheric plasma density irregularities in many contexts tends to be “clumpy” rather than diffuse. This information could be exploited in the inversion scheme if the prior probability function were augmented with a component based on an appropriate model Markov chain. Fully exploiting this information would require processing data from multiple ranges and Doppler frequency bins simultaneously, since the spatial organization occurs equally in bearing, range, and Doppler frequency. That the “clumpy” targets often remain organized for long periods of time suggests that this information should be folded in as well.

7. References

- Ables, J. G. (1974). Maximum entropy spectral analysis, *Astron. Astrophys. Suppl. Ser.* 15: 383.
- Aster, R. C., Borchers, B. & Thurber, C. H. (2005). *Parameter Estimation and Inverse Problems*, Elsevier, New York.
- Capon, J. (1969). High-resolution frequency-wavenumber spectrum analysis, *Proc. IEEE* 57: 1408.
- Chau, J. L. (2004). Unexpected spectral characteristics of VHF radar signals from 150-km region over Jicamarca, *Geophys. Res. Lett.* 31, L23803: doi:10.1029/2004GL021620.
- Chau, J. L. & Hysell, D. L. (2004). High altitude large-scale plasma waves in the equatorial electrojet at twilight, *Ann. Geophys.* 22: 4071.
- Chau, J. L., Hysell, D. L., Kuyeng, K. M. & Galindo, F. (2008). Phase calibration approaches for radar interferometry and imaging configurations: Equatorial spread F results, *Ann. Geophys.* 26: 2333–2343.
- Chau, J. L., Hysell, D. L., Reyes, P. M. & Milla, M. A. (2004). Improved spectral estimations of equatorial spread F echoes at Jicamarca using aperiodic transmitter coding, *J. Atmos. Sol. Terr. Phys.* 66(1543).
- Chau, J. L. & Woodman, R. F. (2001). Three-dimensional coherent radar imaging at Jicamarca: Preliminary results, *J. Atmos. Sol. Terr. Phys.* 63: 253–261.
- Chau, J. L. & Woodman, R. F. (2004). Observations of meteor-head echoes using the Jicamarca 50 MHz radar in interferometer mode, *Atmos. Chem. Phys.* 4.1680-7324/acp: 511–521.
- Chau, J. L., Woodman, R. F., Milla, M. A. & Kudeki, E. (2009). Naturally enhanced ion-line spectra around the equatorial 150-km region, *Ann. Geophys.* 27: 933–942.
- Cornwall, T. J. (1989). The applications of closure phase to astronomical imaging, *Science* 245 (4915): 263–269.
- Cornwell, T. J. & Evans, K. F. (1985). A simple maximum entropy deconvolution algorithm, *Astron. Astrophys.* 143: 77.

- Daniell, G. J. (1991). Of maps and monkeys, in B. Buck & V. A. Macaulay (eds), *Maximum Entropy in Action*, Clarendon, Oxford, chapter 1, pp. 1–18.
- Farley, D. T. (1969). Incoherent scatter correlation function measurements, *Radio Sci.* 4: 935–953.
- Farley, D. T. (1972). Multiple-pulse incoherent-scatter correlation function measurements, *Radio Sci.* 7: 661.
- Farley, D. T. (1985). Theory of equatorial electrojet plasma waves: New developments and current status, *J. Atmos. Terr. Phys.* 47: 729–744.
- Farley, D. T. & Balsley, B. B. (1973). Instabilities in the equatorial electrojet, *J. Geophys. Res.* 78: 227.
- Farley, D. T. & Hysell, D. L. (1996). Radar measurements of very small aspect angles in the equatorial ionosphere, *J. Geophys. Res.* 101: 5177.
- Gull, S. F. & Daniell, G. J. (1978). Image reconstruction from incomplete and noisy data, *Nature* 272: 686.
- Hassenpflug, G., Yamamoto, M., Luce, H. & Fukao, S. (2008). Description and demonstration of the new Middle and Upper atmosphere Radar imaging system: 1-D, 2-D, and 3-D imaging of troposphere and stratosphere,, *Radio Sci.* 43, RS2013: doi:10.1029/2006RS003603.
- Högbom, J. A. (1974). Aperture synthesis with a non-regular distribution of interferometer baselines, *Astron. Astrophys. Supp.* 15: 417–426.
- Holdsworth, D. A., Tsutsumi, M., Reid, I. M., Nakamura, T., T. & Tsuda (2004). Interferometric meteor radar phase calibration, *Radio Sci.* 39, RS5012: doi:10.1029/2003RS003026.
- Hu, S. & Bhattacharjee, A. (1998). Two-dimensional simulations of gradient-drift turbulence in the daytime equatorial electrojet, *J. Geophys. Res.* 103: 20,749.
- Huuskonen, A., Lehtinen, M. S. & Pirttilä, J. (1996). Fractional lags in alternating codes: Improving incoherent scatter measurements by using lag estimates at noninteger multiples of baud length, *Radio Sci.* 31: 245.
- Hysell, D. L. (1996). Radar imaging of equatorial *F* region irregularities with maximum entropy interferometry, *Radio Sci.* 31: 1567.
- Hysell, D. L. (2007). Inverting ionospheric radio occultation measurements using maximum entropy, *Radio Sci.* 42, RS4022: doi:10.1029/2007RS003635.
- Hysell, D. L. & Chau, J. L. (2002). Imaging radar observations and nonlocal theory of large-scale waves in the equatorial electrojet, *Ann. Geophys.* 20: 1167.
- Hysell, D. L. & Chau, J. L. (2006). Optimal aperture synthesis radar imaging, *Radio Sci.* 41: 10.1029/2005RS003383, RS2003.
- Hysell, D. L., Chau, J. L. & Lakshmanan, S. (2008). Improved spectral estimation of equatorial spread *F* through aperiodic pulsing and Bayesian inversion, *Radio Sci.* 43, RS2010: doi:10.1029/2007RS003790.
- Hysell, D. L., Hedden, R. B., Chau, J. L., Galindo, F. R., Roddy, P. A. & Pfaff, R. F. (2009). Comparing *F* region ionospheric irregularity observations from C/NOFS and Jicamarca, *Geophys. Res. Lett.* 36, L00C01: doi:10.1029/2009GL038983.
- Jaynes, E. T. (1982). On the rationale of maximum-entropy methods, *Proc. IEEE* 70: 939.
- Jaynes, E. T. (1985). Where do we go from here?, in C. R. Smith & W. T. Grandy, Jr. (eds), *Maximum-Entropy and Bayesian Methods in Inverse Problems*, D. Reidel, Norwell, Mass., chapter 2, pp. 21–58.

- Jennison, R. C. (1958). A phase sensitive interferometer technique for the measurement of the Fourier transforms of spatial brightness distributions of small angular extent, *Mon. Not. Roy. Astron. Soc.* 118: 276.
- Kosarev, E. L. (1990). Shannon's superresolution limit for signal recovery, *Inverse Problems* 6: 55–76.
- Kudeki, E., Farley, D. T. & Fejer, B. G. (1982). Long wavelength irregularities in the equatorial electrojet, *Geophys. Res. Lett.* 9: 684.
- Kudeki, E. & Fawcett, C. D. (1993). High resolution observations of 150 km echoes at Jicamarca, *Geophys. Res. Lett.* 20: 1987.
- Kudeki, E., Fejer, B. G., Farley, D. T. & Ierkic, H. M. (1981). Interferometer studies of equatorial F region irregularities and drifts, *Geophys. Res. Lett.* 8: 377.
- Kudeki, E. & Sürücü, F. (1991). Radar interferometric imaging of field-aligned plasma irregularities in the equatorial electrojet, *Geophys. Res. Lett.* 18: 41.
- Kudeki, E. & Woodman, R. F. (1990). A post-statistics steering technique for MST radar applications, *Radio Sci.* 25: 591–594.
- Lehtinen, M. S. (1986). Statistical theory of incoherent scatter radar measurements, *Technical Report 86/45*, Eur. Incoherent Scatter Sci. Assoc., Kiruna, Sweden.
- Lomb, N. R. (1976). Least squares frequency analysis of unevenly sampled data, *Astrophys. Space Sci.* 39: 447.
- Menke, W. (1984). *Geophysical Data Analysis: Discrete Inverse Theory*, Academic, New York.
- Palmer, R. D., Gopalam, S., Yu, T. Y. & Fukao, S. (1998). Coherent radar imaging using Capon's method, *Radio Sci.* 33: 1585.
- Powell, M. J. D. (1970). A hybrid method for nonlinear equations, in P. Rabinowitz (ed.), *Numerical Methods for Nonlinear Algebraic Equations*, Gordon and Breach, London, pp. 87–114.
- Ronchi, C., Similon, P. L. & Sudan, R. N. (1989). A nonlocal linear theory of the gradient drift instability in the equatorial electrojet, *J. Geophys. Res.* 94: 1317.
- Royrvik, O. & Miller, K. L. (1981). Nonthermal scattering of radio waves near 150 km above Jicamarca, Peru, *J. Geophys. Res.* 86: 180.
- Schmidt, R. O. (1986). Multiple emitter location and signal parameter estimation, *IEEE Trans. Antennas Propagat.* AP-34: 276–280, March.
- Semeter, J., Butler, T., Heinselman, C., Nicolls, M., Kelly, J. & Hampton, D. (2009). Volumetric imaging of the auroral ionosphere: Initial results from PFISR, *J. Atmos. Sol. Terr. Phys.* 71(6-7): 738–743.
- Shannon, C. E. & Weaver, W. (1949). *The Mathematical Theory of Communication*, Univ. of Ill. Press, Urbana.
- Sharif, B. & Kamalabadi, F. (2008). Optimal sensor array configuration in remote image formation, *IEEE Trans. Image Proc.* 17(2): 155–166.
- Silver, R. N., Sivia, D. S. & Gubernatis, J. E. (1990). Maximum-entropy method for analytic continuation of quantum Monte Carlo data, *Phys. Rev.* 41(4): 2380.
- Skilling, J. (1989). Classic maximum entropy, in J. Skilling (ed.), *Maximum Entropy and Bayesian Methods*, Kluwer Academic Publishers, Dordrecht, pp. 45–52.
- Skilling, J. (1991). Fundamentals of MaxEnt in data analysis, in B. Buck & V. A. Macaulay (eds), *Maximum Entropy in Action*, Clarendon, Oxford, chapter 2, pp. 19–40.
- Skilling, J. & Bryan, R. K. (1984). Maximum entropy image reconstruction: General algorithm, *Mon. Not. R. Astron. Soc.* 211: 111.

- Sulzer, M. P. (1986). A radar technique for high range resolution incoherent scatter autocorrelation function measurements utilizing the full average power of klystron radars, *Radio Sci.* 21: 1033–1040.
- Tarantola, A. (1987). *Inverse Theory*, Elsevier, New York.
- Thompson, A. R. (1986). *Interferometry and Synthesis in Radio Astronomy*, John Wiley, New York.
- Uppala, S. V. (1993). *Aperiodic radar technique for the spectrum estimation of moderately overspread targets*, Master's thesis, University of Washington.
- Uppala, S. V. & Sahr, J. D. (1994). Spectrum estimation moderately overspread radar targets using aperiodic transmitter coding, *Radio Sci.* 29: 611.
- Virtanen, I. I., Viernen, J. & Lehtinen, M. S. (2009). Phase-coded pulse aperiodic transmitter coding, *Ann. Geophys.* 27: 2799–2811.
- Wernecke, S. J. & D'Addario, L. R. (1977). Maximum entropy image reconstruction, *IEEE Trans. Computers* c-26: 351.
- Wilczek, R. & Drapatz, S. (1985). A high accuracy algorithm for maximum entropy image restoration in the case of small data sets, *Astron. Astrophys.* 142: 9.
- Woodman, R. F. (1997). Coherent radar imaging: Signal processing and statistical properties, *Radio Sci.* 32: 2373.
- Woodman, R. F. (2009). Spread F- An old equatorial aeronomy problem finally resolved?, *Ann. Geophys.* 27: 1915–1934.
- Woodman, R. F. & La Hoz, C. (1976). Radar observations of F region equatorial irregularities, *J. Geophys. Res.* 81: 5447–5466.
- Wu, N. (1984). A revised Gull-Daniell algorithm in the maximum entropy method, *Astron. Astrophys.* 139: 555.

Incoherent Scatter Radar — Spectral Signal Model and Ionospheric Applications

Erhan Kudeki¹ and Marco Milla²

¹University of Illinois at Urbana-Champaign

²Jicamarca Radio Observatory, Lima
Peru

1. Introduction

Doppler radars find a widespread use in the estimation of the velocity of discrete *hard-targets* as described elsewhere in this volume. In case of *soft-targets* — collections of vast numbers of weakly scattering elements filling the radar beam — the emphasis typically shifts to collecting the *statistics* of random motions of the scattering elements — i.e., Doppler spectral estimation — from which thermal or turbulent state of the target can be inferred, as appropriate. For instance, in case of a plasma in thermal equilibrium, e.g., the quiescent *ionosphere*, a Doppler radar of sufficient power-aperture-product can detect, in addition to the plasma drift velocities, the densities, temperatures, and even current densities of charged particle populations of the probed plasma — such Doppler radars used in ionospheric research are known as *incoherent scatter radars* (ISR). In this chapter we will provide a simplified description of ISR spectral theories (e.g., Kudeki & Milla, 2011) and also discuss magnetoionic propagation effects pertinent to ionospheric applications of ISR's at low latitudes. A second chapter in this volume focusing on in-beam imaging of soft-targets by Hysell & Chau (2012) is pertinent to non-equilibrium plasmas and complements the topics covered in this article.

The chapter is organized as follows: The working principles of ISR's and the general theory of incoherent scatter spectrum are described in Sections 2 and 3. ISR spectral features in unmagnetized and magnetized plasmas are examined in Sections 4 and 5, respectively. Coulomb collision process operating in magnetized ionosphere is described in Section 6. Effects of Coulomb collisions on particle trajectories and ISR spectra are discussed in Sections 7 and 8. Finally, Section 9 discusses the magnetoionic propagation effects on incoherent scattered radar signals. The chapter ends with a brief summary in Section 10.

2. Working principles of ISR's

The basic physical mechanism underlying the operation of ISR's is *Thomson scattering* of electromagnetic waves by ionospheric free electrons. Thomson scattering refers to the fact that free electrons brought into oscillatory motions by incident radar pulses will re-radiate like Hertzian dipoles at the frequency of the incident field. The total power of scattered fields in an ISR experiment is a resultant of interference effects between re-radiated field components arriving from free electrons occupying the radar field of view. Furthermore the frequency spectrum of incoherent scatter signal is shaped by the same interference effects in addition

to the distribution of random velocities of the electrons in the radar frame of reference in accordance with a two-way Doppler effect.

The “incoherent scatter” concept refers, in essence, to a scattering scenario where each of the Thomson scattering electrons would have statistically independent random motions. The total scattered power would then be reduced to a simple sum (see below) of the return power of individual electrons in the radar field of view treated as hard targets in terms of a standard radar equation, i.e.,

$$P_r = \frac{P_t G_t A_r}{(4\pi r^2)^2} \sigma_e, \quad (1)$$

with *transmitted power* and *gain* P_t and G_t , respectively, effective area A_r of the receiving antenna, radar range r , and backscatter *radar-cross-section* (RCS) of an individual electron, $\sigma_e \equiv 4\pi r_e^2$, where $r_e = e^2(4\pi\epsilon_0 mc^2)^{-1} \approx 2.181 \times 10^{-15}$ m is the *classical electron radius*.

Ionospheric electron motions are not fully independent — i.e., particle trajectories are partially correlated — however, and, as a consequence, the scattered radar power from the ionosphere deviates from such a simple sum in a manner that depends on several factors including the radar frequency, electron and ion temperatures, as well as ambient magnetic field of the ionospheric plasma. This deviation is just one of many manifestations of the correlations — also known as “collective effects” — between ionospheric charge carriers, including the deviation of the Doppler frequency spectrum of the scattered fields from a simple Gaussian shape (of thermal velocity distribution of electrons) implied by the ideal incoherent scatter scenario. It turns out that the “complications” introduced by the collective effects in the Doppler spectrum of this “not-exactly-incoherent-scatter” from the ionosphere amount to a wealth of information that can be extracted from the ISR spectrum given its proper forward model. This model will be described in the following sections.

Historical note: When ISR’s were first proposed (Gordon, 1958), it was expected that ionospheric scattering from free electrons would be fully incoherent. First ISR measurements (Bowles, 1958) showed that not to be the case. Realistic spectral models compatible with the measurements and correlated particle motions were developed subsequently. Rapid theoretical progress took place in the 1960’s, but issues related to ISR response at small magnetic aspect angles were resolved only very recently (e.g., Milla & Kudeki, 2011) as explained in Section 8.

3. From Thomson scatter to the general formulation of ISR spectrum

Since oscillating free electrons radiate like Hertzian dipoles, it can be shown, using elementary antenna theory, that the backscattered field amplitude¹ from an electron at a distance r to a radar antenna is (using phasor notation)

$$E_s = -\frac{r_e}{r} e^{-jk_0 r} E_i = -\frac{r_e}{r} E_0 e^{-j2k_0 r}, \quad (2)$$

where $E_i = E_0 e^{-jk_0 r}$ is the incident field phasor and $k_0 = \omega_0/c$ is the wavenumber of the incident wave with a carrier frequency ω_0 . It follows that a collection of scattering electrons

¹ Since transmitted and scattered fields are co-polarized we can avoid using a vector notation here.

filling a small radar volume ΔV will produce a scattered field²

$$E_s = - \sum_{p=1}^{N_o \Delta V} \frac{r_e}{r_p} E_{op} e^{-j2k_o r_p} \approx - \frac{r_e}{r} E_o \sum_{p=1}^{N_o \Delta V} e^{j\mathbf{k} \cdot \mathbf{r}_p}. \quad (3)$$

Here N_o is the mean density of free electrons within ΔV and the rightmost expression amounts to invoking a plane wave approximation³ of the incident and scattered fields in terms of scatterer position vector \mathbf{r}_p and a Bragg wave vector $\mathbf{k} = -2k_o \hat{r}$ pointing from the center of subvolume ΔV to the location of the radar antenna (assuming a mono-static backscatter radar geometry).

With electrons in (non-relativistic) motion, scattered field phasor (3) turns into

$$E_s(t) = - \frac{r_e}{r} E_o \sum_{p=1}^{N_o \Delta V} e^{j\mathbf{k} \cdot \mathbf{r}_p(t - \frac{r}{c})} \quad (4)$$

including a propagation time delay r/c of the scattered field from the center of volume⁴ ΔV . It then follows that the auto-correlation function (ACF) of the scattered field is

$$\langle E_s^*(t) E_s(t + \tau) \rangle = \frac{r_e^2}{r^2} |E_i|^2 \sum_{p=1}^{N_o \Delta V} \sum_{q=1}^{N_o \Delta V} \langle e^{j\mathbf{k} \cdot [\mathbf{r}_q(t + \tau - \frac{r}{c}) - \mathbf{r}_p(t - \frac{r}{c})]} \rangle, \quad (5)$$

where angular brackets denote an expected value (ensemble average) operation. Using $\langle e^{j\mathbf{k} \cdot [\mathbf{r}_q - \mathbf{r}_p]} \rangle = \langle e^{j\mathbf{k} \cdot \mathbf{r}_q} \rangle \langle e^{-j\mathbf{k} \cdot \mathbf{r}_p} \rangle = 0$ for statistically independent electrons ($p \neq q$), this reduces to

$$\langle E_s^*(t) E_s(t + \tau) \rangle = \frac{r_e^2}{r^2} |E_i|^2 N_o \Delta V \langle e^{j\mathbf{k} \cdot [\mathbf{r}_q(t + \tau - \frac{r}{c}) - \mathbf{r}_q(t - \frac{r}{c})]} \rangle = \frac{r_e^2}{r^2} |E_i|^2 N_o \Delta V \langle e^{j\mathbf{k} \cdot \Delta \mathbf{r}} \rangle \quad (6)$$

with $\Delta \mathbf{r} \equiv \mathbf{r}_q(t + \tau - \frac{r}{c}) - \mathbf{r}_q(t - \frac{r}{c})$ denoting particle displacements over time intervals τ . Only with (6), i.e., only under a strict incoherent scatter scenario, we can obtain

$$\langle |E_s(t)|^2 \rangle = \frac{r_e^2}{r^2} |E_i|^2 N_o \Delta V, \quad (7)$$

a result that implies a total scattered power which is a simple sum over all scatterers individually described by (1).

Collective effects in general invalidate the results (6) and (7) from being directly applicable. Nevertheless the desired spectral model for ionospheric incoherent scatter can be expressed in terms of (6) and (7) after suitable corrections and transformations. To obtain the model let us first re-express (4) as

$$E_s(t) = - \frac{r_e}{r} E_o n_e(\mathbf{k}, t - \frac{r}{c}) \quad (8)$$

² We assume here that ω_o is sufficiently large so that dispersion effects due to plasma density N_o can be neglected (or treated as perturbation effects). Also, multiple scattering is neglected.

³ Justified for $r > 2k_o \Delta V^{2/3} / \pi$, the far-field condition for an antenna of size $\Delta V^{1/3}$.

⁴ ΔV is sufficiently small for electrons to move only an insignificant fraction of the radar wavelength during an interval for light to propagate across ΔV .

in terms of 3D spatial Fourier transform

$$n_e(\mathbf{k}, t) \equiv \sum_{p=1}^{N_0 \Delta V} e^{-j\mathbf{k} \cdot \mathbf{r}_p t} \quad (9)$$

of the *microscopic* density function $n_e(\mathbf{r}, t) = \sum_p \delta(\mathbf{r} - \mathbf{r}_p(t))$ of the electrons⁵ in volume ΔV . The scattered field spectrum for volume ΔV can then be expressed⁶ as

$$\langle |E_s(\omega)|^2 \rangle = \frac{r_e^2}{r^2} |E_i|^2 \langle |n_e(\mathbf{k}, \omega)|^2 \rangle \Delta V \quad (11)$$

in terms of the electron density frequency spectrum

$$\langle |n_e(\mathbf{k}, \omega)|^2 \rangle \equiv \int_{-\infty}^{\infty} d\tau e^{-j\omega\tau} \frac{1}{\Delta V} \langle n_e^*(\mathbf{k}, t - \frac{r}{c}) n_e(\mathbf{k}, t - \frac{r}{c} + \tau) \rangle \quad (12)$$

which simplifies as

$$\langle |n_e(\mathbf{k}, \omega)|^2 \rangle = N_0 \int_{-\infty}^{\infty} d\tau e^{-j\omega\tau} \langle e^{j\mathbf{k} \cdot \Delta \mathbf{r}} \rangle \equiv \langle |n_{te}(\mathbf{k}, \omega)|^2 \rangle \quad (13)$$

for independent electrons. We also have an identical expression $\langle |n_{ti}(\mathbf{k}, \omega)|^2 \rangle$ describing the density spectrum independent ions in the same volume in terms of ion displacements $\Delta \mathbf{r}$.

While neither $\langle |n_{te}(\mathbf{k}, \omega)|^2 \rangle$ nor $\langle |n_{ti}(\mathbf{k}, \omega)|^2 \rangle$ are accurate representations of the density spectra of electrons and ions in a real ionosphere (because of the neglect of collective effects), it turns out that an accurate model for $\langle |n_e(\mathbf{k}, \omega)|^2 \rangle$ can be expressed as a linear combination of $\langle |n_{te}(\mathbf{k}, \omega)|^2 \rangle$ and $\langle |n_{ti}(\mathbf{k}, \omega)|^2 \rangle$ given by

$$\langle |n_e(\mathbf{k}, \omega)|^2 \rangle = \frac{|j\omega\epsilon_0 + \sigma_i|^2 \langle |n_{te}(\mathbf{k}, \omega)|^2 \rangle}{|j\omega\epsilon_0 + \sigma_e + \sigma_i|^2} + \frac{|\sigma_e|^2 \langle |n_{ti}(\mathbf{k}, \omega)|^2 \rangle}{|j\omega\epsilon_0 + \sigma_e + \sigma_i|^2}, \quad (14)$$

where $\sigma_{e,i}$ denote the AC conductivities of electrons and ions in the medium. This result can be derived (e.g., Kuddeki & Milla, 2011) by enforcing charge conservation (i.e., continuity equation) in a plasma carrying quasi-static *macroscopic* currents $\sigma_{e,i} E$ forced by longitudinal polarization fields⁷ E produced by the mismatch of thermally driven electron and ion density fluctuations $n_{te}(\mathbf{k}, t)$ and $n_{ti}(\mathbf{k}, t)$. Furthermore, Nyquist noise theorem (e.g., Callen & Welton, 1951) stipulates that the required conductivities are related to the thermal density spectra via relations

$$\frac{\omega^2}{k^2} e^2 \langle |n_{te,i}(\mathbf{k}, \omega)|^2 \rangle = 2KT_{e,i} \text{Re}\{\sigma_{e,i}(\mathbf{k}, \omega)\}. \quad (15)$$

⁵ Here $\delta(\cdot)$'s denote Dirac's deltas utilized to highlight the trajectories $\mathbf{r}_p(t)$ of individual electrons.

⁶ This expression can be generalized as a soft-target radar equation

$$P_r = \int \int \frac{|E_i|^2 / 2\eta_0}{4\pi r^2} A_r 4\pi r_e^2 \langle |n_e(\mathbf{k}, \omega)|^2 \rangle \frac{d\omega}{2\pi} dV \quad (10)$$

for backscatter ISR's having a scattering volume defined by the beam pattern associated with the effective area function $A_r(\mathbf{r})$.

⁷ Note that it is the response of individual particles to the quasi-static E that produces the mutual correlations in their motions.

And since $\sigma_{e,i}(\mathbf{k}, \omega)$ can be uniquely obtained from $\text{Re}\{\sigma_{e,i}(\mathbf{k}, \omega)\}$ using Kramer-Kronig relations (e.g., Yeh & Liu, 1972), a full blown solution of the modeling problem can be formulated in terms of “single particle correlations” $\langle e^{j\mathbf{k}\cdot\Delta\mathbf{r}} \rangle$ underlying the thermal density spectra $\langle |n_{te}(\mathbf{k}, \omega)|^2 \rangle$ and $\langle |n_{ti}(\mathbf{k}, \omega)|^2 \rangle$.

This general formulation is as follows (see Appendix 2 in Kudeki & Milla, 2011, for a detailed derivation): In terms of a one-sided integral transformation

$$J_s(\omega) \equiv \int_0^\infty d\tau e^{-j\omega\tau} \langle e^{j\mathbf{k}\cdot\Delta\mathbf{r}_s} \rangle, \quad (16)$$

known as *Gordeyev integral* for species s (e or i for the single-ion case), we have

$$\frac{\langle |n_{ts}(\mathbf{k}, \omega)|^2 \rangle}{N_0} = 2\text{Re}\{J_s(\omega_s)\} \quad \text{and} \quad \frac{\sigma_s(\mathbf{k}, \omega)}{j\omega\epsilon_0} = \frac{1 - j\omega_s J_s(\omega_s)}{k^2 h_s^2}, \quad (17)$$

where $\omega_s \equiv \omega - \mathbf{k} \cdot \mathbf{V}_s$ is a Doppler-shifted frequency in the radar frame due to mean velocity \mathbf{V}_s of species s , $h_s \equiv \sqrt{\epsilon_0 K T_s / N_0 e^2}$ is the corresponding Debye length, and the \mathbf{k} - ω spectrum of electron density fluctuations in the equilibrium plasma is given by (14) or its multi-ion generalizations.

The “general framework” of ISR spectral models represented by (16)-(17) and (14) (as well as (10)) takes care of the macrophysics of the incoherent scatter process due to collective effects, while microphysics details of the process remain to be addressed in the specification of single particle ACF’s $\langle e^{j\mathbf{k}\cdot\Delta\mathbf{r}} \rangle$.

4. Single particle ACF’s $\langle e^{j\mathbf{k}\cdot\Delta\mathbf{r}} \rangle$ for un-magnetized plasmas

We have just seen that ISR spectrum of ionospheric plasmas in thermal equilibrium can be specified in terms of single particle ACF’s $\langle e^{j\mathbf{k}\cdot\Delta\mathbf{r}} \rangle$. In general, an ACF $\langle e^{j\mathbf{k}\cdot\Delta\mathbf{r}} \rangle$ can be explicitly computed if the probability distribution function (pdf) $f(\Delta r)$, where Δr is the component of $\Delta\mathbf{r}$ along \mathbf{k} , is known. Alternatively, $\langle e^{j\mathbf{k}\cdot\Delta\mathbf{r}} \rangle$ can also be computed directly given an ensemble of realizations of Δr for a given time delay τ . In either case, pdf’s $f(\Delta r)$ or pertinent sets of Δr data will reflect the dynamics of random particle motions taking place in ionospheric plasmas.

When Δr is a Gaussian random variable with a pdf

$$f(\Delta r) = \frac{e^{-\frac{\Delta r^2}{2\langle\Delta r^2\rangle}}}{\sqrt{2\pi\langle\Delta r^2\rangle}}, \quad (18)$$

the single-particle ACF

$$\langle e^{j\mathbf{k}\cdot\Delta\mathbf{r}} \rangle = \int e^{jk\Delta r} f(\Delta r) d(\Delta r) = e^{-\frac{1}{2}k^2\langle\Delta r^2\rangle} \quad (19)$$

depends on the mean-square displacement $\langle\Delta r^2\rangle$ of the particles. In such cases incoherent scatter modeling problem reduces to finding the appropriate variance expressions $\langle\Delta r^2\rangle$.

In a non-magnetized and collisionless plasma the charge carriers will move along straight line (unperturbed) trajectories with random velocities \mathbf{v} . In that case the displacement vectors will be

$$\Delta\mathbf{r} = \mathbf{v}\tau \quad (20)$$

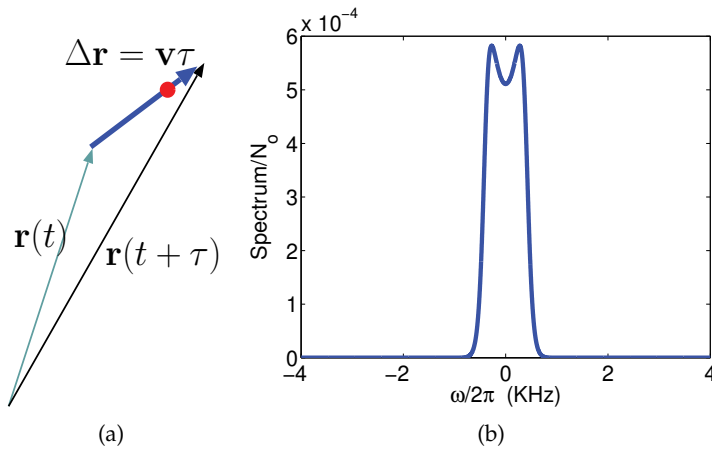


Fig. 1. (a) A cartoon depicting particle displacements Δr in a plasma with straight line charge carrier trajectories, and (b) a sample ISR spectrum for a non-magnetized and collisionless plasma in thermal equilibrium.

over intervals τ . Assuming Maxwellian distributed velocity components v along wavevector \mathbf{k} , we then have Gaussian distributed displacements $\Delta r = v\tau$ with variances

$$\langle \Delta r^2 \rangle = \langle v^2 \rangle \tau^2 = C^2 \tau^2, \quad (21)$$

where $C = \sqrt{KT/m}$ is the thermal speed of the charge carrier. The corresponding single particle ACF is in that case

$$\langle e^{j\mathbf{k} \cdot \Delta \mathbf{r}} \rangle = e^{-\frac{1}{2} k^2 C^2 \tau^2}, \quad (22)$$

which leads (via the general framework equations) to the most basic incoherent scatter spectral model exhibiting double humped shapes as depicted in Figure 6b when (22) is applied to both electrons and ions (with $C = C_e$ and C_i , respectively).

The ACF (22) is also applicable in collisional plasmas so long as the relevant “collision frequency” ν is small compared to the product kC , i.e., $\nu \ll kC$, so that an average particle moves a distance of many wavelengths $\frac{2\pi}{k}$ in between successive collisions. Otherwise, (22) will only be valid until the “first collisions” take place at $\tau \sim \nu^{-1}$. At larger τ , the mean-square displacement $\langle \Delta r^2 \rangle$ as well as the pdf $f(\Delta r)$ will in general depend on the details of the dominant collision process.

Long range Coulomb collisions between charged particles (e.g., electrons and ions) are frequently modeled as a “Brownian motion” process⁸, a procedure which leads (e.g., Kudeki & Milla, 2011) to a Gaussian $f(\Delta r)$ with a variance

$$\langle \Delta r^2 \rangle = \frac{2C^2}{\nu^2} (\nu\tau - 1 + e^{-\nu\tau}). \quad (23)$$

⁸ As discussed in Kudeki & Milla (2011) and here in Section 7, in Brownian motion the position and velocity increments are Gaussian random variables and correspond to stochastic solutions of a first-order Langevin update equation with constant coefficients.

The corresponding single particle ACF is

$$\langle e^{j\mathbf{k}\cdot\Delta\mathbf{r}} \rangle = e^{-\frac{k^2 c^2}{v^2}(\nu\tau - 1 + e^{-\nu\tau})}, \quad (24)$$

having the asymptotic limits (22) as well as

$$\langle e^{j\mathbf{k}\cdot\Delta\mathbf{r}} \rangle = e^{-\frac{k^2 c^2}{v} \tau} \quad (25)$$

for $\nu \ll kC$ and $\nu \gg kC$, respectively. Note that when (25) is applicable, with $\nu \gg kC$, an average particle moves across only a small fraction of a wavelength $\frac{2\pi}{k}$ in between successive collisions. In Coulomb interactions, the time ν^{-1} between “effective collisions” (an accumulated effect of interactions with many collision partners via their microscopic Coulomb fields) can be interpreted as the time interval over which the particle velocity vector rotates by about 90° .

Binary collisions of charge carriers with neutral atoms and molecules — dominant in the lower ionosphere — can be modeled as a Poisson process (Milla & Kudeki, 2009) and treated kinetically using the BGK collision operator (e.g., Dougherty & Farley, 1963). As shown in Milla & Kudeki (2009), in binary collisions with neutrals the mean-squared displacement of charge carriers is still given by (23), but the relevant pdf $f(\Delta r)$ is a Gaussian only for short and long delays τ satisfying $\nu\tau \ll 1$ and $\nu\tau \gg 1$, respectively. At intermediate τ 's the ACF of a collisional plasma dominated by binary collisions will then deviate from (24) and as a result collisional spectra will in general exhibit minor differences between binary and Coulomb collisions except in $\nu \ll kC$ and $\nu \gg kC$ limits (Hagfors & Brockelman, 1971; Milla & Kudeki, 2009).

As the above discussion implies, the single particle ACF in the high collision limit ($\nu \gg kC$) is insensitive to the distinctions between Coulomb and binary collisions and obeys a simple relation (25). In that limit it is fairly straightforward to evaluate the corresponding Gordeyev integrals analytically, and obtain (via the general framework equations) a Lorentzian shaped electron density spectrum (mainly the “ion-line”),

$$\frac{\langle |n_e(\mathbf{k}, \omega)|^2 \rangle}{N_0} \approx \frac{2k^2 D_i}{\omega^2 + (2k^2 D_i)^2}, \quad (26)$$

valid for $kh \ll 1$ (wavelength larger than Debye length), where $D_i \equiv C_i^2/\nu_i = KT_i/m_i\nu_i$ denotes the ion diffusion coefficient in the collisional plasma. This result is pertinent to D-region incoherent scatter observations (see Figure 2) neglecting possible complications due to the presence of negative ions (e.g., Mathews, 1984). Also, from (26) it follows that

$$\langle |n_e(\mathbf{k})|^2 \rangle \equiv \int_{-\infty}^{\infty} \frac{d\omega}{2\pi} \langle |n_e(\mathbf{k}, \omega)|^2 \rangle = \frac{N_0}{2}, \quad (27)$$

which is in fact true in general — i.e., for all types of plasmas with or without collisions and/or DC magnetic field — so long as $T_e = T_i$ and $kh \ll 1$. In view of radar equation (10), this result leads to a well-known volumetric radar cross-section (RCS) formula

$$4\pi r_e^2 \langle |n_e(\mathbf{k})|^2 \rangle = 2\pi r_e^2 N_0 \quad (28)$$

for ISR's that is valid under the same conditions as (27). Hence, RCS measurements with ISR's can provide us with ionospheric mean densities N_0 .

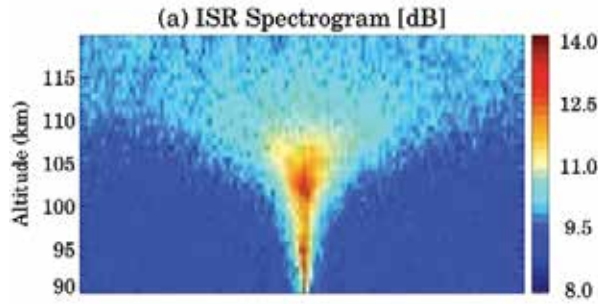


Fig. 2. Collisional D-region spectrograms from Jicamarca Radio Observatory (from Chau & Kudeki, 2006).

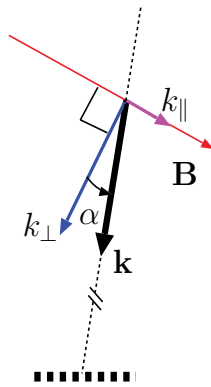


Fig. 3. Backscattering geometry in a magnetized ionosphere parametrized by wavevector components k_{\parallel} and k_{\perp} and aspect angle $\alpha = \tan^{-1}(k_{\parallel}/k_{\perp})$.

5. Incoherent scatter from a magnetized ionosphere

In a magnetized ionosphere with an ambient magnetic field \mathbf{B} , it is convenient to express the scattered wavevector as $\mathbf{k} = \hat{b}k_{\parallel} + \hat{p}k_{\perp}$, where \hat{b} and \hat{p} are orthogonal unit vectors on \mathbf{k} - \mathbf{B} plane which are parallel and perpendicular to \mathbf{B} , respectively, as depicted in Figure 3. We can then express the single particle ACF as

$$\langle e^{j\mathbf{k}\cdot\Delta\mathbf{r}} \rangle = \langle e^{j(k_{\parallel}\Delta r + k_{\perp}\Delta p)} \rangle = \langle e^{jk_{\parallel}\Delta r} \times e^{jk_{\perp}\Delta p} \rangle, \tag{29}$$

where Δr and Δp are particle displacements along unit vectors \hat{b} and \hat{p} . Assuming independent Gaussian random variables Δr and Δp , we can then write

$$\langle e^{j\mathbf{k}\cdot\Delta\mathbf{r}} \rangle = e^{-\frac{1}{2}k_{\parallel}^2\langle\Delta r^2\rangle} \times e^{-\frac{1}{2}k_{\perp}^2\langle\Delta p^2\rangle} \tag{30}$$

in analogy with the non-magnetized case. The assumptions are clearly justified in case of a collisionless ionosphere (or for intervals τ such that $\tau\nu \ll 1$), in which case

$$\langle\Delta r^2\rangle = C^2\tau^2 \tag{31}$$

and, as shown in Kudeki & Milla (2011),

$$\langle\Delta p^2\rangle = \frac{4C^2}{\Omega^2}\sin^2(\Omega\tau/2), \tag{32}$$

where $\Omega \equiv \frac{qB}{m}$ is the particle gyrofrequency. The mean-square displacement (32) which is periodic in τ is can be derived by invoking circular particle orbits with periods $2\pi/\Omega$ and mean radii $\sqrt{2}C/\Omega$ on the plane perpendicular to \mathbf{B} . As a consequence of (31) and (32), ISR spectra in a magnetized but collisionless ionosphere can be derived from the single particle ACF

$$\langle e^{j\mathbf{k}\cdot\Delta\mathbf{r}} \rangle = e^{-\frac{1}{2}k_{\parallel}^2 C^2 \tau^2} \times e^{-\frac{2k_{\perp}^2 C^2}{\Omega^2} \sin^2(\Omega\tau/2)} \quad (33)$$

for electrons and ions.

Note that the ACF (33) becomes periodic and the associated Gordeyev integrals and spectra become singular (expressed in terms of Dirac's deltas) in $k_{\parallel} \rightarrow 0$ limit. Spectral singularities are of course not observed in practice since collisions in a real ionosphere end up limiting the width of single particle ACF's in τ in the limit of small "aspect angles" $\alpha = \tan^{-1}(k_{\parallel}/k_{\perp})$.

Despite the singularities in (33), it turns out that for finite aspect angles α larger than a few degrees, the collisionless result (33) leads us to the most frequently used ISR spectral model at F-region heights. This is true because given a finite k_{\parallel} , the term $e^{-\frac{1}{2}k_{\parallel}^2 C^2 \tau^2}$ in (33) restricts the width of the ACF to a finite value of $\sim (k_{\parallel}C)^{-1}$ even in the absence of collisions (or when collision frequencies are smaller than $k_{\parallel}C$). It can then be shown that for $\tau \ll (k_{\parallel}C)^{-1}$, as well as $\Omega\tau \ll 2\pi$ (easily satisfied by massive ions), the ACF (33) for ions recombines to a simplified form $e^{-\frac{1}{2}k^2 C^2 \tau^2}$ as if the plasma were non-magnetized. Also with finite k_{\parallel} , the ACF (33) for electrons simplifies to $e^{-\frac{1}{2}k^2 \sin^2 \alpha C^2 \tau^2}$, since for the light electrons a condition $k_{\perp}C \ll \Omega$ can be easily invoked to ignore the rightmost exponential in (33) (or even more accurately, replace it with its average value over τ , namely, $1 - \frac{k_{\perp}^2 C^2}{\Omega^2}$). These ion and electron ACF's exhibit similar τ dependencies and lead to similar shaped Gordeyev integrals. The resulting ISR spectra are of the "double humped" type shown in Figure 1b.

6. Modeling the Coulomb collision effects in magnetized plasmas

As we have noted, the form (33) of the single particle ACF indicates that magnetic field effects in ISR response are confined to small aspect angles, which is also the regime where collision effects cannot be neglected (e.g., Farley, 1964; Sulzer & González, 1999; Woodman, 1967) given the non-physical behavior of ACF (33) in $\alpha \rightarrow 0^\circ$ limit.

Historical note: The need to account for the effects of collisions in incoherent scatter theory of ionospheric F-region returns was first pointed out by Farley (1964). Based on a qualitative analysis, Farley recognized that ion Coulomb collisions would be responsible for the lack of O^+ gyroresonance signatures on incoherent scatter observations carried out at 50 MHz at the Jicamarca Radio Observatory located near Lima, Peru. This analysis was later verified by the theoretical work of Woodman (1967) which was based on the simplified Fokker-Planck collision model of Dougherty (1964). Many years later, after the application of modern radar and signal processing techniques to the measurement and analysis of ISR signals (e.g., Kudeki et al., 1999), Sulzer & González (1999) noted that, in addition to ion collisions, electron Coulomb collisions also have an influence on the shape of the ISR spectra at small magnetic aspect angles. Based on a more complex Fokker-Planck Coulomb collision model, Sulzer & González found that the collisional spectrum is narrower (just like the observations of Kudeki et al., 1999) than what the collisionless theory predicts and that the effect of electron collisions extends up to relatively large magnetic aspect angles. Recently, this work has been refined and

extended by Milla & Kudeki (2011). The new procedure allows the calculation of collisional IS spectra at all magnetic aspect angles including the perpendicular-to- \mathbf{B} direction ($\alpha = 0^\circ$) as needed for IS radar applications. In this section, we present the procedure developed by Milla & Kudeki (2011) to model the effects of Coulomb collisions on the incoherent scatter spectrum.

The single-particle ACF $\langle e^{i\mathbf{k}\cdot\Delta\mathbf{r}} \rangle$ in a collisional plasma including a magnetic field can in principle be calculated by taking the spatial Fourier transform of the probability distribution $f(\Delta\mathbf{r}, \tau)$ of the particle displacement $\Delta\mathbf{r}$ appropriate for such plasmas, and $f(\Delta\mathbf{r}, \tau)$ in turn can be derived from the solution $f(\mathbf{r}, t)$ of the Boltzmann kinetic equation with a collision operator, e.g., the Fokker-Planck kinetic equation of Rosenbluth et al. (1957). Although, analytical solutions of simplified versions of the Fokker-Planck kinetic equation are available (e.g., Chandrasekhar, 1943; Dougherty, 1964), determining $f(\Delta\mathbf{r}, \tau)$ would be a daunting task when the full Fokker-Planck equation is considered.

We will discuss here an alternative and more practicable approach that involves Monte Carlo simulations of sample paths $\mathbf{r}(t)$ of particles undergoing Coulomb collisions. A sufficiently large set of samples of trajectories $\mathbf{r}(t)$ can then be used to compute $\langle e^{i\mathbf{k}\cdot\Delta\mathbf{r}} \rangle$ as well as any other statistical function of $\Delta\mathbf{r}$ assuming the random process $\mathbf{r}(t)$ to be ergodic. This alternate procedure requires the availability of a stochastic equation describing how the particle velocities

$$\mathbf{v}(t) \equiv \frac{d\mathbf{r}}{dt} \quad (34)$$

may evolve under the influence of Coulomb collisions.

Assuming that under Coulomb collisions the velocities $\mathbf{v}(t)$ constitute a Markovian random process — meaning that past values of \mathbf{v} would be of no help in predicting its future values if the present value is available — the stochastic evolution equation of $\mathbf{v}(t)$ will be constrained by very strict self-consistency conditions discussed by Gillespie (1996a;b) to acquire the form of a Langevin equation

$$\frac{d\mathbf{v}(t)}{dt} = \mathbf{A}(\mathbf{v}, t) + \bar{\mathbf{C}}(\mathbf{v}, t)\mathbf{W}(t) \quad (35)$$

where vector $\mathbf{A}(\mathbf{v}, t)$ and matrix $\bar{\mathbf{C}}(\mathbf{v}, t)$ consist of arbitrary smooth functions of arguments \mathbf{v} and t , and $\mathbf{W}(t)$ is a random vector having statistically independent Gaussian white noise components

$$W_i(t) = \lim_{\Delta t \rightarrow 0} \mathcal{N}(0, 1/\Delta t), \quad (36)$$

compatible with the requirement that $\langle W_i(t + \tau)W_j(t) \rangle = \delta(\tau)\delta_{ij}$. Here and elsewhere $\mathcal{N}(\mu, \sigma^2)$ denotes the normal random variable with mean μ and variance σ^2 .

A more natural way of expressing the Langevin equation (35) is to cast it in an update form, namely

$$\mathbf{v}(t + \Delta t) = \mathbf{v}(t) + \mathbf{A}(\mathbf{v}, t)\Delta t + \bar{\mathbf{C}}(\mathbf{v}, t)\Delta t^{1/2}\mathbf{U}(t), \quad (37)$$

where Δt is an infinitesimal update interval and $\mathbf{U}(t)$ is a vector composed of independent zero-mean Gaussian random variables with unity variance, i.e., $U_i(t) = \mathcal{N}(0, 1)$.

Note that the Langevin equation describing a Markovian process has the form of Newton's second law of motion, with the terms on the right representing forces per unit mass exerted on plasma particles. Considering the Lorentz force on a charged particle in a magnetized plasma with a constant magnetic field \mathbf{B} , and not violating the strict format of (35), we can modify the equation by adding a term $q\mathbf{v}(t) \times \mathbf{B}/m$ to its right hand side.

Another relevant fact is that a special type of Markov process characterized by a linear $\mathbf{A}(\mathbf{v}, t) = -\beta\mathbf{v}$ and a constant matrix $\bar{\mathbf{C}} = D^{1/2}\bar{\mathbf{I}}$, independent of \mathbf{v} and t , is known as Brownian motion process (e.g., Chandrasekhar, 1942; Uhlenbeck & Ornstein, 1930), which is often invoked in simplified models of collisional plasmas (e.g., Dougherty, 1964; Holod et al., 2005; Woodman, 1967) including our earlier result (24) with $\nu = \beta$. In these models, friction and diffusion coefficients, β and D , are constrained to be related by

$$D = \frac{2KT}{m}\beta \quad (38)$$

for a plasma in thermal equilibrium.

In return for having restricted $\mathbf{v}(t)$ to the space of Markovian processes, we have gained a stochastic evolution equation (35) with a plausible Newtonian interpretation and with the potential of taking us beyond Brownian motion based collision models. Furthermore, the evolution of probability density $f(\mathbf{v}, t)$ of a random variable $\mathbf{v}(t)$ is known to be governed, when $\mathbf{v}(t)$ is Markovian, by the Fokker-Planck kinetic equation having a “friction vector” and “diffusion tensor”

$$\left\langle \frac{\Delta\mathbf{v}}{\Delta t} \right\rangle_c = \mathbf{A}(\mathbf{v}, t), \quad (39)$$

and

$$\left\langle \frac{\Delta\mathbf{v}\Delta\mathbf{v}^T}{\Delta t} \right\rangle_c = \bar{\mathbf{C}}(\mathbf{v}, t)\bar{\mathbf{C}}^T(\mathbf{v}, t), \quad (40)$$

respectively, specified in terms of the input functions of the Langevin equation. This intimate link between the Langevin and Fokker-Planck equations — in describing Markovian processes from two different but mutually compatible perspectives — was first pointed out by Chandrasekhar (1943) and discussed in detail by Gillespie (1996b).

Since the Fokker-Planck friction vector and diffusion tensor for equilibrium plasmas with Coulomb interactions have already been worked out by Rosenbluth et al. (1957) as

$$\left\langle \frac{\Delta\mathbf{v}}{\Delta t} \right\rangle_c = -\beta(v)\mathbf{v} \quad (41)$$

and

$$\left\langle \frac{\Delta\mathbf{v}\Delta\mathbf{v}^T}{\Delta t} \right\rangle_c = \frac{D_{\perp}(v)}{2}\bar{\mathbf{I}} + \left(D_{\parallel}(v) - \frac{D_{\perp}(v)}{2} \right) \frac{\mathbf{v}\mathbf{v}^T}{v^2}, \quad (42)$$

in terms of scalar functions $\beta(v)$, $D_{\parallel}(v)$, $D_{\perp}(v)$, it follows that the Langevin update equation, magnetized version of (37), can be written as

$$\begin{aligned} \mathbf{v}(t + \Delta t) = & \mathbf{v}(t) + \frac{q}{m}\mathbf{v}(t) \times \mathbf{B} \Delta t \\ & - \beta(v)\Delta t \mathbf{v}(t) + \sqrt{D_{\parallel}(v)\Delta t} U_1 \hat{v}_{\parallel} + \sqrt{D_{\perp}(v)\frac{\Delta t}{2}} (U_2 \hat{v}_{\perp 1} + U_3 \hat{v}_{\perp 2}), \end{aligned} \quad (43)$$

where $\hat{v}_{\parallel}(t)$, $\hat{v}_{\perp 1}(t)$, and $\hat{v}_{\perp 2}(t)$ denote an orthogonal set of unit vectors parallel and perpendicular to the particle trajectory and $U_i(t) = \mathcal{N}(0, 1)$ are independent random numbers. For weakly magnetized plasmas of interest here, where Debye lengths are smaller than the mean gyro radii, the “friction coefficient” $\beta(v)$ and velocity-space diffusion

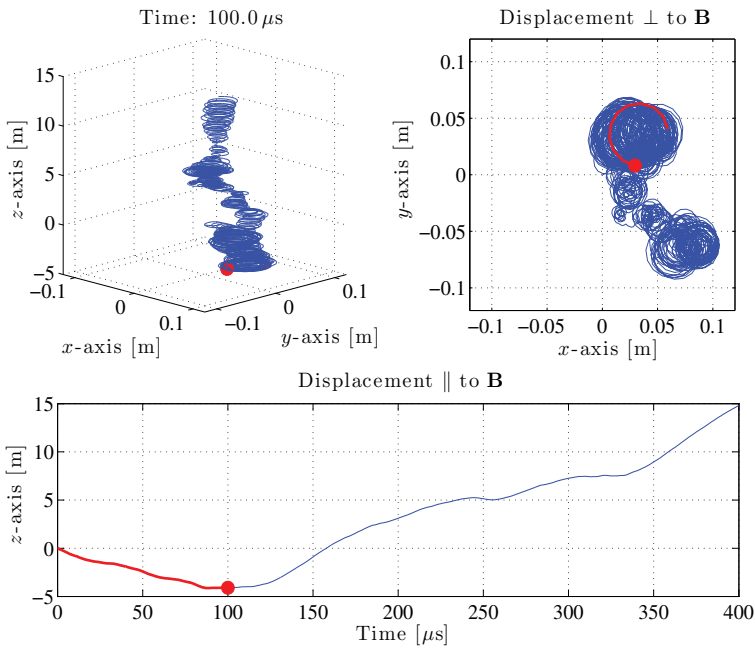


Fig. 4. Sample trajectory of an electron moving in an O+ plasma with density $N_e = 10^{12} \text{ m}^{-3}$, temperatures $T_e = T_i = 1000 \text{ K}$, and an ambient magnetic field $\mathbf{B} = \hat{z}25000 \text{ nT}$. Top left panel depicts the trajectory in 3D space; projection on the x - y plane (the plane perpendicular to \mathbf{B}) is shown on the right; displacements parallel to \mathbf{B} are depicted in the bottom plot (from Milla & Kudeki, 2011).

coefficients $D_{\parallel}(v)$ and $D_{\perp}(v)$ needed in (43) take the forms derived by Rosenbluth et al. (1957) which, for Maxwellian plasmas, have the Spitzer forms given in Milla & Kudeki (2011).

The velocity update equation (43) just described, along with its position counterpart

$$\mathbf{r}(t + \Delta t) = \mathbf{r}(t) + \mathbf{v}(t) \Delta t, \quad (44)$$

constitute our model equations for examining the effects of Coulomb collisions on incoherent scatter response from magnetized plasmas. These equations are used to simulate particle trajectories such as one shown in Figure 4 from which particle displacement statistics needed in ISR spectral models are estimated as explained in Sections 7 and 8.

7. Coulomb collision effects on ion and electron trajectories

7.1 Statistics of ion displacements

First we use the update equations (43) and (44) to simulate sample trajectories $\mathbf{r}(t)$ of an ion, e.g., an oxygen ion O^+ , moving in an ionospheric plasma with suppressed collective interactions but experiencing Coulomb collisions. Using the trajectory data, we can build up the probability distributions of the displacements Δr in directions perpendicular and parallel to the magnetic field for different time delays. Analyzing both distributions (parallel and perpendicular), we notice that their shapes are in essence Gaussian for time delays smaller than the inverse of the corresponding collision frequency. In Figure 5, we show examples

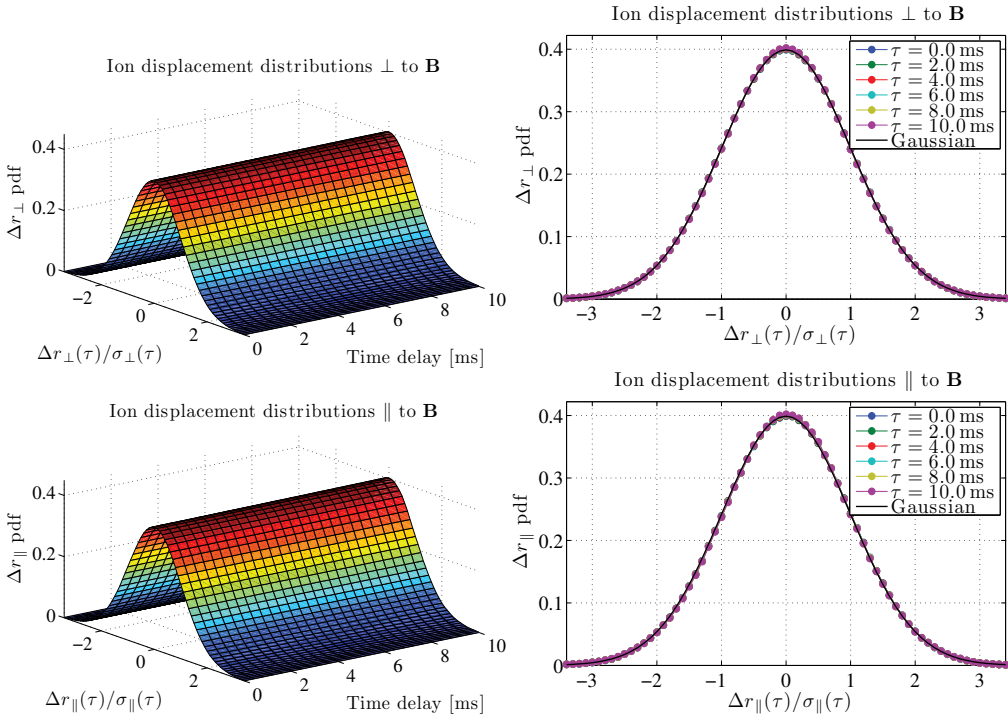


Fig. 5. Probability distributions of the displacements of a test ion in the directions perpendicular (top panels) and parallel (bottom panels) to the magnetic field. On the left, the displacement pdf's are displayed as functions of time delay τ . On the right, sample cuts of the pdf's are compared to a Gaussian distribution. Note that all distributions at all time delays are normalized to unit variance. The displacement axis of each distribution at every delay τ is scaled with the corresponding standard deviation of the simulated displacements (from Milla & Kudeki, 2011).

of the distributions of the ion displacements in the directions perpendicular and parallel to the magnetic field. In this case, we have considered an oxygen ion moving in a plasma with density $N_e = 10^{12} \text{ m}^{-3}$, temperatures $T_e = T_i = 1000 \text{ K}$ and magnetic field $B_0 = 25000 \text{ nT}$. Note that, at every delay τ , the distributions have been normalized to unit variance by scaling the displacement axis of each distribution with the corresponding standard deviation of the particle displacements. On the left panels, the distributions are displayed as functions of τ , while, on the right panels, sample cuts of these distributions are compared to a Gaussian pdf showing good agreement. In addition, we can verify that the components of the vector displacement (i.e., Δr_x , Δr_y , and Δr_z) are mutually uncorrelated.

This analysis implies that ion particle displacements can be represented as jointly Gaussian $\Delta \mathbf{r}$ components, therefore the single-particle ACF takes the form (e.g., Kudeki & Milla, 2011)

$$\langle e^{j\mathbf{k} \cdot \Delta \mathbf{r}} \rangle = e^{-\frac{1}{2}k^2 \sin^2 \alpha \langle \Delta r_{\parallel}^2 \rangle} \times e^{-\frac{1}{2}k^2 \cos^2 \alpha \langle \Delta r_{\perp}^2 \rangle}, \quad (45)$$

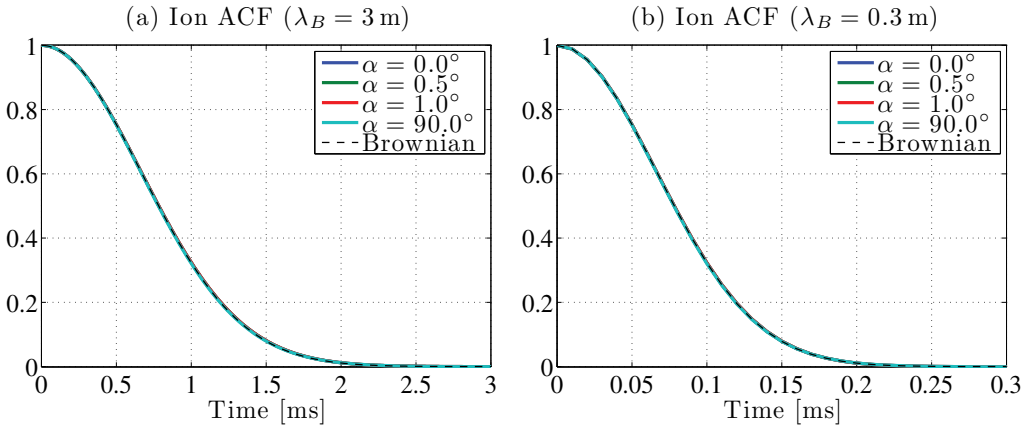


Fig. 6. Simulated single-ion ACF's at different magnetic aspect angles α for two radar Bragg wavelengths: (a) $\lambda_B = 3$ m and (b) $\lambda_B = 0.3$ m. The simulation results (color lines) are compared to theoretical ACF's computed using expression (51) of the Brownian-motion approximation (dashed lines). Note that there is effectively no dependence on aspect angle α (from Milla & Kudeki, 2011).

where, assuming a Brownian-motion process with distinct friction coefficients ν_{\parallel} and ν_{\perp} in the directions parallel and perpendicular to \mathbf{B} , the mean square displacements will vary as

$$\langle \Delta r_{\parallel}^2 \rangle = \frac{2C^2}{\nu_{\parallel}^2} \left(\nu_{\parallel} \tau - 1 + e^{-\nu_{\parallel} \tau} \right) \quad (46)$$

and

$$\langle \Delta r_{\perp}^2 \rangle = \frac{2C^2}{\nu_{\perp}^2 + \Omega^2} \left(\cos(2\gamma) + \nu_{\perp} \tau - e^{-\nu_{\perp} \tau} \cos(\Omega \tau - 2\gamma) \right) \quad (47)$$

in which $\gamma \equiv \tan^{-1}(\nu_{\perp}/\Omega)$, and $C \equiv \sqrt{KT/m}$ and $\Omega \equiv qB/m$ are, respectively, the thermal speed and gyrofrequency of the particles. Furthermore, simulated $\langle \Delta r_{\parallel, \perp}^2 \rangle$ match (46) and (47) with

$$\nu_{\perp} \approx \nu_{\parallel} \approx \nu_{i/i}, \quad (48)$$

where

$$\nu_{i/i} = \frac{N_e e^4 \ln \Lambda_i}{12 \pi^{3/2} \epsilon_0^2 m_i^2 C_i^3} \quad (49)$$

is the Spitzer ion-ion collision frequency given by Callen (2006) and Milla & Kudeki (2011).

The simulations also indicate, in the case of oxygen ions,

$$\langle \Delta r_{\parallel}^2 \rangle \approx \langle \Delta r_{\perp}^2 \rangle \approx C_i^2 \tau^2 \quad (50)$$

for short time delays $\nu_{\parallel} \tau \ll 1$ and $\nu_{\perp} \tau < \Omega_i \tau \ll 1$, in consistency with (46) and (47). Hence (45) simplifies to

$$\langle e^{j\mathbf{k} \cdot \Delta \mathbf{r}_i} \rangle \approx e^{-\frac{1}{2} k^2 C_i^2 \tau^2}. \quad (51)$$

Evidently, the single-oxygen-ion ACF's are essentially the same as in collisionless and non-magnetized plasmas because (a) the ions move by many Bragg wavelengths $\lambda_B = 2\pi/k$

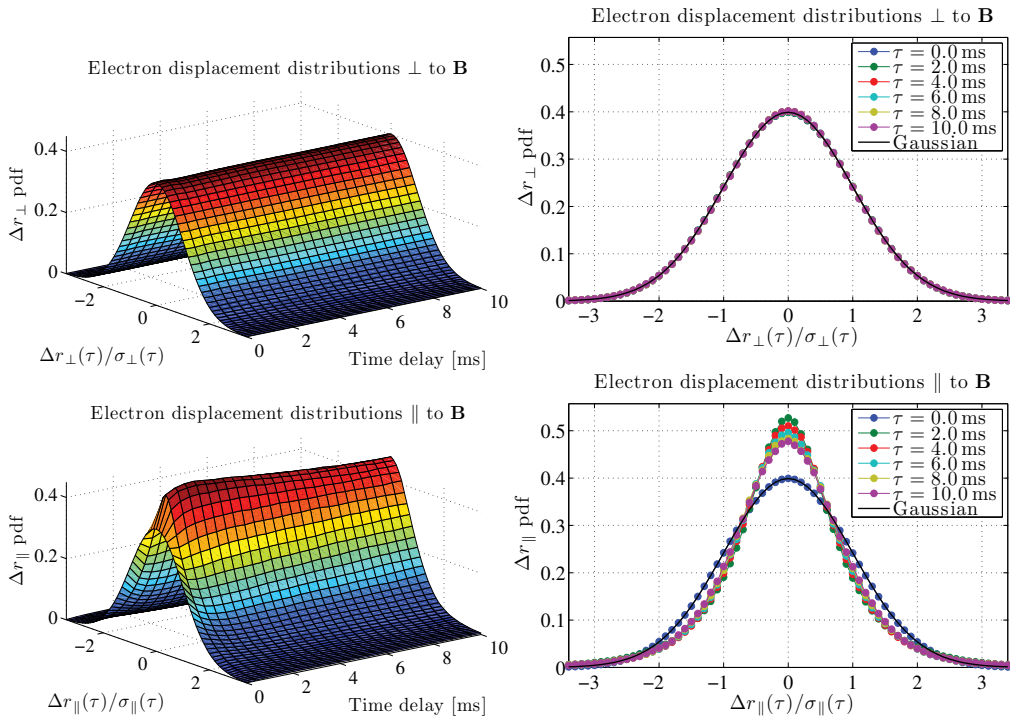


Fig. 7. Same as Figure 5 but for the case of a test electron. All distributions at all time delays are normalized to unit variance. Note that the distributions of the displacements parallel to \mathbf{B} become narrower than a Gaussian distribution (from Milla & Kudeki, 2011).

between successive Spitzer collisions, and (b) the ions are unable to return to within $\lambda_B/2\pi$ of their starting positions after a gyro-period as a consequence of Coulomb collisions. As an upshot, we will be able to handle the ion terms analytically in spectral calculations.

7.2 Statistics of electron displacements

Next, we study the effects of Coulomb collisions on electron trajectories using procedures similar to those applied to ions. In Figure 7, the displacement distributions resulting from an electron moving in an O+ plasma are presented. The top and bottom panels in Figure 7 correspond, respectively, to displacement distributions in perpendicular and parallel directions. On the left, the distributions are displayed as functions of τ , while on the right, sample cuts of the distributions are compared to a Gaussian pdf. As in the ion case, we note that the normalized distributions for perpendicular direction to be invariant with τ and closely match a Gaussian. However, the distributions of parallel displacements change with τ , and the shapes are distinctly non-Gaussian for intermediate values of τ . More specifically, at very small time delays (lower than the inverse of a collision frequency), the distributions are Gaussian, but then, in a few “collision” times, the distribution curves become more “spiky” (positive kurtosis) than a Gaussian. Although, at even longer delays τ the distributions once again relax to a Gaussian shape, it is clear that the electron displacement in the direction parallel to \mathbf{B} is not a Gaussian random variable at all time delays τ .

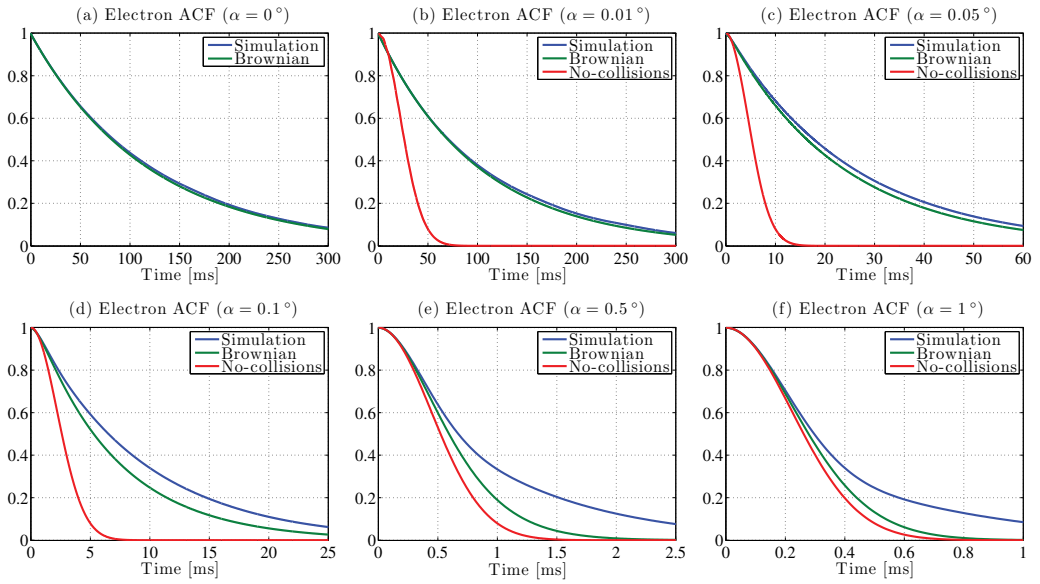


Fig. 8. Electron ACF's for $\lambda_B = 3$ m at different magnetic aspect angles: (a) $\alpha = 0^\circ$, (b) $\alpha = 0.01^\circ$, (c) $\alpha = 0.05^\circ$, (d) $\alpha = 0.1^\circ$, (e) $\alpha = 0.5^\circ$, and (f) $\alpha = 1^\circ$. Note the different time scales used in each plot (from Milla & Kudeki, 2011).

Fitting the simulated $\langle \Delta r_{\parallel, \perp}^2 \rangle$ to match (46) and (47) we find

$$v_{\parallel} \approx v_{e/i} \quad (52)$$

and

$$v_{\perp} \approx v_{e/i} + v_{e/e}, \quad (53)$$

where

$$v_{e/e} = \frac{N_e e^4 \ln \Lambda_e}{12 \pi^{3/2} \epsilon_0^2 m_e^2 C_e^3} \quad (54)$$

and

$$v_{e/i} = \sqrt{2} v_{e/e} = \frac{\sqrt{2} N_e e^4 \ln \Lambda_e}{12 \pi^{3/2} \epsilon_0^2 m_e^2 C_e^3} \quad (55)$$

are the Spitzer electron-electron and electron-ion collision frequencies. However, the Brownian ACF model (45) fails to fit the electron ACF's $\langle e^{j\mathbf{k} \cdot \Delta \mathbf{r}_e} \rangle$ computed with simulated trajectories as shown in Figure 8 for a range of magnetic aspect angles and $\lambda_B = 3$ m. The blue curves correspond to the ACF's calculated with the Fokker-Planck model (simulations), while the green curves are the electron ACF's calculated using expression (45) together with our approximations for v_{\parallel} and v_{\perp} . Additionally, the electron ACF's for a collisionless magnetized plasma are also plotted (red curves). We can see that the Fokker-Planck and the Brownian ACF's matched almost perfectly at $\alpha = 0^\circ$, and also that the agreement is still good at very small magnetic aspect angles (see panels a, b, and c). However, substantial differences between the Brownian and estimated ACF's become evident as the magnetic aspect angle increases (see panels d, e, and f).

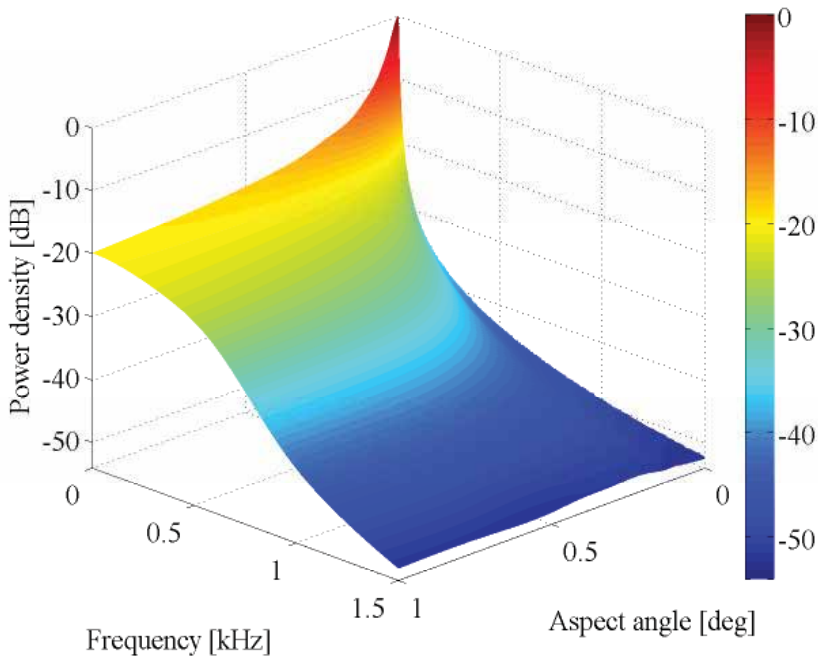


Fig. 9. Collisional incoherent scatter spectra as a function of magnetic aspect angle and Doppler frequency for $\lambda_B = 3$ m (e.g., Jicamarca radar Bragg wavelength). An O+ plasma is considered (from Milla & Kudeki, 2011).

In summary, the single-electron ACF's needed for ISR spectral calculations cannot be obtained from Brownian motion model (45) at small aspect angles. This necessitates the construction of a numerical “library” compiled from Monte Carlo simulations based on the Langevin equation. The fundamental reason for this is the deviation of the electron displacements parallel to \mathbf{B} from Gaussian statistics, despite the fact that displacement variances are well modeled by the Brownian model. Certainly, a non-Gaussian process cannot be fully characterized by a model that specifies its first and second moments only; this is particularly true for the estimation of the characteristic function of the process $\langle e^{j\mathbf{k} \cdot \Delta \mathbf{r}_e} \rangle$ that depends on all the moments of the process distribution.

8. ISR spectrum for the magnetized ionosphere including Coulomb collision effects

The general framework of incoherent scatter theory formulates the spectrum in terms of the Gordoyev integrals or the corresponding single-particle ACFs for each plasma species. As discussed above, in the case of Coulomb collisions, the single-ion ACF can be approximated using the analytical expression (45). However, in the case of the electrons, the approximation of the electron motion as a Brownian process is not accurate, and thus, Monte Carlo calculations were needed to model single-electron ACFs and Gordoyev integrals for different sets of plasma parameters.

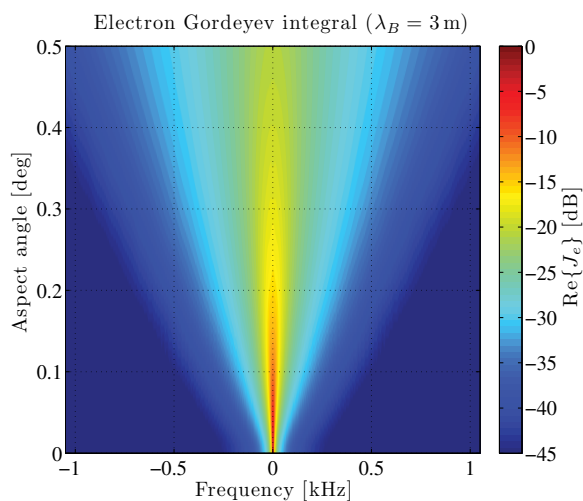


Fig. 10. Electron Gordeyev integral as functions of Doppler frequency and magnetic aspect angle for radar Bragg wavelength $\lambda_B = 3$ m. An O+ plasma with electron density $N_e = 10^{12} \text{ m}^{-3}$, temperatures $T_e = T_i = 1000$ K, and magnetic field $B_0 = 25$ T is considered (from Milla & Kudeki, 2011).

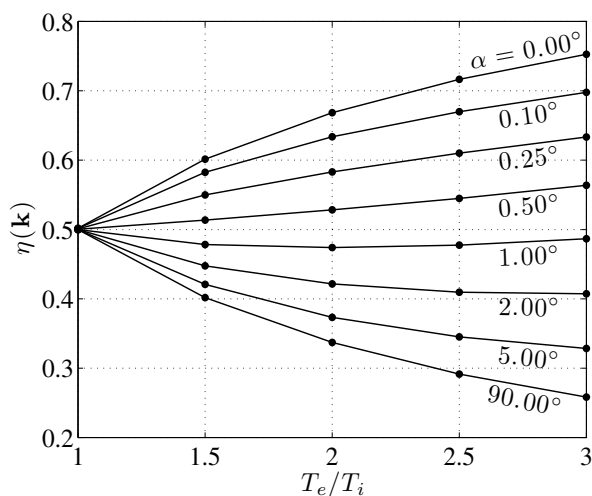


Fig. 11. Electron scattering efficiency factor $\eta(k)$ resulting from the frequency integration of the collisional incoherent scatter spectra as a function of electron-to-ion temperature ratio T_e/T_i and magnetic aspect angle α . An O+ plasma with $N_e = 10^{12} \text{ m}^{-3}$, $T_i = 1000$ K, and $B_0 = 25$ T is considered (from Milla & Kudeki, 2011).

Figure 9 shows a surface plot constructed from full IS spectrum calculations for $\lambda_B = 3$ m (e.g., for the 50 MHz Jicamarca ISR system located near Lima, Peru) using the ACF library constructed with the Monte Carlo procedure for electrons. The underlying electron Gordeyev integral $J_e(\omega)$ is presented in Figure 10 where only $\text{Re}\{J_e(\omega)\} \propto \langle |n_{te}(\mathbf{k}_B, \omega)|^2 \rangle$ is displayed. The plots are displayed as a functions of aspect angle α and Doppler frequency $\omega/2\pi$. In both figures it can be observed how these spectral functions sharpen significantly at small aspect angles. In particular in the case of the IS spectrum, we can see that, just in the range between 0.1° and 0° , the amplitude of the spectrum becomes ten times larger while its bandwidth is reduced by the same factor.

Some interesting features of the IS spectrum caused by collisions can be pointed out. As discussed by Milla & Kudeki (2011), in the absence of collisions, the magnetic field restricts the motion of electrons in the plane perpendicular to \mathbf{B} , forcing them to gyrate perpetually around the same magnetic field lines — this would generate infinite correlation time of the IS signal. With collisions, the electrons manage to diffuse *across* the field lines, and consequently the correlation time of the IS signal becomes finite. As a result, in the limit of $\alpha \rightarrow 0^\circ$, the width of the spectrum becomes proportional to the collision frequency. However, at other magnetic aspect angles, the effects are slightly different. In a few hundredths of a degree from perpendicular to \mathbf{B} ($\alpha > 0.01^\circ$), the shape of the IS spectrum is dominated by electron diffusion *along* the magnetic field lines. As collisions impede the motion of particles, electrons diffuse slower in a collisional plasma than in a collisionless one (where electrons move freely), which implies that the electrons stay closer to their original locations for longer periods of time. As a result, the correlation time of the signal scattered by the electrons also becomes longer, causing the broadening of the IS signal ACF and the associated narrowing of the signal spectrum in this aspect angle regime, as first explained by Sulzer & González (1999).

Spectrum dependence on electron density N_e and temperatures T_e and T_i has been studied by Milla & Kudeki (2011). Since at very small aspect angles the electron Gordeyev integral dominates the shape of the overall incoherent scatter spectrum, Milla & Kudeki (2011) found that in the limit of $\alpha \rightarrow 0^\circ$ the bandwidth of $\text{Re}\{J_e(\omega)\}$, and therefore the IS spectrum, varies according to

$$k^2 C_e^2 \frac{v_\perp}{v_\perp^2 + \Omega_e^2}. \quad (56)$$

Furthermore, using $v_\perp \approx v_{e/i} + v_{e/e}$ from the last section and taking $\Omega_e \gg v_\perp$, we can verify that the bandwidth dependence (56) is proportional to

$$\frac{N_e}{\sqrt{T_e}}. \quad (57)$$

However, as α increases, in a few hundredths of a degree, the dependance of the IS spectral width on N_e and T_e is exchanged, i.e., the bandwidth increases as either the density decreases or the temperature increases. The reason for this is the exchange of roles between particle diffusion in the directions across and along the magnetic field lines. It should be mentioned that collision effects become less significant at even larger aspect angles where the spectrum is shaped by ion dynamics. In that regime, the spectral shapes become independent of N_e as long as $kh_e \ll 1$.

The volumetric radar cross section (RCS) pertinent in ISR applications is given by (e.g., Farley, 1966; Milla & Kudeki, 2006)

$$\sigma_v \equiv 4\pi r_e^2 N_e \eta(\mathbf{k}) \quad (58)$$

where

$$\eta(\mathbf{k}) \equiv \int \frac{d\omega}{2\pi} \frac{\langle |n_e(\mathbf{k}, \omega)|^2 \rangle}{N_e}, \quad (59)$$

is an electron scattering efficiency factor (see Milla & Kudeki, 2006) and depends on the temperature ratio T_e/T_i and magnetic aspect angle α . A plot of this factor obtained from our collisional IS model is shown in Figure 11. As we can observe, if the plasma is in thermal equilibrium (i.e., if $T_e = T_i$), this factor is 1/2 at all angles α and compatible with (28). We can also see that $\eta(\mathbf{k})$ at $\alpha = 0^\circ$ increases in proportion to T_e/T_i . However, at large magnetic aspect angles, the efficiency factor shows a decrease with increasing T_e/T_i . In particular, note that our calculations for $\alpha = 90^\circ$ match the well-known formula $(1 + T_e/T_i)^{-1}$, as expected for moderate values of T_e/T_i and negligible Debye length (e.g., Farley, 1966). Note that for $\alpha \approx 1^\circ$ the factor is approximately independent of T_e/T_i , but otherwise it increases and decreases with the temperature ratio at small and large aspect angles, respectively.

9. Magnetoionic propagation effects on IS spectrum

A radiowave propagating through the ionosphere experiences changes in its polarization caused by the presence of the Earth's magnetic field. In this section, a model for incoherent scatter spectrum and cross-spectrum measurements that takes into account magnetoionic propagation effects is developed.

A mathematical description of radiowave propagation in an inhomogeneous magnetoplasma based on the Appleton-Hartree solution is presented. The resultant wave propagation model is used to formulate a soft-target radar equation in order to account for magnetoionic propagation effects on incoherent scatter spectrum and cross-spectrum models.

9.1 Propagation of electromagnetic waves in a homogeneous magnetoplasma

In the presence of an ambient magnetic field \mathbf{B}_0 , there are two possible and orthogonal modes of electromagnetic wave propagation in a plasma, and, therefore, any propagating field can be represented as the weighted superposition of these characteristic modes. Labeling the modes as ordinary (O) and extraordinary (X), the transverse component of an outgoing (transmitted) electric wave field, at a distance r from the origin, can be written in phasor form as

$$\mathbf{E}^t = A_O \left(\hat{\boldsymbol{\theta}} - j\hat{\boldsymbol{\phi}} \frac{F_O}{Y_L} \right) e^{-jk_o n_{O} r} + A_X \left(\hat{\boldsymbol{\theta}} - j\hat{\boldsymbol{\phi}} \frac{F_X}{Y_L} \right) e^{-jk_o n_X r}, \quad (60)$$

where A_O and A_X are the amplitudes of the O- and X-mode waves with refractive indices

$$n_{O/X}^2 = 1 - \frac{X}{1 - F_{O/X}} \quad (61)$$

specified by Appleton-Hartree equations (e.g., Budden, 1961), in which

$$F_{O/X} = \frac{Y_T^2 \mp \sqrt{Y_T^4 + 4Y_L^2(1-X)^2}}{2(1-X)}, \quad (62)$$

$$X \equiv \frac{\omega_p^2}{\omega^2}, \quad Y_L \equiv \frac{\Omega_e}{\omega} \cos \theta, \quad \text{and} \quad Y_T \equiv \frac{\Omega_e}{\omega} \sin \theta. \quad (63)$$

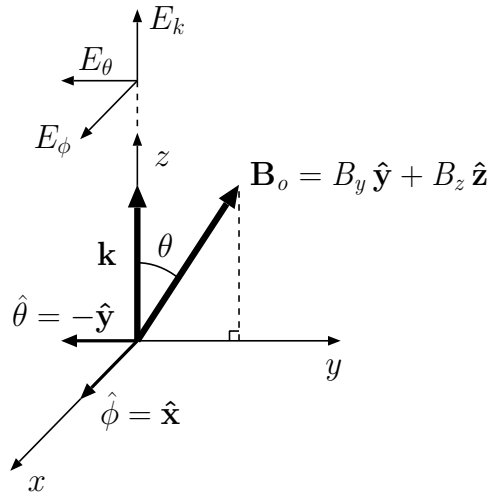


Fig. 12. Coordinate system used for analyzing wave propagation in a magnetized plasma. The magnetic field \mathbf{B}_0 is on the yz -plane and angle θ is measured from \mathbf{B}_0 to the propagation vector \mathbf{k} which is parallel to the $\hat{\mathbf{z}}$ -direction. The wave field \mathbf{E} has three mutually orthogonal components E_k , E_θ , and E_ϕ in directions $\hat{\mathbf{k}} = \hat{\mathbf{z}}$, $\hat{\boldsymbol{\theta}} = -\hat{\mathbf{y}}$, and $\hat{\boldsymbol{\phi}} = \hat{\mathbf{x}}$, respectively. $\hat{\boldsymbol{\theta}}$ is the direction of increasing θ and $\hat{\boldsymbol{\phi}} \equiv \hat{\mathbf{k}} \times \hat{\boldsymbol{\theta}}$.

Above $k_0 = \omega/c$ is the free-space wavenumber, $\omega_p \equiv \sqrt{N_e e^2 / \epsilon_0 m_e}$ and $\Omega_e = eB_0/m_e$ are the plasma- and electron gyro-frequencies, respectively, and θ is the angle measured from the magnetic field vector to the propagation direction $\hat{\mathbf{k}}$. Also, $\hat{\boldsymbol{\theta}}$ and $\hat{\boldsymbol{\phi}}$ are orthogonal unit vectors normal to $\hat{\mathbf{k}}$ as shown in Figure 12.

Note that $F_O F_X = -Y_L^2$ as demanded by the orthogonality of O- and X-mode terms in (60). Thus, $a \equiv \frac{F_O}{Y_L} = -\frac{Y_L}{F_X}$ denotes the axial ratio of elliptically polarized modes in (60), which in turn can be expressed in matrix notation as

$$\begin{bmatrix} E_\theta \\ E_\phi \end{bmatrix} = \begin{bmatrix} e^{-jk_0 n_O r} & e^{-jk_0 n_X r} \\ -jae^{-jk_0 n_O r} & ja^{-1}e^{-jk_0 n_X r} \end{bmatrix} \begin{bmatrix} A_O \\ A_X \end{bmatrix}, \quad (64)$$

where E_θ and E_ϕ are the transverse field components in $\hat{\boldsymbol{\theta}}$ and $\hat{\boldsymbol{\phi}}$ directions. Note that a can take values within the range $0 \leq |a| \leq 1$ and that the limits 0 and 1 correspond to the cases of linearly and circularly polarized propagation modes. Defining $\bar{n} \equiv \frac{n_O + n_X}{2}$ and $\Delta n \equiv \frac{n_O - n_X}{2}$, and considering $E_{\theta,o}$ and $E_{\phi,o}$ as the field components at the origin, the propagating electric field (64) can be recast as

$$\begin{bmatrix} E_\theta \\ E_\phi \end{bmatrix} = \frac{e^{-jk_0 \bar{n} r}}{1 + a^2} \underbrace{\begin{bmatrix} e^{-jk_0 \Delta n r} + a^2 e^{jk_0 \Delta n r} & 2a \sin(k_0 \Delta n r) \\ -2a \sin(k_0 \Delta n r) & a^2 e^{-jk_0 \Delta n r} + e^{jk_0 \Delta n r} \end{bmatrix}}_{\bar{\mathbf{T}}} \begin{bmatrix} E_{\theta,o} \\ E_{\phi,o} \end{bmatrix}, \quad (65)$$

where $\bar{\mathbf{T}}$ is a propagator matrix that maps the fields at the origin into the fields at a distance r . Note that in the case of waves traveling in $-\hat{\mathbf{k}}$ direction, the same matrix $\bar{\mathbf{T}}$ can be used to propagate the fields from a distance r to the origin.

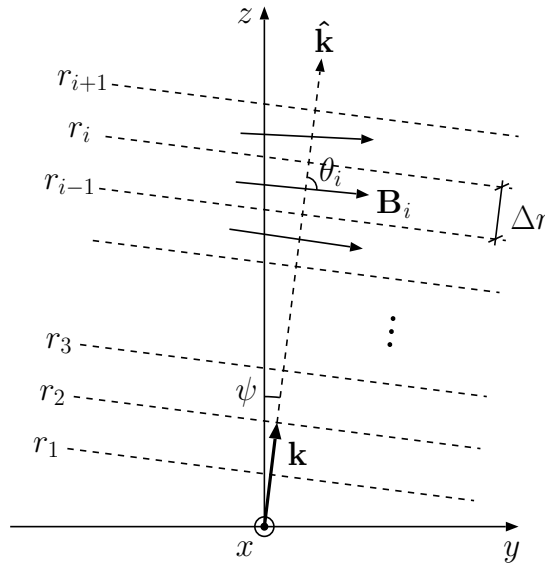


Fig. 13. Geometry of wave propagation in an inhomogeneous magnetized ionosphere.

Using the components of (65), we can re-express the outgoing electric field phasor $E_\theta \hat{\theta} + E_\phi \hat{\phi}$ as

$$\mathbf{E}^t = e^{-jk_o \bar{n}r} \left[e^{-jk_o \Delta nr} \hat{\mathbf{p}}_O \hat{\mathbf{p}}_O^H + e^{jk_o \Delta nr} \hat{\mathbf{p}}_X \hat{\mathbf{p}}_X^H \right] \mathbf{E}_o^t, \tag{66}$$

where \mathbf{E}_o^t is the wave field at the origin,

$$\hat{\mathbf{p}}_O = \frac{\hat{\theta} - ja \hat{\phi}}{\sqrt{1+a^2}} \quad \text{and} \quad \hat{\mathbf{p}}_X = \frac{-ja \hat{\theta} + \hat{\phi}}{\sqrt{1+a^2}} \tag{67}$$

are the orthonormal polarization vectors of the O- and X-mode waves, while $\hat{\mathbf{p}}_O^H$ and $\hat{\mathbf{p}}_X^H$ refer to their conjugate transpose counterparts.

9.2 Model for radiowave propagation in an inhomogeneous ionosphere

A radiowave propagating through an inhomogeneous magnetoplasma will experience refraction and polarization effects. At VHF frequencies, however, ionospheric refraction effects can be considered negligible for most propagation directions because the wave frequency ω exceeds the ionospheric plasma frequency ω_p by a wide margin (i.e., $X \ll 1$). But for the same set of frequencies, polarization changes are still significant despite the fact that the electron gyrofrequency Ω_e is much smaller than the wave frequency ω (i.e., $Y \ll 1$). The reason for this is that the distances traveled by the propagating fields are long enough (hundreds of kilometers) so that phase differences between wave components propagating in distinct modes accumulate to significant and detectable levels. Taking these elements into consideration and noting that, at VHF frequencies, the longitudinal components of the wave fields are negligibly small (as $X \ll 1$ and $Y \ll 1$), waves propagating through the ionosphere can be represented as TEM (transverse electromagnetic) waves.

Consider plane wave propagation in an inhomogeneous magnetized ionosphere in an arbitrary direction $\hat{\mathbf{k}}$. To model the electric field of the propagating wave, we can divide the

ionosphere in slabs of equal width (see Figure 13) perpendicular to the propagation direction such that within each slab the physical plasma parameters (as electron density, electron and ion temperatures, and magnetic field) can be considered constants.⁹ The transverse component of the wave electric field propagates from the bottom to the top of the i -th slab according to (66), that is

$$\mathbf{E}_i = \underbrace{e^{-jk_o\bar{n}_i\Delta r} \left[e^{-jk_o\Delta n_i\Delta r} \hat{\mathbf{p}}_O \hat{\mathbf{p}}_O^H + e^{jk_o\Delta n_i\Delta r} \hat{\mathbf{p}}_X \hat{\mathbf{p}}_X^H \right]}_{\bar{\mathbf{T}}_i} \mathbf{E}_{i-1}, \quad (68)$$

which is the superposition of the O- and X-modes of magnetoionic propagation detailed in the previous section. Above, $\bar{\mathbf{T}}_i$ denotes the i -th propagator matrix (expressed in cartesian coordinates), where $k_o \equiv 2\pi/\lambda_o$ is the free-space wavenumber, Δr is the width of the slab, and where $\bar{n}_i \equiv \frac{n_{O,i} + n_{X,i}}{2}$ and $\Delta n_i \equiv \frac{n_{O,i} - n_{X,i}}{2}$ are the mean and half difference between the refractive indices of the propagation modes in the i -th layer. The polarization vectors of the O- and X-modes are

$$\hat{\mathbf{p}}_O = \frac{\hat{\boldsymbol{\theta}} - ja_i \hat{\boldsymbol{\phi}}}{\sqrt{1 + a_i^2}} \quad \text{and} \quad \hat{\mathbf{p}}_X = \frac{-ja_i \hat{\boldsymbol{\theta}} + \hat{\boldsymbol{\phi}}}{\sqrt{1 + a_i^2}} \quad (69)$$

where $a_i \equiv \frac{F_{O,i}}{Y_{L,i}} = -\frac{Y_{L,i}}{F_{X,i}}$ is the polarization parameter, and $\hat{\boldsymbol{\theta}}_i$ and $\hat{\boldsymbol{\phi}}_i$ are a pair of mutually orthogonal unit vectors perpendicular to $\hat{\mathbf{k}}$ whose directions depend on the relative orientation of the propagation vector \mathbf{k} and the magnetic field \mathbf{B}_i (see Figure 12). Neglecting reflection from the interfaces between slabs, the field components of an upgoing plane wave propagating in the $+\hat{\mathbf{k}}$ direction (at a distance $r_i = i\Delta r$ from the origin) can be computed by the successive application of the propagator matrices; that is,

$$\mathbf{E}_i^u = \bar{\mathbf{T}}_i \cdots \bar{\mathbf{T}}_2 \bar{\mathbf{T}}_1 \mathbf{E}_o^u, \quad (70)$$

where \mathbf{E}_o^u is the wave field at the origin (perpendicular to $\hat{\mathbf{k}}$), and $\bar{\mathbf{T}}_1 \cdots \bar{\mathbf{T}}_i$ are the propagator matrices from the bottom layer to the i -th layer. Similarly, taking advantage of the bidirectionality of the propagator matrices, the field components of a downgoing plane wave propagating in the $-\hat{\mathbf{k}}$ direction (from the i -th layer to the ground) can be written as

$$\mathbf{E}_o^d = \bar{\mathbf{T}}_1 \bar{\mathbf{T}}_2 \cdots \bar{\mathbf{T}}_i \mathbf{E}_i^d, \quad (71)$$

where \mathbf{E}_i^d is the field at the top of the i -th layer.

In radar experiments, the transverse field component of the signal backscattered from a radar range $r_i = i\Delta r$ can be modeled as

$$\mathbf{E}_o^r \propto \kappa_i \underbrace{\bar{\mathbf{T}}_1 \bar{\mathbf{T}}_2 \cdots \bar{\mathbf{T}}_i \bar{\mathbf{T}}_i \cdots \bar{\mathbf{T}}_2 \bar{\mathbf{T}}_1}_{\bar{\mathbf{\Pi}}_i} \mathbf{E}_o^t, \quad (72)$$

where \mathbf{E}_o^t and \mathbf{E}_o^r are the fields transmitted and received by the radar antenna in the $\hat{\mathbf{k}}$ direction. Above, $\bar{\mathbf{\Pi}}_i$ denotes a two-way propagator matrix that accounts for the polarization effects on

⁹ In the ionosphere, electron density and plasma temperatures can be considered to be functions of altitude $f(z)$. Thus, the values of these physical parameters at any position \mathbf{r} from a radar placed at the origin are given by $f(r \cos \psi)$ where r is the radar range and ψ is the zenith angle.

the waves incident on and backscattered from the radar range r_i (upgoing and downgoing waves, respectively). In addition, κ_i is a random variable related to the radar cross section (RCS) of the scatterers at the range r_i (e.g., randomly moving ionospheric electrons).

We now consider an $\hat{\mathbf{x}}$ polarized radar antenna transmitting

$$\hat{\mathbf{p}}_1 = \frac{\hat{\mathbf{k}} \times \hat{\mathbf{k}} \times \hat{\mathbf{x}}}{|\hat{\mathbf{k}} \times \hat{\mathbf{k}} \times \hat{\mathbf{x}}|} \quad (73)$$

polarized waves field in $\hat{\mathbf{k}}$ direction. On reception, the same antenna would be co-polarized with incoming fields of identical polarization direction $\hat{\mathbf{p}}_1$. For an orthogonal $\hat{\mathbf{y}}$ polarized antenna

$$\hat{\mathbf{p}}_2 = \frac{\hat{\mathbf{k}} \times \hat{\mathbf{k}} \times \hat{\mathbf{y}}}{|\hat{\mathbf{k}} \times \hat{\mathbf{k}} \times \hat{\mathbf{y}}|} \quad (74)$$

would be the polarization direction of co-polarized fields. Let's assume that these two antennas, located at the geomagnetic equator, scan the ionosphere from north to south to construct power maps of the backscattered signals. In every pointing direction, narrow pulses are transmitted so that range filtering effects (due to the convolution of the pulse shape with the response of the ionosphere) can be ignored. In transmission, only the first antenna ($\hat{\mathbf{x}}$ polarized) is excited, while, in reception, both antennas are used to collect the backscattered signals. The two antennas then provide us with co- and cross-polarized output voltages

$$v_1(\hat{\mathbf{k}}) \propto \kappa_i \hat{\mathbf{p}}_1^T \bar{\mathbf{\Pi}}_i \hat{\mathbf{p}}_1 \quad \text{and} \quad v_2(\hat{\mathbf{k}}) \propto \kappa_i \hat{\mathbf{p}}_2^T \bar{\mathbf{\Pi}}_i \hat{\mathbf{p}}_1, \quad (75)$$

sampled at each range r_i , where the two-way propagator matrix $\bar{\mathbf{\Pi}}_i$ (defined above) is dependent on the electron density and magnetic field values along $\hat{\mathbf{k}}$ up to the radar range r_i . As κ_i is a random variable, the statistics of voltages (75) would be needed to characterize the scattering targets. For instance, the mean square values of v_1 and v_2 can be modeled as

$$\langle |v_1|^2 \rangle \propto \sigma_v \Gamma_1 \quad \text{and} \quad \langle |v_2|^2 \rangle \propto \sigma_v \Gamma_2, \quad (76)$$

where $\sigma_v = \langle |\kappa_i|^2 \rangle$ is the volumetric RCS of the medium, which is dependent on the electron density, temperature ratio, and magnetic aspect angle at any given range. In addition, Γ_1 and Γ_2 are polarization coefficients defined as

$$\Gamma_1 = \left| \hat{\mathbf{p}}_1^T \bar{\mathbf{\Pi}}_i \hat{\mathbf{p}}_1 \right|^2 \quad \text{and} \quad \Gamma_2 = \left| \hat{\mathbf{p}}_2^T \bar{\mathbf{\Pi}}_i \hat{\mathbf{p}}_1 \right|^2. \quad (77)$$

To simulate radar voltages using the model described above, an ionosphere with the electron density and T_e/T_i profiles displayed in Figure 14 was considered. In addition, the magnetic field was computed using the International Geomagnetic Reference Field (IGRF) model (e.g., Olsen et al., 2000). Finally, the simulations were performed for a 50 MHz radar at the location of the Jicamarca ISR in Peru and antenna polarizations $\hat{\mathbf{x}}$ and $\hat{\mathbf{y}}$ were taken to point in SE and NE directions as at Jicamarca.

Let us first analyze magnetoionic propagation effects on the simulated radar voltages, disregarding scattering effects. For this purpose, polarization coefficients Γ_1 and Γ_2 are displayed in Figure 15 as functions of distance and altitude from the radar (in the plots, the positive horizontal axis is directed north). Note that, at low altitudes, where there is

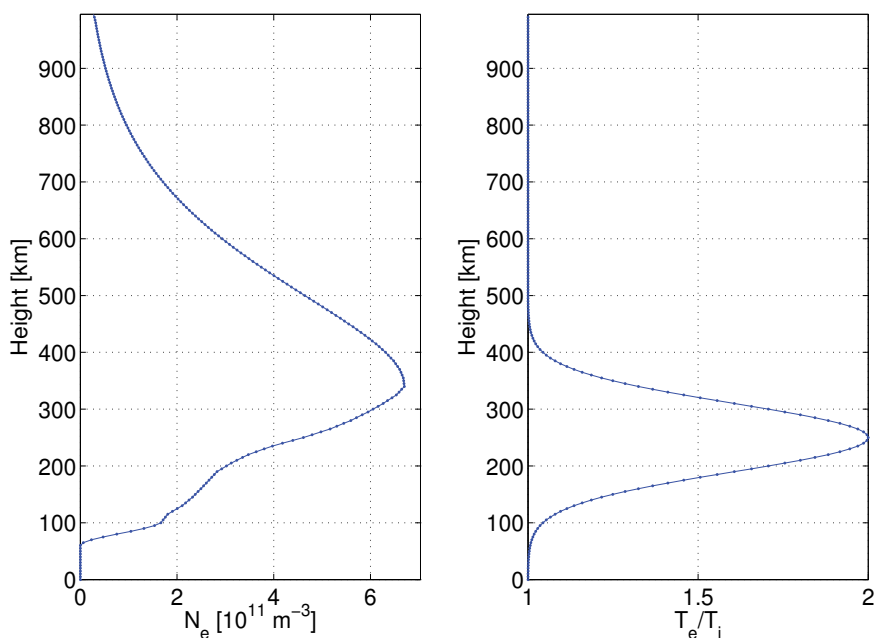


Fig. 14. Electron density and T_e/T_i profiles as functions of height.

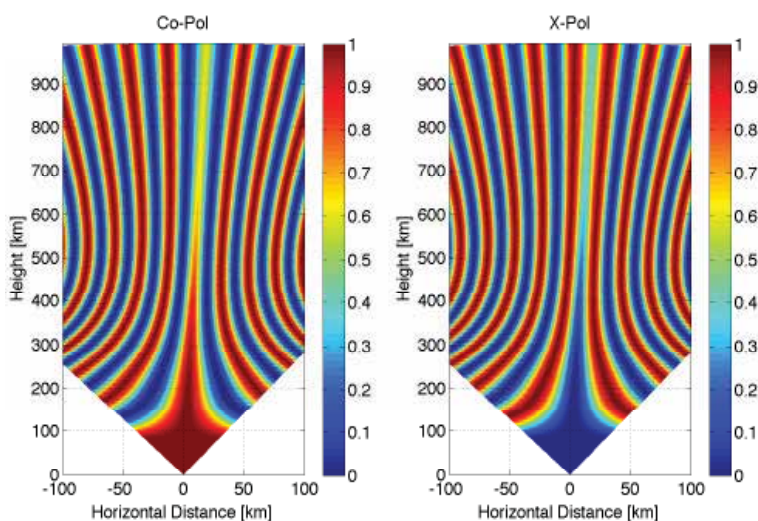


Fig. 15. Polarization coefficients for the mean square voltages detected by a pair of orthogonal linearly polarized antennas placed at Jicamarca. The antennas have very narrow beams and scan the ionosphere from north to south probing different magnetic aspect angle directions. Note that, for most pointing directions, the polarization of the detected fields rotates (Faraday rotation effect), except in the direction where the beam is pointed perpendicular to \mathbf{B} , in which case, the type of polarization changes from linear to circular (Cotton-Mouton effect).

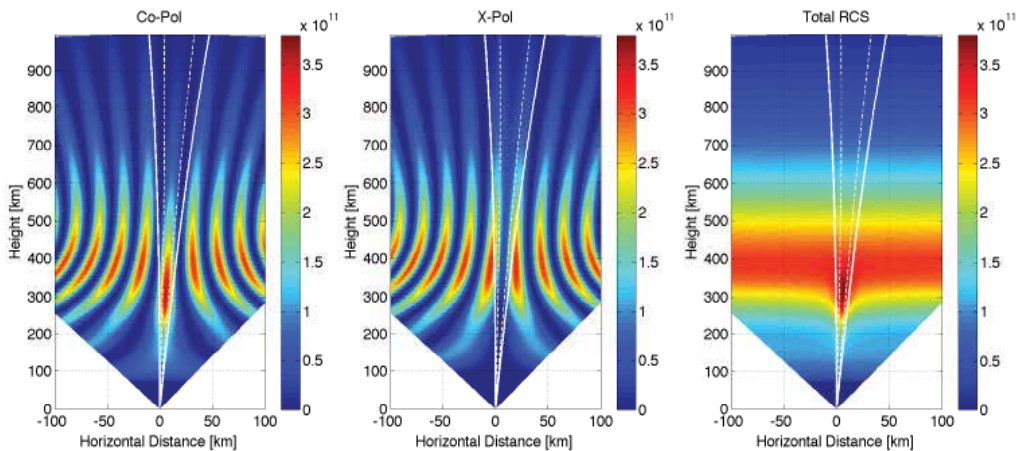


Fig. 16. Co-polarized (left panel), cross-polarized (middle panel), and total (right panel) backscattered power detected by a pair of orthogonal linearly polarized antennas (see caption of Figure 15). Power levels are displayed in units of electron density. In each plot, the dashed white lines indicate the directions half a degree away from perpendicular to \mathbf{B} , while the continuous lines correspond to the directions one degree off.

no ionosphere, signal returns will be detected only by the co-polarized antenna (i.e., by the same antenna used on transmission). However, as the signal propagates farther through the ionosphere, magnetoionic effects start taking place. We can appreciate that, for most of the propagation directions, the polarization vector of the detected field rotates such that signal from one polarization goes to the other as the radar range increases (Faraday rotation effect). Note, however, that there is a direction in which the wave polarization does not rotate much. In this direction, the antenna beams are pointed perpendicular to the Earth's magnetic field, and it can be observed that the polarization of the detected fields varies progressively from linear to circular as a function of height (Cotton–Mouton effect). Finally, note that at higher altitudes, where the ionosphere vanishes, no more magnetoionic effects take place, and the polarization of the detected signal approaches a final state.

Next, scattering and propagation effects are considered in the simulation of the backscattered power collected by the pair of orthogonal antennas described above. The incoherent scatter volumetric RCS formulated in the previous section is used in the calculations. In Figure 16, the simulated co-polarized (left panel) and cross-polarized (middle panel) power data are displayed as functions of distance and altitude from the radar. In addition, the right panel depicts the total power detected by both antennas. Note that power levels are displayed as volumetric radar cross sections divided by $4\pi r_e^2$ (i.e., power levels are in units of electron density). In each plot, the dashed white lines indicate the directions half a degree away from perpendicular to \mathbf{B} , while the continuous lines correspond to the directions one degree off.

In the plots, we can observe that there is negligible backscattered power at low altitudes. At higher altitudes between approximately 200 and 700 km (where polarization effects are significant), co- and cross-polarized power maps exhibit features that are similar to the ones observed in Figure 15. Note, however, that there is an enhancement of the detected power in the direction where the antenna beams are pointed perpendicular to \mathbf{B} ; this can be observed more clearly in the plot of the total power (right panel of Figure 16). This feature

is characteristic of the incoherent scatter process for probing directions perpendicular to \mathbf{B} and for heights where electron temperature exceeds the ion temperature (i.e., $T_e > T_i$) as described before. At even higher altitudes, scattered signals become weaker and weaker as the ionospheric electron density vanishes.

To model incoherent scatter radar measurements using the propagation model presented in this section, an extra level of complexity has to be considered because, within the range of aspect angles illuminated by the antenna beams, propagation and scattering effects vary quite rapidly. For this reason, the measured backscattered radar signals need to be carefully modeled taking into account the shapes of the antenna beams. A model for the beam-weighted incoherent scatter spectrum that considers magnetoionic propagation and collisional effects is formulated next.

9.3 Soft-target radar equation and magnetoionic propagation

In this section, the soft-target radar equation is reformulated using the wave propagation model described above. Consider a radar system composed of a set of antenna arrays (located in the same area) with matched filter receivers connected to the antennas used in reception. The mean square voltage at the output of the i -th receiver can be expressed as

$$\langle |v_i(t)|^2 \rangle = E_t K_i \int dr d\Omega \frac{d\omega}{2\pi} \frac{|\mathcal{T}(\hat{\mathbf{r}})|^2 |\mathcal{R}_i(\hat{\mathbf{r}})|^2}{k^2} \Gamma_i(\mathbf{r}) \frac{|\chi(t - \frac{2r}{c}, \omega)|^2}{4\pi r^2} \sigma_v(\mathbf{k}, \omega), \quad (78)$$

where t is the radar delay, E_t is the total energy of the transmitted radar pulse, and K_i is the i -th calibration constant (a proportionality factor that accounts for the gains and losses along the i -th signal path). Integrals are taken over range r , solid angle Ω , and Doppler frequency $\omega/2\pi$. In addition, $\mathbf{k} = -2k_0 \hat{\mathbf{r}}$ denotes the relevant Bragg vector for a radar with a carrier wavenumber k_0 and associated wavelength λ . Above, $\mathcal{T}(\hat{\mathbf{r}})$ and $\mathcal{R}_i(\hat{\mathbf{r}})$ are the antenna factors of the arrays used in transmission and reception. Note that $|\mathcal{T}(\hat{\mathbf{r}})|^2$ and $|\mathcal{R}_i(\hat{\mathbf{r}})|^2$ are antenna gain patterns and the product $|\mathcal{T}(\hat{\mathbf{r}})|^2 |\mathcal{R}_i(\hat{\mathbf{r}})|^2$ is the corresponding two-way radiation pattern. The polarization coefficient $\Gamma_i(\mathbf{r})$ is defined as

$$\Gamma_i(\mathbf{r}) = \left| \hat{\mathbf{p}}_t^\top \bar{\mathbf{\Pi}}(\mathbf{r}) \hat{\mathbf{p}}_i \right|^2, \quad (79)$$

where $\hat{\mathbf{p}}_t$ and $\hat{\mathbf{p}}_i$ are the polarization unit vectors of the transmitting and receiving antennas, and $\bar{\mathbf{\Pi}}(\mathbf{r})$ is the two-way propagator matrix for the wave field components propagating along $\hat{\mathbf{r}}$ (incident on and backscattered from the range r). Note that $\hat{\mathbf{p}}_t$ and $\hat{\mathbf{p}}_i$ are normal to $\hat{\mathbf{r}}$ because propagating fields are represented as TEM waves. In addition, $\chi(t, \omega)$ is the radar ambiguity function and $\sigma_v(\mathbf{k}, \omega)$ is the volumetric RCS spectrum, functions that have been defined before. Similarly, the cross-correlation of the voltages at the outputs of the i -th and j -th receivers can be expressed as

$$\langle v_i(t) v_j^*(t) \rangle = E_t K_{i,j} \int dr d\Omega \frac{d\omega}{2\pi} \frac{|\mathcal{T}(\hat{\mathbf{r}})|^2 \mathcal{R}_i(\hat{\mathbf{r}}) \mathcal{R}_j^*(\hat{\mathbf{r}})}{k^2} \Gamma_{i,j}(\mathbf{r}) \frac{|\chi(t - \frac{2r}{c}, \omega)|^2}{4\pi r^2} \sigma_v(\mathbf{k}, \omega), \quad (80)$$

where $K_{i,j}$ is a cross-calibration constant (dependent on gains and losses along the i -th and j -th signal paths), and $\Gamma_{i,j}(\mathbf{r})$ is a cross-polarization coefficient defined as

$$\Gamma_{i,j}(\mathbf{r}) = \left(\hat{\mathbf{p}}_i^\top \bar{\mathbf{\Pi}}(\mathbf{r}) \hat{\mathbf{p}}_t \right) \left(\hat{\mathbf{p}}_j^\top \bar{\mathbf{\Pi}}(\mathbf{r}) \hat{\mathbf{p}}_t \right)^*. \quad (81)$$

Note that dispersion of the pulse shape due to wave propagation effects has been neglected in our model.

Denoting by $S_i(\omega)$ the self-spectrum of the signal at the output of the i -th receiver and applying Parseval's theorem, we have that

$$\langle |v_i(t)|^2 \rangle = \int \frac{d\omega}{2\pi} S_i(\omega). \quad (82)$$

Likewise, the cross-spectrum $S_{i,j}(\omega)$ and the cross-correlation of the signals at the outputs of the i -th and j -th receivers are related by

$$\langle v_i(t)v_j^*(t) \rangle = \int \frac{d\omega}{2\pi} S_{i,j}(\omega). \quad (83)$$

Assuming that the ambiguity function is almost flat within the bandwidth of the RCS spectrum $\sigma_v(\mathbf{k}, \omega)$ (which is a valid approximation in the case of short-pulse radar applications), we can use equations (78) and (80) to obtain the following beam-weighted spectrum and cross-spectrum models:

$$S_i(\omega) = E_t K_i \int dr \frac{|\chi(t - \frac{2r}{c})|^2}{4\pi r^2} \int d\Omega \frac{|\mathcal{T}(\hat{\mathbf{r}})|^2 |\mathcal{R}_i(\hat{\mathbf{r}})|^2}{k^2} \Gamma_i(\mathbf{r}) \sigma_v(\mathbf{k}, \omega) \quad (84)$$

and

$$S_{i,j}(\omega) = E_t K_{i,j} \int dr \frac{|\chi(t - \frac{2r}{c})|^2}{4\pi r^2} \int d\Omega \frac{|\mathcal{T}(\hat{\mathbf{r}})|^2 \mathcal{R}_i(\hat{\mathbf{r}}) \mathcal{R}_j^*(\hat{\mathbf{r}})}{k^2} \Gamma_{i,j}(\mathbf{r}) \sigma_v(\mathbf{k}, \omega), \quad (85)$$

where

$$\chi(t) = \frac{1}{T} f^*(-t) * f(t) \quad (86)$$

is the normalized auto-correlation of the pulse waveform $f(t)$. In the radar equations (84) and (85), the polarization coefficients $\Gamma_i(\mathbf{r})$ and $\Gamma_{i,j}(\mathbf{r})$ effectively modify the radiation patterns; thus, the spectrum shapes are dependent not only on the scattering process but also on the modes of propagation. This dependence further complicates the spectrum analysis of radar data and the inversion of physical parameters.

10. Summary

In this chapter we have described the operation of ionospheric incoherent scatter radars (ISR) and the signal spectrum models underlying the operation of such radars. ISR's are the premier remote sensing instruments used to study the ionosphere and Earth's upper atmosphere. First generation operational ISR's were built in the early 1960's — e.g., Jicamarca in Peru and Arecibo in Puerto Rico — and ISR's continue to play a crucial role in our studies of Earth's near space environment. These instruments are primarily used to monitor the electron densities and drifts, as well as temperatures and chemical composition of ionospheric plasmas. The latest generation of ISR's include the AMISR — advanced modular ISR — series which are planned to be deployed around the globe and then re-located depending on emerging science needs. With increasing ISR units around the globe, there will be a larger demand on radar engineers and technicians familiar with ISR modes and the underlying scattering theory. For that reason, in our presentation in this chapter, as well as in our recent papers (Kudeki & Milla, 2011; Milla & Kudeki, 2011), we have taken an "engineering approach" to describe the theory of the incoherent scatter spectrum. Complementary physics based descriptions of the same processes can be found in many of the original ISR papers included in references.

11. Acknowledgements

This chapter is based upon work supported by the National Science Foundation under Grant No. 0215246 and 1027161.

12. References

- Bowles, K. L. (1958). Observation of vertical-incidence scatter from the ionosphere at 41 mc/sec, *Physical Review Letters* 1(12): 454–455.
- Budden, K. G. (1961). *Radio Waves in the Ionosphere*, Cambridge University Press, Cambridge, United Kingdom.
- Callen, H. B. & Welton, T. A. (1951). Irreversibility and generalized noise, *Physical Review* 83(1): 34–40.
- Callen, J. D. (2006). *Fundamentals of Plasma Physics*, Chapter 2 – Coulomb Collisions. URL: <http://homepages.cae.wisc.edu/callen/book.html>
- Chandrasekhar, S. (1942). *Principles of Stellar Dynamics*, University of Chicago Press, Chicago.
- Chandrasekhar, S. (1943). Stochastic problems in physics and astronomy, *Reviews of Modern Physics* 15(1): 1–89.
- Chau, J. L. & Kudeki, E. (2006). First E- and D-region incoherent scatter spectra observed over Jicamarca, *Annales Geophysicae* 24(5): 1295–1303.
- Dougherty, J. P. (1964). Model Fokker-Planck equation for a plasma and its solution, *The Physics of Fluids* 7(11): 1788–1799.
- Dougherty, J. P. & Farley, D. T. (1963). A theory of incoherent scattering of radio waves by a plasma 3. Scattering in a partly ionized gas, *Journal of Geophysical Research* 68: 5473–5486.
- Farley, D. T. (1964). The effect of Coulomb collisions on incoherent scattering of radio waves by a plasma, *Journal of Geophysical Research* 69(1): 197–200.
- Farley, D. T. (1966). A theory of incoherent scattering of radio waves by a plasma 4. The effect of unequal ion and electron temperatures, *Journal of Geophysical Research* 71(17): 4091–4098.
- Gillespie, D. T. (1996a). The mathematics of Brownian motion and Johnson noise, *American Journal of Physics* 64(3): 225–240.
- Gillespie, D. T. (1996b). The multivariate Langevin and Fokker–Planck equations, *American Journal of Physics* 64(10): 1246–1257.
- Gordon, W. E. (1958). Incoherent scattering of radio waves by free electrons with applications to space exploration by radar, *Proceedings of the IRE* 46(11): 1824–1829.
- Hagfors, T. & Brockelman, R. A. (1971). A theory of collision dominated electron density fluctuations in a plasma with applications to incoherent scattering, *The Physics of Fluids* 14(6): 1143–1151.
- Holod, I., Zagorodny, A. & Weiland, J. (2005). Anisotropic diffusion across an external magnetic field and large-scale fluctuations in magnetized plasmas, *Physical Review E* 71(4): 1–11.
- Kudeki, E., Bhattacharyya, S. & Woodman, R. F. (1999). A new approach in incoherent scatter *F* region $E \times B$ drift measurements at Jicamarca, *Journal of Geophysical Research* 104(A12): 28145–28162.
- Kudeki, E. & Milla, M. A. (2011). Incoherent scatter spectral theories—Part I: A general framework and results for small magnetic aspect angles, *IEEE Transactions on Geoscience and Remote Sensing* 49(1): 315–328.

- Mathews, J. D. (1984). The incoherent scatter radar as a tool for studying the ionospheric D-region, *Journal of Atmospheric and Terrestrial Physics* 46(32): 975–986.
- Milla, M. A. & Kudeki, E. (2006). F-region electron density and T_e/T_i measurements using incoherent scatter power data collected at ALTAIR, *Annales Geophysicae* 24(5): 1333–1342.
- Milla, M. A. & Kudeki, E. (2009). Particle dynamics description of “BGK collisions” as a Poisson process, *Journal of Geophysical Research* 114(7): 1–4.
- Milla, M. A. & Kudeki, E. (2011). Incoherent scatter spectral theories—Part II: Modeling the spectrum for modes propagating perpendicular to \mathbf{B} , *IEEE Transactions on Geoscience and Remote Sensing* 49(1): 329–345.
- Olsen, N., Sabaka, T. J. & Tøffner-Clausen, L. (2000). Determination of the IGRF 2000 model, *Earth, Planets and Space* 52(12): 1175–1182.
- Rosenbluth, M. N., MacDonald, W. M. & Judd, D. L. (1957). Fokker-Planck equation for an inverse-square force, *Physical Review* 107(1): 1–6.
- Sulzer, M. P. & González, S. A. (1999). The effect of electron Coulomb collisions on the incoherent scatter spectrum in the F region at Jicamarca, *Journal of Geophysical Research* 104(A10): 22535–22551.
- Uhlenbeck, G. E. & Ornstein, L. S. (1930). On the theory of the Brownian motion, *Physical Review* 36(5): 823–841.
- Woodman, R. F. (1967). *Incoherent scattering of electromagnetic waves by a plasma*, PhD thesis, Harvard University, Cambridge, Massachusetts.
- Yeh, K. C. & Liu, C. H. (1972). *Theory of Ionospheric Waves*, Vol. 17 of *International Geophysics*, Elsevier.

Part 6

Other Advanced Doppler Radar Applications

Volcanological Applications of Doppler Radars: A Review and Examples from a Transportable Pulse Radar in L-Band

Franck Donnadieu

¹*Clermont Université, Université Blaise Pascal, Observatoire de Physique du Globe de Clermont-Ferrand (OPGC), Laboratoire Magmas et Volcans, Clermont-Ferrand*
²*CNRS, UMR 6524, LMV, Clermont-Ferrand*
³*IRD, R 163, LMV, Clermont-Ferrand France*

1. Introduction

Many types of radar systems have been applied to the study of a wide range of volcanic features. Fields of application commonly include volcano deformation by interferometric synthetic aperture radar (InSAR), mainly satellite-based (e.g. Froger et al., 2007) but also ground-based like LISA (Casagli et al., 2009), digital elevation model generation using satellite or airborne InSAR measurements, surface products mapping by amplitude images of satellite radars, characterization of unexposed deposits by ground-penetrating radars (Russell & Stasiuk, 1997), monitoring of active lava domes and flows by either ad-hoc ground-based radars (e.g. Malassingne et al., 2001; Macfarlane et al., 2006; Wadge et al., 2005, 2008) or commercial ones (Hort et al., 2006; Vöge & Hort, 2008, 2009; Vöge et al., 2008), and quantitative characterization of explosive activity by means of fixed weather radars (large ash plumes) and transportable radars (Strombolian activity, weak ash plumes). A thorough review of all radar applications in volcanology is beyond the scope of this chapter which, instead, focuses on recent investigations of explosive eruptive regimes enhanced by the developments of dedicated transportable ground-based radars, by the recent advances made in signal interpretation using eruption models, and by the important concerns raised by ash plume hazards.

Below, weather and transportable radar systems used hitherto to monitor and study tephra emissions are first reviewed along with their advantages and limitations. Some differences relevant to the study of radar signals of volcanic origin are also described. Then I present a unique transportable pulse Doppler radar named VOLDORAD, operating in the L-band and dedicated to the study of explosive activity. Because it can be set up close to an eruptive vent and sound at a high rate the interior of even heavily particle-laden plumes within small beam volumes right above the emission source, many features of processes and dynamics of volcanic emissions can be characterized at different time scales from the spatiotemporal analysis of echo signals. Examples are provided of records obtained with VOLDORAD at

several volcanoes in different sounding conditions and various types of volcanic activity, from Strombolian lava jets to weak ash plumes. They are meant to illustrate the many capabilities of this type of radar and the interpretation of the variety of Doppler signatures in terms of volcanic processes.

2. Radar monitoring of explosive eruptions

2.1 Ash plume hazards and tephra dispersal forecast

Volcanic ash plumes generate important hazards as widespread ash fallout may cause serious perturbations to surrounding population and infrastructures. In addition, volcanic ash clouds derived from eruptive columns, even of moderate size, can generate direct hazards to aviation, as recently highlighted by the 2010 Eyjafjöll eruption in Iceland. The air traffic was disrupted over Europe for several days, causing a loss of about 1.7 billion dollars to airlines. Although no significant damage to aircraft was reported for this eruption, over 120 aircraft encounters with volcanic ash have nevertheless been documented between 1973 and 2008 (Schneider, 2009). The tracking of large ash clouds has therefore become a main concern in the last decades, as attested by the creation of Volcanic Ash Advisory Centers (VAAC) to provide their expertise to civil aviation in case of significant volcanic eruptions. Volcanic ash transport and dispersion (VATD) models are used to forecast the location and movement of ash clouds over hours to days in order to define hazards to aircraft and to communities downwind. Inputs are eruption source parameters such as plume height, mass eruption rate, duration, and mass fraction of fine ash (Mastin et al., 2009). Values of such parameters are frequently unconstrained in the first minutes or hours after an eruption is detected, and also change during an eruption (e.g. plume height), requiring rapid reevaluation. Dispersion model forecast are routinely validated, verified against all available observations, including field observations, combination of tephra deposits analysis and theoretical models, or in-situ measurements and sampling (aircraft). However remotely-sensed measurements by satellite imagery, ground-based radars and lidars, or better a combination of all, are the most efficient tools for real-time response owing to their continuous data acquisition and potential for automatic processing and rapid parameter quantification (Fig. 1).

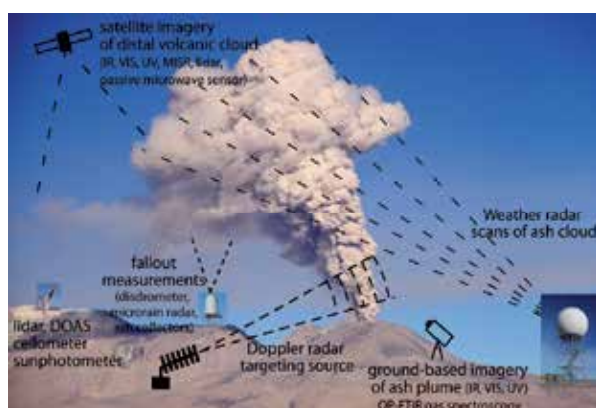


Fig. 1. Synergetic potential of integrated remote-sensing techniques for ash plume monitoring. Photo: Sabancaya volcano, courtesy of J.-L. Le Penec.

2.2 Ash plume monitoring

Long-range trajectory tracking of ash clouds is achieved primarily by means of satellite imagery. Although Delene et al. (1996) showed the utility of a satellite-based microwave imager passively measuring radiations (19-85 GHz) of millimetric volcanic particles from an ash cloud of Mount Spurr in 1992, satellite visible-infrared radiometric observations from geostationary platforms are usually exploited (e.g., Rose et al., 2000). The evolution of the ash cloud spatial distribution, in particular, can be imaged at intervals of 15-30 min. Important parameters can be further retrieved like the approximate plume height assuming thermal equilibrium with the atmosphere (non unicity of solutions for altitudes above the tropopause), and the concentration and size of distal particles (< 20 microns) transported in the atmosphere, assuming particle sphericity and vertically homogeneous concentration. Using these assumptions, the mass of SO₂ and ash can be integrated on successive images (e.g. Wen & Rose, 1994). Scollo et al. (2010) also showed the potential of Multiangle Imaging SpectroRadiometer (MISR) working in four wavelengths in visible and near-infrared bands, for the 3-D reconstruction of ash plume shape, and for the retrieval of column height, optical depth, type and shape of the finest particles, among the most sensitive inputs for ash dispersal modeling.

Yet, the exploitation of satellite images for monitoring purposes is limited by (1) the presence of clouds at higher levels, (2) an insufficient acquisition rate for event onset detection, (3) a relatively poor spatial resolution, (4) errors of the "split-window" method (brightness temperature difference) when the volcanic plume lies over a very cold surface or when the plume lies above a clear land surface at night where strong surface temperature and moisture inversions exist (Prata et al., 2001). In addition, low ash content and/or small ash plumes might not be clearly observed and near-source emissions are obscured by the emitted tephra. For these reasons, ground-based radar systems represent an optimal complementary solution for real-time monitoring of these phenomena, by providing higher spatial resolution and data acquisition rates, as well as the ability to make observations at night and under any weather conditions. Real-time monitoring of ash plumes is crucial, in particular for the initialization of dispersion models. In this respect, essential input parameters such as plume height, mass flux, and particle concentration can be assessed quantitatively from radar data and directly contribute to improve ash dispersion forecasts.

2.2.1 Radar monitoring of ash plumes

2.2.1.1 Weather radar observations

2.2.1.1.1 Characteristics and advantages

Although ash plume hazards to aviation safety raised concerns early on about the detection capacity of ash clouds by airborne radar (Musolf, 1994; Stone, 1994), most observations of large volcanic ash clouds have been opportunely carried out by fixed meteorological radars of national weather services. Weather radars operate at microwave frequencies from S band (7.5-15 cm wavelength, generally about 10 cm) up to C band (3.75-7 cm wavelength, commonly around 6 cm), X band (2.5-3.75 cm wavelength, commonly around 3 cm) and Ka band (0.75-1.11 cm wavelength, often around 1 cm). With peak powers up to 250 kW or even higher, they have sufficient sensitivity to detect volcanic ash clouds with small particle sizes. Pulsed systems ensure a relatively high spatial range resolution of a few hundreds of

meters. Reflector antennas provide half-power beam-widths of a few degrees. These systems usually scan in azimuth and elevation, within a few minutes, allowing the maximum plume height to be tracked through time, along with the spatial variations of its reflectivity. Most have a Doppler capability to measure radial wind velocity, that can be used to infer information on internal velocities of ash clouds and retrieve information on turbulence, which has seldom been used. New generation radars are dual-polarized, which may further help to discriminate ash from hydrometeors.

Powerful weather radars, operating continuously at minute-scale acquisition rate and in all weather, have been used occasionally to track large ash clouds, chiefly since the first radar observations of Hekla eruption in 1970 and Augustine in 1976, because the information held in their records is many fold and potentially very useful for risk mitigation. Scan images of the ash cloud provide reflectivity variations in horizontal and vertical planes. Time evolutions of its height and lateral spreading can then be retrieved, along with its ascent rise rate and lateral transport speed. Mass and volume of radar-detected ash, as well as particle concentrations in the cloud can be estimated provided the grain size distribution can be constrained (from ash fall or other).

2.2.1.1.2 Observations

Harris et al. (1981), Harris & Rose (1983) and Rose & Kostinski (1994) first collected observations of ash plumes from Mt. St. Helens in 1980-1982 using 5 cm and 23 cm radar systems. They tracked the position of the ash cloud of March 19 1982, and estimated its volume ($2000 \pm 500 \text{ km}^3$), the concentration of ash ($0.2\text{-}0.6 \text{ g/m}^3$), reflectivity factors of $4\text{-}5 \text{ mm}^6/\text{m}^3$ ($6\text{-}7 \text{ dBZ}$), and the total mass of ash erupted ($3\text{-}10 \times 10^8 \text{ kg}$). For the famous paroxysmal eruption of May 18 1980, they obtained a mass of $5 \times 10^{11} \text{ kg}$, an ash volume of 0.2 km^3 , and particle concentration of $3\text{-}9 \text{ g/m}^3$, for the ash cloud downwind of Mount St. Helens, 1.5-2 h after its eruption (horizontal speed 135 km/h). Reflectivity factors found for these dense (but distal) ash clouds ($7\text{-}60 \text{ mm}^6/\text{m}^3$ or $8\text{-}18 \text{ dBZ}$) are several orders of magnitude smaller than those for severe weather considered routinely detectable by airborne weather radar and dangerous for aviation. Eruption-column rise rates and horizontal drift of ash clouds of Mount Pinatubo, Philippines, in 1991, were also tracked using two military C-band weather radars 40 km away (Oswalt et al., 1996). During the second eruption of June 12, 1991, radars indicated an apparent column rise rate in excess of 400 m/s . Radar height measurements were typically 10 to 15 percent lower than ash cloud heights inferred from satellite temperature analyses. Radar observations also suggested that higher eruption columns correlated with greater particle size and density within the column. Using a C-band radar Rose et al. (1995) found that most intense reflections in an ash cloud of Mount Spurr in 1992 came from particles 2 to 20 mm in diameter and with a total particle mass concentration of <0.01 to 1 g/m^3 . The radar did not detect distal parts of the ash cloud, which have an atmospheric residence time of longer than 30 minutes, because the larger more reflective ash particles drop out. Maki and Doviak (2001) observed ash plumes of Mount Oyama on Miyake Island, Japan, in 2000, with a 5-cm (C band) radar, and proposed a method to obtain the time-dependent size distribution of ash particles from the time dependence of the reflectivity factor. Lacasse et al. (2004) reported observations of the ash cloud of the Icelandic Hekla volcano in 2000 with a C-band radar at Keflavík international airport. Reflectivity factors in the range 30 to $>60 \text{ dBZ}$ characterized the eruption column above the vent due to the dominant influence of lapilli and ash (tephra) on

the overall reflected signal, whereas values of between 0 and 30 dBz characterized the cloud advected downwind. The plume head had a mean ascent rate of 30 to 50 m/s up to 12 km in altitude (upper limit of the radar). Using the same radar, Marzano et al. (2006a, 2010a) found maximum reflectivities of 34 dBZ for the 2004 ash cloud of Grímsvötn volcano (260 km away), at a height of 6 km (minimum detection altitude). From an inversion technique based on a classification scheme of particles, they estimated ash concentrations of up to 6 g/m³, and ashfall rates of up to 31 kg/h. Likewise, for the 2010 Eyjafjöll eruption, Marzano et al. (2011) determined an ash mass of up to 15×10⁸ kg on April 16, and 8×10⁷ kg on May 5. Recently, Marzano et al. (2010b) used volume scan data acquired in the S-band by a NEXRAD WSR-88D ground-based weather radar at Augustine volcano in Alaska in 2006 (Wood et al., 2007). From their model-based technique, ash aggregate concentrations of up to 0.2g/m³ were found to correspond to measured reflectivities of up to 55 dBZ at an ash column height of about 4 km. Maki et al. (2001) first reported observations of ash plumes from Mount Oyama in Japan by a 3-cm wavelength polarimetric mobile radar about 40 km away. They discussed the possibility of detecting volcanic ash particles and estimating their size distribution from polarimetric radar parameters such as the differential reflectivity and specific differential phase shift.

2.2.1.1.3 Limitations

As seen previously, ground-based weather radar systems are powerful tools for volcanic ash cloud detection and quantification. Their Doppler capacity has not, so far, been much exploited in the study of ash clouds and could aid understanding of the interplay between their dynamics and their environmental conditions (wind, atmospheric properties such as humidity and temperature profiles, etc). Their main limitations are, in general: (i) their limited sensitivity tending to render invisible to the radar the cloud parts where particle concentration is too low (ultimately all of the ash cloud). This leads to an underestimation of the ash cloud lateral extension, and also of its height because the top of the ash column may be coarse-depleted. Another source of error on column heights, and hence an underestimation of height-derived eruption rates, may come from the incomplete filling of the highest volume scanned by the plume top. The sensitivity of the ground-based radar measurements will decrease as the ash cloud moves farther away. (ii) By using single-polarization weather radar, however, it is fairly difficult to discriminate between ash, hydrometeors, and mixed particles. Ice nucleation and subsequent loss in reflectivity also make ash detection more difficult (Marzano et al., 2006b). These authors suggest that polarimetric radars may improve discrimination of the impact of cloud ice and liquid water on ash aggregates. According to Hannesen and Weipert (2011), however, significant overlap exists between meteorological targets and volcanic ash, so that, even if all polarimetric observables of dual-polarized radars are used, automatic detection might be tricky. With polarimetric data, however, the retrieval of volcanic parameters could be improved by taking into account the mixed particle composition and their shape (Marzano et al., 2012). (iii) Path attenuation effects are not always negligible. According to Marzano and Ferrauto (2003), in the case of hydrometeors, any radar technique above S band should take into account, and possibly remove, path attenuation effects in order to correctly convert measured reflectivity into rain rate. For ash clouds, Marzano et al. (2006b) concluded that C-band may offer some advantages in terms of radar reflectivity response and negligibility of path attenuation. While still tolerable at X-band, the path attenuation cannot be handled at

Ka-band. The advantage of higher frequencies (X-, Ka-band) is the potential diminution of the overall size of the system and a higher sensitivity to fine particles, hence a better detection at low ash concentration. For near-source soundings, path attenuation effects are presumably very important up to X-band and possibly non negligible up to L-band because of the high particle concentrations and sizes (commonly pluri-decimetric), especially in the gas thrust region. Further investigations are needed, even at L-band. (iv) Weather radars cannot track ash clouds over the long-term, due to the low atmospheric residence time of reflective coarse particles. (v) Their maximum detection range is generally within 200-300 kilometers of their fixed location. Portable radar systems overcome the limitation of observing ash clouds from a far distance and always the same volcano. In many respects, the synergetic role of satellite imagery in tracking volcanic ash, particularly after the initial stages of an eruptive event is obvious. (vi) Weather radars are unable to image the lowest few kilometers of the ash column when the volcano is too far away (and the top if above the beam), preventing early detection and retrieval of the near-source ash plume characteristics. To avoid some of these shortcomings, institutes in charge of volcano monitoring have started to integrate nearby dedicated radars into their instrumental networks.

2.2.1.2 Radars dedicated to volcano monitoring

Given the benefits of continuous quantitative retrieval of parameters such as height and mass loading which are crucial to initiate dispersion models, permanent volcano monitoring using weather radars has become more widely used. Ground-based weather radar networks are currently operational at several volcanoes, in Alaska, Iceland, Italy and Guadeloupe. The U.S. Geological Survey first experimented in 1997 with a ground-based Doppler radar at the National Center for the Prevention of Disasters (CENAPRED) in Mexico to track the dispersal of ash plumes of Popocatepetl volcano and at least two eruptions were successfully captured. In addition to the near contiguous network of weather-monitoring Doppler radar NEXRAD operated by the U.S. National Weather Service, the U.S. Geological Survey also deployed a new truck-transportable C-band Doppler radar (MiniMax-250C) during the 2009 eruptions of Redoubt Volcano, Alaska (Hoblitt and Schneider, 2009). Results for 17 ash plumes detected by the radar compared favorably well with those of a nearby WSR-88D NEXRAD operated by the Federal Aviation Administration. The sector-scanning strategy (45°) of the new mobile radar advantageously allowed event onset detection within less than a minute. Heights (9-19 km) and vertical rise rates of the ash columns (25-60 m/s) have been determined. The high radar reflectivity values of the central core of the eruption column (50-60 dBZ) were interpreted as being the result of rapid formation of volcanic ash-ice aggregates (Schneider, 2012).

The X-band is generally preferable providing higher sensitivity with respect to lower frequency bands typically used for weather observations. The Japanese government recently set up an X-band polarimetric radar near Sakurajima volcano, able to monitor its recurrent vulcanian ash plumes (M. Maki, pers. comm.). Since November 2010, the Icelandic Met Office has had on loan from the Italian Civil Protection a mobile X-band dual-polarization radar for volcano monitoring. This radar (75 km from the volcano), along with the fixed weather C-band radar in Keflavík (257 km from the volcano), monitored the ash plumes of Eyjafjöll in 2010 and Grimsvötn in 2011 (Arason et al., 2011, 2012). These authors used in particular the radar time-series of the plume heights to calculate the mean eruptive flow

rate. From the polarimetric X-band dataset of this eruption, Hannesen and Weipert (2011) quantified ash concentrations of up to 100 g/m^3 and ash fall rates of up to $100 \text{ kg/m}^2/\text{h}$ at a height of 4.5 km from all polarimetric observables. They emphasize, however, the limits of ash quantification, the ambiguity in the separation of precipitation and ash that makes automatic detection still difficult, and the signal weakness from distant ash that prevents radar observations. Vulpiani et al. (2011) explored the benefits of the mobile dual polarization X band radar (DPX 4) operated by the Department of Civil Protection at the airport of Catania Fontanarossa (30 km to the South) to monitor Etna and offer support to the decisions of the authorities that regulate and control air traffic. In an ash plume fed from a lava fountain, maximum reflectivities of 35 dBZ were measured at medium distances of 10-40 km from the volcano. Estimated mass concentrations vary up to a few g/m^3 , although most are below 1 g/m^3 . The instrumental monitoring network of Etna operated by the Istituto Nazionale di Geofisica e Vulcanologia (INGV) also comprises, since 2009, and this is unique, a permanent ground-based L-band Doppler radar of the Observatoire de Physique du Globe de Clermont-Ferrand (OPGC, France) targeting the summit craters (Donnadieu et al., 2009a, 2012). Named VOLDORAD 2B, this radar is similar to the transportable volcano Doppler radar (VOLDORAD) successfully applied in several volcanic contexts (Dubosclard et al., 1999, 2004; Donnadieu et al., 2003, 2005), as illustrated later in this chapter (cf. section 7.1, fig. 16). The permanent radar at Etna should complement observations from the INGV monitoring network to constrain the inputs of the tephra dispersal models run automatically to perform tephra dispersal forecast (Scollo et al., 2009).

2.2.1.3 Fallout measurements

A compact X-band continuous wave, low power (10 mW) Doppler Radar (PLUDIX, 9.5 GHz frequency of operation), originally designed as a rain gauge disdrometer, was utilized to measure the terminal settling velocities and infer sizes of plume fallout at Mount Etna in 2002 (Scollo et al., 2005) and Eyjafjallajökull in 2010 (Bonadonna et al., 2011). PLUDIX-derived particle size distributions agree reasonably well with sieve-derived grain size distributions, but only for diameter range above 500 microns, and so should be used within a few kilometers from the source. Such measurements, along with deposit sampling and other methods shown in figure 1, can usefully complement other radar observations of the ash plume/cloud (Fig. 1) by providing the particle size distribution necessary to accurately retrieve the loading parameters (total mass, mass concentrations, mass flux of tephra).

2.2.1.4 Compact portable Doppler radars for near-source measurements

The growing need to get insight into the dynamics of explosive eruptions and to measure eruptive parameters at the source has led to the development of several active remote sensing compact instruments in the last decade or so. The first attempt to bring transportable sounders close to volcanic craters to measure the near-source dynamics was achieved by Weill *et al.* (1992) who successfully determined vertical velocities in the range 20-80 m/s for over 100 mild Strombolian explosions at Stromboli using a Doppler sodar. This cumbersome acoustic sounder could operate only at a few hundred meters from the vent and, hence, was not well suited to the sounding of larger magnitude, hazardous eruptions. Besides, velocity determinations using sodar require the knowledge of sound velocity at the jet temperature and gas composition, which was not available. Two main types of dedicated portable radars have since been used with the primary goal of studying

eruption near-source dynamics through their Doppler capability: commercial micro rain radars, that are continuous-wave frequency-modulated and working at 24 GHz (Seyfried & Hort, 1999; Hort et al., 2003, 2006) and the VOLDORAD system, an L-band pulsed volcano Doppler radar (e.g., Dubosclard et al., 1999, 2004; Donnadieu et al., 2005). Being set up at a chosen location and aiming directly at the emission source (instead of rotation scanning), these compact radar systems can advantageously sound the gas thrust region and provide source eruptive parameters like eruption velocities, but also capture short-lived weak explosive activity, not visible to satellites or weather radars. They have higher temporal (<1 s) and spatial resolutions (tens to hundreds of meters) and higher sensitivity. A comparison of some characteristics of weather radars and transportable volcano Doppler radars is presented in Table 1.

	Location	Max. range	Min. range	Acquisition rate	Volume scanned	Power consumption	Frequency bands
Weather radars	Fixed	100-300 km	Few km	Few min	km ³	100s of kW	S, C, X, Ka
Portable radars	Chosen	10-15 km	10s-100s m	≤ 1 s	10 ⁴ -10 ⁸ m ³	Few mW to few 10s of W	L, X, Ka

Table 1. Characteristics of weather and transportable radars for the monitoring of volcanic eruptions. Note in particular the difference in temporal and spatial resolution.

Hort and Seyfried (1998) and Seyfried and Hort (1999) measured mean vertical velocities of about 10 m/s for 12 lava jets during very low activity at Stromboli volcano with a commercial portable FM-CW radar Doppler anemometer 200-300 m away from the eruptive vent. Using the same instrument, Hort et al. (2003) found an increase in eruption duration, much higher velocities and indirect evidence of mean particle size decrease after a rain storm. Gerst et al. (2008) reconstructed the 4D velocity (directivity) of Strombolian eruptions at Erebus and Stromboli from 3 FM-CW radars. FM-CW radars have a narrower field of view (around 1° or so at 3 dB) and can thus target a precise sector of the volcanic emission but, on the other hand, lack the integrated information of longer wavelength pulse radars with a wider beam aperture and deeper range gates. L-band frequency signals are very little attenuated by hydrometeors or volcanic particles and can sound the interior of very dense particle-laden plumes. VOLDORAD also has a higher temporal resolution (<0.1 s).

Donnadieu et al. (2005) showed very detailed time series of power and maximum radial velocities of a Strombolian explosion at Etna and an ash plume at Arenal, acquired at high rate (<0.1 s) with VOLDORAD. Donnadieu et al. (2003, 2005) and Dubosclard et al. (2004) further showed evidence of strong correlation between volcanic tremor and maximum radar velocities for several Strombolian episodes, suggesting the influence of gas bubble dynamics in the conduit on tremor generation at Etna. Using VOLDORAD, Gouhier & Donnadieu (2008) first quantified the mass of tephra of Strombolian explosions at Etna (50-200 tons) from a new power inversion method. From the analysis of the shape of Doppler spectra of 200 Strombolian explosions, Gouhier & Donnadieu (2010) found that 80% of the load is ejected within a 40° dispersion cone and that, for 2/3 of the explosions, ejecta are distributed uniformly within this cone. Using measured maximum radial velocities, at-vent particle and gas velocities can be retrieved, and source gas fluxes estimated when the vent diameter is known (Gouhier & Donnadieu, 2011). Comparing thermal data with records from a FM-CW

at Stromboli, Scharff et al. (2008) found a correlation between the radiative energy of Strombolian lava jets and the backscattered energy, suggesting that both methods record the relative variations of mass. They also found pulsations in the power time series of 40% of the eruptions, likely reflecting variations in mass eruption rate and originating in multiple consecutively exploding bubbles.

Scharff et al. (2012) also report the pulsed release (2-5 s) of ash clouds from the dome of Santiaguito with particle radial velocities between 10 and 25 m/s, and preceded by a vertical dome uplift of about 50 cm, as recorded with a FM-CW radar. Using VOLDORAD, Donnadieu et al. (2008) had already reported staccato pressure release in the ash emissions of Arenal volcano, along with a variety of ash plume dynamics from short-lived explosive events with radial velocities of up to 90 m/s, to sustained pulsed ash jetting and to passive dilute ash emissions. Donnadieu et al. (2011) successfully reconstructed the 3D vector of the ash plume transport speed from the echo onsets in contiguous range gates.

3. Specificity of radar signals of volcanic origin

3.1 Examples of meteorological signals

While abundant literature describes the effects of meteorological targets on weather radar signals, few studies characterize volcanic targets from a radar perspective. Not only the dynamics of volcanic eruptions strongly differs from that of common meteorological phenomena but also the target properties. This section points out some differences relevant to the study of radar signals of volcanic origin, for measurements near the emission source and in the distal part of ash clouds.

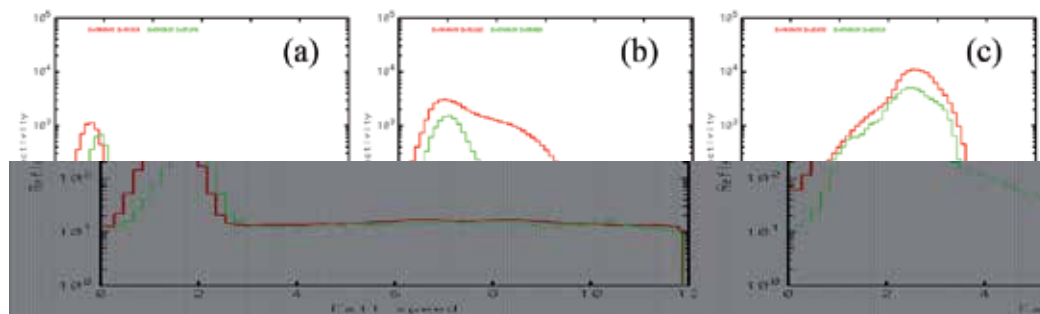


Fig. 2. Examples of meteorological Doppler spectra from a 24 GHz Micro Rain Radar. Reflectivity is shown versus radial velocity (i.e. fall speed with vertical beam) at a 1 hour interval (6:05 U.T. in red and 07:05 U.T. in green) on 21/12/2011: (a) snow crystals at 1430-1730 m a.s.l., (b) mixture of melting snow and water droplets in the radar bright-band (930-1230 m a.s.l.), (c) melt water droplets at 430-730 m a.s.l.. Data of MRR4 at Aulnat Airport (France): courtesy of Yves Pointin (OPGC).

Typical Doppler spectra of meteorological targets showing reflectivity versus fall speeds are presented in figure 2. Because the sounding is vertical, radial velocities (toward the radar) directly indicate fall speeds, unlike in the oblique radar soundings of volcanic emissions. At altitude, low reflectivity snow crystals fall at low speed (Gaussian shape spectrum). At intermediary altitude, a mixture of melting snow and water droplets (radar bright-band)

produces more complex spectrum shapes, whereas at lower altitude melt water droplets produce rainfall with high reflectivity ($Z > 40$ dBZ) and higher fall speeds up to 10 m/s. Note the relatively low velocities and spectrum width, as compared with the volcanic emission recorded by VOLDORAD (right panel in figure 3).

3.2 Volcanic features relevant to radar investigations

The contrasted radar signatures from meteorological targets and volcanic emissions are particularly conspicuous in figure 3 showing Doppler spectra recorded by VOLDORAD for rainfall and at the base of a weak ash plume during an explosive event. Whereas the rainfall shows narrow power distribution with a similar weak intensity and a well defined mode at 12 m/s over many range gates, volcanic tephra backscatter much more power spread over a radial velocity range from -30 to +60 m/s in just the two range gates above the eruptive vent.

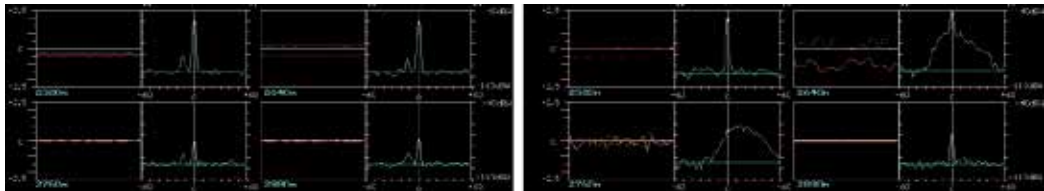


Fig. 3. Doppler spectra recorded by VOLDORAD for rainfall and tephra emission. The snapshots show the signals and power spectral density recorded in 4 range bins (120 m deep) between 2520 and 2880m on 18 February 2004, with a beam elevation angle of 27°. Central ground clutters are not filtered. *Left: rainfall; right: ash plume event.*

In addition to the sounding geometry effect, the large contrasts in echo power and velocity distribution (spectrum shape) observed in signals of volcanic origin relative to meteorological ones come at first order from the target sizes, velocity field, trajectories, with huge variations of these in amplitude in time and space, especially near the volcanic source.

The sizes of tephra currently range from decimetric or even metric to micronic particles (6 orders of magnitude) close to the vent while only particles microns to tens of microns in diameter can remain in the atmosphere for days. While Strombolian eruptions consist of the recurrent ejection of small-medium volumes of incandescent lava bombs and lapilli with commonly minor amounts of ash to heights of tens to hundreds of meters, the fragmentation of lava and particle dispersion are much higher in eruptions generating ash plumes. From a radar perspective, the backscattered power is strongly controlled by the larger particles. Consider for instance that an order of magnitude change in particle size leads to an increase by a factor of 10^6 in the reflectivity factor in the Rayleigh domain. However, the relative proportions of each size also counts, so the particle size distribution is of primary importance, albeit challenging to measure accurately over the full size range. Importantly, particles exceeding several centimeters (lapilli and blocks) present in most volcanic tephra emissions, prevent the use of the Rayleigh approximation to quantify near-source products and the Mie formulation must be used at all infra-metric wavelengths.

Because volcanic emissions are made up of a mixture of hot gases, lava and solid fragments of various sizes ejected at high speed (tens to hundreds of m/s) from a vent, their dynamics

is complex and rapidly varying in time and space. The moments and shapes of Doppler spectra also fluctuate rapidly, with spatial variations among the range gates related to the dimension of the phenomenon with respect to the sounded volumes. The power spectral density results in particular from the complex combination of the particle velocity field and particle load distribution, i.e. the amount of particles, their velocities and trajectories. Being either short-lived or sustained, volcanic emissions can be roughly viewed as two-phase flows generally oriented vertically upward with a continuum of dynamic behaviors from inertial large blocks mostly following ballistic trajectories soon after their ejection down to the finest low-inertia particles nearly following the gas behavior involving a stronger deceleration soon after their emission. Crosswinds also affect the particles' motion differentially according to their diameter and residual momentum. Gravity further implies that ejecta are propelled upward while others fall out simultaneously and both imprint their signature in near-source radar measurements.

Volcanic emissions are generally highly turbulent close to the source (gas thrust region and convective part) and less turbulent in the distal cloud. The effect of turbulence in the cloud is difficult to assess because the particle behavior is highly size-dependent, from inertial large blocks to gas-entrained fine particles. Although assumed not to be dominant in radar measurements near the source where large particles are present, the turbulence effects affecting overall the small particles should nevertheless tend to increase the spectral width, as observed in radar meteorology.

3.3 Target properties

At second order, the intrinsic properties of the targets, their movements and chemico-physical evolution, also play a role in the measured reflectivity. Because volcanic tephra generally originate from the violent fragmentation of magma by the expanding gas, their shape is also complex and their surface highly irregular at various scales. The effects of shape and roughness of volcanic particles on reflectivity have been little investigated at radar wavelengths. Yet they might be non negligible, at least at short wavelength, as suggested for meteorological targets. In examining the effects of ice crystal shapes on reflectivity at 3 mm wavelength, Okamoto (2002) found, for instance, 8 and 5 dB effects of non-sphericity and orientation respectively, for particle sizes approaching the wavelength. In the volcanic case, the analysis is further complicated by in-flight modifications of the ejecta shape and orientation, especially close to the source. Large lava fragments, in particular, deform in-flight due to their plastic nature, as attested by the specific shapes of volcanic bombs (e.g. fusiform), or break up upon impact with other ejecta and because of high strain rates imposed by acceleration, rotation, and drag force. It must be expected that most fragments have a rapidly changing orientation in flight, especially close to the source where turbulence occurs.

Water vapor being the dominant gas species exsolved from magma (commonly >85%), major condensation by the cold atmosphere occurs during eruptions. There is 2.4 factor difference between the dielectric factors of ash (0.39: Adams et al., 1996; Oguchi et al., 2009; Rogers et al., 2011) and liquid water (0.93). According to studies by Oguchi et al. (2009) from 3 to 13 GHz, a water film coating 10-20% of the radius of a sub-millimetric volcanic particle is sufficient to raise the radar cross section to that of a whole liquid water particle (0.93 dielectric factor). Water vapor further promotes the nucleation of ice (0.197 dielectric factor)

in ash plumes at high altitude, depending on the vertical atmospheric temperature profile, and favors aggregation of ash particles. Thus, ice formation has a double effect on reflectivity, acting both on the dielectric properties and the size (aggregation). Although the influence of temperature on the dielectric properties of rocks seems rather limited up to 900°K (Campbell & Ulrichs, 1969), possible effects of magmatic temperatures need to be checked. The decrease of rock permittivity with silica content observed by these authors has direct consequences in terms of radar retrievals from eruption products of different composition, from basaltic to dacitic or rhyolitic for instance. As the combined contributions of all these effects might significantly change the reflectivity of ash plumes, they need to be further characterized physically, along with the relevant volcanic particle characteristics, in order to improve the accuracy of volcanic retrievals from radar returns.

4. VOLDORAD, a dedicated volcanological Doppler radar

4.1 Description of the transportable radar

VOLDORAD is a ground-based pulse volcano Doppler radar specifically designed at the Observatoire de Physique du Globe de Clermont-Ferrand (OPGC) for the monitoring of the surface volcanic activity of variable intensity. It can be deployed rapidly near an eruptive vent and target the near-source activity to measure in real-time the eruptive velocities and backscattered power and give information about the amount and rate of tephra emission.



Fig. 4. (*left*): The transportable volcano Doppler radar VOLDORAD 2 deployed at Arenal. The PC and radar in the car trunk are connected to the antenna system via a switch box and fed by a small generator. *Upper inset*: Radar with PC for data storage and real-time monitoring and GPS receiver for time synchronization; *lower inset*: antenna (square array of Yagi) aiming at the summit to sound ash emissions. Photos: courtesy of S. Valade, OPGC (2009).

Fig. 5. (*right*): Principles of near-vent soundings with VOLDORAD.

The signal wavelength (23.5cm) was chosen (i) to sound the interior of dense lava jets and ash-laden plumes, as well as (ii) to avoid attenuation by hydrometeors because cloudy, foggy, rainy, or snowy conditions often occur at volcano summits. It also results from a compromise between transportability (weight, size), variable measurement distances (0.2-12 km) imposed by field conditions, and the HF hardware facilities available at the OPGC.

Acquisition, reception and pre-processing units are mounted on a suspended frame inside a protective metal container (60 cm, 50 kg). A PC controls the radar acquisition, being synchronized to UTC time through a GPS or ethernet connexion, and is used for real-time visualization of Doppler spectra and data storage. The 23 elements' square array antenna is mounted on a tripod adjustable for site and azimuth, and can be easily dismantled for transport. The 3 dB beam width is 9°, equivalent to site and azimuth resolutions of about 160 m at 1 km. The 300 W power consumption is provided through a small electric generator or AC. Owing to its modularity and limited weight (~70 kg), the ensemble is easily transportable, fits in a 4WD vehicle, and can be set up quickly in a volcanic environment. This radar can thus be used for short-term scientific campaigns, as well as over the long term for monitoring purposes.

A number of settings have been designed to be selectable to best adapt to the activity and the sounding conditions. The pulse duration is selectable from 0.4 to 1.5 μ s so that the range bin radial resolution can be chosen between 60 and 225 m according to the target dimensions and the type of information searched for. The pulse repetition frequency can be 50, 100 or 200 μ s. The non ambiguous maximum range at a 100 microsecond repetition frequency is 12 km. The gain attenuation can be varied by 50 dB through 10 dB steps to best adapt to the eruption intensity. The format of the data stored on the PC hard disk can be chosen in order to adjust the space memory consumption to the duration of the record campaign: either the time series of the raw digitized signal can be recorded, i.e. after coherent integrations in the time-domain, or alternatively only the spectra are saved, i.e. after integrations in the frequency domain.

4.2 Echoing mechanism

A powerful short radio frequency pulse (duration τ) is periodically transmitted into the atmosphere through a switch and a directive antenna which concentrates the energy in a narrow beam. Just after the pulse transmission, the switch connects the antenna to a radio frequency receiver. If targets are located in the antenna beam, part of the pulse energy is backscattered toward the antenna. These radar echoes are fed via a switch to the receiver for amplification and filtering. At the receiver output, the electromagnetic signal is detected and converted into digital data which are then processed and recorded.

Like in the case of atmospheric sounding, two main mechanisms give rise to radar echoes in the case of volcanic targets (Sauvageot, 1992; Doviak and Zrnic', 1993; Dubosclard et al., 1999): (i) Rayleigh ($D < \lambda/4$) or Mie scattering ($D \geq \lambda/4$) from distributed targets, and (ii) Bragg scattering from spatial irregularities of the refractive index induced by turbulent eddies inside the hot jet, and supposedly of secondary importance in the volcanic case because of the large reflectivity of tephra. In addition to the distance of the sounded volumes, the radar reflectivity (η) is deduced from the intensity of the echo signal by using the radar equation:

$$P_r = C_r \frac{\eta}{r^2} \quad (1)$$

where P_r is the echo power measured by the radar receiver and C_r a constant including the radar parameters such as transmitted power, pulse duration, wavelength, antenna

characteristics, gain or half power beamwidth. In the simplest case of Rayleigh scattering ($D < \lambda/4$), η is expressed as:

$$\eta = \frac{\pi^5}{\lambda^4} |K|^2 Z \quad (2)$$

where K is the complex dielectric constant of the targets ($|K|^2 = 0.39$ for ash (Adams et al., 1996; Oguchi et al., 2009; Rogers et al., 2011) and Z the radar reflectivity factor. For spherical targets, Z is given by:

$$Z = \int_0^{\infty} N(D) D^6 dD \quad (3)$$

where $N(D)dD$ is the number of targets per unit volume whose diameters are between D and $D+dD$. Z is generally expressed in dBZ units, defined by:

$$Z(\text{dBZ}) = 10 \text{Log} [Z(\text{mm}^6 \cdot \text{m}^{-3})] \quad (4)$$

For Mie scattering ($D \geq \lambda/4$), one generally uses the so-called equivalent radar reflectivity factor (Doviak and Zrnich, 1993), which is defined as the radar reflectivity factor of a small particle population satisfying the Rayleigh approximation and that would return the same received power. Interestingly, Z characterizes only the target and holds information on the number and size of particles, and thus on the particle concentration. The reflectivity factor obtained from radar measurements is usually calibrated using the dielectric factor of liquid water (0.93) and must be corrected for volcanic ash as the dielectric factor of the latter is lower (0.39):

$$Z_{\text{ash}} = \frac{|K|_{\text{water}}^2}{|K|_{\text{ash}}^2} Z_{\text{water}} = 2.38 Z_{\text{water}} \quad (5)$$

Finally, the radial velocity (V_r) of the target is calculated from the frequency shift between the transmitted and received signals. The velocity component along the antenna line of sight (toward or away from the radar) causes the returned frequency f_r to be different from the transmitted frequency f_t (Doppler effect), and is proportional to the Doppler shift f_d :

$$f_d = f_r - f_t = -\frac{2V_r}{c} f_t = -\frac{2V_r}{\lambda} \quad (6)$$

Note that a negative Doppler shift ($f_r < f_t$) corresponds to a target with a radial component of motion away from the antenna (positive radial velocity) and *vice versa*. Furthermore, if the velocity vector is normal to the antenna direction, the Doppler shift is zero. In volcanic soundings, the antenna beam can be set either to point upward, e.g. from the volcano slope toward the summit, or downward, for instance aiming toward the eruptive vent from the crater rim. In these cases, contributions of rising and falling particles to the spectra are reversed (Fig. 6).

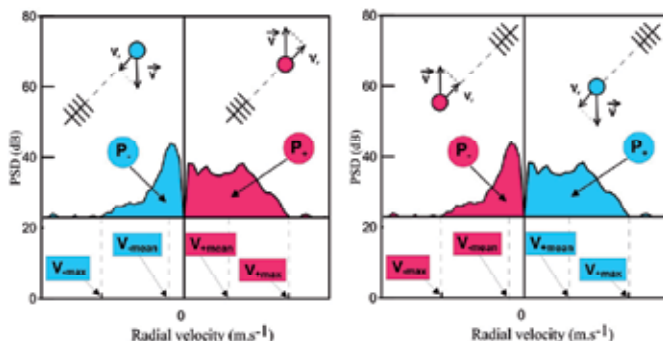


Fig. 6. Volcanic particle contributions to Doppler spectra in different sounding conditions. (a) When the antenna points upward (e.g. at summit craters from the flanks), ascending volcanic particles in red induce echoes with an along-beam velocity component away from the radar (positive radial velocity range, right part of spectrum), whereas falling particles in blue induce radial velocities toward the radar (negative radial velocity range, left part of spectrum). (b) The contributions are reversed when the antenna beam points downward (e.g. down towards a crater from the rim).

For a given range gate and for each component of the complex raw signals, N_c successive digitized samples (coherent integrations) are added together and then averaged in the time domain. This integration process acts as a low-pass filter reducing the high frequency noise and improving the signal-to-noise ratio. In order to avoid aliasing, the value of N_c must be adapted to expected maximum eruption velocities, in such a way that the Nyquist frequency f_N is higher than any Doppler frequency:

$$f_N = \frac{1}{2N_c T_r} \quad (7)$$

where T_r is the pulse repetition period of the radar. From (6) and (7) it results that the maximum radial velocity which can be measured without ambiguity is given by:

$$V_{\max} = \frac{\lambda}{4N_c T_r} \quad (8)$$

After N_c pulses have been integrated, the coherent integration stage is repeated until a sequence of 64 integrated complex data is obtained. For each range gate, the 64 coherently integrated complex data are used as a time series input to a FFT (Fast Fourier Transform) algorithm in order to obtain the power spectrum of the radar echo. The frequency resolution (frequency interval between two consecutive spectral lines) is given by:

$$\Delta f = \frac{1}{64 N_c T_r} \quad (9)$$

Therefore, the corresponding velocity resolution is:

$$\Delta V = \frac{\lambda}{128 N_c T_r} \quad (10)$$

A mean spectrum can be finally calculated from the averaging in the frequency domain of several consecutive spectra (incoherent integrations) to reduce the noise fluctuations in the resulting Doppler spectra and improve the detection of the spectral line(s) corresponding to the volcanic echoes.

5. Insight into the dynamics of Strombolian activity

In addition to measuring eruptive parameters near the emission source, the main advantage of portable Doppler radars with respect to weather radars resides in the fact that they can be set up close to an eruptive vent and target just one direction at the base of the volcanic flow to retrieve near-source parameters. They are thus able to monitor phenomena of limited spatial dimensions with better spatial resolution and higher acquisition rate. In this respect, they are particularly useful for studying Strombolian activity and small scale ash plumes, generally invisible to remote weather radars and satellites. Although VOLDORAD can also be used to monitor strong ash-laden plumes, given its wavelength, examples of records on such types of activity are provided respectively in this section and the next.

5.1 Information retrieved from the shape of Doppler spectra

5.1.1 Ejecta dispersion

Given the relatively low amount of ash produced during typical Strombolian activity, the echo power is mostly controlled by large blocks that mostly follow ballistic trajectories. An illustration of the strong control of the ejecta's spatial distribution on the shape of Doppler spectra is the discrimination between lava bubble outbursts and lava jets (Fig. 7). When the magma column is high in the conduit, large gas bubbles may deform the lava surface to form lava bubbles several tens of meters in diameter, whose outburst disrupts the surrounding lava film and produces the hemispherical ejection of big lava lumps (decimetric to metric) seen above the crater rim (Fig. 7a). Contrastingly, in the vast majority of events, gas slug explosions occur within the conduit and produce oriented jets of gas and more fragmented lava, generally vertical, that can be captured by the radar beam when (if) pyroclasts go beyond the crater rim (Fig. 7c). Velocity and mass load angular distributions of pyroclasts are, as expected, more uniform for hemispherical lava bubbles that can burst at the free surface and more Gaussian-shaped for lava jets that are subjected to conduit wall friction (Fig. 8). In the case of hemispheric lava bubbles, the uniform mass load and velocity distribution of pyroclasts over the range of ejection angles produce an equal echo power over the range of radial velocities, leading to top-hat shaped spectra (Fig. 7b). In the case of lava jets, the power spectral distribution results from the competing effects of particle velocities and the distribution of ejection angles. As shown in figure 8b, measured maximum radial velocities do not result from particles with the highest velocities in the jet axis, nor from those having the most radial trajectories, but from particles ejected at about 20° to the jet axis (when vertical). Therefore Doppler spectra commonly appear rather triangular when shown in dB (Fig. 7d). Gouhier & Donnadieu (2010) found that, for most Strombolians explosions at Etna, 80% of the tephra mass is ejected within a dispersion cone of about 40°.

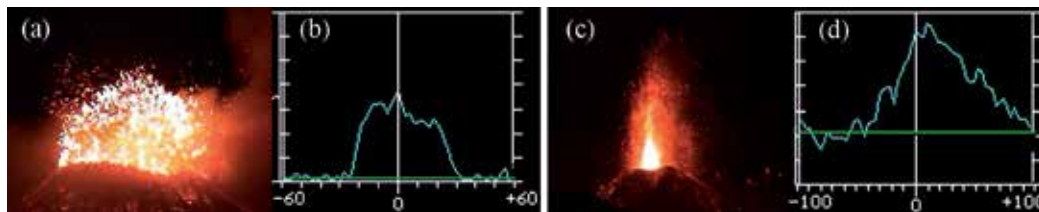


Fig. 7. Shapes of Doppler spectra associated with Strombolian activity. Outburst of a hemispherical lava bubble (a) and associated top-hat Doppler spectrum (b) at Etna’s SE Crater (04/07/2001, 21:43’06). (c) Vertical lava jet at Laghetto (29/07/2001, 21:20’56) and the recorded triangular spectrum (d) (power in dBW vs. radial velocity in m/s).

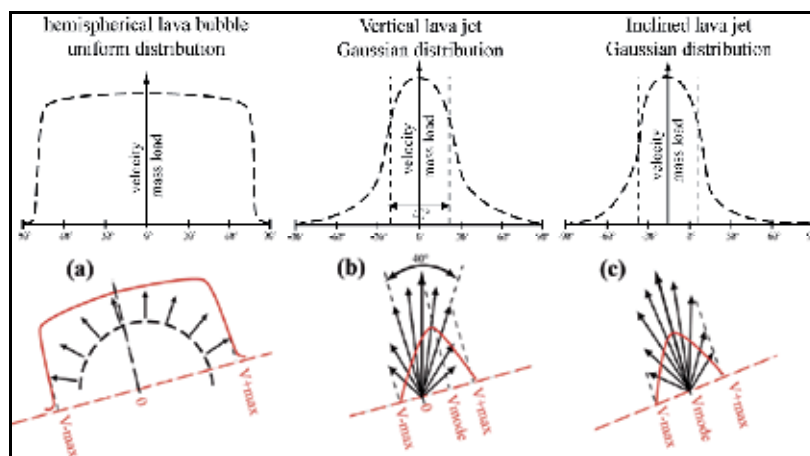


Fig. 8. Ejecta angular distributions (*top*) for lava bubbles (a), vertical jets (b) and inclined jets (c) and associated characteristics of Doppler spectra in red (*bottom*). (a): similar to Fig. 7a & 7b; (b): similar to Fig. 7c & 7d; (c): case of a jet inclined toward the radar.

All intermediary types of pyroclast ejection may exist, including lava jets with low directivity, leading to varied spectrum shapes. The latter can be further complicated by other factors related to the lava state in the conduit and crater, or to gas slug characteristics (overpressure, length) that may enhance fragmentation and produce more fine particles more closely coupled to the gas dynamics.

5.1.2 Inclination of lava jets

Strombolian activity is often imagined as an axi-symmetric dispersion of ejecta around the vertical, but departures are frequently observed from one explosion to another, and ejection in a preferential direction may even persist if conduit conditions are favorable. Relative variations of the ejecta dispersion axis from the vertical, i.e. the inclination of lava jets or lava bubble outburst, can be tracked from the mode of the radial velocities, i.e. the velocity associated with the maximum power in the main range gate (Fig. 8b,c). The velocity mode is shifted toward the maximum negative radial velocities (aiming upward) when the lava jet has an inclination component toward the radar (Fig. 8c) and vice versa. The power distribution in contiguous gates also puts constraints on the ejection geometry and

velocities. In figure 9, for instance, ejecta emitted below the 840 m range bin do not reach the 600 m range bin, falling ejecta reaching the 720 m and 960 m bins where the negative parts of the spectra look alike. The absolute inclination angle cannot be retrieved directly firstly because velocities and power distribution vary strongly between explosions and also only the inclination angular component in the beam's vertical plane can be retrieved. Gerst et al. (2008) solved this problem by using simultaneously 3 FM-CW radars to calculate the directivity of Strombolian eruptions and reconstruct time series of the 3-D directivity vector every second. Another solution is to best match the power spectral distribution in the different range gates (e.g., Fig. 9) from ballistic models and Mie scattering theory (Gouhier & Donnadieu, 2010).

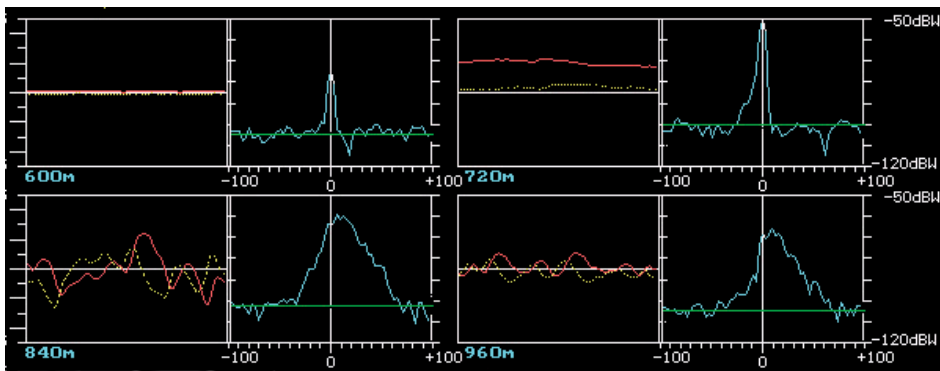


Fig. 9. Doppler spectra recorded in 4 range bins during lava jet activity at Etna. For each gate the raw signals (left) and spectra (right) seen in real-time are shown. The spatial distribution of the power spectral density in the 840 m range gate above the eruptive crater and in contiguous range gates (720 and 960 m) gives information about the dynamics of the lava jets (Laghetto cone, 29/07/2001).

5.2 Information from spectral moments

5.2.1 Mean diameter

Dubosclard et al. (2004) have shown that, in the case of Strombolian activity, the negative power spectral density (when aiming upward) of the range gates above the vent is mostly associated with falling particles. Therefore, the mean negative radial velocity weighted by the power spectral density has been used to retrieve the average particle diameter in the jet, commonly found to be between 1 and a few cm in diameter. Importantly, Gouhier & Donnadieu (2008) pointed out that the radar-equivalent mean diameter retrieved from Doppler spectra differs significantly from the true mode of the particle size distribution which, indeed, corresponds to the most frequent diameter encountered. Thus the radar-equivalent mean diameter cannot be used directly as the true modal diameter. In the gas thrust region of volcanic jets, the power spectrum is very wide, unlike in radar meteorology, and the physical interpretation of the radar-equivalent mean diameter is complex. Because the offset factor depends upon the reflectivity at a given radar wavelength, itself dependent on the number and diameter of particles which vary over a wide range, the conversion requires the Mie scattering formulation.

5.2.2 Eruptive velocities

Initial velocities are of great interest because they control the height reached by the pyroclasts and are related to the gas overpressure. In measuring particle velocities continuously and at high rate, Doppler radars potentially hold information on these parameters and on the detailed kinetics of the jets. Although the variations of measured radial velocities closely reflect the kinetics of the volcanic jet, retrieving absolute initial particle velocities from measured maximum radial velocities is not straightforward, in general, because (i) the latter are associated with oblique trajectories, as illustrated in figure 8b-c, (ii) the distance between the range gate's lower boundary and the emission source must be taken into account; it also controls which particle size induces the measured maximum velocities (Gouhier & Donnadieu, 2011). In order to confidently retrieve initial (at-vent) velocities, eruption models with suitable laws are needed, along with accurate knowledge of the sounding geometry and crater configuration. Velocity calibration can be further supported by an analysis of video-derived velocities. By sounding the volcanic emission near their source, it turns out often that maximum radial velocities, commonly in the range of a few tens to 160 m/s are not very different from eruptive velocities during Strombolian activity at Etna for example. Gouhier & Donnadieu (2011) analyzed 247 Strombolian explosions during the paroxysmal phase of the July 4 2001 eruptive episode of Etna's SE crater and found time-averaged values of 95 ± 24 m/s for initial particle velocities, 37.6 ± 1.9 m/s for the bulk jet velocity, and 118 ± 36 m/s for the initial gas velocity. Note that the initial gas velocity is highly dependent upon the chosen model law, as the gas velocity decrease with height is exponential and more quantitative observations are needed, using complementary techniques like high-rate thermal infrared imagery.

5.2.3 Detailed dynamics at short time scales

Much can be learned from the analysis of time series of echo power and velocities on the eruption dynamics at various time scales, ranging from a single explosion through to an entire eruptive episode, to a series of eruptions. Figure 10 shows such time series for a Strombolian explosion at Yasur volcano, Vanuatu, similar to that shown in figure 11.

The maximum along-beam velocities associated with rising ejecta show a very sharp increase up to a peak near 120 m/s within 0.21 s, attesting to initial accelerations of over 560 m/s^2 (i.e. 57 g). Measured velocities then regularly decrease for 6-7 s, then reach a plateau at 20-30 m/s with sparse, short fluctuations up to 50 m/s. Interestingly, during the strong velocity phase, ample fluctuations associated with short power increases can be seen pulsating every ~ 1.5 s, suggesting rapid variations in the discharge rate. This could be caused either by the successive explosions of trains of closely packed gas bubbles rather than a single large slug, or by flow oscillations related to the high speed motion of a compressible fluid and conduit irregularities. The sharp onset in echo power in the 344 m range gate for both P- and P+ shows that rising particles with motion components both toward and away from the antenna (pointing downward) contribute to the signal. The former are dominant as the bulk flow is vertically directed. The first break in slope is likely associated with ejecta leaving the gate through its upper boundary. P- then gently increases up to its peak amplitude nearly 3 s later, as more pyroclasts fill up the probed volume. About 6 s after the onset, P+ becomes dominant whereas P- starts to decrease, indicating the contribution from block fallout. Comparing with figure 11, it can be inferred that most of the

explosion momentum occurs during the first 6-7 s and corresponds to the main discharge of large ballistic blocks and dense lapilli- and ash-laden plume, with an initial maximum followed by a rapid decrease. The following phase, with lower velocities and echo power, results from the final emptying of the gas slug tail causing the relatively milder release of gas and finely fragmented ash at lower concentrations.

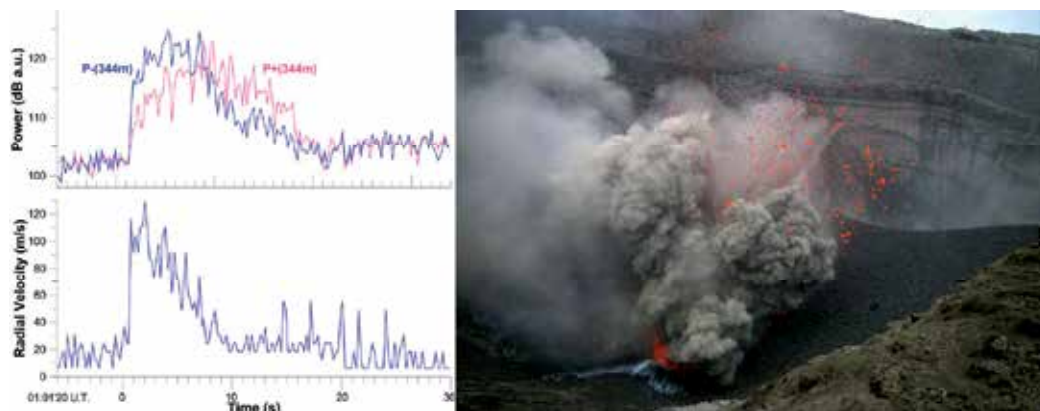


Fig. 10. (left): Time series of power (*top*) and maximum radial velocities (*bottom*) of a Strombolian outburst recorded by VOLDORAD aiming downward into Yasur's southern crater on 27/09/2008. Data are smoothed with 3 incoherent integrations (0.21 s).

Fig. 11. (*right*): Strombolian explosion at southern crater of Yasur volcano, Vanuatu. Incandescent pluridecimeteric lava blocks resulting from the magma surface disruption by the pressurized gas slug are visible ahead of the ash plume (about a hundred meters high) generated by the magma fragmentation during gas pressure release. Photo courtesy: A. Finizola (2008).

5.2.4 Tephra mass loading

Gouhier & Donnadieu (2008) presented a method to estimate the particle loading parameters (mass, number, volume) of eruptive jets from the inversion of the echo power. The inversion algorithm uses the complete Mie (1908) formulation of electromagnetic scattering by spherical particles to generate synthetic backscattered power values. Assuming a log-normal shape for the particle size distribution, they estimated the total mass of tephra emitted during Strombolian explosions at Etna at around 58 and 206 tons for low and high concentration lava jets respectively. Derived parameters such as mass flux, particle kinetic and thermal energy, and particle concentration can also be estimated. As for particle concentrations, they must be regarded as minima in the case of small scale phenomena (relative to the range gate dimensions) like lava jets, because they are spatially highly heterogenous and might not completely fill the sounded volume. More reliable concentration values could be obtained when several range gates are filled completely, such as one expects from large ash plumes. For instantaneous events like Strombolian explosions, a total mass can be calculated from the echo power maximum amplitude assuming that all particles are present in the beam at the instant of the peak power. The instantaneous mass flux that can be derived in this way differs, however, from the initial mass flux as the power

peak does not occur at the signal onset (Fig. 10). The initial mass flux can be estimated from the mass corresponding to the first break in slope of the power curve (cf. 5.2.3.) divided by the time difference between the break in slope and the onset.

The particle size distribution being the main unknown, the tephra mass can be computed as a function of diameter for different reflectivity factors (Z). As seen from the curve shape in figure 12a, the uncertainty on mass is much less for lapilli and blocks than for ash at VOLDORAD's wavelength. This is also demonstrated in figure 12b: for a given tephra volume, Z is much lower for small particles and increases linearly with diameter (in log-log plot), up to particle diameters approaching a quarter of the wavelength (5.9 cm, end of the Rayleigh domain), and beyond this value fluctuates in a lower range. The curve in figure 12a corresponds to the value of Z calculated from the power peak amplitude of figure 10. It can be used to infer a minimum tephra mass of several tons for the high momentum first phase, reasonably assuming an average diameter for ballistic blocks of more than 4 cm. This leads to an initial mass flux of ≥ 10 tons/s for a period of low activity at Yasur, consistent with values of 26-74 tons/s found by Gouhier & Donnadieu (2008) for larger Strombolian outbursts at Etna.

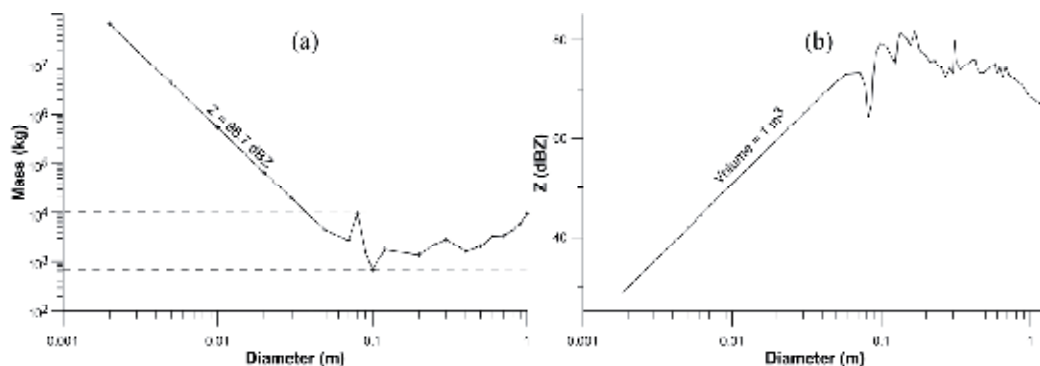


Fig. 12. (a) Tephra mass associated with a given reflectivity factor (Z), as a function of diameter. The curve shown corresponds to the value of Z calculated for the eruption of Yasur volcano in Fig.10. (b) Radar reflectivity factor associated with a tephra volume of 1 m^3 , as function of diameter, calculated with sounding conditions at Arenal volcano.

For sustained tephra emissions, like ash plumes, the mass flux evolution could be tracked through an integration of the mass of rising particles over time. This is not straightforward, however, because (i) falling particles should be removed, (ii) the particle size distribution must be assumed to be constant with time, and (iii) the integration timestep is not the data acquisition rate that would otherwise cause redundancy but is instead related to the average transit time of rising particles through the considered range gates, and (iv) all tephra are not ascending at the same velocity because of their wide range of sizes, and therefore they have different transit times, (v) the particle transit time will vary with time according to velocity variations (e.g. short-lived events). One method to retrieve the time variations of mass flux could be, at first order, to use the P^+/P^- ratio to find the proportion of rising particles and integrate the power-derived mass curve using as a timestep the range gate dimension along the flow direction divided by the bulk (power-weighted) flow velocity.

5.2.5 Gas flux estimates

Although maximum velocities measured by the radar result from particles, initial gas velocities can be estimated at first order using the corrections seen in section 5.2.2. and adequate model laws for the coupling of gas and particle velocities and gas velocity decrease with height. The volume and mass gas fluxes Q^g can also be estimated from the initial gas velocity (V_0^g) and vent section, the radius (r) of which can be observed in the field or inferred from modeling of acoustic signals:

$$Q_{vol}^g = \pi r^2 \times V_0^g \quad (11)$$

$$Q_{mass}^g = \rho^g \times Q_{vol}^g \quad (12)$$

where ρ^g is the gas density at the considered atmospheric pressure (elevation) and temperature; water vapor being the ultra-dominant species, its density can be used for ρ^g . Note that gas fluxes evolve similarly to the maximum radial velocities and therefore have a large peak at the explosion onset followed by a rapid decrease in a matter of seconds. Averaging over the duration of the emission for a large number of Strombolian explosions, Gouhier & Donnadieu (2011) found volume and mass gas fluxes of $3\text{-}11 \times 10^3 \text{ m}^3/\text{s}$ and $0.5\text{-}2 \text{ ton/s}$ during the paroxysmal stage of a Strombolian eruptive episode of the SE crater at Etna. Radar-derived gas flux estimates at the source can then be compared with fluxes inferred from other ground-based techniques, like combined OP-FTIR gas spectroscopy and SO_2 flux measurements by DOAS, or ground-based thermal imagery.

6. Investigations of ash plumes with VOLDORAD

There is a continuum in the types of activity between Strombolian explosions seen previously and ash plumes. Ash plumes display a variety of behaviours depending on whether they are short-lived or sustained (steady state or not), whether they are jet plumes or buoyant plumes according to their momentum (mass loading, particle size distribution, fluxes), and also depending on environmental conditions including crosswind, elevation of the emission point, humidity and atmospheric temperature profiles, among the main ones. As an example, figure 13 shows three ash plumes with varying ash concentration and momentum, and also differently affected by the wind advection.



Fig. 13. Examples of various ash plumes at Arenal and Popocatepetl volcanoes. (a): low concentration buoyant plume bent over by wind advection at Arenal. (b): vertical jet plume, a few hundreds of meters in height, on same day (May 23, 2005). (c): dense ash plume of Popocatepetl buoyantly rising to about 2 km in height and drifting to the North on July 28 2007. Photos courtesy: Hotel Kioro Arenal and CENAPRED.

Ash is the major tephra component and is the main source of the ensuing hazards to humans, infrastructures and aviation, as shown by the 2010 eruption of Eyjafjallajökull in Iceland. This is because fine ash can remain in the atmosphere for hours to days, forming an ash cloud in the distal part. Although termed an ash plume, the proximal part does not comprise only ash, especially in the gas thrust and convective regions sounded by VOLDORAD. Below, examples are described which give insight into the ash plume dynamics close to the source.

6.1 Discriminating ballistics and ash

Tephra emissions are commonly explosive, having initial excess momentum compared with purely buoyant plumes. Therefore the explosive emission driven by the expansion of overpressured gas propels ash, lapilli and blocks in the air. Ash-sized particles closely follow the turbulent gas regime whereas inertial blocks mainly follow ballistic trajectories. So both are strongly decoupled, although a continuum of dynamic behaviors occurs in between for intermediary particle sizes. Because the spatiotemporal distribution of their velocity field and mass loading are contrasted, the dynamics of ballistics and ash can be discriminated when radar targeting the gas thrust region of the volcanic jet. Figure 14 illustrates the distinctive Doppler signatures for a jet plume at Arenal volcano similar to that shown in figure 13b and recorded with the beam aiming upward (27°) toward the summit. Although not obvious from the analysis of the time sequence of Doppler spectra the discrimination becomes particularly conspicuous on velocigrams. The velocigrams represent the power spectral density (dB color scale) as a function of radial velocities (y-axis) and time (x-axis) in 5 contiguous 120 m-wide range bins from 2367 to 2847 m. The 2607 m range bin, located above the vent, first records the jet plume onset. A 3-D representation of the velocigram at 2607 m is shown in the inset (cf. also book cover image). The ballistics are characterized by a short-lived signal (10-15 s) rapidly transiting through the gates. Range gates above the vent show positive radial velocities shifting to negative in a matter of seconds, as a result of the progressive bending of the ballistic trajectories through the radar beam.

Contrastingly, blocks only enter range gates located down-beam with negative radial velocities. So the time evolution of the spectral shape of this signal holds information about the ejection geometry (height, angles, orientation) and mass load spatial distribution, in addition to source parameters retrieved in section 5. Single streaks from individual blocks are sometimes visible on the velocigrams, and power-derived sizes are often decimetric. Considering lapilli to block sizes ranging between 0.04-1 m, Valade & Donnadieu (2011) found a mass of ballistics in the range 0.5-7 tons, i.e. a dense rock equivalent volume of 0.2-2.8 m³, for a similar event at Arenal. The second signal characterizes the ash plume, with lower backscattered power (by 10-20 dB), longer duration (>1 mn), slower transit through the gates, and with only negative velocities because the wind pushes the ash toward the radar. Interestingly, these characteristic maximum radial velocities may be used to constrain the effect of the wind and the buoyant ascent velocity. Although clearly smaller than for ballistics, the particle size distribution in the ash plume is poorly constrained, and so is the ash mass. Also, the longer duration and wider spatial coverage of the ash cloud requires spatial and temporal integration to obtain the total mass, which is nevertheless presumably greater than the mass of ballistics.

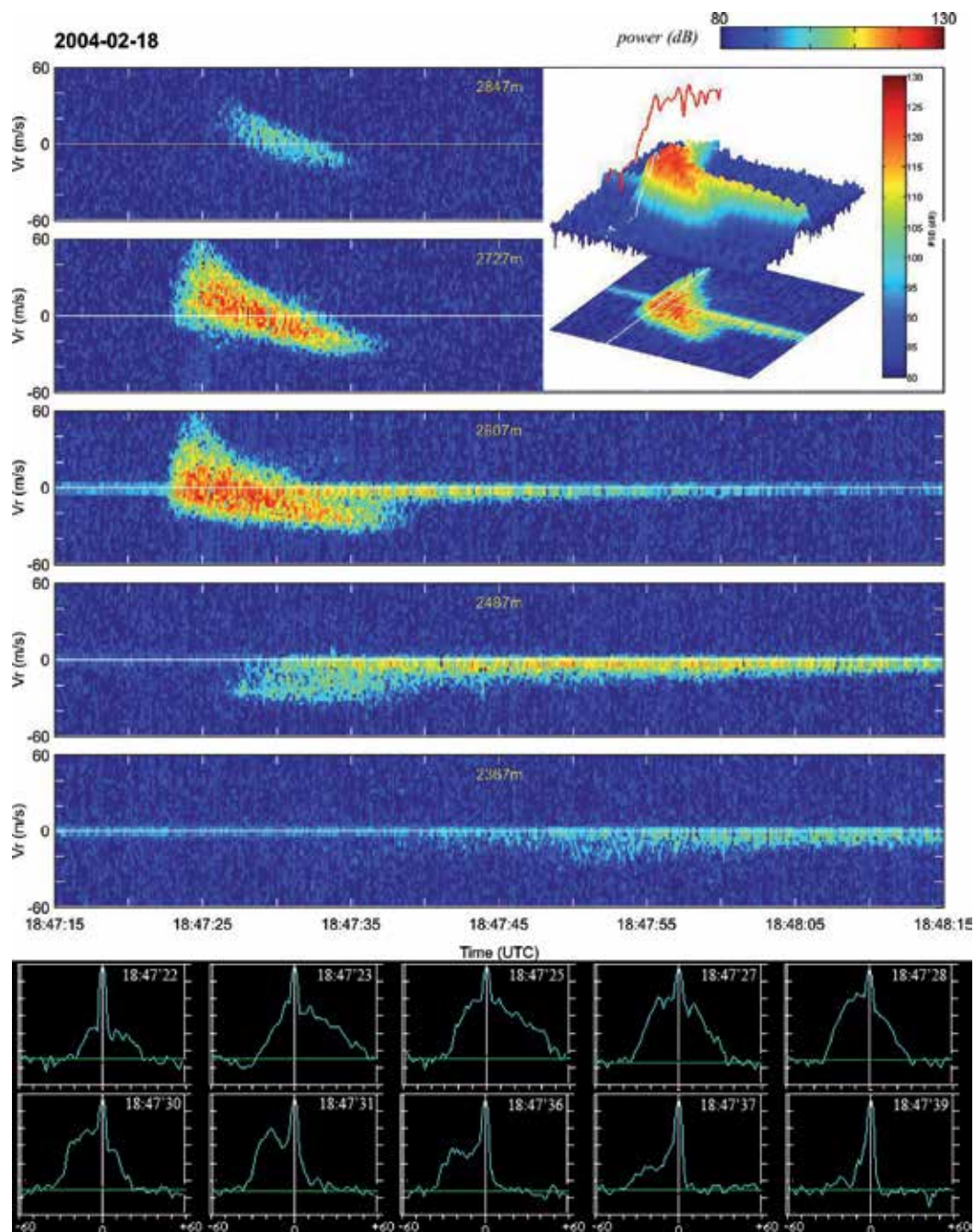


Fig. 14. Distinctive Doppler signatures of ballistics and ash dynamics for a jet plume at Arenal volcano (18/02/2004 at 18:47 U.T.). *Top*: velocigrams of 5 contiguous range bins. Inset: 3-D velocigrams of the 2607 m range bin above the vent. *Bottom*: Doppler spectra at 2607 m, showing power spectral density (dB arbitrary units) versus radial velocity (-60 to +60 m/s); central peaks with constant power value are non filtered ground echoes.

6.2 Ash plume dynamics

The onset impulsivity of the same jet plume is nicely displayed on the time series of figure 15a, showing a sharp onset in maximum radial velocities, rapidly peaking over 80 m/s and then decreasing exponentially over about 10 seconds. The power maximum amplitude is also at the onset, indicating a mass flux maximum at the beginning, and P+ decreases rapidly after a few seconds and then more gently after about 10 s from the onset. The contribution of falling ballistics keeps P- high for a longer time. The 10 second phase of strong velocities and echo power corresponds to the initial mushroom-like ash plume head heavily charged with large blocks which dominate the signal. After this phase, radial velocities remain steady and low (10-20 m/s) and the power decreases more gently. The ballistics might therefore come from the disruption of the solidified lava plug by the gas overpressure accumulated underneath. This would clear the vent or fracture and open a way to a milder sustained gas release remobilizing variable quantities of ash and possibly fragmenting the lava to form juvenile ash.

Not all tephra emissions are impulsive at Arenal, and there are a wide variety of eruptive behaviors (Mora et al., 2009; Valade et al., 2012). Some emissions comprise mainly ash and are sustained typically for a minute or so (Fig. 15b). In contrast to the impulsive signal of jet plumes (Fig. 15a), the peak in echo power comes about 10 s after the onset. The second striking feature is the large oscillations correlated between P+ and P-, and having a remarkable periodicity of about 3 s. This indicates pulsations in the amount of material emitted, suggesting a staccato pressure release (Donnadieu et al., 2008). This observation supports the clarinet model of Lesage et al. (2006) for the volcanic tremor at Arenal, in which intermittent gas flow through fractures produces repetitive pressure pulses. The repeat period of the pulses is stabilized by a feedback mechanism associated with standing or traveling seismic waves in the magmatic conduit. Moreover, these rhythmic variations might well be a common feature of persistently active volcanoes with intermediate lava composition. In eruptions of Santiaguito volcano, Guatemala, Scharff et al. (2012) also observed multiple explosive degassing pulses occurring at intervals of 3-5 s, with common velocities of 20-25 m/s.

Figure 15c illustrates the signature of a larger ash plume of Popocatepetl, in Mexico, reaching a few kilometers above the volcano. Because its summit culminates at nearly 5450 m a.s.l., even small ash plumes generate hazards to the aviation, to the surrounding infrastructures and airports and the 30 million inhabitants living within 100 km of the volcano in important cities like México and Puebla. Its crater is 600 by 800 m wide with a growing lava dome inside. The relatively low velocities (<35 m/s) measured at 5085 m, along with the velocity peak not reached immediately after the onset, suggest low excess momentum and a mainly buoyant uprise, like most ash plumes in 2007 at Popocatepetl. Note that, in the case of ash plumes, radial velocities might reflect plume velocities more closely because convection and turbulence create eddies entraining particles that would tend to generate echoes with radial velocities toward and away from the radar, with comparable amounts of echo power in the absence of wind. From the time lag of P- relative to P+, however, it can be inferred that wind was blowing with some component toward the radar, i.e. to the north. In addition the power backscattered in 3 range gates simultaneously reveals that the horizontal dimension of the plume at the beam level was 2-3 times the radial resolution, i.e. >300 m. The comparable level of echo power at 5085 m and 5235 m, along

with the similar evolution of P+ at 5235 m and P- at 5085 m during the first seconds of the main emission indicate that the plume axis was near the boundary between these range gates, i.e. at a slant distance of 5160 m. This plus the fact that the main emission is shortly preceded by a weaker emission at 4935 m suggests that the ash plume originated from the northern part of the dome, closer to the radar.

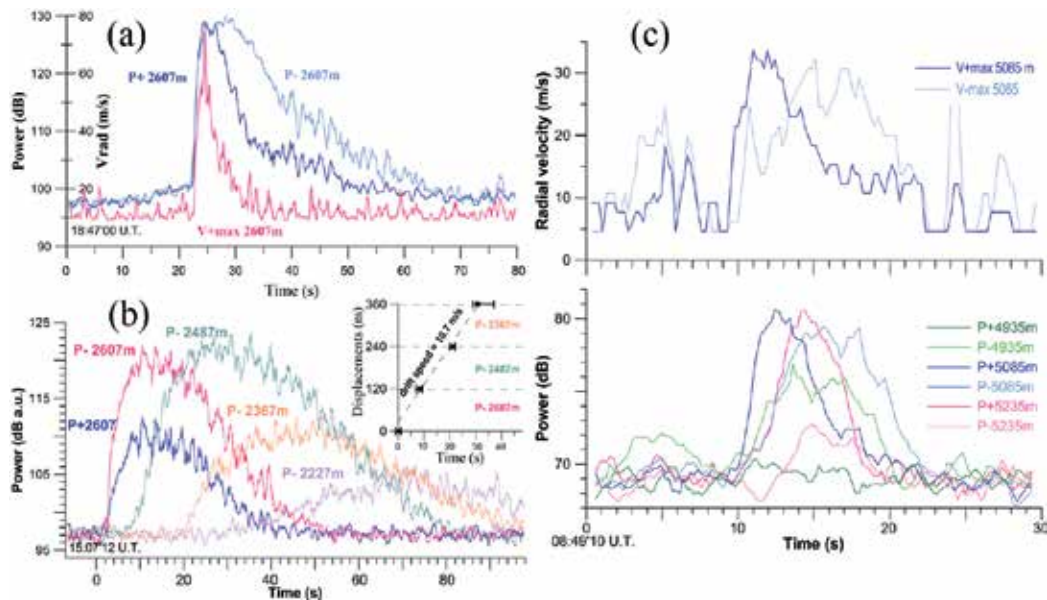


Fig. 15. Time series of echo power and velocities recorded by VOLDORAD (aiming upward) for (a) an impulsive jet plume (18/02/2004, 18:47) and (b) a sustained mild ash emission (11/02/2005, 15:07) at Arenal, and (c) a buoyantly rising ash plume at Popocatepetl (25/01/2007, 08:49).

6.3 Transport speed of ash plumes

The wind has a strong influence on ash plume dynamics, causing it to bend and, importantly for model-derived mass eruption rate estimates, be lower in height. When some wind component exists in the direction of the beam, radar echoes reflect the radial component of the drifting ash plume. As seen in figure 15b for a weak ash plume at Arenal, the near-source displacements of the plume can be tracked through echo onsets induced by ash entering successive probed volumes in the radar beam. When plotting the along-beam displacement versus time, a constant transport velocity is commonly reached within a few seconds of the initial ash emission (10.7 m/s along-beam in this case), as wind advection and buoyancy take over momentum. The departure of the first data point, i.e. the emission onset, from the general trend gives a relative indication of the slant distance of the vent to the radar. As shown by Donnadieu et al. (2011), the plume azimuth and uprise angles can further be constrained by comparing the amplitude decrease of the radar echoes as a function of distance from the source with results from a simple geometric plume model. This allows the three dimensional vector of the ash cloud transport speed to be reconstructed with an accuracy of a few percent. This method may have applications for determining pyroclasts fluxes, for

volcano monitoring, for the modeling of tephra dispersal, and for remote measurements of volcanic gas fluxes for which the plume transport speed is needed.

7. Other applications of transportable radars

Beyond their main use to measure near-source eruptive parameters, compact Doppler radars can be utilized for a number of other applications in volcano monitoring. The identification of erupting vents using range gating and the tracking of rockfalls are illustrated in this section; possible investigations on fallout are discussed in the concluding section.

7.1 Discrimination of active vents

The summit areas of active volcanoes have complex and evolving morphologies, often comprising multiple craters, themselves possibly nesting several vents, all potentially active simultaneously with various dynamics. The relatively good spatial resolution (tens of meters) of dedicated ground-based radars often allows the spatial discrimination of the surface activity and, in particular, the identification of the eruptive vents. This information is obviously very useful in volcano monitoring to locate the activity in real-time. Note that large wavelength signals, such as that used by VOLDORAD (L band) can penetrate through dense ash-laden plumes or lava fountains and give information on possible activity occurring in craters behind.

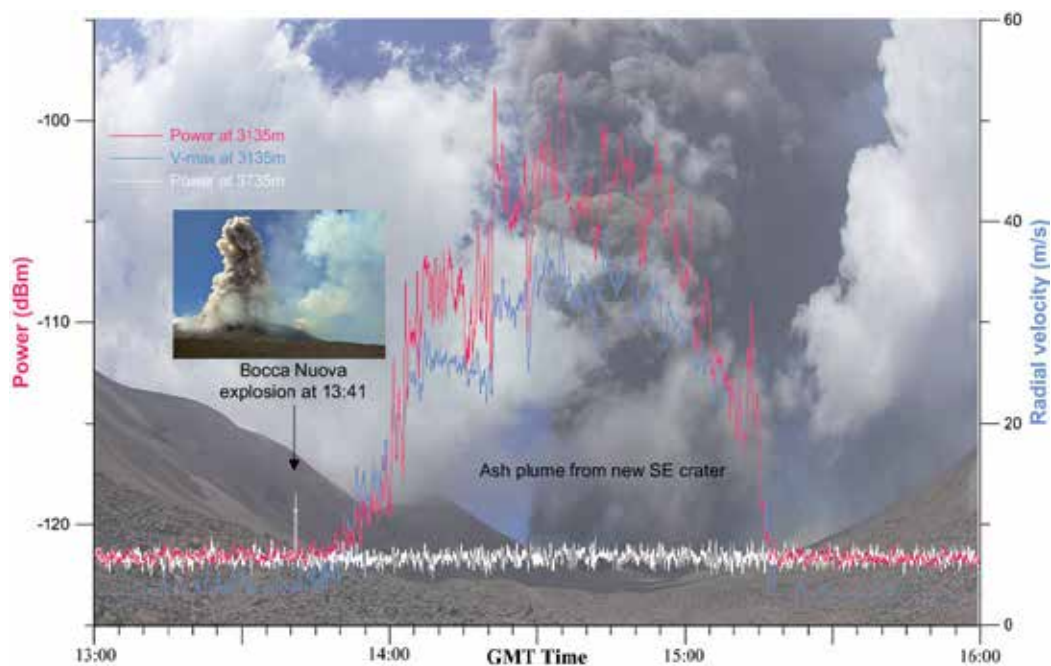


Fig. 16. Spatial discrimination of active craters of Etna using range gating (VOLDORAD 2B). Simultaneous tephra emissions of Bocca Nuova and new SE Crater at Etna on July 9 2011 are discriminated using echoes in range gates at 3735 m and 3135 m respectively (Radar data: OPGC-INGV; Photo courtesy: Tom Pfeiffer, www.volcanodiscovery.com).

At Etna, a ground-based Doppler radar operated jointly by the INGV in Catania and the OPGC in Clermont-Ferrand has been continuously monitoring the tephra emissions of the summit craters since 2009 (Donnadieu et al., 2009a, 2012) from a shelter at La Montagnola, about 3 km to the south. Echoes are recorded in 11 range bins, 150 m deep and 9° wide in azimuth and elevation, defining a 1650 m-long truncated conical volume covering the summit craters. These were very active in 2010-2012, showing different eruptive styles, including short-lived ash plumes (e.g. new SE Crater April 8 2010; Bocca Nuova, August 25 2010) and large ash columns several kilometers high sustained for several hours from lava fountains, such as the eruptive episodes of the new SE Crater in 2011 (Donnadieu, 2012; <http://www.obs.univ-bpclermont.fr/SO/televolc/voldorad/>).

Figure 16 presents records from VOLDORAD 2B of simultaneous activity of Bocca Nuova and new SE Crater during cloudy weather. Radar monitoring is not hampered by clouds that sometimes make visual observations impossible. As shown by the echo power curves from the range gates at 3135 m and 3735 m, the short-lived explosion forming a weak plume at Bocca Nuova can be discriminated from the strong and dense column fed from the lava fountain originating in the new SE Crater and sustained for about 1.5 h. While the former cause a power increase of only a few dB, the latter result in much more powerful echoes (> 20 dB), with a progressive onset and more abrupt waning phase. Radial velocities in the convective ash and lapilli plume above the lava fountain commonly reach 30-40 m/s.

7.2 Tracking of rock falls

Not only the explosive activity can be monitored using transportable radars, but also lava flow or dome instabilities (Wadge et al., 2005; Hort et al., 2006). Viscous basaltic andesite lava flows continuously outpour from the summit of Arenal volcano and slowly flow on top of loose pyroclastic material down the steep and unstable upper slopes. Due to the joint actions of cooling and pushing by new lava, instabilities occur and generate repeated rock falls, sometimes evolving into small pyroclastic flows. While monitoring the ash emissions with VOLDORAD 2 from the west between January 26 and March 4 2009, signals from very frequent rock falls could be recorded in several range gates because their lowest part hit the volcano's upper slopes, where destabilizations occurred toward the SW.

The radar signature of rock falls is characterized by echoes with only radial velocity components toward the radar in contiguous bins at slant distances consistent with the location of the volcano's upper slopes (4013 and 3878 m on Fig.17). Radial velocities are typically low (<20 m/s). The amplitude of the backscattered power is less in closer bins, as expected if not all the destabilized material goes all the way down the slope. As seen from the power curves, signal onsets are delayed from the most remote range gates to the closest, as the destabilized material tumbles down. It is interesting that many small rock fall events detected by the radar are not always well recorded on seismograms, and thus both techniques appear complementary as noticed by Vöge et al. (2008).

An estimate of maximum block velocities during rock falls (V_{rf}) can be retrieved from the radial velocities (V_r) measured by the radar on the upper slopes when the geometry is known:

$$V_{rf} = V_r \times \frac{1}{\cos(\alpha)\cos(\theta_{rf} - \theta_{ant})} \quad (13)$$

where α is the azimuth difference between the rock fall direction and the beam axis, θ_{rf} the average angle of rock fall relative to the horizontal and θ_{ant} the elevation angle of the beam.

Approximate angle values determined from field observations ($\alpha \approx 45^\circ$, $\theta_{rf} \approx 35^\circ$, and $\theta_{ant} \approx 22^\circ$ for the lowest part of the beam) lead to rock falls velocities equal to 1.45 times the measured radial velocities. With maximum radial velocities commonly in the range 7-14 m/s, the upper range of rock fall velocities is 10 to 20 m/s. Likewise, average rock fall speeds can be estimated from the time delays of power onsets in successive range gates and the gate radial resolution.

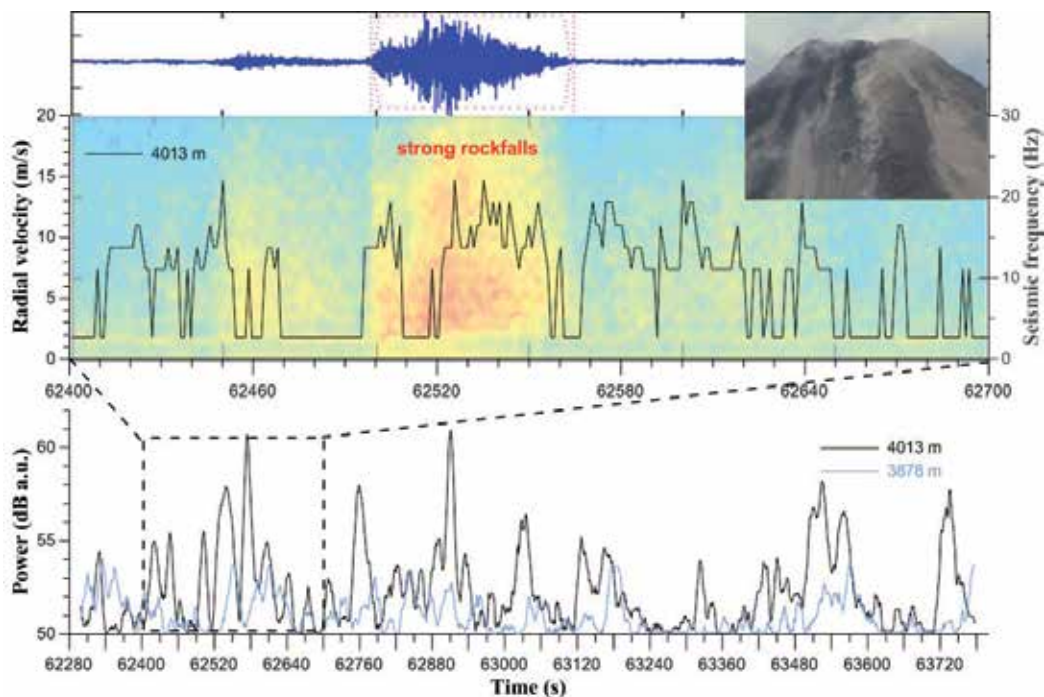


Fig. 17. Radar and seismic signals associated with rock falls at Arenal (02/02/2009). *Bottom*: 25 minute record of power from two range gates hitting the volcano upper slopes, where rock falls are detected by VOLDORAD; *middle*: maximum radial velocity (component towards radar) superimposed on a color spectrogram showing the seismic frequency content associated with rock fall events; *top*: seismic trace of a large rock fall and view of Arenal's summit from north showing lava flows and rock falls producing dust (seismic data courtesy of M. Mora; photo © F. Donnadieu, 14/05/2006).

In theory, the volume of rock falls could be determined from the power measured by the radar. In the case of Arenal, however, the size distribution of the fragments tumbling down the flanks is unknown and challenging to measure. Also, rock falls occurring in corridors can be masked by topographic obstacles or take place in other directions not visible to the radar so that it is likely that not all the falling material is detected and some events can even remain undetected by the radar. Nevertheless, as most rock falls are generated in

preferential directions during long periods of activity, transportable Doppler radars can be used to track this type of activity in order to assess the state of the activity, the stability of the lava flow or dome, and better understand the destabilization processes (Hort et al., 2006). They could be further used to correlate the rock fall activity, linked to the lava effusion rate, to the emissions of tephra. As both types of event could be recorded by the radar, such a comparative quantified analysis over a representative time sequence spanning several weeks could provide information on the eruptive behavior of the volcano and the dynamics of its upper plumbing system.

8. Conclusion and future prospects

Illustrations provided in this chapter show the many capabilities of Doppler radars to investigate and monitor volcanic phenomena in real-time and in all weather conditions. The L-band portable volcano Doppler radar of the OPGC is particularly useful for monitoring explosive activities of variable intensity from a chosen location. Owing to its 23.5 cm wavelength, VOLDORAD is able to sound the interior of dense particle-laden volcanic jets. By directly probing the jets near the vent, quantified eruption source parameters can be retrieved in different volumes with a high spatiotemporal resolution.

A major challenge in the mitigation of ash plume-related risks is to determine the relative mass flux of volcanic material propelled into the atmosphere, in particular the mass transport rate in the cloud at the neutral buoyancy level. The mass transport rate represents only a fraction of the total flux of magma erupted at the vent (magma mass eruption rate), which also includes the effusive activity (lava flows, lava dome) as well as all the lava falling back into the crater and its immediate surroundings contributing to the growth of pyroclastic cones (e.g. ballistics). The proportion of material propelled into the atmosphere strongly controls the hazards to humans and infrastructures, the economic costs and environmental consequences, but also represents an essential input to volcanic ash transport and dispersion models. Its estimation in near real-time could allow models to be constantly refined by comparing their predictions with measurables from ground-based and satellite remote sensing methods and ground deposit data. Model inputs from deposit observations (e.g. thickness) to quantify eruption characteristics cannot be done in real-time as this requires the collection of many fallout samples at remote locations. Although models allow the tephra mass flux to be estimated from the ash column height, the latter needs to be accurately measured and defined, in particular with regard to the strong effect of crosswinds. This can be achieved most reliably through a combination of methods, but radars appear particularly relevant in this case. Weather radars can provide the plume height, within the uncertainties discussed in section 2, along with characteristics of the ash cloud including transport speed estimates. Compact Doppler radars sounding the plume base at a high acquisition rate should help discriminate the mass eruption rate from the mass transport rate and link models of plume ascent to models of tephra dispersal by providing crucial source kinetic and mass loading parameters. The radar echo power is also related to the amount of material ejected and can be inverted to retrieve the mass. Among the most stringent assumptions for this is the particle size distribution in the sounded volumes. It can be inferred from direct measurements of fallout (rain radar, disdrometer etc) or deposit sampling, in situ sampling by aircraft, or comparison with data from similar

eruptions. We could more ambitiously imagine vertical soundings by transportable Doppler radars from underneath wind-advected ash clouds to provide the vertical distribution of both the particle concentration and fallout velocities, owing to their directive antenna and range gating capability. Tracking the time evolution of these parameters would give access to the internal dynamics of ash clouds and sedimentation processes. Terminal fall velocities could in turn be related to the particle size distribution that could be compared with field deposits and results from tephra dispersal models. Fallout measurements from ground collectors and several continuously operating laser or microwave disdrometers would improve understanding of the relationship between particle size and fall velocity, and the spatial heterogeneities often observed in ground deposits.

Unfortunately, a comprehensive real-time technique that can provide the erupted mass associated with the whole particle-size spectrum does not yet exist. This could only be derived from a combination of complementary techniques. This argues for a synergetic strategy for the assimilation of multiple datasets quantitatively describing the different parts of a plume from the gas-thrust region through the convective region to the buoyant distal cloud. As described in this chapter, the proximal region can be well quantified by radars, and developments are expected with multiple/complementary frequencies and dual polarimetry. The cross-correlation of data from radars and complementary passive remote-sensing methods, particularly ground-based imagery (IR, VIS, UV), is also a potentially powerful tool to retrieve crucial parameters like particle size distribution, gas and tephra mass fluxes. Ground-based radars are not useful for long-term volcanic cloud tracking because the large ash particles, that provide strong radar signals fall out soon after an eruption. C-band radars, for instance, do not detect ash particles with diameter $<1\text{-}100\ \mu\text{m}$ in drifting volcanic clouds that can persist in the atmosphere for several days or more (Rose et al., 1995). Thus, for the long-range tracking of ash clouds, satellite-based imagers (IR, VIS, UV, microwave) bring an obvious synergetic contribution, along with MISR and lidars, more sensitive to micron- to submicron-sized particles and aerosols, ceilometers, sun photometers, and DOAS mainly for SO_2 . An important objective of future works should aim at comparing and calibrating data from different instruments and/or acquired at different wavelengths, always cross-validated with field data (e.g. Bonadonna et al., 2011, 2012; Donnadieu et al., 2009b; Gouhier et al., 2011). Further coupling with other geophysical methods, in particular seismic and acoustic, seems promising to investigate the eruptive behavior of a volcano from down the conduit up through the magma-air interface where explosions occur, up to the surface where the dynamics of the tephra emissions can be recorded. Finally, back to figure 1, the synergetic integration of source-targeting Doppler radars, medium-range weather radars (few tens-hundreds km), and satellite- and ground-based imagery, combined with traditional monitoring networks and field methods, is a promising approach to improve the assessment of ash plume-related hazards, the forecast from tephra dispersal models and the mitigation of associated risks. In order to retrieve accurate eruption parameters, future research should focus on joint measurements of ash plume characteristics at different levels by means of complementary techniques. To this purpose, a good strategy would be to (i) carry out well-targeted multi-method experiments on volcanoes showing either recurrent activity or sudden resumption of activity, and (ii) operate long-term observations at selected laboratory volcanoes having a well-instrumented monitoring network.

9. Acknowledgments

I am much indebted to the OPGC staff for developments of the radar system, in particular G. Dubosclard, R. Cordesses, C. Hervier, J. Fournet-Fayard, P. Fréville, C. Bernard, C. Reymond, and for implementation of databases (S. Rivet, P. Cacault). I am also grateful to C. Hervier, T. H. Druitt, M. Gouhier, S. Valade for assistance in data acquisition in the field, and to E. Bonny, A. Clenet, J. Doloire, M. Gouhier, A. Maillat, L. Perrier, L. Pouchol, N. Rodriguez, S. Saumet, D. Tailpied, P. Tinard and S. Valade for help in data processing of the different campaigns. Y. Pointin kindly provided data on meteorological signals. All these colleagues are warmly acknowledged. External partners facilitated radar soundings: Universidad de Costa Rica (M. Mora, G. Alvarado, L.-F. Brenes, F. Arias and C. Ramirez), DGMWR in Port Vila Vanuatu (E. Garaebiti, C. Douglas), UNAM-CENAPRED in Mexico. Radar measurements from VOLDORAD 2B on Etna were obtained in the frame of a collaboration between OPGC and INGV Catania (M. Coltelli, S. Scollo, M. Prestifilippo). Field campaigns were supported by the French CNRS INSU programs 2003-ACI Risques Naturels, ANR-06-CATT-02 Arc-Vanuatu, 2010-TERMEX-MISTRALS, 2011-2012 CT3, and by the European project VOLUME FP6-018471.

This is Laboratory of Excellence CLERVOLC contribution n° 12.

10. References

- Adams, R.J., Perger, W.F., Rose, W.I., & Kostinski, A. (1996). Measurements of the complex dielectric constant of volcanic ash from 4 to 19 GHz. *J. Geophys. Res.*, 101, B4, pp. (8175-8185).
- Arason, P., Petersen, G. N., Bjornsson, H. (2011). Observations of the altitude of the volcanic plume during the eruption of Eyjafjallajökull, April–May 2010. *Earth Syst. Sci. Data*, 3, pp. (9–17).
- Arason, P., Bjornsson, H., Petersen, G. N., Roberts, M. J., & Collins M. (2012). Resonating eruptive flow rate during the Grímsvötn 2011 volcanic eruption. *30th Nordic geological winter meeting*, 9-12 January 2012, Reykjavík, Iceland.
- Bonadonna, C., Folch, A., Loughlin, S., Puempel, H. (2012). Future developments in modelling and monitoring of volcanic ash clouds: outcomes from the first IAVCEI-WMO workshop on Ash Dispersal Forecast and Civil Aviation. *Bull. Volcanol.*, 74, 1, pp. (1-10).
- Bonadonna, C., Genco, R., Gouhier, M., Pistolesi, M., Cioni, R., Alfano, F., Hoskuldsson, A., & Ripepe M. (2011). Tephra sedimentation during the 2010 Eyjafjallajökull eruption (Iceland) from deposit, radar, and satellite observations. *J. Geophys. Res.*, 116, B12202.
- Casagli, N., Tibaldi, A., Merri, A., Del Ventisette, C., Apuani, T., Guerri, L., Fortuny-Guasch, J., & Tarchi D. (2009). Deformation of Stromboli Volcano (Italy) during the 2007 eruption revealed by radar interferometry, numerical modelling and structural geological field data. *J. Volcanol. Geotherm. Res.*, 182, pp. (182–200).
- Campbell, M.J., & Ulrichs, J. (1969). Electrical properties of rocks and their significance of Lunar Radar Observations. *J. Geophys. Res.*, 74, 25, pp. (5867-5881).

- Delene, D.J., Rose, W.I., & Grody, N.C. (1996). Remote sensing of volcanic clouds using special sensor microwave imager data. *J. Geophys. Res.*, 101, B5, pp. (11579-11588).
- Donnadieu, F., Dubosclard, G., Allard, P., Cordesses, R., Hervier, C., Kornprobst, J., & Lénat, J.-F. (2003). Sondages des jets volcaniques par radar Doppler : applications à l'Etna. *Rapport quadriennal C.N.F.G.G. 1999-2002*, pp. (119-124).
- Donnadieu, F., Dubosclard, G., Cordesses, R., Druitt, T.H., Hervier, C., Kornprobst, J., Lénat, J.-F., Allard, P., & Coltelli, M. (2005). Remotely monitoring volcanic activity with ground-based Doppler radar. *E.O.S. Trans.*, 86, 21, pp. (201-204).
- Donnadieu F., Gouhier M., Fournet-Fayard J., Hervier C., 2008. Applications of pulsed ground-based Doppler radar to the study and monitoring of volcanoes, Ground-based radar observations for volcanoes workshop, Univ. Reading UK, pp. (6-8).
- Donnadieu, F., Hervier, C., Fréville, P., Fournet-Fayard, J., Fournol, J.-F., Menny, P., Reymond, C., & Bernard, C. (2009a). The VOLDORAD 2B radar: Operational handbook, Note OPGC 07.09, Univ. Blaise Pascal Clermont-Ferrand.
- Donnadieu F., Roche O., Clarke A., Gurioli L., (2009b). Advances in studies of volcanic plumes and pyroclastic density currents. Report of the IAVCEI Commission on Explosive Volcanism, workshop in Clermont-Ferrand (France), 26-29 October 2009, 18pp.
- Donnadieu, F., Valade, S., & Moune, S. (2011). Three dimensional transport speed of wind-drifted ash plumes using ground-based radar. *Geophys. Res. Lett.*, 38, L18310, doi:10.1029/2011GL049001.
- Donnadieu, F. (2012). VOLDORAD, In: *Observatoire de Physique du Globe de Clermont-Ferrand web site*, 2012, < <http://www.obs.univ-bpclermont.fr/SO/televolc/voldorad/>>.
- Donnadieu, F., Coltelli, M., Scollo, S., Fréville, Hervier, C., P., Prestifilippo, M., Rivet, S., Cacault, P., Fournet-Fayard, J., Bernard, C., & Reymond, C. (2012). Doppler radar monitoring of the explosive activity at Etna's summit craters with VOLDORAD 2B: toward an integrated approach. MEMOVOLC meeting, Jan. 17-18, Clermont-Ferrand, France.
- Doviak, R. J. and D. S. Zrnić, 1993: Doppler Radar and Weather Observations. Academic Press. Cambridge University Press, 562 pp.
- Dubosclard, G., Cordesses, R., Allard, P., Hervier, C., Coltelli, M., & Kornprobst, J. (1999). First testing of a volcano Doppler radar (Voldorad) at Mount Etna, Italy. *Geophys. Res. Lett.*, 26, pp.(3389-3392).
- Dubosclard G., Donnadieu, F., Allard, P., Cordesses, R., Hervier, C., Coltelli, M., Privitera, E., & Kornprobst, J. (2004). Doppler radar sounding of volcanic eruption dynamics at Mount Etna. *Bull. Volcanol.*, 66, 5, pp. (443-456), DOI : 10.1007/s00445-003-0324-8.
- Froger, J.-L., Remy, D., Bonvalot, S. and Legrand, D. (2007). Two scales of inflation at Lastarria-Cordon del Azufre volcanic complex, central Andes, revealed from ASAR-ENVISAT interferometric data. *Earth Planet. Sc. Lett.* 255, pp. (148-163).
- Gerst, A., Hort, M. Kyle, P. R., & Vöge, M. (2008). 4D velocity of strombolian eruptions and man-made explosions derived from multiple Doppler radar instruments. *J. Volcanol. Geotherm. Res.*, 177 (3), pp. (648-660),

- doi:10.1016/j.jvolgeores.2008.05.022.
- Gouhier, M., Harris, A., Calvari, S., Labazuy, P., Guéhenneux, Y., Donnadieu, F., & Valade, S. (2011). Lava discharge during Etna's January 2011 fire fountain tracked using MSG-SEVIRI. *Bull. Volcanol.*, *in press*.
- Gouhier, M., & Donnadieu, F. (2008). Mass estimations of ejecta from Strombolian explosions by inversion of Doppler-radar measurements. *J. Geophys. Res.*, 113, B10202, doi:10.1029/2007JB005383.
- Gouhier, M., & Donnadieu, F. (2010). The geometry of Strombolian explosions: insight from Doppler radar measurements. *Geophys. J. Int.*, 183, pp. (1376–1391), doi: 10.1111/j.1365-246X.2010.04829.x
- Gouhier, M., & Donnadieu, F. (2011). Systematic retrieval of ejecta velocities and gas fluxes at Etna volcano using L-Band Doppler radar. *Bull. Volcanol.*, 73, pp. (1139–1145).
- Hannesen, R., & Weipert, A. (2011). An algorithm to detect and quantify volcanic eruptions using polarimetric X-band radar data. Int. Workshop on X-band Weather Radar, 14-16 Nov. 2011, Delft, Netherlands.
- Harris, D. M., Rose, W.I.Jr., Roe, R., & Thompson, M.R. (1981). Radar observations of ash eruptions. In: *The 1980 Eruptions of Mount St. Helens, Washington*, edited by P. W. Lipman and D. R. Mullineaux, U.S. Geol. Surv. Prof. Pap. 1250, pp. (323–333).
- Harris, D. M., & Rose, W.I.Jr. (1983). Estimating particle sizes, concentrations, and total mass of ash in volcanic clouds using weather radar. *J. Geophys. Res.*, 88, C15, pp. (10969–10983), doi:10.1029/JC088iC15p10969.
- Hoblitt, R. P., & Schneider, D. J. (2009). Radar observations of the 2009 eruption of Redoubt Volcano, Alaska: Initial deployment of a transportable Doppler radar system for volcano-monitoring. American Geophysical Union, Fall Meeting 2009, abstract #V43A-2209.
- Hort, M., & Seyfried, R. (1998). Volcanic eruption velocities measured with a micro radar. *Geophys. Res. Lett.* 25, 1, pp.(113–116).
- Hort, M., Seyfried, R., & Vöge M. (2003). Radar Doppler velocimetry of volcanic eruptions: theoretical considerations and quantitative documentation of changes in eruptive behaviour at Stromboli Volcano, Italy. *Geophys. J. Int.*, 154, pp. (515–532), doi:10.1046/j.1365-246X.2003.01982.x.
- Hort, M., Vöge, M., Seyfried, R., & Ratdomopurbo, A. (2006). In situ observation of dome instabilities at Merapi Volcano, Indonesia: A new tool for hazard mitigation. *J. Volcanol. Geotherm. Res.*, 153, pp. (301–312), doi:10.1016/j.jvolgeores.2005.12.007.
- Lacasse, C., Karlsdóttir, S., Larsen, G., Soosalu, H., Rose, W. I., & Ernst, G.G.J. (2004). Weather radar observations of the Hekla 2000 eruption cloud, Iceland. *Bull. Volcanol.*, 66, pp. (457–473), doi:10.1007/s00445-003-0329-3.
- Lesage, P., Mora, M.M., Alvarado, G.E., Pacheco, J., & Métaixian J.-P. (2006). Complex behavior and source model of the tremor at Arenal volcano, Costa Rica. *J. Volcanol. Geotherm. Res.*, 157, pp. (49–59).
- Macfarlane, D. G., Wadge, G., Robertson, D. A., James, M. R., & Pinkerton, H. (2006). Use of a portable topographic mapping millimeter wave radar at an active lava flow. *Geophys. Res. Lett.*, 33, L03301, doi:10.1029/2005GL025005.

- Maki M., & Doviak, R. J. (2001). Volcanic ash size distribution determined by weather radar. *IEEE Int. Geosc. Rem. Sens. Symp., IGARSS '01.*, 2001, vol.4, pp. (1810 - 1811), doi: 10.1109/IGARSS.2001.977079.
- Maki M., Iwanami, K., Misumi, R., Doviak, R. J., Wakayama, T., Hata, K., & Watanabe, S. (2001). Observation of volcanic ashes with a 3-cm polarimetric radar. *Proc. 30th Radar Meteorol. Conf.*, 18-24 July, Munich, Germany, P5.13, p. (226-228).
- Malassingne, C., Lemaitre, F., Briole, P., & Pascal, O. (2001). Potential of ground based radar for the monitoring of deformation of volcanoes. *Geophys. Res. Lett.* 28, 851-854.
- Marzano, F.S., & Ferrauto, G. (2003). Relation between weather radar equation and first-order backscattering theory. *Atmos. Chem. Phys.*, 3, pp. (813-821).
- Marzano, F. S., Barbieri, S., Vulpiani G., & Rose W.I. (2006a). Volcanic ash cloud retrieval by ground-based microwave weather radar. *IEEE Trans. Geosc. Remote Sens.*, 44 (11), pp. (3235-3246), doi:10.1109/TGRS.2006.879116.
- Marzano, F.S., Vulpiani, G., & Rose W.I. (2006b). Microphysical characterization of microwave radar reflectivity due to volcanic ash clouds. *IEEE Trans. Geosc. Remote Sens.*, 44, pp. (313-327), doi:10.1109/TGRS.2005.861010.
- Marzano, F.S., Barbieri, S., Picciotti, E., & Karlsdóttir, S. (2010a). Monitoring sub-glacial volcanic eruption using C band radar imagery. *IEEE Trans. Geosc. Remote Sens.*, 48, 1, pp. (403-414).
- Marzano, F. S., Marchiotto, S., Barbieri, S., Textor, C., & Schneider, D. (2010b). Model-based Weather Radar Remote Sensing of Explosive Volcanic Ash Eruption, *IEEE Trans. Geosc. Remote Sens.*, 48, pp. (3591-3607).
- Marzano, F. S., Lamantea, M., Montopoli, M., Di Fabio, S., & Picciotti, E. (2011). The Eyjafjöll explosive volcanic eruption from a microwave weather radar perspective. *Atmos. Chem. Phys. Discuss.*, 11, pp. (12367-12409), doi:10.5194/acpd-11-12367-2011.
- Marzano, F. S., Picciotti, E., Vulpiani, G., & Montopoli, M. (2012). Synthetic signatures of volcanic ash cloud particles from X-band dual-polarization radar. *IEEE Trans. Geosc. Remote Sens.*, 50, 1, pp. (193-211).
- Mastin, L. G., Guffanti, M., Servranckx, R., Webley, P., et al. (2009). A multidisciplinary effort to assign realistic source parameters to models of volcanic ash cloud transport and dispersion during eruptions. *J. Volcanol. Geotherm. Res.*, 186, pp. (10-21).
- Mie, G. (1908). Beiträge zur Optik trüber Medien, speziell kolloidaler Metallösungen. *Ann. Phys.*, 330, 3, pp. (377-445).
- Mora, M.M., Lesage, P., Donnadieu, F., Valade, S., Schmidt, A., Soto, G., Taylor, W., & Alvarado, G. (2009). Joint Seismic, Acoustic and Doppler Radar observations at Arenal Volcano, Costa Rica: preliminary results. In: *The VOLUME project*, Bean, C. J., Braiden, A. K., Lokmer, I., Martini, F., & O'Brien, G. S. , pp. (330-340), VOLUME Project Consortium, ISBN 978-1-905254-39-2, Dublin.
- Musolf, M. (1994). Airborne radar detection of volcanic ash. In: *First International Symposium on Volcanic Ash and Aviation Safety*, Casadevall, T.J. (Ed.), *U.S. Geol. Surv. Bull.*, 2047, pp. (387-390), Seattle, Washington, U.S.A.

- Oguchi, T., Udagawa, M., Nanba, N., Maki, M., & Ishimine, Y. (2009). Measurements of dielectric constant of volcanic ash erupted from five volcanoes in Japan. *IEEE Trans. Geosc. Remote Sens.*, 47, 4, pp. (1089 - 1096).
- Okamoto, H. (2002). Information content of the 95-GHz cloud radar signals: Theoretical assessment of effects of non sphericity and error evaluation of the discrete dipole approximation. *J. Geophys. Res.*, 107, D22, 4628.
- Oswalt, J. S., Nichols, W., & O'Hara, J. F. (1996). Meteorological observations of the 1991 Mount Pinatubo eruption, In: *Fire and Mud: Eruptions and Lahars of Mount Pinatubo, Philippines*, Newhall C. G., & Punongbayan R. S., pp. (625–636), Univ. of Wash. Press, Seattle.
- Prata, F., Bluth, G., Rose, W.I., Schneider, D., & Tupper, A. (2001). Comments on 'Failures in detecting volcanic ash from a satellite-based technique'. *Remote Sens. Environ.*, 78, 3, pp. (341–346).
- Rogers, A.B., Macfarlane, D.G., Robertson, D.A. (2011). Complex permittivity of volcanic rock and ash at millimeter wave frequencies. *IEEE Remote Sens. Lett.*, 8, 2, pp. (298–302).
- Rose, W.I., Kostinski, A.B. (1994). Radar remote sensing of volcanic clouds. In: *First International Symposium on Volcanic Ash and Aviation Safety*, Casadevall, T.J. (Ed.), *U.S. Geol. Surv. Bull.*, 2047, pp. (391–395), Seattle, Washington, U.S.A.
- Rose, W. I., Kostinski, A. B., & Kelley, L. (1995). Real-time C band radar observations of 1992 eruption clouds from Crater Peak vent, Mount Spurr Volcano, Alaska. In: *The 1992 eruptions of Crater Peak vent, Mount Spurr Volcano, Alaska*, Keith, T. (Ed.), pp. (19-26), *U.S. Geol. Surv. Bull.*, 2139.
- Rose, W. I., Bluth, G. J. S., & Ernst, G. G. J. (2000). Integrating retrievals of volcanic cloud characteristics from satellite remote sensors – A summary. *Phil. Trans. R. Soc. A*, vol. 358, 1770, 1585–1606.
- Russell, J. K., & Stasiuk, M. V. (1997). Characterization of volcanic deposits with ground-penetrating radar. *Bull. Volcanol.*, 58, pp. (515–527).
- Sauvageot, H. (1992). *Radar meteorology*, Artech House, ISBN 0890063184, Boston.
- Scharff, L., M. Hort, A. J. Harris, M. Ripepe, J. Lees, and R. Seyfried (2008), Eruption dynamics of the SW crater of Stromboli volcano, Italy. *J. Volcanol. Geotherm. Res.*, 176, pp. (565–570).
- Scharff, L., Ziemer, F., Hort, M., Gerst, A., & Johnson J.B. (2012). A Detailed View Into the Eruption Clouds of Santiaguito Volcano, Guatemala, Using Doppler radar. *J. Geophys. Res.*, in revision.
- Schneider, D.J. (2009). Explosive volcanic eruptions: what can radar do for you? *2^d Nat. Symp. on Multifunction Phased Array Radar*, November 18-20, 2009, Norman, OK, USA.
- Schneider, D.J. (2012). The Use of a Dedicated Volcano Monitoring Doppler Weather Radar for Rapid Eruption Detection and Cloud Height Determination. *92nd American Meteorological Society Annual Meeting*, Jan. 22-26 2012, New Orleans, LA, USA.
- Scollo, S., Coltelli, M., Prodi, F., Folegani, M., & Natali, S. (2005). Terminal settling velocity measurements of volcanic ash during the 2002–2003 Etna eruption by an X-band

- microwave rain gauge disdrometer. *Geophys. Res. Lett.*, 32, L10302, doi:10.1029/2004GL022100.
- Scollo, S., Prestifilippo, M., Spata, G., D'Agostino, M., & Coltelli, M. (2009). *Nat. Hazards Earth Syst. Sci.*, 9, pp. (1573–1585).
- Scollo, S., Folch, A., Coltelli, M., & Realmuto, V. J. (2010). Three-dimensional volcanic aerosol dispersal: A comparison between Multiangle Imaging Spectroradiometer (MISR) data and numerical simulations. *J. Geophys. Res.*, 115, D24210.
- Seyfried, R., & Hort, M. (1999). Continuous monitoring of volcanic eruption dynamics: A review of various techniques and new results from a frequency-modulated radar Doppler system. *Bull. Volcanol.*, 60, pp. (627–639).
- Stone, M. (1994). Application of contemporary ground-based and airborne radar for the observation of volcanic ash. *In: First International Symposium on Volcanic Ash and Aviation Safety*, Casadevall, T.J. (Ed.), U.S. Geol. Surv. Bull., 2047, pp. (391–395), Seattle, Washington, U.S.A.
- Valade, S. & Donnadieu, F. (2011). Ballistics and ash plumes discriminated by Doppler radar. *Geophys. Res. Lett.*, 38, L22301, doi:10.1029/2011GL049415.
- Valade, S., Donnadieu, F., Lesage, P., Mora, M.M., Harris, A. & Alvarado, G.E. (2012). Explosion mechanisms at Arenal volcano, Costa Rica: an interpretation from integration of seismic and Doppler radar data. *J. Geophys. Res.*, 117, B1, doi:10.1029/2011JB008623.
- Vöge, M., & Hort, M. (2008). Automatic classification of dome instabilities based on Doppler radar measurements at Merapi volcano, Indonesia: Part I. *Geophys. J. Int.*, 172, pp. (1188–1206), doi:10.1111/j.1365-246X.2007.03605.x.
- Vöge, M., Hort, M., Seyfried, R., Ratdomopurbo, A. (2008). Automatic classification of dome instabilities based on Doppler radar measurements at Merapi volcano, Indonesia: Part II. *Geophys. J. Int.*, 172, pp. (1207–1218), doi:10.1111/j.1365-246X.2007.03665.x.
- Vöge, M., & Hort, M. (2009). Installation of a Doppler Radar monitoring system at Merapi Volcano, Indonesia. *IEEE Trans. Geosc. Remote Sens.*, 47, 1, pp. (251–271), doi:10.1109/TGRS.2008.2002693.
- Vulpiani, G., Montopoli, M., Picciotti, E., & Marzano F.S. (2011). On the use of a polarimetric X-band weather radar for ash clouds monitoring. *Proc. 35th Radar Meteorol. Conf.*, 26-30 September, Pittsburgh, PA, USA, P.101.
- Wadge, G., Macfarlane, D.G., Robertson, D.A., Hale, A.J., Pinkerton, H., Burrell, R.V., Norton, G. E., & James, M.R. (2005). AVTIS: A novel millimetre-wave ground based instrument for volcano remote sensing. *J. Volcanol. Geotherm. Res.*, 146, 307–318.
- Wadge, G., Macfarlane, D.G., Odbert, H.M., James, M.R., Hole, J.K., Ryan, G., Bass, V., De Angelis, S., Pinkerton, H., Robertson, D.A., & Loughlin, S. C. (2008). Lava dome growth and mass wasting measured by a time series of ground-based radar and seismicity observations. *J. Geophys. Res.*, 113, B08210, doi:10.1029/2007JB005466.
- Wen, S., & Rose, W.I. (1994). Retrieval of sizes and total masses of particles in volcanic clouds using AVHRR bands 4 and 5. *J. Geophys. Res.*, 99, pp. (5421–5431).

- Weill, A., Brandeis, G., & Vergnolle, S. (1992). Acoustic sounder measurements of vertical velocity of volcanic jets at Stromboli volcano. *Geophys. Res. Lett.*, 19, 23, pp. (2357-2360).
- Wood, J., Scott, C., & Schneider, D. (2007). WSR-88D radar observations of volcanic ash. World Meteorological Organization, *Proc. 4th Int. Workshop Ash*, Mar. 26–30, 2007, Rotorua, New Zealand.

Doppler Radar Tracking Using Moments

Mohammad Hossein Gholizadeh and Hamidreza Amindavar
*Amirkabir University of Technology, Tehran
Iran*

1. Introduction

A Doppler radar is a specialized radar that makes use of the Doppler effect to estimate targets velocity. It does this by beaming a microwave signal towards a desired target and listening for its reflection, then analyzing how the frequency of the returned signal has been altered by the object's motion. This variation gives direct and highly accurate measurements of the radial component of a target's velocity relative to the radar. Doppler radars are used in aviation, sounding satellites, meteorology, police speed guns, radiology, and bistatic radar (surface to air missile).

Partly because of its common use by television meteorologists in on-air weather reporting, the specific term "Doppler Radar" has erroneously become popularly synonymous with the type of radar used in meteorology.

The Doppler effect is the difference between the observed frequency and the emitted frequency of a wave for an observer moving relative to the source of the waves. It is commonly heard when a vehicle sounding a siren approaches, passes and recedes from an observer. The received frequency is higher (compared to the emitted frequency) during the approach, it is identical at the instant of passing by, and it is lower during the recession. This variation of frequency also depends on the direction the wave source is moving with respect to the observer; it is maximum when the source is moving directly toward or away from the observer and diminishes with increasing angle between the direction of motion and the direction of the waves, until when the source is moving at right angles to the observer, there is no shift. Since with electromagnetic radiation like microwaves frequency is inversely proportional to wavelength, the wavelength of the waves is also affected. Thus, the relative difference in velocity between a source and an observer is what gives rise to the Doppler effect.

Now, suppose that we have received an unknown waveform from the target. This waveform is a result of reflection from a fluctuating target in presence of clutter and noise. The received signal is often modeled as delayed and Doppler-shifted version of the transmitted signal. So not only the Doppler estimation, but the joint estimation of the time delay and Doppler shift provides information about the position and velocity of the target. So we should focus on the joint estimation of both parameters. There are many works for estimating the joint time delay and Doppler shift, with advantages and disadvantages apiece. Among these methods, Wigner Ville (WV) method has proven to be a valuable tool in estimating the time delay and Doppler shift. WV method is a time-frequency processing. It possesses a high resolution in the time-frequency plane and satisfies a large number of desirable theoretical properties [Chassande-Mottin & Pai, 2005]. In fact, these properties are the fundamental motivation

for the use of the narrowband(wideband) WV transformation for detecting a deterministic signal with unknown delay-Doppler(-scale) parameters. WV's practical usage is limited by the presence of non-negligible cross-terms, resulting from interactions between signal components. Alternative approaches are proposed for eliminating or at least suppressing the cross-terms [Chassande-Mottin & Pai, 2005; Orr et al., 1992; Tan & Sha'ameri, 2008]. Generally speaking, cross-term suppression may be divided into two categories: signal-independent and signal-dependent paradigm. Coupling the Gabor transformation with the WV distribution is a signal-independent procedure that reveals a cross-term suppression approach through exploitation of partial knowledge about signals to be encountered [Orr et al., 1992]. For signal-dependent method, it is possible to apply an adaptive window over WV distribution where the kernel parameters are determined automatically from the parameters of the input signal. This kernel is capable of suppressing the cross-terms and maintain accurate time-frequency resolution [Tan & Sha'ameri, 2008]. Besides the WV method, there are other time-frequency techniques such as wavelet transform. Wavelet approach combines the noise filtering and scaling together, yielding a reduction in complexity [Niu et al., 1999]. There is also another procedure using the fractional lower order ambiguity function (FLOAF) for joint time delay and Doppler estimation [Ma & Nikias, 1996]. Now another view is presented. It is assumed that the transmitted signal follows an N -mode Gaussian mixture model (GMM). GMM can be used for different transmitted signals. Especially, it presents an accurate modeling for actual signals transmitted in the sonar and radar systems [Bilik et al., 2006]. The received signal is affected by the noise, time delay and Doppler where the conglomerate effects on the signal cause peculiar changes on the moments of received signal. Using moments is a powerful procedure which is used for different applications, specially in parameter estimation. Some people use the moment method to estimate the parameters of a Gaussian mixture in an environment without noise [Fukunaga et al., 1983]. Some apply the method for better parameter estimation in a faded signal transmitted through a communication channel which is suffered from multipath. The method can be implemented using a non-linear least-squares algorithm to represent a parameterized fading model for the instantaneous received path power which accounts for both wide-sense stationary shadowing and small-scale fading [Bouchereau & Brady, 2008]. The most prominent and novel models for the envelope of a faded signal are Rician and Nakagami. There are estimators for the Nakagami- m parameter based on real sample moments. The estimators present an asymptotic expansion which provides a generalized closed-form expression for the Nakagami- m parameter without the need for coefficient optimization for different ratios of real moments [Gaeddert & Annamalai, 2005]. There are also approaches that show the K-factor in Rician model is an exact function of moments estimated from time-series data [Greenstein et al., 1999].

In this chapter, we analyze the effect of noise, time delay, and Doppler on the moments of received signal and exploit them for estimating the position and velocity of the target. We note that in the new method, the noise power is assumed unknown which is estimated along with the time delay and Doppler shift. The new approach exhibits accurate results compared to the existing methods even in very low SNR and long tailed noise. Then, the estimated parameters are used for tracking a maneuvering target's position and velocity. There exist other practical methods for tracking targets such as Kalman filtering [Park & Lee, 2001]. However, when the target motion is nonlinear and/or clutter and/or noise are non-Gaussian, this approach fails to be effective. Instead, unscented Kalman filter (UKF) and extended Kalman filter (EKF) come into use [Jian et al., 2007]. However, in long tailed noise, Kalman filtering results are

unsatisfactory. To overcome these difficulties, particle filtering (PF) is utilized [Jian et al., 2007].

Although particle filtering performs better than Kalman filtering in noisy environment, but it also diverges in low SNRs and cannot be trustable in this range of SNR. In addition, this method requires much more processing. We note that Kalman filtering, extended Kalman, unscented Kalman and particle filtering are recursive in nature. The new procedure proposed in this chapter is not recursive and can be used in the non-Gaussian, non-stationary noise, and nonlinear target motion. In here, the target tracking is performed based on the estimated time delay and Doppler. Since the accuracy of the time delay and Doppler estimation are high enough even in the severe noise, the results in tracking are acceptable compared to other rival approaches.

In section II the moment concept is reviewed and moment method is described as the base item in our estimations. Section III provides a model for the received signal. This signal has been influenced by unknown noise, delay and Doppler. It is shown in Section IV that it is possible to estimate Doppler by using the moments of the received random signal. The method is also useful for delay estimation. The noise power and its behavior play a prominent role in our work. So some analysis in this field is presented in this section too. After the parameter estimation, section V is devoted to explain about how the tracking a target is done based on the estimated delay and Doppler. And finally, section VI contains results that illustrate the effectiveness of the proposed method.

2. Moment concept

In probability theory, the moment method is a way in which the moments of a discrete sequence are used to determine its distribution.

Suppose that X is a random variable, and $f_X(x)$ is the probability density function (PDF) of this random variable. The moments of the random variable X is calculated from the following equation:

$$m_n = E(X^n) = \int_{-\infty}^{\infty} x^n f_X(x) dx = \int_{-\infty}^{\infty} x^n dF_X(x) dx, \quad (1)$$

which $F_X(x)$ is the cumulative distribution function (CDF) of the random variable X , and $E(\cdot)$ is the expectation value.

On the other hand, the moment generating function (MGF) of this random variable is calculated as follows:

$$M_X(u) = E(e^{uX}), \quad u \in \mathbb{C}. \quad (2)$$

Note that the equation will be hold if the expectation value exists.

In here, to obtain the moments of a random variable, the relation between the moment and the moment generating function is use instead of using equation (1). This relation can be demonstrated as follows:

$$\begin{aligned} M_X(u) &= E(e^{uX}) = \int_{-\infty}^{\infty} e^{ux} f_X(x) dx = \\ &= \int_{-\infty}^{\infty} (1 + ux + \frac{u^2x^2}{2!} + \dots) f_X(x) dx = 1 + um_1 + \frac{u^2m_2}{2!} + \dots \end{aligned} \quad (3)$$

This equation is hold when the moments m_n are finite, i.e. $|m_n| < \infty$.

The moment method claims that using the moment of the random variable X , the PDF of X is completely determined. So if we have:

$$\lim_{n \rightarrow \infty} E \left(X_n^k \right) = E \left(X^k \right), \quad \forall k \quad (4)$$

then, the sequence $\{X_n\}$ has the same distribution as the X . we use (4) for parameter estimation, i.e. The left side of the equation is obtained statically, and the right side is calculated analytically. These two sides should be equal.

To begin our discussion, a model should be considered for our signals. Next section is focused on finding the suitable model.

3. Signal model

We consider the baseband representation of the received signal, which can be expressed as the sum of the desired signal component and non-stationary background noise. The signal component is represented by the linear sum of many non-coherent waveforms whose arrivals at the receiver are governed by a Poisson process [Zabin & Wright, 1994]. The receiver includes two sensors to measure the received signal in presence of background noise:

$$\begin{aligned} y_1(t) &= s(t) + \omega_1(t), \\ y_2(t) &= s(t - \tau) \exp(j2\pi t \varepsilon) + \omega_2(t), \end{aligned} \quad (5)$$

where τ and ε denote the time delay and Doppler respectively, and $s(t)$ is the desired received signal modeled at any time instance t to follow a real N-mode Gaussian mixture distribution [Isaksson et al., 2001]:

$$s(t) \sim \sum_{i=1}^N p_i N \left(\mu_{s_i}, \sigma_{s_i}^2 \right). \quad (6)$$

The processes $\omega_1(t)$ and $\omega_2(t)$ are real zero-mean additive white Gaussian noises (AWGN) with powers of $\sigma_{\omega_1}^2$ and $\sigma_{\omega_2}^2$ respectively. These powers are not constant in practice due to nonhomogeneous environment, but are assumed as random variates which are estimated subsequently. The signal and noise are supposed to be uncorrelated, but the noises $\omega_1(t)$ and $\omega_2(t)$ are possibly correlated.

4. Parameter estimation

In this section, for a random variable X , the moment generating function (MGF), $M_x(u)$, and its asymptotic series are used to determine the moments m_{xj} :

$$M_x(u) = E(e^{uX}) = 1 + um_{x1} + \frac{u^2 m_{x2}}{2!} + \dots, \quad u \rightarrow 0. \quad (7)$$

4.1 Time delay estimation

The statistical properties of the signal and noise which are represented in (5) are known. Therefore, their MGF is available, by assuming finite moments of signal and noise. Although the signal follows a Gaussian mixture distribution, the conglomerate effect of the time delay

n	Moment	Central moment	Cumulant
0	1	1	–
1	μ	0	μ
2	$\mu^2 + \sigma^2$	σ^2	σ^2
3	$\mu^3 + 3\mu\sigma^2$	0	0
4	$\mu^4 + 6\mu^2\sigma^2 + 3\sigma^4$	$3\sigma^4$	0

Table 1. Normal distribution moments

and Doppler creates a non-stationary signal, as seen in (5). At first, by using both sensors in the receiver, the time delay is predicted, then this estimated delay facilitates determination of the Doppler shift subsequently. The time delay estimation is described here and discussions about the Doppler estimation are provided in the sequel. It is required to consider the MGF of the normal distributed variate as the starting ground for the next steps:

$$M(u) = \exp(\mu u + 0.5\sigma^2 u^2), \quad (8)$$

where μ and σ are the mean and variance of normal distribution. The related moments are depicted in table (I). We suppose the received noise-free signal in the second sensor is denoted by:

$$r(t) = s(t - \tau) \exp(j2\pi t\epsilon). \quad (9)$$

First, we assume there is no Doppler i.e. $r(t) = s(t - \tau)$, and the noise variances, $\sigma_{\omega_1}^2$ and $\sigma_{\omega_2}^2$, are constant. As mentioned above, we utilize the MGF for the estimation purposes. The noise terms in both sensors have normal distributions. Since the noise terms in (5) and signal $s(t)$ are independent, the difference between MGF of two received signals $y_1(t)$ and $y_2(t)$ in (5) is derived from the noise-free terms $s(t)$ and $r(t)$. Since $r(t)$ is the delayed replica of $s(t)$, it includes two blocks. When the second sensor has not sensed the received signal yet, $r(t)$ merely contains the noise $\omega_2(t)$ and its MGF can be calculated by (8), but, as soon as the transmitted signal arrives at this sensor, $y_2(t)$ shows a similar behavior to $y_1(t)$. This suitable observation could be used for the time delay estimation.

So, MGF of signal detected at the first sensor is considered as a reference for our estimation in the second sensor. Indeed, the moments of $y_1(t)$ are extractable from this known MGF by using (7). These moments are employed as the reference for comparing among results retrieved from the second sensor. In the second sensor, a rectangular running window is implemented on $y_2(t)$ and this window helps to extract different segments of $y_2(t)$ step by step. The window length depends on two parameters. First, it must be long enough to be trustable in calculating the estimated moments, on the other hand, it should not be so long that damages the real-time characteristics of estimator. Anyway, there is a trade-off between these two factors. The window length is considered constant and moves from the beginning

of the signal to the end. Besides the length, the overlap between adjacent frames is another item that is determined according to the required accuracy and tolerable complexity in the time delay estimation. At the beginning of signal block, the windowed signal includes only the noise part of $y_2(t)$, because of delay τ , so it exhibits different moments in comparison with $y_1(t)$. While the first point of window reaches the onset of delayed signal $s(t - \tau)$, the estimated moments become similar to the moments of $y_1(t)$. Mean square error (MSE) criterion is applied for observing the measure of this similarity. At first, we observe large MSE values, but, the window progression leads to a decrease in MSE and after the τ seconds delay point, we get a small amount for MSE nearly equal to zero and will remain constant up to the end of observation time.

Now, Doppler is considered and $r(t)$ is obtained from (9). Doppler changes the constant amount of MSE which had happened after τ seconds. It means that after the delay point, Doppler increases MSE gradually, but this phenomenon is not an annoying event in time delay estimation, even it helps to find the time delay, because this increasing in MSE takes place from the delay point, so it causes the delay point to be the point which has minimum value for MSE.

In figure (1), the Doppler effect on the MSE behavior is showed for three different SNRs. Time delay is equal to 300 microseconds. In SNR=+10dB, the result is clear. In two other SNRs, the minimum point is almost matched well with the actual amount of delay, i.e. 300.

We assume the windowed signal in the k -th step of window moving is denoted by y_{2k} and the i -th moment of this windowed signal is presented as $\hat{m}_{y_{2k},i}$. Therefore, the k -th window whose related moments $\hat{m}_{y_{2k},i}$ are the most similar to those of $y_1(t)$, $m_{y_1,i}$, can be estimated by:

$$\hat{k} = \arg \min_k \sum_{i=1}^L \left| m_{y_1,i} - \hat{m}_{y_{2k},i} \right|^2, \quad (10)$$

where in here, L is considered 4, and it would reveal a desirable result [Fukunaga et al., 1983]. In fact, when $L=4$, we use 4 moments of signal. So we have 4 equations that are applied to determine the unknown parameter. Although there is only one unknown parameter, but the noise signal does not let us find the parameter by only one equation. But the use of four equations is enough. Note that if more accuracy is needed, L can be considered larger. So, the delay point, $\hat{\tau}$, is the first point of \hat{k} -th window.

Despite the presence of Doppler, the proposed moment method estimates the time delay precisely. Consequently, this method can consider the time delay and Doppler simultaneously, and thus, is able to estimate the joint time delay and Doppler accurately.

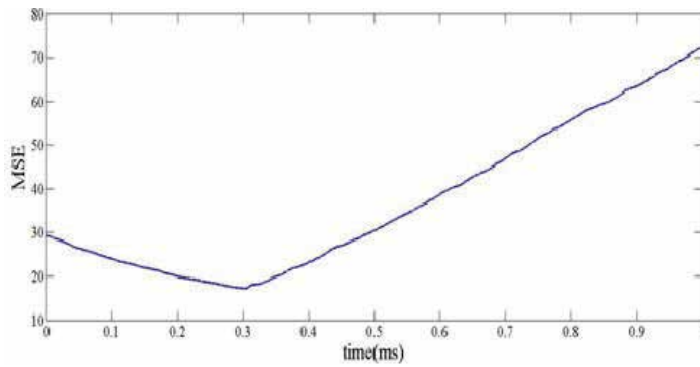
4.2 Doppler estimation

In this section, we can consider the estimated delay $\hat{\tau}$ as the time origin for the received signal in the second sensor:

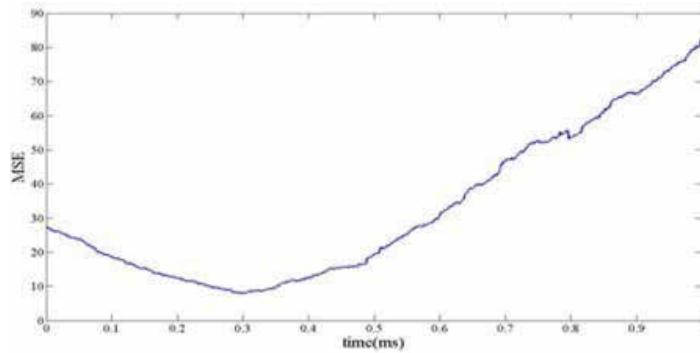
$$y_2(t + \hat{\tau}) = r(t + \hat{\tau}) + \omega_2(t + \hat{\tau}), \quad t \geq 0. \quad (11)$$

According to (9) and (11), we have:

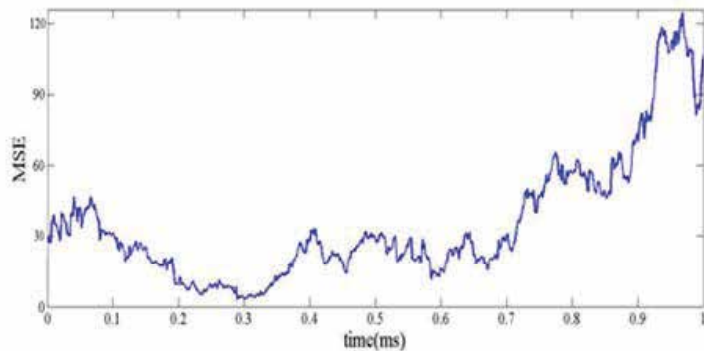
$$y_2(t + \hat{\tau}) = s(t) \exp(j2\pi(t + \hat{\tau})\varepsilon) + \omega_2(t + \hat{\tau}), \quad t \geq 0. \quad (12)$$



a) SNR=+10 dB



b) SNR= 0 dB



c) SNR=-10 dB

Fig. 1. MSE between the signal $y_1(t)$ moments and the windowed parts of signal $y_2(t)$ moments. a) SNR=+10dB, b) SNR=0dB, c) SNR=-10dB

Doppler and noise effect on the moments of $y_2(t + \hat{\tau})$ should be noticed. Instead of $y_2(t + \hat{\tau})$, we work on the real part:

$$y_{2r}(t + \hat{\tau}) = s(t) \cos(2\pi(t + \hat{\tau})\varepsilon) + \omega_2(t + \hat{\tau}), \quad t \geq 0. \tag{13}$$

$y_{2r}(t + \hat{\tau})$ includes the noise and signal, and the signal is also affected by Doppler which changes the moments of the signal. Therefore, we prefer to obtain MGF of $y_{2r}(t + \hat{\tau})$ firstly, then, the moments are obtained from this MGF by (7). The noise-free signal in (13) is independent from the noise $\omega_2(t + \hat{\tau})$, so MGF of $y_{2r}(t + \hat{\tau})$ is:

$$M_{y_{2r}}(u) = M_r(u)M_{\omega_2}(u), \tag{14}$$

where $M_r(u)$ is MGF of the first term in right side of (13), and:

$$M_{\omega_2}(u) = \exp\left(0.5\sigma_{\omega_2}^2 u^2\right). \tag{15}$$

The time varying variance will be comprehensively discussed in the sequel. Here, the problem is to estimate $M_r(u)$. $s(t)$ follows a Gaussian mixture distribution in (6). The presence of the cosine term changes the first term in the right side of (13) to a non-stationary process. Although the cosine term is time variant, fortunately, it is deterministic.

Now, we obtain $M_r(u)$:

$$\begin{aligned} M_s(u) &= \sum_{i=1}^N p_i \exp\left(\mu_{s_i} u + 0.5\sigma_{s_i}^2 u^2\right) \Rightarrow \\ M_r(u; t) &= \sum_{i=1}^N p_i \exp\left(\mu_{s_i} u + 0.5\sigma_{s_i}^2 \cos^2(2\pi(t + \hat{\tau})\varepsilon)u^2\right). \end{aligned} \tag{16}$$

Both $M_r(u)$ and $M_{\omega_2}(u)$ are expressed as the series for $u \rightarrow 0$, then by multiplying these two series and ordering their terms, MGF of $y_{2r}(t + \hat{\tau})$ is asymptotically obtained in the context of (7):

$$\begin{aligned} M_{y_{2r}}(u) &= M_r(u) M_{\omega_2}(u) \\ &= \left(1 + um_{r1} + \frac{u^2 m_{r2}}{2!} + \frac{u^3 m_{r3}}{3!} + \frac{u^4 m_{r4}}{4!} + \dots\right) \\ &\times \left(1 + um_{\omega_2 1} + \frac{u^2 m_{\omega_2 2}}{2!} + \frac{u^3 m_{\omega_2 3}}{3!} + \frac{u^4 m_{\omega_2 4}}{4!} + \dots\right) \\ &= 1 + u(m_{r1} + m_{\omega_2 1}) + \frac{u^2(m_{r2} + m_{\omega_2 2} + 2m_{r1}m_{\omega_2 1})}{2!} \\ &+ \frac{u^3(m_{r3} + m_{\omega_2 3} + 3m_{r1}m_{\omega_2 2} + 3m_{r2}m_{\omega_2 1})}{3!} \\ &+ \frac{u^4(m_{r4} + m_{\omega_2 4} + 6m_{r2}m_{\omega_2 2} + 4m_{r1}m_{\omega_2 3} + 4m_{r3}m_{\omega_2 1})}{4!} + \dots \end{aligned} \tag{17}$$

The moments extracted from $M_r(u)$ are shown in Table (II). There exists also another problem. The resulting moments of $y_{2r}(t + \hat{\tau})$ are time dependent. Since the cosine term is deterministic, the time average of the moments can be substituted instead. Let's define:

$$\zeta_i(\varepsilon) = \frac{1}{T} \int_0^T \cos^i(2\pi(t + \hat{\tau})\varepsilon) dt, \tag{18}$$

n Moment
0 1
1 $\sum_{i=1}^N p_i \mu_{s_i}$
2 $\sum_{i=1}^N p_i (\mu_{s_i}^2 + \sigma_{s_i}^2 \cos^2(2\pi(t + \hat{\tau})\varepsilon))$
3 $\sum_{i=1}^N p_i (\mu_{s_i}^3 + 3\mu_{s_i} \sigma_{s_i}^2 \cos^2(2\pi(t + \hat{\tau})\varepsilon))$
4 $\sum_{i=1}^N p_i (\mu_{s_i}^4 + 6\mu_{s_i}^2 \sigma_{s_i}^2 \cos^2(2\pi(t + \hat{\tau})\varepsilon) + 3\sigma_{s_i}^4 \cos^4(2\pi(t + \hat{\tau})\varepsilon))$

Table 2. Moments extracted from $M_r(u; t)$

where T is the observation time. Note that for dependency of $\zeta_i(\varepsilon)$ on ε , the moments of $y_{2r}(t + \hat{\tau})$ are dependent on ε too. Finally, for obtaining the time-independent moments of $y_{2r}(t + \hat{\tau})$, $m_{y_{2r},i}$, it suffices that all “ $\cos^i(2\pi(t + \hat{\tau})\varepsilon)$ ” terms in the time-dependent moments to be substituted by $\zeta_i(\varepsilon)$. The final moments are depicted in table (III).

Since now, the moments were obtained analytically, it means we only calculated the right side of equation (4). On the other hand, the moments of the observed signal in the second receiver can be calculated statistically by:

$$\tilde{m}_i = \frac{1}{T} \int_0^T y_{2r}^i(t + \hat{\tau}) dt. \quad (19)$$

Now the left side of the equation (4) is also obtained. Both of these two procedures must yield same results. Thus, ε should be selected in such a way that this equality holds. To do this, MSE criterion is used again:

$$\text{MSE} = \sum_{i=1}^L \left| m_{y_{2r},i} - \tilde{m}_i \right|^2. \quad (20)$$

Similar to the previous section, L is considered as 4. So Doppler of the received signal $y_{2r}(t + \hat{\tau})$ is estimated:

$$\hat{\varepsilon} = \arg \min_{\varepsilon} \sum_{i=1}^L \left| m_{y_{2r},i} - \tilde{m}_i \right|^2. \quad (21)$$

4.3 Noise power estimation

The noise power estimation is similar to Doppler estimation. Indeed, these two estimations are done simultaneously. It could be seen that the moments do not merely depend on Doppler.

n Moment
0 1
1 $\sum_{i=1}^N p_i \mu_{s_i}$
2 $\sum_{i=1}^N p_i (\mu_{s_i}^2 + \sigma_{s_i}^2 \zeta_2(\epsilon)) + \sigma_\omega^2$
3 $\sum_{i=1}^N p_i (\mu_{s_i}^3 + 3\mu_{s_i} \sigma_{s_i}^2 \zeta_2(\epsilon)) + 3\sigma_\omega^2 \sum_{i=1}^N p_i \mu_{s_i}$
4 $\sum_{i=1}^N p_i (\mu_{s_i}^4 + 6\mu_{s_i}^2 \sigma_{s_i}^2 \zeta_2(\epsilon) + 3\sigma_{s_i}^4 \zeta_4(\epsilon)) + 3\sigma_\omega^4 + 6\sigma_\omega^2 \sum_{i=1}^N p_i (\mu_{s_i}^2 + \sigma_{s_i}^2 \zeta_2(\epsilon))$

Table 3. Final moments extracted from $M_{y_{2r}}(t + \hat{t})$

They depend onto the noise power as well. So, in (20), MSE includes two parameters, the noise power and Doppler of the received signal, and should be minimized according to both of them:

$$(\hat{\epsilon}, \hat{\sigma}_{\omega_2}^2) = \arg \min_{\epsilon, \sigma_{\omega_2}^2} \sum_{i=1}^L \left| m_{y_{2r},i} - \tilde{m}_i \right|^2. \tag{22}$$

Now it is the time to discuss about the variable variance of the noise. This means that in (14) the noise variance is considered unknown. We can estimate the noise variance given N_1 signal-free samples which are at hand occasionally. So, $\sigma_{\omega_2}^2$ becomes a random variate. Since the noise $\omega_2(t + \hat{t})$ is assumed Gaussian, the N_1 -sample based estimated variance is chi-square distributed with N_1 degrees of freedom:

$$\hat{\sigma}_{\omega_2}^2 = \frac{1}{N_1} \sum_{i=1}^{N_1} \omega_{2,i}^2, \quad \hat{\sigma}_{\omega_2}^2 \sim \chi_{N_1}^2. \tag{23}$$

Hence, the average MGF of the noise over σ^2 is obtained in (14) as:

$$\begin{aligned} \bar{M}_{\omega_2}(u) &= \frac{1}{\sqrt{(1 - \hat{\sigma}_{\omega_2}^2 u^2 / N_1)^{N_1}}} \\ &= 1 + 0.5 \hat{\sigma}_{\omega_2}^2 u^2 + (0.125 + 1/4N_1) \hat{\sigma}_{\omega_2}^4 u^4 + \dots \end{aligned} \tag{24}$$

In this non-stationary noise scenario due to $\hat{\sigma}_{\omega_2}^2$, the procedure presented for Doppler estimation in the previous part does not change, only MGF and the moments of the normal

distribution considered previously for the noise should be substituted by the ones determined in (24).

5. Radar tracking

In the basic section, we said that the proposed parameter estimation can be useful for the tracking of a target. As mentioned, there are various methods for the target tracking which present specific mathematical algorithms. These methods have different performance levels, but most of them are recursive, so that at any time, the data is obtained by using previous data and improving them. Now, some of the most common procedures and their problems are expressed and then, the proposed moment method are described in detail.

5.1 Kalman filter

The Kalman filter is the central algorithm to the majority of all modern radar tracking systems. The role of the filter is to take the current known state (i.e. position, heading, speed and possibly acceleration) of the target and predict the new state of the target at the time of the most recent radar measurement. In making this prediction, it also updates its estimate of its own uncertainty (i.e. errors) in this prediction. It then forms a weighted average of this prediction of state and the latest measurement of state, taking account of the known measurement errors of the radar and its own uncertainty in the target motion models. Finally, it updates its estimate of its uncertainty of the state estimate. A key assumption in the mathematics of the Kalman filter is that measurement equations (i.e. the relationship between the radar measurements and the target state) and the state equations (i.e. the equations for predicting a future state based on the current state) are linear, i.e. can be expressed in the form $y = A.x$ (where A is a constant), rather than $y = f(x)$. The Kalman filter assumes that the measurement errors of the radar, and the errors in its target motion model, and the errors in its state estimate are all zero-mean Gaussian distributed. This means that all of these sources of errors can be represented by a covariance matrix. The mathematics of the Kalman filter is therefore concerned with propagating these covariance matrices and using them to form the weighted sum of prediction and measurement [Ristic et al., 2004].

In situations where the target motion conforms well to the underlying model, there is a tendency of the Kalman filter to become "over confident" of its own predictions and to start to ignore the radar measurements. If the target then manoeuvres, the filter will fail to follow the manoeuvre. It is therefore common practice when implementing the filter to arbitrarily increase the magnitude of the state estimate covariance matrix slightly at each update to prevent this.

5.2 Extended Kalman Filter (EKF)

This method is a class of nonlinear tracking algorithms that provides much better results than the Kalman filter.

Nonlinear tracking algorithms use a nonlinear filter to cope with the following cases:

- The relationship between the radar measurements and the track coordinates is nonlinear.
- The errors are nonlinear.
- The motion model, is non-linear.

In this case, the relationship between the measurements and the state is of the form $h = f(x)$ (where h is the vector of measurements, x is the target state and $f(\cdot)$ is the function relating the two). Similarly, the relationship between the future state and the current state is of the form $x(t+1) = g(x(t))$ (where $x(t)$ is the state at time t and $g(\cdot)$ is the function that predicts the future state). To handle these non-linearities, the EKF linearizes the two non-linear equations using the first term of the Taylor series and then treats the problem as the standard linear Kalman filter problem. Although conceptually simple, the filter can easily diverge (i.e. gradually perform more and more badly) if the state estimate about which the equations are linearized is poor. The unscented Kalman filter and particle filters are attempts to overcome the problem of linearizing the equations.

5.3 Particle Filtering (PF)

Another example of nonlinear methods is particle filtering. This method makes no assumptions about the distributions of the errors in the filter and neither does it require the equations to be linear. Instead it generates a large number of random potential states ("particles") and then propagates this "cloud of particles" through the equations, resulting in a different distribution of particles at the output. The resulting distribution of particles can then be used to calculate a mean or variance, or whatever other statistical measure is required. The resulting statistics are used to generate the random sample of particles for the next iteration. However, this method also has some problems that restrict the use. This method requires large computational operations and face severe difficulties for real-time applications. On the other hand, this method is also not able to have suitable results in very low SNRs. In these SNRs, PF is not able to bring us to a reasonable particle, and even using Sampling Importance Re-sampling (SIR) method can not lead us to better results [Ristic et al., 2004]. In SIR method, a weighted set of particles is used. These new weighted particles can face and eliminate the noise more powerfully and present better estimation in low SNRs.

5.4 The proposed moment method

In this section, we are going to solve the problems we are faced in PF. This is done based on the time delay and Doppler estimated in the previous section. Three sensors are used. They are located on the vertices of an equilateral triangle. One of the sensors is a transmitter and receiver, the other two sensors only serve as the receiver. The arrangement of the sensors and their positions relative to the target is depicted in figure (2). The target is in the far field of the sensors.

A signal is emitted from the first sensor to the target. When this signal comes into contact with the target, generally speaking, it is scattered in many directions. The signal is thus partly reflected back, hence, all three sensors receive this reflected signal. According to the earlier discussions, the time delay and Doppler of the received signal in each sensor could be estimated.

First, the target position is determined. Suppose the time interval between sending the signal from the transmitter and receiving it in each sensor is shown by T_i for $i = 1, 2, 3$, which i denotes the sensor number. We also use R_i as the distance between the target and the i -th receiver. Since the transmitter is beside the first receiver, we have:

$$R_1 = \frac{1}{2} T_1 \times C_e, \quad (25)$$

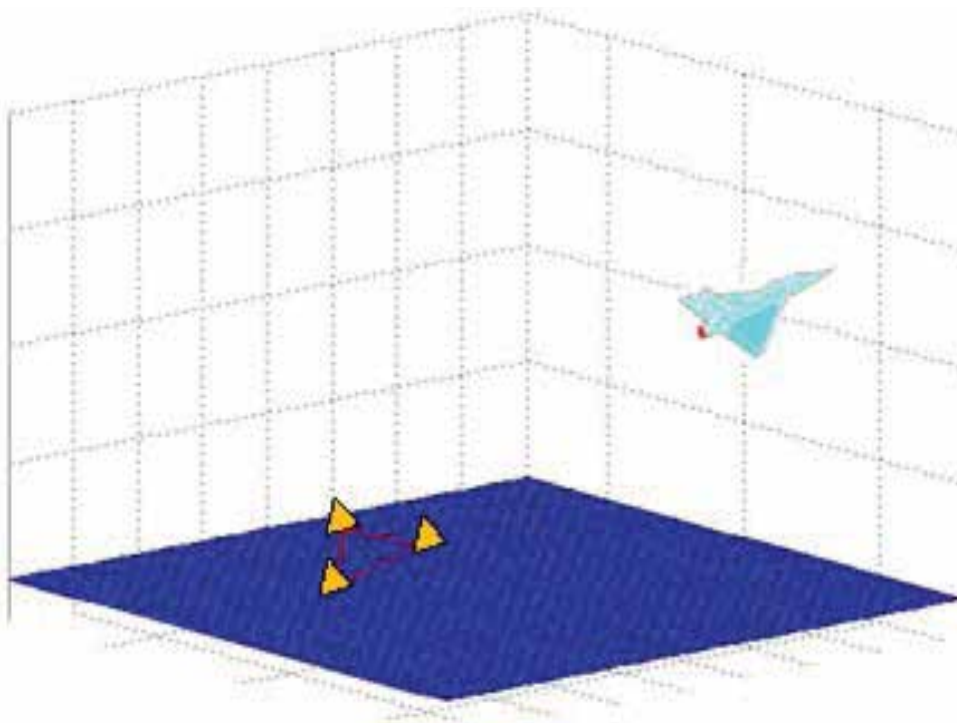


Fig. 2. The arrangement of the three sensors and their positions relative to the target

which C_e is the velocity of the emitted signal that is equal to the light speed. For two other receivers that are not near the transmitter, the distance is calculated as:

$$R_i = (T_i - \frac{T_1}{2}) \times C_e, \quad i = 2, 3. \quad (26)$$

Each sensor provides the locus of the target on a sphere of radius R_i centered at that sensor. As mentioned before, these sensors are located on the vertices of an equilateral triangle.

It can be shown mathematically that the intersection of these three spheres is at two points. To prove this, the equations for the three spheres are considered, and then the intersection of them is obtained. Without losing the generality, we assume that the three points where the sensors are located in, are showed by A, B and C. The points are respectively in $(x_0, 0, 0)$, $(-x_0, 0, 0)$ and $(0, y_0, 0)$ in Cartesian coordinates and are showed in figure (3).

At first, the equations of two spheres with centers A and B and radii R_1 and R_2 are obtained:

$$\begin{aligned} (x - x_0)^2 + y^2 + z^2 &= R_1^2, \\ (x + x_0)^2 + y^2 + z^2 &= R_2^2. \end{aligned} \quad (27)$$

The first equation is subtracted from the second one:

$$\begin{aligned} 2xx_0 - (-2xx_0) &= R_2^2 - R_1^2 \Rightarrow \\ 4xx_0 &= R_2^2 - R_1^2 \Rightarrow x = \frac{R_2^2 - R_1^2}{4x_0}. \end{aligned} \quad (28)$$

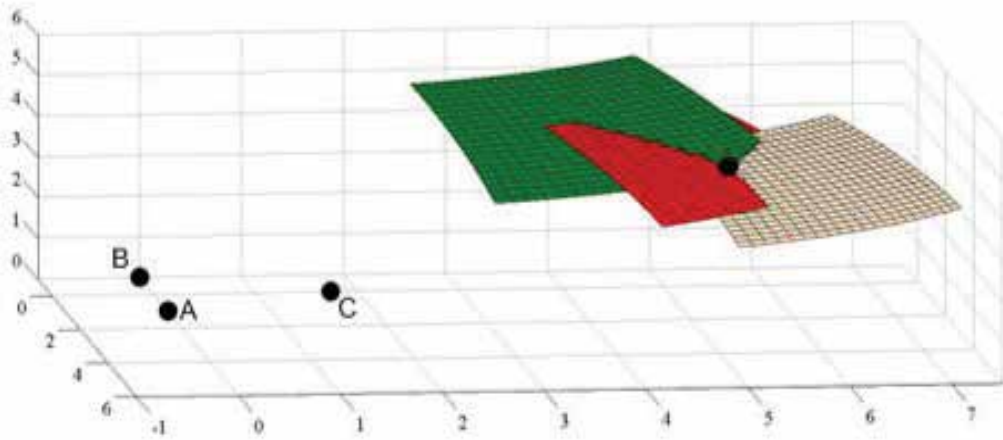


Fig. 3. The position of the three sensors and the intersection of three spheres related to the sensors

Now, the obtained value x is put in the one of the equations (27). We select the first one:

$$\left(\frac{R_2^2 - R_1^2}{4x_0} - x_0 \right)^2 + y^2 + z^2 = R_1^2 \Rightarrow$$

$$y^2 + z^2 = R_1^2 - \left(\frac{R_2^2 - R_1^2}{4x_0} - x_0 \right)^2. \quad (29)$$

For convenience, the right side of the second equality of (29) is showed by R_{cir}^2 . Thus, the intersection of the two spheres is a circle with the following equation:

$$y^2 + z^2 = R_{cir}^2, \quad (30)$$

Which is located in the plane $x = \frac{R_2^2 - R_1^2}{4x_0}$.

Then the intersection of this circle and the third sphere should be obtained. The third sphere has the center C and radius R_3 . So its equation is:

$$x^2 + (y - y_0)^2 + z^2 = R_3^2. \quad (31)$$

The left side of the equation (31) is extended, and the circle equation is used in it:

$$\begin{aligned} x^2 + (y - y_0)^2 + z^2 &= -2yy_0 + y_0^2 + x^2 + y^2 + z^2 \\ &= -2yy_0 + y_0^2 + \left(\frac{R_2^2 - R_1^2}{4x_0} \right)^2 + R_{cir}^2 \Rightarrow \\ y &= \frac{y_0^2 + \left(\frac{R_2^2 - R_1^2}{4x_0} \right)^2 + R_{cir}^2}{2y_0}. \end{aligned} \quad (32)$$

So, x and y coordinates of the intersection point is:

$$\begin{aligned} x &= \frac{R_2^2 - R_1^2}{4x_0} \\ y &= \frac{y_0^2 + \left(\frac{R_2^2 - R_1^2}{4x_0}\right)^2 + R_{cir}^2}{2y_0}. \end{aligned} \quad (33)$$

Using this two values and the equation (31), the third coordinates is also calculated:

$$z = \pm \sqrt{R_3^2 - \left(\frac{R_2^2 - R_1^2}{4x_0}\right)^2 - \left(\frac{y_0^2 + \left(\frac{R_2^2 - R_1^2}{4x_0}\right)^2 + R_{cir}^2}{2y_0} - y_0\right)^2}. \quad (34)$$

As mentioned, this intersection contains only two points which are located in the two sides of the plane xy and in front of each other. But in reality, only one of these points has a positive height and coincides with the coordinate of a target in sky.

After this proof, we continue our discussion about the tracking. On the one hand, the target position is achievable by using R_i s, and on the other hand, the equations (25) and (26) inform about the relation between R_i s and T_i s. Therefore, the target position can be determined if T_i is known. For calculating this parameter, it should be considered as the signal's time delay to reach to the i -th receiver. Let's assume the first sensor in the section (IV), is the transmitter now, and the second sensor in there is one of the three receivers in here. By using the proposed moment method three times, the time delay can be estimated for all the three receivers. T_i is denoted as the estimated time delay for i -th receiver. Now, all unknowns are obtained, so the position is easily predicted.

Finally, the target velocity should be obtained. The receivers compute three values for Doppler, $\hat{\epsilon}_i$, by the proposed moment technique. Since the transmitter and the first receiver are at the same sensor, the velocity component along the connecting line between the target and the first sensor is:

$$v_1 = \frac{d}{dt} \|\mathbf{R}_1\| = \frac{C}{2f_t} \hat{\epsilon}_1, \quad (35)$$

where $\|\cdot\|$ represents Euclidean norm, and \mathbf{R}_1 is the vector connecting the first sensor to the target. C is the speed of light and f_t is the frequency of the emitted signal. Using v_1 , we determine the velocity components along the connecting line between the target and two other sensors (receivers):

$$v_i = \frac{C}{f_t} \hat{\epsilon}_i - v_1, \quad i = 2, 3. \quad (36)$$

In the next section, there are results that compare the different methods available for estimating the time delay and Doppler. There are also some results about tracking a target which has a nonlinear motion. In the parameter estimation results, the proposed moment method is compared with the methods Wigner-Ville (WV), fractional lower order ambiguity function (FLOAF) and wavelet, and in the tracking part, there is a comparison between the proposed method and EKF and PF ones.

6. The results

To prove the procedures were presented in this Chapter, several different tests have been conducted. The results are divided into two categories. At first, the proposed method for estimating the joint time delay and Doppler is examined and compared with other conventional methods. Then, the efficiency of this method in the tracking of the maneuver target is also investigated.

6.1 Parameter estimation results

To estimate the time delay and Doppler parameters, the following assumptions are considered:

- The transmitted desired signal follows a trimodal Gaussian mixture distribution presented in equation (6) with the following mean and standard deviation related to the three modes:
 $\sigma_{s_1} = \sigma_{s_2} = \sigma_{s_3} = 1,$
 $\mu_{s_1} = 2, \mu_{s_2} = 5, \mu_{s_3} = 8,$

And the probability distribution of the modes is considered as below:

$$p_1 = 0.3, p_2 = 0.3, p_3 = 0.4 .$$

- The observation time of the signal is considered 1 millisecond.
- The time delay can be within the observation time of the signal, and in here, it is assumed 300 microseconds.
- Doppler value, $\omega_\varepsilon = 2\pi\varepsilon$, is a number between 0 and 2π that provides a 2π rotation for the frequency shift. Now, Doppler is assumed 0.8π .

The test is done for different SNR values from -10dB to +10dB, and for each SNR, the operation is performed 1000 times. The figure (4) depicts the error existed in the estimation of the time delay for the conventional methods and the proposed moment one. This error is depicted as MSE, calculated from 1000 times of simulation implementation, versus SNR. We have used normalized MSE in our results:

$$MSE(\hat{\tau}) = E \left[\left(\frac{\hat{\tau} - \tau}{\tau} \right)^2 \right], \quad (37)$$

where τ is the actual time delay, and $\hat{\tau}$ is the estimated value of this parameter. The conventional methods are WV [Chassande-Mottin & Pai, 2005], wavelet method [Niu et al., 1999] and FLOAF [Ma & Nikias, 1996].

As shown in Figure (4), all methods are convincing in high SNRs, but in low SNRs, especially negative ones, WV and FLOAF methods are completely unable to estimate the time delay. Wavelet method also has relatively unsuitable results, so that it presents very little reduction in MSE value from SNR=-10dB to SNR=0dB. But the moment method in the both high and low SNRs provides precise answers.

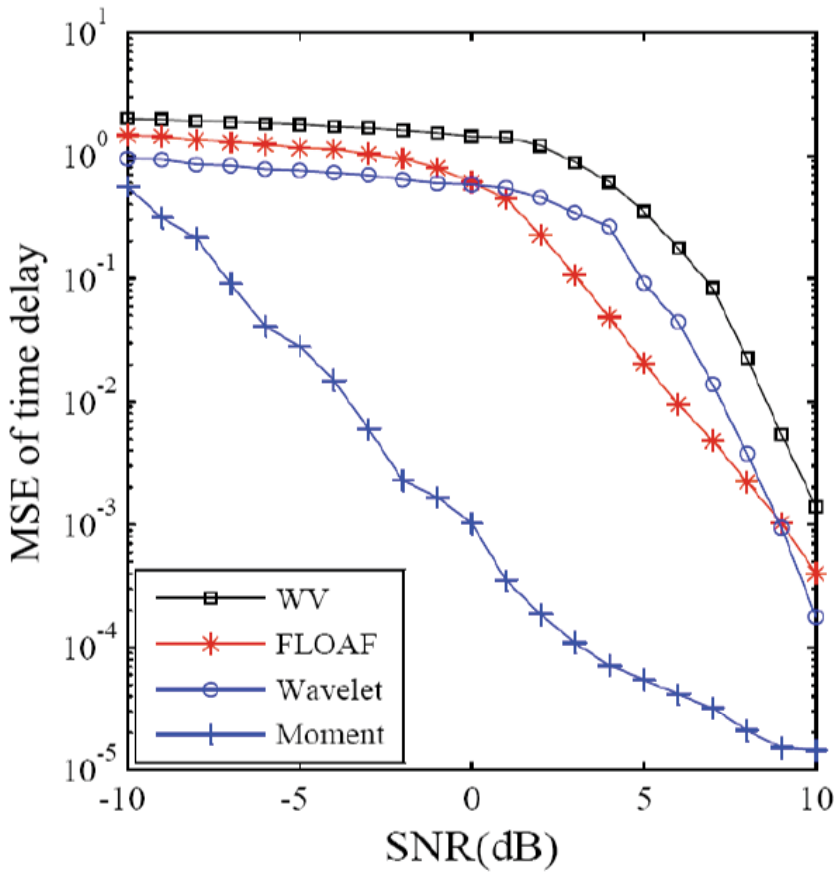


Fig. 4. MSE of estimated time delay in the conventional and proposed methods.

There is a similar observation for Doppler that is showed in figure (5). The error is also as MSE versus SNR. In this figure, the conventional methods are WV [Chassande-Mottin & Pai, 2005] and FLOAF [Ma & Nikias, 1996].

As portrayed in figure (5), WV offers very good results in high SNRs which is expectable. But in the low SNRs, the interaction terms are relatively large and this method fails. So in low SNRs, FLOAF presents more suitable results in comparison with WV. Again in this figure, the power of moment method is absolutely visible.

It is worth mentioning that the obtained results are in an unknown noise power scenario. The moment method also can estimate the noise power. It is important that in addition to parameter estimation, our method can also predict the noise power. This capability helps to recognize the noise environment, and ameliorates noise encountering. To judge the performance of the proposed moment method for estimating the unknown noise power, MSE between the actual and the estimated noise power is portrayed in figure (6). For instance, MSE is 10^{-5} in SNR 8. It means that in this SNR, we have an error between the actual noise power

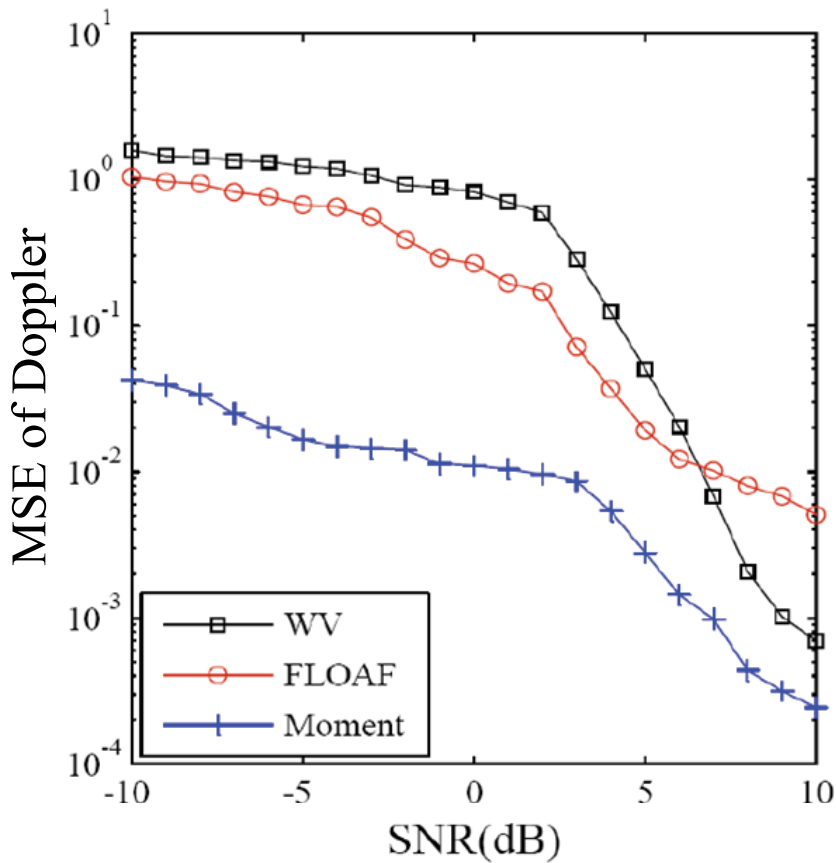


Fig. 5. MSE of estimated Doppler in the conventional and proposed methods.

and the value which our method has estimated for it, and the normalized mean square value of this error is equal to 10^{-5} .

6.2 Radar tracking results

In the following, radar tracking results are presented based on the time delay and Doppler estimations. The original frequency of the signal emitted from the radar, f_t , is considered 10GHz. A target is at cartesian coordinate $(10000m, 10000m, 10000m)$. It moves with the velocity $v_x = 10m/s, v_y = 10m/s$. In the first 25 sec, $v_z = -10$ m/s and in the following 75 sec, $v_z = +20$ m/s. At first, for SNR=+10dB, test is done for the non-recursive proposed moment method and two recursive conventional methods: EKF [Park & Lee, 2001] and PF [Jian et al., 2007]. The results have been traced for 100 epochs with one second interval and can be seen in figures (7) and (8) as MSE of the estimated position and velocity.

Two points are worth noting in this figures. EKF and PF methods are recursive, so the related curves are decreasing and at first, have not acceptable results. We need some time to have suitable results. In vital application like military, less needed time leads us to a better real-time system and gives the opportunity to react faster. So, a non-recursive method can be valuable.

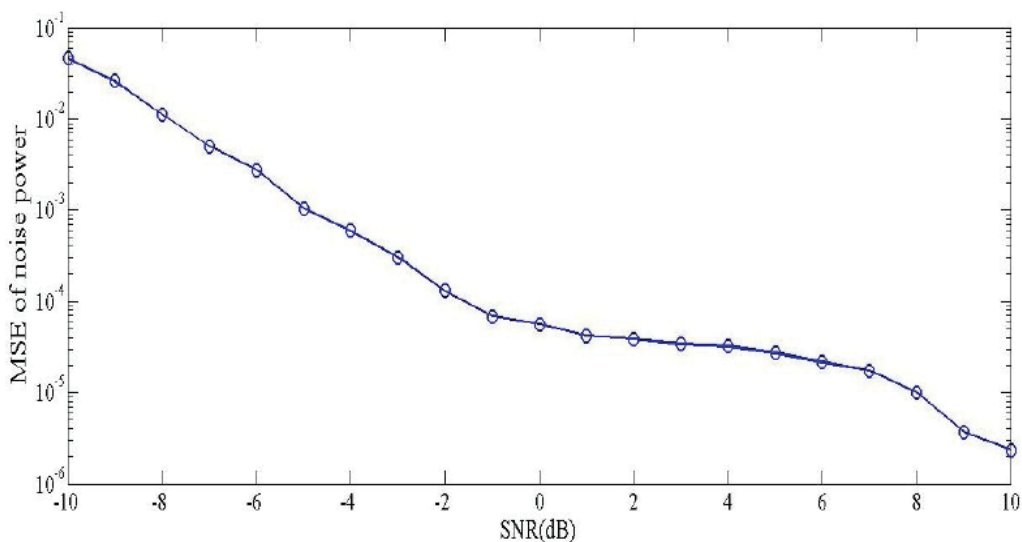


Fig. 6. MSE of estimated noise power in the proposed method

In addition to have a high precision, the moment method is non-recursive, trustable from the beginning, and provides a rapid reaction.

The second point in figures (7) and (8) is the existence of a bulge around the time 25 seconds, where the third component of the speed has changed and made a nonlinear motion. There is no bulge in the curves relating to the moment method, because in this method, the estimation at any time is independent from the other times, so it has no problem in nonlinear motions. In the figures we magnify the results around time 25 seconds and show them in linear scale to depict the bulge obviously. We cannot present all results together in linear scale, because moment results are too small in comparison with EKF and PF results.

To further examine the ability of the proposed method, the test is done at different SNRs. The results of this experiment is showed in figures (9) and (10). In the figures, MSE of the position and velocity estimation is portrayed for our moment method.

In figures (7) and (8), MSE is versus time , and SNR is constant and equal to +10dB. Thus the figures (7) and (8) show the superiority of the proposed method on the two other ones. But in figures (9) and (10), MSE is versus SNR. The power of moment method in the low SNR is quite satisfactory, while the other methods, the EKF and PF, either do not respond or provide answers that are not reliable.

Finally, a necessary point should be noted. We see that our method has much better results in comparison with other ones. The better results are not only because of using moments. Moment method helps us as a tool to encounter the undesired signals logically. In fact, in the first step, we recognize the environment more precisely by a suitable model of noise. Then after the modelling, although the noise is unknown, but the moments of its model are known and used for our estimations. So we can control the noise behaviour. This procedure cannot be found in other methods.

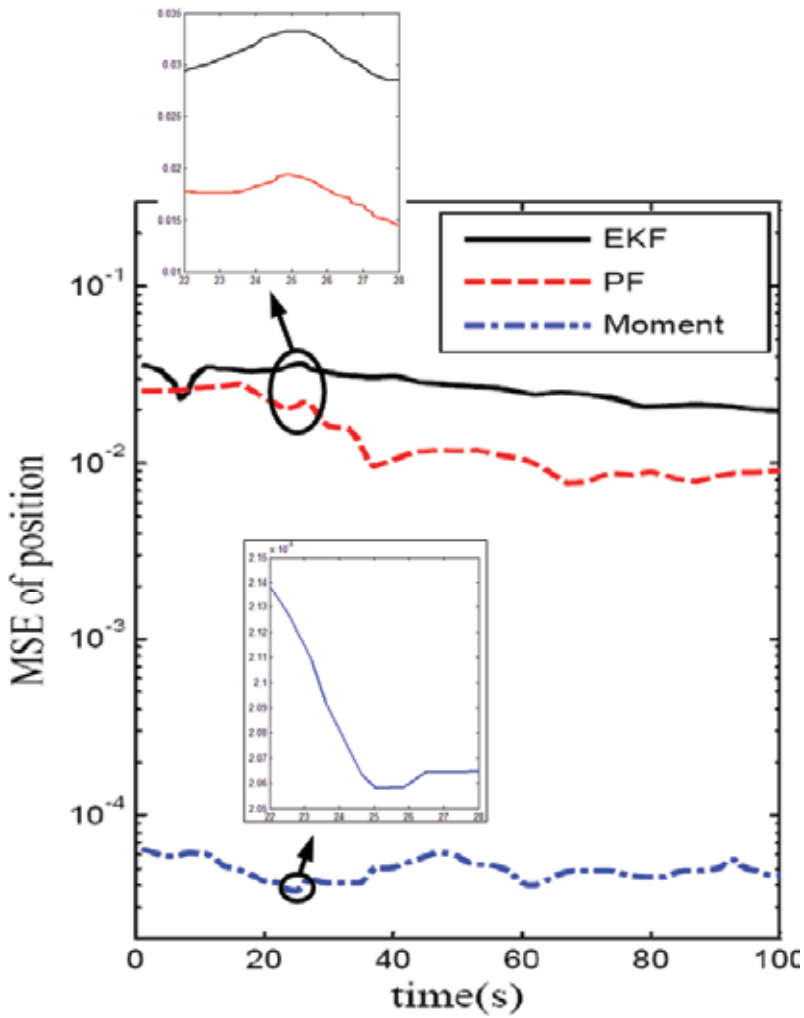


Fig. 7. MSE of estimated position in the conventional and proposed methods for SNR=+10 dB.

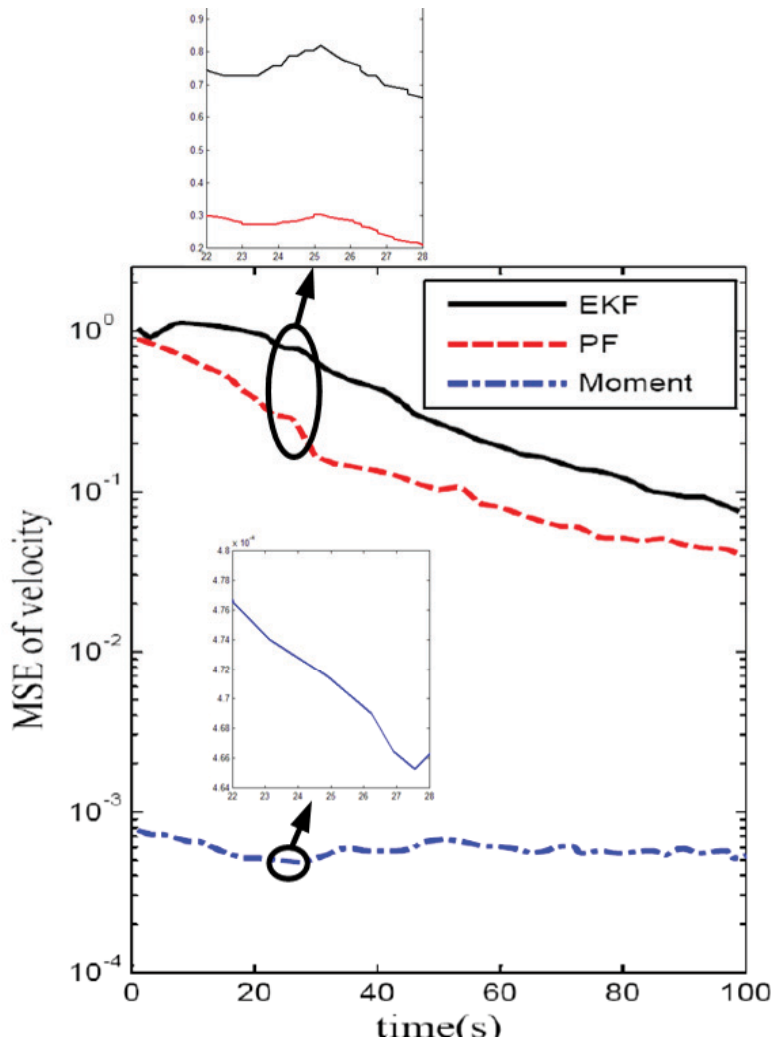


Fig. 8. MSE of estimated velocity in the conventional and proposed methods for SNR=+10 dB.

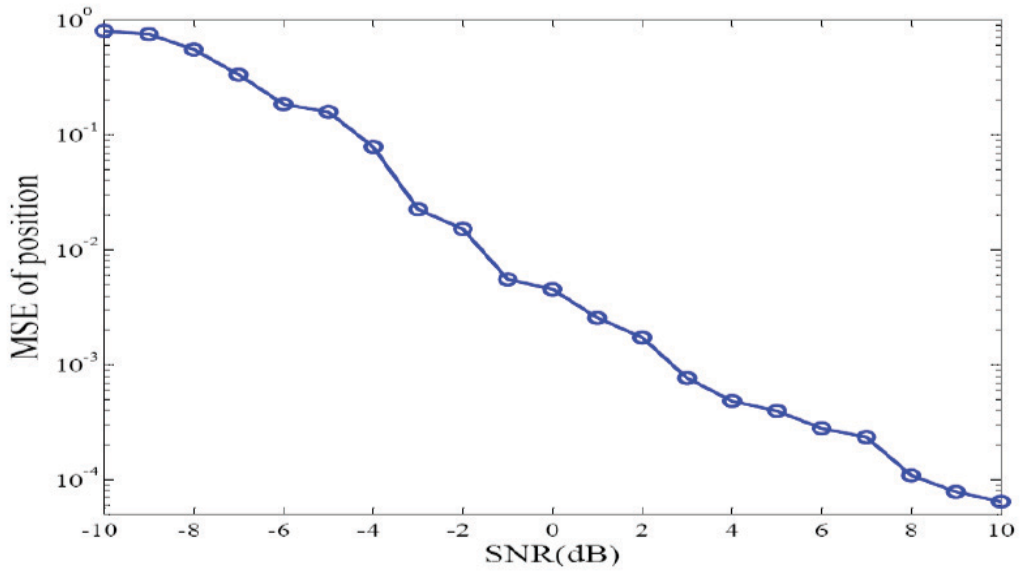


Fig. 9. MSE of estimated position in the proposed method.

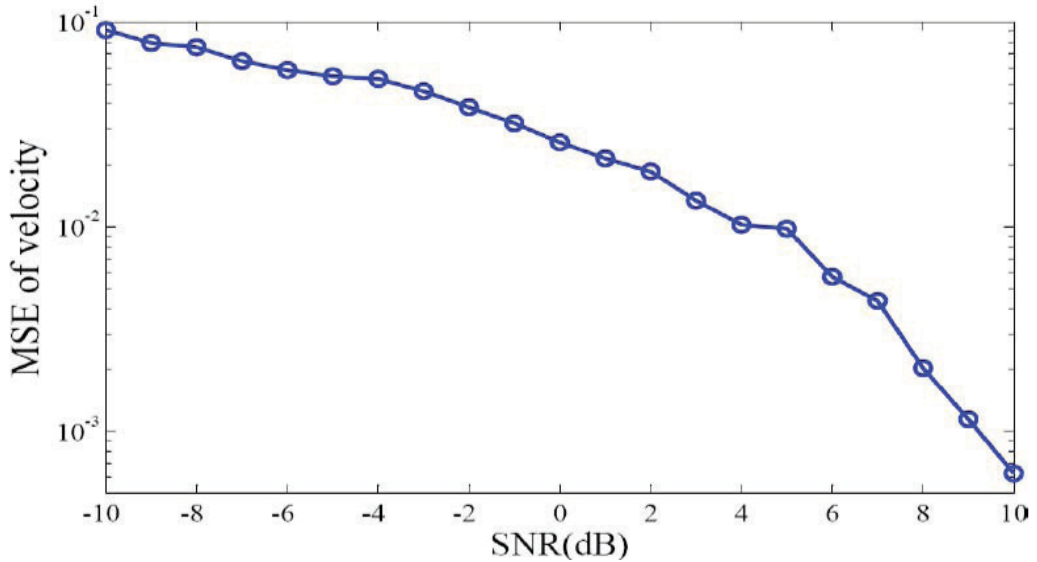


Fig. 10. MSE of estimated velocity in the proposed method.

7. Conclusion

In this chapter, we review different novel methods in joint time delay and Doppler estimation. Each of them has some advantages and disadvantages. The disadvantages are studied and we find a new method which can almost obviate the most of these disadvantages. The new method is based on moment. It exploits the time delay, Doppler, and noise effects exerted onto the moments of the received data. The insight on the moments of the received signal is the criteria for joint estimation of time delay and Doppler. Since the moments of the noise could be obtained, these moments can facilitate separating the main signal from the noise even in a severe noisy environment. So, our estimation in low SNR has suitable results. In addition, we do not encounter with undesirable cross-terms discussed in WV method. After introducing our estimation method, its application in Doppler radar is declared.

The estimated delay and Doppler are used in the target tracking and predicting the position and velocity of the target in a noisy background. So it is applicable in the radar trackers. Test results provide a plausibility of the both estimations and tracking. The estimated position and velocity are completely accurate even in very low SNRs. The tracking can be extended to multiple targets. Based on the features described for mono-target tracking, it is expected to have acceptable results in multiple targets tracking. Multi tracking in low SNRs is one of the most important roles of a Doppler radar which is reachable based on the presented method.

8. References

- [1] Bilik, I., Tabrikian, J., Cohen, A. (2006). "GMM-based target classification for ground surveillance Doppler radar," *IEEE Trans. on Aerospace and Electronic Systems*, vol. 42, no. 1, January.
- [2] Bouchereau, F., Brady, D. (2008). "Method-of-moments parameter estimation for compound fading processes," *IEEE Trans. Comm.*, vol. 56, no. 2, pp. 166-172.
- [3] Chassande-Mottin, E., Pai, A. (2005). "Discrete time and frequency Wigner-Ville distribution: Moyal's formula and aliasing," *IEEE Signal Processing Letters*, vol. 12, no. 7, pp. 508-511, July.
- [4] Fukunaga, K., Flick, T. E. (1983). "Estimation of the parameters of a Gaussian mixture using the method of moments," *IEEE Trans. Pattern Analysis and Machine Intelligence*, vol. pami-5, no. 4, pp. 410-416, July.
- [5] Gaeddert, J., Annamalai, A. (2005). "Some remarks on Nakagami-m parameter estimation using method of moments," *IEEE Comm. Letters*, vol. 9, no. 4, pp. 313-315.
- [6] Greenstein, L. J., Michelson, D. G., Erceg, V. (1999). "Moment-method estimation of the Ricean K-factor," *IEEE Comm. Letters*, vol. 3, no. 6, pp. 175-176.
- [7] Isaksson, A. J., Horch, A., Dumont, G. A. (2001). "Event-triggered deadtime estimation from closed-loop data," *In Proc. American Control Conf.*, Arlington, VA, USA, June.
- [8] Jian, W., Yonggao, J., Dingzhang, D., Huachun, D., Taifan, Q. (2007). "Particle filter initialization in non-linear non-Gaussian radar target tracking," *Journal of Systems Engineering and Electronics*, vol. 18, no. 3, pp. 491-496.
- [9] Ma, X., Nikias, C. L. (1996). "Joint estimation of time delay and frequency delay in impulsive noise," *IEEE Trans. Signal Processing*, vol. 44, pp. 2669-2687, November.
- [10] Niu, X., Ching, P., Chan, Y. (1999). "Wavelet based approach for joint time delay and Doppler stretch measurements," *IEEE Trans. on Aerospace and Electronic Systems*, vol. 35, no. 3, pp. 1111-1119.

- [11] Orr, R. S., Morris, J. M., Qian, S. E. (1992). "Use of the Gabor representation for Wigner distribution crossterm suppression," *ICASSP-92*, vol.5, pp. 29-31, March.
- [12] Park, S. T., Lee, J. G. (2001). "Improved Kalman filter design for three-dimensional radar tracking," *IEEE Trans. on Aerospace and Electronic Systems*, vol. 37, no. 2, pp. 727-739, April.
- [13] Ristic, B., Arulampalam, S., Gordon, N. (2004). "Beyond the Kalman Filter: Particle filters for tracking applications," *Artech House*.
- [14] Tan, J. L., Sha'ameri, A. Z. B. (2008). "Adaptive optimal kernel smooth-windowed wigner-ville for digital communication signal," *EURASIP Journal on Advances in Signal Processing*.
- [15] Zabin, S. M., Wright, G. A. (1994). "Nonparametric density estimation and detection in impulsive interference channels. I. Estimators," *IEEE Trans. on Communications*, vol. 42, no. 2/3/4, pp. 1684-1697, February/March/April.

Edited by Joan Bech and Jorge Luis Chau

Doppler radar systems have been instrumental to improve our understanding and monitoring capabilities of phenomena taking place in the low, middle, and upper atmosphere. Weather radars, wind profilers, and incoherent and coherent scatter radars implementing Doppler techniques are now used routinely both in research and operational applications by scientists and practitioners. This book brings together a collection of eighteen essays by international leading authors devoted to different applications of ground based Doppler radars. Topics covered include, among others, severe weather surveillance, precipitation estimation and nowcasting, wind and turbulence retrievals, ionospheric radar and volcanological applications of Doppler radar. The book is ideally suited for graduate students looking for an introduction to the field or professionals intending to refresh or update their knowledge on Doppler radar applications.

Photo by eugeneseergeev / iStock

IntechOpen

